The Warm ISM in the Sgr A Complex: Mid-J CO, Atomic Carbon, Ionized Atomic Carbon, and Ionized Nitrogen Line Observations with the Herschel-HIFI and the NANTEN2/SMART Telescopes

Inaugural-Dissertation
zur
Erlangung des Doktorgrades
der Mathematisch-Naturwissenschaftlichen Fakultät
der Universität zu Köln

vorgelegt von

Pablo García F.

aus Arica, Chile.

Berichterstatter:	Prof. Dr. Jürgen Stutzki (Universität zu Köln)
(Gutachter)	Prof. Dr. Simon Trebst (Universität zu Köln)

Tag der mündlichen Prüfung: 25.06.2015

To my Son and Mother.

"The amazing thing is that every atom in your body came from a star that exploded. And, the atoms in your left hand probably came from a different star than your right hand. It really is the most poetic thing I know about physics: You are all stardust. You couldn't be here if stars hadn't exploded, because the elements - the carbon, nitrogen, oxygen, iron, all the things that matter for evolution - weren't created at the beginning of time. They were created in the nuclear furnaces of stars, and the only way they could get into your body is if those stars were kind enough to explode. So, forget Jesus. The stars died so that you could be here today."

L. Krauss, *A Universe From Nothing*

"Even the smallest person can change the course of the future."

J.R.R. Tolkien, *The Fellowship of the Ring*

Contents

Abstract

The interstellar medium (ISM) in the few central hundred parsecs of the Galaxy has physical properties that differ strongly from the rest of the ISM in the Galaxy. In the present work, large-scale submillimeter heterodyne observations towards the Sgr A Complex (located in the Galactic Center) covering $\sim$ 300 arcminutes^2, obtained in the frame of the Herschel EXtraGALactic Guaranteed Time key Program (HEXGAL) with the Herschel-HIFI satellite and complementary data with the NANTEN2/SMART telescope are presented. The observed species are: CO(J=4-3) at 461.0 GHz observed with the NANTEN2/SMART telescope, [CI] $^3P_1$ - $^3P_0$ at 492.2 GHz, [CI] $^3P_2$ - $^3P_1$ at 809.3 GHz, [NII] $^3P_1$ - $^3P_0$ at 1461.1 GHz, and [CII] $^2P_{3/2}$ - $^2P_{1/2}$ at 1900.5 GHz observed with the Herschel-HIFI satellite. The observations are presented in 1 kms^{-1} spectral resolution, and spatial resolutions ranging from 46 to 28 arcseconds. The frequency bandwidth of the three lower frequency lines largely allows to cover the emission found within $\pm$200 kms^{-1}, while in the two high frequency lines, the upper LSR velocity is limited to +94 kms^{-1} for the [NII] line due to baseline instabilities, and to +144 kms^{-1} for the [CII] line, due to the available spectrometer bandwidth. The spatial distribution of the emission in all lines is very widespread. The bulk of the carbon monoxide emission is found toward Galactic latitudes below the Galactic plane, and all major known molecular clouds are identified. Both neutral atomic carbon lines have their brightest emission associated with the +50 kms^{-1} cloud. Their spatial distribution at this LSR velocity describes a crescent-shape structure, which is probably the result of interaction with the energetic event (one or several supernovae explosions) that gave origin to the non thermal Sgr A-East source. The [CII] and [NII] emissions have most of their flux associated to the thermal Arched-Filaments and the H-Region, with also bright spots in [CII] emission towards the Central Nuclear Disk. Out of the large number of astronomical sources (Arched-Filaments, the H-Region, more than ten molecular clouds, the Circum Nuclear Disk, the Sickle H II region, gas streamers, high velocity gas, and high velocity compact clumps) detected in these datasets, the Arched-Filaments and the High Velocity Gas Clouds were selected for a preliminary analysis of their physical conditions, while future work related to the +50 kms^{-1} and +20 kms^{-1} Clouds is outlined.

Zusammenfassung

Das interstellare Medium (ISM) in den wenigen zentralen hundert Parsec der Milchstraße hat physikalische Eigenschaften, die stark unterschiedlich sind vom Rest des ISM in unserer Galaxis. In der vorliegenden Arbeit werden großräumige Submillimeter Heterodyn-Beobachtungen in Richtung des Sgr A Komplexes im Galaktischen Zentrum, die etwa 300 arcminutes^2 abdecken und im Rahmen von HEXGAL, dem Herschel EXtraGALactic Guarateed Time Program, mit dem Herschel-HIFI Satelliten gewonnen wurden, sowie komplementäre Daten vom NANTEN2/SMART Teleskop vorgestellt. Die beobachteten Übergänge sind: CO(J=4-3) bei 461.0 GHz, beobachtet mit dem NANTEN2/SMART Teleskop, [CI] $^3P_1$ - $^3P_0$ bei 492.2 GHz, [CI] $^3P_2$ - $^3P_1$ bei 809.3 GHz, [NII] $^3P_1$ - $^3P_0$ bei 1461.1 GHz und [CII] $^2P_{3/2}$ - $^2P_{1/2}$ bei 1900.5 GHz beobachtet mit dem Herschel-HIFI Satelliten. Die Beobachtungen werden mit 1 kms^{-1} spektraler Auflösung präsentiert, wobei die Winkelauflösung zwischen 46 und 28 Bogensekunden liegt. Die Frequenzbandbreite der drei Linien bei niedrigeren Frequenzen erlaubt es die Emission innerhalb ±200 kms^{-1} abzudecken, während für die beiden Linien bei hoher Frequenz die obere LSR-Geschwindigkeit auf +94 kms^{-1} für [NII] aus Gründen der Basislinien-Stabilität und auf +144 kms^{-1} für [CII] aus Gründen der verfügbaren Bandbreite der Spektrometer limitiert ist. Die räumliche Verteilung der Emission in allen Linien ist sehr weit ausgedehnt. Der Großteil der Emission von Kohlenstoffmonoxid befindet sich bei Galaktischen Breiten unterhalb der Galaktischen Ebene und alle wichtigen bekannten Molekülwolken werden identifiziert. Die hellsten Emissionen beider Linien des neutralen Kohlenstoffs sind mit der 50 kms^{-1} Wolke assoziiert. Ihre räumliche Verteilung bei dieser LSR-Geschwindigkeit beschreibt eine sichelförmige Struktur, die wahrscheinlich das Ergebnis von Wechselwirkung mit dem energiereichen Ereignis (eine oder mehrere Supernova-Explosionen) ist, das den Ursprung der nicht-thermischen Sgr A-East Quelle darstellt. Die Emission von [CII] und [NII] ist hauptsächlich assoziiert mit den thermalen Bogenfilamenten (Arched Filaments) und der H-Region, mit zusätzlichen hellen Stellen in Richtung der Zentralen Nuklearen Scheibe (Central Nuclear Disk). Aus den vielen astronomischen Quellen (Arched-Filaments, die H-Region, über zehn Molekülwolken, die Central Nuclear Disk, die Sichel (Sickle) H II Region, Gas-streamer, Hochgeschwindigkeits-Gas und kompakte Hochgeschwindigkeits-Klumpen), die in den Datensätzen detektiert wurden, wurden die Arched-Filaments und die Hochgeschwindigkeits-Gaswolken für eine vorläufige Analyse der physikalischen Bedingungen des Gases ausgewählt, während weitere zukünftige Arbeiten, die die +50 kms^{-1} und +20 kms^{-1} Wolken betreffen, umrissen werden.

Chapter 1

The Sgr A Region

The Galactic Center (GC[1]), located at 8.34 ± 0.16 kpc (Reid et al., 2014) from the Sun in the Sagittarius (Sgr[2]) constellation, is one of the most remarkable places in the Milky Way harboring an overwhelming variety of astronomical sources under extraordinary physical conditions. From larger to smaller scales, the region between Galactic longitude l = −1°.5 to 3°.5, and Galactic latitude range b = ± 0°.75, known as the Nuclear Bulge (Mezger et al., 1996), harbors five major giant molecular clouds (GMCs[3]): Sgr A, Sgr B, Sgr C, Sgr D, and Bania's Clump 2 (Oka et al., 1998; Bania, 1980; Stark & Bania, 1986). The densest GMCs within this region are located in the so called Central Molecular Zone (CMZ[4]), extending from l = −1°.0 to 1°.5, which contains all Sgr GMCs, and a massive black hole within Sgr A (Ghez et al., 2008; Gillessen et al., 2009).

1.1 The Central Molecular Zone

The CMZ has been observed in practically the entire electro-magnetic spectrum, from centimeter wavelengths (Yusef-Zadeh et al., 1984; Law et al., 2008), millimeter wavelengths in a large variety of molecules (Nagayama et al., 2007; Ott et al., 2014; Jones et al., 2013, 2012; Bally et al., 1987; Oka et al., 1998; Sawada et al., 2001; Oka et al., 2012, 2007), atomic, molecular, and dust observations in the sub-mm[5] range (Martin et al., 2004; Tanaka et al., 2011; Pierce-Price et al., 2000; Schuller et al., 2009; Bally et al., 2010), Far- and Mid-Infrared observations accessible only from space (Molinari et al., 2011; Stolovy et al., 2006), optical

[1] Galactic Center
[2] Sagittarius
[3] Giant Molecular Clouds
[4] Central Molecular Zone
[5] Sub-Millimeter

imaging (Figer et al., 2004) and, in the high energy range, from a few tenths of keV up to TeV (Watson et al., 1981; Sidoli et al., 2001; Hunter et al., 1997; Aharonian et al., 2006), spanning a wide range of spectral and spatial resolutions. The large amount of astronomical data have produced the following picture of the Nuclear Bulge:

1.1.1 Kinematics

The velocity field in the Nuclear Bulge is extremely complex, deviating strongly from the (average) circular motion of the gas in the Galactic disk orbiting around the Galactic Center as seen from CO(1-0) observations (Dame et al., 2001). Molecular and atomic emission is detected at "forbidden" LSR[6] velocities ranging from -200 kms^{-1} to $+200$ kms^{-1}. Nowadays, there is a relatively broad consensus that the overall observed LSR velocity field in the GC is the response of the gas to presence of a stellar (old population) bar potential with semi-major axis between 3.1 and 3.5 kpc, inclined between 15°- 30° measured from the Galactic Center toward positive Galactic longitudes, also referred to as the "thick bar" (Binney et al., 1991; Jenkins & Binney, 1994; Mezger et al., 1996; Oka et al., 1998), coexisting with another bar-like structure with inclination angle between 25°- 45° and semi-major axis of 4 kpc identified in ongoing star formation spots such as methanol masers, also referred to as the "thin bar" (Romero-Gómez et al., 2011; Green et al., 2011). The total gravitational potential at this scale is dominated by the stellar component since the stellar-to-gas mass ratio is ~ 0.01 (Güsten & Philipp, 2004). The orbits for a barred gravitational potential inside the co-rotation radius are divided into two families for the inner Lindblad resonances: the X_1 orbits along the semi-major axis of the stellar bar, and X_2 orbits which exist perpendicular to the semi-major axis of the bar, as seen in the schematic view of the GC in Figure 1.1, from the work of Bally et al. (2010). The gas flows from the outer X_1 orbits to the innermost X_2 orbits and then it is further transported to the inner 10 pc at which center a massive black hole (Sgr A*) of mass ~ $4{\times}10^6$ $M_\odot$ (Ghez et al., 2008; Gillessen et al., 2009) dominates the gravitational potential. Within and between the X_1 and X_2 orbits, there are several spots where cloud-cloud collisions are expected to occur. The X_1 orbits become self-interacting at their apocenter, and it is thought that the Bania's Clump 2 is transiting this part, as shown in Figure 1.1. At the pericenter of the X_1 orbits, the X_1 and X_2 orbits become very crowded, so that star forming burst-like regions such as Sgr B2 can occur (Tanaka et al., 2011; Etxaluze et al., 2013). In the region where the X_2 orbits are located, the gas seems to be arranged in a twisted ring-like structure as proposed by Molinari et al. (2011). Cloud-cloud collisions certainly contribute to the complex velocity field observed toward the GC region,

[6]Local Standard of Rest

as well as supernovae explosions that can inject large amounts of mechanical energy ($\sim 10^{40}$ erg s^{-1}) from their stellar winds (Crocker et al., 2010). Overall, the interpretation of the observed LSR velocity distribution at different positions in the CMZ is a challenging task.

1.1.2 Physical Conditions

The physical conditions of the molecular gas in the CMZ are very different from the physical conditions of gas in the Galactic disk. The total stellar, molecular, and atomic mas of the CMZ is $\sim 6{\times}10^9$ $M_\odot$, $\sim 5{\times}10^7$ $M_\odot$ ($\sim$ 10% of the total molecular mass in the Milky Way), and $\sim 3{\times}10^6$ $M_\odot$, respectively (Güsten & Philipp, 2004; Dahmen et al., 1998; Huettemeister et al., 1993, 1998; Nagayama et al., 2007), while individual GMCs have molecular masses $\geq 3{\times}10^6$ $M_\odot$ (Martin et al., 2004). The molecular mass distribution is not symmetric with respect to l = 0°, with about 3/4 of the gas at positive Galactic longitudes and LSR velocities (Mezger et al., 1996). Deriving molecular masses for GMCs in the GC from CO(1-0) observations is not a trivial task since the CO-to-H_2 conversion factor χ, which is defined as the proportionality factor between the CO(1-0) integrated line intensity W_{CO} and the column density of molecular hydrogen N_{H_2} (Dahmen et al., 1998, and references therein), used for GMCs in the Galactic plane (Hunter et al., 1997; García et al., 2014) can not be applied within the CMZ. The main reasons for this are: (1) the CO(1-0) emission is not optically thick everywhere, and (2) GMCs are far from virialization for a significant fraction of the gas, assumptions that have to be fulfilled in order to have a physical relationship between the CO(1-0) luminosity and the molecular mass (Dahmen et al., 1998; Oka et al., 2001). Given the very large LSR velocity widths ΔV(FWHM) of GMCs in this region ≥ 15 kms^{-1} (Güsten & Philipp, 2004; Huettemeister et al., 1993; Sawada et al., 2001), their virial masses are usually one order of magnitude larger than their molecular masses. The average volume density n(H_2) of GMCs in the CMZ is more than two orders of magnitude higher than typical values of GMCs in the Galactic disk (García et al., 2014), and is found to be $\geq 10^4$ cm^{-3} depending on the density tracer (Mezger et al., 1996; Oka et al., 2011, 1998; Martin et al., 2004; Oka et al., 2007), while the inter-cloud medium has typical values around $\sim 10^2$ cm^{-3}. Despite the large volume densities, the emission observed from different molecules has optical depths (τ) that vary from optically thin to moderately optically thick regions with typical values for ^{12}CO, CS, and NH_3 around $\tau_{^{12}CO} <$ 1 - 5, $\tau_{CS} \sim$ 2 - 3, $\tau_{NH_3} \sim$ 3 - 10 (Huettemeister et al., 1993, 1998; Dahmen et al., 1998; Oka et al., 1998; Sawada et al., 2001; Martin et al., 2004; Nagayama et al., 2007, and references therein). The dust has a very uniform temperature of $\sim$ 21 K derived from different continuum measurements, with less than 10% of the

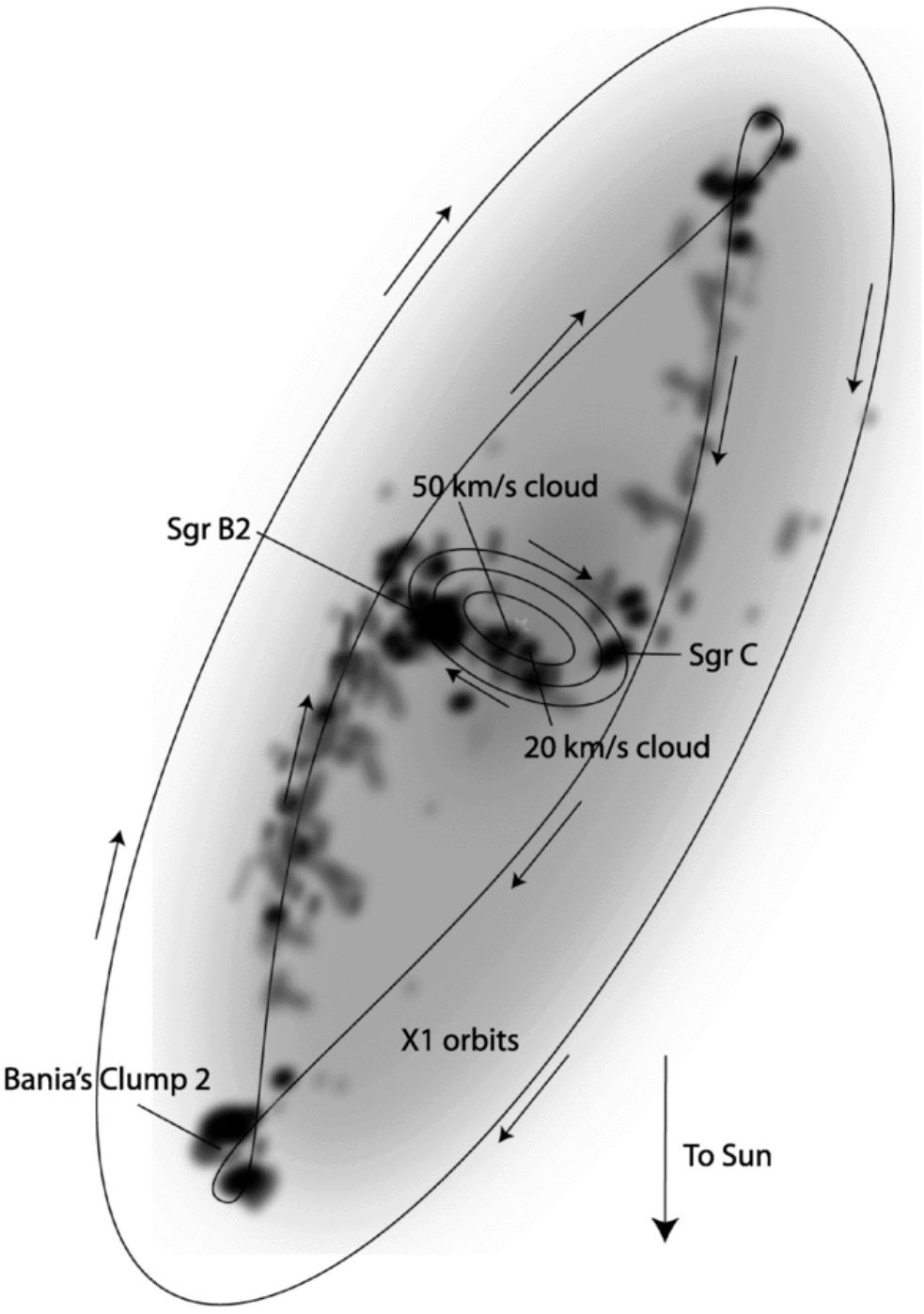

Figure. 1.1: *Schematic view of the X_1 and X_2 family orbits as shown in Bally et al. (2010), Figure 21.*

total FIR[7] luminosity coming from gas with temperatures > 29 K (Pierce-Price et al., 2000; Bally et al., 2010; Molinari et al., 2011). For the gas, warm and hot

[7]Far Infrared

gas coexists within the CMZ: the bulk of the gas is warm with relatively uniform kinetic temperature (T_{kin}) ranging from 30 K to 70 K (Güsten & Philipp, 2004; Oka et al., 2011; Ao et al., 2013; Nagayama et al., 2007; Ott et al., 2014), and a hot component with $T_{kin} > 80$ K up to 300 K (Oka et al., 1998; Huettemeister et al., 1993, 1998; Riquelme et al., 2013). Both dust and gas components are immersed in a pervasive thermal plasma of electron temperature $T_e \leq 7000$ K (Mezger et al., 1996), while a much hotter plasma with $T_e \sim 10^8$ K has also been observed within the central ±80 pc, whose origin has been suggested to be several supernovae or a single hypernova explosion occurred $\sim 10^4$ years ago (Mezger et al., 1996; Oka et al., 2007; Lau et al., 2015, and references therein). The Galactic magnetic field reaches its highest values in the Nuclear Bulge. Crocker et al. (2010) found a lower limit ≥ 50 μG, while values above 1 mG are not unusual (Mezger et al., 1996; Han, 2013). These values a several times the ones found in the Galactic disk (Güsten & Philipp, 2004). Under these extreme physical conditions, GMCs seem not to be gravitationally bound but rather in pressure equilibrium with the hot gas external pressure (Oka et al., 1998, 2001).

1.2 The Sgr A Complex

From all GMCs in the CMZ, the Sgr A Complex is the one containing the dynamical center of the Milky Way. The bolometric luminosity of the central parsec in the GC is $\sim 10^8$ $L_\odot$ and accounts for $\sim 0.3\%$ of the bolometric luminosity of the Galaxy. Given this low luminosity, it is thought that the Milky Way would resemble a "weak Seyfert Galaxy" as when seen from a distance of 700 kpc, with an angular resolution of 0.05" (Mezger et al., 1996). Understanding the physical conditions and dynamics of the Sgr A Complex is crucial to understand unresolved CMZ in other Galaxies.

The Sgr A Complex, extending ~ 100 pc around Sgr A*, contains a large diversity of astronomical sources confined in a small volume, whose emission can be detected across the entire spectral domain. Table 1.1 summarizes many of theses sources for which their name (first column), approximated position or extent (from the second to the fifth column), LSR velocity (sixth column), ΔV(FWHM) when available (seventh column), and the observations from which all parameters were obtained (eighth column), are shown. Some of the sources in Table 1.1 are: the non thermal shell Sgr A-East and the H II region Sgr A-West (Yusef-Zadeh & Morris, 1987a), the Central Nuclear Disk (CND[8]) (Requena-Torres et al., 2012), the Radio-Arc and several Non Thermal Filaments (NTFs[9]) running

[8] Circum Nuclear Disk
[9] Non Thermal Filaments

perpendicular to the Galactic plane and possible associated with the poloidal structure of the magnetic field in this region (Yusef-Zadeh & Morris, 1987b; Lang et al., 1999b, 2010), the Arched Thermal Filaments (Serabyn & Guesten, 1987; Lang et al., 2002), the H-Region containing several H II regions (Lang et al., 2001; Yusef-Zadeh & Morris, 1987a; Zhao et al., 1993), the Sickle H II region and Pistol star (Yusef-Zadeh & Morris, 1987b; Timmermann et al., 1996; Lang et al., 1997), the three massive Quintuplet, Arches, and Nuclear star clusters (Cotera et al., 1996; Lang et al., 1999a; Chatzopoulos et al., 2015), several Molecular Clouds (MCs[10]) such as the -30 kms^{-1}, $+20$ kms^{-1}, $+50$ kms^{-1} among others (Güsten et al., 1981; Serabyn & Guesten, 1987; Zhao et al., 1993), water and methanol masers (Caswell et al., 2010, 2011), X-ray point-like sources such as 1E-1743.1-2843B (Porquet et al., 2003), and High Velocity Compact Clumps (HVCCs[11]) (Oka et al., 2008). Along the same l.o.s.[12] but outside this region, gas at high LSR velocities associated to X_1 orbits and absorption features at LSR velocities -55 kms^{-1}, -30 kms^{-1}, and -5 kms^{-1} associated with the loci of the 3 kpc, 4.5 kpc, and local arms (Oka et al., 1998; Jones et al., 2012, Luna et al., in preparation) are found. At these Galactic longitudes, the foreground spiral arms are characterized by small ($\Delta V \leq 5$ kms^{-1}) velocity widths.

In Figures 1.2 and 1.3, the sources in Table 1.1 are shown on 20 cm VLA[13] continuum emission (Lang et al., 2010) and on the Mopra N_2H^+(1-0) integrated intensity map (Jones et al., 2012), respectively. In Figure 1.2, all point-like sources, and extended structures better traced by the continuum emission are shown. The diagonal solid line represents the Galactic plane at b = 0°. The dotted line, enclosing a large fraction of the map, represents the area covered by the observations in the present work. In Figure 1.3, the MCs traced by the molecular emission and the extent of the CND are shown. The complexity of the region is evident from both figures. The molecular masses ($\sim 10^5$ $M_\odot$) and volume densities ($\sim 10^4$ cm^{-3}) of the $+20$ kms^{-1} and $+50$ kms^{-1} clouds are similar, being the $+20$ kms^{-1} cloud the most massive cloud in the Sgr A Complex, sharing also a similar chemistry. The latter is not the case for the so called HCO^+ clouds (around the positions of M+0.11−0.08 and M+0.07−0.08), where an enhancement of HCO^+ emission is seen, revealing a somewhat different chemistry (Minh et al., 2005). The lack of auto-absorptions in the 86 GHz and 110 GHz bands indicates that the optical depth in the Sgr A Complex must be lower than in the Sgr B2 cloud (Minh et al., 1992).

The position of the different clouds along the l.o.s. is still a matter of debate. The $+20$ kms^{-1} and $+50$ kms^{-1} clouds were identified by Ho et al. (1991) to

[10]Molecular Cloudss
[11]High Velocity Compact Clumps
[12]line-of-sight
[13]Very Large Array

Source	Equatorial Coordinates (2000)				V_{lsr}	ΔV_{lsr}	Obs.
	R.A. ($^h\ ^m\ ^s$)	DEC. ($^\circ\ '\ ''$)	R.A. ($^h\ ^m\ ^s$)	DEC. ($^\circ\ '\ ''$)	(kms^{-1})	(kms^{-1})	
H II Regions, Masers, Shell Structures, X-ray sources, Stars, and Star Clusters							
Sgr A*	17 45 39.9	−29 00 28.1	...	...	...	...	20,6 cm[16]
Sgr A-West	17 45 39.4	−29 00 24.0	...	...	...	...	20,6 cm[16]
Sgr A-East	17 45 47.0	−29 00 12.0	...	...	...	...	20,6 cm[16]
A	17 45 52.1	−28 59 27.2	...	...	...	...	20,6 cm[16]
B	17 45 52.2	−28 59 38.1	...	...	...	...	20,6 cm[16]
C1	17 45 52.6	−28 59 58.4	...	...	...	...	20,6 cm[16]
C2	17 45 52.2	−29 00 04.8	...	...	...	...	20,6 cm[16]
D	17 45 51.6	−29 00 22.2	...	...	...	...	20,6 cm[16]
E	17 45 40.8	−29 04 32.7	...	...	...	...	20,6 cm[16]
F	17 45 38.1	−29 03 29.5	...	...	...	...	20,6 cm[16]
G	17 45 38.3	−29 05 42.8	...	...	...	...	20,6 cm[16]
I1	17 45 41.7	−28 58 16.0	...	...	...	...	20,6 cm[16]
I2	17 45 41.4	−28 58 26.5	...	...	...	...	20,6 cm[16]
I3	17 45 53.8	−28 58 04.5	...	...	...	...	20,6 cm[16]
M	17 45 36.6	−29 00 37.7	...	...	...	...	20,6 cm[16]
M1(H_2O) maser	17 45 36.4	−29 05 50.0	...	...	13.0	10.0	22 GHz[2]
M2(H_2O) maser	17 45 37.9	−29 05 45.0	...	...	−19.0	10.0	22 GHz[2]
M3(H_2O) maser	17 45 37.5	−29 03 50.1	...	...	28.0	30.0	22 GHz[2]
M4(H_2O) maser	17 46 01.9	−29 03 58.7	...	...	−19.0	−10.0	22 GHz[2]
M(CH_3OH) maser	17 46 07.6	−28 45 20.9	...	...	41.0	50.5	6.7 GHz[1]
H1(HII)	17 45 32.1	−28 56 12.7	...	...	−39.0	42.0	H110α[16,18]

H2(HII)	17 45 28.6	−28 56 03.8	...	...	−58.0	48.0	H110α[16,18]
H3(HII)	17 45 29.9	−28 54 36.6	...	...	−42.0	38.0	H110α[16,18]
H4(HII)	17 45 33.4	−28 54 07.8	...	...	−31.0	42.0	H92α[16,18]
H5(HII)	17 45 38.5	−28 53 27.7	...	...	−36.0	46.0	H110α[16,18]
H6(HII)	17 45 38.5	−28 53 07.9	...	...	...	...	20,6 cm[16]
H7(HII)	17 45 35.1	−28 53 34.4	...	...	...	...	20,6 cm[16]
H8(HII)	17 45 37.7	−28 57 34.3	...	...	...	...	20,6 cm[16]
H9(HII)	17 45 37.6	−28 52 42.0	...	...	...	...	6,3.6 cm[8]
H10(HII)	17 45 37.8	−28 52 34.0	...	...	...	...	6,3.6 cm[8]
H11(HII)	17 45 38.8	−28 52 31.0	...	...	...	...	6,3.6 cm[8]
H12(HII)	17 45 43.7	−28 52 26.0	...	...	...	...	6,3.6 cm[8]
H13(HII)	17 45 43.9	−28 51 33.0	...	...	...	...	6,3.6 cm[8]
G0.12+0.02(Arches-Cluster)	17 45 50.5	−28 49 27.8	...	...	...	...	H(1.6μm), K'(2.1μm)[3]
G0.07+0.04	17 45 37.8	−28 51 20.1	...	...	−25.0	50.0	CS(2-1)[7,9]
G0.10+0.02(Banana)	17 45 46.8	−28 50 25.4	...	...	−25.0	60.0	[OIII] 88 μm[15]
AFGL2004(Quintuplet)	17 46 13.9	−28 49 48.0	...	...	...	...	6,3.6 cm GHz[6]
G0.15−0.05(Pistol-Star)	17 46 15.3	−28 50 04.0	...	...	111.0	55.9	H92α[5,17]
G0.18−0.04(Sickle)	17 46 12.2	−28 48 11.9	...	...	40.0	52.0	[OI] 63 μm[5,15,17]
1E_1743.1-2843B	17 46 21.0	−28 43 44.0	...	...	...	...	2-10 keV[10,12]
Large Scale Filamentary Structures							
Northern-Thread	17 45 36.0	−28 51 15.0	17 45 11.0	−28 46 25.0	-	-	20,6,3.6,2 cm[7]
Southern-Thread	17 45 26.0	−28 56 55.0	17 45 10.0	−28 54 32.0	-	-	20,6,3.6,2 cm[7]
E1-Filament	17 45 54.0	−28 47 09.0	17 45 47.0	−28 49 39.0	−25.0	50.0	CS(2-1)[1,9,14]
E2-Filament	17 45 47.0	−28 46 09.0	17 45 42.0	−28 49 39.0	−25.0	50.0	CS(2-1)[1,9,14]
W1-Filament	17 45 33.0	−28 47 10.0	17 45 35.0	−28 50 40.0	−25.0	50.0	CS(2-1)[1,9,14]

W1-Filament	17 45 31.0	−28 48 10.0	17 45 30.0	−28 50 10.0	−25.0	50.0	CS(2-1)[1,9,14]
Radio-Arc	17 46 29.8	−28 51 39.0	17 45 49.5	−28 45 20.0	-	-	20,6 cm[1,10,17]
Molecular Clouds, High Velocity Clump, and Circum-Nuclear Disk							
Circum-Nuclear Disk (CND)	−50"(offset)	−50"(offset)	+50"(offset)	+50"(offset)	150.0	−150.0	CO(6-5)[13]
M1−0.13−0.08	17 45 37.7	−29 05 36.2	...	...	11.0	12.5	$NH_3(1,1)$[4]
M2−0.13−0.08(+20 kms^{-1} Cloud)	17 45 40.0	−29 04 45.0	...	...	17.0	12.5	$NH_3(1,1)$[4]
M−0.02−0.07(+50 kms^{-1} Cloud)	17 45 50.7	−28 59 22.9	...	...	50.0	15.0	$NH_3(1,1)$[4]
M+0.06−0.04	17 45 55.1	−28 54 20.8	...	...	48.0	12.5	$NH_3(1,1)$[4]
M+0.07−0.08	17 46 05.9	−28 55 05.0	...	...	51.0	15.0	$NH_3(1,1)$[4]
M+0.10−0.01	17 45 53.8	−28 51 21.6	...	...	52.0	12.5	$NH_3(1,1)$[4]
M+0.11−0.08	17 46 11.6	−28 53 02.0	...	...	53.0	15.0	$NH_3(1,1)$[4]
M+0.25+0.01	17 46 10.5	−28 43 03.0	...	...	30.0	15.0	$NH_3(1,1)$[4]
M+0.02−0.05(−15 kms^{-1} Cloud)	17 45 51.8	−28 56 42.5	...	...	−15.0	10.0	$NH_3(1,1)$[4]
M+0.04+0.03(−30 kms^{-1} Cloud)	17 45 35.9	−28 53 11.0	...	...	−30.0	10.0	CS(2-1), H92α, H110α[14,18]
CO+0.02−0.02	17 45 44.7	−28 55 46.3	...	...	110.0	100.0	CO(1-0), HCN(1-0)[11]

Table. 1.1: *Sources in the Sgr A Complex: The first column shows the source's name. From the second to the fifth columns, the position of each source is indicated. Columns sixth and seventh show the central radial velocity and velocity width. The last column shows the observed emission from which the parameters were derived. The upper indexes are: Caswell et al. (2010)[1], Caswell et al. (2011)[2], Cotera et al. (1996)[3], Güsten et al. (1981)[4], Lang et al. (1997)[5], Lang et al. (1999a)[6], Lang et al. (1999b)[7], Lang et al. (2001)[8], Lang et al. (2002)[9], Lang et al. (2010)[10], Oka et al. (2008)[11], Porquet et al. (2003)[12], Requena-Torres et al. (2012)[13], Serabyn & Guesten (1987)[14], Timmermann et al. (1996)[15], Yusef-Zadeh & Morris (1987a)[16], Yusef-Zadeh & Morris (1987b)[17], and Zhao et al. (1993)[18].*

be behind Sgr A-East based on the presence of a red-shifted component of the gas but no blue-shifted gas component in NH_3 observations. On the other hand, the +20 kms^{-1} cloud is placed in front of Sgr A-East by Okumura et al. (1991) implying that the cloud is moving toward the GC. Coil & Ho (2000) used NH_3(1,1) and NH_3(2,2) VLA observations of the central 15 pc of the GC and used kinematic criteria to put the +20 kms^{-1} cloud in front of the CND. The LSR velocity of the emission is red-shifted when approaching to the GC, which determines the flux of the gas towards the GC, while the lack of blue-shifted emission would imply that the +50 kms^{-1} cloud is behind and next to Sgr A-East. More recently, Ferrière (2012) compiled a large number of observational results to make a consistent 3-dimensional picture of the inner 10 pc of the GC. In their results, they put the +20 kms^{-1} and +50 kms^{-1} clouds on opposite sides of the GC, being the +50 kms^{-1} cloud behind and around Sgr A-East, while the +20 kms^{-1} cloud is located in front of the GC. For a detailed view of the positions along the l.o.s. of several structures in the inner 10 pc of the GC, see their Figure 4.

1.3 The Present Work

In the sub-mm/FIR range, from 650 μm to 158 μm (460 GHz to 1.9 THz), great effort has been made to understand the physics behind the Sgr A Complex and the numerous astronomical sources within it. On the one hand, previous heterodyne observations of this region, ranging from a few targeted positions, with moderate spectral resolution, to large scale observations with moderate spatial resolution, have largely contributed to understand the kinematics and excitation mechanisms of the warm gas in the GC (Genzel et al., 1990; Poglitsch et al., 1991; Mizutani et al., 1994; Martin et al., 2004). More recently, small scale observations with high spatial and spectral resolutions have become available for the shorter wavelengths in this spectral domain with the Stratospheric Observatory for Infrared Astronomy (SOFIA[14]) as shown in the observations of the CND by Requena-Torres et al. (2012). On the other hand, several high resolution continuum observations covering the whole CMZ have been crucial to estimate volume densities, temperatures and characterize the spatial morphology of the warm gas in this region (Mezger et al., 1989; Pierce-Price et al., 2000; Bally et al., 2010; Molinari et al., 2011). Observation with ground-based telescopes in this frequency domain are particularly difficult given the poor atmospheric transmission. In the present work I present observations of the entire Sgr A Complex at high angular ($\leq$ 46") and spectral (1 kms^{-1}) resolution in most of main cooling lines (except for the two [OI] transitions at 146 μm and 63 μm) in the sub-mm/FIR regime of the ISM[15] (CO(J=4-3), [CI] $^3P_1$ - $^3P_0$, [CI] $^3P_2$ - $^3P_1$, and [CII] $^2P_{3/2}$ - $^2P_{1/2}$) and

[14] Stratospheric Observatory for Infrared Astronomy
[15] Inter Stellar Medium

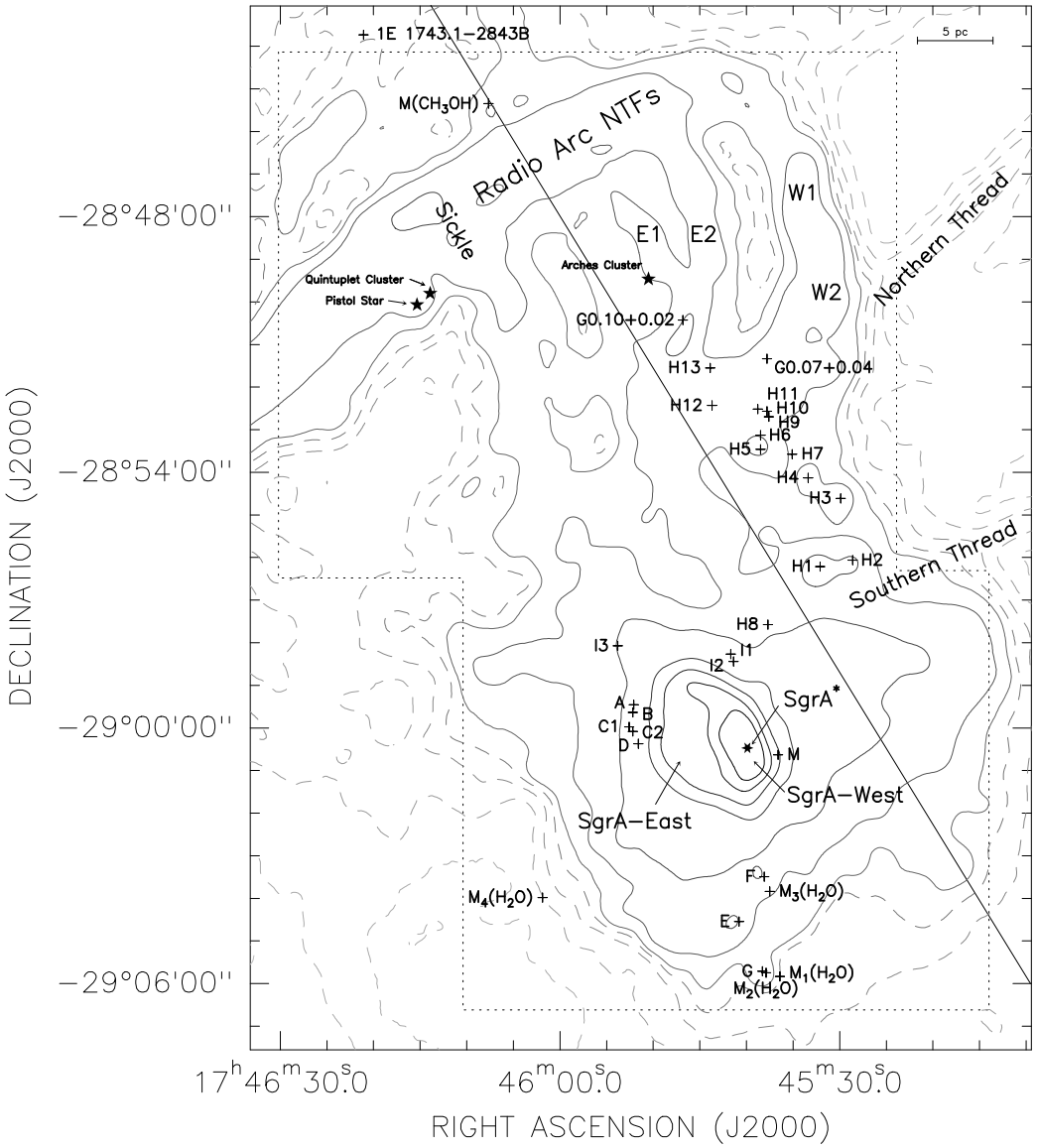

Figure. 1.2: *20 cm continuum observations at 30" spatial resolution from Yusef-Zadeh & Morris (1987a). Following Lang et al. (2010), contours levels are at 10, 15, 20, 25, 30, 35, 50, 100, 300, 500, 700, and 900 times the level of 8.5 mJy beam^{-1}. The solid straight line shows the position of the Galactic plane at b = 0°.*

H II regions ([NII] $^3P_1$ - $^3P_0$) obtained with the Herschel-HIFI[16] satellite and the NANTEN2/SMART[17] telescope.

The present work is organized as follows: in Chapter 2, the physical background and modeling tools for the present work are explained; in Chapter 3, the data

[16]Heterodyne Instrument for the Far-Infrared
[17]Sub-Mm Array Receiver for Two frequencies

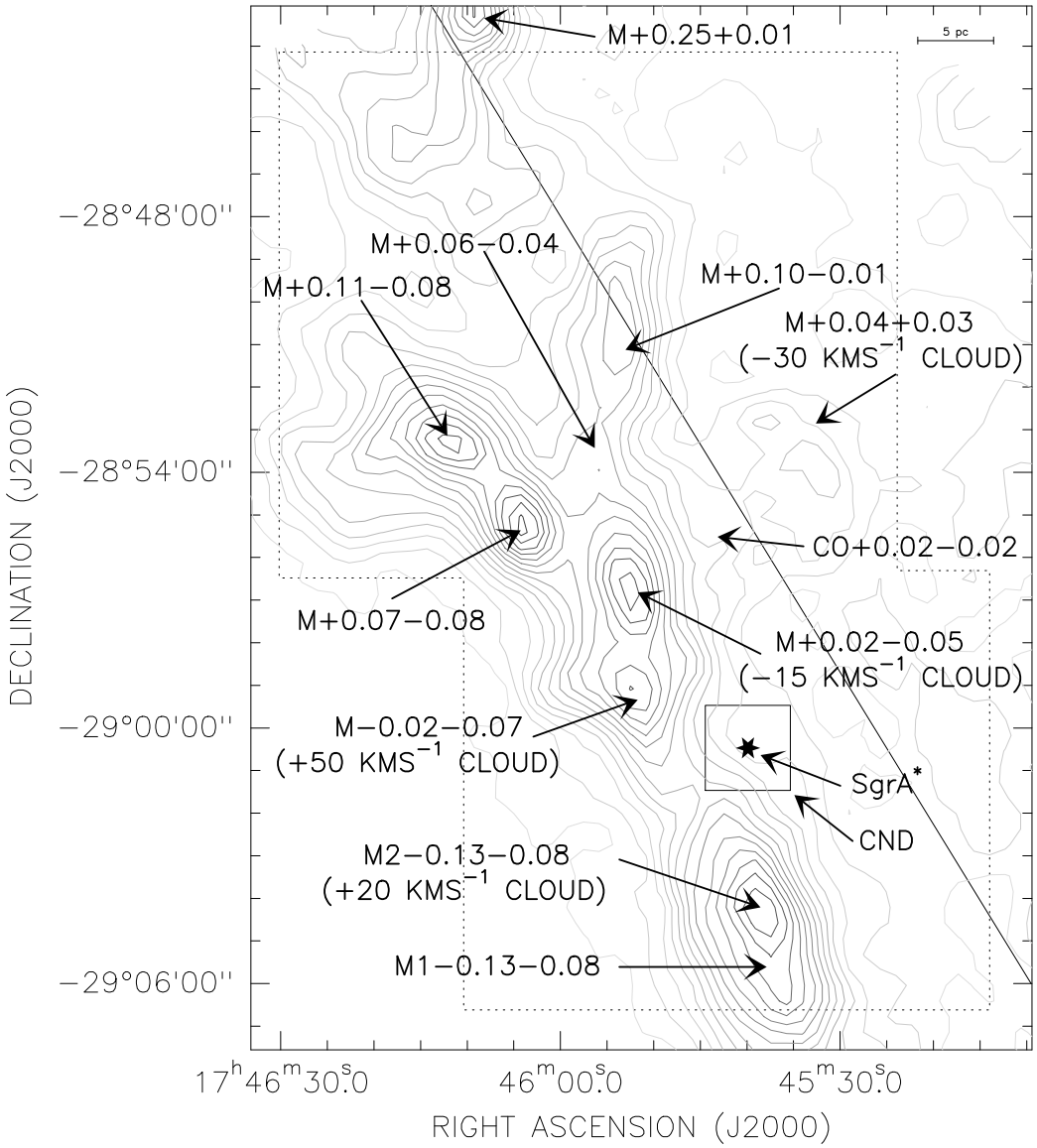

Figure. 1.3: *N_2H^+(1-0) (diazenylium) integrated intensity map between −75 and +110 kms^{-1} of the Mopra archive (Jones et al., 2012). The spatial resolution is 44" with 3.6 kms^{-1} spectral resolution. The first contour is located at 1.08 K kms^{-1} equivalent to 5×σ, while the contour increment is 5 K kms^{-1}. The positions of the molecular clouds (arrows) are taken from Güsten et al. (1981). The solid straight line shows the position of the Galactic plane at b = 0°.*

acquisition campaign and data reduction process are described; in Chapter 4, the emission morphology of the main sources detected in the observations is discussed. Out of the vast number of sources in these datasets, the Arched-Filaments were selected in Chapter 5 for a preliminary analysis of the physical conditions of the gas within them, while the physical conditions of the HVG[18] at the X_1 orbits

[18]High Velocity Gas

is investigated in Chapter 6. In Chapter 7, ongoing and future work related to the +20 kms^{-1} and +50 kms^{-1} Clouds is discussed. Finally, in Chapter 8, the main work done in this thesis is summarized.

Chapter 2

Physical Background

In the present Chapter, the main physical processes used to interpret the sub-mm observations in the present work are discussed. From the formation of the observed species, through the interaction of their emitted radiation with matter, and the models used in interpreting the measured intensities, this chapter outlines the conceptual physical framework on which all results of the present work are based.

The topics of this chapter are based on texts in astrophysics such as: *Physics of the Interstellar and Intergalactic Medium* (Draine, 2011), *The Physics and Chemistry of the Interstellar Medium* (Tielens, 2005), *Radiative Processes in Astrophysics* (Rybicki & Lightman, 1979), *The Alchemy of the Heavens: Searching for Meaning in the Milky Way* (Croswell, 1996), and *Tools of Radio Astronomy* (Wilson et al., 2009). They are complemented with publications and lectures on physics and astrophysics of different authors addressing specialized topics, with references given accordingly in the text. This chapter is intended to be a compendium of previous work in the literature, in order to provide the reader with the necessary astrophysical terminology of the physical processes related to this work.

2.1 Atoms and Ions: Carbon, Nitrogen and their Ionized Species

The second most common metal in the universe, carbon (^{12}C), is formed in stellar interiors (at temperatures $\sim 10^8$ K) by nuclear fusion. Its formation occurs in the so called *triple-α process* in which two α particles (^4He atoms) fusion to form Beryllium-8 (^8Be), which then further combines with another α particle to form ^{12}C. These reactions are extremely important in the evolution of stars as energy

reservoir, because they give rise to the so called CNO[1]-Cycle (where the first stable isotopologue of nitrogen ^{14}N is also created), which is one of the most important energy sources of stars (Croswell, 1996). Once carbon and nitrogen, formed in the stellar interiors, are released into the ISM due to stellar evolution, they can be ionized by photons (or particles) with energies ≥ 11.26 eV and 14.53 eV, respectively (Tielens, 2005). In the context of the present work, the ionization process occurs mainly within PDRs[2] and H II regions. In the case of nitrogen, the ionization occurs only within H II regions, were the UV field contains photons that are energetic enough to remove at least one electron from the external atomic orbits, while in the case of carbon, ionizing emission can arise from both, the H II region and the PDR (Abel, 2006).

The energy state transitions of the observed atoms and ions in the present work originate from the spin-orbit interaction of electrons, the so called *fine-structure* transitions (Herzberg, 1945). Neutral atomic carbon has ground state energy levels $^3P_0$, $^3P_1$, and $^3P_2$, with increasing energy. Given the low densities in the ISM, when a neutral carbon electron is excited to one of the ^3P states, it will almost certainly decay via a "forbidden" transition (expressed within "[ ]") which are all transitions between energy states that do not occur via the most probable path, namely, electric dipole transitions but rather via magnetic dipole ones (Rybicki & Lightman, 1979), such as the [CI] ^{3}P$_1$ - ^{3}P$_0$ and [CI] ^{3}P$_2$ - ^{3}P$_1$ transitions at 609.1 μm and 370.4 μm, respectively, observed in the present work. When neutral carbon is ionized, one of the two electrons in the $2P$ energy level is removed, yielding the $^2P_{1/2}$ and $^2P_{3/2}$ energy states. Hence, a single transition [CII] ^{2}P$_{3/2}$ - ^{2}P$_{1/2}$ at 157.7 μm occurs in ionized carbon, which is also observed in the present work. On the other hand, once nitrogen is ionized, it becomes a carbon-like species. The [NII] ^{3}P$_1$ - ^{3}P$_0$ and [NII] ^{3}P$_2$ - ^{3}P$_1$ transitions produce photons with wavelengths at 205 μm and 122 μm, respectively. In the present work, only the 205 μm transition has been observed because of instrumental limitations.

2.2 The Carbon Monoxide (CO) Molecule

After carbon and oxygen and their isotopologues are released into the ISM, they can combine to form carbon monoxide in the gas-phase using several pathways (see Röllig & Ossenkopf (2013b) for examples of chemical reactions leading to CO formation). On the other hand, CO can get dissociated by photons with energies ∼ 11.11 eV, which are usually produced in regions where massive stars

[1] Carbon-Nitrogen-Oxygen
[2] Photon-Dominated Regions

dominate the radiation field (Tielens, 2005).

In terms of CO energy levels, the fact that two different atoms (carbon and oxygen) constitute the CO diatomic molecule adds two extra degrees of freedom to the movement of the gas particle, when compared to single atoms: rotation and vibration of the nuclei. It can be shown that the relative contribution of electrons and nuclei movements to the total energy of the diatomic molecule is approximately (Rybicki & Lightman, 1979):

$$E_{e^-} : E_{vib} : E_{rot} = 1 : \left(\frac{m}{M}\right)^{1/2} : \frac{m}{M}, \tag{2.1}$$

where m and M are the electron and nuclear masses. Therefore, the easiest way for a molecule to move to higher energy states is to fill the rotational energy states first, giving rise to the so called *rotational spectrum*, with some transitions in the sub-mm regime, such as the CO(J=4-3) line. From Quantum Mechanics, it can be shown that the energy difference between rotational levels is given by (Herzberg, 1966; Rybicki & Lightman, 1979):

$$\Delta E_{n,J\to J+1} = E_{n,J+1} - E_{n,J} \tag{2.2}$$

$$= 2B(J+1)\Big[1 - \frac{4\hbar^2(J+1)^2}{k_n \mu r_\circ^4}\Big], \tag{2.3}$$

where $B = \hbar^2/2\mu r_\circ^2$ is the so called *rotational constant*, k_n is referred to as the *spring constant*, $r_\circ$ is the equilibrium intermolecular distance, and $\mu = M_1 M_2/(M_1 + M_2)$ is the reduced mass. Equation 2.3 shows that the rotational transitions have frequencies $\nu_{J\to J+1} = \Delta E_{n,J\to J+1}/h$ that scale linearly with the upper angular momentum quantum number $J + 1$.

2.3 Radiation

As described in the previous sections, matter made out of atoms/molecules emits/absorbs energy when changing their energy state. Once released, this radiation propagates through space. In the astronomical context, radiation (photons) emitted by an astronomical source can be assumed to travel in straight lines or "rays" since the spatial scales of the radiation emitter (source) are much larger than the wavelength of the corresponding radiation. This is a fundamental assumption from which the energy carried by an infinitesimal set of rays can be determined. From geometrical arguments, it can be shown that, the amount of energy crossing an area dA, normal to the direction of propagation of the rays coming from a solid angle $d\Omega$, within a time interval dt and frequency interval $d\nu$ can be expressed as (Rybicki & Lightman, 1979):

$$dE = I_\nu dA dt d\Omega d\nu, \tag{2.4}$$

where I_ν is defined as the *specific intensity*, and has units of ergs cm^{-2} s^{-1} str^{-1} Hz^{-1}. It can be also shown from energy conservation and geometrical arguments that I_ν, in vacuum, is a constant property of the electromagnetic field along a given ray, depending only on the direction in space where the radiation is coming from and its frequency.

In the same way, it is useful to define the *specific energy density* u_ν as the amount of energy that is contained in the volume defined by the distance traveled by the rays in a time dt. Given the fixed light speed c, u_ν satisfies (Draine, 2011):

$$dE = u_\nu dV d\Omega d\nu \tag{2.5}$$
$$= u_\nu dA c dt d\Omega d\nu. \tag{2.6}$$

Combining Equations 2.4 and 2.6, the relationship $u_\nu = I_\nu/c$ is obtained.

2.4 The Planck Function, Brightness (T_b) and Radiation (T_R) Temperatures

The Planck function characterizes the radiation (photons) across the electromagnetic spectrum of matter in thermodynamic equilibrium with surrounding radiation. Its derivation follows from calculating u_ν in Equation 2.5 for photons within a blackbody (opaque and non-reflective body, or equivalently with very high optical depth, as defined in Equation 2.14) at uniform temperature T. The expression for u_ν can be obtained by multiplying the density of states (number of states per solid angle per volume per frequency) of photons within the box (Rybicki & Lightman, 1979):

$$\rho_s = \frac{2\nu^2}{c^3}, \tag{2.7}$$

by the average energy of each state for a given frequency ν:

$$\overline{E} = \frac{h\nu}{\exp(h\nu/kT) - 1}, \tag{2.8}$$

where h and k are the Planck and Boltzmann constants, respectively. Then, with the relationship between I_ν and u_ν shown in the previous section, the Plank function $B_\nu(T)$ satisfies:

$$I_\nu = B_\nu(T) = \frac{2h\nu^3/c^2}{\exp(h\nu/kT) - 1}. \tag{2.9}$$

Therefore, in the particular case of a blackbody in LTE[3] with its environment, the functional form of the specific intensity I_ν equals the Planck function $B_\nu(T)$.

[3] Local Thermodynamic Equilibrium

This particular case does rarely apply in astronomical environments since matter is usually not in LTE. Nonetheless, in order to express the measure specific intensity I_ν in more convenient units, the *radiation temperature* $T_{R,\nu}$ is defined as (Wilson et al., 2009):

$$T_{R,\nu} = J_\nu(T) \tag{2.10}$$

$$= \frac{h\nu}{k}\frac{1}{\exp(h\nu/kT)-1}, \tag{2.11}$$

with $J_\nu(T)$ the *normalized Planck function*. In case of a blackbody emitter in the sub-mm range, the *Rayleigh-Jeans (R-J) approximation* ($h\nu \ll kT$), yields for $T_{R,\nu}$ (Guan et al., 2012):

$$T_{R,\nu} \approx T_b - \frac{h\nu}{2k}\Big[1 - \frac{1}{6}\frac{h\nu}{kT_b} + O(\epsilon^2)\Big], \tag{2.12}$$

with $\epsilon = h\nu/kT$, and T_b the *brightness temperature* of the blackbody $B_\nu(T_b)$. The $h\nu/2k$ factor in Equation 2.12 is called the *Rayleigh-Jeans Correction* in the case of the R-J approximation, and is included in the calibration of sub-mm observations in the present work (See Appendix A), while the $O(\epsilon^2)$ can be neglected for ϵ very small.

2.5 Radiative Transfer

The case in which radiation does not encounter any matter along its traveling path is not common. In practice, light does encounter matter which affects the value of I_ν by adding/removing energy as it travels across it. Therefore, the propagation of such radiation has to consider the variations of I_ν along the path s. This behavior is described by the radiative transfer equation as follows (Wilson et al., 2009):

$$\frac{dI_\nu}{ds} = -\alpha_\nu I_\nu + j_\nu. \tag{2.13}$$

From Equation 2.13, the variation of I_ν along the the path s, is governed by the terms on the right side. The first term, $\alpha_\nu I_\nu$ describes the decrease in I_ν by the quantity of light absorbed through the *absorption coefficient* $\alpha_\nu = \rho\kappa_\nu$, where ρ is the mass density of the medium, and κ_ν (in units of $\mathrm{cm}^{-2}\ \mathrm{gr}^{-1}$) is referred to as the *opacity coefficient*. In the second term, the *emission coefficient* j_ν in units of ergs $\mathrm{cm}^{-3}\ \mathrm{s}^{-1}\ \mathrm{str}^{-1}\ \mathrm{Hz}^{-1}$ accounts for the light added by spontaneous emission of the medium. Since s (the path I_ν travels across the medium) is difficult to measure, a more convenient approach is to rewrite Equation 2.13 as a function of more accessible quantities. By defining the *optical depth* as:

$$d\tau_\nu = \alpha_\nu ds, \tag{2.14}$$

and introducing the source function S_ν:

$$S_\nu = \frac{j_\nu}{\alpha_\nu}, \tag{2.15}$$

Equation 2.13 can be rewritten as:

$$\frac{dI_\nu}{d\tau_\nu} = -I_\nu + S_\nu. \tag{2.16}$$

whose general solution, using the Ansatz $I_\nu(\tau_\nu) = f(\tau_\nu)e^{-\tau_\nu}$, is given by:

$$I_\nu(\tau_\nu) = I_\nu(0)e^{-\tau_\nu} + \int_0^{\tau_\nu} e^{-(\tau_\nu - \tau_\nu')} S_\nu(\tau_\nu') d\tau_\nu', \tag{2.17}$$

where the first term corresponds to the initial intensity attenuated by the optical depth along the path, and the second term shows the integrated source emission attenuated by absorption. In the particular case when S_ν is assumed to be constant, Equation 2.17 can be written as (Rybicki & Lightman, 1979):

$$I_\nu(\tau_\nu) = I_\nu(0)e^{-\tau_\nu} + S_\nu(1 - e^{-\tau_\nu}). \tag{2.18}$$

Furthermore, assuming that level population of the two different states (lower and upper) giving rise to the radiation at frequency ν can be described by a single temperature T_{ex} (see Section 2.6), it can be shown that $S_\nu = B_\nu(T_{ex})$. Expressing Equation 2.18 in terms of $J_\nu(T)$ defined in Equation 2.11 yields:

$$J_\nu(T_R) = J_\nu(T_{bg})e^{-\tau_\nu} + J_\nu(T_{ex})(1 - e^{-\tau_\nu}), \tag{2.19}$$

where T_{bg} is the contribution to the measured emission from the Cosmic Background (in the simplest scenario where no other emission source contributes to $I_\nu(0)$) that fills the sky almost isotropically, at temperature 2.73 K (Fixsen, 2009). This background radiation is removed from the measured intensities by subtracting $J_\nu(T_{bg})$ from Equation 2.19, yielding (Simon, 1997):

$$T_R^* = f[J_\nu(T_{ex}) - J_\nu(T_{bg})](1 - e^{-\tau_\nu}), \tag{2.20}$$

known as the *detection equation* where T_R^* is the measured radiation temperature by the telescope, for which the atmospheric and instrumental contributions to the radiation have been removed, and the *filling factor* f is a number between 0 and 1 that accounts for the coupling of the telescope beam to the astronomical source, describing the fraction of the beam that is filled by it.

2.6 Mechanisms of Line emission: Einstein Coefficients

As it has been shown in Equation 2.16, the macroscopic variation of the specific intensity I_ν is the result of the interplay between absorbing and emitting material

along the rays paths. On a microscopic level, the emission/absorption of photons of frequency ν by a system with quantized energy levels l (lower) and u (upper) can be characterized by three main processes, as A. Einstein first proposed (Rybicki & Lightman, 1979):

1. *Spontaneous Emission:* occurs when a photon of frequency ν is emitted in the absence of a radiation field. The transition $u \rightarrow l$ is then characterized by the Einstein-A coefficient A_{ul} in units of s^{-1}, representing the probability of such transition and defining the lifetime of the system at the energy state u as $t = A_{ul}^{-1}$.

2. *Absorption:* occurs when, in the presence of a radiation field, the system undergoes an energy transition from $l \rightarrow u$, with the probability per unit time of the process being proportional to the *mean specific intensity*. The energy difference between states l and u is not infinitely sharp, but it has a functional form depending on frequency defined as the *normalized line profile function* $\phi(\nu)$, where:

$$\int_0^\infty \phi(\nu) d\nu = 1. \tag{2.21}$$

   To properly estimate which photons of frequency ν' within $\nu \pm \Delta\nu$ will be absorb, the estimation of the mean specific intensity is "weighted" by $\phi(\nu)$ as:

$$\overline{J} = \int_0^\infty \underbrace{\overbrace{\left[\frac{1}{4\pi}\int_\Omega I_\nu d\Omega\right]}^{\text{mean specific intensity}} \phi(\nu)}_{\text{weighted mean specific intensity}} \, d\nu. \tag{2.22}$$

   With these definitions, the transition probability per unit time for the absorption process from $l \rightarrow u$ is $B_{lu}\overline{J}$, where B_{lu} is referred to as the Einstein-B coefficient.

3. *Stimulated Emission:* occurs when an photon of frequency ν' within $\nu \pm \Delta\nu$ interacts with matter at energy state u, originating the de-excitation of the state with the transition $u \rightarrow l$. Using the same arguments described for the absorption case, it is clear that this process is described by $B_{ul}\overline{J}$, where the energy after the process is $2h\nu$.

In LTE, the number of transitions to the state l must equal the number of transitions out of the same state, to the state u. Given that the number of transitions in each

case is proportional to the number density of atoms in each state (n_l and n_u), this can be written as (Rybicki & Lightman, 1979):

$$\overbrace{n_l B_{lu} \overline{J}}^{\text{out of state } l} = \overbrace{n_u A_{ul} + n_u B_{ul} \overline{J}}^{\text{into state } l}. \tag{2.23}$$

Solving for $\overline{J}$ yields:

$$\overline{J} = \frac{A_{ul}/B_{ul}}{(n_l/n_u)(B_{lu}/B_{ul}) - 1}. \tag{2.24}$$

On the other hand, the Boltzmann law relates the population densities of the states l and u as:

$$\frac{n_l}{n_u} = \frac{g_l}{g_u} \exp(h\nu/kT_{ex}), \tag{2.25}$$

where g_l and g_u are the statistical weights of each state, and T_{ex} is referred to as the *excitation temperature*. Thus, replacing Equation 2.25 in 2.24 yields:

$$\overline{J} = \frac{A_{ul}/B_{ul}}{(g_l B_{lu}/g_u B_{ul}) \exp(h\nu/kT_{ex}) - 1}. \tag{2.26}$$

In LTE, and assuming that $\overline{J}$ varies little over the small frequency interval $\Delta\nu$, the mean specific intensity in Equation 2.22 equals the Planck function $B_\nu(T)$. The latter sets constrains to the Einstein coefficients so the must fulfill:

$$g_l B_{lu} = g_u B_{ul}, \textit{and} \tag{2.27}$$

$$A_{ul} = \frac{2h\nu^3}{c^2} B_{ul}. \tag{2.28}$$

From Equations 2.27 and 2.28 it can be noticed that there is no dependence on temperature, implying that they hold whether or not matter is in LTE, constituting a connection between microscopic processes such as emission and absorption of photons.

2.6.1 Radiative Transfer Described by Einstein Coefficients

Since the Einstein coefficient describe the emission/absorption mechanisms of the material from the microscopic physics, they can be used to described the macroscopic behavior of the radiation as it passes through a medium as shown in Section 2.5, by expressing the emission and absorption coefficients j_ν and α_ν as function of A_{ul}, B_{ul}, and B_{lu}. By definition, the monochromatic *spontaneous* emission coefficient relates to the energy dE of the energy state l, at frequency ν by:

$$dE = j_\nu dV dt d\nu d\Omega. \tag{2.29}$$

Since photons with frequencies ν' within $\nu \pm \Delta\nu$ will also contribute to dE, the most simple assumption is to characterize their distribution around ν by the normalized line profile function $\phi(\nu)$, as is was done for the absorption case. Thus, for emission at frequency ν distributed over a 4π solid angle, dE can be expressed as:

$$dE = \frac{h\nu}{4\pi} n_u A_{ul} \phi(\nu) dV dt d\nu d\Omega. \tag{2.30}$$

Then, it follows (Draine, 2011):

$$j_\nu = \frac{h\nu}{4\pi} n_u A_{ul} \phi(\nu). \tag{2.31}$$

In Equation 2.30, the contribution of *stimulated emission* to dE is missing. As previously discussed, given its proportionality to I_ν, it is better to treat it as "negative" absorption, including it in the absorption coefficient α_ν. Since the total energy dE removed by the absorption process (proportional to $n_l B_{lu} \bar{J}$) is decreased by the stimulated emission process (proportional to $n_u B_{ul} \bar{J}$), following Equation 2.22 it can be shown that, the total absorbed energy in a volume dV, in a frequency range $d\nu$ and solid angle $d\Omega$ is given by:

$$dE = -\frac{h\nu}{4\pi} \phi(\nu) [n_l B_{lu} - n_u B_{ul}] I_\nu dV dt d\nu d\Omega. \tag{2.32}$$

If the absorption term dominates, than the variation of dE is < 0, while the opposite is true when stimulated emission is the major contributor to dE. Now, considering the variation of dE along a ray path s, defining a volume $dV = dA \times s$, Equation 2.32 can be written as:

$$\frac{d}{ds}\Big(\overbrace{\frac{dE}{dA dt d\nu d\Omega}}^{I_\nu} \Big) = -\frac{h\nu}{4\pi} \phi(\nu) [n_l B_{lu} - n_u B_{ul}] I_\nu, \tag{2.33}$$

from which, using Equation 2.13, the absorption coefficient can be recognized as (Rybicki & Lightman, 1979):

$$\alpha_\nu = \frac{h\nu}{4\pi} \phi(\nu) (n_l B_{lu} - n_u B_{ul}). \tag{2.34}$$

Using Equations 2.31 and 2.34, the source function can be expressed in terms only of the Einstein coefficients as:

$$S_\nu = \frac{j_\nu}{\alpha_\nu} = \frac{n_u A_{ul}}{n_l B_{lu} - n_u B_{ul}} \tag{2.35}$$

which, using the relationships between Einstein coefficients in Equations 2.27 and 2.28 becomes:

$$S_\nu = \frac{2h\nu^3}{c^2} \Big(\frac{g_u n_l}{g_l n_u} - 1 \Big)^{-1}. \tag{2.36}$$

Then, for matter in LTE with itself (but not necessarily with the radiation field), the population of levels l and u can be described by the Boltzmann law in Equation 2.25, so the source function equals the Planck function:

$$S_\nu = \frac{2h\nu^3}{c^2}\Big(\exp(h\nu/kT_{ex}) - 1\Big)^{-1} = B_\nu(T_{ex}). \tag{2.37}$$

In this case, the energy state of matter is referred to as LTE.

2.7 Estimation of Column Densities from Observations

In astronomy, a useful way to measure the amount of material of a given species along the l.o.s. is the so called *column density* N which relates directly to the volume density n integrated along a path s as (Rybicki & Lightman, 1979):

$$N = \int n ds. \tag{2.38}$$

In order to obtain an expression for N as a function of measurable quantities, it can be noticed that, from Equations 2.14, 2.25, 2.27, and 2.28, the total optical depth (integrated over frequency) can be expressed as:

$$\int \tau_\nu d\nu = \overbrace{\int \frac{A_{ul}c^2}{8\pi\nu^2}\Big[\exp(\frac{h\nu}{kT_{ex}}) - 1\Big]\phi(\nu)d\nu}^{f(\nu)} \overbrace{\int n_u ds}^{N_u}. \tag{2.39}$$

To evaluate $f(\nu)$, a few simplifications can be made. In sub-mm observations, the bandwidth of the detectors is of the order of a few GHz, much smaller than the observed frequencies (between 460 GHz and 1.9 THz in the present work). Therefore, all functions explicitly depending on ν can be approximated by the observed frequency $\nu_{u\to l}$ of the transition $u \to l$. With this, Equation 2.39 yields:

$$\int \tau_\nu d\nu \approx \frac{A_{ul}c^2}{8\pi\nu_{u\to l}^2}\Big[\exp(\frac{h\nu_{u\to l}}{kT_{ex}}) - 1\Big] N_u \overbrace{\int \phi(\nu)d\nu}^{\equiv 1}. \tag{2.40}$$

Equation 2.40 is linked to the observations by solving Equation 2.19 for τ_ν, and integrating over the frequency domain yields:

$$\int \tau_\nu d\nu = -\int \ln\Big(1 - \frac{T_R^*}{f(J_\nu(T_{ex}) - J_\nu(T_{bg}))}\Big)d\nu, \tag{2.41}$$

The right side in Equation 2.41 contains the filling factor parameter f. In the context of GC observations, given the very widespread emission in sub-mm lines

observed in the present work, it is assumed that the telescope beam is completely coupled with the astronomical source so $f = 1$. Since T_R^* is usually expressed as a function of radial velocity, the integral on the right side can be converted by using the Jacobian determinant of the coordinate conversion $dv = \frac{c}{\nu} d\nu$. Assuming optically thin emission ($\tau_\nu \ll 1$) and a weak background compared to the emission from the source ($T_{bg} \ll T_{ex}$), Equation 2.41 can be rewritten as:

$$\int \tau_\nu d\nu \approx \frac{\nu_{u\to l}}{cJ_\nu(T_{ex})} \int T_R^* dv. \tag{2.42}$$

Thus, equaling the expressions in Equations 2.39 and 2.42 it is obtained:

$$\left(\frac{A_{ul}c^2}{8\pi\nu_{u\to l}^2}\right)\left(\frac{h\nu_{u\to l}}{kJ_\nu(T_{ex})}\right)N_u = \left(\frac{\nu_{u\to l}}{cJ_\nu(T_{ex})}\right)\int T_R^* dv, \tag{2.43}$$

and solving for N_u, the column density of the upper state u is given by:

$$N_u = \frac{8\pi k}{A_{ul}c^3 h}\nu_{u\to l}^2 \int T_R^* dv. \tag{2.44}$$

In the optically thick case, Equation 2.44 has to take into account the large optical depth, so it has to be corrected by a factor $\tau/(1 - e^{-\tau})$ (Goldsmith & Langer, 1999). In general, to determine the level population of all energy levels is not a trivial problem. Only when assuming thermodynamic equilibrium, i.e., that the population of all levels is described by a single temperature T, N_u can be related to the total column density of the same species N_{tot} as (Goldsmith & Langer, 1999; Draine, 2011):

$$N_u = \frac{N_{tot}}{Q(\mathrm{T})} g_u e^{-E_u/kT}, \tag{2.45}$$

with Q(T) the *partition function* defined as:

$$Q(\mathrm{T}) = \sum_i^{levels} g_i e^{-E_i/kT}. \tag{2.46}$$

The way in which total column densities are obtained in the present section relays on several assumptions that are almost never fulfilled in the ISM. More realistic estimates for column densities are obtained through the detailed treatment of the mechanisms responsible for the population of a given energy level. In Equation 2.23, excitation and de-excitation of the level populations due to collisions with other partners are not considered (electrons, atoms, or molecules) for simplicity but they can play an important role depending on the kinetic temperature and volume density of the studied ISM.

2.8 Collisional Excitation and Critical Density

An atom or molecule can not only change its energy state by spontaneous emission, or due to the interaction with an external electromagnetic field, but also due to collisions with other partners, which may play an important role in the cooling/heating mechanism of the ISM. If the following collision occurs:

$$\chi_l + \theta \rightarrow \chi_u + \theta, \tag{2.47}$$

with χ_l and χ_u a species at energy level l prior to the collision and u after, and θ another species acting as collision partner (which does not change its energy state after the collision), the process can be characterized by the collision rates:

$$C_{ul} = n_{coll}(\theta)\gamma_{ul};\ C_{lu} = n_{coll}(\theta)\gamma_{lu}, \tag{2.48}$$

for downwards (C_{ul}) and upwards (C_{lu}) transitions, where n_{coll} is the collision partner number density and γ_{ul} is the collision rate coefficient defined as (Draine, 2011; Tielens, 2005):

$$\gamma_{ul} = \langle \sigma(v)_{ul} v \rangle = \int_0^\infty (\sigma(v)_{ul} v) f(v) dv, \tag{2.49}$$

with $\sigma(v)_{ul}$ the collisional cross section for the transition $u \rightarrow l$, v the relative velocity between both species, and $f(v)$ the distribution probability that the relative velocity between the species is found in the velocity interval $v, v + \Delta v$. For LTE, $f(v)$ has the form of a Maxwellian distribution:

$$f(v) = 4\pi \Big(\frac{\mu}{2\pi kT} \Big)^{3/2} v^2 e^{-\mu v^2/2kT}, \tag{2.50}$$

characterized by the kinetic temperature T, and where μ is the reduce mass of both species. The functional form of $\sigma(v)_{ul}$ depends strongly on the type of interaction between the collision partners. Depending on the range of the interacting potential, they are usually divided into: (a) long range Coulomb interaction ($\propto r^{-1}$) for ion-ion, ion-electron, and electron-electron interactions, (b) intermediate range ($\propto r^{-4}$) dipole induced interactions for ion-neutrals (atoms or molecules) or electron-neutrals interaction, and (c) short range interactions for neutrals-neutrals interactions.

The downwards and upwards collision coefficients are not independent from each other. From the *law of mass action* it can be easily shown that C_{lu} and C_{ul} satisfy (Draine, 2011):

$$\frac{C_{lu}}{C_{ul}} = \frac{g_u}{g_l} e^{-E_{ul}/kT}, \tag{2.51}$$

with g_u and g_l the statistical weights of each level. Equation 2.51 has the same form as Equation 2.25 for the population of the two levels.

For the collision partner θ, there is a critical density $n_{crit,u}(\theta)$ at which the depopulation of level u by collisional processes equals the spontaneous and induced emission depopulation processes. This can be written as:

$$n_u \sum_{l<u} C_{ul} = n_u \sum_{l<u} B_{ul} J_\nu + n_u \sum_{l<u} A_{ul} \implies \tag{2.52}$$

$$n_{crit,u}(\theta) \sum_{l<u} \gamma_{ul} = n_\gamma \sum_{l<u} A_{ul} + \sum_{l<u} A_{ul} \implies \tag{2.53}$$

$$n_{crit,u}(\theta) = \frac{\sum_{l<u}(1+n_\gamma)A_{ul}}{\sum_{l<u}\gamma_{ul}}, \tag{2.54}$$

where Equation 2.28 was used as well as the definition of the specific energy density u_ν as $J_\nu = (c/4\pi)u_\nu$, and the so called *photon occupation number* $n_\gamma = (c^3/8\pi h\nu^3)u_\nu$ was defined, to obtain the expression for $n_{crit,u}(\theta)$ in Equation 2.54, in which radiative trapping has not been considered, namely, all produced photons escape the source. The sums in all the expressions above go over all possible final levels to which the state u can decay.

When considering radiative trapping, Equation 2.54 can be slightly modified to the following expression (Draine, 2011):

$$n_{crit,u}(\theta) = \frac{\sum_{l<u}(1+n_\gamma)A_{ul}\langle\overline{\beta(\tau_\nu)}\rangle}{\sum_{l<u}\gamma_{ul}}, \tag{2.55}$$

with $\langle\overline{\beta(\tau_\nu)}\rangle$ the direction-averaged and line profile-averaged escape probability of the photons as a function of opacity τ_ν. Usually, $\langle\overline{\beta(\tau_\nu)}\rangle$ takes three different functional forms depending on the geometry of the source (van der Tak et al., 2007). Under the assumption of an expanding spherical shell, also called the *Large Velocity Gradient* (LVG[4]) approximation (Mihalas, 1978; de Jong et al., 1980), $\langle\overline{\beta(\tau_\nu)}\rangle$ is:

$$\langle\overline{\beta(\tau_\nu)}\rangle_{LVG} = \frac{1-e^{-\tau_\nu}}{\tau_\nu}. \tag{2.56}$$

In the case of pure spherical symmetry and homogeneous medium, $\langle\overline{\beta(\tau_\nu)}\rangle$ takes the form (van der Tak et al., 2007):

$$\langle\overline{\beta(\tau_\nu)}\rangle_{sph} = \frac{1.5}{\tau_\nu}\Big[1 - \frac{2}{\tau_\nu^2} + \Big(\frac{2}{\tau_\nu} + \frac{2}{\tau_\nu^2}\Big)e^{-\tau_\nu}\Big]. \tag{2.57}$$

Finally, for a plane-parallel "slab" geometry, $\langle\overline{\beta(\tau_\nu)}\rangle$ yields (van der Tak et al., 2007):

$$\langle\overline{\beta(\tau_\nu)}\rangle_{slab} = \frac{1-e^{-3\tau_\nu}}{3\tau_\nu}. \tag{2.58}$$

[4]Large Velocity Gradient

Therefore, for a collision partner density much larger than the critical density, collisions are expected to thermalize the gas.

2.9 Photon-Dominated Regions

Massive stars ($M_\star > 8$ M$_\odot$), such as O, B and Wolf-Rayet stars, have surface temperatures larger than 15.000 K. At these high temperatures, most of their (blackbody) emission peaks at FUV[5] wavelengths, producing a very strong radiation field between 6 eV < $h\nu$ < 13.6 eV, or 912 - 2070 Å. Radiation above the Lyman limit will ionized atomic hydrogen completely giving rise to the so called H II regions, while the FUV will ionized other species such as carbon (with ionization energy ~ 11.26 eV) and dissociate molecules such as carbon monoxide (with ionization energy ~ 11.11 eV). The strength of the radiation field is usually expressed in the so called "Habing" units (Habing, 1968):

$$G_\circ = \frac{U_{FUV}}{U^H_{FUV}} = \frac{U_{FUV}}{4.6 \times 10^{-17}\ ergs\ cm^{-3}\ \text{Å}^{-1}}, \tag{2.59}$$

while another standard unit is the so called "Draine field" (Draine, 1978), which relates to $G_\circ$ as $\chi = 1.7 G_\circ$. Both standard units are based on measurements of FUV radiation sources within the solar neighborhood. *Photon-Dominated Regions* (PDRs) are the regions of the ISM whose chemistry and heating/cooling mechanisms are governed by this incident FUV field. This definition encompasses the transition zones between H II regions and the general ISM as well as diffuse and translucent interstellar clouds. Galaxies harboring sites of massive star formation can reprocess a large fraction of their total luminosity (~ 10%) through dense PDRs.

The structure of PDRs is governed by the density and the intensity of the incident FUV radiation field. Both quantities produce two distinctive zones: the photo-ionization and photo-dissociation fronts. These structures are produced by FUV photons that penetrate a molecular cloud, ionizing, dissociating, and heating the gas. Figure 2.1 shows an schematic view of a PDR in a plane-parallel geometry taken from Hollenbach & Tielens (1999). From left to right in the figure, the hydrogen-ionizing photons are absorbed in a thin ($N_H \sim 10^{19}$ cm^{-2} or $A_v \sim 10^{-2}$) transition zone. The FUV photons with energies less than 13.6 eV will dissociate molecular hydrogen and molecular oxygen, and will ionize carbon, producing a H/C$^+$/O atomic surface layer in which only carbon remains ionized. Then, at higher depths ($A_v \sim 2$) the transition from atomic hydrogen to molecular hydrogen happens. After this layer, and because of dust attenuation,

[5] Far Ultraviolet

the carbon balance shifts from C^+ to C and CO at $A_v \sim 4$ forming the C^+/C/CO layer. Finally, at large optical depths ($A_v > 10$), O_2 can be formed through the O + OH reaction, getting excited by infrared pumping. Given its large ionization potential (13.62 eV), oxygen remains neutral over the entire PDR (before turning into molecular form), being its two fine-structure transitions at 63 μm and 146 μm tracers of almost the whole PDR.

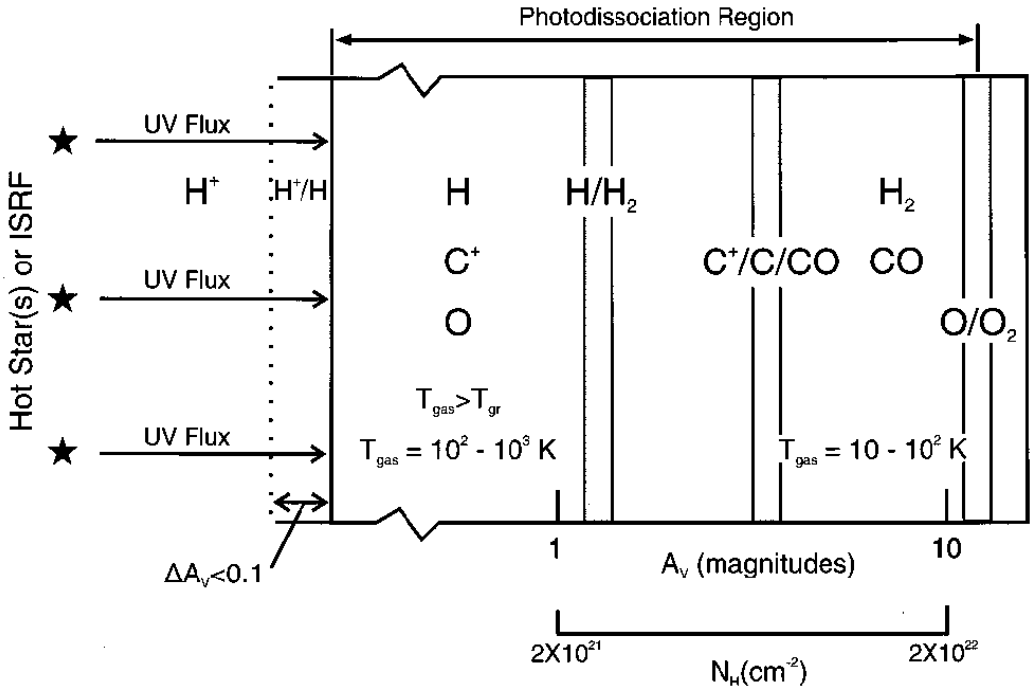

Figure. 2.1: *Schematic view of the PDR structure in a plane-parallel geometry shown in Figure 3 of Hollenbach & Tielens (1999).*

2.9.1 Heating Mechanisms

The most efficient heating mechanisms in PDRs (under standard physical conditions) are mainly four, which are briefly described in the following:

The first one is *photo-electric heating on dust and PAHs*[6] *grains*, being the former a mixture of amorphous silicates and carbonaceous material, containing nearly 100% of the Si, Mg and Fe, approximately 30% of the oxygen and about 70% of the available carbon. These elements do not vaporize until temperatures are well above 1200 K. Hence, they are not available for gas-phase chemistry in PDRs (van Dishoeck, 2014). The latter are neutral, organic compounds containing

[6]Polycyclic Aromatic Hydrocarbons

only carbon and hydrogen that consist of multiple aromatic rings, in which the electrons are delocalized. The mechanism consists of electrons being released from the dust grains or PAHs surfaces by incoming photons. After the ionization barrier has been reached, the remaining kinetic energy of these electrons will then heat the gas through collisions with the other particles constituent of the gas. Typically, between 0.1% - 1% of the FUV energy is converted into gas heating in this process, while the rest is emitted as FIR dust continuum radiation. This mechanism is more efficient in poorly ionized dust and PAHs particles, given the lower ionization energies required.

A second process is *photo-pumping of* H_2 followed by collisional de-excitation of the resulting vibrationally excited states (Klessen & Glover, 2014). Under the influence of FUV radiation, H_2 is radiatively pumped into its electronically ($v > 0$) excited states. Then, it decays into the electronic ground state ($v = 0$) by cascading via high vibrational levels ($\lambda \sim 5.2 - 36.5\ \mu$m) giving rise to optical and infrared fluorescent emission. For high enough densities ($n > n_{crit} \sim 10^4$ cm^{-3}), the rotational exited H_2 molecules can be collisionally de-excited, heating the gas accordingly, while for $n < n_{crit}$, the lifetime of the lowest rotational levels is long enough so that collisions play anyway a role in depopulating them. This heating mechanism is, at the same time, an important agent in the destruction of H_2. If photons decay to the vibrational continuum level in the ground electronic state, then H_2 is destroyed by photo-dissociation. This happens in $\sim$ 15% of the transitions. For column densities exceeding 10^{14} cm^{-2}, FUV photons capable of dissociating H_2 are absorbed at the edge of the molecular cloud, which avoids H_2 to get further dissociated deeper into the cloud. In this regime, the FUV absorption lines become optically thick, and the H_2 molecule becomes *self-shielded* against the impinging FUV field.

A third process is *dust-gas heating*. Since dust and gas are usually not in LTE, if the gas temperature T_{gas} is lower than the dust temperature T_{dust} (e.g., in protostar envelopes), then gas-grain collisions can warm up the gas, while for the inverse case, when $T_{dust} < T_{gas}$, such as in the case of PDRs and the diffuse ISM, the process acts as a cooling mechanism. Finally, a fourth process is caused by *cosmic-ray heating*, which are highly energetic relativistic particles, with $\sim$ 99% nuclei and $\sim$ 1% electrons. This process is the dominant heating source at the densest parts of the PDR, where the FUV field has been almost completely attenuated. According to the cosmic ray spectrum, most of the heating and ionization they produce is carried out by the least energetic particles with energies of $\sim$ 100 MeV or below (Klessen & Glover, 2014). Other heating mechanisms such as, photo-ionization of carbon, X-ray heating, turbulent heating, shock heating, and gravitational heating, could become important under extreme physical conditions such as the ones found in the Sgr A Complex, where strong X-ray radiation, large turbulent motions, shocks, and a super massive black hole control much of the

dynamics of the ISM in the GC.

2.9.2 Cooling Mechanisms

Dust and gas in PDRs cool in different ways. Dust in PDRs (including PAHs emission features) is very bright in the FIR continuum because most of the total gas+dust cooling (> 99% of the impinging FUV radiation) occurs in this way (Tielens, 2005; Draine, 2011). Although dust temperatures are much less than the gas temperature, dust particles have much more ways (phonons) available for efficient cooling, making it the dominant cooling agent. On the other hand, gas can cool only via discrete high-lying ($\Delta E \sim 100$ - 300 K) emission lines. Among them, the most important lines are the FIR fine-structure lines of [OI] (at 63 μm and 146 μm) and [CII] (at 158 μm) at the surface of the PDRs and rotational lines of carbon monoxide deeper into the PDR. The former atomic lines are used to probe the temperature and density of the emitting gas, while their relative importance in the cooling process depends strongly on the chemical composition and density of the gas. At low densities ($n \ll n_{crit}(C^+) \sim 10^3$ cm^{-3}), C^+ is the dominant cooling agent, while O takes over for high densities ($n > n_{crit}(O) \sim 5{\times}10^5$ cm^{-3}). In terms of their opacities, theoretical studies suggest that the [OI] 63 μm line is optically thick, while the [CII] 158 μm line is marginally optically thin ($\tau \lesssim 1$) (Draine, 2011).

As previously explained, photo-pumping of H_2 in the near-infrared can also contribute to the cooling. Also, atomic fine-structure lines of [CI] (at 609 μm and 370 μm), [SiII] (at 35 μm), as well as rotational transitions of other molecules such as CO^+, CN, C_2, OH, and H_2O contribute to the overall cooling. The total cooling line intensity is of the order of $10^{-2} - 10^{-3}$ of the total FIR continuum intensity. At extinctions $A_v > 4$, gas-grain collisions can cool the gas keeping the gas temperature slightly below the dust temperature.

2.9.3 The Origin of the [CII] Emission

Usually, carbon in H II regions is present in the form of [CIII], but observations have shown that there is also [CII] emission coming from the same spatial extent. [CII] can be collisionally excited by collisions with H, H_2, and e^-. Then, radiative decay is efficient as long as the electron density n_e, hydrogen density n(H), and molecular hydrogen density n(H_2) are lower than their corresponding critical densities n_{crit}: $3{\times}10^5$ cm^{-3}, $5{\times}10^3$ cm^{-3}, and 50 cm^{-3}, respectively. Given the geometry of the source and the beam size of the observations, [CII] emission coming

from H II regions can be confused and considered to be arising from the PDR. This would overestimate the [CII] intensities, affecting the modeling of the physical conditions such as density and FUV field. Abel (2006) analyzed this problem by noticing that there is a strong correlation between the [CII] $^2P_{3/2}$ - $^2P_{1/2}$ line arising from both PDR and H II regions and the [NII] $^3P_1$ - $^3P_0$ line originating only within the H II region. This correlation is shown in Figure 2.2 (Figure 6 in their paper) in which, a power-law fit between the ionized carbon and ionized nitrogen emission from the H II region yields:

$$\log(CII) = 0.937\log(NII) + 0.689 \quad [\text{ergs cm}^{-2}\ \text{s}^{-1}]. \tag{2.60}$$

Abel (2006) showed that between 10% and up to 60% of the detected [CII] emission can arise from H II regions being the main physical parameters controlling this contribution the electron density (controlling the excitation of ionized carbon), the size of the H II region with respect to the size of the PDR where [CII] is detected (determining the physical extent over which [CII] emission can arise from), and the stellar continuum (controlling the [CIII] → [CII] transition).

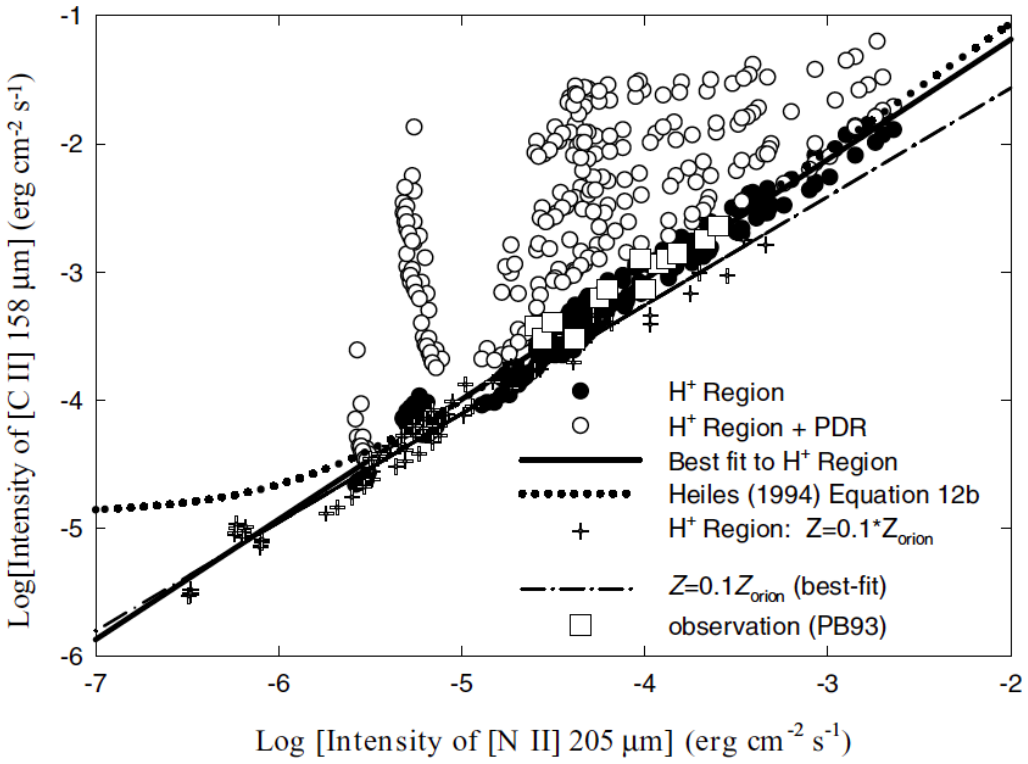

Figure. 2.2: *C^+ contribution from H II regions to the observed C^+ emission in PDRs as shown by Abel (2006), Figure 6.*

2.10 Chemistry in the ISM

The main chemical reactions in the ISM are summarized in Table 2.1, taken from van Dishoeck (2014). The formation, destruction and recombination reactions in the gas-phase and on the dust grain surfaces are listed in the first and second columns, while typical rate coefficients are given in the third column of the table. The rate coefficients of a reaction between species X and Y is given by κn(X)n(Y), where n(X) and n(Y) are the densities of the species and κ is the reaction coefficient in units of cm^3 s^{-1}. Given the low densities in space, only two-body processes are usually considered. In the following, the reactions shown in Table 2.1 are briefly described.

Bond Formation Processes		rate coefficient (cm^3 s^{-1})
Radiative association	$X + Y \rightarrow XY + h\nu$	10^{-17} - 10^{-14}
Grain surface formation	$X + Y : g \rightarrow XY + g$	$\sim 10^{-17}$
Associative detachment	$X^- + Y \rightarrow XY + e$	$\sim 10^{-9}$
Bond Destruction Processes		
Photodissociation	$XY + h\nu \rightarrow X + Y$	10^{-10} - 10^{-8} s^{-1}
Dissociative recombination	$XY^+ + e \rightarrow X + Y$	10^{-7} - 10^{-6}
Collisional dissociation	$XY + M \rightarrow X + Y + M$	$\sim 10^{-26}$ cm^6 s^{-1}
Bond Rearrangement Processes		
Ion-molecule exchange	$X^+ + YZ \rightarrow XY^+ + Z$	10^{-9} - 10^{-8}
Charge-transfer	$X^+ + YZ \rightarrow X + YZ^+$	10^{-9}
Neutral-neutral	$X + YZ \rightarrow XY + Z$	10^{-11} - 10^{-9}

Table. 2.1: *Summary of main chemical reactions in the ISM taken from van Dishoeck (2014).*

2.10.1 Gas Phase Chemistry

The main formation path of new molecules in the gas-phase chemistry is radiative association in which the binding energy of the new species is carried away by the emission of a photon. Given its low reaction rate, it is a very inefficient process when compared to collision timescales, which are around ten orders of magnitude faster. A second process is associative detachment which is much faster than radiative association. The efficiency of the process depends on the formation rate of negative ions.

Among the destruction processes of molecules in gas-phase is photodissociation. In this case, a molecule can be dissociated directly, or via decay of excited electronic states into the vibrational continuum of the ground state as it is the case of H_2. Other important molecules that are dissociated in this way are CO and N_2. Dissociative recombination with electrons can efficiently destroy molecular ions. One of the important reactions of this process is the destruction of H_3^+, a key species in the chemistry of the ISM (van Dishoeck, 2014). Finally, collisional dissociation is important only in very high temperature (T > 3000 K) and high density regions.

Some species can be created by rearranging the energy bounds in molecules that already exist. The ion-molecule reaction is very fast down to temperatures of 10 K, but for certain molecules with permanent dipole moment such as in the reaction $C^+ + H_2O$, they can be 10 - 100 times faster because long-range attraction is enhanced. Other mechanisms for rearranging energy bounds are charge-transfer and neutral-neutral interactions.

2.10.2 Grain Surface Chemistry

The efficiency of grain surface chemistry depends on four necessary steps for the reaction to occur: the chance that a particle (atom or molecule) sticks to the dust grain upon collision, the mobility of the particle on the grain surface, the probability that the molecule formation takes place, and the probability that the product is released again into the gas phase (desorption).

For the reaction to occur, it is usually assumed that at least one of the reactants hops on the grain surface to meet the other reaction partner and via collision, produces the reaction. This process is called *Langmuir-Hinshelwood mechanism*. It is also possible (but more unlikely) that the atom or molecule lands directly on the reaction partner on the grain surface with enough energy to produce the reaction. This process is known as the *Ely-Rideal mechanism*. Deep in the grains, the penetration of UV photons and cosmic-rays can dissociate molecules and trigger further reactions (van Dishoeck, 2014).

The interaction between gas and dust grain is basically governed by the collision rate of the gas species with dust particles and the desorption of the final molecules back into the gas phase. For the former, an analytic expression for the accretion rate κ_{acc} is found to be (Whittet, 2003):

$$\kappa_{acc} = v\sigma_{dust}n_{dust}S(T_{gas}, T_{dust}), \tag{2.61}$$

where v is the impact velocity of the species, σ_{dust} is the collision cross section of the dust particles, n_{dust} is the density of dust particles and $S(T_{gas}, T_{dust})$ is the so called *sticking coefficient* depending on gas and dust temperatures. Usually, $S(T_{gas}, T_{dust})$ is taken to be 1 for heavy species at low temperatures. Particles hitting the dust grain can be physically adsorbed or *physisorbed*, namely, they stick with weak van der Waals forces to the grain, or they can be chemically adsorbed or *chemisorbed* in which case, the bound to the grain is a much stronger covalent bound. Hence, chemisorbed species are much less mobile than physisorbed ones on the surface of the dust grains. Regarding the desorption of molecules, some of the mechanisms that can return the reaction product to the gas phase are: (a) thermal sublimation, (b) UV photodesorption, (c) cosmic-ray induced spot heating, (d) cosmic-ray whole grain heating, (e) exothermicity from chemical reactions, and (f) ice mantle explosions (van Dishoeck, 2014).

2.10.3 Chemical Networks

The main reactions in the chemistry of oxygen, carbon, nitrogen, sulfur and silicon are shown in Figures 2.3 and 2.4 from Hollenbach & Tielens (1999). Chemical networks are in general very complex. In the example for oxygen and carbon, only small species are considered, while species with more than one carbon atom have been neglected. In panel (a) of Figure 2.3, the oxygen reactions are shown. This element gets quickly in equilibrium with its ionized form while in regions with low FUV, oxygen chemistry is initialized by the reaction $O^+ + H_2$ and following reactions with H_2 produce H_2O^+ and H_3O^+. The carbon network is shown in panel (b) of Figure 2.3. The balance between carbon and its ionized form is driven by photo-dissociation and radiative recombination reactions. For cold and low density PDRs, reactions with pumped molecular hydrogen become very important. On the other hand, in warm, high-density PDRs, important reactions are with thermal molecular hydrogen.

In Figure 2.4 panel (a), the chemical network for nitrogen is shown. This chemistry is started with the reaction $N + H_2 \rightarrow NH + H$, where H_2 is vibrationally excited. Given its large ionization potential, only neutral and molecular nitrogen are considered in the network. Deep in the PDR, nitrogen can be liberated again from its molecular form by the reactions with He^+, ionized by cosmic-rays. In panel (b) and (c) of the same figure, the sulfur and silicon chemical networks are shown. For sulfur, given its low ionization potential (10.4 eV), only the atomic and ionized forms are considered in PDRs. Given that reactions with H_2 are endothermic, as it is the case for nitrogen as well, starting the sulfur chemical reactions is difficult. A more likely reaction occurs with vibrationally excited H_2 to form SH^+. For silicon, given its low ionization potential (8.2 eV), its ionized

form dominates until extinctions $A_v \lesssim 6$. Radiative recombination yields neutral silicon while for higher extinctions, SiO becomes the dominant sulfur-bearing species.

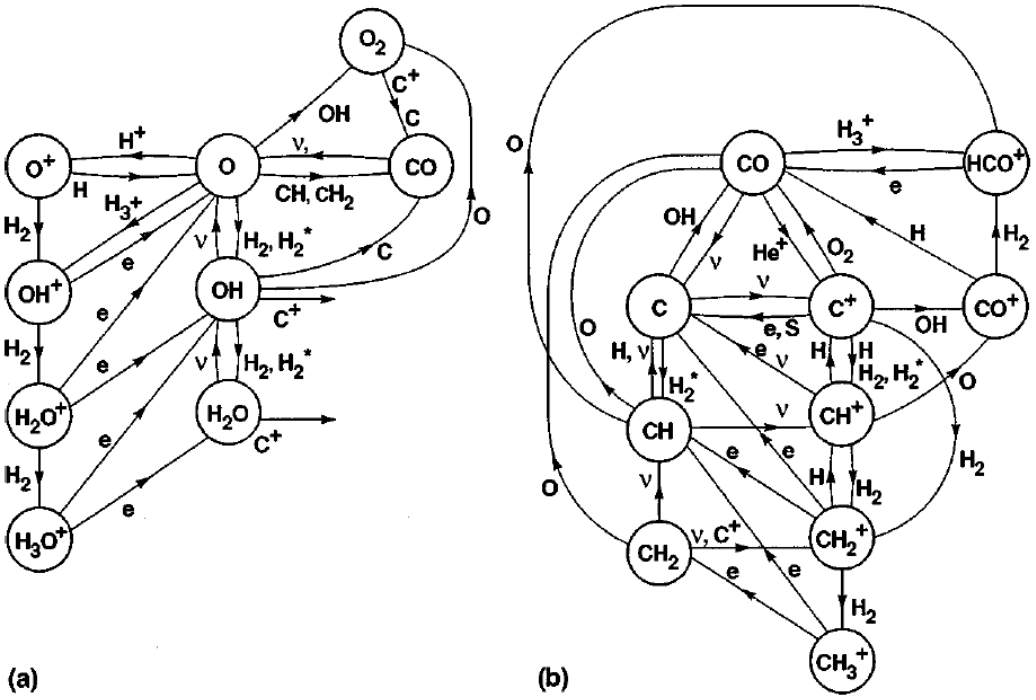

Figure. 2.3: *Chemical network of (a) oxygen and (b) carbon bearing species in PDRs shown in Figure 9 of Hollenbach & Tielens (1999).*

2.11 Modeling Software

In the following, the software used to obtain some of the physical parameters of the analyzed sources in the present work are briefly described. In Section 2.11.1, the KOSMA[7]-τ software for PDR modeling of the emission in the Arched-Filaments shown in Chapter 5 is reviewed. In Section 2.11.2, the RADEX software used to investigate the physical properties of the HVG clouds in Chapter 6 is described.

2.11.1 The KOSMA-τ PDR Model

The KOSMA-τ PDR model (τ as acronym for Tel Aviv University (TAU), in Israel) has been developed over the last twenty years at the I. Physikalisches

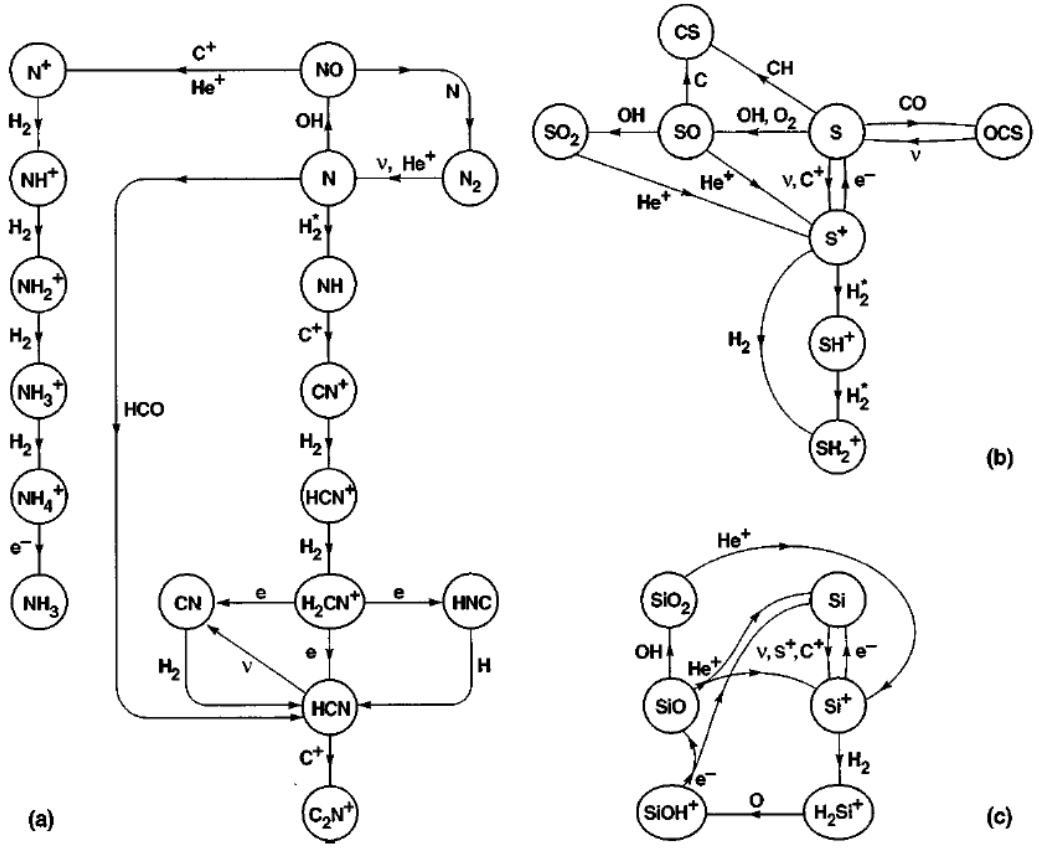

Figure. 2.4: *Chemical network of nitrogen (a), sulfur (b), and silicon (c) bearing species in PDRs shown in Figure 10 of Hollenbach & Tielens (1999).*

Institut, of the Universität zu Köln, in collaboration with the Tel Aviv University, by continuously improving and adding new features to reproduce the complex structure in PDRs (Stoerzer et al., 1996; Cubick et al., 2008; Röllig et al., 2013a). The model aims to retrieve the physical conditions of a PDR by reproducing the observed emission of millimeter and submillimeter cooling lines from the ISM. In its clumpy version (Cubick et al., 2008), the observed ISM is described as an ensemble of small clumps (not spatially resolved) within the telescope's beam, which are individually in virial equilibrium. The KOSMA-τ model calculates the physics and chemistry for each individual (spherical) clump exposed to an isotropic FUV field. Once the species distribution within each clump has been computed, the non-LTE radiative transfer for the clump is calculated, so its surface brightness $\bar{I}$ is obtained. By combining the individual intensities of all clumps, the clumps ensemble intensity can be obtained (Cubick et al., 2008). In this process, any type of absorption between the clumps is neglected. This is a good first order approximation since, under normal conditions, the velocity dispersion of the clumps avoids, at least partially, the l.o.s. crowding. The gas velocity dispersion in the GC (a few times 10 kms^{-1}) is much larger than in standard PDRs in the Galactic disk (a few times 1 kms^{-1}), with

an average H_2 volume density of $\sim$ 100 times the one in the disk (see Chapter 1), implying that local crowding could play a role in the Galactic Centre PDRs.

The radial density structure $n(r)$ of each individual clump is given in Cubick et al. (2008) (Equation 1) by:

$$n(r) = \begin{cases} n_s(\frac{r}{R_{cl}})^{-\beta}, & \text{for } 0.2R_{cl} < r < R_{cl} \\ n_\circ, & \text{for } r \leq 0.2R_{cl} \end{cases} \tag{2.62}$$

with R_{cl} the radius of the clump, $n_s = n_{H,s} + 2n_{H_2,s}$ the total hydrogen nucleus number density at the clump's surface, and $n_\circ$ a constant. The density profile is constant for $r < 0.2R_{cl}$ and varies outside with a power law index $\beta = -1.5$ for $0.2R_{cl} < r < R_{cl}$. Following Cubick et al. (2008), the clump's ensemble is defined by a power law as:

$$\frac{dN_{cl}}{dM_{cl}} = AM_{cl}^{-\alpha}, \tag{2.63}$$

with $\alpha = 1.8$ (Heithausen et al., 1998), and follows the "mass-size" relationship:

$$M_{cl} = CR_{cl}^{-\gamma}, \tag{2.64}$$

with $\gamma = 2.3$, consistent with the fractal nature of the ISM (Stutzki et al., 1998).

The chemistry in the KOSMA-τ PDR model yielding the composition of each clump is governed by chemical equilibrium, shown in Equation 1 of Sternberg & Dalgarno (1995):

$$\frac{dx_i}{dt} = \sum_{jl} k_{ijl}(T)x_j x_l + \sum_j [\Gamma_{ij}(z) + \xi_{ij}]x_j - x_i\Big(\sum_{jl} k_{jil}(T)x_l + \sum_j [\Gamma_{ji}(z) + \xi_{ji}]\Big), \tag{2.65}$$

where $x_i = n_i/n$ is the relative abundance of species i (ratio of species density n_i and the total hydrogen density n), $k_{ijl}(T)$ are the temperature-dependent reaction rate coefficients in which species j and l react to form species i, and $\Gamma_{ij}(z)$ and ξ_{ij} are the photon and cosmic-rays destruction rates of species j yielding species i. Equation 2.65 is solved for the steady-state case ($dx_i/dt = 0$). In the case of the KOSMA-τ PDR model, pure gas-phase reactions are assumed, except for the formation of H_2 on grain surfaces (Sternberg & Dalgarno, 1995; Röllig et al., 2006). The reaction rates in Equation 2.65 are taken from the UMIST[8] data base (McElroy et al., 2013).

Once the chemical composition of the clump is obtained, its emitted intensity is driven by the cooling rate (Λ) of the gas which counteracts its heating rate (Γ).

[8] http://udfa.ajmarkwick.net/

The total heating rate Γ_{tot} is described by Röllig et al. (2006) in their Equation 13 as:

$$\Gamma_{tot} \approx \Gamma_{PE}^{net} + \Gamma_{H_2}^{net} + \Gamma_{H_2,formation}. \tag{2.66}$$

Equation 2.66 shows how the total heating of the gas is the result of competing cooling and heating mechanisms of three different physical processes: (1) the *net photo-electric heating rate*, given by $\Gamma_{PE}^{net} = \Gamma_{PE} - \Lambda_{rec}$, with Γ_{PE} the heating rate due to the photo-electric effect, and Λ_{rec} the cooling rate due to electron recombination; (2) the *net collisional de-excitation heating rate*, given by $\Gamma_{H_2}^{net} = \Gamma_{H_2^\star} - \Lambda_{H_2}$, with $\Gamma_{H_2^\star}$ the heating rate due to collisional de-excitation of vibrationally excited $H_2^\star$, and Λ_{H_2} the cooling rate through H_2 transitions in the optical range for high temperature gas; and (3) the *H_2 formation heating rate* $\Gamma_{H_2,formation}$ which may contribute significantly for UV fields $\chi < 10^3$ and densities $n < 10^4$ cm^{-3} (Sternberg & Dalgarno, 1989; Röllig et al., 2006).

The clump's surface brightness $\bar{I}$ is calculated in Röllig et al. (2006), Equation 17, as:

$$\bar{I} = \frac{2\pi \int_0^R I(p) p dp}{\pi R^2}, \tag{2.67}$$

where $I(p)$ refers to the specific intensity (function of Λ) along a ray with impact parameter p. The beam averaged intensity of the whole ensemble is then obtained by the multiplication of $\bar{I}$ with the clump projected area and the clumps number density spectrum. It is then integrated over the mass ensemble (see Equation 23 in Cubick et al. (2008)), in which the filling factor due to the ensemble's projected area ($\Omega_{ensemble}$) with respect to the beam size (Ω_B) has been considered.

2.11.2 RADEX

In order to obtain physical parameters of the ISM under regimes far from LTE (low densities), the **RADEX** program (van der Tak et al. (2007), `http://www.sron.rug.nl/~vdtak/radex/radex.php`) performs non-LTE radiative transfer calculations assuming an isothermal homogeneous medium under the *Statistical Equilibrium* approach, which consists in, assuming a local excitation mechanism of the gas, solving for the balance of excitation and de-excitation rates for a given state i as follows:

$$\frac{dn_i}{dt} = 0 = \sum_{j \neq i}^{N} n_j P_{ji} - n_i \sum_{j \neq i}^{N} P_{ij}, \tag{2.68}$$

where P_{ij} and P_{ji} are the destruction and formation rate coefficients of level i, and no assumption about chemical processes of the modeled species is made. The

RADEX code can handle up to seven collision partners for each species (see Table D.1 for a list of the collision partners of the modeled species in the present work) and uses atomic and molecular collisional data from the LAMBDA[9] archive (Schöier et al. (2005), http://home.strw.leidenuniv.nl/~moldata/), which allows to constrain the column densities of the observed species N, the kinetic temperature of the gas T_{kin}, and the H_2 volume densities $n(H_2)$. The program offers three options for the geometrically average escape probability of photons β as a function of opacity τ: the static, spherically symmetric, and homogeneous medium $\beta_{sphere}(\tau)$; the plane parallel slab geometry $\beta_{slab}(\tau)$; and the expanding spherical shape geometry or LVG approximation $\beta_{LVG}(\tau)$ (Mihalas, 1978; de Jong et al., 1980) shown in Equation 2.56 and used in this work. The continuum contribution to the rate equations may be composed of (1) an external component which arises outside the emitting region (CMB[10] and ISRF[11]) and (2) an internal continuum that arises within the emitting region (dust emission). The principal input parameters for the software is a grid of T_{kin}, N, and $n(H_2)$ values and the measured line width $\Delta V(FWHM)$ of the observed line. The main outputs are the excitation temperature T_{ex}, the opacity τ, and the radiation peak temperature T_R than can be directly compared to the observed antenna temperatures corrected for the optical efficiency of the telescope, under the assumption that the source fills the telescope's beam completely, namely, the filling factor equals unity. A detailed description of the **RADEX** software can be found in van der Tak et al. (2007).

[9] Leiden Atomic and Molecular Database
[10] Cosmic Microwave Background
[11] Inter Stellar Radiation Field

Chapter 3

Data Reduction

In the present chapter, I describe the data acquisition and data reduction process implemented for the observed sub-mm lines in the present work. I also briefly describe the main characteristics of the receivers involved in the data acquisition: the Herschel-HIFI and NANTEN2/SMART heterodyne receivers. Observations with the different receivers are treated separately due to the different difficulties involved in each data reduction process. I conclude with a summary of the main parameters characterizing the observations.

3.1 Herschel-HIFI Data

With the Herschel-HIFI instrument (Roelfsema et al., 2012) onboard the Herschel Satellited (Pilbratt et al., 2010), four sub-mm lines towards the Sgr A Complex were observed in the frame of the Herschel Guaranteed Time HEXGAL[1] key Program (P.I. Rolf Güsten, MPIfR): [CI] $^3P_1$ - $^3P_0$, [CI] $^3P_2$ - $^3P_1$, [NII] $^3P_1$ - $^3P_0$, and [CII] $^2P_{3/2}$ - $^2P_{1/2}$. The [NII] $^3P_1$ - $^3P_0$ and [CII] $^2P_{3/2}$ - $^2P_{1/2}$ lines have special difficulties in terms of data quality that are treated separately. The spatial distribution of the integrated intensities in the Herschel-HIFI datasets of the [CI] $^3P_1$ - $^3P_0$, [CI] $^3P_2$ - $^3P_1$, [NII] $^3P_1$ - $^3P_0$, and [CII] $^2P_{3/2}$ - $^2P_{1/2}$ transitions are shown in Figures 3.1, 3.2, 3.3, and 3.4, respectively. In the following, I describe the receiver, observing modes, and method used in the data reduction process of the Herschel-HIFI observations.

[1] Herschel EXtraGALactic

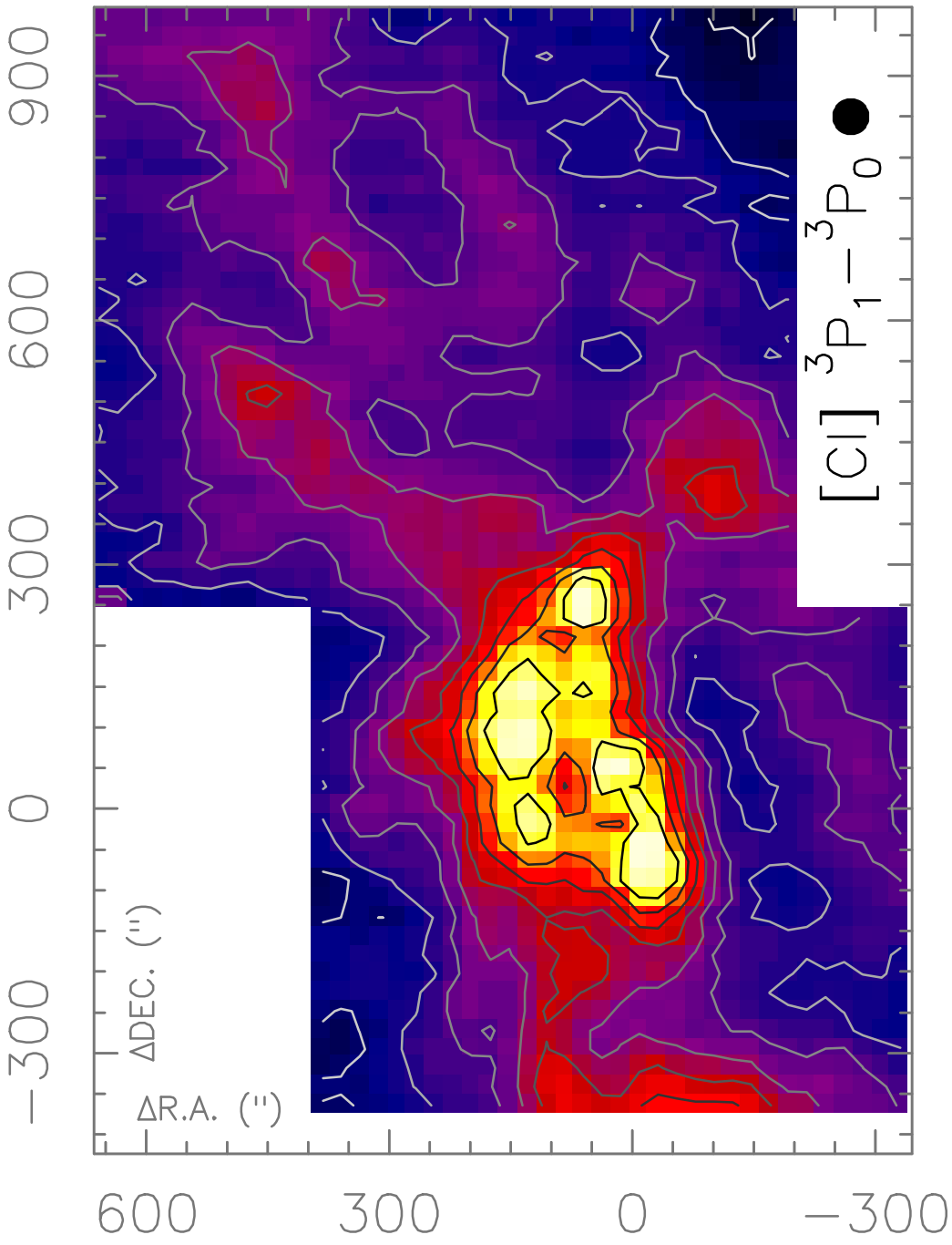

Figure. 3.1: *[CI](1-0) Integrated intensity between ±200 kms^{-1}. The ΔR.A. and ΔDEC. angular offsets are measured with respect to the position of Sgr A* in the Equatorial (J2000) coordinate reference frame. The filled black circle represents the map spatial resolution.*

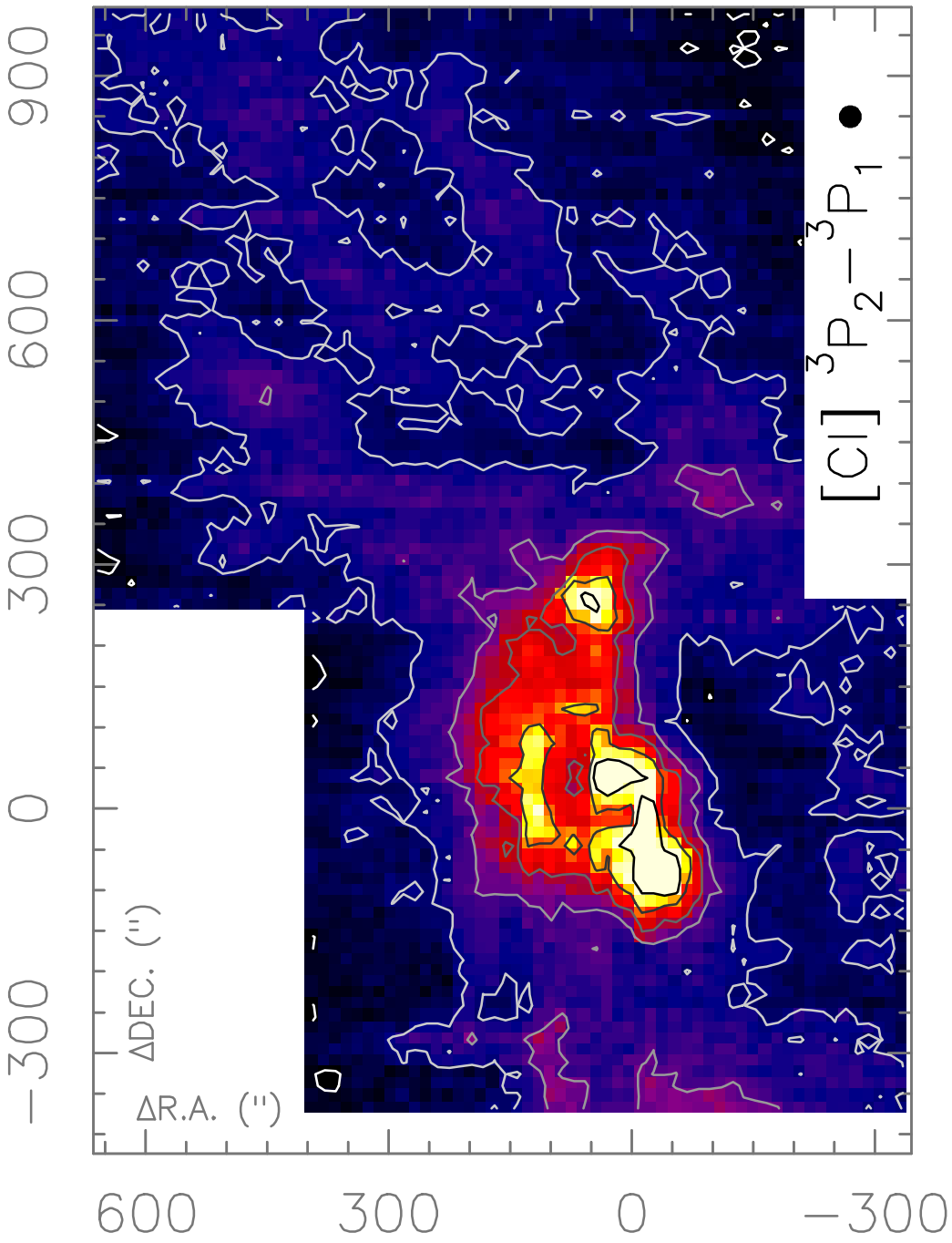

Figure. 3.2: *[CI](2-1) Integrated intensity between ±200 kms^{-1}. The ΔR.A. and ΔDEC. angular offsets are measured with respect to the position of Sgr A* in the Equatorial (J2000) coordinate reference frame. The filled black circle represents the map spatial resolution.*

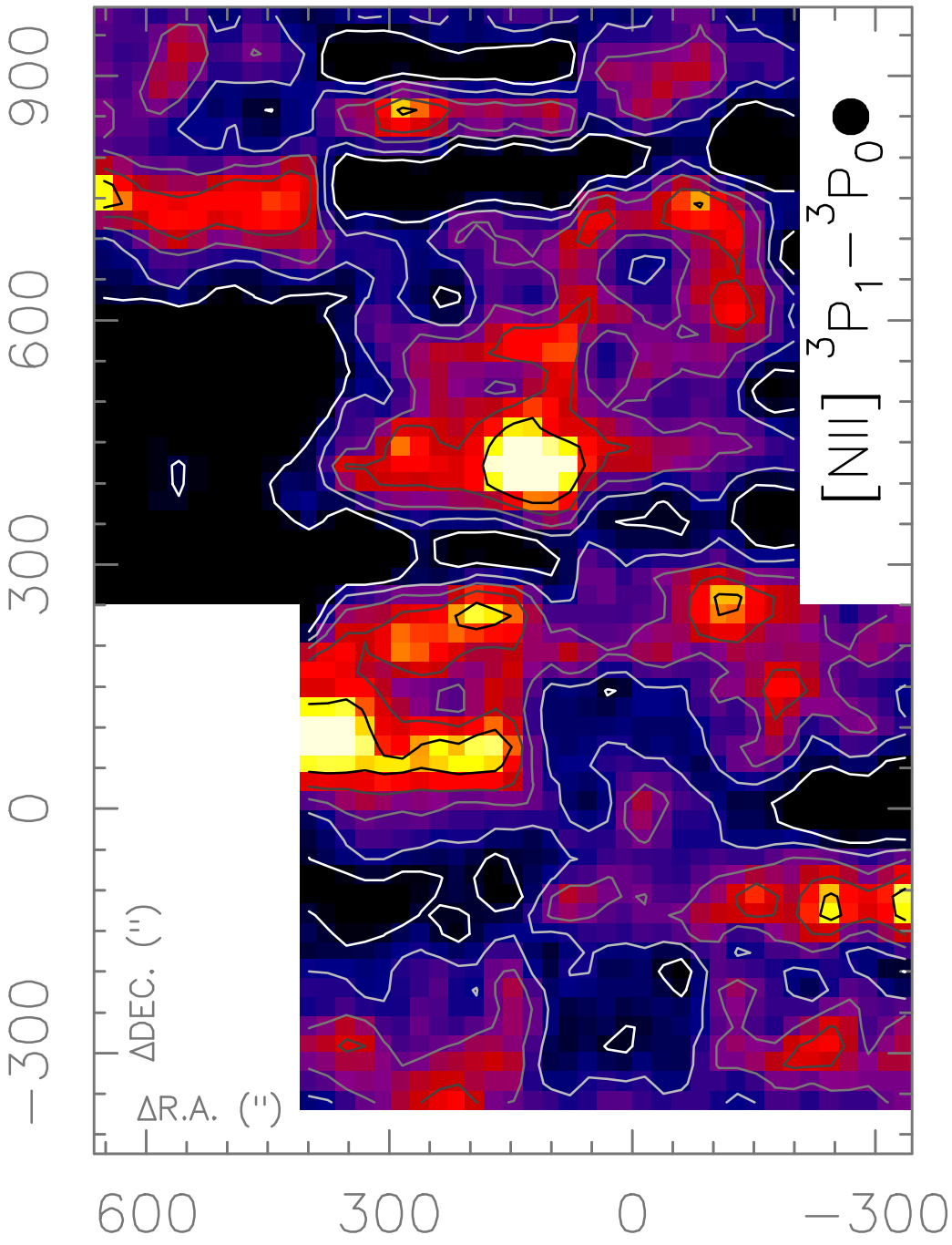

Figure. 3.3: *[NII] Integrated intensity between −200 kms^{-1} to +94 kms^{-1}. The ΔR.A. and ΔDEC. angular offsets are measured with respect to the position of Sgr A* in the Equatorial (J2000) coordinate reference frame. The filled black circle represents the map spatial resolution.*

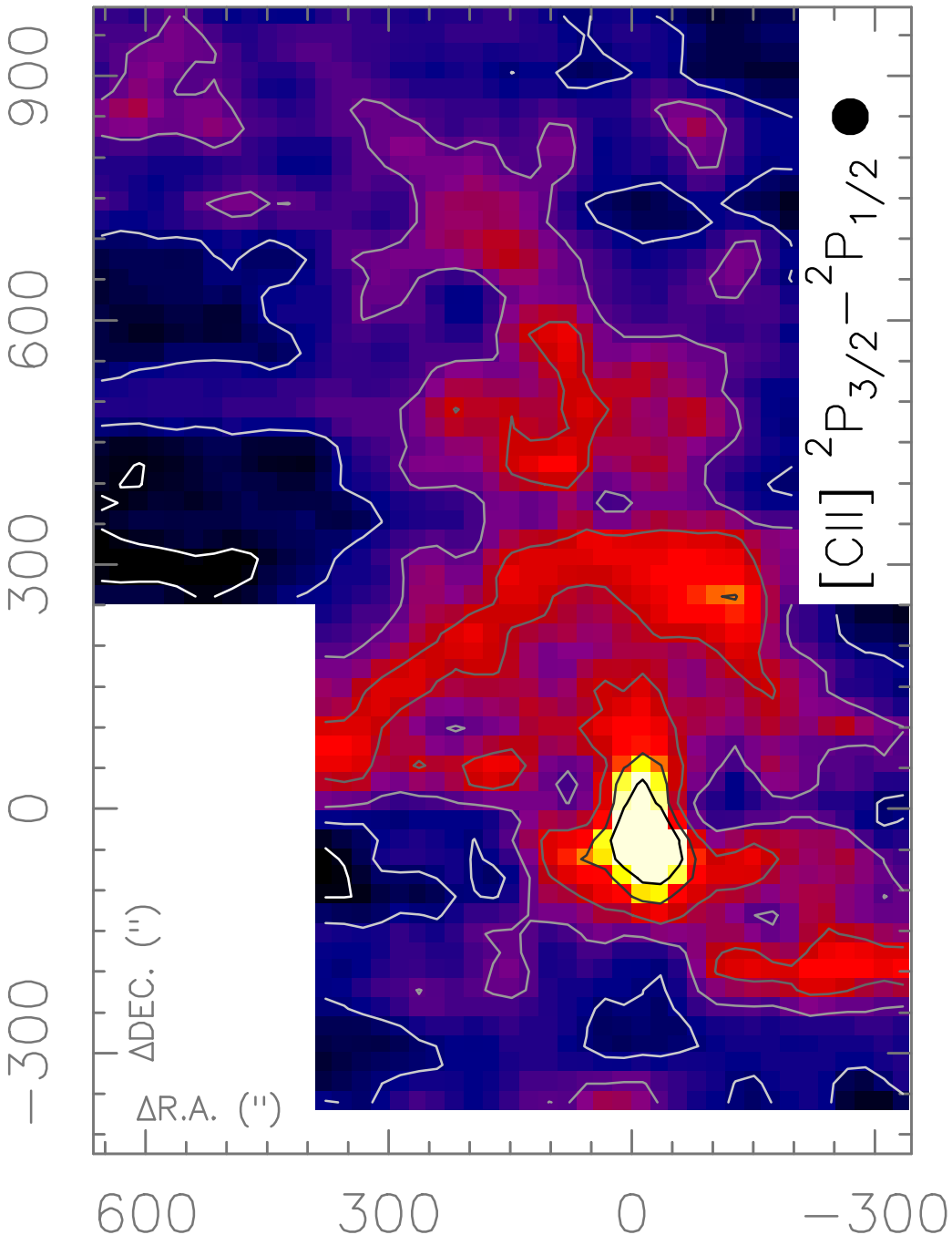

Figure. 3.4: *[CII] Integrated intensity between −200 kms^{-1} to +145 kms^{-1}. The ΔR.A. and ΔDEC. angular offsets are measured with respect to the position of Sgr A* in the Equatorial (J2000) coordinate reference frame. The filled black circle represents the map spatial resolution.*

3.1.1 The HIFI Receiver

The Herschel Heterodyne Instrument for the Far-Infrared (HIFI) is a double sideband (DBS[2]) single pixel receiver, with a total of 7 mixer bands, ranging in frequency continuously from 480 GHz to 1250 GHz and from 1410 up to 1910 GHz. The mixing devices are SIS[3] mixers for bands 1 to 5 (4 GHz bandwidth) and HEBs[4] for bands 6 and 7 (2.4 GHz bandwidth, given by state-of-the-art HEBs at the time of construction). Each band is in turn divided into 2 subbands, denoted with the letters "a" and "b", each one associated to a different Local Oscillator (LO[5]) chain, so that the total subbands available in the HIFI instrument are 7×2. The backend used for the observations of the present work consists of two Wide-Band Acousto-Optical Spectrometers (WBSs[6]), one for each measured vertical (V) and horizontal (H) polarizations. The spectral resolution of the WBS is 1.1 MHz and possesses a total bandwidth of 4 GHz. The bands 1a, 3a, 6a, and 7b, correspond to the [CI](1-0), [CI](2-1), [NII], and [CII] observed atomic transitions, respectively. The pointing accuracy of the telescope was estimated to be ~ 2". A detailed description of the receiver can be found in de Graauw et al. (2010) and Roelfsema et al. (2012), while a detailed description of the HIFI capabilities and observing modes can be found in the HIFI Observer's Manual (http://herschel.esac.esa.int/Docs/HIFI/pdf/hifi_om.pdf).

3.1.2 HIFI Observing Strategy

The Herschel-HIFI observations were carried out in Equatorial coordinates reference frame and two observing modes were used for different frequency bands: the *"OTF[7] Map With Position-Switch Reference"* observing mode for the [CI](1-0) line, and the *"OTF Map With Load Chop And Position-Switch Reference"* observing mode for the [CI](2-1), [NII], and [CII] lines. The choice between them is mainly driven by the Allan stability time of the receiver at a given frequency relative to the time spent by the instrument in measuring a single OTF line. If the stability time is larger than the OTF time, then the first observing mode is more efficient. In the other case, chopping to an internal load in a shorter time than the Allan stability time becomes necessary and the second observing mode is used. For 1 GHz bandwidth and at a resolution of 1 kms^{-1}, the Allan stability times of the HIFI receiver in these bands are: 120 s (band 1a), 40 s

[2]Double SideBand
[3]Superconductor Insulator Superconductor
[4]Hot Electron Bolometers
[5]Local Oscillator
[6]Wide-Band Acousto-Optical Spectrometers
[7]On The Flight

(band 3a), 15 s (band 6a), and 10 s (band 7b), as shown by Roelfsema et al. (2012).

For the observations of the [CI](1-0) line with the *"OTF Map With Position-Switch Reference"* observing mode, the total observed area of the map is composed by two subregions A and B. Each map consists of 33 OTF lines, with a spacing of 22.5", spanning in total 742.5" perpendicular to the scanning direction. In turn, each OTF line consists of 40 independent points, with an average spacing of 22.2", covering in total 888.0" in the scanning direction. The backend readout period ON source was set to 2 seconds and one reference position (OFF) measurement was performed every OTF line. A calibration load measurement was done after each OTF line, while the telescope slewed to the reference position.

The observations of the high frequency lines, [CI](2-1), [NII], and [CII], were performed with the *"OTF Map With Load Chop And Position-Switch Reference"* observing mode. The observations settings of the [CI](2-1) line are similar to those of the [CI](1-0) line. The total map was split into two subregions A and B. For region A, the observed map consists of 44 OTF lines, with a spacing of 14.5", spanning in total 638.0" perpendicular to the scanning direction, with each OTF line consisting of 52 points, with an average spacing of 14.4", covering in total 748.8". For region B, the observed map consists of 52 OTF lines, with a spacing of 14.5", spanning in total 754.0" perpendicular to the scanning direction. Each OTF line consists of 61 points, with an average spacing of 14.4", covering in total 878.4". In both maps, the integration time ON source was 2 s, with 1 OFF and calibration load measurement per OTF line.

In the observations of the [NII] and [CII] lines, the subregions A and B were further split into 3 sections, yielding the maps A1, A2, A3, B1, B2, and B3. In both lines, the average spacing between OTF lines (10.5") and between points of the same OTF line (10.2") is the same for all maps. For the [NII] observations, the integration time on the source was 1 s, with 1 OFF measurement each 6 OTF lines for all maps, except for B2 where 1 OFF measurement was done each 4 OTF lines. Maps A1, A2, and A3 consist of 60 OTF lines spanning in total 630.0". In maps A1 and A3, each OTF line consists of 26 independent points covering in total 265.2". In map A3, each OTF line consists of 20 independent points covering in total 204.0". The B1, B2, and B3 maps consist of 72 OTF lines spanning in total 756.0" perpendicular to the scanning direction while their OTF lines consists of 28, 29, and 26 independent points, covering in total 285.6", 295.8", and 265.2", respectively for each map. For the [CII] observations, the integration time on the ON source position was also 1 s, with 1 OFF measurement each 6 OTF lines for all "A" maps, and each 4 OTF lines for the "B" maps. Maps A1, A2, and A3 consist of 60 OTF lines spanning in total 630.0". In maps A1 and A3, each OTF line consists of 27 independent points covering in total 275.4".

In map A2, each OTF line consists of 20 independent points covering in total 204.0". The B1, B2, and B3 maps consist of 72 OTF lines spanning in total 756.0" perpendicular to the scanning direction. In maps B1 and B2, each OTF line consists of 29 independent points covering 295.8". For map B3, the number of independent point in each OTF is 28, covering 285.6".

The *"OTF Map With Load Chop And Position-Switch Reference"* is very efficient in producing integration times ON source that are shorter than the Allan stability times of the high frequency lines but, on the downside, it yields an irregular sampling pattern of the observed area leading to observed maps that are under sampled in the scanning direction, given the beam size at the observed frequency. An example of the irregular sampling pattern is shown in Figure 3.5 for the [CII] line. The figure shows the sampling pattern for the sub-regions A2 (left panel) and B2 (right panel). The absolute Equatorial coordinates of the central position (0,0) of each map are given at the top of each panel. The beam size at this frequency is 11.2", and is represented by the plotted circles. Also, both polarizations H (solid circle) and V (dashed circle) are shown. The beams of the two polarizations are shifted due to a small misalignment from the construction process, measured to be -1.0" in the "Y " and 0.0" in the "Z" focal plane coordinates of the receiver (Roelfsema et al., 2012). The angular separation between two consecutive spectra is 5.1", while the separation for the spectra immediately before and after the chop to the load is 15.3", larger than the beam at this frequency. The separation of the OTF lines in the DEC. direction is 10.5", almost the size of the beam. From the figure, it can be seen that the original measured map is under sampled in the scanning direction (R.A.) due to the used observing mode. In the DEC. direction, the map is beam sampled by construction of the observing proposal. The same sampling pattern is present in the [NII] observations though the under sampling degree is lower given the larger beam size. In the case of the [CI](2-1) line, the separations of the consecutive spectra is 7.2", and 21.6" for the spectra just before and after the chop to the load, while the angular space between OTF lines is 14.5". Given the much larger beam size of 26.2" at this frequency, the under sampled area is much less than in the previous cases.

3.1.3 HIFI Data Reduction Process

In the following, I describe the common steps for all observed lines involved in the data reduction process of the Herschel-HIFI observations. For the [NII] and [CII] datasets, and due to the presence of instabilities in the calibrated baselines, a few different steps had to be implemented in order to obtain the observations datasets. These cases are explained separately in the text.

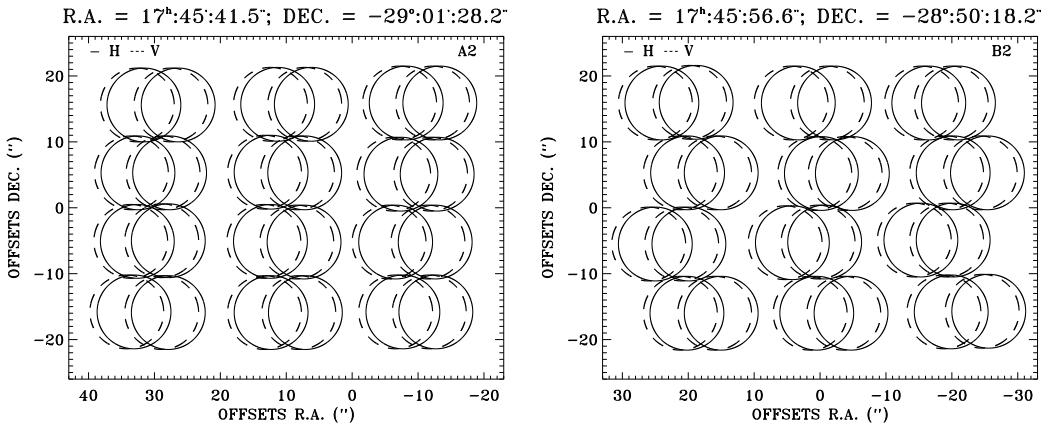

Figure. 3.5: *Examples of the [CII] observed grid in two different regions of the entire observed map. The left panel shows the sampling grid of the A2 sub map while the right panel does it for the B2 sub map. The beam size at this frequency is represented by the circle's size. In both panels, the H polarization (solid line) and V polarization (dashed line) measured positions are shown. The slight misalignment between both beams is -1.0" in the "Y " and 0.0" in the "Z" focal plane coordinates of the HIFI instrument. Due to the* "OTF Map With Load Chop And Position-Switch Reference" *observing mode used for the high frequency lines, the observed maps are under sampled.*

In general, the standard data reduction software package of the Herschel-HIFI observations (and also of the other two instruments on board the Herschel Satellite: the Photodetector Array Camera & Spectrometer for Herschel (PACS[8]) and the Spectral and Photometric Imaging Receiver (SPIRE[9])), is the Herschel Interactive Processing Environment (HIPE[10]). Nonetheless, I follow a different approach in the present work and, instead of using this very RAM and PCU capacity demanding package, for most of the data reduction process I took advantage of the widely used Continuum and Line Analysis Single-dish Software (CLASS[11]), which is part of the more extended GILDAS[12] software (https://www.iram.fr/IRAMFR/GILDAS/). This software allows compatibility with different versions of the software, something that was an issue with the consecutive releases of the HIPE versions at the time when this data reduction process took place, and an easy handle of very large datasets, making fast and easy the fitting and subtraction of baselines from the observed spectra together with a variety of different functions useful to extract the relevant information contained in the datasets such integrated intensity maps, position-velocity diagrams, etc.

Given the 4 GHz SISs bandwidth of bands 1a and 3a, the 2.5 GHz HEBs

[8]Photodetector Array Camera & Spectrometer for Herschel
[9]Spectral and Photometric Imaging Receiver
[10]Herschel Interactive Processing Environment
[11]Continuum and Line Analysis Single-dish Software
[12]Grenoble Image and Line Data Analysis Software

bandwidth of bands 6a and 7b, and the 4×1 GHz bandwidth of the WBS backend, a single spectrum of the Herschel-HIFI data is divided either into 4 subbands (for bands 1a and 3a), or 3 subbands (for bands 6a or 7b). As a consequence of a none uniform temperature inside the WBS, effects such as drifting among the 1 GHz subbands can appear. Therefore, in order to obtain the full spectrum it is necessary to stitch the subbands properly. This part of the data reduction process was performed in HIPE using the "Stitch" Task (full name *herschel.ia.toolbox.spectrum.StitchSpectrumTask*). This task takes the overlapping region among the subbands, calculates the average values in that range separately, bring them to the same continuum level, and glue the subbands together. And example of this procedure is shown in Figure 3.6 for the observed [CI](1-0) line. The colors represent the four different 1 GHz WBS subbands. The velocity resolution at this frequency is 0.305 kms^{-1}. The overlapping regions between subbands are enclosed between vertical dashed lines. The results of the stitching procedure is shown in the full spectrum (black line) on the same plot. The displacement in the continuum level towards higher antenna temperatures of the end product spectrum is artificially introduced for display purposes.

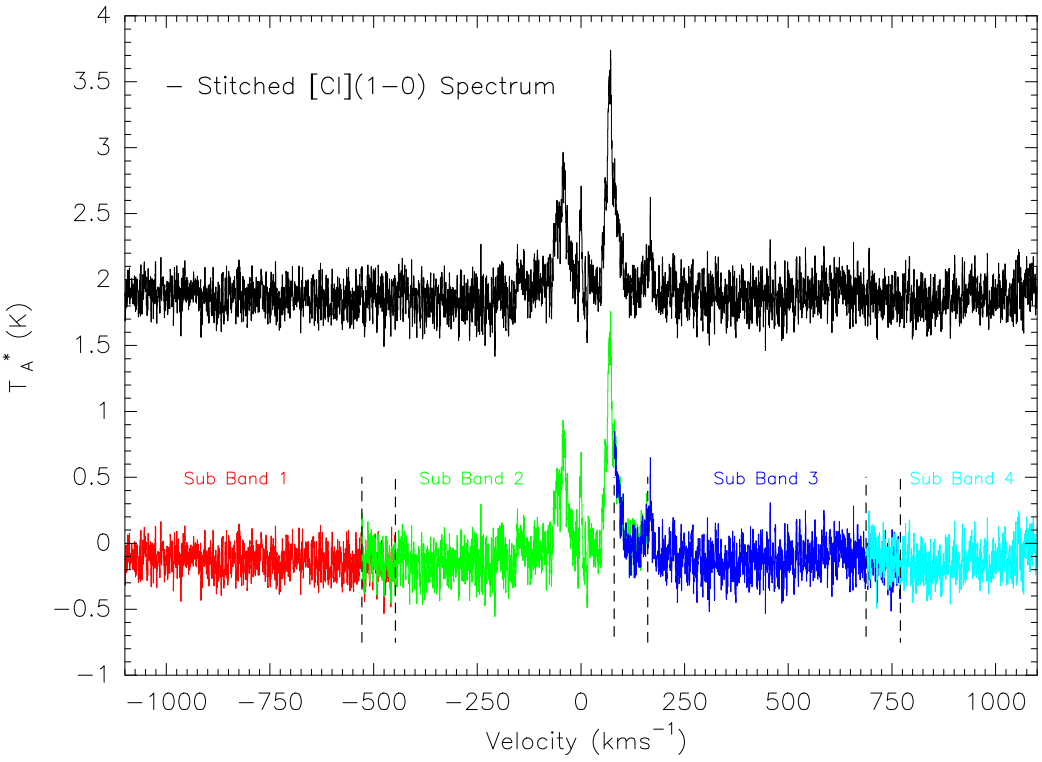

Figure. 3.6: *[CI](1-0) spectrum showing the 1 GHz wide subbands before (colors) and after (black) the stitching procedure. The dashed vertical lines encompass the overlapping spectral region between consecutive subbands. After the stitching procedure, the full spectrum is used in the data reduction process.*

After all spectra for all four observed lines were stitched together, the raw spectra were exported to CLASS compatible FITS[13] files to further continue the data reduction process in the CLASS module. This was done using the "Hiclass" task in HIPE. The temperature scale of the data after this process was in the forward beam antenna temperature scale T_A^* (see Appendix A for a definition of this antenna temperature scale).

The first step in the data reduction process using the CLASS software was to resample the spectra to the desired velocity resolution. In the case of the Sgr A Complex, and in general in the Galactic Center Region, the emission lines cover a very wide LSR velocity range, between ±200 kms^{-1}. For this reason, a 1 kms^{-1} velocity resolution was chosen. This velocity resolution ensures that the emission lines are still spectrally resolved, increasing at the same time the signal-to-noise ratio of the spectra, given the higher spectral resolution of the original data (see Table 3.1 for the original spectral resolution of the different lines).

The baseline subtraction for each spectrum was done using the "base" function in the CLASS software. The function requires the definition of LSR velocity windows to be excluded of the base line fitting procedure. The line emission is enclosed inside the selected LSR velocity windows so only the continuum level is fitted and subtracted from the original spectrum, leaving the line emission alone. The selection of the LSR velocity windows was done for each OTF line individually, and applied for all spectra within the same OTF line. Even tough the emission varies significantly across a single OTF line, the large LSR velocity coverage of the 4 GHz bandwidth, specially in bands 1a and 3a, and the excellent stability of the baseline, allowed to select a single velocity window for a given OTF line, and apply it to all spectra within the same OTF line. In this way, the "base" function fits a polynomial of order "n", with "n" between 1 and 3 for the datasets in the present work, and subtracts the fitted function from the original spectrum, removing the continuum level and characterizing the spectrum with a corresponding noise level calculated as the rms[14] noise temperature ($T^*_{A,rms}$) in the region outside the defined LSR velocity windows. Usually, spectra that have anomalies in their baselines can be discarded by setting a threshold in the $T^*_{A,rms}$ value tolerated for the data. Given the excellent stability of the Herschel-HIFI receiver in bands 1a and 3a, none of the spectra were discarded. The baseline fitting procedure for the [NII] and [CII] lines, in bands 6a and 7b respectively, has different difficulties that required a slightly different treatment of the LSR velocity windows selection and the setting of a $T^*_{A,rms}$ threshold in order to discard some spectra with bad baselines. Unfortunately, the HEB mixers in bands 6a and 7b present what seems to be a reflection in the electrical amplification

[13] Flexible Image Transport System
[14] root-mean-square

chain which leads to distortion of the baselines in the spectra measured at this frequencies (Higgins , 2011). In the following we address the impact of such electrical perturbation in the measured data and the procedure define to minimize the impact on the final datasets:

- **The [NII] line**: in band 6a, the spectra present a baseline oscillation at one edge of the bandpass, between +94 kms^{-1} and +170 kms^{-1}, in both V and H polarizations. This perturbation is shown in Figure 3.7, as a red line in the same LSR velocity range. The spectrum shown is the average spectrum of the H polarization over the whole dataset. Unfortunately, given the very wide velocity dispersion of the line, this perturbation affects regions of the bandpass where emission is present. The exact origin of such anomaly is still not clear until the date of the present work, but a preliminary analysis points at a jump in the power level of the LO of this band. In order to minimize the impact of this oscillation on the final dataset, before subtraction the baseline from the spectra, the average T_A^* value between +94 kms^{-1} and +170 kms^{-1} was calculated and assigned to the measured antenna temperature. The result of this procedure is shown as a black dashed line in the same figure. The baseline fitting in this case is difficult since the continuum level of the line is artificially changed by setting the measured antenna temperatures to the calculated average value. I investigated the effect of a polynomial of order 0 and 1 subtracted from the data and the best results were obtained with the latter, so I adopted that value for the baseline fitting of all spectra. Higher polynomial orders are not suitable given the source line width-to-bandwidth ratio at this frequency ~ 0.5. In this way, the useful LSR velocity extent of this dataset comprehends from -200 kms^{-1} to +94 kms^{-1} only.

- **The [CII] line**: in band 7b, the V polarization HEB mixer suffers from a too high LO power pumping which yields an impedance mismatch between the mixer and the first LNA[15] as shown by Higgins (2011). Since both polarizations share the same LO chain, optimizing the LO power for one of the polarizations yields unavoidable the other polarization to get either a too low (in the case of the H polarization HEB mixer) or too high (in the case of the V polarization HEB mixer) LO power. In the Herschel-HIFI observation scheme, it was decided to operate the H polarization HEB mixer at their optimum level, namely, at a mixer current of 0.045 mA, and the V polarization mixer current was left to follow (Higgins , 2011). As a consequence, some of the V polarization spectra present large distortions of their baselines.

[15]Low Noise Amplifier

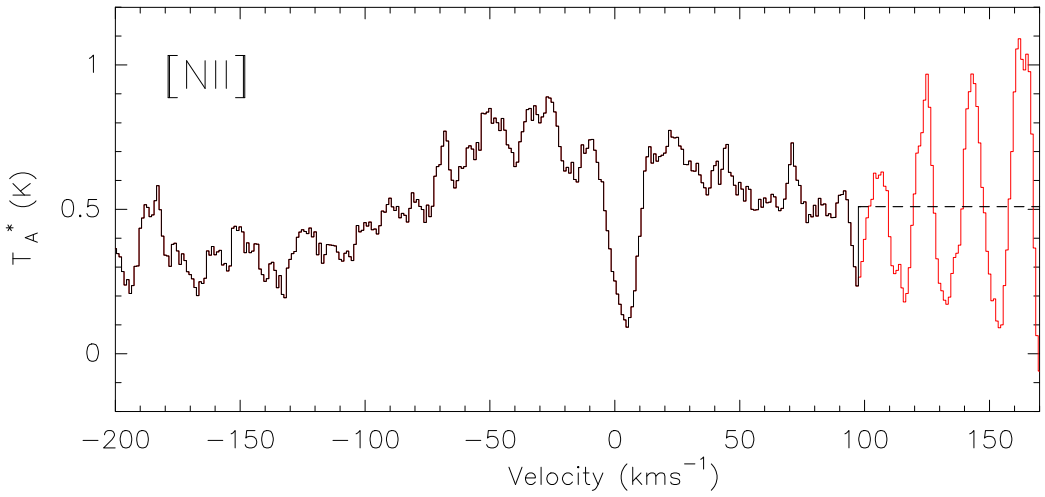

Figure. 3.7: *[NII] average spectrum of the V polarization observations over the whole map. The red line signalizes the distortion of the baseline between +94 kms^{-1} and +170 kms^{-1} present in all the spectra. The dashed line over the same LSR velocity interval shows the result of the method utilized in getting rid of the distortion by replacing the measured antenna temperatures by their average value within the same LSR velocity interval.*

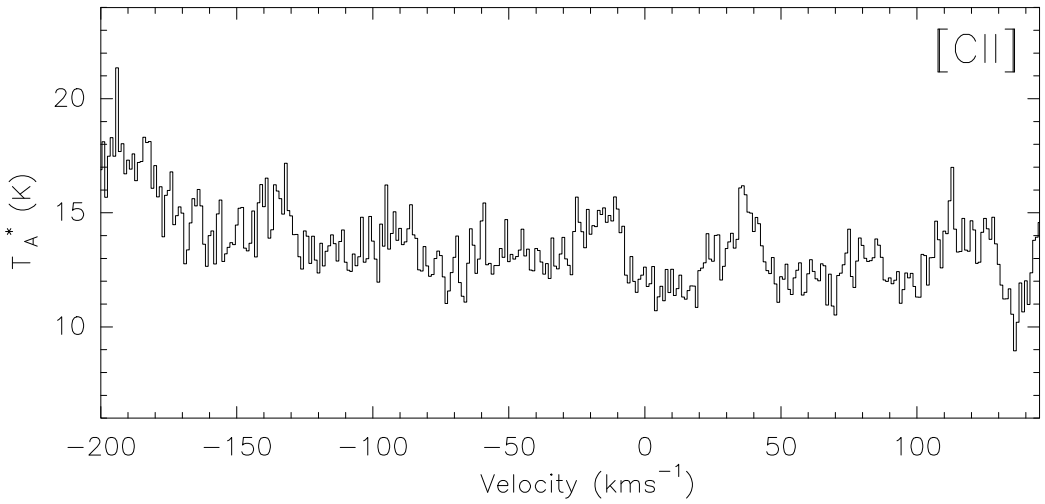

Figure. 3.8: *[CII] average OTF line of the V polarization spectra. The curvature of the average spectrum together with the distortion of the baseline across the bandpass are the product of an overpump of the V polarization mixer due to a too high LO power (Higgins , 2011). Such spectra were filtered out by setting the $T^*_{A,rms}$ threshold to 2.3 K.*

An example of the V polarization spectra is shown in Figure 3.8. The figure shows the average spectrum of one OTF line measured in the B1 sub map ($\delta(J2000)$ offset = +236.3"). Given the very large line width of the emission, usually extending from −200 kms^{-1} to +200 kms^{-1}, and the small velocity coverage of the 2.5 GHz bandwidth at this very high

frequencies ($\sim$ 400 kms^{-1}), it is impossible to make use of the spectra that present such baselines distortions. Therefore, a $T^{*}_{A,rms}$ = 2.3 K threshold was implemented to filter them out from the V polarization dataset. This threshold produced that $\sim$ 25% of the observed spectra in the V polarization were filtered out. Currently, there is a development of a new pipeline to improve the data quality of the measured V polarization spectra by removing the distortion of the baselines, but this is still work in progress and this is not expected to be finished before 2016.

3.1.4 Emission Contamination in the Reference Position

The four lines observed with the Herschel-HIFI receiver in the present work suffer from contamination in the reference position. This occurs when the emission of an astronomical sources is so extended that a clean reference position can not be found within a few arcminutes of the source's position, which is necessary due to time stability arguments of the receiver. Ideally, the clean reference position should be as close as possible to the observed region, so the time difference between the ON source and OFF measurements is kept small. The emission contamination in the reference position causes that some of the emission in the observed map is subtracted from the data, modifying the observed line shape of the emission artificially. The case of the Galactic Center is a standard case of very extended emission where finding a clean position close to the Galactic Center at l = 0°.000, b = 0°.000 is nearly impossible. In the case of the Herschel-HIFI observations, they all share the same OFF position at $\alpha(J2000) = 17^{h}$ 44' 33", $\delta(J2000) = -28°$ 52' 08", while the center of the maps is located at $\alpha(J2000) = 17^{h}$ 45' 39.9", $\delta(J2000) = -29°$ 00' 28.1", yielding an average angular distance between the ON source and OFF measurement of $\sim$ 8'. The average angular distance between the ON source and OFF position guarantees that both measurements are carried out with the receiver at almost the same stability conditions, but as a drawback, it also yields the contamination of the reference position in all four observed lines. An example of emission contamination in the reference position affecting the measured spectra is the large emission dip in the center of Figure 3.7. In order to account for the subtracted emission from the data, we modeled the emission at the reference position and added it back to each individual spectrum. The full procedure is explained in detail in Appendix B.

After the baseline subtraction and OFF emission recovery processes were performed, all datasets were brought to their final spatial resolution using the Grenoble Graphic (GREG[16]) software, also part of the GILDAS package. The

[16]Grenoble Graphic

spatial resolution of the [CI](1-0) and [CI](2-1) datasets, 46" and 26.7" respectively, is slightly higher than the beam size ~ 6% (for beam sizes of 43.1" and 26.2", respectively) due to the Gaussian convolution kernel of size one-third of the telescope beam width. The spatial resolution of the [NII] and [CII] data were set to the spatial resolution of the [CI](1-0) dataset to improve the signal-to-noise ratio. The $T^*_{A,rms}$ noise distribution of all Herschel-HIFI datasets are shown in Figure 3.9. The figures shows for each line: the spatial distribution of the noise (color scale) and the corresponding $T^*_{A,rms}$ noise histogram on top of the spatial map. As expected, the $T^*_{A,rms}$ noise at the edges of all spatial maps is higher than in the inner parts due to the smaller amount of spectra used by the convolution process to calculate the corresponding spectrum at a given grid position. In the histograms, a Gaussian fit was performed to the histograms to characterize the noise distribution of the datasets. The typical noise of the datasets is taken to be the Gaussian center C_{fit}, and the standard deviation σ_{fit} of the distribution is also given. All relevant parameters of the final datasets are summarized in Table 3.1.

3.2 NANTEN2/SMART Data

Complementary observations of the CO(4-3) line towards the Sgr A Complex were carried out with the NANTEN2/SMART Telescope. Other sub-mm observations such as the [CI](1-0) line were carried out to obtain a cross calibration between the Herschel-HIFI and NANTEN2/SMART observations. The spatial distribution of the integrated intensity in the NANTEN2/SMART dataset of the CO(J=4-3) transition is shown in Figure 3.10. In the following, I describe the receiver, observing modes, and method used in the data reduction process of the NANTEN2/SMART observations.

3.2.1 The SMART Receiver

The Sub-Mm Array Receiver for Two frequencies (SMART) is a DBS 2×8 pixel heterodyne receiver operating at 460 GHz and 810 GHz frequencies simultaneously. The tunable range of the two frequencies spans from 435 GHz to 495 GHz for the 460 GHz channel, and from 795 GHz to 880 GHz for the 810 GHz channel, with an intermediate frequency (ν_{IF}) of 4 GHz and 1.5 GHz, respectively. The mixing devices are 4 GHz bandwidth SISs mixers for both channels. During the data acquisition campaign, two different backends were used: Acousto-Optical Spectrometers (AOSs[17]) and eXtended bandwidth Fast

[17] Acousto-Optical Spectrometers

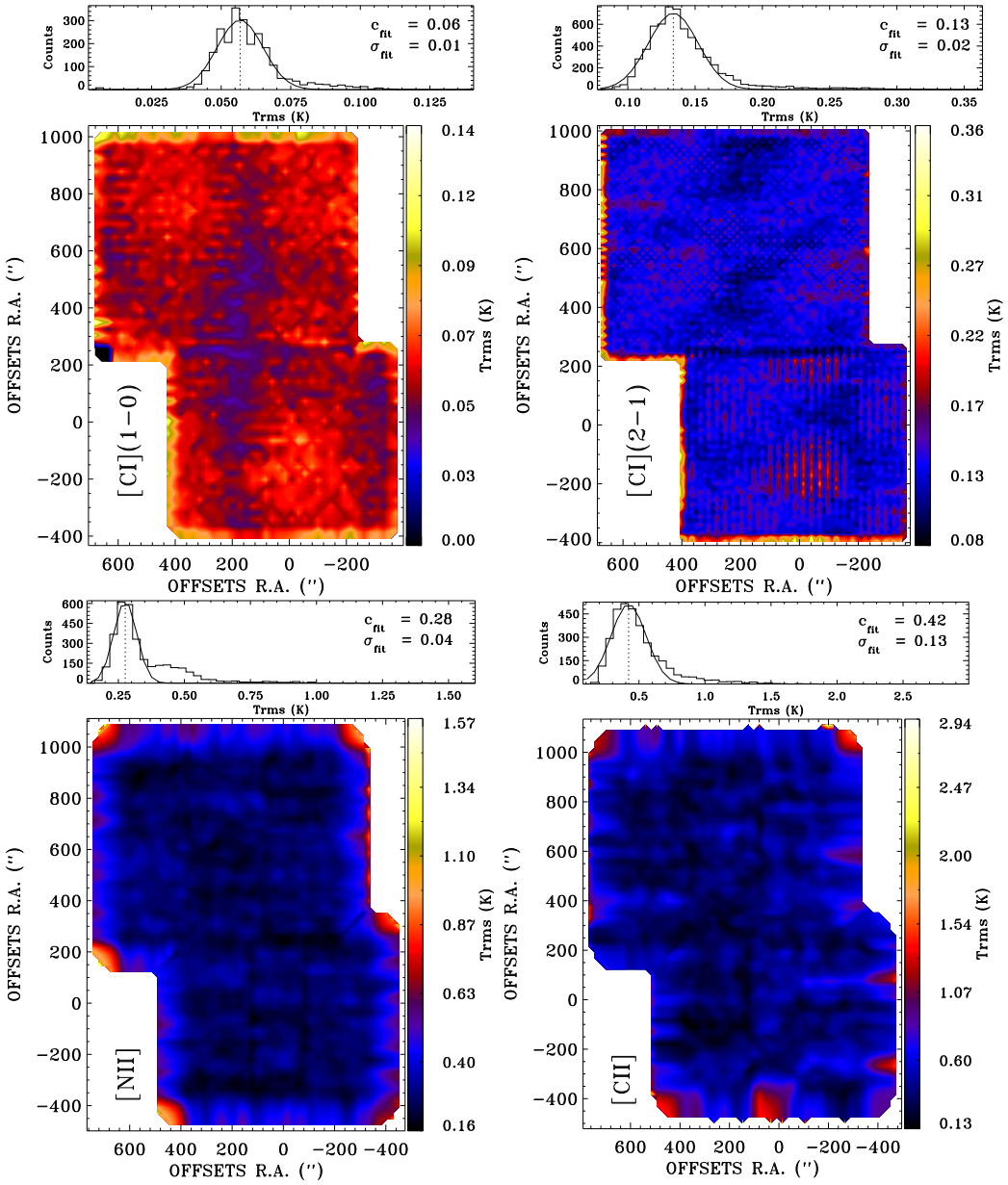

Figure. 3.9: *[CI](1-0), [CI](2-1), [NII], and [CII] $T^{*}_{A,rms}$ noise distributions. For each panel, the spatial noise distribution as well as the histogram of the noise distribution is shown. The spatial maps are centered at $\alpha(J2000) = 17^{h}\ 45'\ 39.9''$, $\delta(J2000) = -29°\ 00'\ 28.1''$. From the spatial maps, the noise is higher at the edges of the maps, as expected, given the fewer spectra at the borders to calculate the resampled spectrum. From the histograms, a Gaussian fit (solid curve) shows the typical noise of each map C_{fit} (Gauss center shown as a vertical dashed line) and the standard deviation of the distributions σ_{fit}.*

Fourier Transform Spectrometers (XFFTSs[18]). The AOSs were used from the

[18] eXtended bandwidth Fast Fourier Transform Spectrometers

beginning of the data acquisition campaign until August 2013. They posses a 1 GHz bandwidth with 1.04 MHz spectral resolution corresponding to 0.68 kms^{-1} at 460 GHz. About 75% of the data were observed using the AOSs as backends before switching to the new XFFTSs. The area observed with the AOSs backends comprehends from −650" to +100" in Galactic latitude offsets, and from −900" to +900" in Galactic longitude offsets as seen in Figure 3.13. The XFFTSs were installed on September 2013. They posses a total bandwidth of 2.5 GHz and a spectral resolution of 88.5 KHz, corresponding to 0.05 kms^{-1} at 460 GHz. The area observed with these state-of-the-art backends comprehends from +100" to +450" in Galactic latitude offsets, and from −550" to +900" in Galactic longitude offsets. With both backends, we measured essentially the same antenna temperatures within calibration errors. This is shown in Appendix C where the measured antenna temperatures by the AOSs and XFFTSs are compared. The typical pointing error of the 4 m NANTEN2/SMART telescope was within ∼ 10".

3.2.2 SMART Observing Strategy

The observations of the CO(4-3) line were carried out in the Galactic coordinates reference frame using the OTF observing mode and with an array angle of 0°. Since the SMART receiver is an array, the sampling spacing is mainly driven by the angular separation of the pixels on the sky and the beamsize of the telescope at the observed frequency. The latest update of the telescope pointing model, namely, the determination of the Nasmyth rotation constants, yielded an angular separation between consecutive pixels of ∼ 85" in both "X" and "Y" focal plane coordinates (projected on the sky). Since the receiver detects the sky signal at 460 GHz and 810 GHz simultaneously, the sampling spacing is driven by the high frequency beamsize, which is 24.5" at 810 GHz. Therefore, and in order to guarantee a Nyquist sampled map, the sampling spacing was chosen to be 8.5". This spatial sampling gives origin to the basic sampling unit of the SMART receiver called *"footprint"*. A footprint is a map of 340"×170" (or in terms of the pixel separation (4×85")×(2×85")) that is Nyquist sample at 810 GHz and oversampled at 460 GHz, which helps to further increase the signal-to-noise ratio of the lower frequency line after spatial resampling to the angular resolution consistent with the beamsize. The integration time ON source per OTF spectrum was set to 3 s. This is mainly due to the Allan stability time (Allan , 1966) estimated for the receiver. The spatial sampling together with the integration time ON source per spectrum implies a total of 30 s per measured OTF line, short enough so the Allan stability time at the high frequency channel is not exceeded. After each OTF line an OFF position measurement was performed, and a calibration load measurement was done every two OFF measurements. Under normal circumstances, the total time spent in a single footprint with the

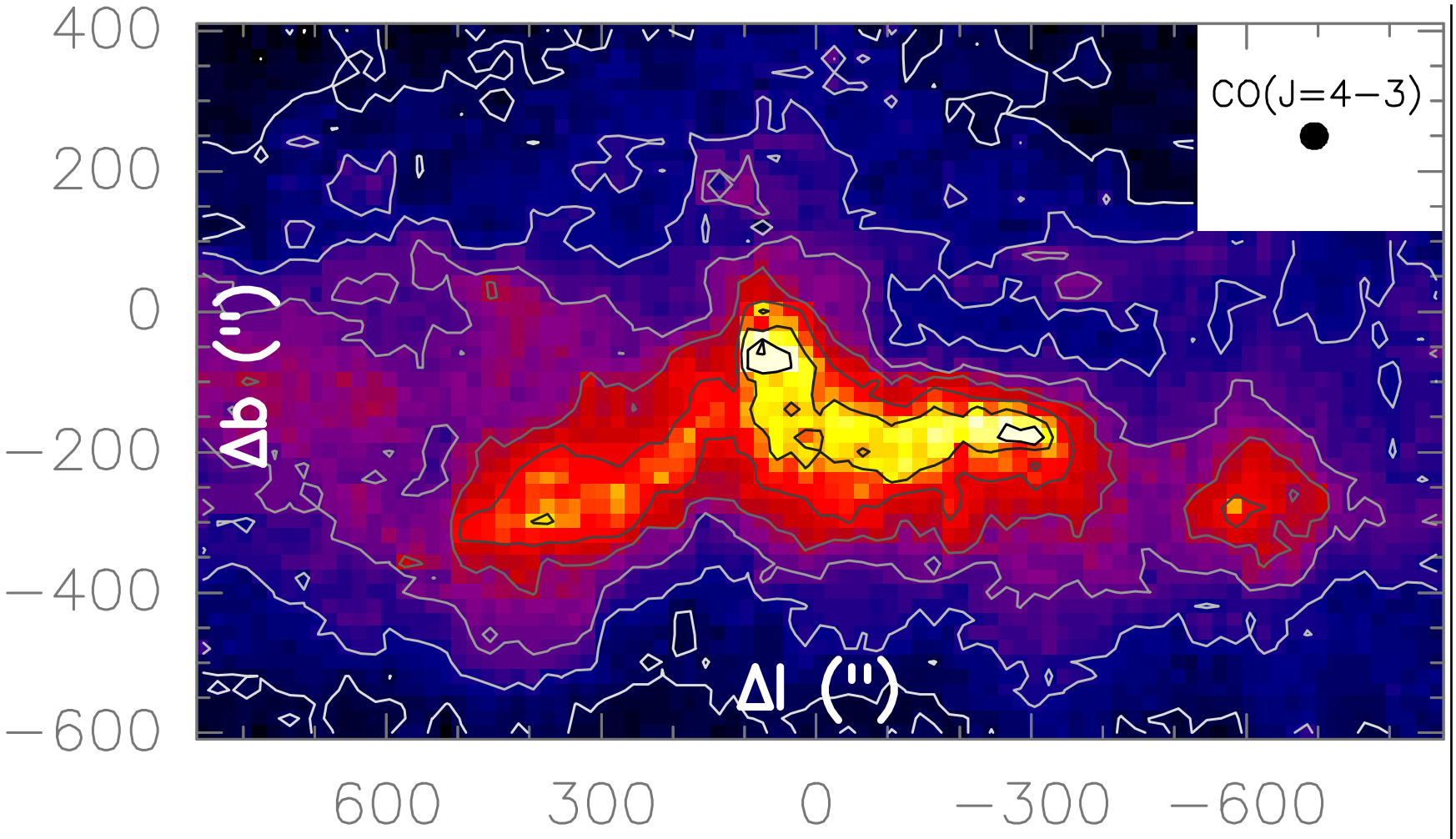

Figure. 3.10: *CO(4-3) Integrated intensity between ±200 kms^{-1}. The Δl and Δb angular offsets are measured with respect to the origin of the Galactic coordinates reference frame. The filled black circle represents the map spatial resolution.*

previous mentioned setting was ~ 25 minutes.

The identification of a clean reference position for the observations is a major problem for large scale surveys of the Galactic Center. As previously mentioned, all Herschel-HIFI observed lines suffered from emission contamination in the reference position that could be recovered largely because the receiver has only one pixel and no atmosphere had to be taken into account for the data calibration process. In the case of the NANTEN2/SMART observations, the picture is much more complicated since, during the OFF measurement, each of the eight pixels at 460 GHz is pointing through the atmosphere, at a different position on the sky separated by 85". This means that not only a single clean position has to be found to be used as a reference but a whole area. This difficulty inherent to both, the observed source and the receiver array, set a constrain to the selected reference position to be very far from the Galactic Center, in order to guarantee a clean reference position for all pixels simultaneously. Therefore, and based on the CO(2-1) observations of Sawada et al. (2001), the $l = +0°.497$, $b = +0°.980$ position was chosen. This position is located ~ 1° away from the Galactic Center at $l = 0°.00$, $b = 0°.000$. In order to check if, despite of the location of the reference position, there was still emission contamination, we observed the reference position against an even further OFF position previously checked for emission contamination. The observations showed no emission in a footprint scale containing the position of the eight pixels at the reference position, at least down to a $3\times T^{*}_{A,rms}$ significance level. A detailed description of the procedure is presented in Appendix B.

Unfortunately, selecting a position far away from the astronomical source has also some major drawbacks, specially in terms of the receiver stability and airmass between ON source and OFF measurements. As a product of these difficulties, major baseline distortions appear in the calibrated spectra, which makes the observing efficiency defined here as the ratio between the number of selected spectra after the data reduction process, divided by the total amount of spectra, very low ~ 0.4. On top of this, the extreme weather conditions at the telescope site, nearly 5000 m altitude in the Chilean Andes, the extreme dry conditions of the site which make the electronics very difficult to cool down, and the very high frequencies at which the receiver operates, make the overall data acquisition process a very challenging task.

3.2.3 SMART Data Reduction Process

The data reduction process of the NANTEN2/SMART CO(4-3) observations is divided into two major stages. The first stage, comprehends the standard data

reduction process starting with defining the antenna temperature scale that is going to be used and ending with the baseline subtracted spectra, dropping out the continuum information, so the line intensity information can be analyzed. The second stage is related to filter out spectra that have distorted baselines due to the several difficulties involved in the data acquisition process, among them: (a) a far reference position ($\sim 1^\circ$ from the central position of the observed map) selected to avoid emission contamination of all eight pixels at 460 GHz; (b) the extreme weather conditions at the telescope site make it difficult for the electronics to properly cool down due to the very low water vapor in the ambient causing a very inefficient heating exchange with the ambient, leading to damage of some parts of the electronic equipment, for instance, the LO chain; and (c) instabilities in the electronic system given the high frequencies at which the receiver is operated. Finding the spectra that present problems in their baselines in an automatized way is not a trivial task, and it requires the implementation of fully automatic selection filters that allow to get rid of them. Of course, an identification by eye of such spectra is possible, but given the more than 10^5 spectra processed, that approach is just unfeasible. In the following, we describe both stages of the data reduction process:

3.2.3.1 Data Reduction Process: First Stage

The first step in data reduction process is to produce antenna temperature calibrated spectra out of the measured raw "counts" stored in FITS format files. In order to do so, the *kalibrate* module of the *Kosma Software* is used (see Appendix A for a detail explanation on the calibration process). The *Kosma Software* is the control software of the NANTEN2/SMART telescope and has been developed over the last 20 years at the I. Physikalisches Institut of the University of Cologne, Germany. Nowadays, it is operated successfully in ground based (3 meter KOSMA telescope, now at the Yangbajain Astronomical Observatory, China) and the SOFIA observatory). The output of the *kalibrate* module is a CLASS compatible file. In CLASS, the spectra were brought to the forward beam antenna temperature scale T_A^* (see Appendix A for a definition of this antenna temperature scale).

In order to fit a baseline for each spectrum in CLASS, given the large extent of the observed region and the very changing emission profiles, the total observed area was divided into 100"×100" subregions to define a common LSR velocity windows and polynomial order for all spectra within a subregion. Usually, and because of the reasons previously mentioned, several spectra have very distorted baselines, so in order to properly set the LSR velocity windows and define the order of the polynomial to be fitted for the baseline subtraction, I selected the spectra, within the 100"×100" map, that had the flattest baseline as templates

for the definition of the baseline fitting parameters for the sub region. **This is the most crucial step in the whole data reduction process because: (a) an average spectrum is calculated from the selected spectra to define the LSR velocity windows and polynomial order that will be use for the baseline subtraction of all spectra within the 100"×100" map; and (b) the selected spectra are used in the second stage of the data reduction process to generate the statistics that allow to filter out spectra with baseline distortion that could not be filtered out in any other way**. In Figure 3.11, an example of a selected 100"×100" subregion is shown. From the figure, it can be seen that some spectra show large baseline distortions. In this particular case, the spectra with observation numbers between 841 and 1564 were selected to construct the average spectrum for selecting the LSR velocity windows and setting the polynomial order for the baseline subtraction of all spectra in the subregion.

With the two parameters for the baseline subtraction already defined (LSR velocity windows and polynomial order) for the average template spectrum, a baseline is fitted and subtracted from the spectra. After this procedure, it is decided whether a spectrum is kept in the dataset based on three parameters: (1) $T^*_{A,rms}$ noise calculated in the baseline fitting procedure, (2) signal sideband atmospheric opacity τ_s obtained from the calibration process during the removal of the atmospheric contribution to the spectrum, and (3) the system temperature T_{sys} that contains information of the receiver temperature T_{REC} and atmospheric opacity, quantifying the whole performance of the receiver, from frontend to backend. Usually, spectra taken under poor weather conditions, or with the receiver not properly tuned will deviate from some expected values in this three parameters, so they can be discarded. Typical values for these three parameters in the data reduction process of the NANTEN2/SMART data were T_{rms} = 2 K, τ_s = 0.7 (which implies an attenuation of the sky signal by the atmosphere of about 50%), and T_{sys} = 800 K. Any spectrum which at least one of the three parameter above the corresponding thresholds was discarded.

3.2.3.2 Data Reduction Process: Second Stage

After all spectra measured under not very good weather conditions or with the receiver not optimally tuned were discarded, there are still many spectra which, having passed all three excluding criteria previously mentioned in the Section 3.2.3.1 ($T^*_{A,rms}$, τ_s, and T_{sys}), present large anomalies in their baselines. In the following, the problem of the baseline distortion is explained in detail and an empirical solution is given to filter out the spectra presenting such baselines anomalies.

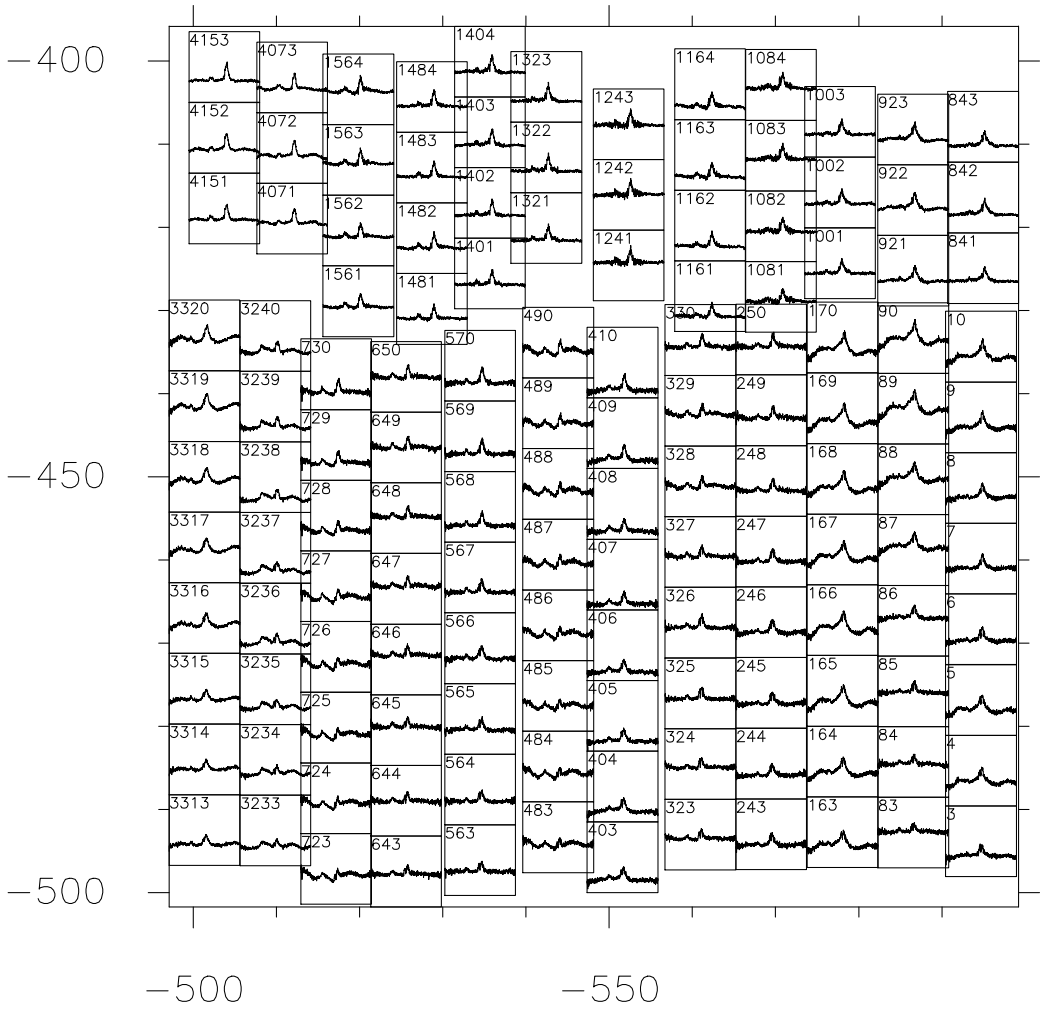

Figure. 3.11: *Example of a selected 100”×100” subregion from the NANTEN2/SMART CO(4-3) observations for the data reduction process. The observation number of each spectrum is shown within each cell (see the text for details).*

3.2.3.2.1 Baseline Anomalies A typical case of baseline distortions is shown on the lower left panel of Figure 3.12. The twenty spectra shown in the figure were measured in two consecutive OTF lines, with an OFF position measurement before each OTF line, and a calibration load measurement immediately before the first OFF. The spatial sampling is 8.5” with an integration time of 3 s ON source. All spectra were measured with the same pixel NANTEN2-A07. As can be clearly seen from the measured OTF lines, the baselines shapes change drastically over the scan, which is not to be expected since the spatial sampling is less than one fourth of the beamsize. The scanning direction goes from −240” to −180” in Galactic longitude offsets. Since the baseline distortions appear at random positions in the scans, they can not be attributed to a too large time difference between the ON source and OFF integrations. One of the main difficulties that such baseline distortions produce is that, given the very large line widths of the

observations towards the Sgr A Complex, it is difficult to discard whether the distortion is indeed an artifact or it is a real emission feature. This is why, and in order to distinguish between both cases, it is necessary to always consider a spatial region large enough (in our case 100"×100", or ∼ 4×beamsize at 460 GHz), so neighboring spectra can be compared. If the distortion is treated as a standard optical standing wave, for a period of ∼ 250 kms^{-1}, the cavity length between the detector and the reflection surface is of the order of 40 cm which is too short for any characteristics length in the optical path of the telescope. If the distortion is not related to reflections in the optical path but rather to reflections in the transport of the signal traveling along electronic cables, a more realistic propagation velocity would be around half of the speed of light, yielding a cavity length (or rather cable length in this case) of the order of 20 cm. This would put the origin of the interference inside the SMART cryostat or in the IF[19] processing unit. Given the very far away reference position adopted for the NANTEN2/SMART observations, instabilities created from the constant movement of the telescope between the ON source and OFF position can not be discarded, but preliminary analysis of observations of other sources, with reference positions of the order of a few arcminutes, seem to show the same behavior. So far, the origin of the interference remains unknown, and there is ongoing work to solve the problem.

The upper left panel of Figure 3.12 shows two spectra (S1 and S2 in the OTF scans below) for a more detail comparison between flat (black) and distorted (red) baselines. The difference between baselines results evident. Both spectra were measured under extreme good weather conditions with τ_s = 0.19, and with the receiver properly tuned as seen in the common system temperature of T_{sys} = 667 K. The vertical solid lines in the figure show and example of the LSR velocity window selection. After a polynomial of first order is fitted and subtracted from both observations, the resulting spectra are shown on the right panel of Figure 3.12. As shown in the figure, the calculated noise values outside the LSR velocity window are 0.31 K and 0.89 K for the flat and distorted baseline spectra, respectively. Although the noise level of the baseline distorted spectrum is around three times the one of the flat baseline spectrum, a 0.89 K noise level is quite decent for a single spectrum at these frequencies. Based on its $T^*_{A,rms}$, τ_s, and T_{sys} parameter values, it is not possible to reject spectrum S2 automatically unless a visual inspection of the spectrum is done. The large amount of spectra (above 10^5) obtained during the data acquisition campaign makes such a visual inspection, in a case by case basis, impossible. Therefore, I developed three filters to discard such spectra in a fully automatized way. This procedure is describe in the following section.

[19]Intermediate Frequency

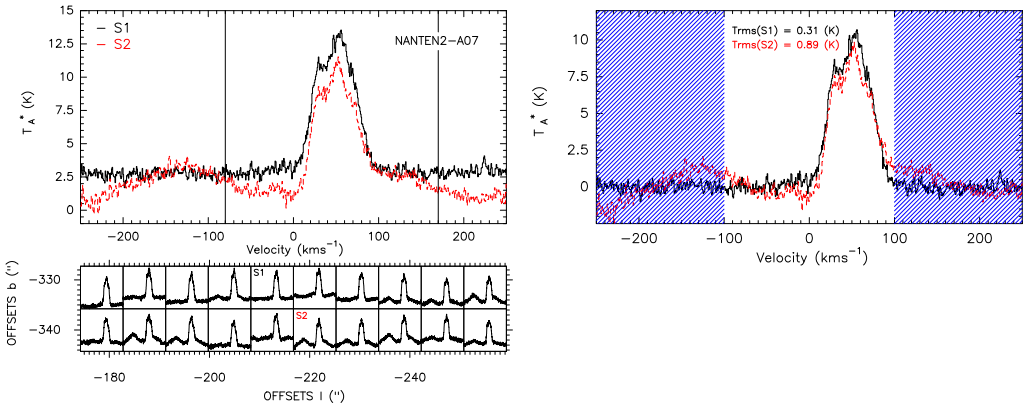

Figure. 3.12: *Left lower panel: CO(4-3) OTF lines showing typical baseline distortions. Left upper panel: S1 and S2 spectra selected from the OTF lines for comparison. The solid vertical lines show the LSR velocity windows selected for the baseline subtraction in both cases. Right panel: S1 and S2 spectra after the baseline subtraction. The dashed area exemplifies the velocity ranges in which the implemented filters for the second stage data reduction process were calculated.*

3.2.3.2.2 Filters: In order to remove the spectra with baseline distortions that were not filtered out by the $T^*_{A,rms}$, τ_s, or T_{sys} criteria, three consecutive filters were implemented. The LSR velocity range, where the calculations of the filters are performed, is shown on the right panel of Figure 3.12, as blue dashed areas on both sides of the emission line. Each filter output was feed into the next one, so at the end of the third filter, an output file containing *almost* only flat baseline spectra was obtained. In the following, I describe the filters implemented that are applied to each 100"×100" subregion. The process is iteratively repeated until the whole observed map has gone through all the filters.

The first filter is the *"amplitude"* filter. This filter checks for bad calibrated spectra (spectra with negative intensities) in the region where emission is expected to be found. In the example shown in Figure 3.12, this region is the one enclosed between the blue dashed areas. The filter calculates the minimum and maximum measured antenna temperatures T^*_A within that region, then it compares their absolute values and, if the absolute value of the minimum T^*_A is larger than the maximum T^*_A measured, the spectrum is rejected. This procedure is applied to each spectrum within the 100"×100" area selected.

The second filter is the *"integrated intensity"* filter. It receives as input, the output file from the *"amplitude"* filter, performs all calculations within the blue dashed areas shown in Figure 3.12, and stores them separately for computing the statistics corresponding to the 100"×100" subregion in memory. As a first step, the integrated intensity of the average spectrum obtained from the previously selected spectra in the first stage of the data reduction process is calculated. In

the second step, the filter performs the same calculation individually for each spectrum within the 100"×100" subregion. As third step, all integrated intensities of the individual spectra are divided by the calculated values of the average spectrum, so for each spectrum within the subregion, two numbers are obtained: the integrated intensity ratio (spectrum/average) towards negative (I^{-}_{ratio}) and positive (I^{+}_{ratio}) LSR velocities. In the fourth step, the average integrated intensity ratio ($\langle I^{-}_{ratio}\rangle$ and $\langle I^{+}_{ratio}\rangle$) and its corresponding standard deviation (σ^{-}_{ratio} and σ^{+}_{ratio}) is calculated from the values obtained from all spectra. Finally, all spectra that have at least one integrated intensity ratio outside the $\langle I^{-/+}_{ratio}\rangle \pm \sigma^{-/+}_{ratio}$ range, are rejected.

The third filter is the *"integrated intensity difference"* filter. It receives as input, the output file from the *"integrated intensity"* filter. The overall procedure is the same as the one explained for the second filter, only the computed function is different. For a given LSR velocity, the filter calculates the square of the antenna temperature difference between the current spectrum in memory and the average spectrum. Then, all values are integrated across the corresponding LSR velocity interval on each side of the spectrum. The differences obtained from all spectra are normalized to one to make them comparable. After this, the same statistical analysis as in the second filter is applied: the average square difference ($\langle I^{-}_{diff}\rangle$ and $\langle I^{+}_{diff}\rangle$) and the corresponding standard deviation are calculated. In this way, the lower the I_{diff} value, the more similar the emission between the spectrum and the average spectrum is, so all spectra with at least one value larger than $\langle I^{-/+}_{diff}\rangle + \sigma^{-/+}_{diff}$ were rejected. After all filters have been applied to the entire dataset, more than 90% of the baseline distorted spectra were rejected. A final visual inspection of the selected spectra was performed to throw away the small number of baseline distorted spectra that could not be discarded in the filtering process.

The principal assumption in the implementation of all filters is that, within any 100"×100" subregion of the total observed map, the emission profile does not change dramatically so that the average spectrum calculated from the best quality spectra is a fair representation of the overall shape of the line within the same region. This assumption is well supported in the sense that, a 100"×100' region contains only eight telescope beams at 460 GHz. Given that the spatial sampling is 8.5", equivalent to nearly one fifth of the beam, only a small change in the line profile is expected when moving from one position to the next. All parameters such as the subregion size, LSR velocity range, tolerance of the rejecting criteria (1×σ, 2×σ, etc., below or above the calculated average value) can be varied to further improve the rejection of the baseline distorted spectra.

With the spectra obtained after the data reduction process, the final dataset was created using the GREG package. Again, the spatial resolution (40") of the

dataset is slightly higher than the beamsize (37.4”) at this frequency. The $T^*_{A,rms}$ noise distribution of the CO(4-3) NANTEN2/SMART dataset is shown in Figure 3.13. As in the case of the Herschel-HIFI observations, the color scale shows the spatial distribution of the $T^*_{A,rms}$ noise while the corresponding noise histogram is shown on top of the map. From the figure, it can be seen that the $T^*_{A,rms}$ noise is larger at the edges of the map as expected, and that the noise in the region observed with the XFFTSs (from +100” to +450” in Galactic latitude offsets) is slightly higher than the noise of the region observed with the AOSs. This is only due to the lower total integration time we obtained for the XFFTSs observations. This can be also seen in the deviation from the Gaussian profile of the noise histogram. The relevant parameters of the final dataset are summarized in Table 3.1.

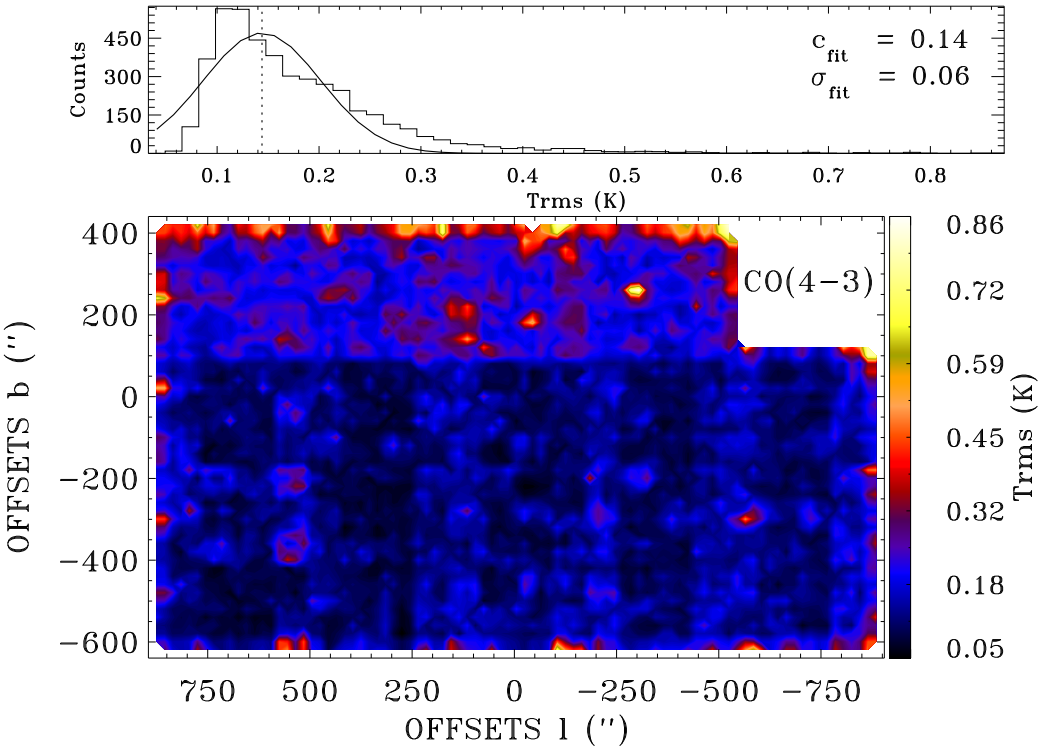

Figure. 3.13: *CO(4-3) $T^*_{A,rms}$ noise distribution. The spatial noise distribution (bottom) as well as the histogram of the noise distribution (top) is shown. The noise distribution spatial map is centered at the l = 0°.000, b = 0°.000 position. From the spatial map, the noise is higher at the edges of the maps, as expected, given the fewer spectra at the borders to calculate the resampled spectrum. Also, the upper region of the map, measured with the newly installed XFFTSs has a slightly higher noise than the rest of the map measured with the AOSs due to a shorter total integration time. From the histogram, a Gaussian fit (solid curve) shows the typical noise of the map C_{fit} (Gauss center shown as a vertical dashed line) and the standard deviation of the distribution σ_{fit}.*

3.3 Summary of Observations

A summary of the main parameters describing the scientific version datasets of all observed lines is presented in Table 3.1. The central position of all Herschel-HIFI observed maps is $\alpha(J2000) = 17^h\ 45'\ 39.9''$, $\delta(J2000) = -29°\ 00'\ 28.1''$ in Equatorial coordinates, while the NANTEN2/SMART observations are centered at $l = 0°.000$, $b = 0°.000$ in Galactic coordinates. The columns in Table 3.1 counted from left to right contain: telescope name; observed line name; transition frequency (ν_{obs}); telescope beamsize at the observed frequency (Θ_{FWHM}); final spatial resolution of the dataset (Θ); forward efficiency of the telescope (F_{eff}); typical noise in the dataset ($T^*_{A,rms}$); original LSR velocity resolution (ΔV_{res}); resampled spectral resolution (ΔV_f); LSR velocity coverage of the observations (ΔV_{range}); and energy of the upper level above the ground state for the observed line (E_u). Recently, Müller & Jellema (2014) revised the aperture (η_A) and main beam (B_{eff}) efficiencies of the Herschel-HIFI satellite based on all Mars observations acquired during operations (see Appendix A.2). They found significant deviations in both values from the ones obtained by Roelfsema et al. (2012). The new values have an impact on the flux density conversion (K-to-Jy factor) used for point-like sources, and on calculated main beam temperatures (T_{mb}). Since we have adopted the T^*_A temperature scale, the observations in the present work are not affected by the new values. In Chapter 4, the datasets presented here are analyzed in the context of their emission morphology. The interplay between different gas states along the l.o.s. are mirrored in the detected emission of the several observed species so their analysis will shed some light on the physical conditions of the ISM in the Sgr A Complex.

Table. 3.1: *Summary of main datasets parameters after the data reduction process for the Herschel-HIFI and NANTEN2/SMART observations.*

Telescope	Line	ν_{obs} (GHz)	Θ_{FWHM} (")	Θ (")	F_{eff}	$T^{*}_{A,rms}$ (K)	ΔV_{res} (kms^{-1})	ΔV_{f} (kms^{-1})	ΔV_{range} (kms^{-1})	E_u (K)
NANTEN2/SMART	CO(J=4-3)	461.0	37.4	40.0	0.86	0.14	0.677[a]/0.050[b]	1.0	−200 to +200	55
Herschel-HIFI	[CI] $^3P_1$ - $^3P_0$	492.2	43.1	46.0	0.96	0.06	0.305	1.0	−200 to +200	25
Herschel-HIFI	[CI] $^3P_2$ - $^3P_1$	809.3	26.2	28.0	0.96	0.13	0.185	1.0	−200 to +200	60
Herschel-HIFI	[NII] $^3P_1$ - $^3P_0$	1461.1	14.5	46.0	0.96	0.28	0.103	1.0	−200 to +94	70
Herschel-HIFI	[CII] $^2P_{3/2}$ - $^2P_{1/2}$	1900.5	11.2	46.0	0.96	0.42	0.079	1.0	−200 to +144	90

[a]For AOSs
[b]For XFFTSs

Chapter 4

Emission Morphology

In the following, I discuss the spatial distribution of the emission in all lines, and across the ±200 kms^{-1} LSR velocity range in the present work. The data are presented in channel maps of integrated intensity in units of K kms^{-1} ($I = \int T_A^*(v)\, dv$). For each map, the central LSR velocity is given. The spatial resolution in each dataset is shown as a filled black circle in each map. For all observations, the Right Ascension (R.A.) and Declination (DEC.) offsets, and Galactic longitude (l) and Galactic latitude (b) offsets are with respect to the central position mentioned in Chapter 3. Given the large spatial and angular extent of the datasets, extra channel or integrated intensity maps are displayed when necessary for a better overview on the discussion of particular astronomical sources. In those figures, the NANTEN/SMART data have been rotated to the Equatorial (J2000) coordinate system for better comparison with the Herschel-HIFI observations. The channel maps of all datasets are shown in Appendix F.

4.1 Average Spectrum of the Observed Sub-mm Lines

The average spectrum of the observed sub-mm lines is shown in Figure 4.1. The spectra were obtained by bringing all data sets to a common 46" angular resolution and averaging all spectra within the area covered by the Herschel-HIFI observations. If one considers the average spectrum as a single-point observation, it would be roughly equivalent to a spectrum taken with a spatial resolution of ≈ 50 pc. The bulk of the carbon monoxide and atomic carbon emission is concentrated in the major MCs toward positive LSR velocities, while the emission of the ionized material is more symmetric with respect to 0 kms^{-1}. Given the low

rms noise of the Herschel-HIFI and NANTEN2/SMART observations, even weak emission at very high LSR velocities (V_{lsr} > +150 kms^{-1}) in the [CI](1-0) and CO(4-3) lines is detected in the average spectrum. Absorption features along the l.o.s. associated with the loci of spiral arms are observed in the CO(4-3) average spectrum: at −5 kms^{-1} the most prominent absorption feature associated with the local arm is seen, while other weaker absorption features at −30 kms^{-1} and −55 kms^{-1} are associated to the 3 kpc and 4.5 kpc spiral arms (Oka et al., 1998; Jones et al., 2012; Dame et al., 2001; Dame & Thaddeus, 2008). The average [CII] spectrum also shows some correspondence with the absorption LSR velocity of the spiral arms along the l.o.s., while no clear absorption signatures are seen in the carbon average spectra. It is important to notice that, absorption due to foreground spiral arms is expected to be narrow with $\Delta V(FWHM) \leq 5$ kms^{-1} for the CO(1-0) transition (Oka et al., 1998). Therefore, broader absorption features in the warm gas could (at least partially) originate due to in situ absorption. For instance, the absorption feature at −5 kms^{-1} seen in the average CO(4-3) spectrum has a line width $\Delta V(FWHM) \approx 10$ kms^{-1}.

4.2 Molecular Clouds Between −80 kms^{-1} and +90 kms^{-1}

Most of the molecular clouds within the Sgr A Complex are located between −80 kms^{-1} up to +90 kms^{-1}. From negative to positive LSR velocities, the first major feature is M+0.04+0.03 (−30 kms^{-1} Cloud), containing the gas associated to the Arched-Filaments (Serabyn & Guesten, 1987; Zhao et al., 1993), ranging from ∼ −70 kms^{-1} up to 0 kms^{-1}, covering the upper half of the Herschel-HIFI maps. Figure 4.2 shows 5 kms^{-1} integrated intensity maps of the [CII] (color scale) and [NII] (contours) emission, with the corresponding central LSR velocity of the maps shown in the bottom of each panel. The red squares depict the positions of two peaks in CS(2-1) emission detected by Serabyn & Guesten (1987), tracing high density material, while the red star shows the position of the massive Arches Cluster. The emission in both lines is very widespread and closely follows the 20 continuum emission shown in Figure 1.2, moving from the H-Region, with a local intensity peak in both lines at the position of the H1-H2 sources, to the Arched Filaments, going through G0.07+0.04, and moving from the W1/W2 filaments to the E1/E2 filaments and the "Banana" as the LSR velocity approaches 0 kms^{-1}. From the maps, a strong spatial correlation between the [CII] and [NII] lines is observed, indicating that there is a significant contribution to the observed [CII] emission from H II regions and not only from PDRs (Abel et al., 2005). The case of the G0.07+0.04 is particularly interesting since it is thought that, at this position, the gas is interacting with the Northern Thread (Lang et al., 1999b). In a preliminary analysis, the central LSR velocity of the H92α average

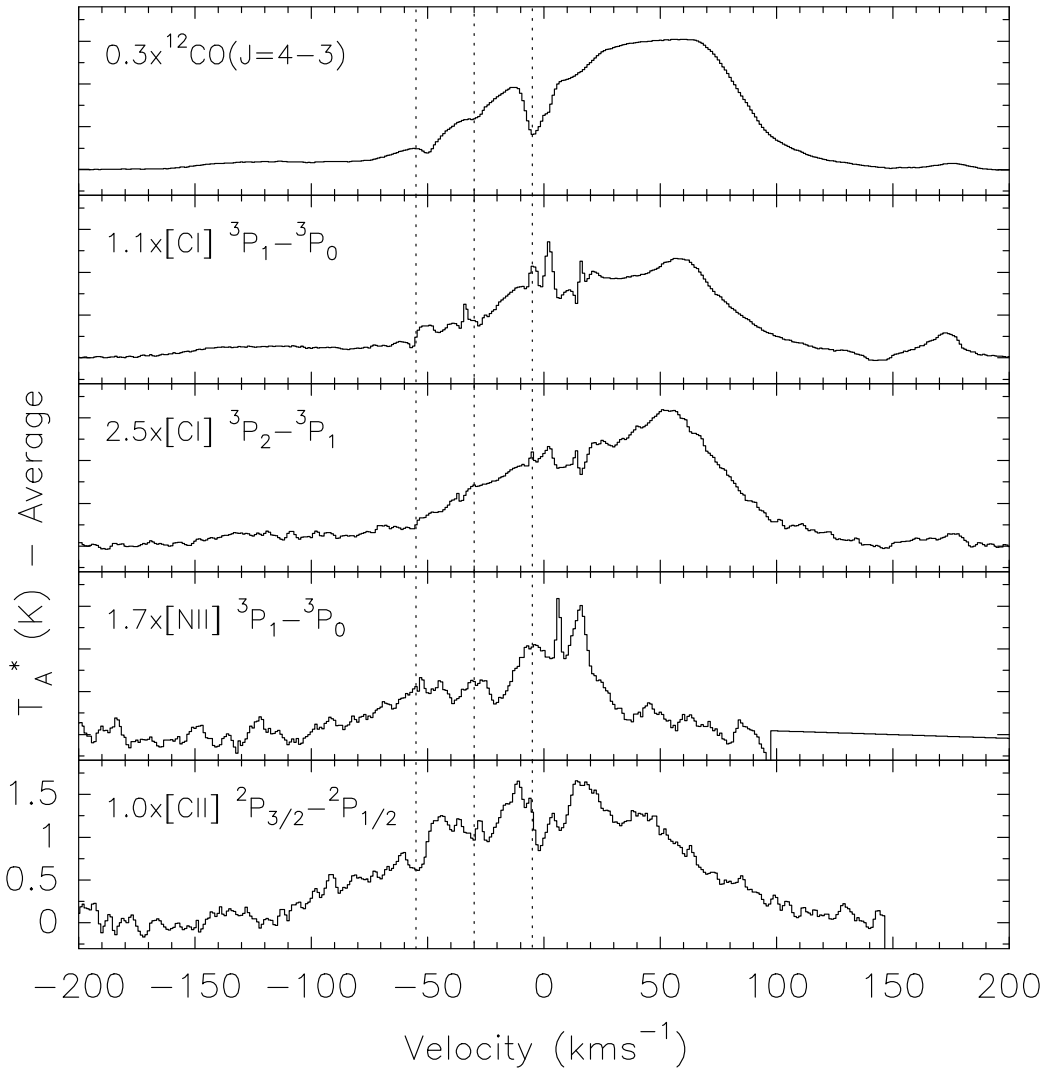

Figure. 4.1: *Average spectra of the sub-mm lines observed in the present work. Each average spectrum is made out of 46" spatial resolution maps and within the area covered by the Herschel-HIFI observations. Dotted vertical lines denote the loci in radial velocity of the 3 kpc, 4.5 kpc, and local spiral arms.*

spectrum in this region shown by Lang et al. (2001) is shifted by around ∼ 30 kms^{-1} towards more negative velocities with respect to the bulk of carbon and carbon monoxide emission along the same l.o.s. Such a large velocity shift is not seen at other positions of the Arched Filaments, and might be indicating that the ionized material is being drifted away from G0.07+0.04 by the interaction with the local magnet field. The peak [CII] intensity (∼ 9.2 ± 0.4 K) occurs within the Arched Filaments at $\Delta\alpha(J2000) = -82.2$", $\Delta\delta(J2000) = +490.4$", and V_{lsr} −45 kms^{-1} , while the peak intensity of the [NII] line (∼ 2.7 ± 0.4 K) occurs at $\Delta\alpha(J2000) = -107.2$", $\Delta\delta(J2000) = +720.3$", and V_{lsr} −26 kms^{-1}. Figure 4.3 shows the emission distribution of the CO(4-3) (colors) and [CI](1-0) (contours). The behavior of the [CI](2-1) line is very similar to the [CI](1-0)

emission (as expected), so I focus the discussion on the lower frequency line. At large negative LSR velocities, there is a gas streamer connecting the H-Region with the lower part of the Arched Filaments, where one of the CS(2-1) peaks is located (see Section 4.2.1). The bulk of the emission detected from the CO(4-3) and [CI](1-0) lines is displaced with respect to the position of the filaments and with respect to the CS(2-1) emission peaks (red squares) detected by Serabyn & Guesten (1987), and it is weak in comparison to the rest of the emission in the data cubes. The position of the most intense emission in the CO(4-3) line is at the center of the maps, as seen for example at −18 kms^{-1}, between M+0.04+0.03 (−30 kms^{-1} Cloud) and M+0.02−0.05 (−15 kms^{-1} Cloud), while local maxima of the carbon emission coincide with the position of these two clouds. In the top panels of Figure 4.4, at −11 kms^{-1}, a lane of emission (both in carbon and carbon monoxide) going from the the position of M+0.02−0.05, through the Galactic Center and connecting with another cloud, south of the CND, that is probably part of the +20 kms^{-1} Cloud, is seen. Serabyn & Guesten (1987) suggested that the lack of ionized material in the region around M+0.02−0.05, the so called *molecular bridge*, could be the result of the tidal disruption of material in infall toward the CND. This seems to be supported by the morphology of the warm gas in our observations (see Section 4.2.1).

From 0 kms^{-1} to +90 kms^{-1}, there is a large number of molecular clouds outlined in different temperature and density tracers at lower frequencies. I refer to them following the nomenclature used by Güsten et al. (1981) who identified their NH_3(1,1) peak positions, as shown in Figure 1.3. Given the molecular nature of the MCs, these are brighter in the CO(4-3) emission than in any other line in our data. From 0 kms^{-1} to +20 kms^{-1}, the brightest feature is the M2−0.13−0.08 (+20 kms^{-1} Cloud), seen at $\Delta l < 0$". The emission lane that crosses the GC from the *molecular bridge* to connect with the +20 kms^{-1} Cloud is still clearly visible at +8 kms^{-1}, as seen in the bottom panel of Figure 4.4. These streamers are traced almost uninterruptedly by the [CI](1-0) and the [CI](2-1) emission, since no major absorption features are present in these lines within the −11 kms^{-1} to +8 kms^{-1} LSR velocity range. From the morphological point of view, this suggests that the molecular bridge and the +20 kms^{-1} Cloud are part of the same structure that is being tidally disrupted in the gravitational field of the Nuclear Cluster which dominates the gravitational potential for radii 2 - 30 pc (Longmore et al., 2013). In this case, the emission gap between the bridge and the +20 kms^{-1} Cloud in the CO(4-3) emission is, at least partially, due the strong absorption of the local arm along the l.o.s..

For $\Delta l > 0$", two CO(4-3) emission features appear at $\Delta l = +400$", $\Delta b = -400$", and $\Delta l = +750$", $\Delta b = -150$". The former surrounds the M+0.11−0.08 cloud as seen in the N_2H^+(1-0) emission from the Mopra observations (Jones et al., 2012), and it is associated to the M+0.11−0.11 dense cloud observed in CS(1-0) and

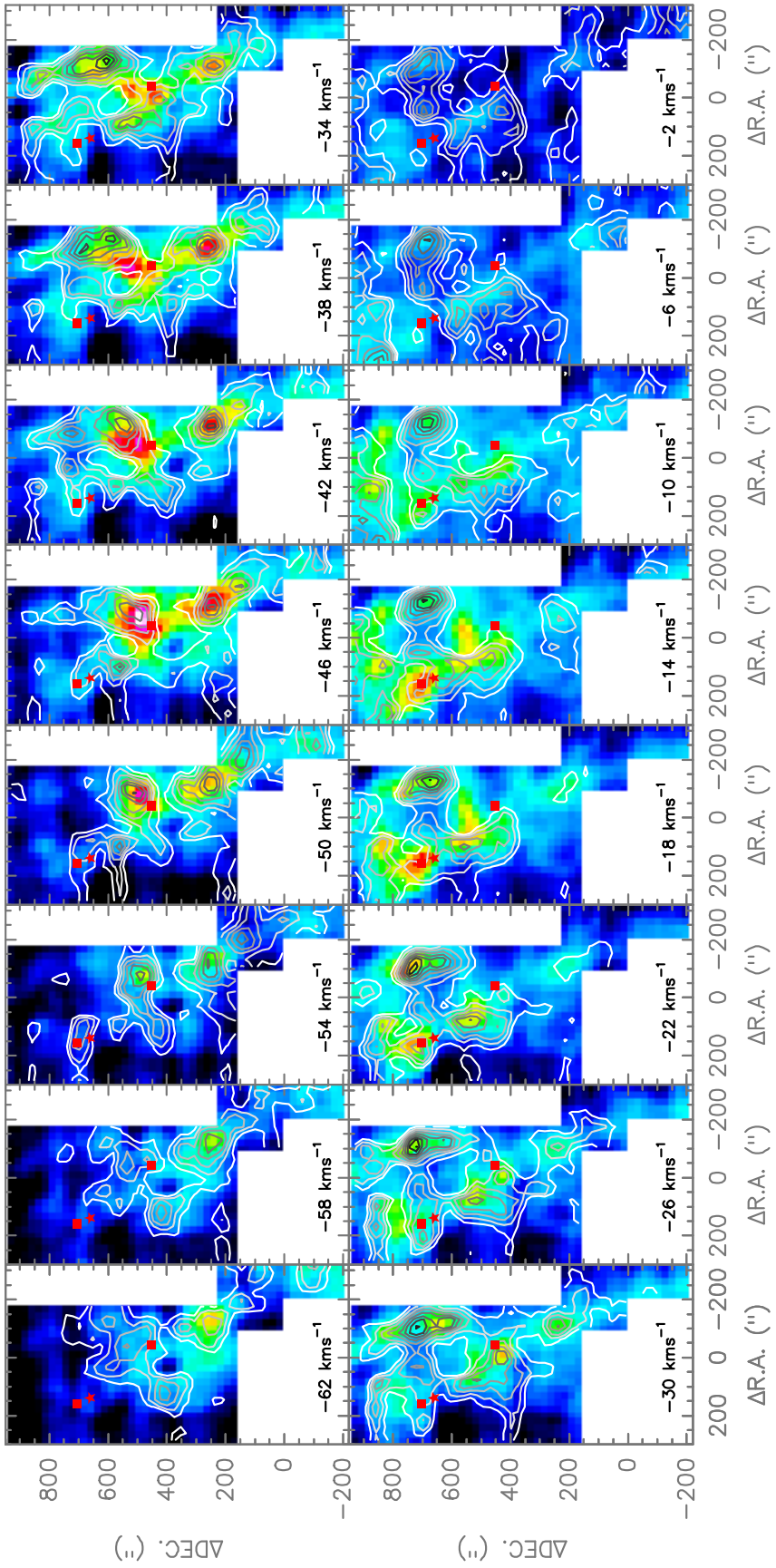

Figure. 4.2: *Integrated intensity maps (5 kms^{-1} wide) of the [CII] (color scale) and [NII] (contours) lines, tracing the ionized material towards the Arched Filaments E1, E2, W1, and W2 and the H-Region as shown in Figure 4.1. The red star shows the location of the Arches Cluster, while red squares show the positions of two CS(2-1) peaks detected by Serabyn & Guesten (1987), tracing high density material. The central LSR velocity of the maps is shown in each panel.*

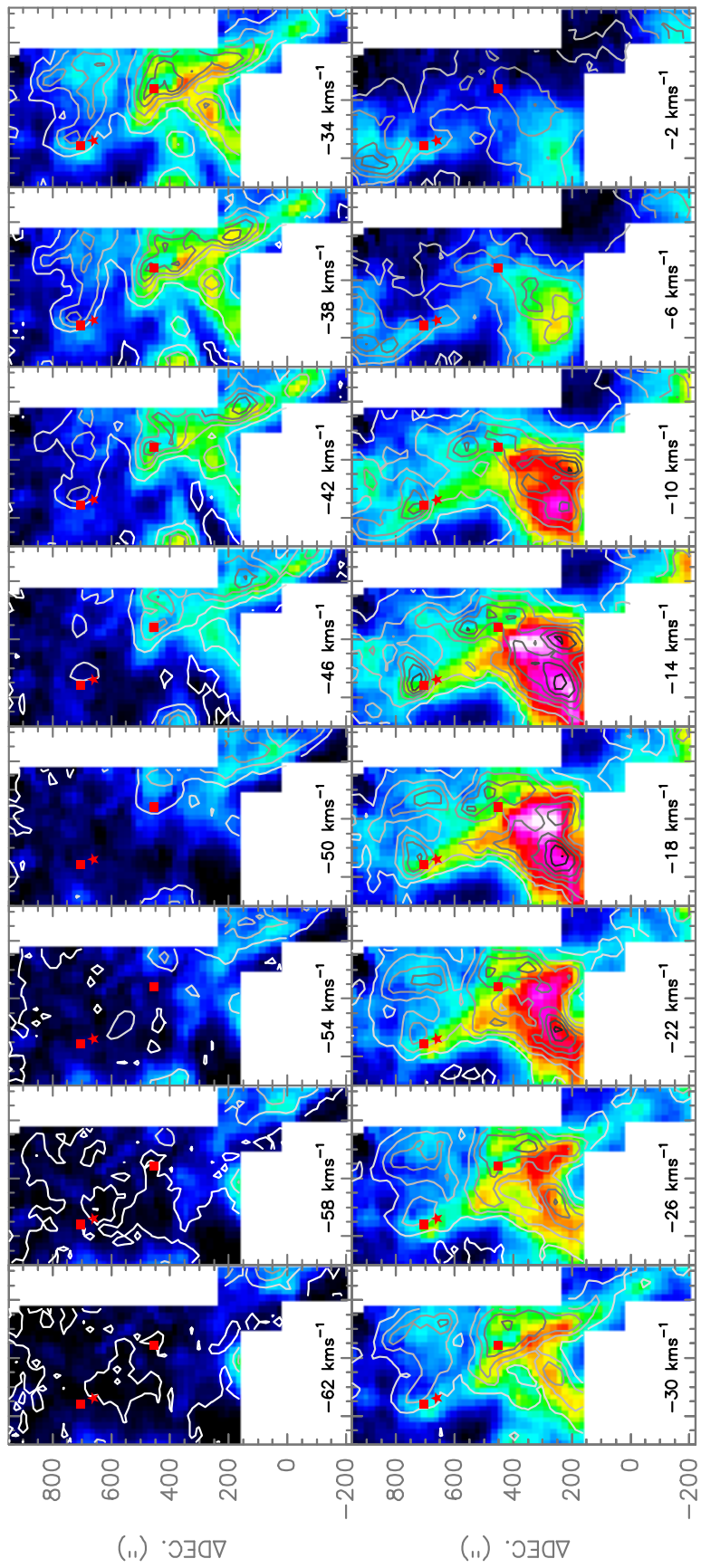

Figure. 4.3: *Integrated intensity maps (5 kms^{-1} wide) of the CO(4-3) (color scale) and [CI](1-0) (contours) lines in the bottom panels, tracing the molecular and atomic material towards the Arched Filaments E1, E2, W1, and W2 and the H-Region as shown in Figure 4.1. The red star shows the location of the Arches Cluster, while red squares show the positions of two CS(2-1) peaks detected by Serabyn & Guesten (1987), tracing high density material. The central LSR velocity of the maps is shown in each panel.*

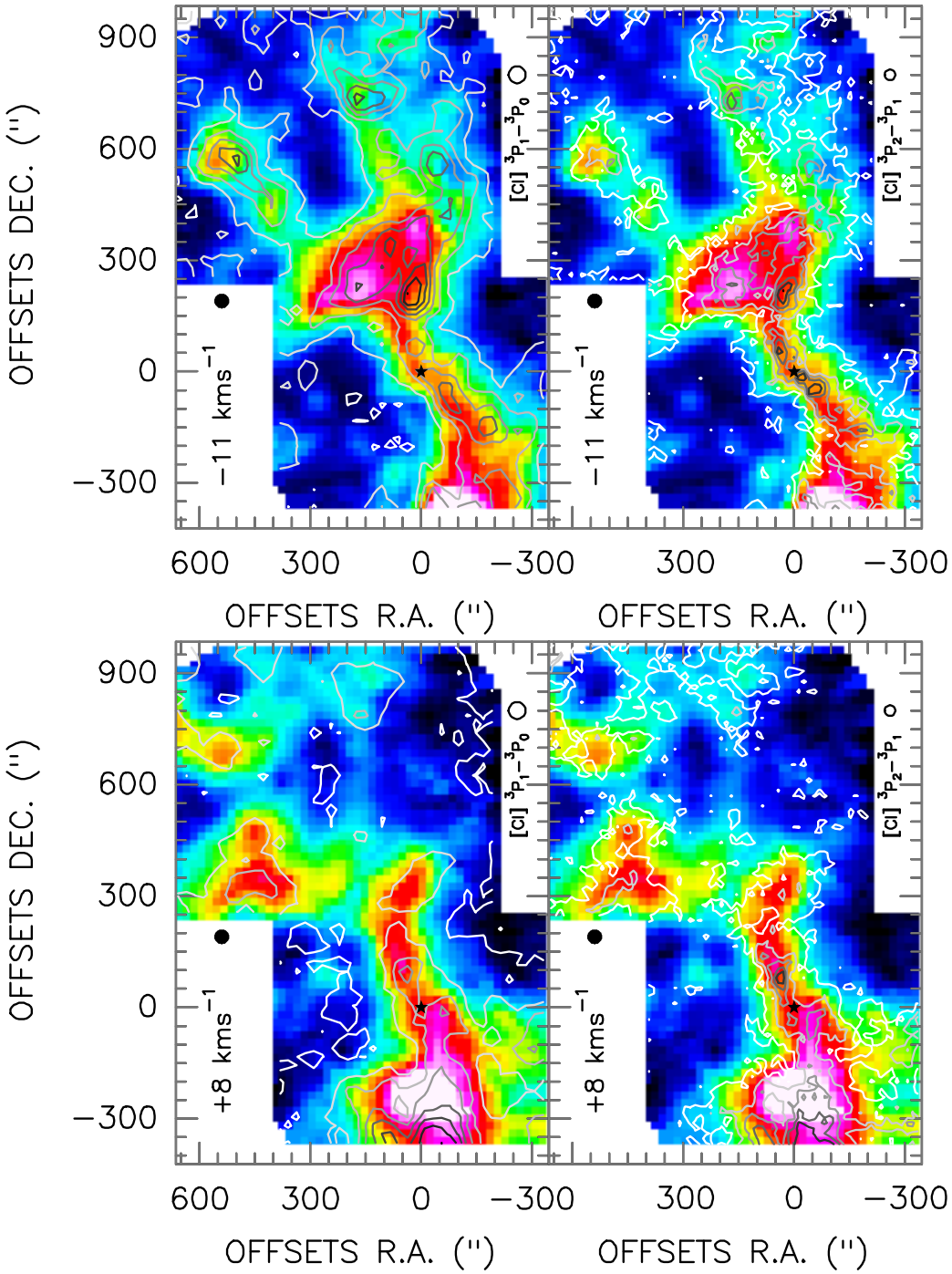

Figure. 4.4: *Channel maps at −11 kms^{-1} (top panels) and +8 kms^{-1} (bottom panels) of the CO(4-3) (color scale) emission, while the [CI](1-0) (left panels) and [CI](2-1) (right panels) lines are shown as contours. Open circles show the spatial resolution of the carbon lines, while the black filled circles show the spatial resolution of the carbon monoxide line. The ⋆ symbol shows the position of Sgr A⋆. The color scale is the same in all panels.*

CS(2-1) by Tsuboi et al. (1997), while the latter is slightly shifted with respect

to a local N_2H^+(1-0) peak, not covered in the Güsten et al. (1981) observations, and coincides spatially with the edge of the Sickle H II region. Both features anti-correlate with the 20 cm continuum emission measured by Yusef-Zadeh & Morris (1987a). This is illustrated in the 3 kms^{-1} wide CO(4-3) integrated intensity map shown in Figure 4.5 at central LSR velocity +29 kms^{-1}. The contours in the figure show the Sickle H II region depicted in the 20 cm continuum emission (left panel), the M+0.11−0.08 cloud traced by the diazenylium line, and the position of the M+0.11−0.11 cloud (right panel). Their CO(4-3) emission extends up to ∼ +40 kms^{-1} where these structures are still recognizable. The atomic carbon line observations follow the same trend as the carbon monoxide observations in this LSR velocity range. There are [CII] and [NII] detections towards the Sickle H II region, while no clear detection is seen towards the M+0.11−0.08 cloud. In general, the [CII] emission is widespread while the [NII] emission anti-correlates spatially at some spots with the lower frequency lines as can be expected from gas adjacent to H II regions. An example of this is seen in the channel maps, at LSR velocity +18 kms^{-1}, where a local maximum in the [NII] emission is located just next to the CO(4-3) emission of the +20 kms^{-1} Cloud at $\Delta\alpha(J2000) \sim -150$”, $\Delta\delta(J2000) \sim -250$”.

Most of the neutral atomic carbon emission and molecular emission is found within the LSR velocity range +20 kms^{-1} up to +90 kms^{-1}. The peak intensities in the datasets are: $T_A^* = 22.11 \pm 0.09$ K, at Δl = −64.9”, Δb = −259.3”, and V_{lsr} +63 kms^{-1} for the CO(4-3) line, $T_A^* = 8.14 \pm 0.05$ K, at $\Delta\alpha(J2000) = +152.1$”, $\Delta\delta(J2000) = +73.0$”, and $V_{lsr} = +53$ kms^{-1} for the [CI](1-0) line, and $T_A^* = 6.98 \pm 0.13$ K, at $\Delta\alpha(J2000) = +155.2$”, $\Delta\delta(J2000) = +80.1$”, and $V_{lsr} = +55$ kms^{-1} for the [CI](2-1) line, all of them associated in space and LSR velocity to M−0.02−0.07 (+50 kms^{-1} Cloud). For $\Delta l < +150$”, when going from +20 kms^{-1} to +50 kms^{-1}, the CO(4-3) emission moves across Galactic longitude from the +20 kms^{-1} Cloud (Δl = −350”, Δb = −250”) continuously to connect with the +50 kms^{-1} Cloud at around Δl = −350”, Δb = −250”. This behavior is also seen in both atomic carbon lines from which, at LSR velocities between +50 kms^{-1} and +60 kms^{-1}, the +50 kms^{-1} Cloud stands out as a crescent-shaped feature, with its concave side oriented to the non thermal shell source Sgr A-East, which is thought to be the remnant of a supernova(e) explosion(s) with energy ∼ 4× 10^{52} ergs (Yusef-Zadeh & Morris, 1987a; Mezger et al., 1989; Coil & Ho, 2000). At +67 kms^{-1}, a similar crescent-shaped structure in CO(4-3) emission is seen. This is shown in Figure 4.6, where contours show the 20 cm continuum emission and the position of Sgr A* is represented by the ⋆ symbol. This indicates that the emission detected from the +50 kms^{-1} Cloud is in close relationship with the energetic event that originated in the Sgr A-East region. The emission tracing the +50 kms^{-1} Cloud extends up to +90 kms^{-1}.

For $\Delta l > +150$”, the CO(4-3) emission between +20 kms^{-1} and +90 kms^{-1} traces

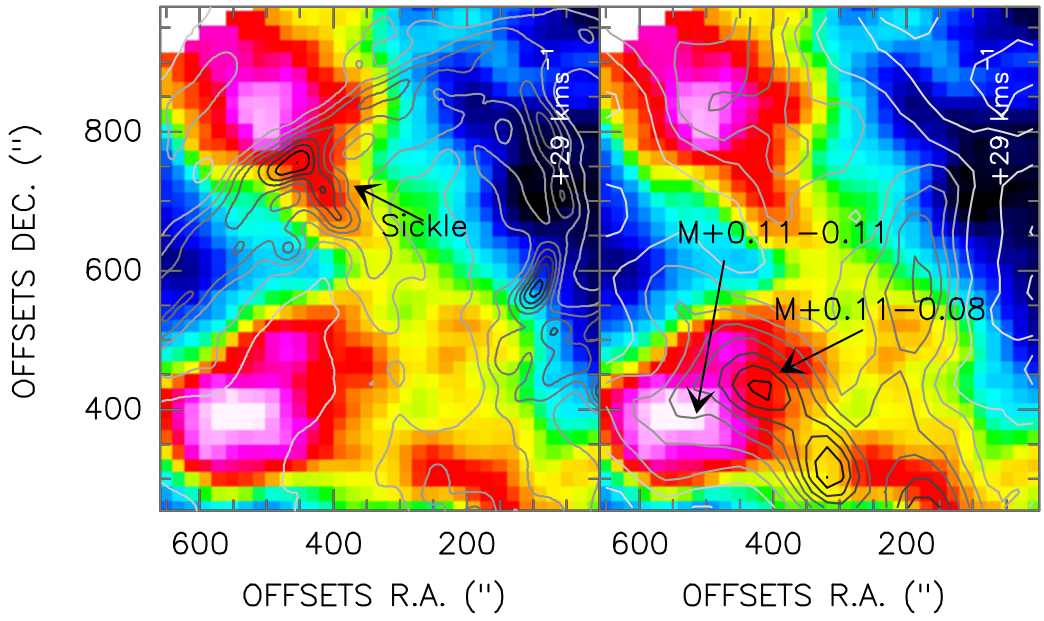

Figure. 4.5: *Integrated intensity map (3 kms^{-1} wide) of the CO(4-3) emission (color scales) centered at +29 kms^{-1} with superimposed contours of the 20 cm continuum emission measured by Yusef-Zadeh & Morris (1987a) showing the Sickle H II region (left panel), and N_2H^+(1-0) contours of the integrated intensity map between −75 and +110 kms^{-1} from the Mopra observations by Jones et al. (2012) showing the emission distribution of the M+0.11−0.08 cloud and the position of the M+0.11−0.11 cloud from Tsuboi et al. (1997) (right panel). The CO(4-3) emission related to the Sickle H II region is located at the edge of the H II region while the CO(4-3) emission related to the M+0.11−0.11 cloud is shifted at this LSR velocity with respect to the peak emission of the cold gas traced by diazenylium.*

the M+0.07−0.08, M+0.11−0.08, M+0.06−0.04, and M+0.10−0.01 molecular clouds and gas associated to the Sickle H II region, as mentioned before. The CO(4-3) emission peak in this region is shifted with respect to the global [CI](1-0) intensity peak, around +57 kms^{-1}, and is comparable in magnitude to the one detected toward the +50 kms^{-1} Cloud, having a similar morphology than the emission below Δl = +150", for LSR velocities between +56 kms^{-1} and +63 kms^{-1}. This is not the case for the atomic carbon lines. The emission from the [CI](1-0) and [CI](2-1) lines, above $\Delta\delta(J2000)$ = +250", is much weaker toward these molecular clouds and shows a highly asymmetric spatial distribution. Given the symmetric distribution in the CO(4-3) lines and the very asymmetric distribution of the [CI](1-0) and [CI](2-1) emission, it is likely that a different heating mechanism between both regions is responsible for the gas excitation. Minh et al. (2005) attributed the enhancement of the HCO^+(1-0) emission in this region to the interaction of the gas with the shocks waves produced by the Sgr A-East supernova remnant. The [CII] emission, between +20 kms^{-1} and to +90 kms^{-1} is much weaker than at negative LSR velocities and in general follows the

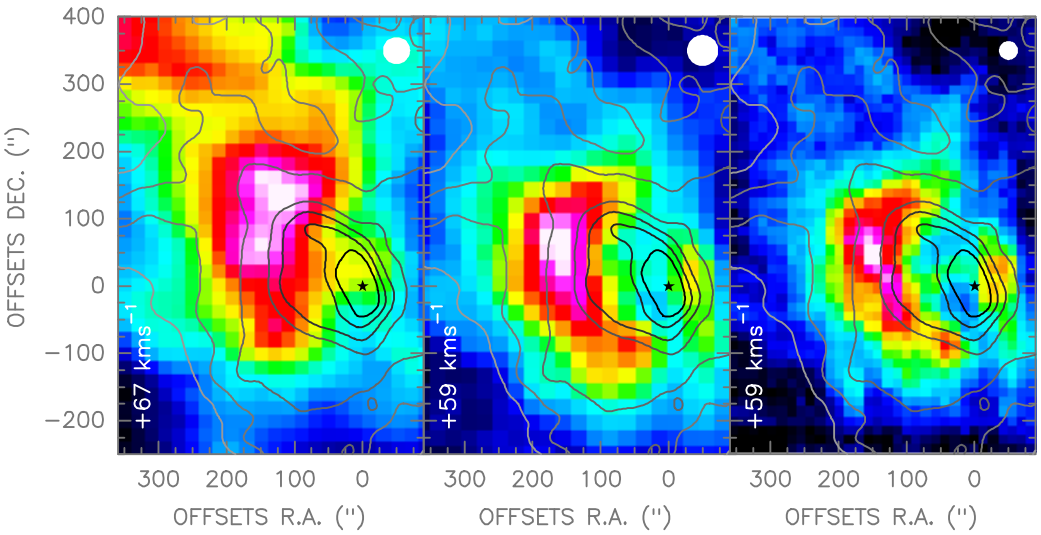

Figure. 4.6: *Integrated intensity maps (3 kms^{-1} wide) of the CO(4-3), [CI](1-0), and [CI](2-1) emission (color scales) for the +50 kms^{-1} Cloud. The filled white circles represent the spatial resolution of the data, and the central LSR velocity of the maps in given in each panel. The 20 cm continuum emission from the Sgr A-East region measured by Yusef-Zadeh & Morris (1987b) is shown as contours. The crescent-shape in all three sub-mm lines at different LSR velocities surrounding the Sgr A-East region reveals the interaction of the +50 kms^{-1} Cloud with the non thermal source.*

distribution of the molecular gas traced by CO(4-3) below the Galactic plane.

Between +20 kms^{-1} and +70 kms^{-1}, there is a prominent emission lane going from $\Delta\alpha(J2000) \sim +150$", $\Delta\delta(J2000) \sim +400$" to $\Delta\alpha(J2000) \sim +400$", $\Delta\delta(J2000) \sim +50$". The feature is tangent to the convex side of the +50 kms^{-1} Cloud. Since the [NII] emission decreases significantly for LSR velocities above +20 kms^{-1}, the same feature is barely detected in the [NII] line. This is shown in Figure 4.7, where the [CII] and [NII] emission in contours is overlaid on the CO(4-3) emission in colors. Again, the ⋆ symbol represents the position of Sgr A*. The composite 8.0, 4.5, and 3.6 μm Spitzer/IRAC image of the Sgr A Complex in Chambers et al. (2014) shows bright emission at the same position, indicating a lower opacity than towards the positions of the bulk molecular gas. The A-I H II regions associated to the +50 kms^{-1} Cloud (Yusef-Zadeh & Morris, 1987a) are located towards the opposite side of the cloud and closer to the GC. I found no H II sources listed in the literature that correlate with the position of the [CII] emission lane. In general, the [NII] emission is more confined spatially than the [CII] emission, reflecting their different origin, with [NII] emission associated mainly to H II regions and [CII] emission tracing different stages of the ISM, including a contribution from H II regions.

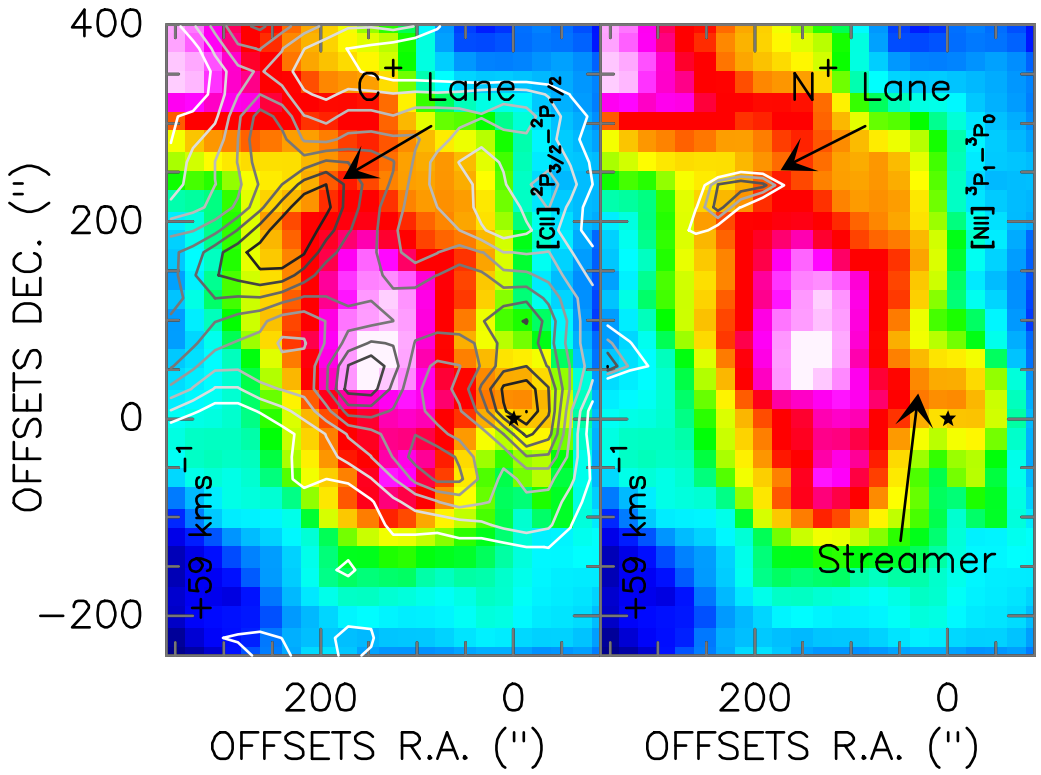

Figure. 4.7: *Integrated intensity map (3 kms^{-1} wide) of the CO(4-3) emission (color scale) from the +50 kms^{-1} Cloud centered at +58 kms^{-1} with [CII] (left) and [NII] (right) emission as contours overlaid on the maps. The first contour of the high frequency lines is set at a 5×σ significance level, with σ the typical noise of the map. The ⋆ symbol represents the position of Sgr A⋆. A prominent [CII] emission lane is found tangent to the convex side of the +50 kms^{-1} Cloud, with a small [NII] counterpart.*

It is interesting to notice that most of the flux in the neutral atomic and molecular lines is located at Galactic latitudes below the Galactic plane (b < 0°), while the flux of the ionized material traced by the [NII] and [CII] peaks above the Galactic plane, running from $\Delta\alpha(J2000) = -350$", $\Delta\delta(J2000) = -300$", to $\Delta\alpha(J2000) = +450$", $\Delta\delta(J2000) = +1000$" in the Herschel-HIFI maps. Given the offset of the dynamical center of the Milky Way (Sgr A⋆) from the center position of the Galactic coordinate system, the location of the ionized and neutral material with respect to b = 0° is not particularly meaningful but the fact that both materials are found at different positions in the Sgr A Complex could indicate a different evolutionary state of the gas moving along a ring-like structure (Molinari et al., 2011) whose passage through the closest point to the bottom of the gravitational potential could trigger the star formation process (Longmore et al., 2013).

4.2.1 Gas Streamers

Gas streamers are seen at several locations in the GC and were first reported by Ho et al. (1991). They are thought to be the result of material from MCs (such as the +20 kms^{-1} and +50 kms^{-1} Clouds) trapped by the central gravitational potential. They are brighter in emission from warm gas than from cold gas as their are heated on their way towards the GC (Ho et al., 1991). Using NH_3 observations, Coil & Ho (2000) reported the detection of the *southern streamer* stretching from the +20 kms^{-1} towards the CND but not reaching the GC. No detection of the northern part of the streamer is seen in their data, probably due to low density of the gas. Nonetheless, the southern and northern parts of the streamer are clearly traced by CO(4-3), [CI](1-0), and [CI](2-1) emission in our data, as it is shown in Figure 4.4, at positive LSR velocities. In the CO(4-3) line, the northern and southern parts of the streamer appear as a single continuous structure (at least in projection) going through the CND, and are remarkable similar to the streamer shown at negative velocities also shown in Figure 4.4 (upper panels), suggesting that they could be physically related. The streamers would appear as separated entities only because of the accidental massive absorption feature at −5 kms^{-1}. If this were the case, it would imply that there is warm gas connecting the −15 kms^{-1} Cloud with the +20 kms^{-1} Cloud. In the same work, Coil & Ho (2000) showed that the +20 kms^{-1} and +50 kms^{-1} Clouds are connected by a thin molecular ridge of gas (also referred to as the *eastern streamer*), not seen in dust maps, and suggested that both clouds may constitute part of the same large scale structure of gas lying along the Galactic plane. Since NH_3 traces only the densest part of the gas, they fail to detect intermediate densities of the warm gas traced by CO(4-3). The eastern streamer is seen in CO(4-3), [CI](1-0), and [CI](2-1) emission, in the velocity range +20 kms^{-1} to +50 kms^{-1}, moving from the position of the +20 kms^{-1} Cloud towards the location of the +50 kms^{-1} Cloud, surrounding the CND.

Using ^{13}CO(3-2) observations, Zylka et al. (1990) detected another streamer, very small in spatial extent (see their Figure 5d), reaching from the +50 kms^{-1} Cloud towards the CND. The same feature is detected in the CO(4-3) line going from Δl = +175", Δb = −200" to Δl = +225", Δb = −100", between +45 kms^{-1} and +70 kms^{-1}. The streamer is signalized in the right panel of Figure 4.7, reaching towards the GC. It has a very small spatial extent and is weak in the carbon line emission. This streamer is also detected in 1.3 mm dust continuum tracing free-free and thermal dust in the analysis done by Zylka et al. (1998).

A *far western streamer* going from the H-Region towards the −30 kms^{-1} Cloud and connecting with the Arched Filaments, but not going through the GC was discussed in Section 4.2. The structure runs almost parallel to the Galactic plane and can be seen in CO(4-3) emission between $\sim$ −50 kms^{-1} up to $\sim$ −25 kms^{-1}

as an almost straight line going from Δl = −50” to Δl = −400”, at constant Δb = +50”. Atomic carbon emission is also found towards some portions of the far western streamer. Since this feature does not go through the GC, it could have a different origin than the streamers previously mentioned. Nonetheless, it could reflect gas under tidal disruption orbiting the GC. The *far western streamer* should not be confused with the *western streamer* on the western side of Sgr A-East, extending in the north-south direction detected by McGary et al. (2001).

4.2.2 Emission Around and Within the CND

In the Herschel-HIFI maps, the CND is contained within a square of side length 100”, centered at the $\Delta\alpha(J2000)$ = 0”, $\Delta\delta(J2000)$ = 0” position. This area contains the high resolution (9.5”) CO(6-5) emission observed by Requena-Torres et al. (2012). In the NANTEN/SMART CO(4-3) maps measured in Galactic coordinates, this area is centered at Δl ∼ −202”, Δb ∼ −165”. Figure 4.8 shows the average emission within the 100”×100” area containing the CND. The emission extends from −150 kms^{-1} to +150 kms^{-1} in all lines but [NII], where the line is barely detected between −10 kms^{-1} and +30 kms^{-1}. Overall, the CO(4-3), [CI](1-0), [CI](2-1), and [CII] average spectra are very similar. All present a clear emission bump at +50 kms^{-1}, where emission from the northern lobe of the CND dominates, while toward negative velocities, where the southern lobe is present, the average emission decreases showing also the strong absorption features from the loci of spiral arms along the l.o.s. in the molecular and ionized emission.

Toward negative velocities, above −50 kms^{-1}, there is an “excess” in [CII] emission with respect to the molecular and neutral atomic emission. This “excess” is indeed tracing a very bright [CII] spot toward the southern part of the CND, where the peak of the integrated CO(6-5) intensity is also found (Requena-Torres et al., 2012). This can be clearly seen in the channel maps at LSR velocity −63 kms^{-1} shown in Figure 4.9 (number 1). The red square in the figure represents the spatial extent of the CND while the ⋆ symbol shows the position of Sgr A*. The bright [CII] spot is detected in both atomic carbon lines and in the carbon monoxide line. In these transitions, two emission peaks are distinguishable, instead of the single emission peak in the [CII] emission. No significant [NII] emission is detected at this position. Outside the northern part of the CND, there is second spot (number 2 in Figure 4.9) at position Δl ≈ −75”, Δb ≈ −100” detected in CO(4-3) and in [CI](1-0) and [CI](2-1) at $\Delta\alpha(J2000)$ ≈ +25”, $\Delta\delta(J20004)$ ≈ +150”. This feature shows up for the first time at around −75 kms^{-1} and it is still visible up to −55 kms^{-1} where the 3 kpc absorption features appears. There is neither [NII] nor significant [CII] emission detected at this position. A third spot of emission (number 3 in Figure 4.9), located just outside

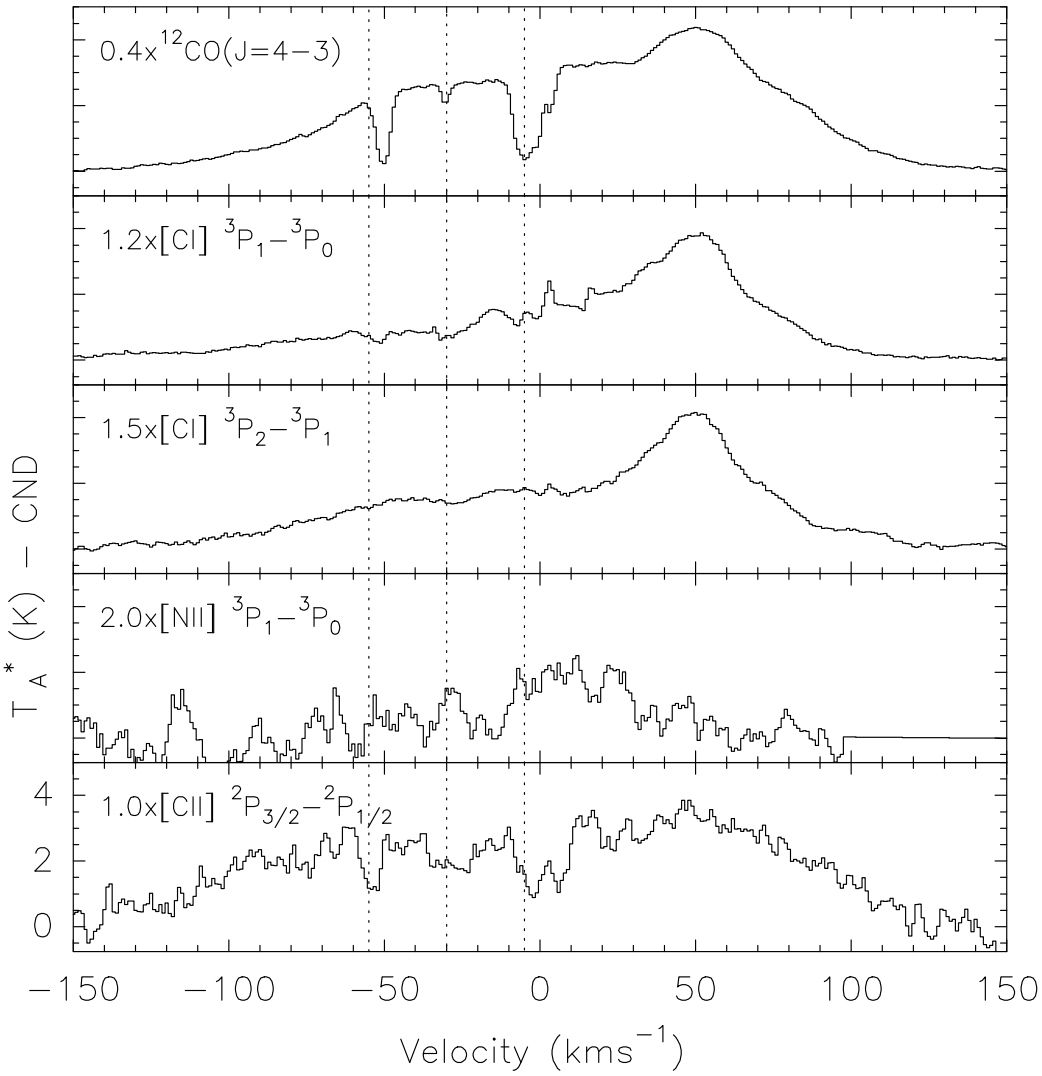

Figure. 4.8: *Circum Nuclear Disk (CND) average spectra in the sub-mm/FIR lines presented in this work. The plots were created by averaging the spectra within a 100"×100" area centered at the position of Sgr A⋆, from data cubes with a common 46" spatial resolution. Vertical dotted lines show the loci of the 3 kpc, 4.5 kpc, and local arm spiral features at ∼ −55 kms^{-1}, ∼ −30 kms^{-1}, and ∼ −5 kms^{-1}, respectively.*

the CND northern part, is detected in CO(4-3) at Δl ≈ -125", Δb ≈ -220", and barely detected in [CI](1-0) and [CI](2-1) at $\Delta\alpha(J2000) \approx +100$", $\Delta\delta(J20004) \approx +25$", traceable between -100 kms^{-1} and -55 kms^{-1}, before it washes out with the rest of the emission. Neither [NII] nor [CII] significant emission is detected at this position. The different atomic carbon intensities between the second and third spots of bright CO(4-3) emission could be an indication of different excitation mechanisms for sources only 2 arcminutes apart in the vicinity of the CND. Towards very high positive LSR velocities, a similar bright spot is found associated to the northern lobe of the CND where the CO(6-5) emission also shows a local maximum (Requena-Torres et al., 2012). The spot is located at Δl

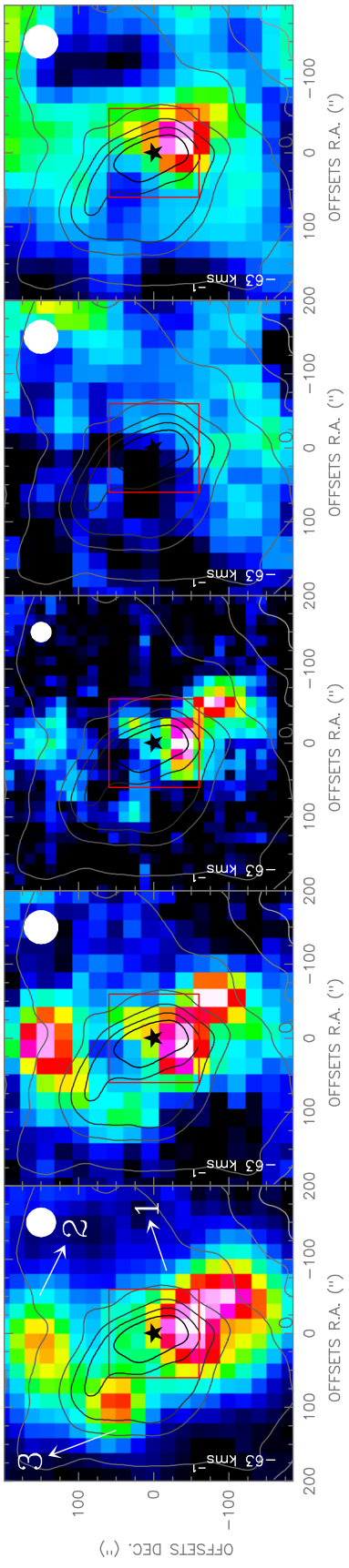

Figure. 4.9: *From left to right: CO(4-3), [CI](1-0), [CI](2-1), [NII], and [CII] emission at LSR velocity −63 kms^{-1} around and within the CND, denoted by the read box. The 20 cm continuum observations by Yusef-Zadeh & Morris (1987a) are shown as contours. Filled white circles represent the spatial resolution in each panel. The ⋆ symbol represents the position of Sgr A*.*

≈ +25”, Δb ≈ −50” in the CO(4-3) line and at $\Delta\alpha(J2000) \approx +35$”, $\Delta\delta(J20004) \approx$ +50” in the carbon lines. The feature is detected in all lines, except in [NII] , as can be seen in the channel map at +105 kms^{-1}.

4.2.3 High Velocity Gas Detected in [CI](1-0) and CO(4-3)

Towards the l.o.s. to the Sgr A Complex, and at high LSR velocities ($|V_{lsr}| > 100$ kms^{-1}), the gas is expected to be orbiting in the family of X_1 orbits around the GC (Jenkins & Binney, 1994). The HVG at these orbital velocities is detected in low-J CO observations, while mid-J detections are difficult due to weak emission at those frequencies. Given the low rms noise in the sub-mm datasets in the present work, it is possible to detect this gas in the CO(4-3) and the [CI](1-0) lines. At negative LSR velocities, HVG is detected between −160 kms^{-1} and −100 kms^{-1} at the lower right part of the CO(4-3) channel maps and in the lower left corner of the [CI](1-0) line images. This structure seems to have two velocity components along the l.o.s., judging from ^{13}CO(1-0) observations of the ongoing Mopra CMZ CO(1-0) Survey (M. Burton, private communication). Between −96 kms^{-1} to −73 kms^{-1}, a remarkably commentary-like structure is seen in both lines. In the CO(4-3) maps, it ranges from Δl ∼ +350”, Δb ∼ 50” to Δl ∼ +650”, Δb ∼ −400”. In the [CI](1-0) maps, the structure spans from $\Delta\alpha(J2000) = +100$” to $\Delta\alpha(J2000) = +550$”, at approximately constant Declination $\Delta\delta(J2000) =$ +600”.

At positive LSR velocities, two structures with LSR velocities above +100 kms^{-1} are identified. The first one can be traced between LSR velocities +100 kms^{-1} to +150 kms^{-1}, and is located in the upper left and upper right regions of the CO(4-3) and [CI](1-0) channel maps, respectively. This emission was already detected in CS(2-1) by Serabyn & Guesten (1987) but no further analysis was made. At even larger LSR velocities, between +155 kms^{-1} and +180 kms^{-1}, a very large structure covering almost entirely the observed area is detected in both lines. Figure 4.10 shows the [CI](1-0) (colors) and CO(4-3) (contours) emission of this HVG component at the +175 kms^{-1}. There is a good spatial correlation between both lines, being the carbon emission more widespread than the carbon monoxide emission. From Figure 4.1, the peak intensities in both lines are around ∼ 0.25 K in the average spectra. This structure is particularly interesting since it appears completely separated from the bulk of the gas in the X_2 orbits, assumed to be at radial velocities < +100 kms^{-1} in the direction of the Sgr A Complex.

In the datasets of the neutral species, the HVCC CO+0.02−0.02 previously observed by Oka et al. (2008) with high spatial resolution in CO(1-0) and HCN(1-0), is detected. The HVCC is clearly detected in CO(4-3), [CI](1-0), and

[CI](2-1), between +100 kms^{-1} and +150 kms^{-1}. The compact source is located at the center of the map in all observations. The [CII] detection is marginal with the emission just above the lowest contour at 3σ significance level, with σ the characteristic noise of the data as summarized in Table 3.1.

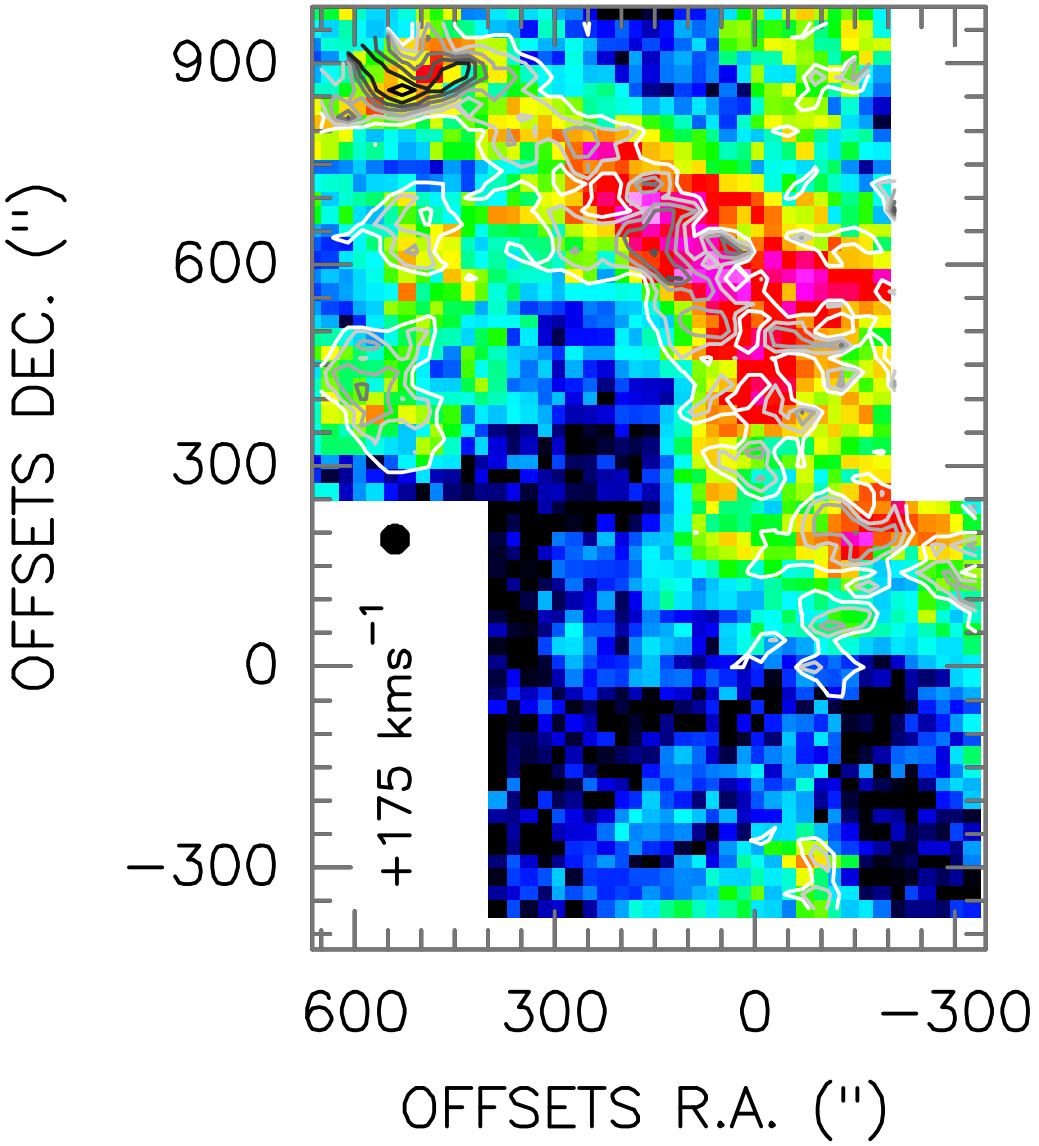

Figure. 4.10: *Channel map of the [CI](1-0) (color scale) and CO(4-3) (contours, black being the largest value) emission of the HVG component at +175 kms^{-1}. The filled black circle shows the 46" angular resolution of the [CI](1-0) data. The structure belongs to the X_1 orbits in the gravitational potential of the GC. The emission from both lines show large spatial coincidence, though intensity ratios can have large variations, specially towards the CO(4-3) peak, at the upper left corner of the image.*

Chapter 5

The Arched Thermal Filaments

5.1 Introduction

In the GC, several bubble-like and arc-like structures are seen (Price et al., 2001). Some of these structures are closely related to massive star clusters or SNRs[1], such as the "Radio Arc Bubble" (Rodríguez-Fernández et al., 2001), located south from the Quintuplet Cluster (in Galactic coordinates) and thought to be produced by the interaction of the molecular material with several supernovae explosions (Tsuboi et al., 1997); or the Arched-Filaments, which are arc-like structures that originated presumably from the interaction of the gas with the radiation field of the massive Arches Cluster (Simpson et al., 2007). In this chapter, I analyzed the sub-mm emission detected towards the Arched-Filaments in the context of PDRs using the KOSMA-τ PDR model of clumpy clouds as described in Section 2.11.1.

The Arches Cluster, first discovered by Cotera et al. (1996), is located at a projected distance of ~ 26 pc from Sgr A*. Its mass is ~ $2{\times}10^4$ $M_\odot$ with a radius of ~ 0.19 pc. It has an age between 2 - 2.5 Myr, young enough so no supernovae explosions in the cluster have occurred so far. The bolometric luminosity of its ~ 160 OB stars is L_{bol} ~ 10^8 $L_\odot$ (Figer, 2008), and a Lyman continuum flux between $4{\times}10^{51}$ s^{-1} and $1{\times}10^{51}$ s^{-1} has been derived (Figer, 2008; Simpson et al., 2007). In the last years, 19 isolated Wolf-Rayet and O super giants stars have been found scattered throughout the inner 50 pc of the GC with no association to any of the three massive star clusters in the GC: Arches, Quintuplet, and Nuclear Cluster (Mauerhan et al., 2010; Dong et al., 2011, 2012), showing that the gravitational interactions in the GC can remove massive stars from their parent stellar cluster, affecting the ISM with their strong radiation field, as they travel across the GC

[1] Supernova Remnants

region.

In terms of its kinematics, Stolte et al. (2008) estimated the 3-dimensional velocity of the Arches Cluster to be 232 ± 30 kms^{-1} after obtaining its spatial velocity from stellar proper motions 212 ± 29 kms^{-1} and combining it with the measured LSR velocity of the cluster +95 ± 8 kms^{-1} obtained by Figer et al. (2002). More recently, Clarkson et al. (2012) recalculated the proper motions of the Cluster obtaining 172 ± 15 kms^{-1} which is only slightly lower than the previous value. The large spatial velocity of the cluster suggests that it must be in a noncircular orbit, if the cluster is to be found within the X_2 orbits (Stolte et al., 2008). On the other hand, the positive LSR velocity of the cluster agrees in sign with X_2 orbit simulations, but the high space velocity is inconsistent with the maximum X_2 orbital velocity of 120 kms^{-1} suggested by the stellar bar model of Englmaier & Gerhard (1999). Overall, and given the short orbital time $\lesssim$ 1 Myr for a stellar cluster to orbit the GC, it is probable that the Arches and Quintuplet clusters are no longer spatially related with their parent MCs (Simpson et al., 2007).

Star Clusters such as the Arches and Quintuplet Clusters are not expected to live longer than ~ 10 Myr due to the strong tidal forces in the GC (Kim et al., 1999; Portegies Zwart et al., 2002). Stolte et al. (2008) found that the Arches Cluster has completed at most one orbit around the GC in its lifetime, and that it will approach closer than 10 pc to the GC only if its projected distance from Sgr A* (~ 26 pc), is very close to its Galactocentric radius (Clarkson et al., 2012). Recently, the estimation of the cluster's tidal radius (> 2.5 pc), suggests that its closest approach to Sgr A* is larger than 120 pc (M. W. Hosek Jr., private communication), suggesting that the projected distance from the GC is far from its Galactocentric radius.

In Figure 5.1, the Arched-Filaments are shown in the 20 cm continuum emission from Yusef-Zadeh & Morris (1987a). From H85α recombination and continuum observations at 10 GHz, Pauls et al. (1976) found that the emission from the Arched-Filaments originates mainly in a thermal plasma of electron temperature ~ 7000 K, while similar electron temperatures were found by Lang et al. (2001) across and along the filaments. As it was shown in Chapter 4, most of the ionized [CII] and [NII] emission is associated to the Arched-Filaments, and it appears at negative LSR velocities, while little [CI](1-0), [CI](2-1), and CO(4-3) emission is found towards the filaments, when compared with the rest of the emission in the datasets. Minh et al. (2005) found that at negative LSR velocities in the Sgr A Complex, HCO^+, HNCO and SiO have low column densities. This is consistent with the composite Spitzer/IRAC-3 color image (8.4 μm, 4.5 μm, and 3.6 μm) in Chambers et al. (2014) tracing dust emission, where dark areas indicate large

column densities. On the other hand, Bally et al. (1987, 1988) and Serabyn & Guesten (1987) have shown that the Arched-Filaments are closely associated to a system of dense molecular clouds traced, for instance, by CS(2-1) observations (see the Peak 1 and Peak 2 positions in Serabyn & Guesten (1987)).

In terms of previous PDR modeling work, Genzel et al. (1990) used [CII] observations (67 kms^{-1} spectral resolution and 55" spatial resolution), [OI] at 63 μm, mid-infrared, FIR, and radio continuum to model the emission from the G0.07+0.04 region of mas $\sim 2{\times}10^4$ $M_\odot$. They interpreted the [CII] emission coming from partially ionized interfaces between fully molecular and fully ionized gas. From the estimated [CII]/[OI] 63 μm ratio $\sim$ 1, they inferred a hydrogen volume density of a few times 10^3 cm^{-3} and a H_2 mass per beam $\sim$ 500 $M_\odot$ assuming an abundance ratio $C^+/H_2 \sim 3{\times}10^{-4}$ and optically thin emission. Genzel et al. (1990) found that the emission of all measured lines was better reproduced by PDR models (Hollenbach et al., 1991) than by J-shock ionization or magneto-hydrodynamic models (Hollenbach & McKee, 1989), in which collisions between neutrals and charge particles ionize the gas. Martin et al. (1984) showed that only models taking clumpiness into account can match the observed line intensities and linewidth of various CO isotopic transitions. In the following, I describe the positions selected and the procedure used to model the sub-mm emission observed towards the Arched-Filaments.

5.2 Selected Positions in the Arched-Filaments

I have selected seven positions within the Arched-Filaments and two positions close to them in order to investigate the physical conditions of the gas under the influence of the FUV field from the Arches Cluster. The positions are shown in Figure 5.1 and summarized in Table 5.1. The criterion in selecting the positions is mainly based on the [CII] and [NII] emission distribution shown in Chapter 4, which is most intense and closely follows the 20 cm continuum (Yusef-Zadeh & Morris, 1987a) in the Arched-Filaments, as can be seen in Figure 4.2. In Figure 5.1, the selected positions E1, E2-N, E2-S, G0.10+0.02, W1, W2, G0.07+0.04, P1, and P2 are shown as red crosses, while the red open circles represent the 46" spatial resolution of the sub-mm datasets. The blue crosses in the figure show the closest 20 cm continuum emission peaks to the positions in the sub-mm datasets grid, except for positions P1 and P2, where the blue crosses show the CS(2-1) peak positions in Serabyn & Guesten (1987). Also shown are several H II regions (black crosses) that together conform the H-Region (see Chapter 4). The E1, E2-N, E2-S, and G0.10+0.0 (also known as the "banana" in Timmermann et al. (1996)) positions are tracing the two sub-filaments forming the Eastern-Filament, while the W1, W2, and G0.07+0.04 positions are tracing the Western-Filament.

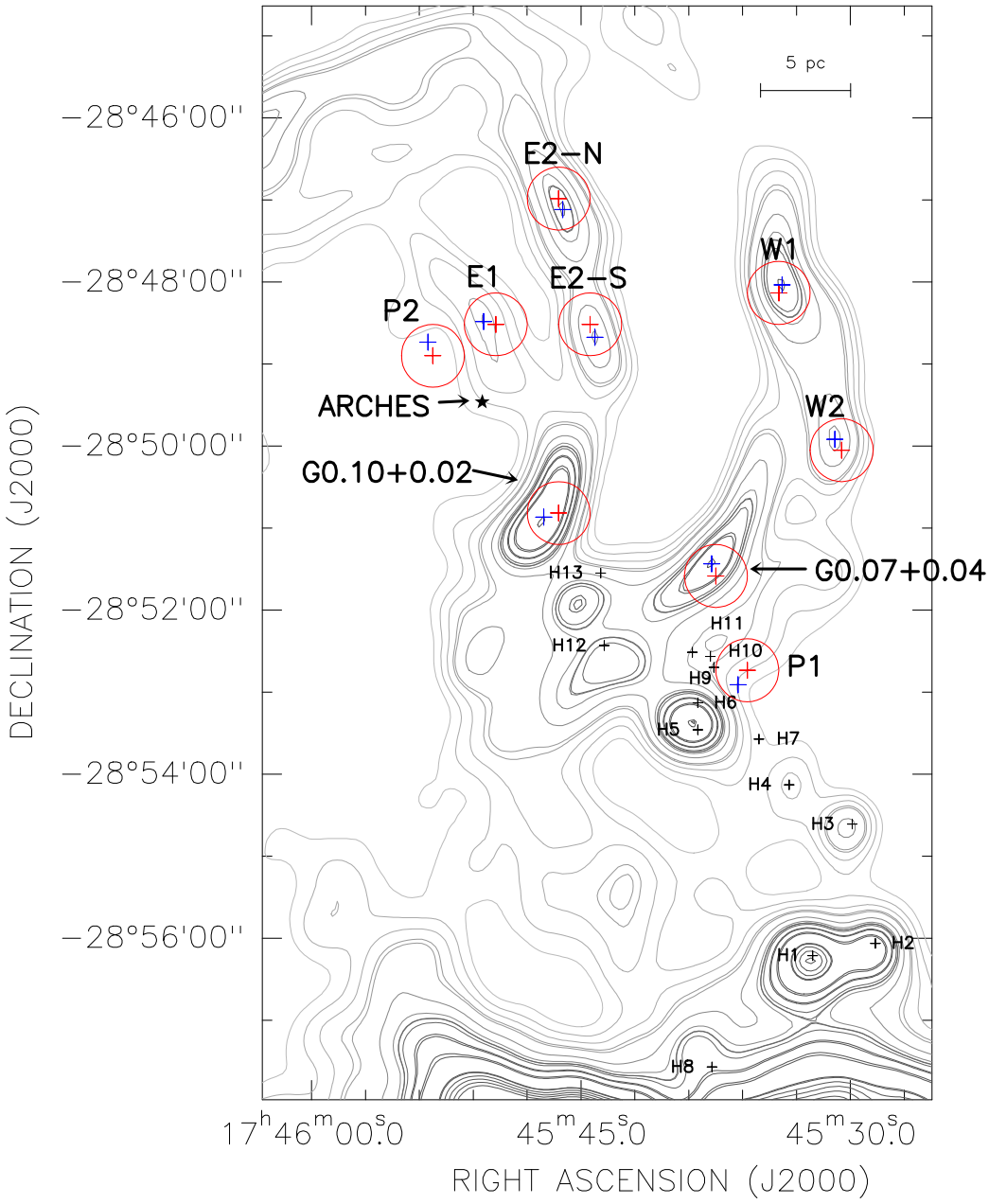

Figure. 5.1: *1.4 GHz VLA contours of the Arched-Filaments with selected positions for PDR analysis overplotted. Blue crosses depict the continuum emission peaks of the E1, E2-N, E2-S, W1, W2, G0.07+0.04, and G0.10+0.02 structures, and the CS(2-1) peaks in Serabyn & Guesten (1987). Red crosses show the closest position to the blue crosses in the grid of our data, while the red circles represent the 46" spatial resolution in the sub-mm observations. Black crosses show the position of the several H II regions conforming the so called* H-Region.

The G0.07+0.04 region is particularly interesting since the gas there is thought to be interacting with the Northern-Thread NTF, resolved for the first time in the

high resolution 6 cm continuum images of Lang et al. (1999b). The magnetic field is aligned with the thread, indicating the possible interaction of the ionized, neutral atomic, and molecular material with the pervasive large-scale, dipolar magnetic field in the GC. These selected positions are also seen as local maxima in the 3.6 cm continuum observations of Lang et al. (2001). The P1 and P2 positions are coincident with high density gas traced by CS(2-1) observations in Serabyn & Guesten (1987), and are located at the edges of the E and W filaments. Given the high density towards these positions, PDR models are expected to reproduce the emission if the exciting mechanism of the gas is mainly due to the FUV field from the Arches Cluster. In Table 5.1, the $\Delta\alpha$ and $\Delta\delta$ columns contain the offsets of the selected positions with respect to the maps center located at Sgr A*, while the $\Delta\alpha(shift)$ and $\Delta\delta(shift)$ columns contain the angular offsets of the selected positions with respect to the closest 20 cm continuum maximum in Figure 5.1. The last two columns in the table contain the absolute coordinates of the selected positions in the Equatorial (J2000) coordinate system.

The CO(4-3) integrated intensity between -65 kms^{-1} and 0 kms^{-1} is shown in Figure 5.2 (contours) for the Arched-Filaments, together with the 20 cm continuum emission from Yusef-Zadeh & Morris (1987a). The selected positions in Table 5.1 are shown as black crosses, while the position of the Arches Cluster is indicated by the ★ symbol. The emission associated to the H-Region to the south-west of the figure is also shown. Most of the warm molecular material in the -30 kms^{-1} Cloud traced by the CO(4-3) emission is displaced to the south from the Arched-Filaments, and it is connected to the gas streamers shown in Figure 4.4. It is interesting to notice that the peak CO(4-3) emission is sandwiched between the 20 cm continuum emission from the Arched-Filaments, and the 20 cm continuum emission associated to the Sgr A-East SNR to the south. In Chapter 7, the close association of the +50 kms^{-1} Cloud with the Sgr A-East SNR at positive LSR velocities is shown. If the CO(4-3) emission from the -30 kms^{-1} Cloud and from the +50 kms^{-1} Cloud are both indeed related to the 20 cm continuum emission from Sgr A-East, then the idea that MCs in the GC are a single entity ripped apart in the strong gravitational potential of the central 30 pc of the GC as the gas orbits around it, would be supported by the observations in the present work.

5.3 Integrated Emission at Selected Positions

In Appendix D, Figures D.1 to D.9 show the measured sub-mm spectra at the selected positions in Table 5.1. The sub-mm observations are complemented with public HCO^+(1-0) and $H^{13}CO^+$(1-0) Mopra observations by Jones et al. (2012) and with unpublished CO(1-0) and ^{13}CO(1-0) observations of the ongoing

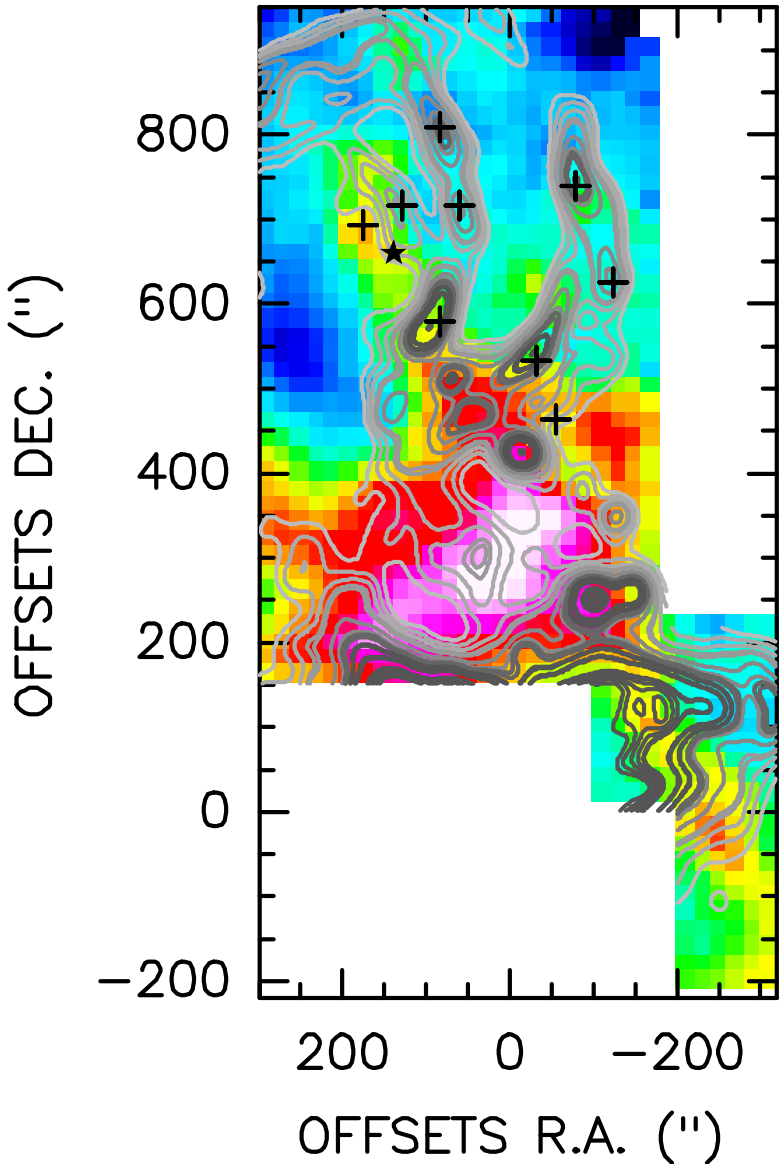

Figure. 5.2: *Integrated CO(4-3) emission between −65 kms^{-1} and 0 kms^{-1} (colors) and 20 cm continuum emission (contours) from Yusef-Zadeh & Morris (1987a) for the Arched-Filaments. The black crosses represent the selected positions in Table 5.1 (red crosses in Figure 5.1), while the ★ symbol denotes the position of the Arches Cluster.*

Mopra CMZ Survey (M. Burton, priv. communication). I also had access to their optically thin $C^{18}O$(1-0) observations, but no detections were found above the noise level. Each figure labels the observed species and transition, and the $T^*_{A,rms}$ noise of the spectrum. The LSR velocities of the foreground spiral arm features are shown as vertical dashed lines (see Chapter 4). From Figures D.1 to D.9, the complexity of the line profiles in all observed species is evident. They are the result of the complex kinematics of the gas in the velocity field of the GC, the interaction of the gas with the Arches Cluster radiation field, together

Position	$\Delta\alpha$ (")	$\Delta\alpha(shift)$ (")	$\Delta\delta$ (")	$\Delta\delta(shift)$ (")	$\alpha(J2000)$ $h\ m\ s$	$\delta(J2000)$ $^\circ\ '\ ''$
E1	+129.1	+9.0	+717.0	+2.0	17 45 49.74	−28 48 31.1
E2-N	+83.1	−3.0	+809.0	−8.0	17 45 46.24	−28 46 59.1
E2-S	+60.1	−3.5	+717.0	−9.5	17 45 44.48	−28 48 31.1
W1	−77.9	−2.5	+740.0	+6.0	17 45 33.96	−28 48 08.1
W2	−123.9	+5.0	+625.0	+8.0	17 45 30.45	−28 50 03.1
G0.07+0.04	−31.9	+3.0	+533.0	+9.0	17 45 37.47	−28 51 35.1
G0.10+0.02	+83.1	+11.0	+579.0	−3.0	17 45 46.24	−28 50 49.1
P1	−54.9	+6.9	+464.0	−10.7	17 45 35.71	−28 52 44.1
P2	+175.1	+3.7	+694.0	+10.0	17 45 53.25	−28 48 54.1

Table. 5.1: *Arched-Filaments selected positions shown in Figure 5.1. The $\Delta\alpha$ and $\Delta\delta$ values are the angular offsets with respect to the position of Sgr A*, while the $\Delta\alpha(shift)$ and $\Delta\delta(shift)$ angular offsets are measured with respect to the 20 cm continuum (Yusef-Zadeh & Morris, 1987a) emission peaks closest to the positions in the grid of the datasets in the present work. The absolute Equatorial (J2000) coordinates of the selected positions are shown in the last two columns of the table.*

with in-situ and foreground absorption features that control the shape of the observed profiles. Therefore, merely identifying the number of independent gas components along the l.o.s. is not a trivial task. Oka et al. (2005) showed that separating the broad spectra towards the GC into cloud components is difficult and can be somewhat arbitrary. In order to obtain the integrated intensities at each position and for each line, it is necessary to simultaneously investigate the line profiles of different species in order to find a coherent picture of how many and in which LSR velocity range, the gas component(s) are located. For this purpose, I followed three approaches: (1) integrating the original spectrum as it was measured, (2) fitting a high order polynomial that will interpolate between LSR velocities where absorption features from spiral arms (seen also sometimes in emission) are found in the spectrum, as done in Requena-Torres et al. (2012) for the spectra measured towards the CND, and (3) fitting multiple Gaussians that will also interpolate between absorption features in order to recover the missing emission. An example of the three approaches is given in Figure 5.3, which shows the CO(4-3) spectrum of position W1, taken from Appendix D. The vertical dashed lines indicate the LSR velocity of spiral arms features along the l.o.s. while vertical dotted lines show the LSR velocity integration limits for the POLY and SPEC approaches. The black boxes at the bottom of the spectrum show the regions that were masked out for the fitting procedure. The gray dotted spectra show the residuals from the fit procedures. In the top panel of the figure, the GAUSS approach was used to recover the CO(4-3) integrated emission. From the panel, it can be seen that a double Gaussian profile (blue line) can very well reproduce and recover the missing emission due to absorption features. The [CI](1-0) Gaussian fit (pink line) was overplotted on the CO(4-3) spectrum to

check the consistency between the Gaussians profiles of both lines in terms of their fitted central LSR velocities and linewidths. The bottom panel shows the high order polynomial POLY approach (red line). In the case of W1, similar integrated intensities are found from the GAUSS and POLY approaches, but larger differences are found for other lines and positions.

The integrated intensities are summarized in Table 5.2 for the first (SPEC), second (POLY) and third (GAUSS) methods. Roughly, the intensities derived from the GAUSS and POLY methods are similar and larger than the ones of the SPEC method, as expected. In general, a single Gaussian can fit well the observed profiles in the LSR velocity range of the gas associated with the Arched-Filaments (for LSR velocities < 0 kms^{-1}), under the assumption that most of the deviation of the line profile from a Gaussian profile is either due to absorption (local or along the l.o.s.) or particular kinematics of the gas. An exception is found in the [CI](1-0) spectrum of position P1 in Figure D.6, which clearly shows signatures of non symmetric, red-shifted gas, possible due to gas being pushed away from the local stellar winds of the several H II regions (H6, H9, H10, and H11) that surround it.

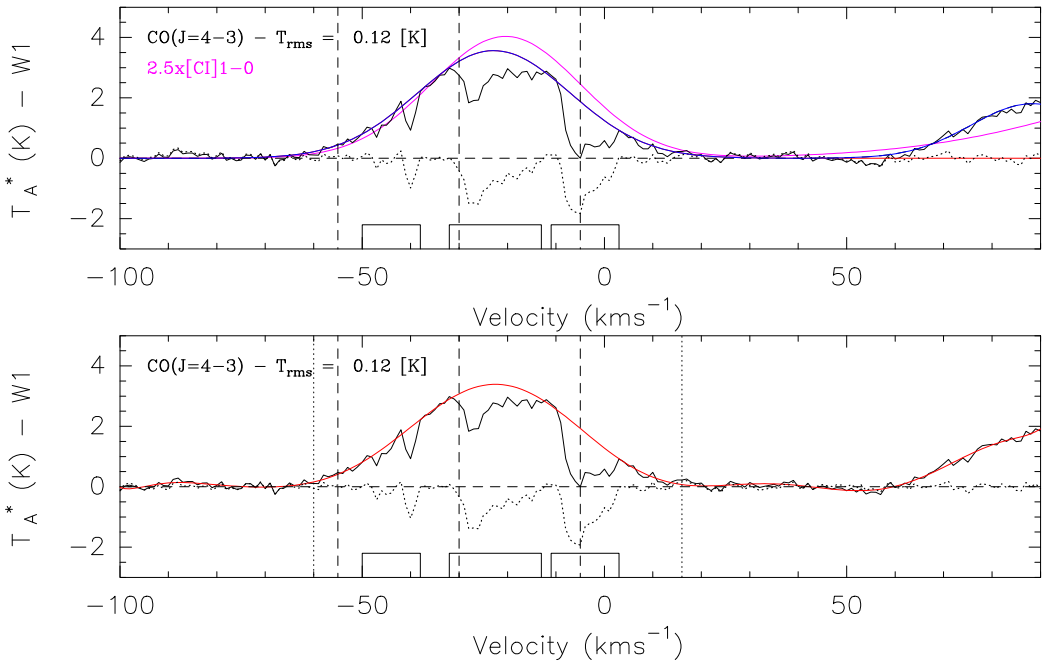

Figure. 5.3: *Gaussian (top blue line) and polynomial (bottom red line) fit results of the CO(4-3) transition for position W1. Vertical dashed lines indicate the position of spiral arms along the l.o.s.. The dotted vertical lines indicate the integration limit for the POLY approach. The [CI](1-0) Gaussian fit (pink line) is overplotted for comparison.*

5.4 [NII] as Tracer of [CII] Emission Originated in H II Regions

In Section 2.9.3, the theoretical relationship derived by Abel (2006) between the [CII] emission originated in PDRs and in H II regions as traced by [NII] observations was shown in Equation 2.60. As a reminder, Equation 2.60 shows the [CII] intensity expected to arise from H II regions, while the rest of the emission above the prediction is attributed to PDRs, under the assumption that the H II and PDR regions are in pressure equilibrium. In order to explore this relationship between the ionized species in the present work, the spatial distribution of the [CII] and [NII] integrated emission is shown in Figure 5.4. The map in Figure 5.4 was constructed by integrating the [CII] and [NII] spectra between -70 kms^{-1} and $+20$ kms^{-1}, and calculating their ratios in units of ergs cm^{-2} s^{-1} str^{-1}. For each ratio, only integrated intensities with detections above the 3σ significance level, with σ the corresponding propagated noise in the LSR velocity integration interval, were considered. This is the reason why some positions have no ratios derived (white areas). The grid points in the datasets are shown as black crosses, and the red ★ symbol shows the position of the Arches Cluster. The 20 cm continuum emission from Yusef-Zadeh & Morris (1987a) and the selected positions in Table 5.1 are shown as black contours and white circles (of the size of the spatial resolution of the data), respectively. The upper panel in Figure 5.4 is an histogram of the integrated intensity ratios in the spatial map. In the histogram, a Gaussian profile was fitted to characterize the distribution, from which the central ratio (C_H) and standard deviation (σ_H) are given. As it can be seen from the figure, most the [CII]/[NII] ratios are lower than 10 across the map, while the highest values are located close to the southern edge of the Radio-Arc, to the western edge of the W1 filament, to northern edge of Sgr A-East, and to the western edge of the M+0.11−0.08 cloud.

The left panel in Figure 5.5 shows a scatter plot of the [CII] and [NII] integrated intensities in Figure 5.4. The selected positions in Table 5.1 are shown as color points, with their corresponding error bars. The relationship in Equation 2.60 from Abel (2006) is shown as a dashed straight line. Most points fall below the prediction, as expected from Figure 5.4, since for 150 K kms^{-1} integrated intensity of the [NII] line, the predicted [CII]/[NII] ratio is $\sim$ 7.4, increasing with decreasing [NII] integrated intensities. The right panel in Figure 5.5 shows the same scatter plot than in the left panel, but only for the selected positions in Table 5.1 identified by colors. For each position, the integrated intensities using the GAUSS (filed squares), POLY (filled diamonds), and SPEC (filled circles) methods, and their corresponding error bars, are shown. Even in the upper limit for the integrated intensities obtained from the GAUSS and POLY methods, only positions E1, E2-N, G0.07+0.04, P1, and P2 reach the Abel (2006) prediction,

while positions E2-S, W1, W2, and G0.10+0.02 fall well below it.

In the following, I discussed some of the reasons why such discrepancy might arise between the measured and predicted integrated intensities between the [CII] and [NII] lines in the Arched-Filaments region: (1) as shown in Appendix A, the best temperature scale to represent the true convolved antenna temperature of the warm gas in the present work is the T_A^* temperature scale, in which the calibrated data have been divided by the forward efficiency (F_{eff}). Nonetheless, this represents a lower limit to the true convolved antenna temperatures. Since the main beam efficiencies (B_{eff}) for the [CII] and [NII] transitions observed with the Herschel-HIFI satellite are virtually identical $\sim$ 0.58 (Müller & Jellema , 2014), scaling the integrated intensities of both lines by B_{eff}/F_{eff} to put them in the main beam temperature scale (upper limit to the true convolved antenna temperatures) would leave the overall trend in both panels of Figure 5.5 unchanged; (2) an underestimation of the [CII] emission is rather unlikely given that methods GAUSS and POLY are, by definition, upper limits to the integrated intensities. Moreover, the [CII] emission at the G0.07+0.04 position was measured by Genzel et al. (1990) to be $\sim$ 1.2×10^{-3} ergs s^{-1} cm^{-2} str^{-1} within a 55" beam (and 30% calibration error), which is lower than what I have estimated from the SPEC method (lower limit for the integrated intensity) around 1.7×10^{-3} ergs s^{-1} cm^{-2} str^{-1} within the 46" spatial resolution of the datasets. Despite of the slightly different beam sizes, both estimates are consistent within error uncertainties; (3) an overestimation of the [NII] emission is also unlikely since, even when plotting the SPEC [NII] intensities (lower intensity limits shown by the filled circles on the right panel of Figure 5.5) against either the GAUSS or POLY [CII] intensities (upper intensity limits shown by the filled squares and diamonds on the right panel of Figure 5.5), the overall trend does not change significantly; (4) Abel (2006) also explored models with metallicities an order of magnitude lower than the solar value (Z = 0.1 Z_{orion}), which would put the dashed straight line on the right panel of Figure 5.5, between the two groups of points (those matching the prediction and those below it), but such low metallicity values are unlikely for the GC, where larger metallicities than the solar value have been derived (Mezger et al., 1979; Cox & Laureijs, 1989; Shields & Ferland, 1994; Mezger et al., 1996; Yusef-Zadeh et al., 2007); (5) Simpson et al. (2007) found that strong shocks from the Quintuplet Cluster Wolf-Rayet stars can ionize oxygen to [OIV] (with ionization potential $\sim$ 54.9 eV, Draine (2011)) and destroy dust grains. If this were also the case for atomic carbon in the Arched-Filaments and most of the ionized carbon were in the form of [CIII] (ionization potential $\sim$ 24.4 eV, Draine (2011)) rather than in [CII] form due to a strong ultra-violet field from the Arches Cluster, the low [CII] intensities with respect to the predicted ones from the [NII] intensities could be explained. Nonetheless, this would not explain the low [CII] intensities at positions W1 and W2, given their large projected distances to the cluster (> 10 pc), where the radiation field should be strongly reduced; (6) finally

an most likely, it could well be that the main assumptions of the Abel (2006) theoretical work, who assumed the simplified case of an H II region and PDR in pressure equilibrium, for a single massive star, and elemental abundances for the Orion nebula are not matched in the Arched-Filaments region.

A particularly interesting case is the one of the G0.07+0.04 position, where the gas is apparently interacting with Northern-Thread NTF (Lang et al., 1999b), tracing the magnetic field in the GC. Genzel et al. (1990) found that [CII] and H110α observations are blue-shifted by $\sim$ 10 to 15 kms^{-1} with respect to their CO and CS observations, indicating streaming motions between ionized and molecular gas. In Figure 5.6, the sub-mm spectra in the present work, together with the Mopra observations (see Section 5.3) are shown. The gray solid line represents the Gaussian fit results by Lang et al. (2001) to the H92α recombination line in the same region. Vertical dotted lines show the LSR velocity of spiral arms long the l.o.s.. As it can be seen from the figure, the H92α central LSR velocity at ~ -44 kms^{-1} is slightly blue-shifted with respect to the [CII] central LSR velocity at ~ -37 kms^{-1}, and strongly blue-shifted ($\sim$ 30 kms^{-1}) with respect to the neutral atomic and molecular material with central LSR velocity around -14 kms^{-1}, if the emission in the neutral atomic, and molecular spectra is related to a single gas component along the l.o.s., and only appears as several different components because it is strongly absorbed at the positions of the spiral arms, as interpreted in the present work. Certainly, observations of the optically thin C^{18}O(1-0) line with enough signal-to-noise ratio would be needed to disentangle the real number of physical gas components along the l.o.s..

5.5 KOSMA-τ Model Parameters

In order to model the calculated integrated intensities in Table 5.2, the KOSMA-τ PDR model of clumpy clouds (Stoerzer et al., 1996; Cubick et al., 2008; Röllig et al., 2013a) was used. The model can handle several species such as C$^+$, C, O, CO, ^{13}CO, ^{13}C$^+$, ^{13}C, HCO$^+$, H^{13}CO$^+$, H$_3$O$^+$, CH$^+$, with energy level transitions ranging from radio wavelengths up to the FIR domain.

In Table 5.3, the parameter grid for the model is given. On the lower limits for the FUV Draine field χ/χ_D and total hydrogen nucleus number density n(H)$_{s,tot}$ = n(H)$_s$ + 2n(H$_2$)$_s$, the parameter grid was selected to cover the values for the GC estimated by Rodríguez-Fernández et al. (2004) who found that, for MCs with projected distances far from thermal continuum sources, PDRs in the CMZ are illuminated by a FUV radiation field a few times 10^3 larger than the local ISM value, with hydrogen densities of the order of $\sim 10^3$ cm^{-3}. On the upper limits,

Table. 5.2: *Integrated intensities from the Gaussian fit (GAUSS), polynomial fit (POLY), and from the original measured spectrum (SPEC) for the selected Arched-Filaments positions in Table 5.1. The integrated Intensity errors are calculated from the $T^*_{A,rms}$ and $\Delta V(FWHM)$ errors in the GAUSS method, and from the propagation of $T^*_{A,rms}$ over the integrated LSR velocity range for the POLY and SPEC methods. The Mopra (CO(1-0), ^{13}CO(1-0), HCO$^+$(1-0), and H^{13}CO$^+$(1-0)) data were corrected for the extended beam efficiency η_{xb} = 0.65 (Ladd et al., 2005).*

Source	Method	[CII] (K kms^{-1})	[NII] (K kms^{-1})	[CI](2-1) (K kms^{-1})	[CI](1-0) (K kms^{-1})	CO(4-3) (K kms^{-1})	CO(1-0) (K kms^{-1})	^{13}CO(1-0) (K kms^{-1})	HCO$^+$(1-0) (K kms^{-1})	H^{13}CO$^+$(1-0) (K kms^{-1})
P1	GAUSS	260.90 ± 22.30[b]	77.00 ± 15.40[b]	61.10 ± 4.30[b]	91.40 ± 3.00[b]	262.60 ± 8.20[b]	..... [a]	128.92 ± 8.31[b]	61.85 ± 1.08[b]	5.23 ± 0.31
P2	GAUSS	303.80 ± 20.80	81.70 ± 4.10	27.00 ± 1.10	53.40 ± 1.80	237.60 ± 6.00	327.85 ± 18.31	82.00 ± 4.46	32.62 ± 1.54	4.62 ± 0.31
W1	GAUSS	144.90 ± 8.70	117.80 ± 6.10	27.90 ± 0.60	60.10 ± 2.20	140.50 ± 2.90	415.85 ± 13.69	93.69 ± 8.62	15.85 ± 0.92	.....
W2	GAUSS	215.60 ± 4.70	146.20 ± 3.90	33.90 ± 1.20[c]	65.50 ± 2.20[c]	172.40 ± 4.10[a]	633.38 ± 21.23[a]	101.69 ± 6.77	18.62 ± 0.92	.....
G0.10+0.02	GAUSS	308.40 ± 17.70	148.30 ± 9.10	21.70 ± 1.70	42.40 ± 0.80	231.00 ± 4.70	538.62 ± 31.38[c]	74.31 ± 4.00	20.00 ± 0.77	.....
G0.07+0.04	GAUSS	378.90 ± 10.10	125.50 ± 5.10	46.70 ± 1.90	92.00 ± 1.70	234.70 ± 3.50	599.08 ± 28.77	94.62 ± 7.08	31.08 ± 0.46	.....
E2-N	GAUSS	249.20 ± 7.20	71.00 ± 4.70	22.70 ± 0.90	52.60 ± 1.60	113.40 ± 1.80	545.54 ± 19.23	68.00 ± 3.85	25.54 ± 0.77	.....
E2-S	GAUSS	144.40 ± 7.10	93.80 ± 3.70	29.80 ± 1.20	57.00 ± 2.90	162.80 ± 3.50	522.46 ± 19.08	87.69 ± 3.69	20.46 ± 0.92	.....
E1	GAUSS	268.60 ± 14.50	72.30 ± 3.30	55.90 ± 2.00	110.20 ± 2.60	152.10 ± 2.20	590.77 ± 10.46	140.00 ± 3.85	28.46 ± 0.92	4.15 ± 0.31
P1	POLY	317.70 ± 4.10	71.80 ± 3.20	61.20 ± 0.70	91.40 ± 0.60	235.50 ± 1.10	873.08 ± 3.69[a]	114.46 ± 2.15	53.54 ± 0.15	4.00 ± 0.15
P2	POLY	307.30 ± 5.40	75.20 ± 2.70	25.30 ± 0.50	49.20 ± 0.40	241.30 ± 0.70	387.38 ± 3.69	73.23 ± 2.31	35.23 ± 0.31	3.85 ± 0.31
W1	POLY	169.60 ± 4.30	128.40 ± 3.90	28.10 ± 0.50	57.00 ± 0.50	134.90 ± 1.00	421.23 ± 5.85	82.00 ± 4.62	16.31 ± 0.31	.....
W2	POLY	214.90 ± 5.60	139.00 ± 4.50	33.30 ± 0.40	61.60 ± 0.50	138.20 ± 1.10[a]	600.92 ± 5.85[a]	92.00 ± 2.92	16.31 ± 0.15	.....
G0.10+0.02	POLY	301.00 ± 4.50	119.70 ± 3.80	20.80 ± 0.50	42.50 ± 0.40	236.60 ± 0.50	582.77 ± 3.69	69.38 ± 2.00	21.08 ± 0.15	.....
G0.07+0.04	POLY	335.30 ± 3.80	99.40 ± 4.30	47.80 ± 0.70	91.20 ± 0.50	237.00 ± 1.10	668.62 ± 6.62	79.38 ± 3.85	28.62 ± 0.31	.....
E2-N	POLY	231.90 ± 3.70	70.80 ± 3.30	23.00 ± 0.50	53.50 ± 0.50	107.20 ± 1.00	530.31 ± 3.85	61.08 ± 2.46	25.38 ± 0.15	.....
E2-S	POLY	142.10 ± 3.50	91.30 ± 3.60	28.10 ± 0.40	58.70 ± 0.60	147.10 ± 1.00	488.00 ± 8.31	85.85 ± 2.15	19.54 ± 0.15	.....
E1	POLY	277.90 ± 4.70	66.80 ± 3.00	55.10 ± 0.50	109.80 ± 0.40	151.00 ± 1.00	581.08 ± 5.23	117.23 ± 2.92	39.08 ± 0.31	4.00 ± 0.31
P1	SPEC	234.30 ± 4.10	66.00 ± 3.20	60.10 ± 0.70	95.50 ± 0.60	206.40 ± 1.10	484.31 ± 3.69	106.00 ± 2.15	34.15 ± 0.15	3.69 ± 0.15
P2	SPEC	230.70 ± 5.40	65.50 ± 2.70	24.30 ± 0.50	47.90 ± 0.60	226.70 ± 0.70	270.62 ± 3.69	61.38 ± 2.31	23.85 ± 0.31	3.38 ± 0.31
W1	SPEC	143.60 ± 4.30	106.80 ± 3.90	27.00 ± 0.50	53.60 ± 0.50	106.20 ± 1.00	310.15 ± 5.85	75.38 ± 4.62	9.69 ± 0.31	.....
W2	SPEC	198.10 ± 5.60	110.80 ± 4.50	26.30 ± 0.40	53.30 ± 0.50	115.40 ± 1.10	397.85 ± 5.85	74.31 ± 2.92	10.92 ± 0.15	.....
G0.10+0.02	SPEC	264.60 ± 4.50	116.30 ± 3.80	17.40 ± 0.50	40.20 ± 0.40	165.20 ± 0.50	265.54 ± 3.69	59.23 ± 2.00	10.62 ± 0.15	.....
G0.07+0.04	SPEC	241.90 ± 3.80	89.90 ± 4.30	40.50 ± 0.70	71.20 ± 0.50	182.10 ± 1.10	449.54 ± 6.62	65.69 ± 3.85	16.00 ± 0.31	.....
E2-N	SPEC	205.80 ± 3.70	68.70 ± 3.30	19.60 ± 0.50	44.30 ± 0.50	83.20 ± 1.00	349.38 ± 3.85	59.85 ± 2.46	15.69 ± 0.15	.....
E2-S	SPEC	121.60 ± 3.50	89.30 ± 3.60	25.20 ± 0.40	55.70 ± 0.60	117.00 ± 1.00	287.85 ± 8.31	70.92 ± 2.15	10.15 ± 0.15	.....
E1	SPEC	209.50 ± 4.70	62.20 ± 3.00	44.10 ± 0.50	86.70 ± 0.40	130.60 ± 1.00	312.00 ± 5.23	85.08 ± 2.92	22.00 ± 0.31	4.15 ± 0.31

[a] POLY integrated intensity used for PDR modeling procedure instead of the GAUSS integrated intensity.
[b] Integrated intensity calculated from the sum of two fitted Gaussian profiles.
[c] Large extrapolation from measured intensities.

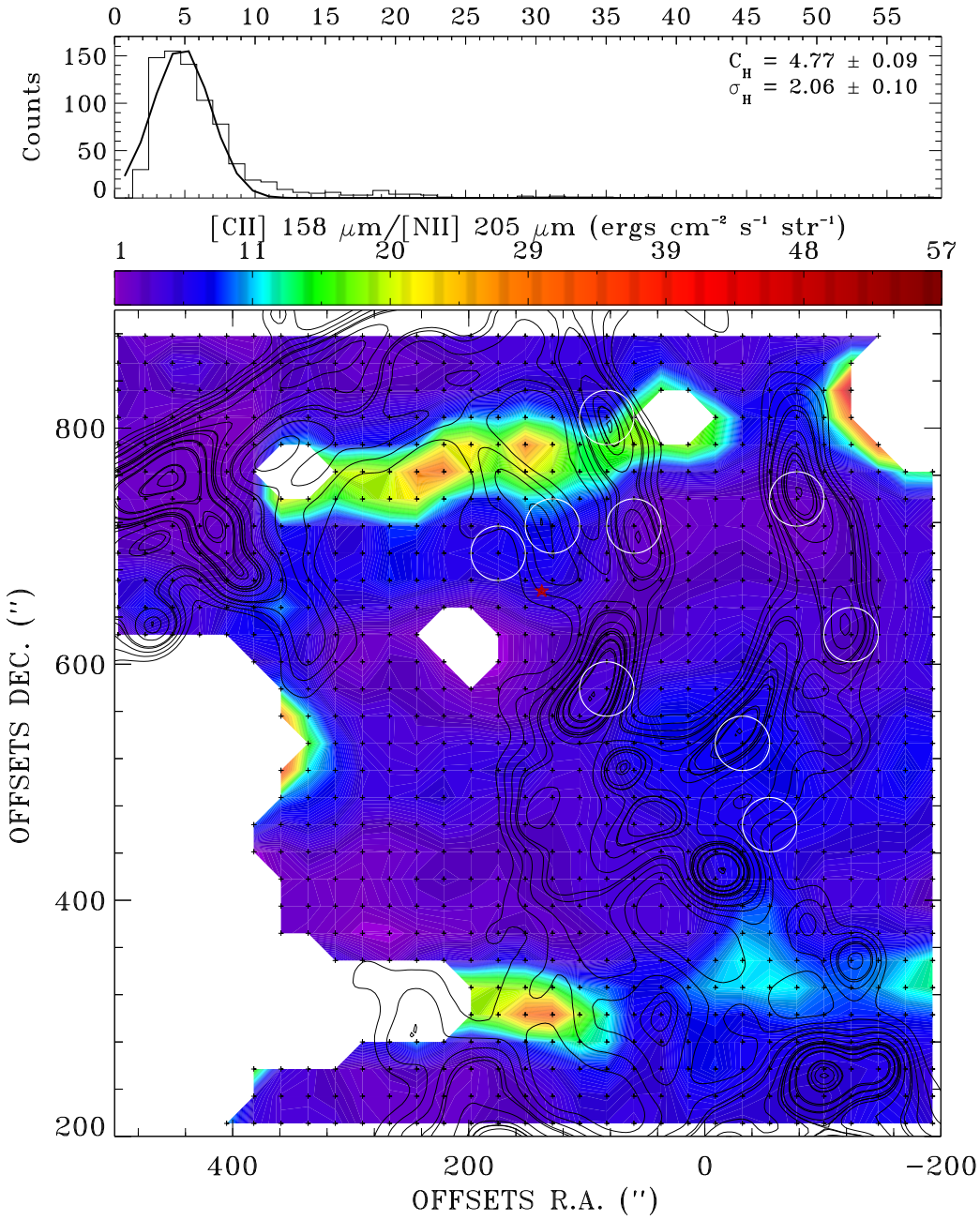

Figure. 5.4: *Bottom panel: spatial distribution of the integrated intensity ratios of the [CII] and [NII] lines between −70 kms^{-1} and +20 kms^{-1}. The 20 cm continuum emission from Yusef-Zadeh & Morris (1987a) and the selected positions in Table 5.1 are shown as black contours and white circles, respectively. Black crosses represent the grid points in the sub-mm datasets. The red ★ symbol shows the position of the Arches Cluster. Upper panel: histogram of the derived ratios in the bottom panel. A Gaussian fit was performed to characterize the central (C_H) and standard deviation (σ_H) of the histogram.*

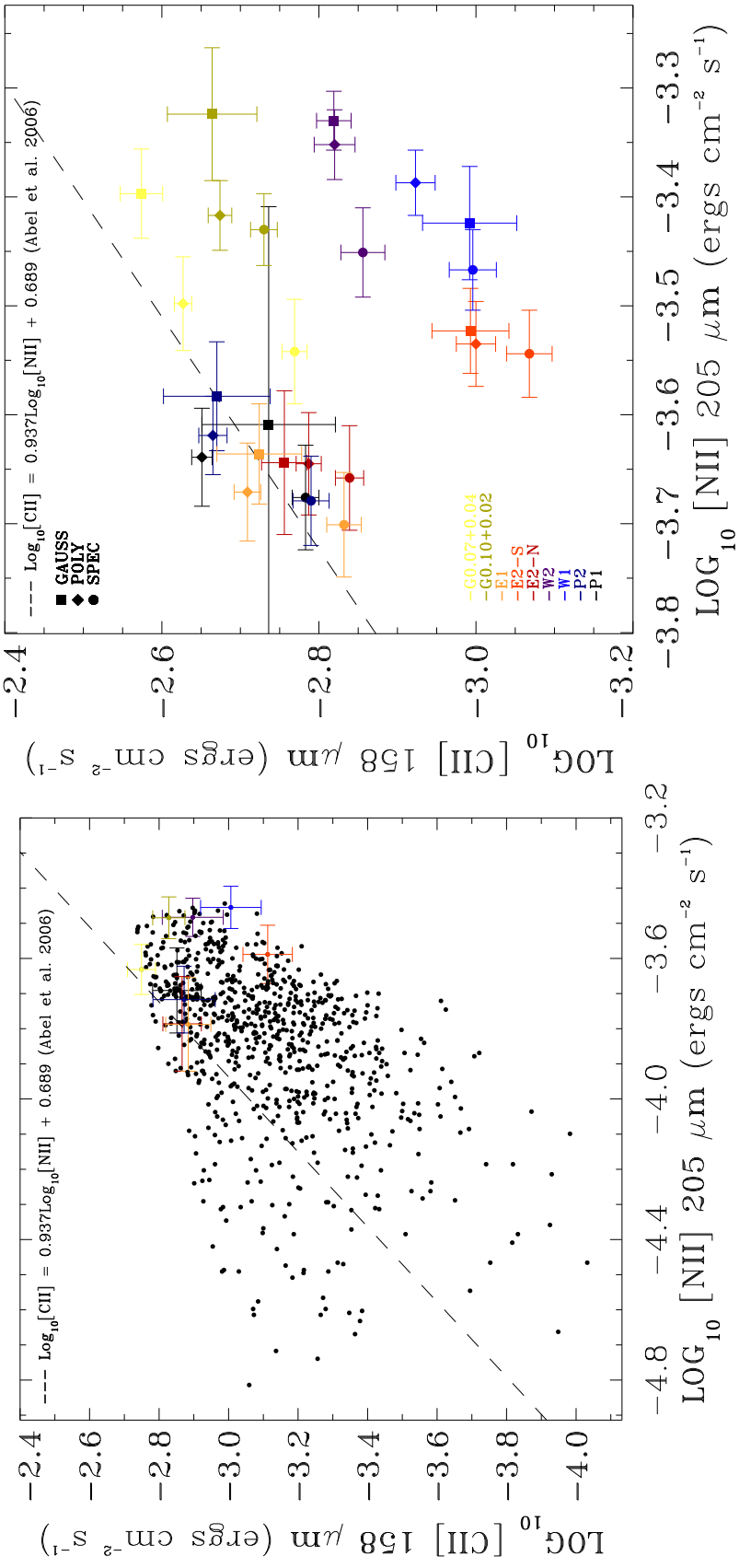

Figure. 5.5: *Left panel: scatter plot of the [CII] and [NII] integrated intensities between −70 kms^{-1} and +20 kms^{-1}. The corresponding values for the selected positions in Table 5.1 are shown as colors (as indicated on the right panel). The Abel (2006) relationship in Equation 2.60 is shown as a dashed straight line. Right panel: same as the left panel but for the selected positions in Table 5.1 and the methods used to estimated their total integrated intensity: GAUSS (filled squares), POLY (filled diamonds), and SPEC (filled circles).*

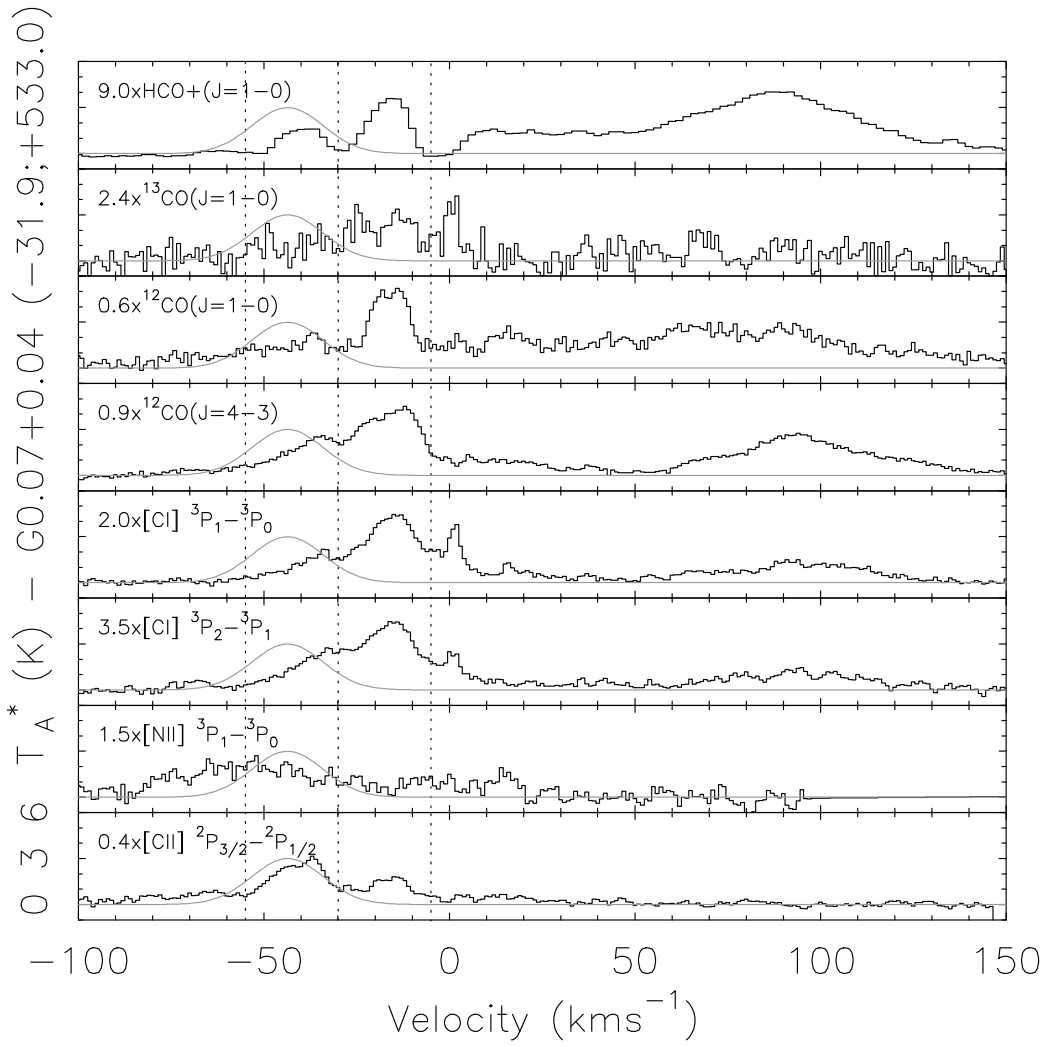

Figure. 5.6: *G0.07+0.04 spectra in the present work (black lines), as described in Section 5.3, and Gaussian fit results to the H92α recombination line emission from Lang et al. (2001) (gray line). The ionized emission is strongly blue-shifted (~ 30 kms^{-1}) with respect to the bulk of the molecular emission.*

the χ/χ_D values found by Simpson et al. (2007) for the Quintuplet Cluster > 10^4, with H_2 volume densities > 10^4 cm^{-3} are covered. The clump masses (M_{cl}) were selected following the FIR line emission modeling of the Milky Way by Cubick et al. (2008), while the limits on low mass (M_{low}) and upper mass (M_{up}) cutoffs of the ensemble mass distribution are standard values used in the KOSMA-τ PDR model.

The Ratio of total to selective extinction (ultraviolet to the optical) $R_v = A_v/E_{B-V}$ is a crucial parameter of the KOSMA-τ PDR model, since it reflects the efficiency of the dust grains, through the dust grain sizes, in reprocessing the FUV field from massive stars. The KOSMA-τ PDR model can handle $R_v = 3.1$, $R_v =$

4.0 and R_v = 5.5 (Röllig et al., 2013a) from the dust models of Weingartner & Draine (2001). From observations between 1 μm and 13 μm of stars in the GC, Rieke & Lebofsky (1985) found R_v = 3.09 ± 0.03, with no significant variation in the region. Their value is virtually the same the lowest one in Weingartner & Draine (2001). Nonetheless, Nishiyama et al. (2006) argued that the value obtained by Rieke & Lebofsky (1985) is inconsistent with ISO[2] observations for wavelengths ≥ 2.4 μm towards the GC and that the extinction law changes from one l.o.s. to another, so its usually assumed universality does not necessarily hold in infrared wavelengths. Nishiyama et al. (2008) obtained for the GC $R_v \approx 1.8$ from their estimated A_v/E_{V-J} = 1.251 ± 0.014 and A_J/E_{V-J} = 0.225 ± 0.007 values in the GC. Very steep FUV extinction (small R_v values) implies a relatively high abundance of small grains, which provide a larger surface area per volume for molecular hydrogen formation (Larson et al., 1996; Larson & Whittet, 2005, and references therein). The extinction law in Nishiyama et al. (2009) varies as $A_\lambda \propto \lambda^{-2.0}$ in the wavelength range of the J, H, and K_s filters, being steeper than the Rieke & Lebofsky (1985) result $A_\lambda \propto \lambda^{-1.6}$. Given that R_v seems to be lower for the GC when compared with the standard Galactic disk value, the lowest R_v value that the KOSMA-τ PDR model can handle was adopted.

The standard value for the H ionization rate due to cosmic-rays (ζ_H) in the Galactic disk is usually taken as $\zeta_H \sim 3 \times 10^{-17}$ s^{-1} (van Dishoeck & Black, 1986; Lee et al., 1996). For the CMZ and using H_3^+ (protonated H_2) observations, Goto et al. (2008) found a much larger value around $\zeta \sim 10^{-15}$ s^{-1}, including the ionization of H and H_2 (with $\zeta_{H_2} = 2\zeta_H$), and where the effect of X-rays and FUV radiation on the derived value may be significant. Combining H_3^+ observations along several l.o.s. towards the GC (whose emission was mostly found toward negative LSR velocities and in diffuse material) and CO observations, Oka et al. (2005) estimated ζ_{H_2} = 2 - 7 × 10^{-15} s^{-1}. From X-ray observations between 2 keV and 6 keV, Yusef-Zadeh et al. (2007) found much larger values for ζ_H in a small region around the Arches Cluster. From the electron energy density of the cluster (6×10^4 eV cm^{-3}), over an area of ∼ 1.6 arcminutes^2, they obtained $\zeta_H \sim 3\times10^{-11}$ s^{-1}, while for a much larger area (285 arcminutes^2) containing the Radio-Arc region, they obtained an electron energy density of ∼ 19 eV cm^{-3} yielding $\zeta_H \sim 10^{-14}$ s^{-1}. The latter region excludes the southern part of the observations in the present work, starting at the northern limit of the +50 kms^{-1} Cloud (see Chapter 7). Given the several orders of magnitude difference between ζ_H values in the literature, I have adopted a wide range for ζ_H, ranging from 10^{-11} s^{-1} to 10^{-15} s^{-1}.

The metallicity (Z) in the GC varies between the solar metallicity value $Z_\odot$ and $3Z_\odot$, with an average value of ∼ $2Z_\odot$ (Mezger et al., 1979; Cox & Laureijs, 1989; Shields & Ferland, 1994; Mezger et al., 1996; Yusef-Zadeh et al., 2007).

[2]Infrared Space Observatory

The KOSMA-τ PDR model handles only $Z = Z_{\odot}$, so this value was assumed for the model. An extrapolation to higher metallicities is not straightforward due to convergence problems in the PDR code. The clump velocity width ($\Delta V(FWHM)$) was set to 1.67 kms^{-1} following Cubick et al. (2008), while the H_2 formation on PAHs was disabled mainly because it is not clear whether this process can actually take place, as suggested by Habart et al. (2003). If enabled, this would produce vast amounts of H_2, having a large impact on the derived model intensities.

The elemental abundances in the CMZ are quite uncertain for several elements. Models of the Galaxy formation usually intend to reproduce the oxygen, carbon, and nitrogen abundances mainly in the Galactic disk, from Galactocentric radius 4 kpc and outwards, given the lack of observational constrains for smaller radii (Mott et al., 2013; Colavitti et al., 2009), making the extrapolation to the inner 100 pc of the Galaxy very uncertain. For the GC, the carbon abundance has been taken to be between at least 3 (Arimoto et al., 1996) and up to 10 times the solar value (Sodroski et al., 1995; Oka et al., 2005). For the He and O atoms, I have assumed that their elemental abundances follow the same behavior as the carbon abundance in the GC and are three times the solar value (Asplund et al., 2005; Simón-Díaz & Stasińska, 2011), while the S elemental abundance is taken from Simpson et al. (2007) from observations of the Arched-Filaments. In the case of the isotopic abundance of ^{13}C, the derived value for the GC in Güsten & Philipp (2004) was used, so its elemental abundance was estimated accordingly.

5.6 KOSMA-τ PDR Model Results

The KOSMA-τ PDR model fit results for the selected Arched-Filaments positions are summarized in Table 5.4. The modeled transitions are: [CII], [NII], [CI](2-1), and [CI](1-0) from the Herschel-HIFI observations; CO(4-3) from the NANTEN2/SMART observations; CO(1-0) and ^{13}CO(1-0) from the unpublished Mopra CMZ Survey; and HCO$^+$(1-0) and H^{13}CO$^+$(1-0) observations from the Mopra archive. From left to right, the columns in Table 5.4 contain the position name, *chi-square* (χ^2) result from the minimization algorithm, the H nucleus number density $n(H)_{s,tot}$, the total clump mass M_{cl}, the FUV field in Draine units χ, the H ionization rate due to cosmic-rays ζ_H, the lower (M_{low}) and upper (M_{up}) limits in the clump masses for the ensemble, and the projected distance of each position from the Arches Cluster d_{proj}, calculated using $R_{\odot}$ = 8.34 kpc (Reid et al., 2014) as heliocentric distance to the GC. For the χ^2 minimization, six free parameters were considered ($n(H)_{s,tot}$, M_{cl}, χ, ζ_H, M_{low}, and M_{up}), and a 20% absolute calibration error was assumed for the calculated integrated intensities of all observed lines, which is representative of the average calibration error of the

Description	Parameter Range
FUV Draine Field (χ/χ_D)	10^2,10^3,10^4,10^5
Clump Mass ($M_{cl}/M_\odot$)	10^{-3},10^{-2},10^{-1},10^0,10^1,10^2,10^3
Total H nucleus number density $n(H)_{s,tot}$ (cm^{-3}) at the clump's surface	10^2,10^3,10^4,10^5,10^6,10^7
M_{low} ($M_\odot$)	0.001 - 0.010
M_{up} ($M_\odot$)	0.011, 0.1, 1, 10, 100, 1000
[a]Ratio of total-to-selective extinction R_v	3.1
[b]H ionization rate due to cosmic-rays ζ_H	10^{-11},10^{-12},10^{-13},10^{-14},10^{-15}
Clump $\Delta V(FWHM)$ (kms^{-1})	1.67
Formation of H_2 on PAHs	NO
Elemental Abundances:	
[He/H]	0.1
[c][C/H]	7.03×10^{-4}
[e][^{13}C/H]	2.81×10^{-5}
[c][O/H]	1.34×10^{-3}
[f][S/H]	2.00×10^{-5}
Isotopic Abundances:	
[d][C/^{13}C]	25

Table. 5.3: *Parameters used for the KOSMA-τ PDR model. Elemental abundances of for all species are taken from Asplund et al. (2005) and Simón-Díaz & Stasińska (2011). [a]Value from Rieke & Lebofsky (1985); [b]Values from Goto et al. (2008); Oka et al. (2005); Yusef-Zadeh et al. (2007); [c]Values scaled by a factor of 3 from elemental abundances; [d]Value from Güsten & Philipp (2004); [e]Value based on isotopic abundance in Güsten & Philipp (2004); [f]Value from Simpson et al. (2007).*

Herschel-HIFI and the NANTEN2/SMART observations, as shown in Chapter 3.

In Figures 5.7 to 5.11, the best fit for the integrated intensities at each position are shown. In general, all integrated intensities at the selected positions in Table 5.1 can be very well fitted by the KOSMA-τ PDR model. This is quite remarkable when considering that the fitted Gaussian profiles to each observed line in Appendix D interpolate between broad absorption features in the line profiles in order to recover the missing emission. The only exception for the good fitting results is the CO(1-0) emission, which is largely underestimated for all positions. Possible reasons for such discrepancy are discussed is Section 5.6.1. Removing the CO(1-0) integrated intensities from the fitting procedure does not alter the fit results significantly. For instance, the best fit model for the P1 position, without the CO(1-0) transition, yields: $\chi^2 = 46$, $\log_{10}$ $n(H)_{s,tot} = 4.7$ cm^{-3}, $M_{cl} = 1142$ $M_\odot$, $\chi = 306$ χ_D, $\log_{10}$ $\zeta_H = -14.0$ s^{-1}, $M_{low} = 0.011$ $M_\odot$, and $M_{up} = 100$ $M_\odot$

Position	χ^2	$\log_{10}$ n(H)$_{s,tot}$ (cm^{-3})	M$_{cl}$ (M$_\odot$)	χ (χ_D)	$\log_{10}\,\zeta_H$ (s^{-1})	M$_{low}$ (M$_\odot$)	M$_{up}$ (M$_\odot$)	d$_{proj}$ (pc)
E1	17	4.2	1078	100	−14.6	0.028	344	2
E2-N	19	4.6	849	910	−14.7	0.035	477	6
E2-S	14	4.6	841	204	−14.5	0.004	426	4
W1	9	4.3	872	100	−14.9	0.021	311	9
W2	14	4.3	776	213	−14.7	0.026	348	11
G0.07+0.04	13	4.7	779	353	−14.1	0.007	12	9
G0.10+0.02	18	4.9	669	1339	−14.8	0.001	65	4
P1	19	4.7	1205	255	−14.1	0.008	96	11
P2	17	5.0	747	1304	−14.5	0.001	70	2

Table. 5.4: *KOSMA-τ PDR model fitting results for selected positions in the Arched-Filaments. From left to right, the position name, chi-square (χ^2) result from the minimization algorithm, H nucleus number density n(H)$_{s,tot}$, total clump mass M$_{cl}$, FUV field in Draine units χ, H ionization rate due to cosmic-rays ζ_H, clump mass lower limit M$_{low}$, clump mass upper limit M$_{up}$, and the projected distance from the Arches Cluster d$_{proj}$, are given.*

with all model integrated intensities well within the 20% error bars of the derived integrated intensities from the observations.

The results from the KOSMA-τ PDR model are shown in Figure 5.12 as a function of projected distance d$_{proj}$ from the Arches Cluster. The upper left panel shows the distribution of the derived FUV field for all positions. Roughly, two groups can be distinguished in the panel: positions P2, G0.10+0.02, and E2-N having $\chi \gtrsim 10^3\ \chi_D$, and positions P1, G0.07+0.04, W1, W2, E1, and E2-S having $\chi \lesssim 4{\times}10^2\ \chi_D$. If the FUV field controlling the gas excitation and chemistry of the gas came only from the stars in the Arches Cluster, the two groups could be reflecting different distances to it. Closer positions to the stellar cluster would experience a much more intense FUV field than further ones, as the FUV field at a distance d scales as d^{-2}. As mentioned in Section 5.1, the Galactocentric radius of the Arches Cluster is quite uncertain. Rodríguez-Fernández et al. (2004) found $\sim 6{\times}10^2\ \chi_D$ for sources far in projected distances from thermal sources. This is very consistent with the limit separating both groups, reinforcing the idea that different distances to the cluster are driving the decrease in the derived FUV fields. The latter, together with the very complex velocity field in the GC, makes it feasible that emission spots that appear close in projected distance in the GC, are actually much further away than what the projected distance between them suggests. For the G0.07+0.04 position, the derived FUV field in Table 5.4 is $\sim 3.5{\times}10^2\ \chi_D$, which is lower than the lower limit of the range derived by Genzel et al. (1990) between $6{\times}10^2\ \chi_D$ - $6{\times}10^3\ \chi_D$. The discrepancy could be understood in terms of the clumpiness of the PDR model. The more clumply the ISM is,

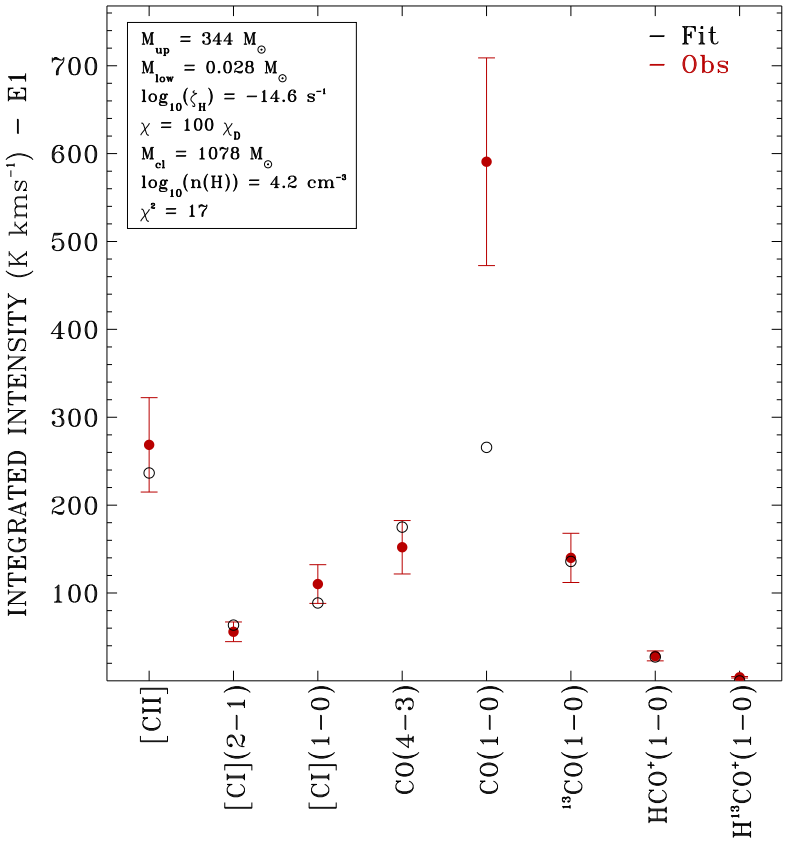

Figure. 5.7: *Measured (filled red circles) and KOSMA-τ PDR model (open black circles) integrated intensities for position E1 in Table 5.1. Error bars for the observed integrated intensities represent an average 20% calibration error for all observed transitions. The best fit parameters shown in the panel inset are summarized in Table 5.4.*

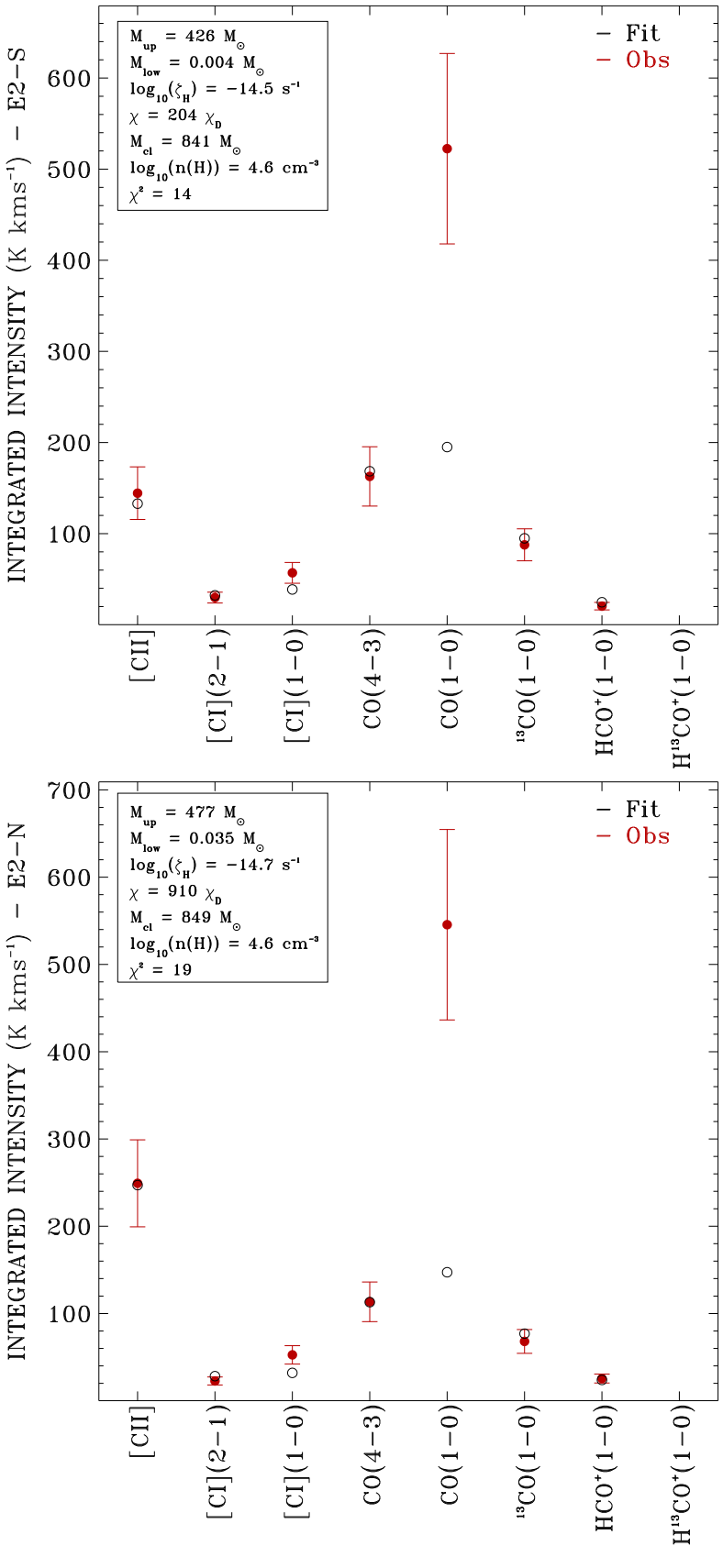

Figure. 5.8: *Measured (filled red circles) and KOSMA-τ PDR model (open black circles) integrated intensities for positions E2-N and E2-S in Table 5.1. Error bars for the observed integrated intensities represent an average 20% calibration error for all observed transitions. The best fit parameters shown in the panel inset are summarized in Table 5.4.*

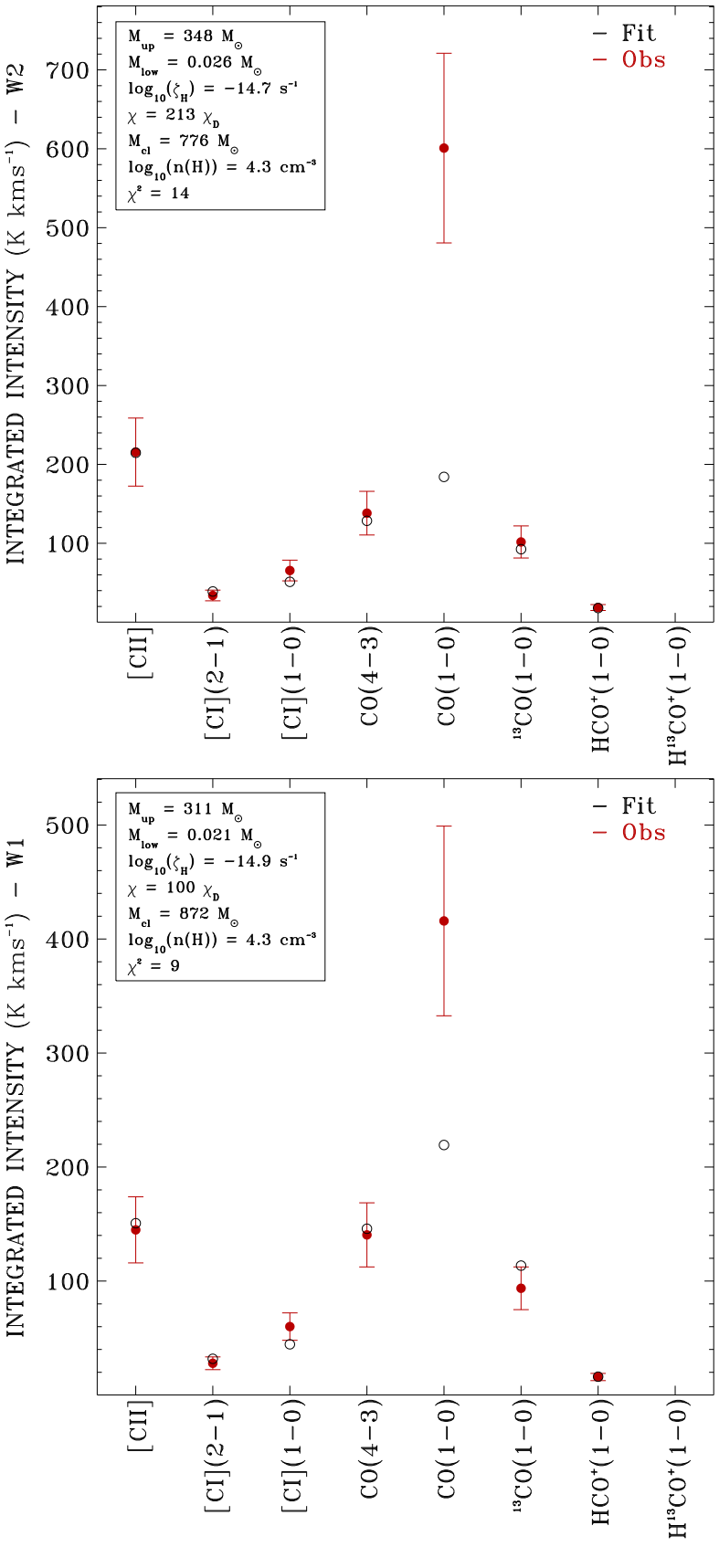

Figure. 5.9: *Measured (filled red circles) and KOSMA-τ PDR model (open black circles) integrated intensities for positions W1 and W2 in Table 5.1. Error bars for the observed integrated intensities represent an average 20% calibration error for all observed transitions. The best fit parameters shown in the panel inset are summarized in Table 5.4.*

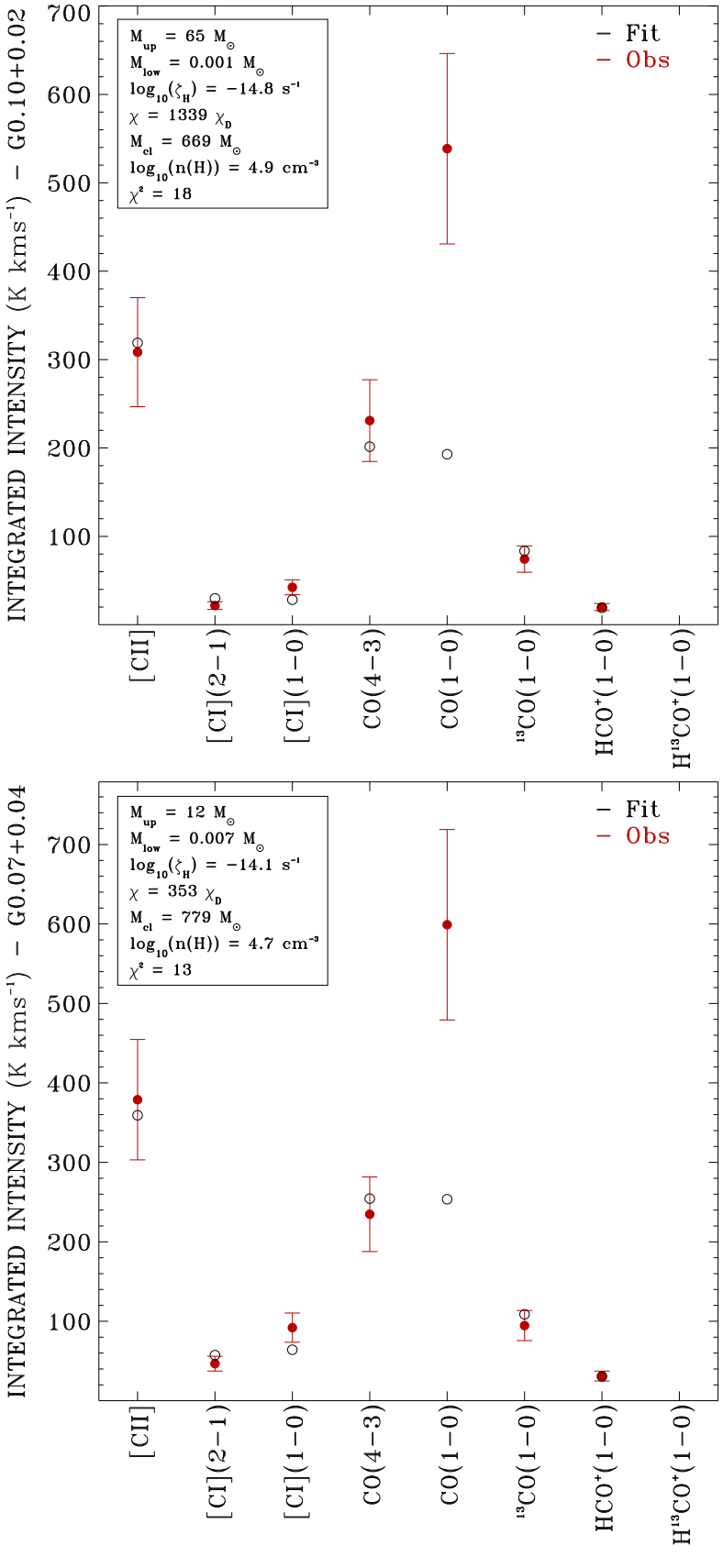

Figure. 5.10: *Measured (filled red circles) and KOSMA-τ PDR model (open black circles) integrated intensities for positions G0.07+0.04 and G0.10+0.02 in Table 5.1. Error bars for the observed integrated intensities represent an average 20% calibration error for all observed transitions. The best fit parameters shown in the panel inset are summarized in Table 5.4.*

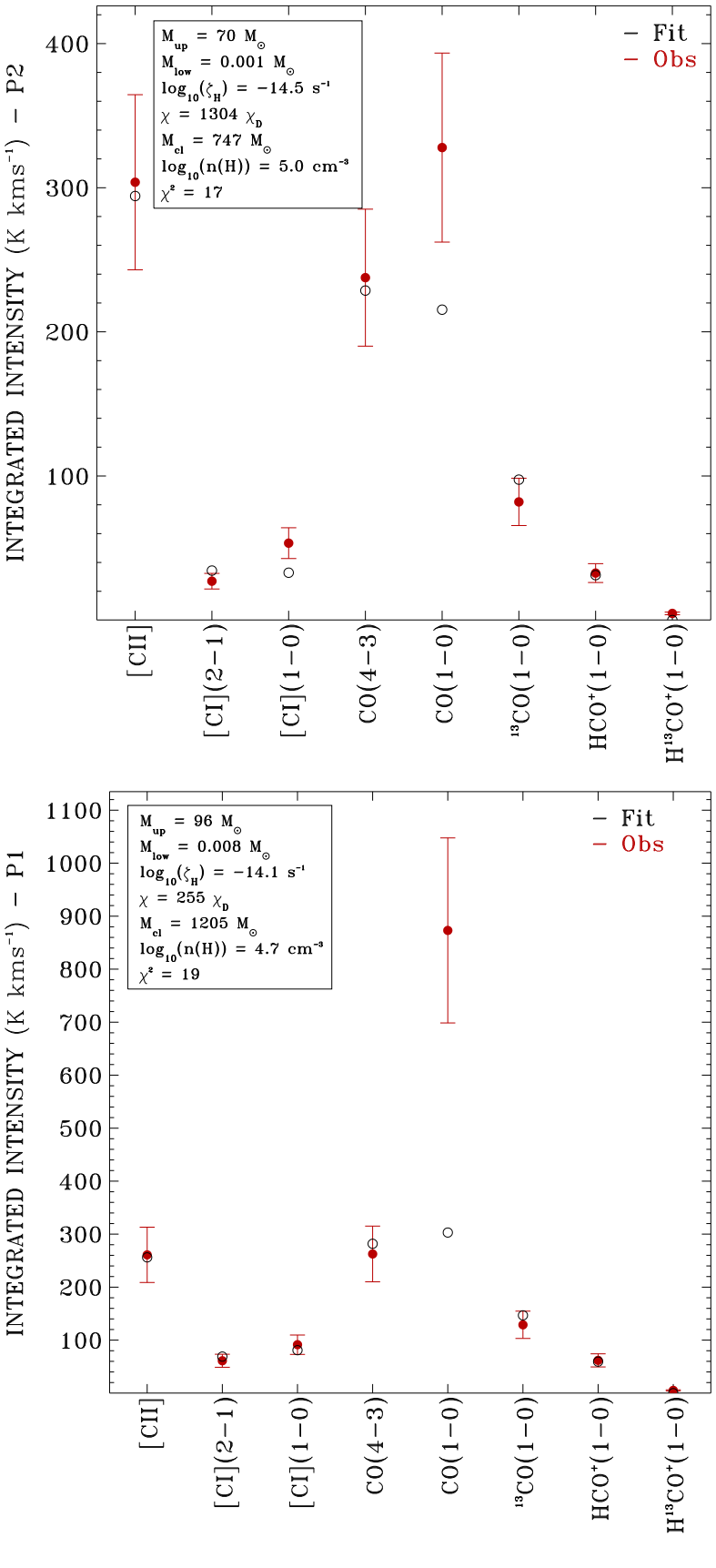

Figure. 5.11: *Measured (filled red circles) and KOSMA-τ PDR model (open black circles) integrated intensities for positions P1 and P2 in Table 5.1. Error bars for the observed integrated intensities represent an average 20% calibration error for all observed transitions. The best fit parameters shown in the panel inset are summarized in Table 5.4.*

the larger is the surface of the clumps exposed to the impinging FUV radiation, producing brighter [CII] emission. Therefore, very strong FUV fields would not be necessary to explain the high [CII] intensities measured in the present work.

The upper right panel in Figure 5.12 shows the variation of $n(H)_{s,tot}$ as a function of projected distance. Hydrogen densities are consistently within the 10^4 cm^{-3} - 10^5 cm^{-3} range for all positions. Interestingly, position E1, W1, and W2 share similarly low FUV fields and $n(H)_{s,tot}$ densities, despite of the large difference in projected distance from the Arches Cluster they have. Positions P2 and G0.10+0.02 are the densest in the sample. In the E2 filament, E2-N and E2-S have the same hydrogen density, but their FUV fields differ by a factor of ~ 4, which could indicate in principle a different distance along the l.o.s. for both segments. Nonetheless, and since E2-N appears very close in projection to the Radio-Arc, it can not be ruled out that its large [CII] intensity compared with E2-S is, at least partially, due to the interaction with the large NTF structure, in which collisions with charged particles could exicite the ionized carbon line. Serabyn & Guesten (1987) derived H_2 densities for P1 and P2 of the order of $\sim 10^4$ cm^{-3}, while hygrogen densities in Table 5.4 are $5{\times}10^4$ cm^{-3} and 10^5 cm^{-3}, respectively. Figure 5.2 shows that the molecular material traced by the CO(4-3) lines is located far from the selected positions, suggesting that the gas is predominantly atomic. This would be consistent with higher H than H_2 densities. The hygroden mass contained within the telescope's beam is shown in the lower right panel of Figure 5.12. Most positions share similar hydrogen masses in the range $\sim$ 700 $M_\odot$ - 900 $M_\odot$ with ony E1 and P1 having $M_{cl} > 10^3$ $M_\odot$. For G0.07+0.04, Genzel et al. (1990) estimated a molecular mass within a 55" beam of $\sim$ 500 $M_\odot$ which is quite consistent with the $\sim$ 780 $M_\odot$ estimate in Table 5.4, for a slightly smaller beam (46").

The derived H ionization rates due to cosmic-rays ζ_H as a function of projected distance from the Arches Cluster are shown in the lower left panel of Figure 5.12. The values obtained for all positions are larger than the 10^{-15} s^{-1} value derived from H_3^+ observations by Goto et al. (2008) and lower than the 10^{-14} s^{-1} obtained by Yusef-Zadeh et al. (2007) from X-ray observations. Goto et al. (2008) disscused that for high ζ_H values, the $N(H_3^+)$ column density no longer scales linearly with ζ_H, but saturates, making it less sensitive to changes in ζ_H. This could be the case for the Arched-Filaments. On the other hand, the value derived by Yusef-Zadeh et al. (2007) is based on the spatial average of the electron energy density. By including the small area around the Arches Cluster, which has an extreme high cosmic-ray ionization rate $\sim 3{\times}10^{-11}$ s^{-1}, the average ζ_H value for the Radio-Arc region containing the Arched-Filaments could be considered an upper limit. From the panel, it can be seen that most of the positions have ζ_H between 10^{-15} s^{-1} and $4{\times}10^{-15}$ s^{-1}, which could be closer to the true average value in the region. The highest ζ_H values around $\sim 10^{-14}$ s^{-1}

are found at positions P1 and G0.07+0.04, which are close in projection. These positions also share very similar FUV fields and H volume densities, with only ∼ 40% difference in mass, suggesting that they are indeed spatially close. Since G0.07+0.04 is thought to be interacting with the Northern-Thread (see Section 5.2), and increase in the H ionization due to cosmic-rays would be expected from the charged particles traveling along the magnetic field lines. Also, the [CII] and [NII] spectra for P1 in Figure D.6 show that the emission is slightly shifted with respect to the molecular and neutral emission. These results suggests that P1 could be also directly influenced by the interation with the magnetic field in the GC.

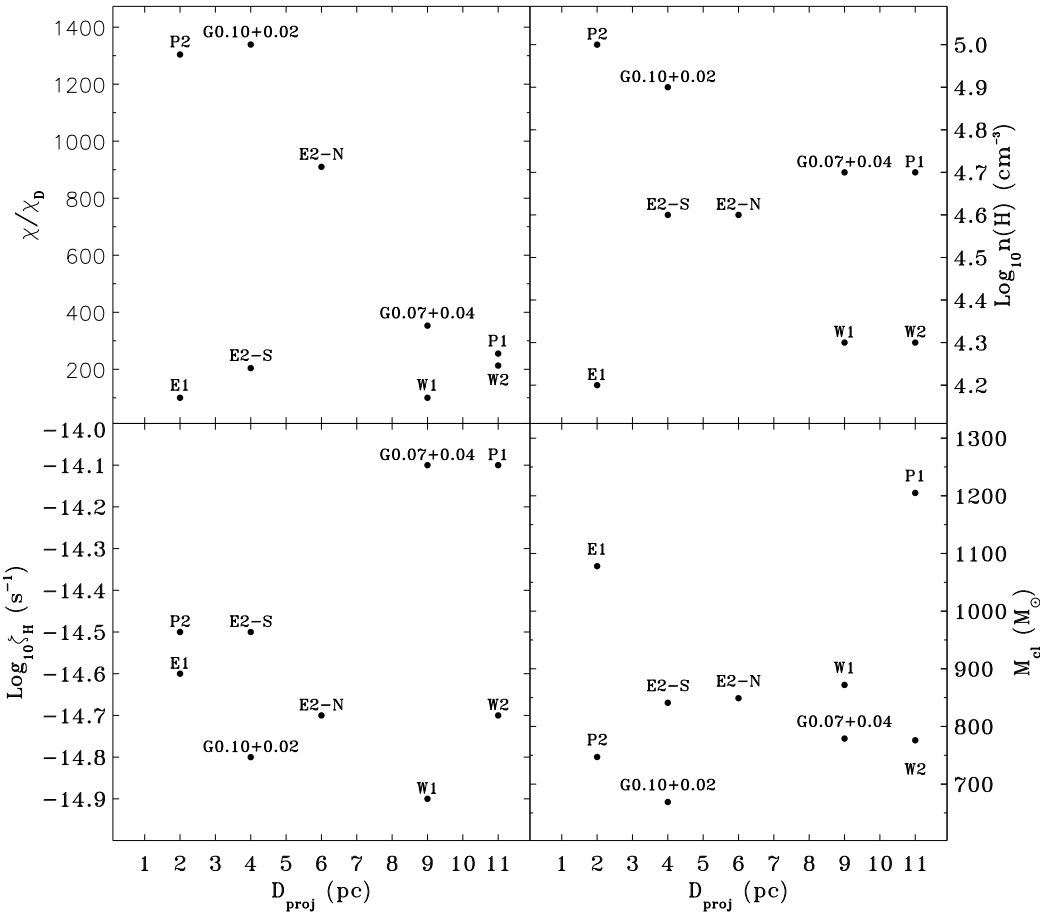

Figure. 5.12: *KOSMA-τ PDR model best fitted parameters in Table 5.4 as a function of projected distance d_{proj} from the Arches Cluster for the selected Arched-Filaments positions. The panels shown the derived FUV field (upper left panel), the H volume density (upper right panel), the H ionization rate due to cosmic-rays (lower left panel), and the hydrogen mass in the beam (lower right panel). The name of each position in given at each point.*

5.6.1 Difference Between Model and Observed CO(1-0) Integrated Intensities

The largest fraction of the obtained χ^2 values in Table 5.4 is controlled by the large difference between measured and modeled CO(1-0) integrated intensities. In order to explore the reason for such discrepancy, Figure 5.13 shows the integrated intensities used for the fitting procedure (GAUS and in some cases POLY as described in the footnotes in Table 5.2), against the predicted integrated intensities from the KOSMA-τ PDR model. Also, the SPEC integrated intensities are plotted in orange for comparison. The solid straight line in the figure represents the identity. For all Mopra observations, I used the extended beam efficiency η_{xb} = 0.65 described in Ladd et al. (2005) at 86 GHz to bring the Mopra observations to a comparable antenna temperature scale with the Herschel-HIFI and NANTEN2/SMART observations. A more appropiate value for the CO(1-0) and ^{13}CO(1-0) observations is 0.55 and 0.57, respectively (Ladd et al., 2005), which lead to an increase of 18% and 14% in the CO(1-0) and ^{13}CO(1-0) emission. In terms of the ^{13}CO(1-0) emission, the 14% correction improves the fitting of the observed intensities in seven out of the nine positions, as it can be seen from the error bars set at 20% of the emission in Figures 5.7 to 5.11. In the case of the CO(1-0) emission, the 18% correction in the observed emission only increases the difference between observed and modeled intensities. From Figure 5.13, even SPEC intensities, which are a lower limit to the true integrated intensities (since the emission loss due to absorption features along the l.o.s. was not recovered in that method), are underestimated by the PDR model. The two positions where observed and model CO(1-0) intensities come closest are P2 and W1, with the former very close to Arches Cluster in projected distance and the later far away from it. This indicates that the difference in CO(1-0) intensities is not controlled by the proximity to the FUV field of the stellar cluster, but rather is locally controlled. The fact that the ^{13}CO(1-0) emission is very well reproduced by the PDR model while the CO(1-0) emission is largely underestimatd is very puzzeling if it is considered that both transitions have very similar critical densities (see Table D.1) and both trace cold ($\sim$ 10 K) gas. The good fit of the ^{13}CO(1-0) emission rules out a calibration problem in the CO(1-0) intensities, as both transitions were observed simultaneously. The large discrepancy between observed and predicted CO(1-0) intensities suggests a rather fundamental difference either in the excitation mechanism of the CO(1-0) line at the selected positons or more likely, the presence of a significant fraction of CO(1-0) emission in the telescope's beam that does not arise from the same volume than the other lines. This would not be surpising if one considers that the l.o.s. towards the Sgr A Complex crosses the entire Galactic disk, where diffuse (low density) molecular gas occupies a considerable fraction of the volume, and that is bright in CO(1-0) emission (Pineda et al., 2014), as weall as MCs which are even brighter in the CO(1-0) transition (Dame & Thaddeus, 2008; García et

al., 2014). Other low-J rotational transitons of the CO molecule would be needed in order to identify if the CO(1-0) "excess" is related to gas within the same volume in the GC or it is in fact originated along the l.o.s..

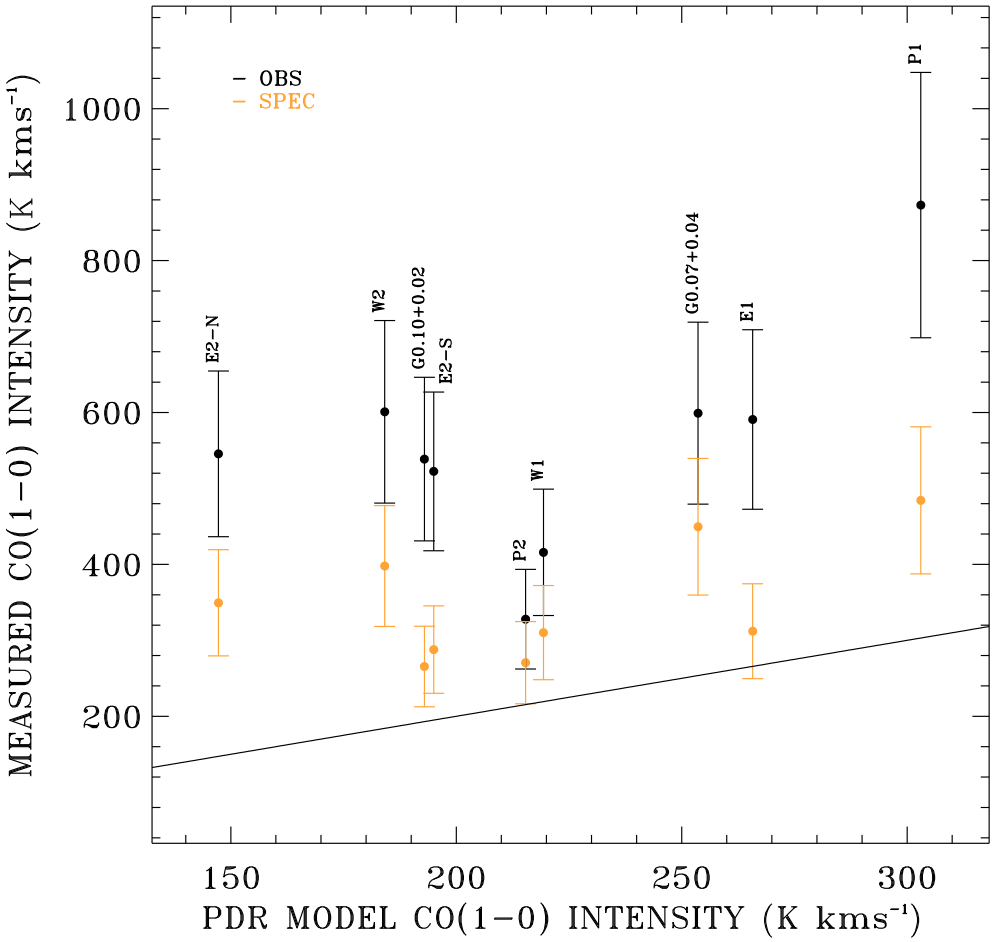

Figure. 5.13: *Comparison between measured and KOSMA-τ PDR model CO(1-0) integrated intensities. The CO(1-0) integrated intensities from the GAUSS (black) and SPEC (orange) methods are shown. Error bars for the observed integrated intensities represent an average 20% calibration error for all observed transitions. The solid straight lines represents the identity.*

5.6.2 Future Work

Follow-up work will further improve the understanding of such complex region as the Arched-Filaments. In particular, the discrepancy in the sub-mm datasets in the present work between the measured and predicted [CII] emission from the observed [NII] intensities, as postulated by Abel (2006), has to be further investigated. Also, complementary low- and mid-J CO observations will help to

understand where the apparent CO(1-0) excess in the Mopra data is coming from, and if the discrepancy is related to model defficiencies or rather to particular physical conditions of the gas in the GC. The assumed approach of representing the emission in all observed atoms an molecules as a single component along the l.o.s. was very sucessful from the modeling point of view, as shown by the KOSMA-τ results in the present chapter, but in the process, double gas components may have been overseen. Therefore, observations of the optically thin $C^{18}O$(1-0) species with enough signal-to-noise ratio are the natural candidates to attack this problem. All these issues will be adressed in a future publication.

Chapter 6

High Velocity Gas Towards the Sgr A Complex

6.1 Introduction

In the next sub sections, the overall kinematics of the gas in the gravitational potential of the GC based on theoretical/numerical works and observations is summarized. Also, the transition from atomic to molecular material as the gas moves from the outer to the inner parts of the GC is reviewed.

6.1.1 The Gravitational Potential and Kinematics of the HVG

The gas dynamics in the GC is extremely complex. Nowadays, the most accepted models of the gas kinematics in the inner 3 kpc of the Milky Way are consistent with a rotating (ω = 63 kms^{-1} kpc^{-1}, Binney et al. (1991)) tri-axial stellar bar whose gravitational potential gives rise to two different family of allowed orbits: the X_1 and X_2 family orbits (Binney et al., 1991; Jenkins & Binney, 1994). The gas starts orbiting in the outer X_1 orbits, moving inwards to the X_2 orbits which are closer to the GC. At the pericenter (apocenter) of the X_1 (X_2) orbits, these family orbits intersect. As gas travels from the X_1 to the X_2 orbits, the gas passes through the so called X_1 "cusped" orbit (Binney et al., 1991), at which the X_1 orbits become self-interacting at their apocenters (See Figure 1.1). Gas in the X_1 cusped orbit remains there for a short time since it is prompted to suffer shocks due to the incoming material from outer X_1 orbits, due to the shocks with gas in the self-interacting region (such as it is the case for Bania's Clump 2) and due to the interaction with material already in the X_2 orbits such as the 1.3 Complex, Sgr B, and Sgr C, as studied in previous works (Riquelme et al., 2010, 2013). The shocks result in the gas loosing energy and angular momentum, falling deeper

in the gravitational potential to the X_2 family orbits, where most of the known molecular clouds and star clusters are located. Huettemeister et al. (1998) used SiO and SiO isotopomers observations to identified shocked gas in the CMZ. Since SiO is thought to be released from the icy grain mantels into the gas phase after shocks destroy the grains, it is a known shocked gas tracer. They concluded that the SiO abundances in the observed molecular clouds are in fact related to the large scale dynamics in the GC, with the highest values found at Galactic longitudes $l > 0°.8$, in regions prompted to undergo shocks.

Although the dominant contributor to the overall gravitational potential in the GC is the stellar component, the gas component can also be important depending on the gas distribution in the CMZ. Within the inner 500 pc of the GC, the gas-to-star fraction is around ~ 0.01 (Güsten & Philipp, 2004). This rather low value does not reflect the contribution of the gas to the gravitational potential at these radii. Given the gas distribution in elongated orbits near the Galactic plane, Binney et al. (1991) estimate that gas in such an arrangement has a substantial contribution to the tangential gravitational force for radii ≤ 500 pc. A schematic view of the X_1 and X_2 orbits and their relationship to gas in the inner Galaxy is shown in Figure 1.1 taken from Bally et al. (2010).

Given the inclination of the stellar bar, ranging from 15° and 30° (Englmaier & Gerhard, 1999; García et al., 2014, and references therein), the X_1 and X_2 orbits are consequently also inclined with respect to the l.o.s.. This traduces into different LSR velocities originating from them, given the difference in the orientation and magnitude of the velocity vector for each one. At $l = 0°$, the projection along the l.o.s. of the velocity vector for X_2 orbits is less than 100 kms^{-1} in modulus, according to the models in Jenkins & Binney (1994), while simulations carried out by Englmaier & Gerhard (1999) suggest that the maximum X_2 LSR velocity is about 120 kms^{-1} for $l < 2°$. Local emission and emission arising from spiral arms in the Galactic plane do not contribute to the emission at these velocities since the former is found within the LSR velocity range ± 20 kms^{-1} (Bally et al., 1987; García et al., 2014), while the latter are seen in narrow absorption features up to ~ -53 kms^{-1}, where the well known near side of the 3 kpc expanding arm is located (Dame & Thaddeus, 2008). Therefore, the high velocity gas detected at LSR velocities larger in modulus than 120 kms^{-1} is very likely tracing gas in the outer parts of the GC, in the Galactic longitude range $|l| < 0°.25$, which is roughly the extent of the CO(4-3) NANTEN2/SMART observations in the present work.

6.1.2 The Transition from Atomic to Molecular Gas

Observations of the ground state of carbon monoxide show a well defined parallelogram-shaped structure in position-velocity diagrams, which is identified with the X_1 cusped orbit (Oka et al., 1998; Dame et al., 2001). The left panel in Figure 6.1 shows the CO(J=1-0) emission distribution of the molecular gas in the GC from Oka et al. (1998). For comparison, the emission distribution of the ground state 21 cm transition of atomic hydrogen, measured by Burton & Liszt (1978), is shown on the right panel of the same figure. The figure itself is taken from Binney et al. (1991). The fact that the position-velocity diagram of the CO(1-0) emission is not filled up with molecular emission outside the parallelogram, as it is the case for the HI emission, is a strong evidence that (most) of the molecular material must be forming when arriving (near) to the X_1 cusped orbit (Binney et al., 1991).

In terms of the atomic mass supply to form the molecular material, mass loss by the star population in the Galactic Bulge is thought to be capable of replenishing the gas in the outer X_1 orbits within 1-2 orbital periods of the stellar bar rotation (Jenkins & Binney, 1994; Mezger et al., 1996). Material influx in the GC is observed at all scales and occurs primarily along the Galactic plane. The inflow mass rate is estimated to be of the order of a few 10^{-2} $M_\odot$ yr^{-1}. The large metallicity in the CMZ $\sim$ 2 $Z_\odot$ (Cox & Laureijs, 1989; Mezger et al., 1979) indicates that, gas in the GC has been processed by stars several times already, which also points out to the Bulge atomic material as the gas supply of the CMZ.

Given the kinetic information and molecular gas formation arguments from the literature, I used millimeter and sub-mm atomic and molecular line detections of high LSR velocity gas towards the l.o.s. to the Sgr A Complex to investigate the physical conditions of the gas in X_1 orbits, that is not located at the very peculiar regions of the cusped X_1 orbit where it becomes self-interacting or where the interaction between X_1 and X_2 orbits is thought to occur, but rather at intermediate locations, where the gas is expected to better trace the average physical conditions of the gas in the X_1 orbits, away from the inner X_2 orbits.

6.2 High Velocity Gas Detections

In the present datasets, six structures were detected at high LSR velocities ($|V_{lsr}|$ > 120 kms^{-1}) in the sub-mm CO(4-3) and [CI](1-0) transitions: four MCs (*HVG1-1C, HVG1-2C, HVG2* and *HVG3*) and two molecular ridges reaching from the X_1 to the X_2 LSR velocities (*B-RIDGE* and *R-RIDGE*). Three of the

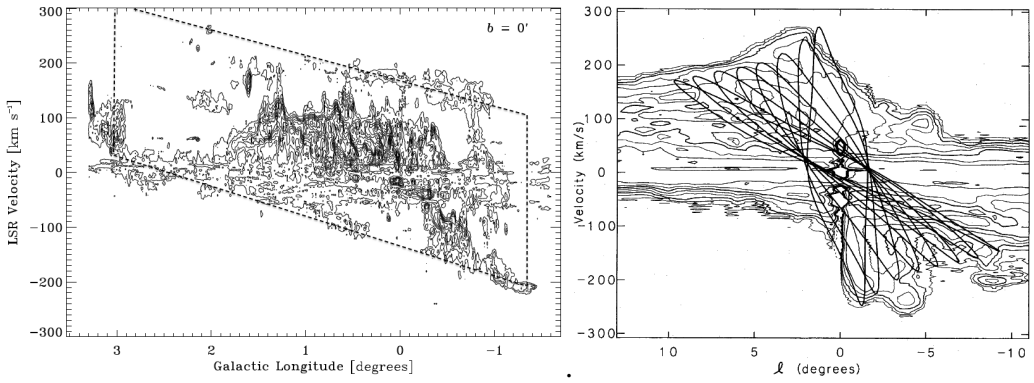

Figure. 6.1: *Left: CO(1-0) emission position-velocity diagram of Oka et al. (1998). The approximate position of the X_1 parallelogram is shown as dashed lines. Right: HI emission position-velocity diagram of Binney et al. (1991) from the data of Burton & Liszt (1978). The lack of carbon monoxide emission beyond the parallelogram structure enclosing the gas is a strong evidence for the formation of the molecular gas when arriving at the X_1 cusped orbit.*

structures are located at negative (*HVG1-1C, HVG1-2C* and *B-RIDGE*) and three at positive (*HVG2, HVG3* and *R-RIDGE*) LSR velocities. At the CO(4-3) peak position of the MCs, the [CI](2-1) line is also detected. Figure 6.2 shows two position-velocity diagrams of the CO(4-3) dataset (measured in Galactic coordinates). The left panel of the figure was obtained by integrating the dataset between $b = +0°.11$ and $b = -0°.17$. The color scale is set so the first contour is drawn at $5\times\sigma$ detection level (with $\sigma = 1.0$ K) and bright emission is saturated. This panel shows the six sources we refer to in this chapter: molecular clouds *HVG1-1C*, *HVG1-2C*, *HVG2*, and *HVG3*, and the two molecular ridges *B-RIDGE* (blue shifted ridge) and *R-RIDGE* (red shifted ridge). The right panel in Figure 6.2 is the same as the former but integrated over the Galactic latitude range $b = -0°.097$ and $b = -0°.17$ to exclude emission related to the CND. The first color is again drawn at $5\times\sigma$ detection level, with $\sigma = 0.5$ K. In terms of molecular clouds, the ones at negative LSR velocities appear below the Galactic plane while the opposite is true for cloud *HVG2* at positive LSR velocities. Given the large spatial extent of the *HVG3* cloud, it shows emission above and below the plane (see Section 6.2.2.2), as it appears in both panels in Figure 6.2. Bally et al. (1988) reported the detection of two diffuse features at +135 kms^{-1} and −150 kms^{-1} above and below Sgr A* in their ^{13}CO(1-0) data. They interpreted these features as part of an expanding ring around the GC, which is now understood as gas moving in the X_1 family orbits (Sawada et al., 2004).

At negative LSR velocities and Galactic longitudes, clouds HVG1-1C, HVG1-2C, and the B-RIDGE appear to be part of the same structure connecting the gas in X_1 orbits to the gas in X_2 orbits at l.o.s. $l = -0°.09$. Nonetheless, at that l.o.s., most of emission related to the B-RIDGE in the integrated Galactic latitude range

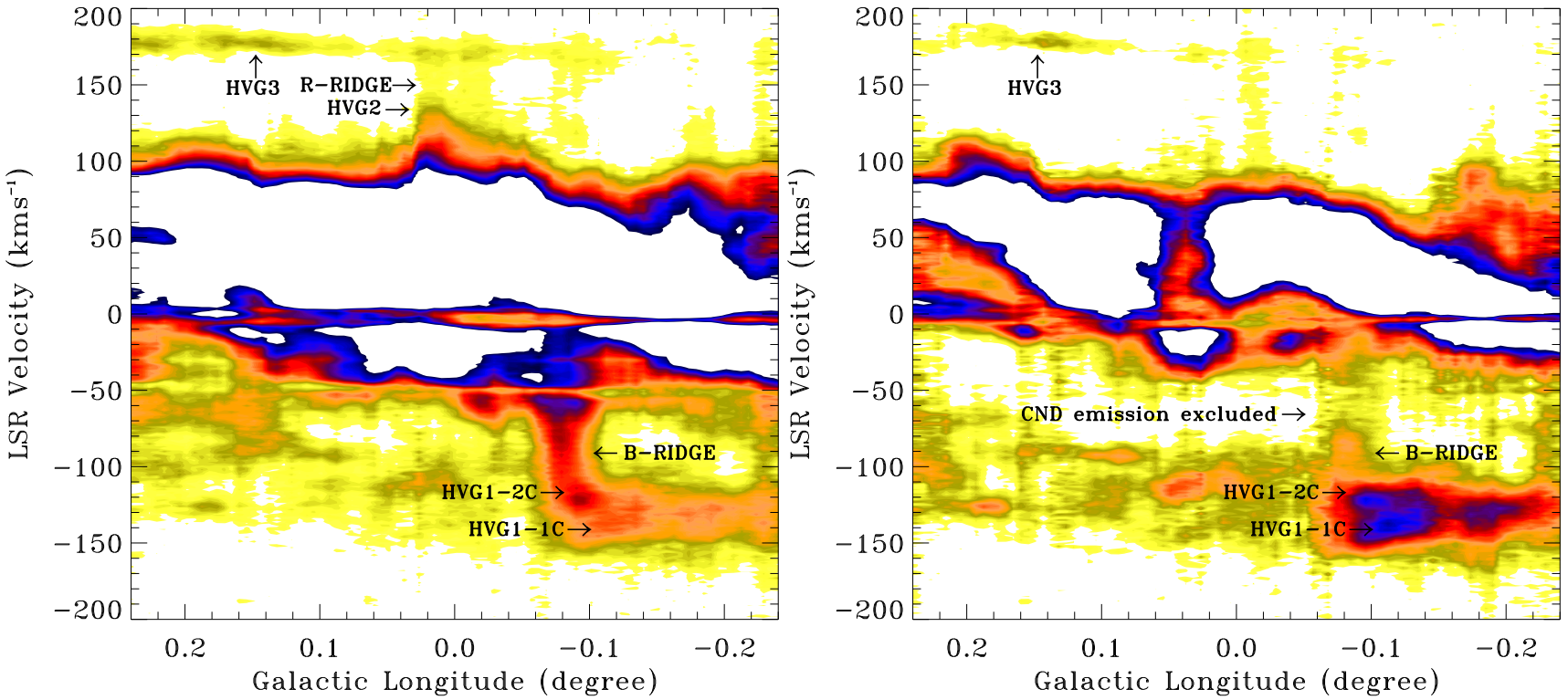

Figure. 6.2: *Left: Position-velocity diagram of the CO(4-3) emission in the present work. Colors of high intensity emission have been saturated in order to better outline the high velocity gas components. The CO(4-3) dataset was integrated between b = +0°.11 and b = −0°.17. The first contour is drawn at 5×σ detection level, with σ = 1.0 K. The position of the four molecular clouds (HVG1-1C, HVG1-2C, HVG2, and HVG3) and the blue shifted (B-RIDGE) and red shifted (R-RIDGE) molecular ridges extending from the X_1 orbits and reaching the inner gas at X_2 orbits are shown. Right: same as left but integrated in the Galactic latitude range between b = −0°.097 and b = −0°.17 to avoid contamination from the CND emission. The first contour is drawn at 5×σ detection level, with σ = 0.5 K*

is confused with the emission arising in the CND, which extends at very high negative velocities, as can be seen from its average spectrum in Figure 4.8. In order to better assess the emission extent of the molecular ridge between clouds HVG1-1C and HVG1-2C, the left panel of the same figure excludes the CND emission by restricting the Galactic latitude integration range to $b = -0°.097$ and $b = -0°.17$. As can be seen from the figure, most of the emission connecting high and low LSR velocities was removed but not all of it. The residual emission which seems to extend from the HVG1-2C towards lower LSR velocities is what I call the B-RIDGE. This is a signature of molecular material connecting the gas at the X_1 orbits with the inner X_2 orbits.

On the positive Galactic longitude and LSR velocity side of the left panel of Figure 6.2, the HVG2, HVG3, and R-RIDGE sources form a similar structure to the one at negative Galactic longitude LSR velocities, but at a different l.o.s. ($l = +0°.20$). In this case, the HVG2 cloud has already moved to lower LSR velocities, to the edge of the bulk of the emission. The symmetry between the positive and negative LSR velocity structures is quite remarkable: both show a lane of emission at large LSR velocities running almost parallel in Galactic longitude and both show emission that abruptly stops at the position of the ridges. One should remember that, in the case of the positive LSR velocity structures, these are located at the far side of the cusped X_1 orbit, so it is expected that the detected emission is weaker.

The low rms noise in the data allows to detect sub-mm emission even though a significant drop is seen in line intensities at these LSR velocities in several lower frequency transitions of other species tracing low $\sim 10^2$ cm^{-3} (CO(1-0)), intermediate $\sim 5{\times}10^2$ cm^{-3} (^{13}CO(1-0), C^{18}O(1-0)), and high $\geq 10^4$ cm^{-3} (CS(1-0)) volume densities (Bally et al., 1987; Dahmen et al., 1998; Oka et al., 1998; Tsuboi et al., 1999). The distribution of the MCs is not symmetric relative to the galactic plane. Gas at these LSR velocities is also seen in CS(1-0) observations of Tsuboi et al. (1999) shown in Figure 6.3. In the figure, the Galactic longitude limits of our CO(4-3) observations are drawn as vertical dashed lines and the positions of the structures shown in Figure 6.2 are also shown for comparison. The first contour level in Figure 6.3 is located at $2{\times}\sigma$ detection level. I interpret the lack of CS(1-0) emission tracing gas with densities $\geq 10^4$ cm^{-3} at the position of the B-RIDGE and R-RIDGE, as these structures being low density diffuse transient features, bringing molecular gas inwards to the inner X_2 orbits. Further investigation would be needed to make a more solid statement about the physical conditions in the B-RIDGE and R-RIDGE. Higher angular resolution CO(4-3) observations would improve the spatial separation of the B-RIDGE from CND emission. This would provide a better determination of the structure of the B-RIDGE emission in the position-velocity diagram. Also, a better signal-to-noise would help to better trace the weak emission of the R-RIDGE connecting the far side of the X_1

orbits with the inner orbits. In the following, I focus on the molecular clouds HVG1-1C, HVG1-2C, HVG2, and HVG3, which are much brighter than the emission in the molecular ridges. In order to compare the carbon monoxide and atomic carbon detections, all observations hereafter are shown in the Equatorial (J2000) coordinate system in which all Herschel-HIFI observations were carried out.

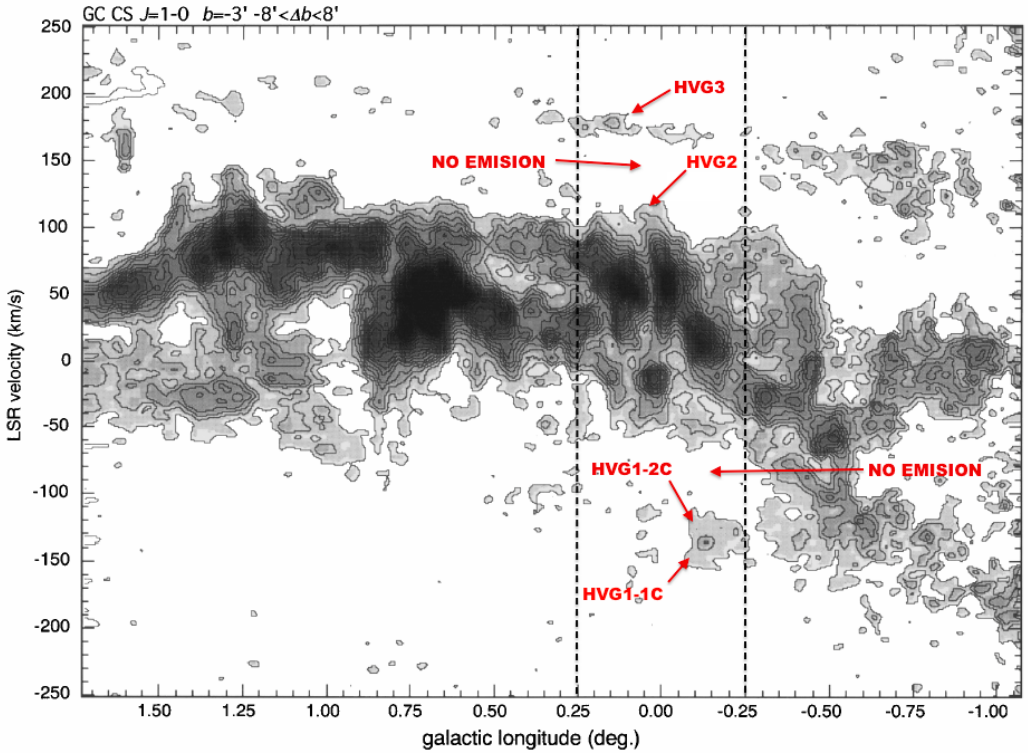

Figure. 6.3: *CS(1-0) position-velocity diagram in Tsuboi et al. (1999). Vertical dashed lines indicate the limits of the CO(4-3) observations. The first contour level is drawn at 2×σ detection level. The positions of the high velocity sources in the datasets are shown. The lack of CS(1-0) emission in the molecular ridges suggests gas with low volume densities.*

6.2.1 HVG at Negative LSR Velocities

The molecular clouds HVG1-1C and HVG1-2C are found along the same l.o.s. and suffer substantial velocity blending. Figures 6.4 and 6.5 show 3 kms^{-1} wide spatial maps of HVG1-1C and HVG1-2C, respectively. The color scale in the figures represents the CO(4-3) emission while contours refer to [CI](1-0) emission. The $\Delta R.A.$ and $\Delta DEC.$ offsets are measured with respect to the position of Sgr A* at $\alpha(J2000) = 17^h\ 45'\ 39.9''$, $\delta(J2000) = -29^\circ\ 00'\ 28.1''$. The ★ symbols

in the figures denote the CO(4-3) emission peak positions summarized in Table 6.1. From the figures, it can be noticed that part of the clouds toward the southern direction is outside the covered area of our surveys. The spatial distribution of the emission in both cases is very similar. The [CI](1-0) emission follows closely the distribution of the CO(4-3) emission (darker contours represent higher intensities). For LSR velocities lower than -110 kms^{-1}, HVG1-2C displays what seems to be an arc-like structure related to the B-RIDGE emission.

The spectra at the CO(4-3) peak positions shown in Table 6.1 are shown in Figures 6.6 and 6.7, for HVG1-1C and HVG1-2C, respectively. In each plot, the offsets from the Sgr A* position are given next to the source's name. In the plots, I have included: (a) [CI](2-1), [CI](1-0), and CO(4-3) sub-mm spectra from the present work, (b) unpublished CO(1-0) and ^{13}CO(1-0) observations part of the ongoing Mopra CMZ Survey (M. Burton, private communication), and (c) HCO$^+$(1-0) emission from the Mopra archive with 2 kms^{-1} velocity resolution (Jones et al., 2012). The C^{18}O(1-0) observations showed no detection above the $3\times\sigma$ detection level, with $\sigma = 0.06$ K. The antenna temperature scale of all the Mopra data shown here has no correction for the extended beam efficiency $\eta_{xb} = 0.65$ (Ladd et al., 2005), unless it is explicitly mentioned, and measured antenna temperatures have been scaled by the factor shown next to each line's name for better display purposes. The position of each cloud along the LSR velocity axis is demarcated by the horizontal bracket on top of the emission.

From the spectra in both figures, it can be seen that sub-mm transitions show the two peaks associated to HVG1-1C and HVG1-2C and have similar shapes. Dahmen et al. (1998) showed that, in general in the CMZ, the CO(1-0) and ^{13}CO(1-0) spectra are indeed very similar, while their ratio varies very little. Because of the large line widths of molecular clouds in the GC, CO(1-0) does not appear to be optically thick but rather has moderate opacities with $\tau \gtrsim 1$, while the optical depth for C^{18}O(1-0) is always $\tau \ll 1$. Since we have no detection in C^{18}O(1-0), this puts limits in the column density at the observed l.o.s.. These facts make me confident that, the dip between both clouds is indeed the physical separation in velocity space between them, and therefore, they are separated physical entities, and not the artificial product of a self-absorption feature at the LSR velocity center of one single cloud. The case of the CO(1-0) spectrum of HVG1-2C is very interesting because it shows clear signs of an undergoing shock, The spectrum is almost identical in shape and velocity extent (~ 70 kms^{-1}) to the ^{13}CO(3-2) observations of the molecular clump "IC443 C" in van Dishoeck et al. (1993) (see their Figure 2). Whether the collision is between the clouds or with some external source (e.g. a SNR) is not clear at the moment, but given the close location of the clouds along the l.o.s. and LSR velocity, it seems likely that this is indeed the collision between clouds in the X_1 orbits. In fact, van Dishoeck et al. (1993) showed that the for the "IC443 C" clump, the shock occurs predominantly

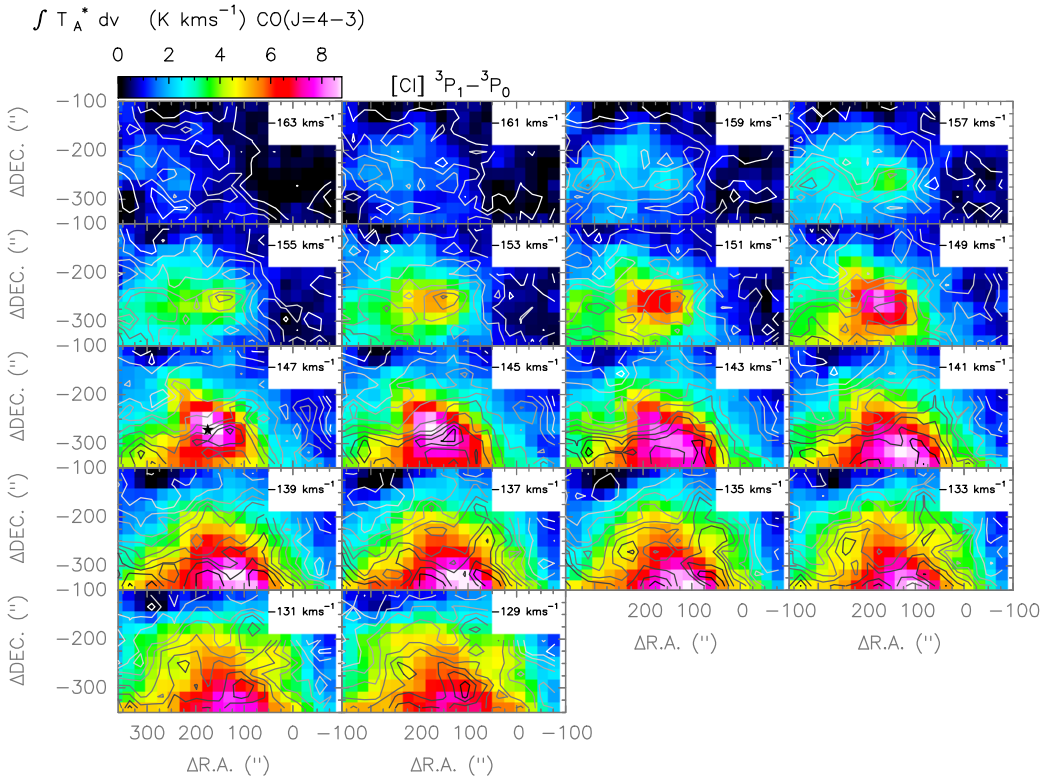

Figure. 6.4: *HVG1-1C spatial map of CO(4-3) (color scale) and [CI](1-0) (contours) emission. The ★ symbol shows the CO(4-3) peak position on the map.*

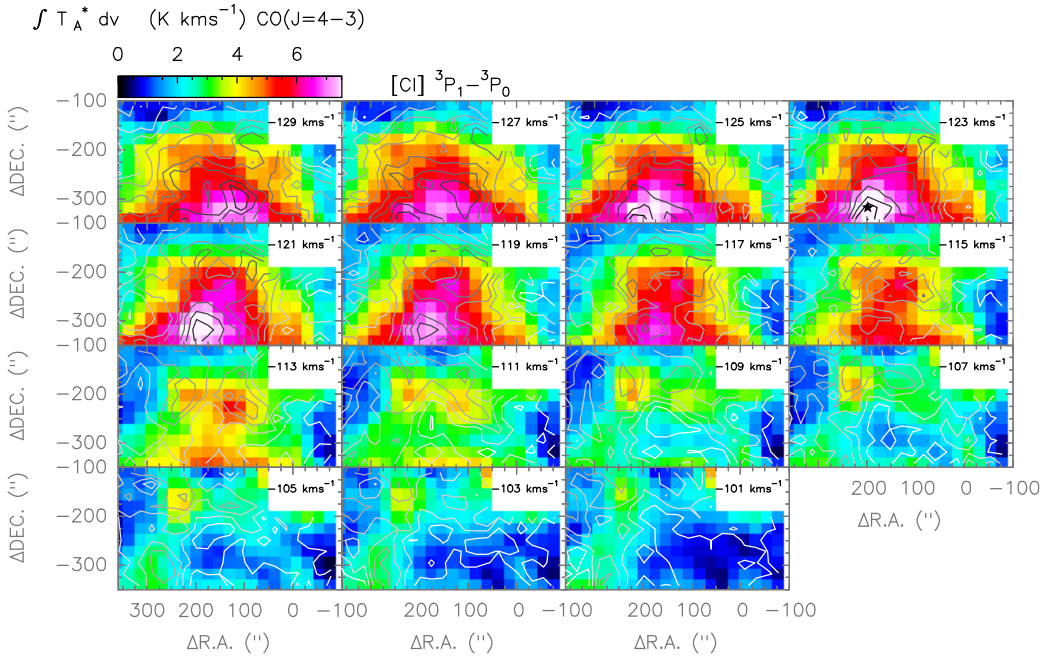

Figure. 6.5: *HVG1-2C spatial map of CO(4-3) (color scale) and [CI](1-0) (contours) emission. The ★ symbol shows the CO(4-3) peak position on the map.*

along the l.o.s.. Detailed shocks analysis is out of the scope of the present thesis,

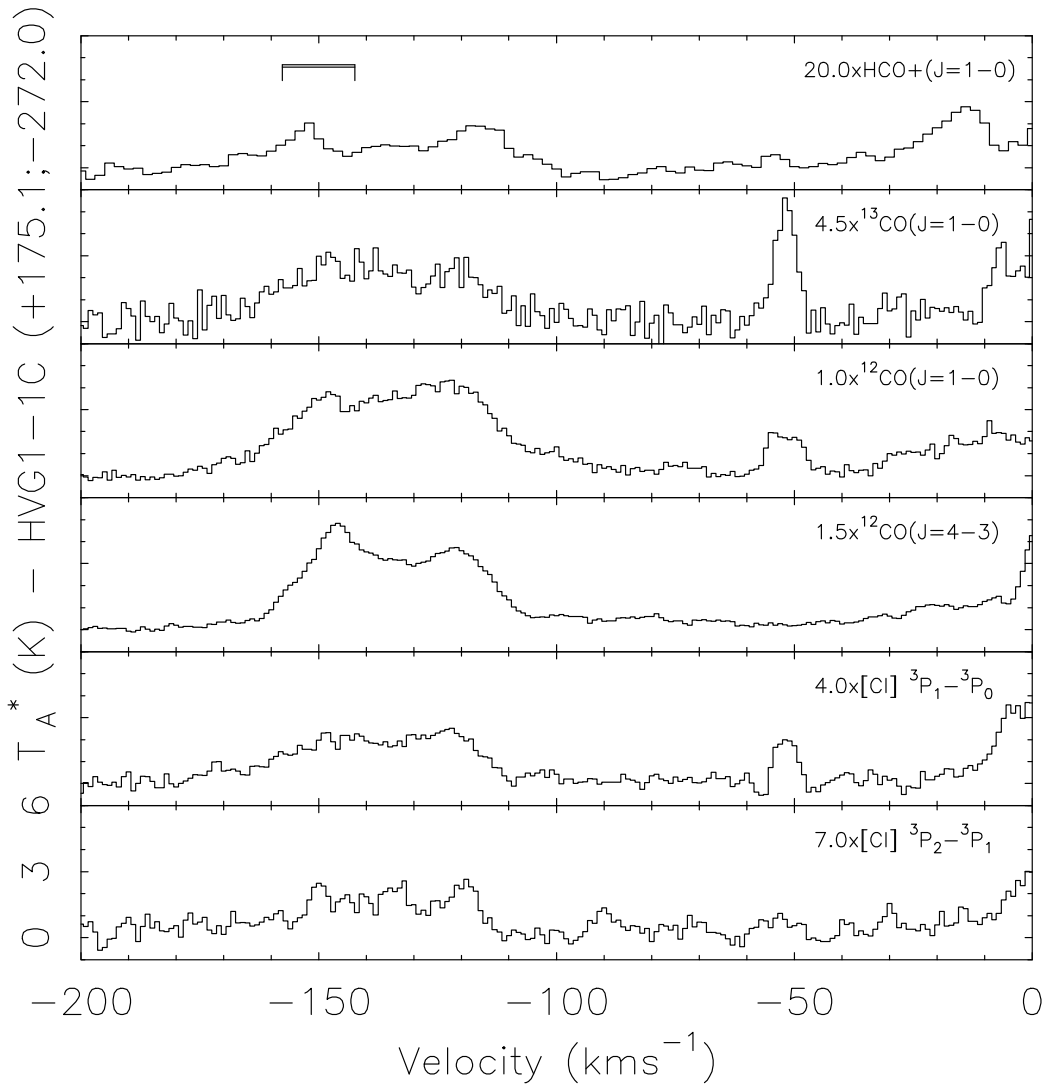

Figure. 6.6: *From bottom to top: [CI](2-1), [CI](1-0), CO(4-3), CO(1-0), ^{13}CO(1-0), and HCO$^+$(1-0) spectra at the CO(4-3) peak position for cloud HVG1-1C. The CO(1-0) and ^{13}CO(1-0) are part of the ongoing Mopra CMZ Survey (M. Burton, priv. communication), while the HCO$^+$(1-0) spectrum is part of the public data archive of the Mopra telescope (Jones et al., 2012). The position of the cloud along the velocity axis is demarcated by the horizontal bracket on top of the emission.*

so I refer the reader to a future publication on these sources.

6.2.2 HVG at Positive LSR Velocities

At positive LSR velocities, two molecular clouds are identified: HVG2 and HVG3. These molecular clouds are on opposite sides of the R-RIDGE, being

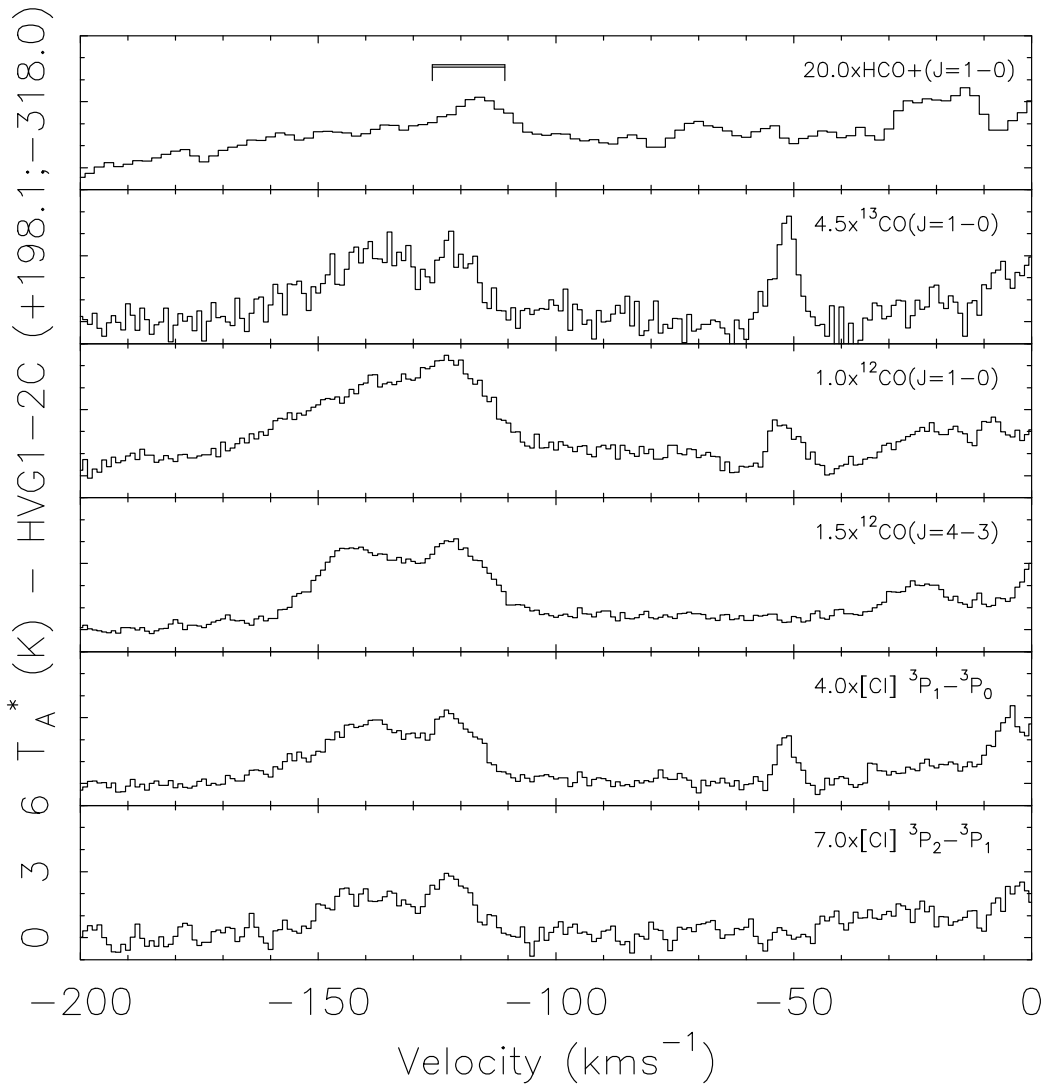

Figure. 6.7: *From bottom to top: [CI](2-1), [CI](1-0), CO(4-3), CO(1-0), ^{13}CO(1-0), and HCO$^+$(1-0) spectra at the CO(4-3) peak position for cloud HVG1-2C. The CO(1-0) and ^{13}CO(1-0) are part of the ongoing Mopra CMZ Survey (M. Burton, priv. communication), while the HCO$^+$(1-0) spectrum is part of the public data archive of the Mopra telescope (Jones et al., 2012). The position of the cloud along the velocity axis is demarcated by the horizontal bracket on top of the emission.*

HVG2 closer in LSR velocity to the bulk of molecular emission in X_2 orbits while HVG3 is the cloud with the largest LSR velocity ($\sim +175$ kms^{-1}) in the datasets. HVG3 is seen in the CS(1-0) emission in Figure 6.3 and HVG2 is detected at $l = -0°.063$.

Source	$\Delta\alpha$ (")	$\Delta\delta$ (")	$\alpha(J2000)$ ($^h\ ^m\ ^s$)	$\delta(J2000)$ ($^\circ\ '\ ''$)	l ($^\circ$)	b ($^\circ$)
HVG1-1C	+175.1	−272.0	17 45 53.25	−29 05 00.1	−0.095	−0.127
HVG1-2C	+198.1	−318.0	17 45 55.00	−29 05 46.1	−0.103	−0.139
HVG2	−123.9	+579.0	17 45 30.45	−28 50 49.1	+0.063	+0.067
HVG3	+589.1	+441.0	17 46 24.81	−28 53 07.1	+0.134	−0.122

Table. 6.1: *HVG cloud's selected positions at the CO(4-3) emission peaks.*

6.2.2.1 HVG2

The spatial distribution of the CO(4-3) (colors) and [CI](1-0) (contours) emission of the HVG2 cloud is shown in Figure 6.8. Almost the entire spatial extent of the cloud is within the covered area in the observed datasets. Serabyn & Guesten (1987) show CS(2-1) observations of these area in an integrated intensity map between +80 kms^{-1} and +140 kms^{-1} tracing high volume densities $\sim 10^5$ cm^{-3}. Figure 6.9 shows their data, measured in Equatorial (1950) coordinates. The red cross indicates the position of the CO(4-3) emission peak while the red square represents the spatial extent in Figure 6.8. Judging from the distribution of the CS(2-1) emission contours in the figure compared to the ones of the [CI](1-0) emission in Figure 6.8, it seems that the cloud is also detected in CS(2-1), as a local maximum found almost adjacent (blue cross) of the CO(4-3) emission peak, though a definitive statement can not be made given the large LSR velocity integration interval used for their figure. Unfortunately, no spectra at any position of this cloud is shown in Serabyn & Guesten (1987), so a direct comparison of the spectral information between the CO(4-3) and CS(2-1) emission can not be made. The detection of CS(2-1) emission in this cloud would immediately imply an increase in volume density with respect to the gas with no CS(2-1) emission given the high critical density necessary to excite the rotational $J = 2 - 1$ level of carbon monosulfide. This is interesting in the context of the molecular gas becoming denser when migrating from the outer X_1 to the inner X_2 orbits, which could be the case of HVG2 given its location along the LSR velocity axis.

In Figure 6.10, the spectra toward the CO(4-3) emission peak in Table 6.1 are shown, as explained in the previous section. Again, the horizontal bracket shows the position of HVG2 along the LSR velocity axis. The same arguments exposed for the case of clouds HVG1-1C and HVG1-2C apply here to consider the cloud as single physical entity and not an artificial component due to self-absorption at +120 kms^{-1}. There is a large velocity blending with a prominent adjacent feature that covers most of Figure 6.9 and that can be seen in the upper part of the CO(4-3) observations shown in Appendix F at $V_{lsr} \geq +100$ kms^{-1}.

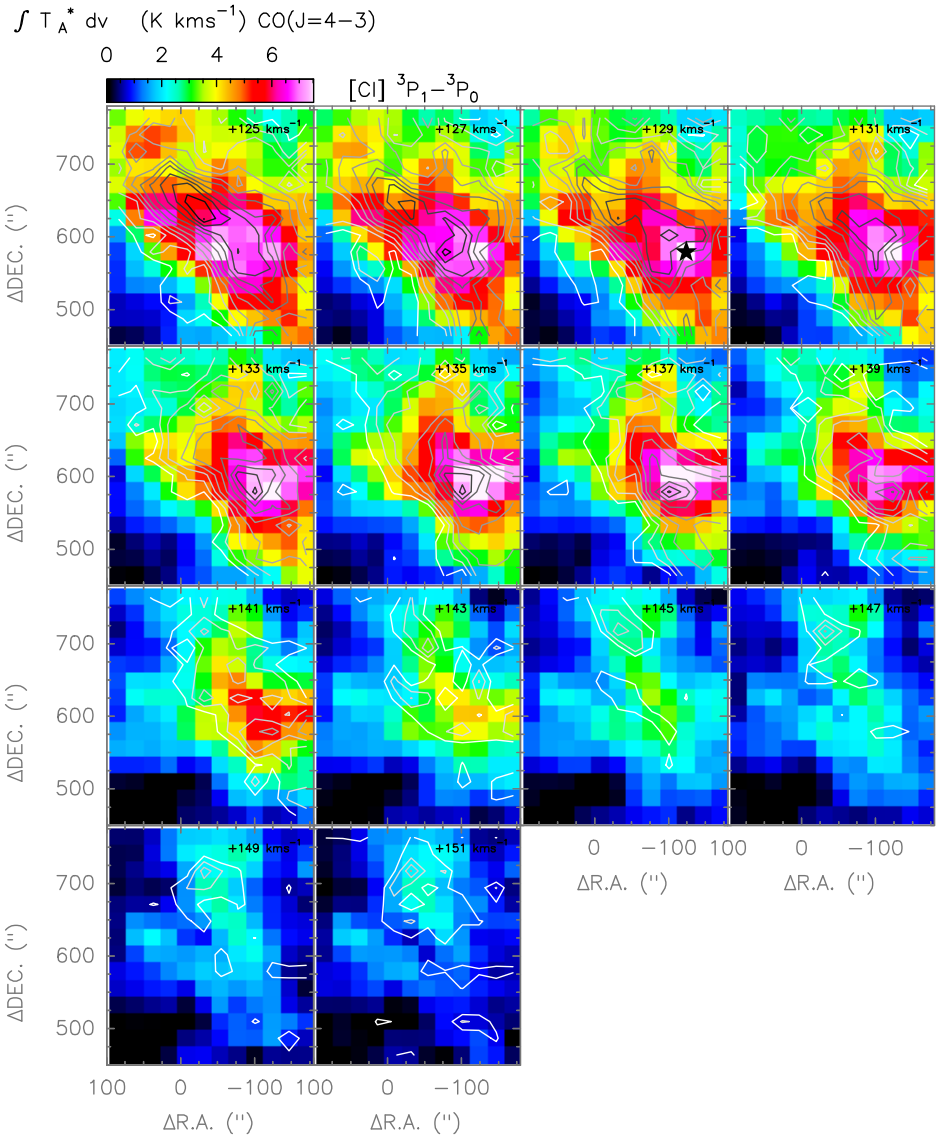

Figure. 6.8: *HVG2 spatial map of CO(4-3) (color scale) and [CI](1-0) (contours) emission. The ★ symbol shows the CO(4-3) peak position on the map.*

6.2.2.2 HVG3

The HVG3 cloud is by far the largest molecular cloud at high LSR velocities in the datasets. Its large radial velocity $V_{lsr} \sim +175$ kms^{-1} places it almost certainly at the X_1 orbits. Its emission is very weak compared to the other HVG clouds and presents no LSR velocity blending with other features along the l.o.s., being completely isolated from the rest of the emission. The CO(4-3) spatial distribution of the HVG3 cloud along LSR velocity is shown in Figure 6.11 with the [CI](1-0) emission shown in contours. Given the higher signal-to-noise ratio of the [CI](1-0) observations, the same figure is repeated in Figure 6.12, where the color scale and contours of both lines have been interchanged. In

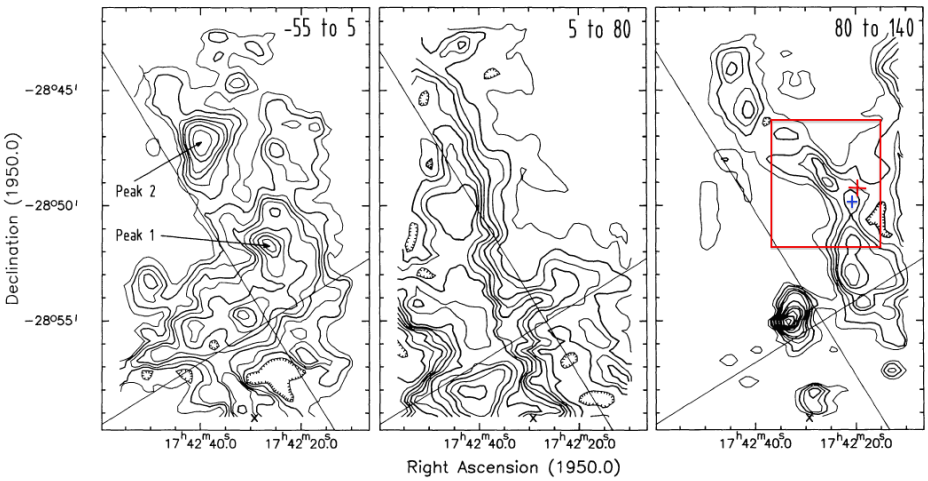

Figure. 6.9: *CS(2-1) observations of Serabyn & Guesten (1987) towards molecular cloud HVG2. The third panel from left to right contains the LSR velocity range including the HVG2 cloud. The red box enclosures the spatial extent of Figure 6.8, while the red cross shows the CO(4-3) emission peak in our data, and the blue cross shows the spatially associated CS(2-1) component to HVG2.*

both figures, the solid straight line represents the Galactic plane at $b = 0°$. From the figures, an arc-like structure is clearly recognizable in both CO(4-3) and [CI](1-0) lines. It develops above the Galactic plane from the the south-west part of the maps at +165 kms^{-1}, crossing the north part at +177 kms^{-1}, where it intersects $b = 0°$, ending below the Galactic plane to the south-east at higher LSR velocities. The [CI](1-0) emission has a tail above the Galactic plane that is detected at all LSR velocities and does not show correspondent CO(4-3) emission.

The large and complex structure of HVG3 is confined in a relative narrow velocity range (for GC standards), with $\Delta V(FWHM)$ 15 kms^{-1} around +175 kms^{-1}. The most striking difference between the spatial distribution of both sub-mm lines is that CO(4-3) emission appears extremely clumpy while [CI](1-0) emission is much more homogeneous and most of it is located toward the western half of the maps, above the Galactic plane. In Figure 6.11, the [CI](1-0) emission peak (▲ symbol) in the integrated intensity maps at +177 kms^{-1} lies above the plane while, in the CO(4-3) case (★ symbol), it is found at +179 kms^{-1} below the plane, within a round-shaped clump. The differences in the spatial distribution of both lines suggests that gas in this LSR velocity range could be composed by several, smaller clumps, than rather a single large arc-like structure. The much weaker [CI](1-0) emission towards the CO(4-3) clumps below the Galactic plane could reflect different excitation conditions. In Figure 2 of Bally et al. (1987), the bottom panel shows integrated ^{13}CO(1-0) emission from their low resolution (6') observations. Their figure shows an arc-like feature above the Galactic plane, from $l = 0°$ towards positive Galactic longitudes that resembles the [CI](1-0)

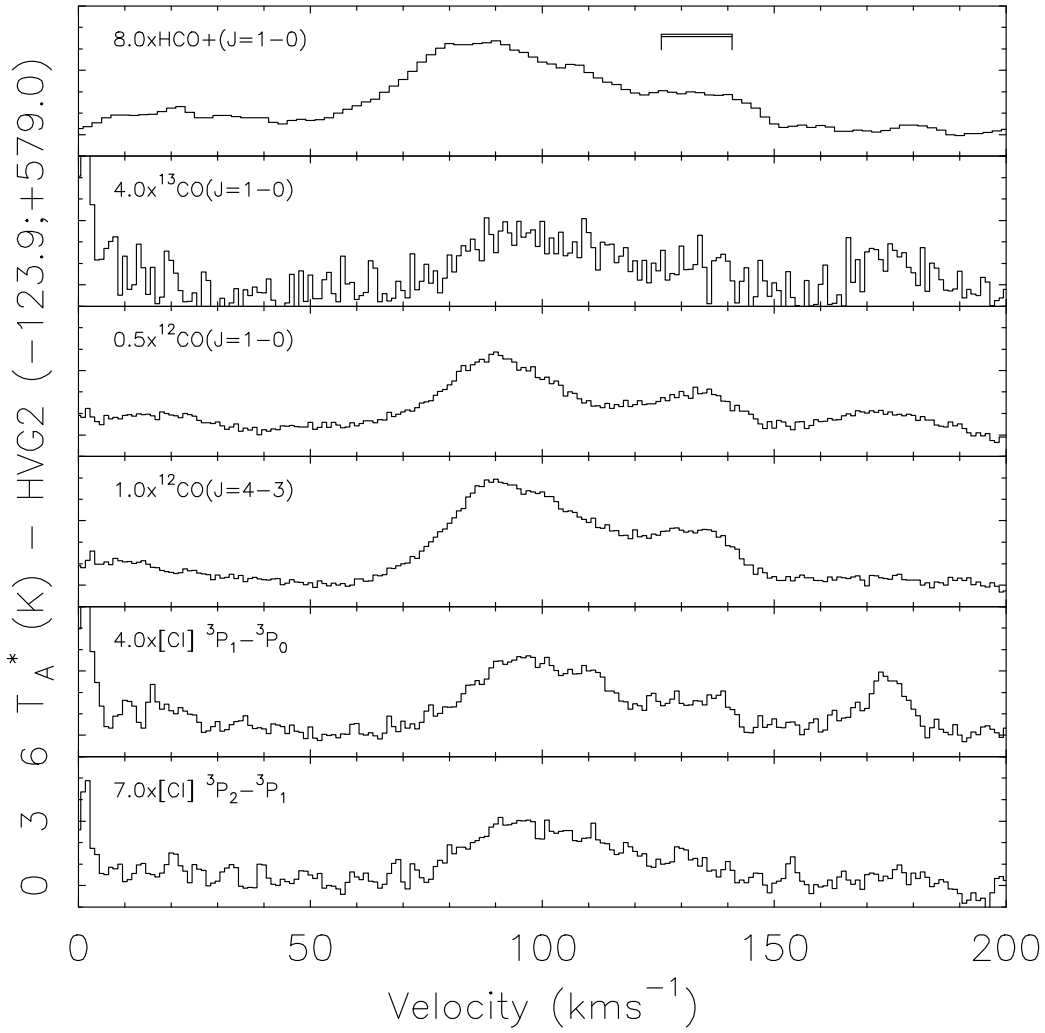

Figure. 6.10: *From bottom to top: [CI](2-1), [CI](1-0), CO(4-3), CO(1-0), ^{13}CO(1-0), and HCO$^+$(1-0) spectra at the CO(4-3) peak position for cloud HVG2. The CO(1-0) and ^{13}CO(1-0) are part of the ongoing Mopra CMZ Survey (M. Burton, priv. communication), while the HCO$^+$(1-0) spectrum is part of the public data archive of the Mopra telescope (Jones et al., 2012). The position of the cloud along the velocity axis is demarcated by the horizontal bracket on top of the emission.*

distribution. No emission below the Galactic plane is found above the lowest emission contour. A more detailed comparison is not possible given the large beam size and the large velocity interval (+100 kms^{-1} to +200 kms^{-1}) used to create the figure. In Figure 6.13, the same observations shown for all previously discussed clouds are shown for HVG3. Almost all lines show only one velocity component at the CO(4-3) emission peak, with the exception of the [CI](2-1) spectrum that presents some distortions in the baseline at these velocities, and the HCO$^+$(1-0) spectrum that shows some weak indication of a double peak component. The weak emission and large separation of the HVG3 cloud from

the bulk emission at lower LSR velocities indicates that this source is probably located at the far side of the X_1 cusped orbit.

6.3 Kinematics and Integrated Intensities

In order to obtain the physical information of the clouds at the positions in Table 6.1, Gaussian fits to the [CI](2-1), [CI](1-0), CO(4-3), CO(1-0), ^{13}CO(1-0), and HCO$^+$(1-0) observed spectra were performed. The quality of the Gaussian fits can be assessed from the spectra in Appendix D. Table 6.2 summarizes the results. From left to right, the columns in Table 6.2 contain: the source's name, the line's name, the characteristic noise of each spectrum $T^*_{A,rms}$, the cloud's LSR velocity center V_{lsr}, the velocity width $\Delta V(FWHM)$, the fitted antenna temperature peak T_{peak}, the integrated intensity I, and the integrated intensity ratio with respect to the CO(4-3) emission $R_{i/CO(4-3)}$. The error in the velocity estimates are the formal Gaussian fit errors while $T^*_{A,rms}$ was used as the error of the fitted peak antenna temperature T_{peak} to compute the error in I. The Mopra CO(1-0), ^{13}CO(1-0), and HCO$^+$(1-0) lines were corrected by the extended efficiency $\eta_{xb} = 0.65$ (Ladd et al., 2005).

In the case of the HVG1-1C cloud, the fitted LSR velocities for all the lines span the range from ~ -150 kms^{-1} to ~ -140 kms^{-1}. Linewidths are large, ranging from ~ 20 kms^{-1} to ~ 25 kms^{-1}, being the largest of the two HVG1 components. For HVG1-2C, LSR velocities are all around ~ -121 kms^{-1} except for the HCO$^+$(1-0) line whose LSR velocity center at -115.6 kms^{-1} largely deviates from the rest. Linewidths are narrower than in the HVG1-1C cloud, ranging from ~ 7 kms^{-1} to ~ 19 kms^{-1}. At positive LSR velocities, the fitted central LSR velocities for HVG2 are all around $\sim +132$ kms^{-1} with the [CI](2-1) central LSR velocity blue-shifted by ~ 10 kms^{-1}, probably due to poor signal-to-noise making the fit difficult. In terms of the linewidths, there is a wide range of values from ~ 13 kms^{-1} to ~ 34 kms^{-1}. For cloud HVG3, central LSR velocities vary from $\sim +170$ kms^{-1} to $\sim +180$ kms^{-1}, while linewidths range from ~ 6 kms^{-1} to ~ 25 kms^{-1}. Given the baseline distortion of the [CI](2-1) line at these LSR velocities, in order to estimate I, the [CI](1-0) spectrum was scaled by 0.8 and its integrated intensity assigned to the [CI](2-1) line in Table 6.2. This procedure is justified as first order approximation since both spectra behave similar as it can be seen in Figures D.10, D.11, and D.12 for the other HVG sources.

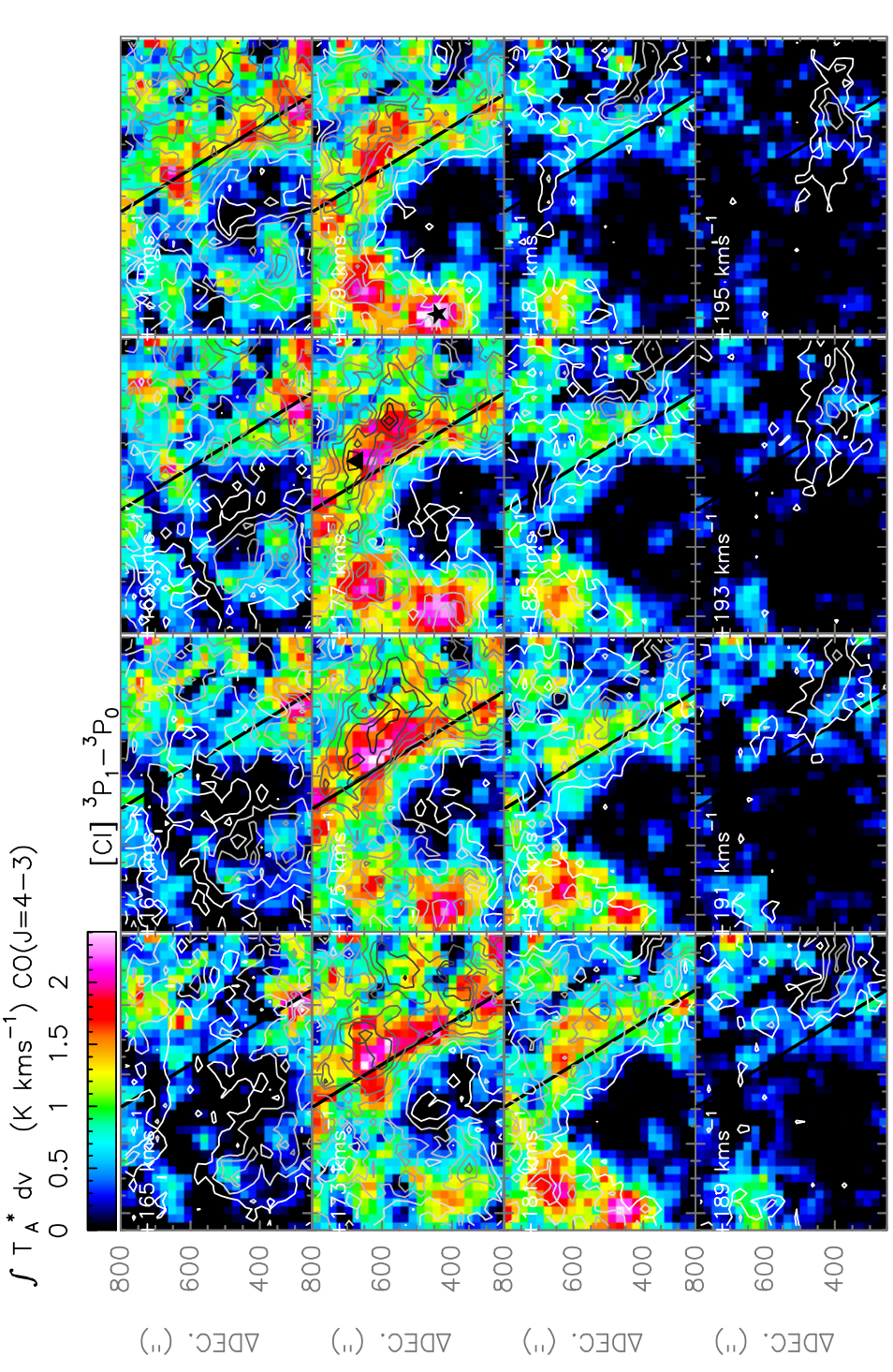

Figure. 6.11: *HVG3 spatial map of CO(4-3) (color scale) and [CI](1-0) (contours) emission. The ★ symbol shows the peak position on the map of the colored emission, while the ▲ symbol shows the peak position of the contoured data. The solid straight line shows the Galactic plane at b = 0°.*

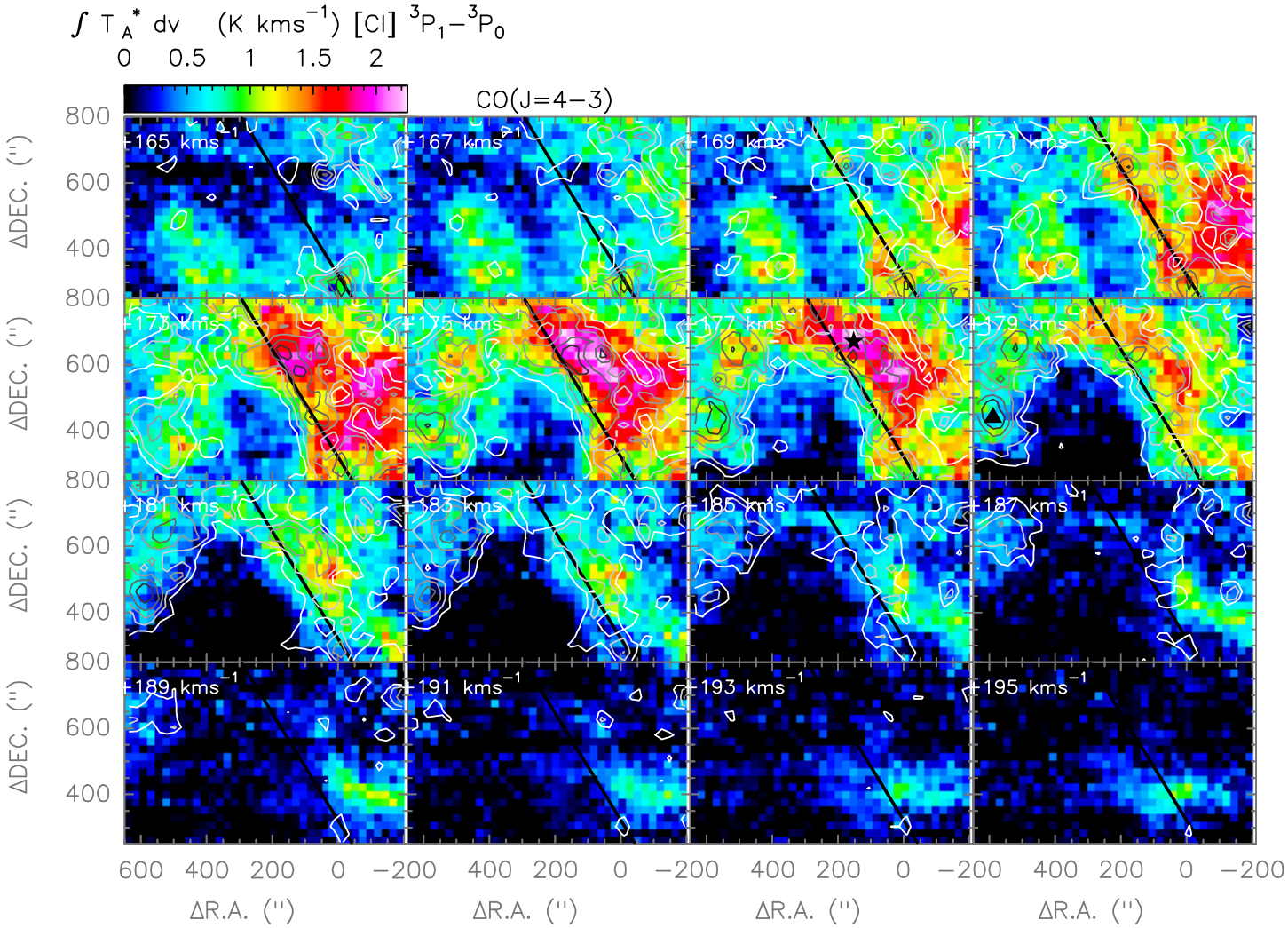

Figure. 6.12: *HVG3 spatial map of [CI](1-0) (color scale) and CO(4-3) (contours) emission. The ★ symbol shows the peak position on the map of the colored emission, while the ▲ symbol shows the peak position of the contoured data. The solid straight line shows the Galactic plane at b = 0°.*

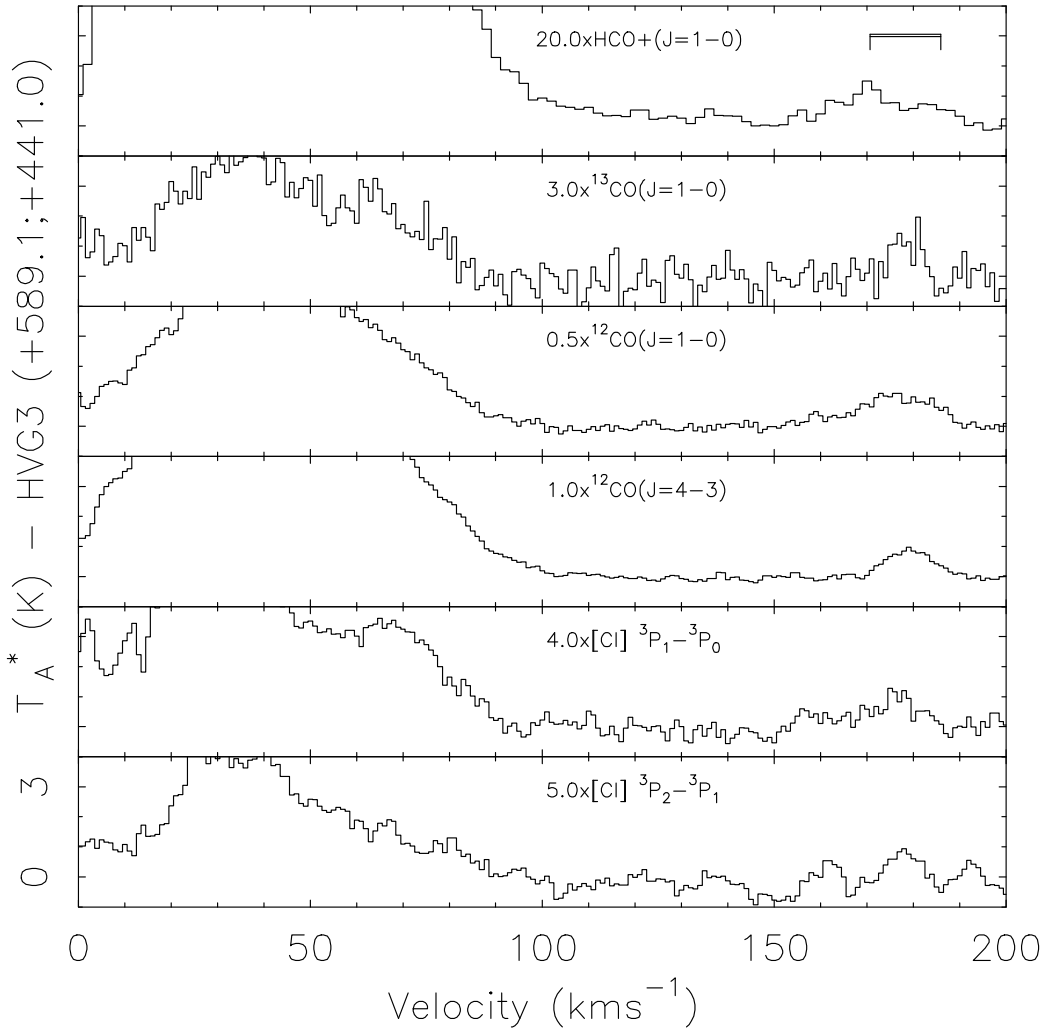

Figure. 6.13: *From bottom to top: [CI](2-1), [CI](1-0), CO(4-3), CO(1-0), ^{13}CO(1-0), and HCO$^+$(1-0) spectra at the CO(4-3) peak position for cloud HVG3. The CO(1-0) and ^{13}CO(1-0) are part of the ongoing Mopra CMZ Survey (M. Burton, priv. communication), while the HCO$^+$(1-0) spectrum is part of the public data archive of the Mopra telescope (Jones et al., 2012). The position of the cloud along the velocity axis is demarcated by the horizontal bracket on top of the emission.*

6.4 Line Ratios for HVG Sources

In order to identify possible trends in the physical conditions of the gas being located at X_1 orbits as it moves towards the more inner orbits (at smaller LSR velocities in modulus), I explored the behavior of the integrated line intensity ratios for each source, as a function of LSR velocities. Since the gas in the GC is known to be warm and dense, I assumed the bulk of the molecular material to be traced by the CO(4-3) transition and used their LSR velocities as a fair representation of the V_{lsr} of the clouds.

Table. 6.2: *Gaussian fit results and integrated intensity ratios for HVG clouds. Intensity errors are calculated from $T^*_{A,rms}$ and $\Delta V(FWHM)$ errors. The Mopra data were corrected by the extended efficiency η_{xb} = 0.65 (Ladd et al., 2005)*

Source	**Line**	$T^*_{A,rms}$ (K)	V_{lsr} (kms^{-1})	$\Delta V(FWHM)$ (kms^{-1})	T_{peak} (K)	I (K kms^{-1})	$R_{i/CO(4-3)}$ (K kms^{-1})
HVG1-1C	[CI](1-0)	0.14	−142.5 ± 1.3	35.7 ± 2.6	0.48 ± 0.02	18.20 ± 5.5	0.312 ± 0.103
	[CI](2-1)	0.08	−140.6 ± 1.3	36.4 ± 3.5	0.25 ± 0.01	9.50 ± 3.2	0.163 ± 0.059
	CO(4-3)	0.39	−145.4 ± 0.2	19.3 ± 0.3	2.84 ± 0.03	58.40 ± 8.1	...
	CO(1-0)	0.46	−146.4 ± 1.0	28.5 ± 1.0	5.06 ± 0.08	153.54 ± 15.0	2.629 ± 0.445
	^{13}CO(1-0)	0.29	−143.1 ± 1.7	32.7 ± 4.1	0.88 ± 0.06	30.62 ± 10.9	0.524 ± 0.200
	HCO$^+$(1-0)	0.03	−149.8 ± 1.7	30.5 ± 4.0	0.11 ± 0.00	3.23 ± 1.0	0.055 ± 0.019
HVG1-2C	[CI](1-0)	0.09	−120.3 ± 0.3	10.2 ± 1.0	0.51 ± 0.04	5.50 ± 1.1	0.111 ± 0.026
	[CI](2-1)	0.06	−121.7 ± 0.5	10.6 ± 1.3	0.36 ± 0.03	4.10 ± 0.8	0.083 ± 0.020
	CO(4-3)	0.28	−121.1 ± 0.4	19.5 ± 0.9	2.38 ± 0.07	49.50 ± 6.3	...
	CO(1-0)	1.00	−120.9 ± 0.3	16.1 ± 1.4	3.52 ± 0.28	60.46 ± 17.9	1.221 ± 0.394
	^{13}CO(1-0)	0.23	−120.4 ± 0.6	7.1 ± 1.2	0.58 ± 0.08	4.46 ± 1.9	0.090 ± 0.040
	HCO$^+$(1-0)	0.05	−115.6 ± 0.4	13.0 ± 0.8	0.12 ± 0.00	1.69 ± 0.6	0.034 ± 0.014
HVG2	[CI](1-0)	0.17	+133.8 ± 0.9	19.8 ± 2.6	0.36 ± 0.03	7.60 ± 3.7	0.102 ± 0.051
	[CI](2-1)	0.08	+122.3 ± 11.6	33.7 ± 15.1	0.18 ± 0.06	6.30 ± 4.0	0.085 ± 0.054
	CO(4-3)	0.19	+130.0 ± 0.5	27.6 ± 1.2	2.53 ± 0.06	74.30 ± 6.4	...
	CO(1-0)	0.60	+131.7 ± 0.4	29.6 ± 1.2	5.92 ± 0.12	186.77 ± 20.4	2.514 ± 0.350
	^{13}CO(1-0)	0.35	+134.2 ± 2.6	13.4 ± 6.7	0.43 ± 0.12	6.15 ± 5.9	0.083 ± 0.080
	HCO$^+$(1-0)	0.03	+132.3 ± 1.7	33.4 ± 3.2	0.34 ± 0.02	12.00 ± 1.6	0.162 ± 0.026
HVG3	[CI](1-0)	0.05	+175.7 ± 0.9	12.7 ± 2.6	0.23 ± 0.02	3.10 ± 0.9	0.287 ± 0.090
	[CI](2-1)	0.06	+178.0 ± 0.7	6.1 ± 1.3	0.18 ± 0.02	2.50[a] ± 1.0	0.231 ± 0.094
	CO(4-3)	0.08	+179.2 ± 0.2	11.2 ± 0.5	0.90 ± 0.02	10.80 ± 1.1	...
	CO(1-0)	0.37	+176.0 ± 0.3	19.8 ± 0.8	3.09 ± 0.06	65.23 ± 8.2	6.040 ± 0.970
	^{13}CO(1-0)	0.25	+178.4 ± 0.7	6.7 ± 1.2	0.68 ± 0.08	4.92 ± 2.0	0.456 ± 0.190
	HCO$^+$(1-0)	0.02	+171.6 ± 1.5	25.1 ± 3.9	0.08 ± 0.00	2.15 ± 0.5	0.199 ± 0.054

[a] [CI](1-0) value scaled by 0.8

In Figure 6.14, the line ratios in Table 6.2 are plotted as a function of CO(4-3) LSR velocity with different ratios identified by colors. For displaying purposes, the intensity ratios were multiplied by the factors shown in the figure, so trends with LSR velocities are more clearly recognizable. From left to right, the ratios displayed are from the HVG1-1C, HVG1-2C, HVG2, and HVG3 clouds, respectively. The solid lines connecting the measurements have been drawn only for displaying purposes so the interpolation for the low LSR velocities ($|V_{lsr}| <$ 120 kms^{-1}) is not intended to accurately reproduce the intensity ratios within the LSR velocity range associated to the X_2 orbits. From a preliminary analysis, I see that within the LSR velocity range containing the gas at X_2 orbits, ratios of the [CI](1-0) and [CI](2-1) intensities with respect to the CO(4-3) intensity are much lower that the ones for $|V_{lsr}| >$ 120 kms^{-1}. All intensity ratios show the same trend: decreasing line ratios with decreasing radial velocity, being the "inner" ratios lower than the "outer" ones at higher LSR velocities, with the exception of HVG2, whose CO(1-0)/CO(4-3) ratio seem to be to high compared with the trend in the other line ratios. It should be noticed that this cloud seems to be much closer to the X_2 orbits as it is shown in Figure 6.2, so the difference in the CO(1-0)/CO(4-3) ratio could be in fact reflecting slightly different physical conditions. I also notice that, though the HCO$^+$(1-0)/CO(4-3) ratios follow the general trend, they are larger at positive LSR velocities than the values at negative LSR velocities. From Table D.1, the HCO$^+$(1-0) and CO(4-3) critical densities at 100 K kinetic temperature are similar: $\sim 2.4\times10^5$ cm^{-3} and $\sim 3.0\times10^5$ cm^{-3} (ignoring radiative trapping), respectively. Since the upper level energy of the HCO$^+$(1-0) transition is low, changes in their integrated intensity ratios are dominated either by changes in the excitation temperature of CO gas, suggesting that gas at the far side of the X_1 orbits could have lower excitation temperatures than the gas at the near side, increasing the HCO$^+$(1-0)/CO(4-3) ratio or, if the excitation temperatures are similar, by a different degree of ionization of the gas traced by the HCO$^+$(1-0) emission.

6.5 Physical Parameters of the HVG Gas

In order to obtain the physical conditions of the HVG gas, such as the H_2 volume density, column density of the observed species, and kinetic temperature of the gas, I modeled the peak intensities in Table 6.2 (T_{peak}) using the RADEX software (van der Tak et al., 2007), as described in Section 2.11.2. The collision partners considered for each species are shown in Table D.1.

In order to reproduce the T_{peak} values, I created a parameter grid for the volume densities of the collision partners, column densities for each species (C, CO, ^{13}CO, HCO$^+$), and kinetic temperature of the gas. For the molecular species, the

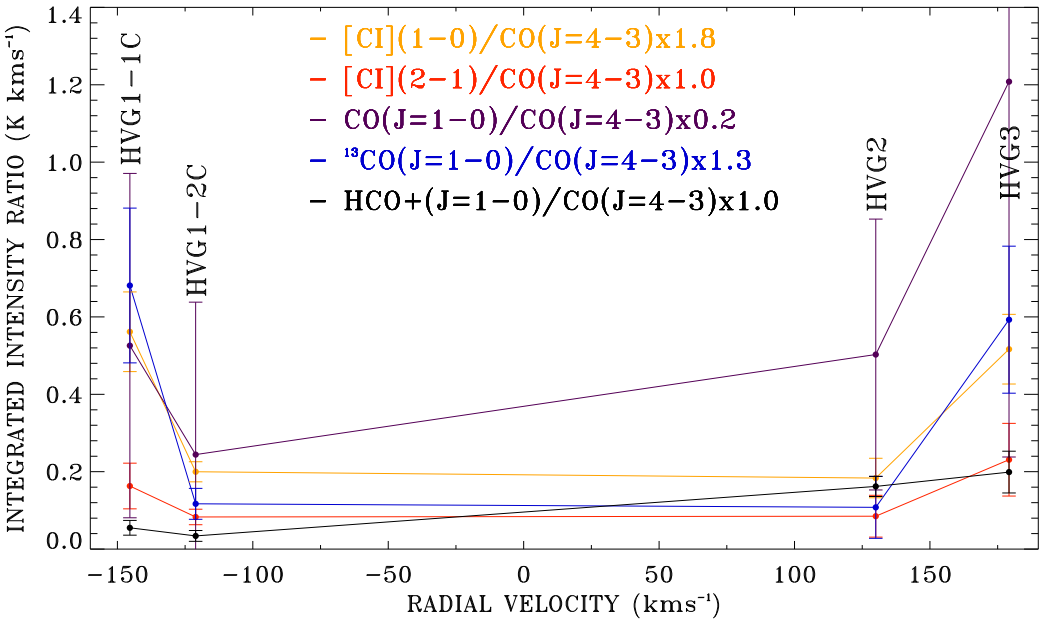

Figure. 6.14: *LSR velocity distribution of line ratios in Table 6.1. Ratios are taken with respect to the CO(4-3) line, whose fitted V_{lsr} values are used to locate the ratios along the LSR velocity axis for each cloud.*

main collision partner is molecular hydrogen, so in Figures E.1 to E.20, only the H_2 volume density n(H_2) is plotted on the x-axis. For the case of atomic carbon, the volume densities for the other collision partners such as H, He, H^+, and e^- had to be provided. In order to do so, I made some assumptions based on available observational evidence: (1) the hydrogen density was assumed to be the same as the one of H_2 since, as previously mentioned in the text, the gas is expected to transit from atomic to molecular form when arriving to the X_1 orbits, so an equipartition of the atomic and molecular content of hydrogen seems to be a good first order approximation, (2) the volume density assumed for He was 0.36×n(H_2) based on the usual Helium correction abundance applied in the Galactic disk for calculations of the molecular mass of MCs (García et al., 2014), and (3) the H^+ and e^- volume densities were assumed to be low and equal to 1 cm^{-3} since, with no massive stellar clusters close to the gas at these LSR velocities capable of providing large amounts of FUV photons, it is not expected that the gas is significantly ionized in the HVG clouds. The column density of each species in shown on the y-axis of Figures E.1 to E.20, spanning different ranges for different species. As expected, the column densities for atomic carbon and carbon monoxide are larger than the one for the isotopologue ^{13}CO, and much larger than the ionized HCO^+, given their large abundance with respect to the other two species (Güsten & Philipp, 2004). For the kinetic temperature grid, I chose five values for the gas temperature: 50 K, 100 K, 200 K, 300 K, and 500 K, based on the work done by Riquelme et al. (2013) tracing shocked gas in the X_1 orbits, in regions where the most prominent shocks occur (Sgr B2, Sgr C, Molecular Loops, etc.). In Figures E.1 to E.20, the model results are shown

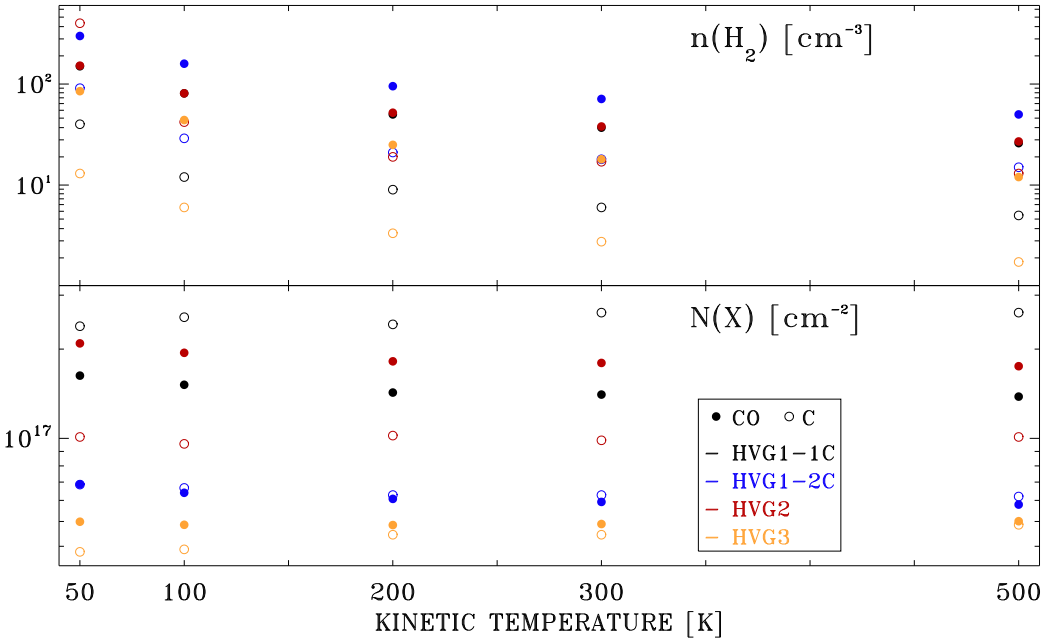

Figure. 6.15: *H_2 volume densities n(H_2) and column densities N(X) for atomic carbon (open circles) and carbon monoxide (filled circles) as a function of kinetic temperature, for the HVG1-1C, HVG1-2C, HVG2, and HVG3 MCs.*

for all HVG clouds, with one figure for each kinetic temperature of the grid. The curves in the plots show the model results consistent with the fitted peak antenna temperatures (T_{peak} values) in Table 6.2, while the dashed areas enclose the 1-σ deviation from the fitted values, with σ equal to the $T^*_{A,rms}$ value of each spectrum. In the cases of atomic carbon and carbon monoxide, the low and high frequency lines are plotted as blue and red circles, respectively. The solid black lines is an interpolation between all grid points consistent with the T_{peak} values in Table 6.2.

Possible physical solutions for the H_2 volume densities, column densities, and kinetic temperatures are found in the intersection of two or more observed lines of the same species. Since I had access only to one transition of the ^{13}CO and HCO^+ species, in the following I discuss the results from the models based only on the C and CO observations. Once the H_2 volume density and kinetic temperature of the gas are determined, they can be used to constrained the column densities of the species with only one transition available. In Figure 6.15, the solutions for H_2 volume densities (upper panel) and column densities (lower panel), indicated by the dashed vertical and horizontal lines in Figures E.1 to E.20, as a function of kinetic temperature, are shown. The values for the different HVG sources are distinguished by colors, while solutions from atomic carbon and carbon monoxide observations are represented as open and filled circles, respectively. The characteristic errors in the determined values are usually of the order of 50%, depending on the shaded area around the intersection point of two given lines. From Figures E.1 to E.20, it can be clearly seen that the two CO observed lines

give much better constrains on the solutions for the column and volume densities, while the atomic carbon curves usually overlap over larger fractions of the model curves, within error uncertainties, making the determination of the column and volume densities more uncertain. The impact of the filling factor on the derived solutions for both physical parameters is discussed in Appendix D, and all results discussed in the following assume a filling factor equal to unity in all cases, which is a common assumption in extended high velocity gas in the CMZ (Riquelme et al., 2013).

From the bottom panel in Figure 6.15, columns densities for both species seem no to be very sensitive to kinetic temperature, as their values do not change much between 50 K and 500 K. As a first order approximation, I determined the C and CO column densities within the telescope's beam for the CO(4-3) peak positions of the HVG clouds as given by their average value over the kinetic temperature range, as summarized in Table 6.3. The two error values in the table correspond to 1-σ deviations from the average value (first value) and to an 50% assumed error in the individual values derived for each cloud, at each kinetic temperature (second value). For H_2 volume densities in the upper panel of Figure 6.15, it can be seen that they can differ up to one order of magnitude between the atomic carbon and carbon monoxide values, as well as between different kinetic temperatures for the same species. The fact that C and CO provide solutions for all kinetic temperatures in the grid means that the kinetic temperature can not be determined from the current observations. As an example, Figure 6.16 shows the variation of kinetic temperature with volume density for HVG1-2C in both, atomic carbon and carbon monoxide observations. In this case, I fixed the column densities of both species at the corresponding values shown in Table 6.3, N(C) = 6.8×10^{16} cm^{-2} and N(CO) = 6.6×10^{16} cm^{-2}, while I refined the kinetic temperature grid, from 1 to 500 K, in steps of 1 K. As it can be seen from the figure, the best models for the low and high frequency transitions (shown by the blue and red curves, respectively) do not intersect, yielding no solution for the kinetic temperature. At very low kinetic temperatures values (< 30 K), the curves from both transitions come closer for both species. Nonetheless, low kinetic temperature for low H_2 volume density gas in the CMZ is rather unrealistic, since the gas in the X_1 orbits is prompted to suffer shocks, as explained in Section 6.1.1. Dahmen et al. (1998) showed that hot thin gas in the CMZ is good approximated by T_{kin} ~ 150 K and n(H_2) ~ $10^{2.5}$ cm^{-3}. From LVG models, Huettemeister et al. (1998) estimated that the dense gas component n(H_2) > 10^4 cm^{-3} is cold with T_{kin} ~ 25, while T_{kin} > 100 K is found in low density gas of a few 10^3 cm^{-3} where SiO is subthermally excited, so the molecular gas in the CMZ is consistent with two kinetic temperature regimes (~ 25 and ~ 150 K) (Riquelme et al., 2013).

The average H_2 volume densities and their corresponding errors in Table 6.3 are calculated in the same way as the column densities, averaging over the kinetic

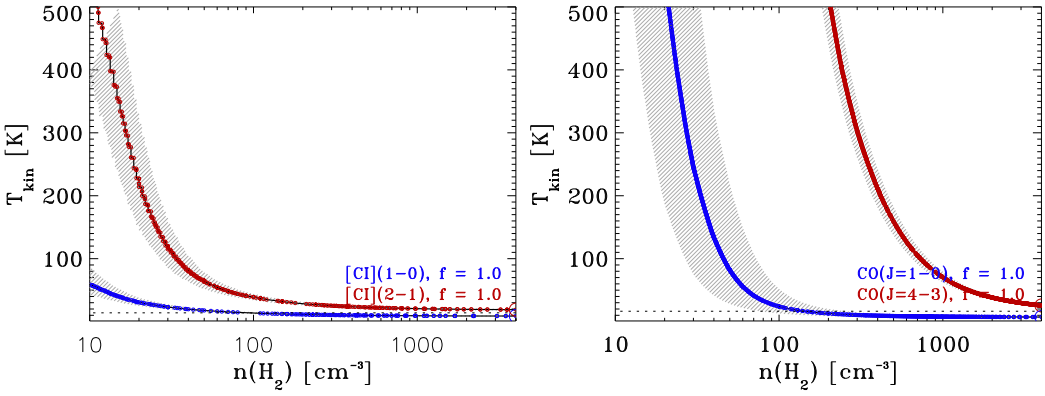

Figure. 6.16: *Kinetic temperature as a function of H_2 volume density n(H_2) at fixed column densities N(C) = 6.8×10^{16} cm^{-2} and N(CO) = 6.6×10^{16} cm^{-2} for HVG1-2C.*

temperature range in Figure 6.15. The variation of the estimated average H_2 volume densities as a function of CO(4-3) LSR velocity is shown in Figure 6.17, in the same way as the integrated intensity ratios were shown as a function of CO(4-3) LSR velocity in Figure 6.14. The error bars were obtained by adding *in quadrature* the errors in Table 6.3. Filled black diamonds and filled gray circles represent the obtained values from the carbon monoxide and atomic carbon observations, respectively. From the figure, all average H_2 volume densities are $\lesssim 10^3$ cm^{-3}, with increasing values as the LSR velocity decreases. This value is lower than the typical $\sim 10^4$ cm^{-3} for MCs in the GC (see Chapter 1). Even though error bars for the atomic carbon observations are large, it is quite remarkably that all n(H_2) densities derived from the C observations are lower than the ones derived from CO, with the exception of the values for HVG2, which is the cloud closest to the bulk of molecular emission in the X_2 orbits. The Interpretation of the derived H_2 volume densities from the atomic carbon observations is not trivial, given the large number of collision partners for this species, and their related uncertainties. How the obtained values for atomic carbon change with different collision partner densities is something that will be explored in a future publication. On the other hand, only H_2 is a relevant collision partner for carbon monoxide, so the overall behavior of n(H_2) is better constrained by those observations. Based on that fact, one concludes that the average H_2 volume densities of the HVG clouds are consistent with the gas at X_1 orbits, and that n(H_2) increases with decreasing LSR velocity as the gas moves inwards to X_2 orbits. More observations are needed to constrain the kinetic temperatures of the gas in order to obtain a more detailed physical picture of the HVG clouds. Finally, the selected peak positions of the CO(4-3) emission for each cloud mean that the results obtained here are probably biased towards higher density regions than the ones traced, for instance, only by the CO(1-0) transition. If this were the case, then one could consider the results in Figure 6.17 as upper limits, what would only reinforce the fact that the derived H_2 volume densities here are much lower than the typical values for MCs in the X_2 orbits.

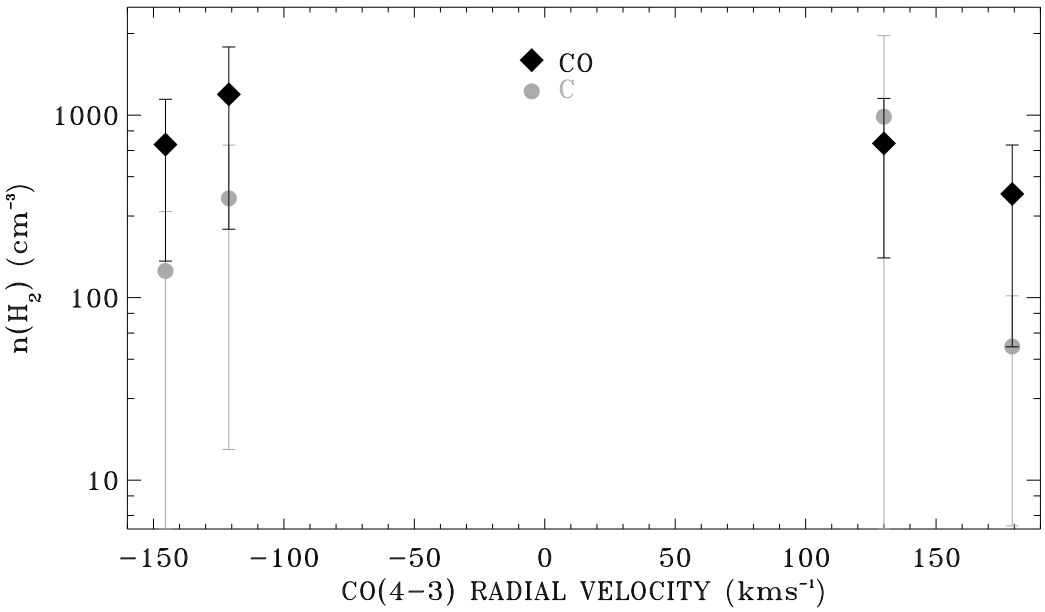

Figure. 6.17: *H_2 volume density n(H_2) as a function of CO(4-3) LSR velocity of HVG clouds in the present work. Black filled diamonds show n(H_2) values derived from the CO observations while gray filled circles show the ones derived from the C observed transitions. Error bars are calculated from adding in quadrature the errors in Table 6.3.*

6.6 Follow-up Work

In order to constrain the kinetic temperature of the gas and to improve the volume densities estimates for the HVG clouds, I have an accepted observing proposal at the IRAM[1] facility (http://www.iram-institute.org/) (proposal-ID: 018-15) targeting the CO(2-1) and ^{13}CO(2-1) transitions, with the possibility to detect also the C^{18}O(1-0) and C^{18}O(2-1) transitions if the observations are carried out under good weather conditions. The low-J CO transitions will constrain the gas kinetic temperature, while observations of the more optically thin isotopologues will also help the constrain the mass contained in the telescope's beam.

Launhardt et al. (2002) found that gas and dust within Galactocentric radius < 120 pc are warmer than those at larger radii, mainly because the FUV field from the GC is not intense at those radii and CO is largely shielded by dust (Dahmen et al., 1998). Nonetheless, the sub-mm detections in the present work at very high LSR velocities, tracing the warm gas, suggest that enough radiation must be present to excite those lines. Goldsmith & Langer (1978) derived the temperature

[1]Institut de Radioastronomie Millimétrique

dependence of the total cooling rate for a variety of molecular hydrogen densities with velocity gradients of 1 kms^{-1} pc^{-1} for a kinetic temperature range from 10 K to 60 K. According to their work, for $n(H_2) \leq 10^3$ cm^{-3}, the cooling is dominated by CO lines of the warm gas, while for 10^3 $cm^{-3} \leq n(H_2) \leq 10^5$ cm^{-3}, atomic carbon, molecular oxygen, and the isotopic species of CO contribute with 30% to 70% of the total cooling, respectively. In order asses the strength of the average FUV field at the position of the X_1 orbits, I have also submitted a SOFIA observing proposal targeting the [CII] line which was not detected in the Herschel-HIFI observations at any of the HVG1-1C, HVG1-2C, and HVG2 clouds above a $3\times T^*_{A,rms}$ significance level, with $T^*_{A,rms} \sim 0.5$ K, and in the case of the extreme positive LSR velocity of HVG3, due to the lack of spectral coverage. Combining the information of all these observations will help to better characterize the physical properties of the gas at the X_1 orbits, towards the l.o.s. to the Sgr A Complex.

Cloud	**N(C)** (cm^{-2})	**N(CO)** (cm^{-2})	**n(H_2)-C** (cm^{-3})	**n(H_2)-CO** (cm^{-3})
HVG1-1C	2.4E+17 ± 1.1E+16 ± 5.3E+16	1.4E+17 ± 9.1E+15 ± 3.2E+16	1.4E+02 ± 1.5E+02 ± 4.3E+01	6.9E+02 ± 5.0E+02 ± 1.8E+02
HVG1-2C	6.8E+16 ± 2.6E+15 ± 1.5E+16	6.6E+16 ± 3.9E+15 ± 1.5E+16	3.5E+02 ± 3.2E+02 ± 1.0E+02	1.3E+03 ± 1.0E+03 ± 3.6E+02
HVG2	1.0E+17 ± 2.4E+15 ± 2.2E+16	1.8E+17 ± 1.2E+16 ± 4.0E+16	9.8E+02 ± 1.7E+03 ± 4.0E+02	7.0E+02 ± 5.0E+02 ± 1.9E+02
HVG3	4.9E+16 ± 3.9E+15 ± 1.1E+16	5.4E+16 ± 6.9E+14 ± 1.2E+16	5.4E+01 ± 4.6E+01 ± 1.5E+01	3.7E+02 ± 3.0E+02 ± 1.0E+02

Table. 6.3: *Average column N and volume n(H_2) densities for HVG clouds. The errors correspond to 1-σ deviations from the average value (first value) and to an 50% assumed error in the individual values derived for each cloud, at each kinetic temperature (second value).*

Chapter 7

The +20 kms^{-1} and +50 kms^{-1} Molecular Clouds

Given the large number of astronomical sources and their complexity in the vast datasets shown in the present work, it is not possible to analyze and model all of them, within the time frame of a PhD thesis. Therefore, in the present chapter I outline part of the future work related to the observed sub-mm lines, in particular, the work related to the emission detected towards the +20 kms^{-1} and +50 kms^{-1} Clouds at the GC. Other sources such as the Sickle H II region and the HCO^+ Cloud (Minh et al., 2005) will be treated as well in follow up publications, based on the preliminary work I have done for this thesis.

7.1 Introduction

The +20 kms^{-1} and +50 kms^{-1} molecular clouds are located within 10 pc of the GC (Genzel et al., 1990; Ferrière, 2012). They are embedded in a clumpy and highly turbulent molecular intercloud medium, with estimated hydrogen mass $\sim 10^6$ $M_\odot$ (in the inner $\sim$ 50 pc of the GC), average density $\sim 10^2$ cm^{-3} and LSR velocities ranging from -40 kms^{-1} to +90 kms^{-1} (Ferrière, 2012). The +20 kms^{-1} Cloud has a mass around 5×10^5 $M_\odot$ with LSR velocities increasing with Galactic longitude from +5 kms^{-1} to +25 kms^{-1} (Minh et al., 2005; Ferrière, 2012). This increase in LSR velocity is related to the presence of another molecular cloud along the same l.o.s., at smaller LSR velocities. Minh et al. (2005) identified these MCs as being two different components at +5 kms^{-1} and +25 kms^{-1} (M$-$0.13$-$0.08b and M$-$0.13$-$0.08a), respectively, based on their morphology and on the enhancement of HNCO and SiO emission only towards the +25 kms^{-1} Cloud. The molecular mass of the +50 kms^{-1} Cloud is 3×10^5 $M_\odot$ (Minh et al., 2005; Ferrière, 2012). The gas kinetic temperature ranges from 50 - 120 K

throughout the clouds (Ferrière, 2012). The physical and chemical properties of these clouds differ strongly from the ones in the Galactic disk (Güsten & Philipp, 2004). Minh et al. (2005) found emission peaks of molecules such has HCO^+, HNCO, and SiO, shifted with respect to the NH_3 peaks (Güsten et al., 1981) indicating changing physical conditions from one position to the other.

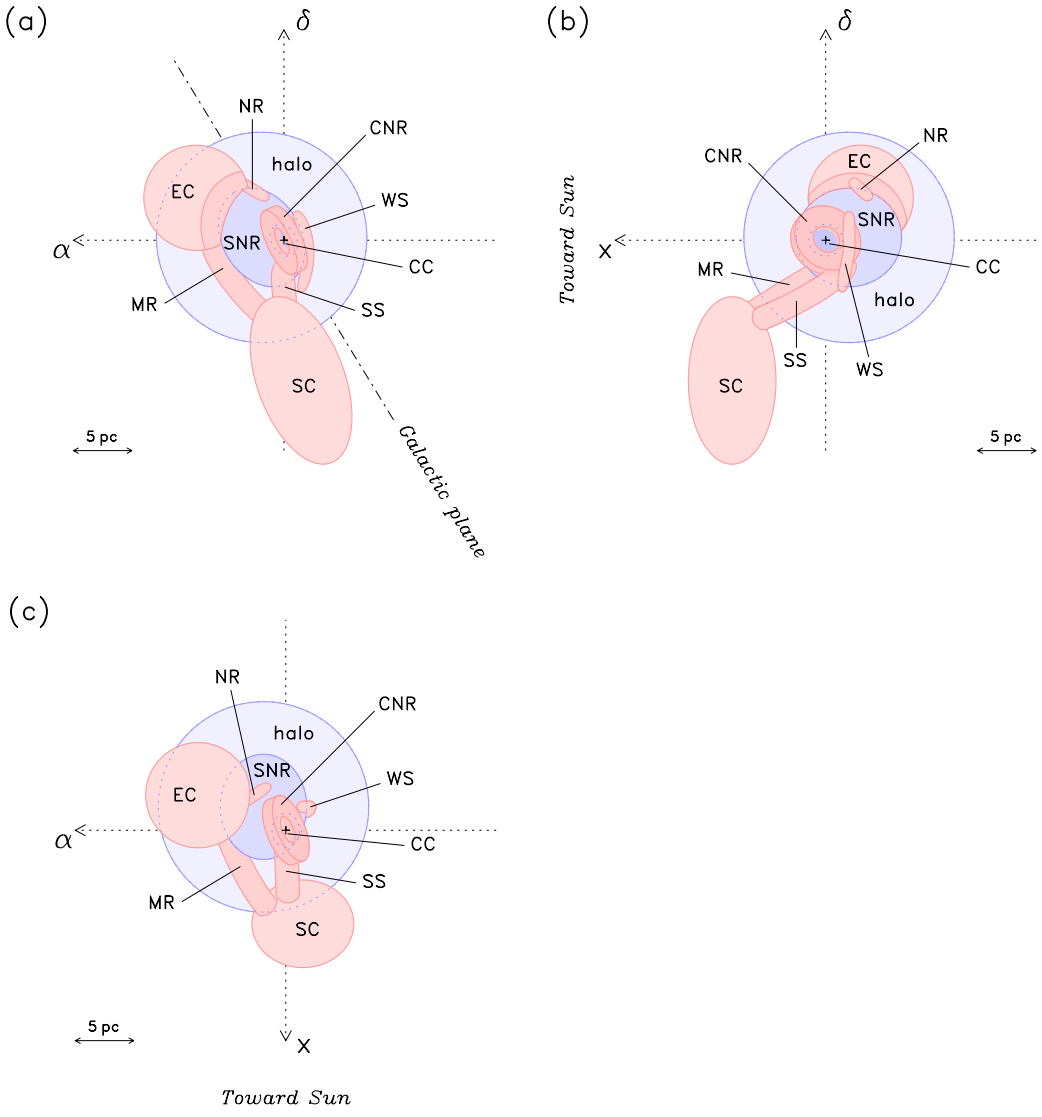

Figure. 7.1: *View of the inner 10 pc of the GC by Ferrière (2012) based on a compilation of observational results: a) in the plane of the sky; b) looking along the α-axis from west to east; and c) looking along the δ-axis from north to south. The relative locations of the +20 kms^{-1} Cloud (SC) and +50 kms^{-1} Cloud (EC) with respect to Sgr A-East (SNR), Central Nuclear Disk (CNR), Sgr A West H II region (CC) and gas streamers (MR, SS, NR, and WS) are shown.*

An overview of the inner 10 pc of the GC containing the +20 kms^{-1} Cloud (SC),

+50 kms^{-1} Cloud (EC), the Sgr A-East SNR, the gas streamers described in Chapter 4, the CND, and other structures not relevant for the present chapter, is shown in Figure 7.1 taken from Ferrière (2012). In their work, they created a three-dimensional picture of the gas based on a compilation of observational results (which are some times contradictory). The most strongly constrained location in the figure is the relative position between the Sgr A-West H II region (CC) and Sgr A-East since the former is clearly identified in absorption (free-free absorption by thermal gas) against the latter (Yusef-Zadeh & Morris, 1987a). The position of the SNR G359.92−0.09 (Yusef-Zadeh & Morris, 1987a), south of Sgr A-East and which was suggested by Coil & Ho (2000) to be interacting with the southern streamer, the +20 kms^{-1} Cloud, and Sgr A-East (Coil & Ho, 2000; Ferrière, 2012), was left out by the authors. The position of the +50 kms^{-1} Cloud next and behind of Sgr A-East seem to be well supported by observational evidence, while the northward LSR velocity gradient measured along the southern streamer automatically positions the +20 kms^{-1} Cloud in front of the CND. In Figure 7.1, the northern ridge (NR) seem to be the northern fraction of the streamer at −11 kms^{-1} and +8 kms^{-1} (if they are indeed the same structure) shown in Figure 4.4.

In terms of the overall kinematics, the +20 kms^{-1} and +50 kms^{-1} Clouds are presumably part of the same dynamical system (Liu et al., 2014) rotating rapidly (∼ 1 Myr orbital time for a stellar cluster) around the GC (Simon et al., 2007; Kruijssen et al., 2014). In the CMZ, it is expected that star clusters and their parent MCs may not be physically related anymore, given that the clusters originated from gas reservoirs already one dynamical time-scale (a few Myr) ago (Kruijssen et al., 2014). At the distance of both clouds from Sgr A*, the gravitational field is likely to be dominated by the Nuclear Cluster or the stellar Bulge, which are thought to be the main contributors to the gravitational potential at radii between 2 - 30 and 30 - 300 pc, respectively (Longmore et al., 2013).

7.1.1 Interaction Between Sgr A-East and the +50 kms^{-1} Cloud

The non thermal Sgr A-East source is interacting with the +50 kms^{-1} Cloud as it can be seen from several observations in the literature (Genzel et al., 1990; Coil & Ho, 2000; Ferrière, 2012, an references therein). This is also seen in Figure 4.6 from the emission morphology of the [CI](1-0), [CI](2-1), and CO(4-3) observations in the present work. Genzel et al. (1990) found blue-shifted C^{18}O(2-1) and CO(7-6) emission from the +50 kms^{-1} Cloud towards Sgr A-East considering it as direct kinematic evidence of expanding gas motions associated with the non thermal source. The morphology of its emission (supposedly

synchrotron), its measured size, and the strong enrichment in heavy elements (overabundance in the center of Sgr A-East ~ 4×[Fe/H]$_\odot$ down to ~ 0.5×[Fe/H]$_\odot$ at the outer parts), have supported the widely accepted conclusion that Sgr A-East is in fact a SNR, filled with hot (1.5×10^7 K) gas (Ferrière, 2012, and references therein). The energy of the supernova explosion has been estimated to be ~ 4× 10^{52} ergs (Yusef-Zadeh & Morris, 1987a; Mezger et al., 1989; Coil & Ho, 2000; Genzel et al., 1990). The age of Sgr A-East is around ~ 10^4 yr, estimated from the observed proper motion and displacement of the neutron star located at its interior and believed to be the remnant of the supernova progenitor (Genzel et al., 1990; Zhao et al., 2013; Lau et al., 2015). The gas in the +50 kms^{-1} Cloud has been accelerated by 100 kms^{-1} due to the interaction with Sgr A-East (Genzel et al., 1990). Also, the detection of 1720 MHz OH masers, without 1665 MHz and 1667 MHz counterparts, along the periphery of Sgr A-East (Yusef-Zadeh et al., 1996, 1999) revealed the presence of shocked molecular gas, providing more evidence that the expanding SNR is interacting with the +50 kms^{-1} Cloud and also possibly with the +20 kms^{-1} Cloud (Ferrière, 2012).

The expansion of Sgr A-East into the +50 kms^{-1} Cloud has not yet reached the entire molecular cloud. The total hydrogen mass swept up is ~ 6×10^4 M$_\odot$, which implies a mean preshock density ~ 10^4 cm^{-3} in the parent MC (Ferrière, 2012). The star formation linked to the A-D H II region complex precedes the shock with Sgr A-East based on the dynamics of the SNR and on the timescales required for the emergence of the H II regions (Serabyn et al., 1992; Lau et al., 2014). Serabyn et al. (1992) found in their high density tracer CS(7-6) observations compressed gas with a similar shape to the carbon observations in Figure 4.6. The gas is blue-shifted and red-shifted only in the crescent-shape, while outside it behaves as a normal MC. Therefore, they proposed a two component model for the dense gas: a normal dense star forming core, and a compression wave which has advance into the cloud from Sgr A-East.

7.1.2 FUV Field Heating the +50 kms^{-1} Cloud

The +50 kms^{-1} Cloud is not only compressed and accelerated by the expanding Sgr A-East shell but also exposed to an intense FUV from the Nuclear Stellar Cluster (Genzel et al., 1990). The cluster has a stellar mass within an angular radius 100" of M$_\star$ ~ 8.94×10^6 M$_\odot$, with Sgr A* at its dynamical center. It extends up to several hundred arcseconds from Sgr A* (Chatzopoulos et al., 2015), and its bolometric luminosity is L$_{bol}$ ~ 2×10^7 L$_\odot$, produced by ~ 100 OB stars, with an estimated age between 4 - 7 Myr (Figer, 2008). If there is no much extinction between the +50 kms^{-1} Cloud and the Nuclear Cluster, the FUV field from the Nuclear Cluster can be as high as χ ~ 10^3 at 10 pc from the center (Genzel et al.,

1990). Genzel et al. (1990) attributed the [CII] emission in the +20 kms^{-1} Cloud being weaker than in the +50 kms^{-1} Cloud, as it can be seen from the emission contours in Figure 7.4, as the +20 kms^{-1} Cloud being further away (in front) of the GC.

As mentioned in Chapter 2, most of the FIR radiation is reprocessed by dust, while the dust size is a crucial parameter in regulating the attenuation of the impinging FUV on the gas from the stellar clusters. The smaller the grains, the more effective they are in attenuating the FUV field from OB stars. The dust grain size within the Sgr A-East region (0.01 μm) is smaller than the dust typical grain size $\sim$ 0.1 μm in the surrounding ISM (Lau et al., 2015). For the compact H II regions (A, B, and C) and the ultra-compact H II region (D) associated to the +50 kms^{-1} Cloud (see Figure 1.3), Lau et al. (2014) modeled the SEDs[1] of regions A-D, finding that all of them require populations of very small (6 - 25 Å) transiently heated grains, large (100 - 1000 Å) equilibrium-heated grains, and PAHs (6-10 Å) in order to fit the 3.6 μm, 4.5 μm, 5.8 μm, and 8.0 μm fluxes observed by Spitzer/IRAC (Stolovy et al., 2006). A different grain size distribution in the GC than in the Galactic disk, would modify the ratio of total to selective extinction R_v, which is an important parameter in photodissociation region models such as the KOSMA-τ PDR model (Stoerzer et al., 1996; Cubick et al., 2008; Röllig et al., 2013a).

7.2 Sub-mm Emission of the +20 kms^{-1} and +50 kms^{-1} Molecular Clouds

The sub-mm emission of the large MCs complex between 0 kms^{-1} and +100 kms^{-1} covers almost the entire region observed in the present work. This is shown in the 5 kms^{-1} wide integrated intensity maps of the CO(4-3) (colors) and [CI](1-0) (contours) emission in Figure 7.2, and for the [CII] (colors) and [NII] (contours) lines in Figure 7.3. The emission of the [CI](2-1) line closely follows the distribution of the [CI](1-0) emission.

From Figure 7.2, it is clear that the [CI](1-0) emission is asymmetrically distributed in the map, being more intense towards the location of the +50 kms^{-1} Cloud between +46 kms^{-1} and +56 kms^{-1}, than at the position of the +20 kms^{-1} Cloud, between +2 kms^{-1} and +30 kms^{-1}. The CO(4-3) emission starts at the +20 kms^{-1} Cloud at low ΔDEC. values, between +2 kms^{-1} and +26 kms^{-1}, where the molecular streamer in Figure 4.4 is also seen. The emission develops

[1] Spectral Energy Distribution Cosmics

upwards to a more symmetric spatial distribution for LSR velocities > +30 kms^{-1} with the emission mainly distributed between the +50 kms^{-1} Cloud, at ΔDEC. values lower than ∼ +250", and the M+0.07−0.08 and M+0.11−0.08 clouds (also referred to as the HCO^+ Cloud in Minh et al. (2005)) above that value. Minh et al. (2005) detected much stronger HCO^+(1-0) emission is M+0.07−0.08 and M+0.11−0.08 than towards the location of the +50 kms^{-1} and +20 kms^{-1} Clouds. They interpreted this as an indication of a large scale process changing the excitation conditions from the GC outwards, possible due to shocks or high energy photons. They also found that the +25 kms^{-1} Cloud has enhanced HNCO and SiO emission that may be the result of the interaction with Sgr A-East or the G359.92−0.09 SNR.

From Figure 7.3, it can be noticed that the spatial distribution of the [CII] and [NII] emission is very widespread for LSR velocities between +2 kms^{-1} and +30 kms^{-1}, with the most intense [CII] emission located at the edge of the Sickle H II region (see Figure 4.5). Interestingly, the [CII] emission is weak at the position of the +20 kms^{-1} Cloud, and it rather surrounds it, as it can be seen when comparing the distribution of the CO(4-3) emission with the [CII] emission between +18 kms^{-1} and +22 kms^{-1} (see also Figure 7.4). Stronger [CII] emission towards the +50 kms^{-1} Cloud than at the +20 kms^{-1} Cloud was also found by Genzel et al. (1990). In their observations, [CII] emission peaked close to the CO peak in the +50 kms^{-1} Cloud, and weaker emission extended over the whole cloud. As expected, this behavior is also observed in the present datasets, as can be seen when comparing the CO(4-3) emission with the [CII] emission between +50 kms^{-1} and +60 kms^{-1} in Figures 7.2 and 7.3 (see also Figure 7.4). They concluded that PDRs models explain better the measured intensities of all the observations in their work than J-shock ionization or magneto-hydrodynamic models (Hollenbach & McKee, 1989). The [CII] emission gets more spatially confined towards the position of the +50 kms^{-1} Cloud with increasing LSR velocity. For radial velocities larger than +62 kms^{-1}, [NII] emission is almost absent, while the remaining [CII] emission is associated almost entirely to the +50 kms^{-1} Cloud and the CND.

7.3 Selected Positions For Analysis

As it was discussed in Section 7.1, part of the molecular gas of the +20 kms^{-1} and +50 kms^{-1} Clouds is interacting with Sgr A-East and it is also exposed to the intense FUV field from the Nuclear Cluster. In order to study the physical conditions of the gas in such harsh environment, I selected 17 representative positions of the main emission features of the +20 kms^{-1} and +50 kms^{-1} Clouds. The selected positions are given in Table 7.1, and their spatial distribution is shown

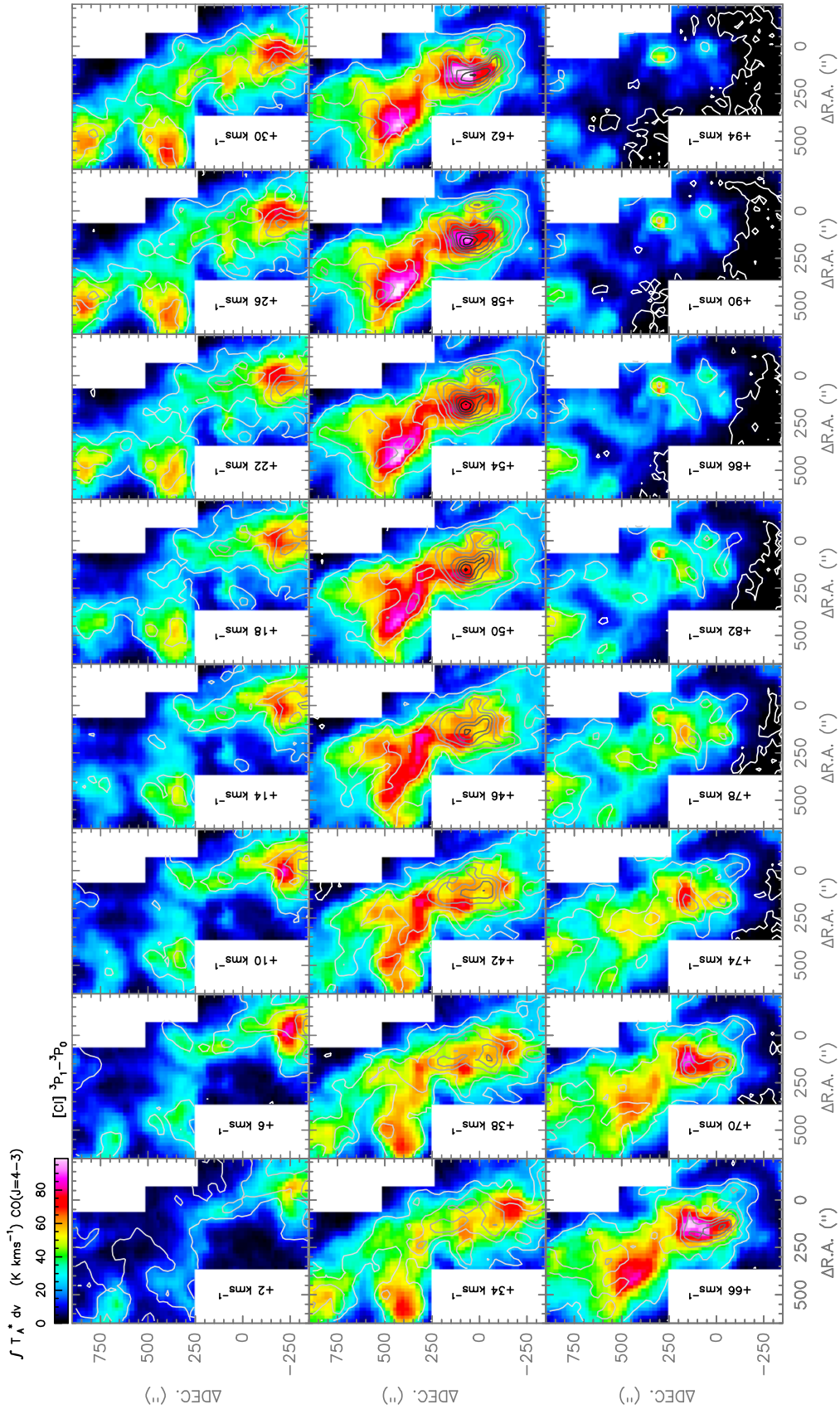

Figure. 7.2: *CO(4-3) (colors) and [CI](1-0) (contours) emission of MCs in the Sgr A Complex. The panels show 5 kms^{-1} wide integrated intensities, with darker contours for higher intensities. The first [CI](1-0) contour is set at 3σ significance level, with σ the typical noise of the map.*

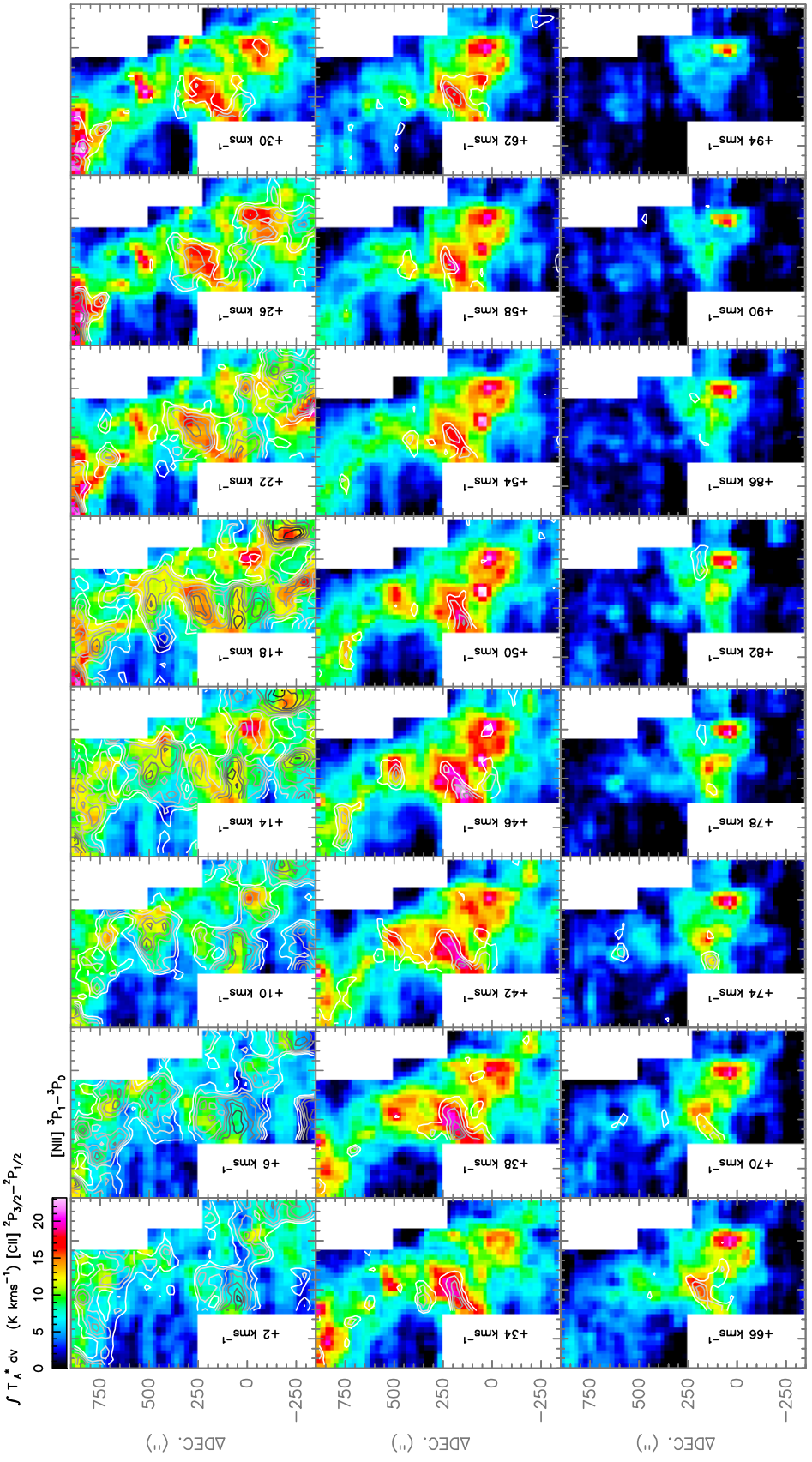

Figure. 7.3: *[CII] (colors) and [NII] (contours) emission of MCs in the Sgr A Complex. The first [NII] contour is set at 5σ significance level, with σ the typical noise of the map.*

in Figure 7.4 with their respective numbers, where the position of the HCO^+ Cloud is also shown. The individual spectra at those positions of all sub-mm observations ([CII], [NII], [CI](2-1), [CI](1-0), and CO(4-3)) from the present work and also from Mopra observations by Jones et al. (2012) (HCO^+(1-0), $H^{13}CO^+$(1-0), HCN(1-0), and $H^{13}CN$(1-0)) are given in Figures 7.5 to 7.13.

Positions 1 to 4 were selected to model the emission from the +20 kms^{-1} Cloud, as it moves north-east with increasing LSR velocity, connecting with the +50 kms^{-1} Cloud, in projection. Their corresponding spectra in Figures 7.5 and 7.6 show that both atomic carbon lines and the $H^{13}CO^+$(1-0) and $H^{13}CN$(1-0) lines suggest a single component between +5 kms^{-1} and +30 kms^{-1}, while the other molecular lines suffer from massive absorption around −5 kms^{-1}. Positions 5 and 6 and 8 to 10 were selected to trace the region interacting with Sgr A-East. The former are tracing the tail of the crescent-shape in the +50 kms^{-1} Cloud. The carbon emission at these positions shows two very distinctive emission peaks around +40 kms^{-1} and +60 kms^{-1} in Figure 7.7 which, in positions 8 and 9 appear as a single entity in Figures 7.8 and 7.9, while the molecular lines show still two components. At positions 10 and 11, it can be seen that the gas is strongly blue-shifted, by more than 100 kms^{-1}, presenting also absorption features due to the spiral arms along the l.o.s. (dashed vertical lines) (see Figures 7.9 and 7.10). Position 7 in Figure 7.8 shows the emission directly coming from the inner parts of the CND, seen in the large LSR velocity extent of the emission in all lines. Position 12 was selected to trace the small streamer reaching from the +50 kms^{-1} Cloud towards the GC, as seen in 1.3 millimeter continuum emission (Coil & Ho, 2000), which also shows very extended emission along the LSR velocity axis in Figure 7.10. Positions 13, 14, and 15 were selected to trace the gas physical conditions across the +50 kms^{-1} Cloud, and in the direction towards the HCO^+ Cloud. Their spectra in Figures 7.11 and 7.12 show a similar behavior in all lines at positive LSR velocities. Finally, in order to investigate the emission along the [CII] lane shown in Figure 4.7, positions 16 and 17 were selected. Together with position 14, they will allow to investigate the change in physical conditions across the [CII] lane as the emission decreases from position 14 to 17. Their spectra are shown in Figures 7.12 and 7.13, respectively.

7.4 Future Work

With the positions selected in Section 7.3, their measured emissions can be used to constrain the physical condition of the gas at those positions, such as H_2 or total hydrogen volume densities, impinging FUV field, and kinetic temperature (among others). Such analysis will done in the context of PDR analysis with the

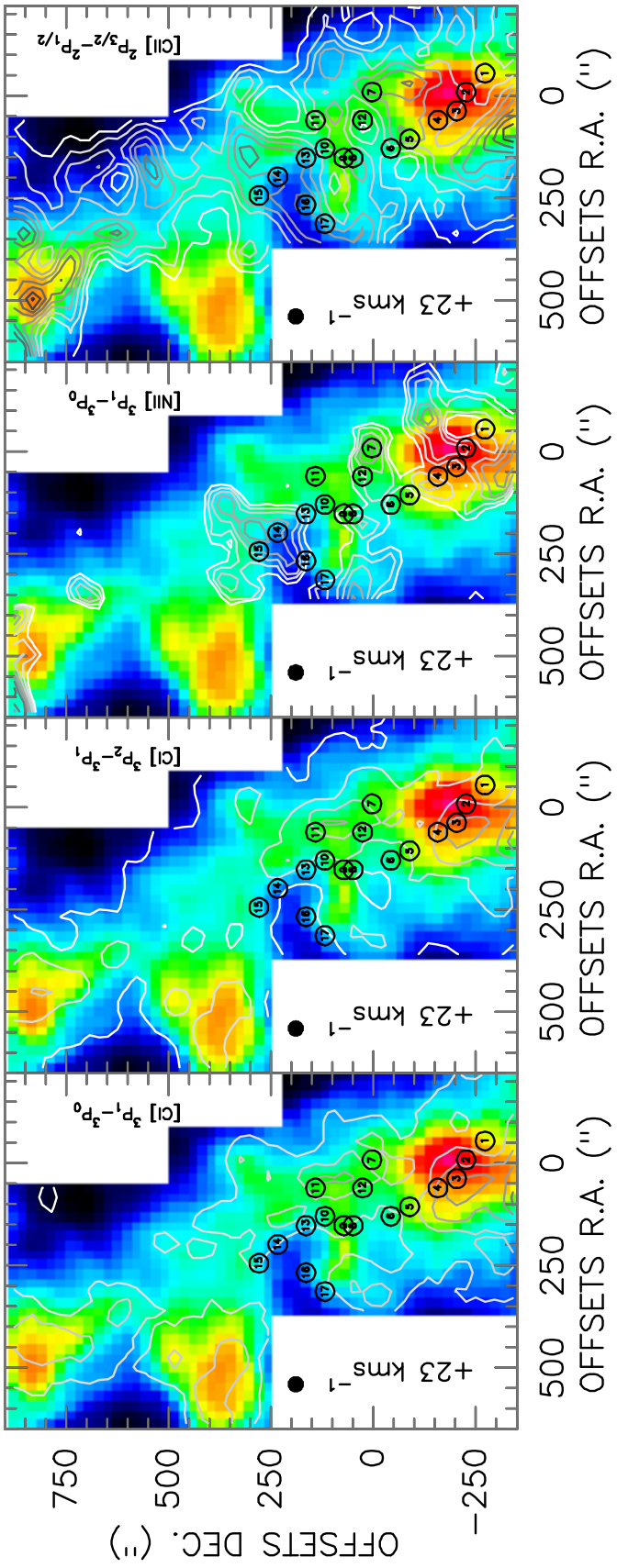
[CII] $^2P_{3/2}-^2P_{1/2}$
[NII] $^3P_1-^3P_0$
[CI] $^3P_2-^3P_1$
[CI] $^3P_1-^3P_0$
+23 kms^{-1}
OFFSETS R.A. (")
OFFSETS DEC. (")
500
250
0
−250
750

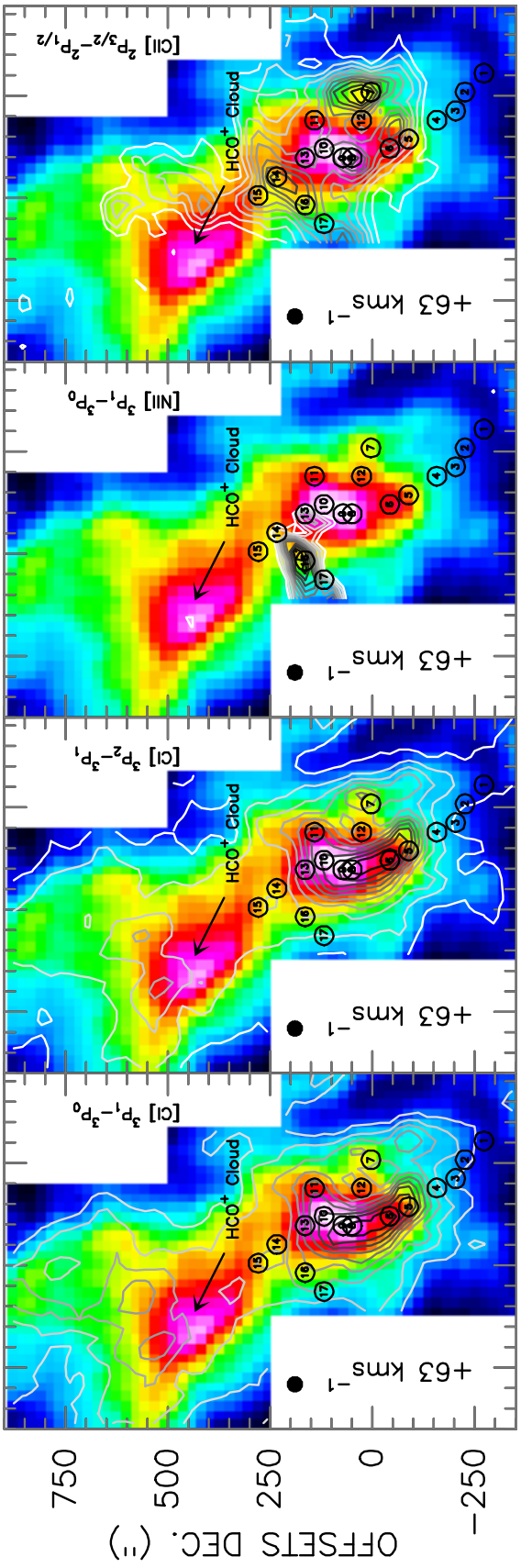

Figure. 7.4: *Selected positions in Table 7.1 (beamsizes from 1-17) for the +50 kms^{-1} and +20 kms^{-1} Clouds in the GC. From left to right, the [CI](1-0), [CI](2-1), [NII], and [CII] emission (contours) is overplotted on the CO(4-3) emission (colors). Upper and lower panels are integrated intensity maps of 5 kms^{-1} width centered at +23 kms^{-1} and +63 kms^{-1}, respectively. The location of the HCO$^+$ Cloud from Minh et al. (2005) is shown in the lower panels.*

#	$\Delta\alpha$ (")	$\Delta\delta$ (")	$\alpha(J2000)$ ($^h\ ^m\ ^s$)	$\delta(J2000)$ ($^\circ\ '\ ''$)	**Source**
1	−54.9	−272.0	17 45 35.71	−29 05 00.1	+20 kms^{-1} Cloud
2	−8.9	−226.0	17 45 39.22	−29 04 14.1	+20 kms^{-1} Cloud
3	+37.1	−203.0	17 45 42.73	−29 03 51.1	+20 kms^{-1} Cloud
4	+60.1	−157.0	17 45 44.48	−29 03 05.1	+20 kms^{-1} Cloud
5	+106.1	−88.0	17 45 47.99	−29 01 56.1	+50 kms^{-1} Cloud
6	+129.1	−42.0	17 45 49.74	−29 01 10.1	+50 kms^{-1} Cloud
7	−8.9	+4.0	17 45 39.22	−29 00 24.1	Sgr A*
8	+152.1	+50.0	17 45 51.50	−28 59 38.1	+50 kms^{-1} Cloud
9	+152.1	+73.0	17 45 51.50	−28 59 15.1	+50 kms^{-1} Cloud
10	+129.1	+119.0	17 45 49.74	−28 58 29.1	+50 kms^{-1} Cloud
11	+60.1	+142.0	17 45 44.48	−28 58 06.1	+50 kms^{-1} Cloud
12	+60.1	+27.0	17 45 44.48	−29 00 01.1	Streamer
13	+152.1	+165.0	17 45 51.50	−28 57 43.1	+50 kms^{-1} Cloud
14	+198.1	+234.0	17 45 55.00	−28 56 34.1	[CII] Lane
15	+244.1	+280.0	17 45 58.51	−28 55 48.1	[CII] Lane
16	+267.1	+165.0	17 46 00.26	−28 57 43.1	[CII] Lane
17	+313.1	+119.0	17 46 03.77	−28 58 29.1	[CII] Lane

Table. 7.1: *Selected positions for the +20 kms^{-1} and +50 kms^{-1} Clouds in the GC.*

KOSMA-τ PDR model.

The first step in the analysis will be to disentangle the emission associated to each component along the l.o.s., within the 0 kms^{-1} and +100 kms^{-1} LSR velocity range. Since atomic and molecular lines show sometimes different components in their spectra (see for instance the spectra at positions 1 and 2 in Figure 7.5), and massive absorption features affect the line profiles, optically thin species will be very useful to distinguish between one o more components along the l.o.s., such as in the case of the +20 kms^{-1} Cloud and the smaller +5 kms^{-1} component detected by Minh et al. (2005) in other species. Currently, there is an ongoing Mopra CMZ Survey (M. Burton, private communication) in the ^{12}CO, ^{13}CO, and C^{18}O ground state transitions. From the observed lines, the C^{18}O(1-0) transitions is certainly optically thin given the low isotopic abundance of oxygen [^{16}O/^{18}O] ~ 200 - 250 (Dahmen et al., 1998; Huettemeister et al., 1998; Güsten & Philipp, 2004) in the GC. This transition will not only help to disentangle different component along the l.o.s., but also to constrain the mass contained within the beamsize of the observations. Its emission can be converted to molecular hydrogen mass through its abundance with respect to H_2 given by [C^{18}O/H_2] = 4×10^{-7} (Dahmen et al., 1998; Huettemeister et al., 1998). I have already used some of the unpublished Mopra observations in Chapters 5 and 6, and I expect to continue such collaboration for the work concerning the +20 kms^{-1} and +50 kms^{-1} Clouds.

The second step of the analysis will be the PDR modeling. For this, I will used the already calculated PDR models for the Arched-Filaments in Chapter 5, for which the nitrogen chemistry will be included to account for the HCN observations. Since the grid parameter for the Arched-Filaments is large in volume density, mass, and FUV field, adequate parameters for the +20 kms^{-1} and +50 kms^{-1} Clouds should be contained within it. In terms of other parameters, some differences may be present. The ratio of total to selective extinction R_v can vary as a consequence of different grain sizes between both regions. This is plausible if one considers that the explosion of the Sgr A-East SNR can destroy the grains over a large fraction of the clouds, affecting the FUV shielding of the gas. Another factor that could be different between the Arched-Filaments and the +20 kms^{-1} and +50 kms^{-1} Clouds is the photoionization rate of hydrogen due to cosmic-rays, which is a rather unknown parameter for the specific location of the clouds. Within the central parsec of the GC, values ranging from $> 1.6\times10^{-15}$ s^{-1} to 10^{-11} s^{-1} have been derived (Goto, 2014), much larger than the values used in the Arched-Filaments models $\leq 10^{-15}$ s^{-1}. Soft X-rays ($h\nu < 1$ keV) can also be more important for clouds closer to the GC because of the influence of the Sgr A-East SNR, affecting the structure of the PDRs and producing rather XDRs[2] (Maloney et al., 1996; Hollenbach & Tielens, 1999). This, together with the past activity of Sgr A* producing X-ray flares that travel through the ISM in the CMZ (Amo-Baladrón et al., 2009; Dogiel et al., 2013), could also affect the gas differently in the +20 kms^{-1} and +50 kms^{-1} Clouds and in the Arched-Filaments.

This future work can be extended to other sources such as the Sickle H II region and the HCO$^+$ Cloud, together with complementary observations of low and mid-J CO transitions from ground based observatories to better constrain the physical conditions of the gas. At higher frequencies, the SOFIA telescope, and its upcoming upGREAT[3] receiver (`http://www3.mpifr-bonn.mpg.de/div/submmtech/heterodyne/upgreat/upgreatmain.html`), will make possible to observe very important cooling lines of the ISM such as the [OI] at 63 μm and 146 μm and high-J CO transition over a large area, and in a reasonable amount of time, so covering the 46" spatial resolution of the datasets in the present work, with good signal-to-noise ratio will become straightforward. As shown in Chapter 4, the number of detected sources within the datasets in the present work is large, and many of them were not treated in detail given the time constrains for a PhD thesis. Nonetheless, this work sets a solid foundation upon which, further research on the physical conditions of the gas in the Sgr A Complex can be continued.

[2]X-ray Dissociation Regions
[3]German Receiver for Astronomy

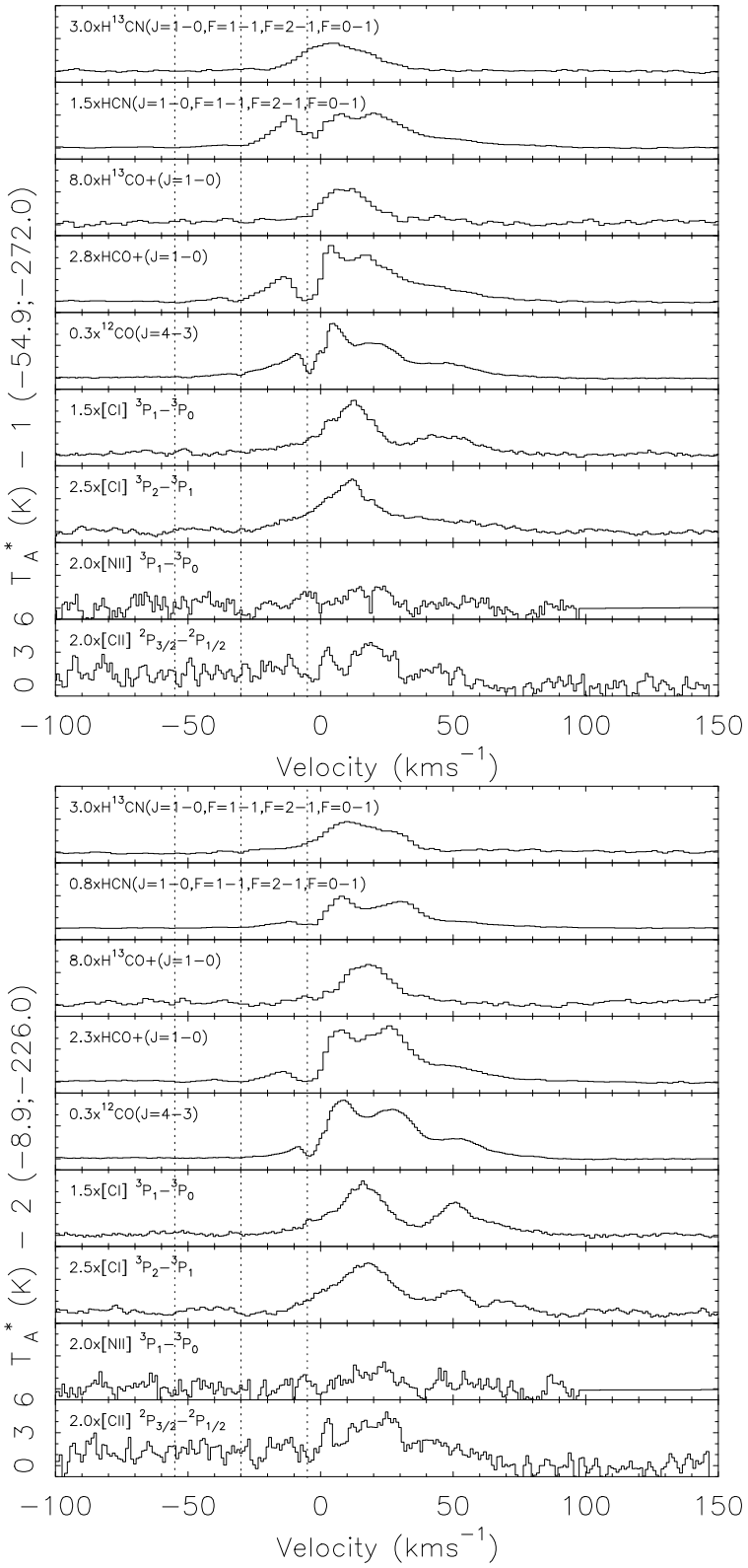

Figure. 7.5: *Positions 1-2: from bottom to top, sub-mm observations ([CII], [NII], [CI](2-1), [CI](1-0), and CO(4-3)) from the present work and Mopra observations by Jones et al. (2012) (HCO^+(1-0), $H^{13}CO^+$(1-0), HCN(1-0), and $H^{13}CN$(1-0)) of the +50 kms^{-1} Cloud and +20 kms^{-1} Cloud in the GC.*

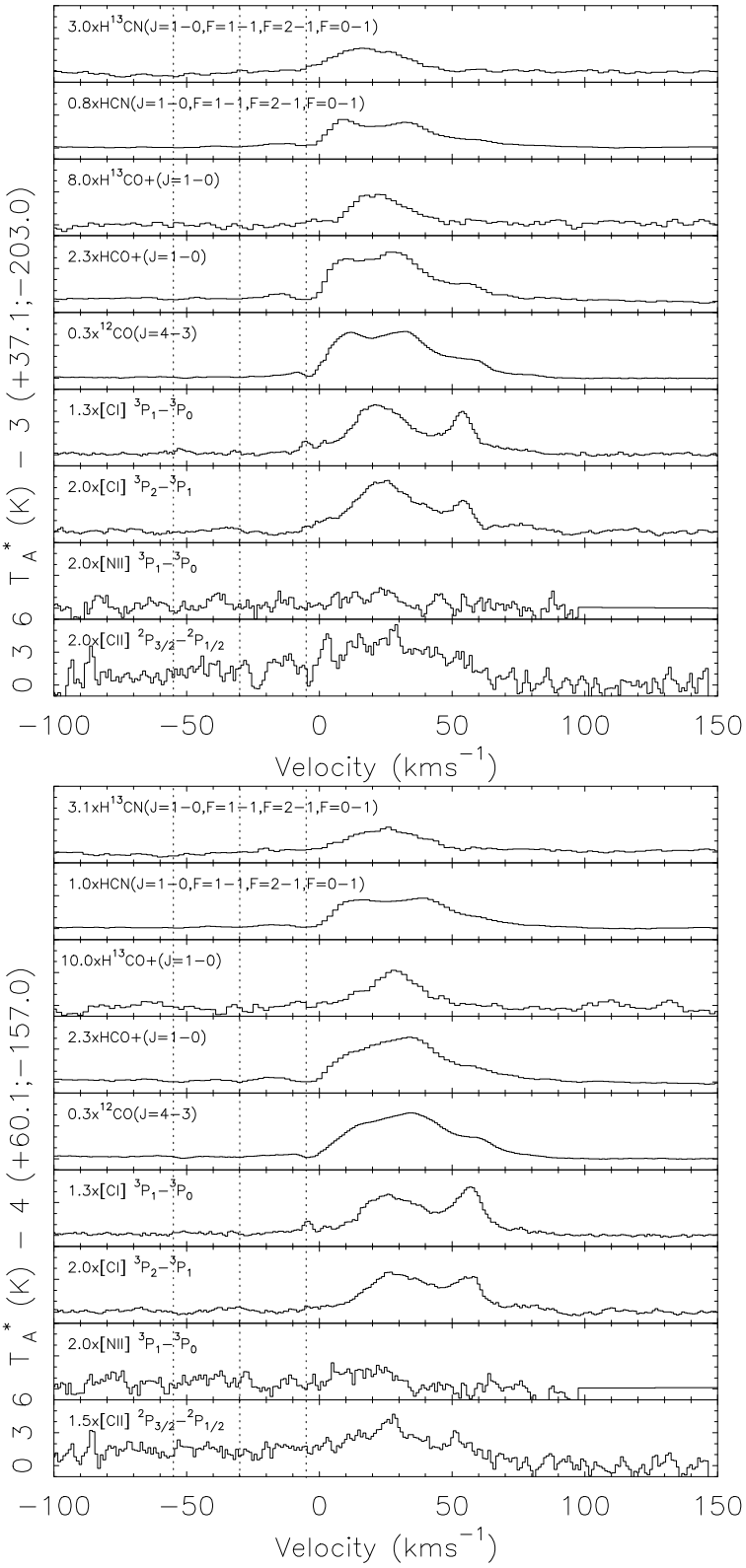

Figure. 7.6: *Positions 3-4: from bottom to top, sub-mm observations ([CII], [NII], [CI](2-1), [CI](1-0), and CO(4-3)) from the present work and Mopra observations by Jones et al. (2012) (HCO^+(1-0), $H^{13}CO^+$(1-0), HCN(1-0), and $H^{13}CN$(1-0)) of the +50 kms^{-1} Cloud and +20 kms^{-1} Cloud in the GC.*

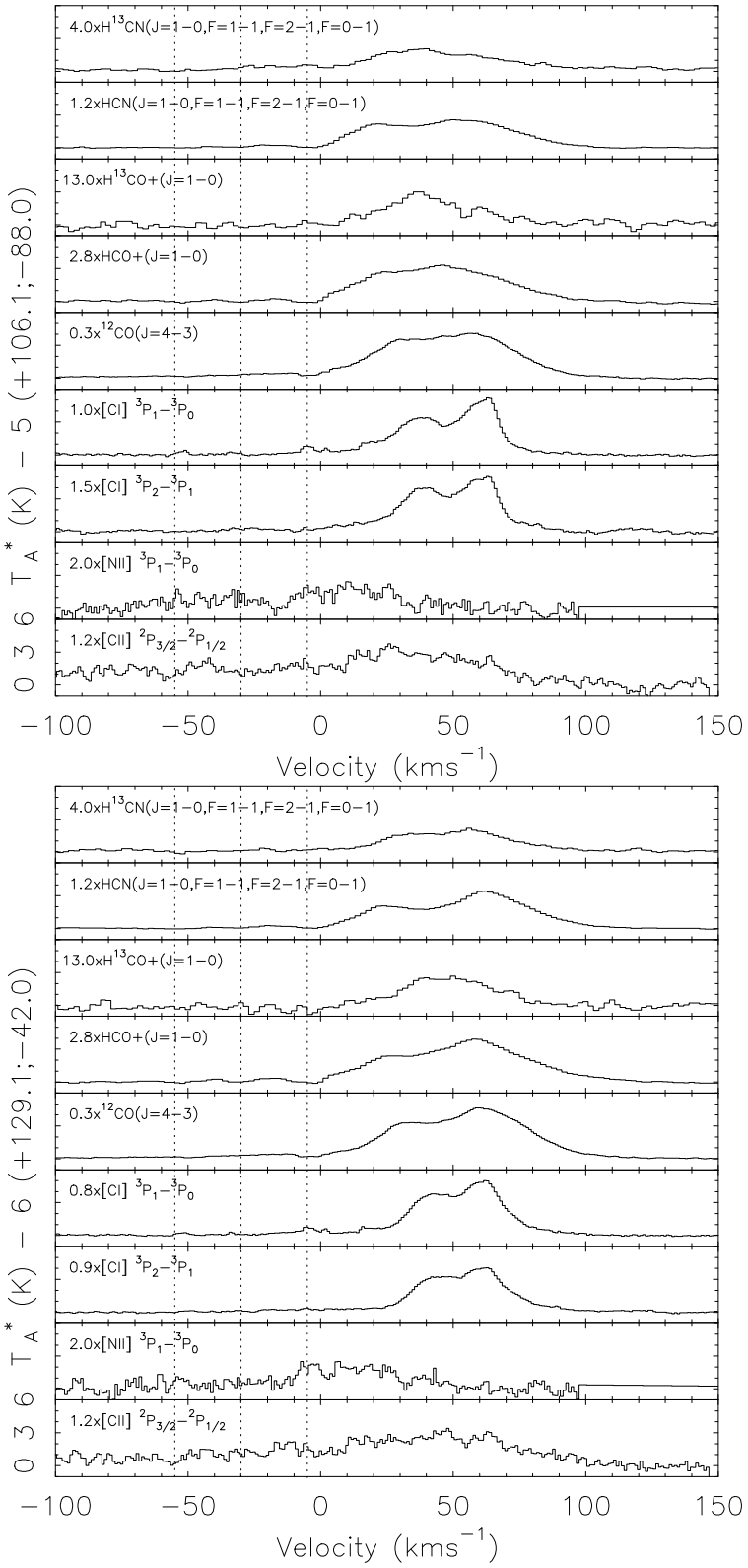

Figure. 7.7: *Positions 5-6: from bottom to top, sub-mm observations ([CII], [NII], [CI](2-1), [CI](1-0), and CO(4-3)) from the present work and Mopra observations by Jones et al. (2012) (HCO^+(1-0), $H^{13}CO^+$(1-0), HCN(1-0), and $H^{13}CN$(1-0)) of the +50 kms^{-1} Cloud and +20 kms^{-1} Cloud in the GC.*

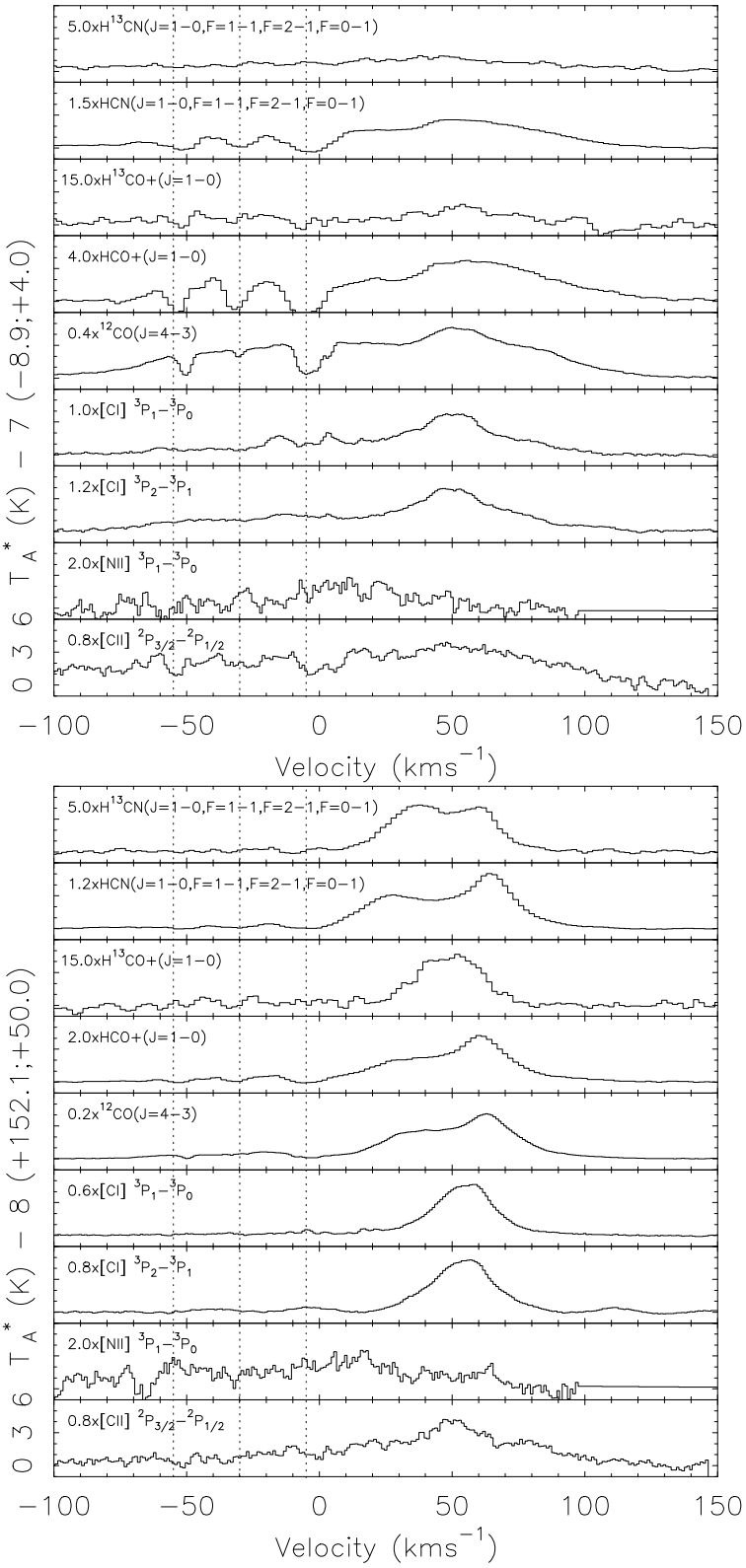

Figure. 7.8: *Positions 7-8: from bottom to top, sub-mm observations ([CII], [NII], [CI](2-1), [CI](1-0), and CO(4-3)) from the present work and Mopra observations by Jones et al. (2012) (HCO^+(1-0), $H^{13}CO^+$(1-0), HCN(1-0), and $H^{13}CN$(1-0)) of the +50 kms^{-1} Cloud and +20 kms^{-1} Cloud in the GC.*

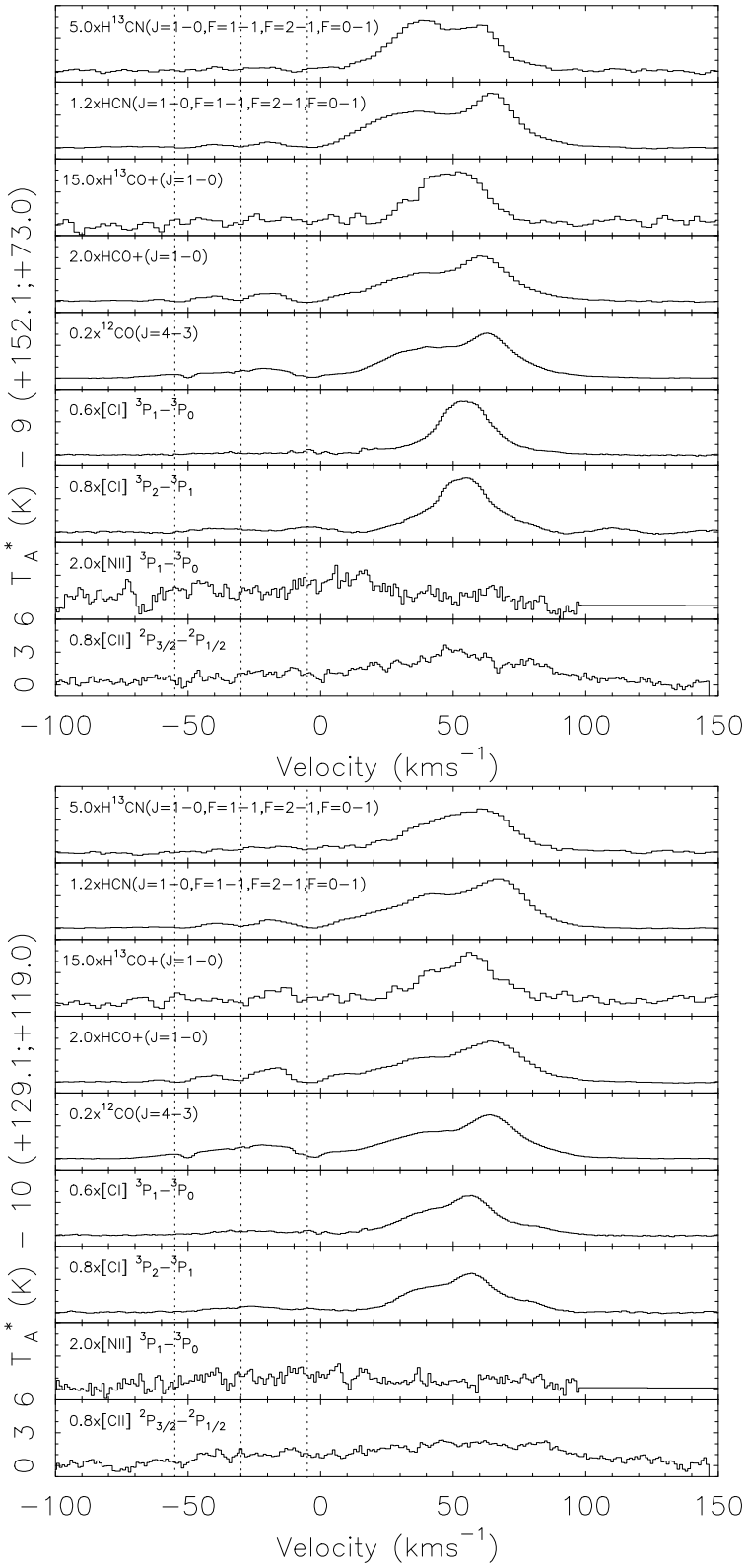

Figure. 7.9: *Positions 9-10: from bottom to top, sub-mm observations ([CII], [NII], [CI](2-1), [CI](1-0), and CO(4-3)) from the present work and Mopra observations by Jones et al. (2012) (HCO^+(1-0), $H^{13}CO^+$(1-0), HCN(1-0), and $H^{13}CN$(1-0)) of the +50 kms^{-1} Cloud and +20 kms^{-1} Cloud in the GC.*

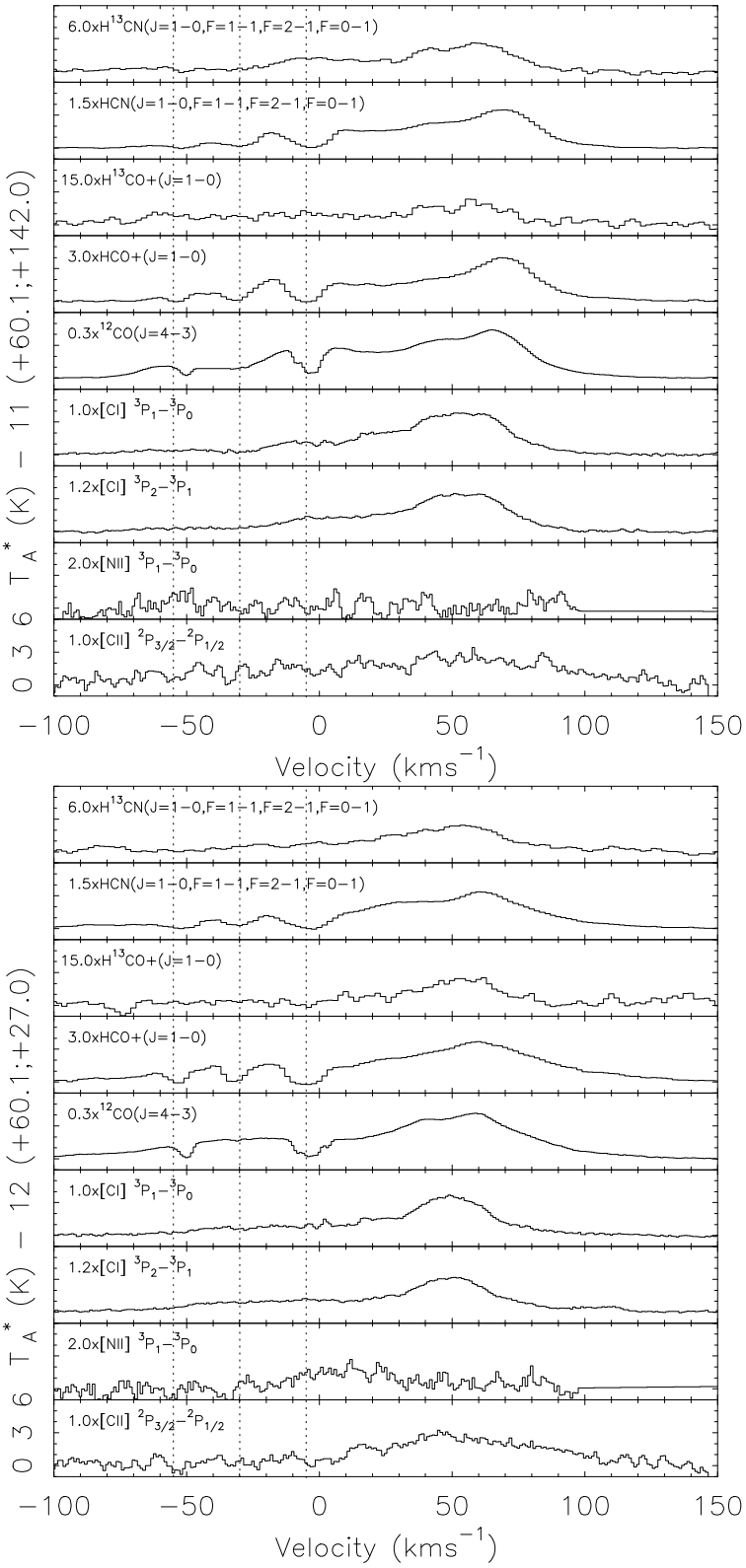

Figure. 7.10: *Positions 11-12: from bottom to top, sub-mm observations ([CII], [NII], [CI](2-1), [CI](1-0), and CO(4-3)) from the present work and Mopra observations by Jones et al. (2012) (HCO^+(1-0), $H^{13}CO^+$(1-0), HCN(1-0), and $H^{13}CN$(1-0)) of the +50 kms^{-1} Cloud and +20 kms^{-1} Cloud in the GC.*

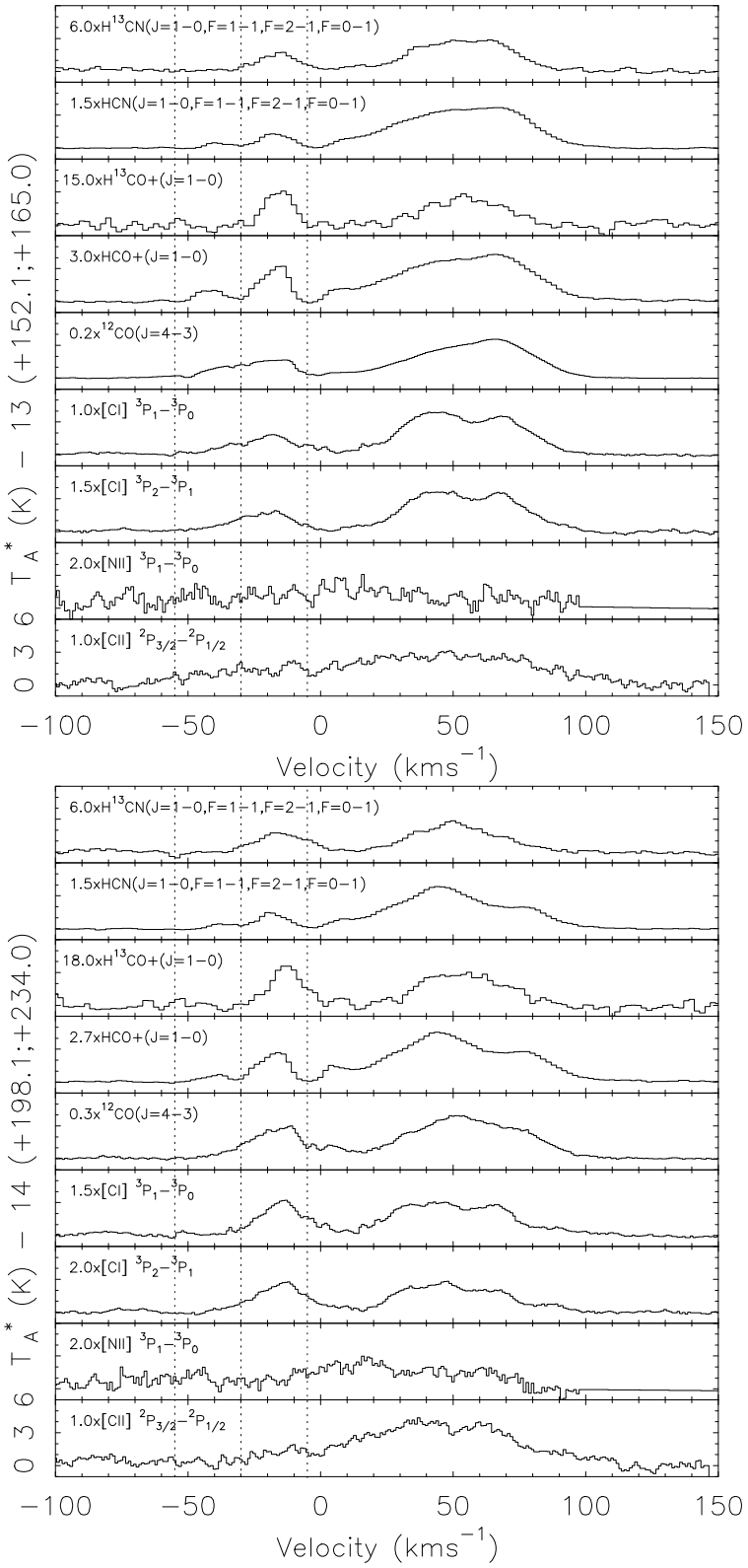

Figure. 7.11: *Positions 13-14: from bottom to top, sub-mm observations ([CII], [NII], [CI](2-1), [CI](1-0), and CO(4-3)) from the present work and Mopra observations by Jones et al. (2012) (HCO^+(1-0), $H^{13}CO^+$(1-0), HCN(1-0), and $H^{13}CN$(1-0)) of the +50 kms^{-1} Cloud and +20 kms^{-1} Cloud in the GC.*

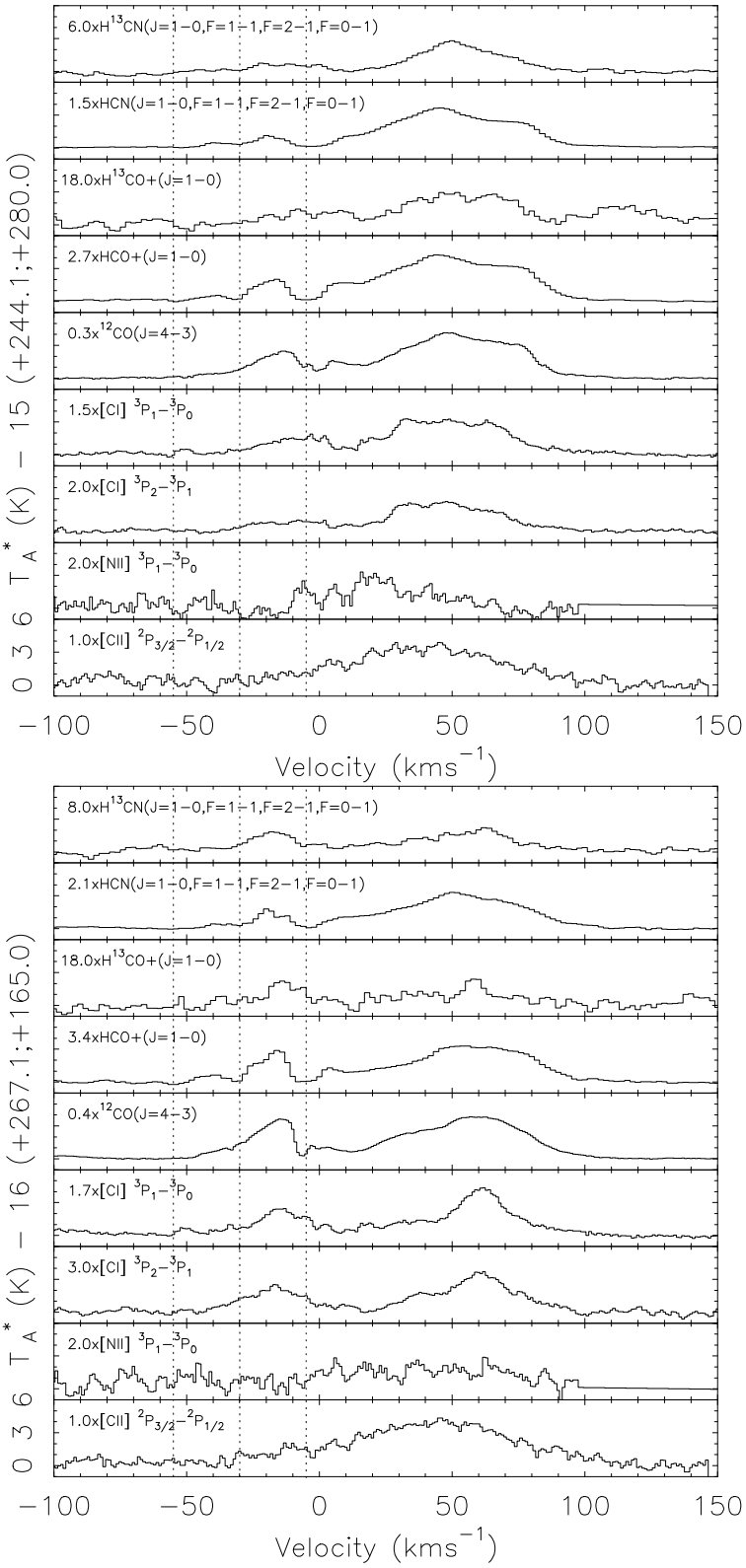

Figure. 7.12: *Positions 15-16: from bottom to top, sub-mm observations ([CII], [NII], [CI](2-1), [CI](1-0), and CO(4-3)) from the present work and Mopra observations by Jones et al. (2012) (HCO^+(1-0), $H^{13}CO^+$(1-0), HCN(1-0), and $H^{13}CN$(1-0)) of the +50 kms^{-1} Cloud and +20 kms^{-1} Cloud in the GC.*

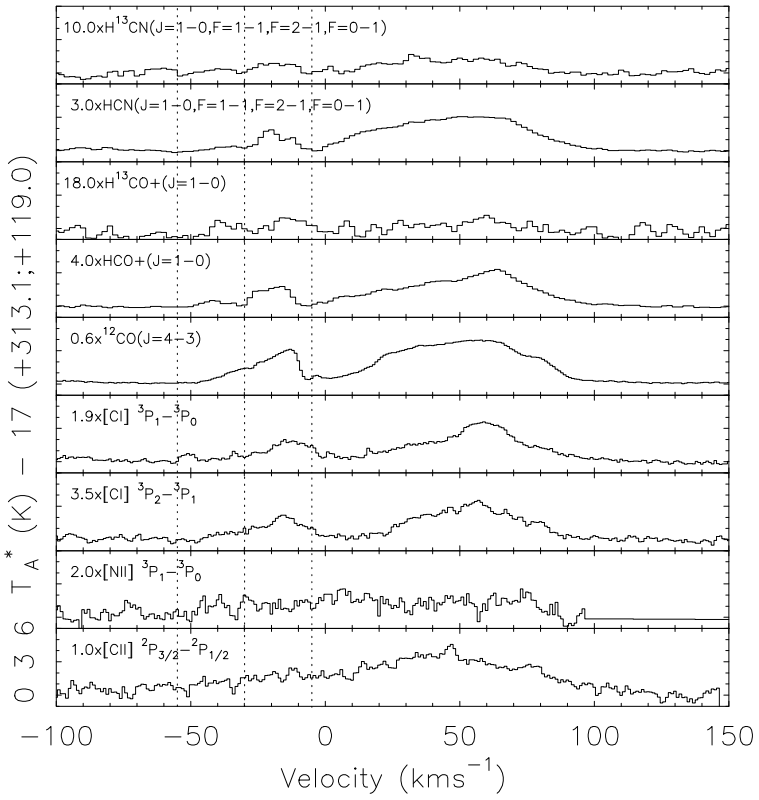

Figure. 7.13: *Position 17: from bottom to top, sub-mm observations ([CII], [NII], [CI](2-1), [CI](1-0), and CO(4-3)) from the present work and Mopra observations by Jones et al. (2012) (HCO^+(1-0), $H^{13}CO^+$(1-0), HCN(1-0), and $H^{13}CN$(1-0)) of the +50 kms^{-1} Cloud and +20 kms^{-1} Cloud in the GC.*

Chapter 8

Summary

In the present work, high spatial ($\lesssim$ 46") and spectral (1 kms^{-1}) resolution observations of the CO(J=4-3), [CI] $^3P_1$ - $^3P_0$, [CI] $^3P_2$ - $^3P_1$, [NII] $^3P_1$ - $^3P_0$, and [CII] $^2P_{3/2}$ - $^2P_{1/2}$ transitions tracing the warm gas in the Sgr A Complex, located at the GC, have been presented. The atomic gas observations were carried out with the Herschel-HIFI satellite in the frame of the Herschel EXtraGALactic Guaranteed Time key Program (HEXGAL) while the molecular gas observations were carried out with the NANTEN2/SMART telescope. These observations are an important contribution to fill in the current observational gap in terms of high resolution (spatially and spectrally) large-scale heterodyne observations of the Sgr A Complex at these sub-mm frequencies.

These vast datasets contain emission associated to a large number of astronomical objects such as: the CND; the NTF Radio-Arc; the Arched Thermal Filaments containing the E1, E2 (northern and southern parts), W1, W2, G0.10+0.02, and G0.07+0.04 segments, and the close by high density CS(2-1) peaks P1 and P2; the H-Region containing several H II regions (from H1 to H13); the Sickle H II region; the eastern, northern, southern, and western and far western gas streamers; several MCs including M1−0.13−0.08, M2−0.13−0.08 also referred to as +20 kms^{-1} Cloud, M−0.02−0.07 also referred to as +50 kms^{-1} Cloud, M+0.06−0.04, M+0.10−0.01, the so called HCO^+ Cloud composed by the M+0.07−0.08, M+0.11−0.08, and M+0.11−0.11 clouds, M+0.02−0.05 also referred to as −15 kms^{-1} Cloud, M+0.04+0.03 also referred to as −30 kms^{-1} Cloud; and the HVCC CO+0.02−0.02. Along the same l.o.s. towards the Sgr A Complex, but outside the region, gas at high LSR velocities associated to X_1 orbits, and absorption/emission features at LSR velocities −55 kms^{-1}, −30 kms^{-1}, and −5 kms^{-1} associated with the loci of the 3 kpc, 4.5 kpc, and local spiral arms are also found within the datasets.

8.1 Data Reduction

The data acquisition and data reduction process of large scale observations towards the GC are very challenging given the large LSR velocity extent of the observed transitions (covering usually a large fraction of the available spectrometer bandwidth at the sub-mm frequencies in the present work), and because of the extended spatial distribution of the emission which makes it difficult to find a spatially close reference (OFF) position (a position without emission at the measured frequency, outside the Earth's atmosphere), necessary to removed telescope and receiver artifacts in the measured spectra, and to remove the atmospheric contributions to them (in the case of ground based telescopes).

The Herschel-HIFI observations suffered from emission contamination at the selected reference position in all observed lines and from baseline distortions related to electronic components of the receiver, such as LOs and LNAs (which are often operated at their limit capacity at these frequencies) in the [NII] and [CII] transitions. I successfully recovered the artificially subtracted emission from the observed spectra by taking advantage of the observing modes used for the observations of the [CI](2-1), [NII], and [CII] lines. The NANTEN2/SMART observing capabilities at 492 GHz helped to recover the emission subtracted from the [CI](1-0) observations. The emission at the reference position in each case was modeled and added back to the measured spectra. For the baseline distortions at the high frequency lines, averaging the measure intensities over the affected fraction of the bandwidth for the [NII] line and rejecting the [CII] spectra with $T^*_{A,rms}$ noise above a certain threshold, largely reduced the baseline distortion problems in the final datasets.

The NANTEN2/SMART observations were planed in a way that no emission contamination would be found at any of the eight positions on the sky observed simultaneously by the 16-pixel SMART heterodyne receiver. Nonetheless, this approach presented a major drawback since avoiding emission contamination implied the selection of a reference positions far away ($\sim 1^\circ$) from the measurements on source (ON positions), yielding large instabilities in the measure baselines of the CO(4-3) spectra, due to a combination factors: the short stability time of the receiver at this high frequency, the movement of the telescope between the OFF and ON positions, and also possibly due to instabilities in some electronic components of the receiver. Since it was not possible to filter out the affected spectra by setting thresholds on the fitted opacities, system temperatures, and $T^*_{A,rms}$ noise level of the spectra, I developed a series of filters that took advantage of the integrated emission of "good" (flat baseline) spectra on each side of the observed line (positive and negative LSR velocities), which were then used on an statistical approach to remove all spectra whose integrated intensities differed largely from the ones derived from the model selected spectrum. After putting

the data through these filters, only good quality spectra remained.

After all datasets were put through the data reduction process, It was shown that the Forward Beam Antenna Temperature scale (T_A^*) does reproduce more accurately the true convolved antenna temperatures of the astronomical source than the Main Beam Antenna Temperature scale (T_{mb}), given the extended emission and error beam pickup of both telescopes. This antenna temperature scale represents at the same time, a lower limit to the true convolved antenna temperatures. A cross-calibration between the measured intensities from the Herschel-HIFI satellite and the NANTEN2/SMART telescope using the [CI](1-0) line yielded that both telescopes measure essentially the same intensities within absolute calibration errors. Therefore, the observations carried out with both telescopes can be safely combined to explore the physical conditions of the ISM in the Sgr A Complex.

8.2 Emission Morphology

The spatial and spectral distribution of the sub-mm emission in the present work is very complex. From negative to positive LSR velocities, the brightest ionized emission closely follows the Arched-Filaments between -70 kms^{-1} and 0 kms^{-1}. The emission develops from the H-Region, reaching G0.07+0.04, and moving from the W1/W2 filament to the E1/E2 filament and to the G0.10+0.02 source. Little neutral atomic carbon (C) and carbon monoxide (CO) emission is found towards the Arched-Filaments in comparison to positive LSR velocities, showing that a large fraction of the gas is ionized in this region. At positive LSR velocities the C and CO observations trace the +20 kms^{-1} Cloud, located south from the CND, with the emission moving continuously towards the +50 kms^{-1} Cloud as the LSR velocity increases. The sub-mm emission associated to the +50 kms^{-1} Cloud shows a very distinctive crescent-shape in the CO(4-3), [CI](1-0), and [CI](2-1) lines, reflecting the strong interaction of the cloud with the Sgr A-East SNR. The carbon emission peaks in the whole datasets are found at the interaction region. The [CII] emission is widely spread within the cloud, while [NII] emission is very weak. At positive Galactic longitudes, the HCO^+ cloud stands out in bright CO(4-3) emission, while carbon emission is much weaker than towards the +50 kms^{-1} Cloud, reflecting different excitation conditions between them. The CO(4-3) emission associated to the Sickle H II region, and to the M+0.11−0.08 and M+0.11−0.11 clouds is found around +29 kms^{-1}.

Prominent gas streamers at -8 kms^{-1} and +11 kms^{-1} traced by the CO(4-3), [CI](1-0) and [CI](2-1) lines seem to be connecting the -15 kms^{-1} Cloud with

the +20 kms^{-1} Cloud on opposite sites of Sgr A*. The emission associated to the CND extends between ±150 kms^{-1}, by far the largest linewidths in the datasets, reflecting the extreme kinematics close to Sgr A*. The average sub-mm spectra of the CND show prominent absorption features around LSR velocities −55 kms^{-1}, −30 kms^{-1}, and −5 kms^{-1}, which are associated to the loci of the 3 kpc, 4.5 kpc, and local spiral arms along the l.o.s.. Three bright emission spots are found close to the CND at negative LSR velocities around −63 kms^{-1} whose intensities in the various observed transitions vary strongly from position to position.

At LSR velocities larger than 120 kms^{-1} in modulus, four HVG components are detected mainly in the CO(4-3) and [CI](1-0) transitions due to the better signal-to-noise ratio at low frequencies, while at the position of their CO(4-3) peak emission, the [CI](2-1) line is also detected. These MCs are most probably located outside the X_2 orbits in the GC, containing all previously mentioned sources, but rather are located at the X_1 orbits. The HVCC CO+0.02−0.02 is detected in the CO(4-3), [CI](1-0), and [CI](2-1) transitions, between +100 kms^{-1} and +150 kms^{-1}.

Out of the vast number of sources contained within these datasets, a few sources were selected for a preliminary analysis on the physical conditions of the gas within them, and to outline future work based on these observations. In the following, I summarized the main results obtained for the selected Arched-Filaments region and HVG clouds, while the strategy for the analysis of the gas related to the +20 kms^{-1} and +50 kms^{-1} Clouds is briefly discussed.

8.2.1 The Arched Thermal Filaments

In a preliminary analysis of the physical conditions of the gas associated to the Arched-Filaments, which is influenced by the strong radiation field of the massive Arches Cluster, the sub-mm emission associated with the Arched-Filaments was investigated. These observations were complemented with public HCO^+(1-0) and $H^{13}CO^+$(1-0) Mopra data (Jones et al., 2012), and with unpublished CO(1-0) and ^{13}CO(1-0) observations from the ongoing Mopra CMZ Survey (M. Burton, priv. communication). First, the theoretical relationship found by Abel (2006) between the [CII] emission originated in H II regions as predicted by the strength of the [NII] intensities, was explored. The measured [CII] intensities fall mostly below the theoretical prediction from the measured [NII] emission, for most of the positions in the datasets. It is argued that the main reason for the discrepancy is that the assumptions on which the theoretical relationship was built, mainly the pressure equilibrium between the H II region and the PDR are not met in the Arched-Filaments region. The emission detected at seven positions in the

filaments (E1, E2-N, E2-S, W1, W2, G0.10+0.02, and G0.07+0.04) and at two positions associated with high density gas (P1 and P2) close to the filaments, was modeled using the clumpy version of the KOSMA-τ PDR model. The integrated intensity of all lines, and at all positions is very well fitted by the model predictions, with the only exception of the CO(1-0) intensities, which are heavily underestimated by the model. It is speculated that the "excess" in CO(1-0) emission could originate from gas not contained within the same volume in the GC, but rather from contributions of foreground MCs along the l.o.s.. The gas is well described by an FUV field between $\sim 10^2$ and 10^3 Draine fields, with hydrogen densities between 10^4 cm^{-3} and 10^5 cm^{-3}, and a hydrogen ionization rate due to cosmic-rays between 10^{-15} s^{-1} and 10^{-14} s^{-1}. The total hydrogen masses in the 46" spatial resolution of the observations is between ~ 700 M$_\odot$ and 1200 M$_\odot$. This is an ongoing work which will be expanded in a future publication.

8.2.2 High Velocity Gas Towards the Sgr A Complex

The physical conditions of the gas in four molecular clouds detected at high LSR velocities, and in the CO(4-3), [CI](1-0), and [CI](2-1) transitions, were investigated. The sub-mm observations of these clouds were also complemented with Mopra observations, as described for the Arched-Filaments. The Mopra observations for which emission above the $3\times T^*_{A,rms}$ significance level was detected at these high LSR velocities were CO(1-0), ^{13}CO(1-0), and HCO$^+$(1-0). The HVG1-1C and HVG1-2C clouds are found at negative LSR velocities around ~ -145 kms^{-1} and -121 kms^{-1}, respectively, while clouds HVG2 and HVG3 are found at positive LSR velocities around $\sim +130$ kms^{-1} and $+179$ kms^{-1}. These large LSR velocities are consistent with the gas orbiting in the X$_1$ orbits around the GC, which are located outside the inner X$_2$ orbits, where the Sgr A Complex is located. Integrated intensity ratios of all observed lines with respect to the CO(4-3) emission show a decreasing trend with decreasing LSR velocities, as the gas approaches to the inner X$_2$ orbits, for which V$_{lsr} < 100$ kms^{-1}. Using non-LTE RADEX calculations, it was shown that the integrated intensity ratios trend is consistent with increasing H$_2$ volume densities, as the gas transits from mainly atomic in the X$_1$ orbits to mainly molecular in the X$_2$ orbits. With the given observations, it was not possible to constrain the kinetic temperature of the gas, but an accepted observing proposal at the IRAM facility of several CO and CO isotopologues lines will help to constrain it. Also, a submitted SOFIA proposal for [CII] observations will allow to estimate the FUV field in which, gas at these orbits is immersed. This ongoing work will also be expanded in a future publication.

8.2.3 The +20 kms^{-1} and +50 kms^{-1} Molecular Clouds

The analysis of the physical conditions of the gas traced by the sub-mm emission from the +20 kms^{-1} and +50 kms^{-1} Cloud will be part of the future work related to this thesis. These clouds are exposed to an intense FUV field from the Nuclear Cluster and are interacting with SNRs such as the Sgr A-East SNR in the case of the +50 kms^{-1} Cloud, and the G359.92−0.09 SNR in the case of the +20 kms^{-1} Cloud. In order to investigate how the gas physical conditions vary across the clouds, 17 positions were selected tracing the emission associated to the +20 kms^{-1} and eastern streamer (positions 1 to 4), the emission associated to the +50 kms^{-1} Cloud (positions 6-5, and 8 to 11), the emission associated to Sgr A* (position 7), and to the small gas streamer from the +50 kms^{-1} Cloud towards Sgr A* (position 12). The change on the gas physical conditions from the +50 kms^{-1} Cloud towards the HCO^{+} Cloud (position 13, 14 and 15) will be also explored, as well as the physical conditions in the [CII] emission lane (positions 14, 16, and 17) at the outer edge of the +50 kms^{-1} Cloud. The already calculated KOSMA-τ PDR models will be used to model the emission, while including the nitrogen chemistry in the PDR model will also help to interpret the HCN and H^{13}CN emission towards these clouds, publicly available in the Mopra archive.

8.3 Outlook

Within the limited time of a PhD thesis, these vast datasets can not be explained in much detail for many of the sources here presented. The focus of this work was on the data reduction of the datasets, and on the preliminary analysis of the gas physical conditions in two sources: the Arched-Filaments and the HVG detected along the l.o.s. towards the Sgr A Complex. Also, future work related to the +20 kms^{-1} and +50 kms^{-1} Clouds was outlined. As it has been shown in this work, the richness of these large datasets will help to shed light on the physical conditions of many sources contained within the Sgr A Complex, and sources located along the same l.o.s., contributing further to the understanding of the physics behind the Galactic Center of the Milky Way.

Bibliography

Abel, N. P. 2006, MNRAS, 368, 1949

Abel, N. P., Ferland, G. J., Shaw, G., & van Hoof, P. A. M. 2005, ApJS, 161, 65

Aharonian, F., Akhperjanian, A. G., Bazer-Bachi, A. R., et al. 2006, Nature, 439, 695

Allan, D. W. 1966, Proc. IEEE, 54, 221

Amo-Baladrón, M. A., Martín-Pintado, J., Morris, M. R., Muno, M. P., & Rodríguez-Fernández, N. J. 2009, ApJ, 694, 943

Ao, Y., Henkel, C., Menten, K. M., et al. 2013, A&A, 550, A135

Arimoto, N., Sofue, Y., & Tsujimoto, T. 1996, PASJ, 48, 275

Asplund, M., Grevesse, N., & Sauval, A. J. 2005, Cosmic Abundances as Records of Stellar Evolution and Nucleosynthesis, 336, 25

Bally, J., Aguirre, J., Battersby, C., et al. 2010, ApJ, 721, 137

Bally, J., Stark, A. A., Wilson, R. W., & Henkel, C. 1987, ApJS, 65, 13

Bally, J., Stark, A. A., Wilson, R. W., & Henkel, C. 1988, ApJ, 324, 223

Bania, T. M. 1980, ApJ, 242, 95

Binney, J., Gerhard, O. E., Stark, A. A., Bally, J., & Uchida, K. I. 1991, MNRAS, 252, 210

Burton, W. B., & Liszt, H. S. 1978, ApJ, 225, 815

Chambers, E. T., Yusef-Zadeh, F., & Ott, J. 2014, A&A, 563, A68

Chatzopoulos, S., Fritz, T. K., Gerhard, O., et al. 2015, MNRAS, 447, 948

Caswell, J. L., Breen, S. L., & Ellingsen, S. P. 2011, MNRAS, 410, 1283

Caswell, J. L., Fuller, G. A., Green, J. A., et al. 2010, MNRAS, 404, 1029

Clarkson, W. I., Ghez, A. M., Morris, M. R., et al. 2012, ApJ, 753, 92

Coil, A. L., & Ho, P. T. P. 2000, ApJ, 533, 245

Colavitti, E., Cescutti, G., Matteucci, F., & Murante, G. 2009, A&A, 496, 429

Cotera, A. S., Erickson, E. F., Colgan, S. W. J., et al. 1996, ApJ, 461, 750

Cox, P., & Laureijs, R. 1989, The Center of the Galaxy, 136, 121

Crocker, R. M., Jones, D. I., Melia, F., Ott, J., & Protheroe, R. J. 2010, Nature, 463, 65

Croswell, K. 1996, The alchemy of the heavens., by Croswell, K.. Oxford University Press, Oxford (UK), 1996, XII + 340 p., ISBN 0-19-286192-1.

Cubick, M., Stutzki, J., Ossenkopf, V., Kramer, C., Röllig, M. 2008, A&A, 488, 623

Dahmen, G., Huttemeister, S., Wilson, T. L., & Mauersberger, R. 1998, A&A, 331, 959

Dame, T. M., Hartmann, D., & Thaddeus, P. 2001, ApJ, 547, 792

Dame, T. M., & Thaddeus, P. 2008, ApJL, 683, L143

de Graauw, T., Helmich, F. P., Phillips, T. G., et al. 2010, A&A, 518, L6

de Jong, T., Boland, W., & Dalgarno, A. 1980, A&A, 91, 68

Dogiel, V. A., Chernyshov, D. O., Tatischeff, V., Cheng, K.-S., & Terrier, R. 2013, ApJL, 771, L43

Dong, H., Wang, Q. D., Cotera, A., et al. 2011, MNRAS, 417, 114

Dong, H., Wang, Q. D., & Morris, M. R. 2012, MNRAS, 425, 884

Draine, B. T. 1978, ApJS, 36, 595

Draine, B. T. 2011, Physics of the Interstellar and Intergalactic Medium by Bruce T. Draine. Princeton University Press, 2011. ISBN: 978-0-691-12214-4.

Englmaier, P., & Gerhard, O. 1999, MNRAS, 304, 512

Etxaluze, M., Goicoechea, J. R., Cernicharo, J., et al. 2013, A&A, 556, AA137

Ferrière, K. 2012, A&A, 540, AA50

Figer, D. F. 2008, IAU Symposium, 250, 247

Figer, D. F., McLean, I. S., & Morris, M. 1999, ApJ, 514, 202

Figer, D. F., Najarro, F., Gilmore, D., et al. 2002, ApJ, 581, 258

Figer, D. F., Rich, R. M., Kim, S. S., Morris, M., & Serabyn, E. 2004, ApJ, 601, 319

Fixsen, D. J. 2009, ApJ, 707, 916

García, P., Bronfman, L., Nyman, L.-Å., Dame, T. M., & Luna, A. 2014, ApJS, 212, 2

Genzel, R., Eisenhauer, F., & Gillessen, S. 2010, Reviews of Modern Physics, 82, 3121

Genzel, R., Stacey, G. J., Harris, A. I., et al. 1990, ApJ, 356, 160

Ghez, A. M., Salim, S., Weinberg, N. N., et al. 2008, ApJ, 689, 1044

Gillessen, S., Eisenhauer, F., Trippe, S., et al. 2009, ApJ, 692, 1075

Girart, J. M., Estalella, R., Ho, P. T. P., & Rudolph, A. L. 2000, ApJ, 539, 763

Goldsmith, P. F., & Langer, W. D. 1978, ApJ, 222, 881

Goldsmith, P. F., & Langer, W. D. 1999, ApJ, 517, 209

Goldsmith, P. F., Langer, W. D., Pineda, J. L., & Velusamy, T. 2012, ApJS, 203, 13

Goto, M. 2014, IAU Symposium, 303, 429

Goto, M., Usuda, T., Nagata, T., et al. 2008, ApJ, 688, 306

Green, J. A., Caswell, J. L., McClure-Griffiths, N. M., et al. 2011, ApJ, 733, 27

Guan, X., Stutzki, J., Graf, U. U., et al. 2012, A&A, 542, L4

Gundlach, K. H., Schicke, M., 2000, Supercond.Sci.Technol., 13, 12, R171

Güsten, R., & Philipp, S. D. 2004, The Dense Interstellar Medium in Galaxies, 253

Güsten, R., Walmsley, C. M., & Pauls, T. 1981, A&A, 103, 197

Habart, E., Boulanger, F., Verstraete, L., et al. 2003, A&A, 397, 623

Habing, H. J. 1968, Bull. Astron. Inst. Netherlands, 19, 421

Han, J. 2013, IAU Symposium, 294, 213

Heithausen, A., Bensch, F., Stutzki, J., Falgarone, E., & Panis, J. F. 1998, A&A, 331, L65

Herzberg, G. 1945, New York: Dover, 1945, of Physics (IOP) Publishing, 2003 Series in Astronomy and Astrophysics, ISBN 0750306246.,

Herzberg, G. 1966, New York: Van Nostrand, Reinhold, 1966,

Higgins, D. 2011, "Advanced Optical Calibration of the Hershcel HIFI Heterodyne Spectrometer" PhD Thesis, National University of Ireland, Maynooth

Ho, P. T. P., Ho, L. C., Szczepanski, J. C., Jackson, J. M., & Armstrong, J. T. 1991, Nature, 350, 309

Hollenbach, D., & McKee, C. F. 1989, ApJ, 342, 306

Hollenbach, D. J., Takahashi, T., & Tielens, A. G. G. M. 1991, ApJ, 377, 192

Hollenbach, D. J., & Tielens, A. G. G. M. 1999, Reviews of Modern Physics, 71, 173

Horn, J., Siebertz, O., Schmülling, F., et al. 1999, Experimental Astronomy, 9, 17

Huettemeister, S., Dahmen, G., Mauersberger, R., et al. 1998, A&A, 334, 646

Huettemeister, S., Wilson, T. L., Bania, T. M., & Martin-Pintado, J. 1993, A&A, 280, 255

Hunter, S. D., Bertsch, D. L., Catelli, J. R., et al. 1997, ApJ, 481, 205

Jenkins, A., & Binney, J. 1994, MNRAS, 270, 703

Jones, P. A., Burton, M. G., Cunningham, M. R., et al. 2012, MNRAS, 419, 2961

Jones, P. A., Burton, M. G., Cunningham, M. R., Tothill, N. F. H., & Walsh, A. J. 2013, MNRAS, 433, 221

Kim, S. S., Morris, M., & Lee, H. M. 1999, ApJ, 525, 228

Klein, B., Hochgürtel, S., Krämer, I., et al. 2012, A&A, 542, L3

Klessen, R. S., & Glover, S. C. O. 2014, arXiv:1412.5182

Kramer, C., 1997, Calibration of spectral line data at the IRAM 30m radio telescope, Version 2.1, January 24th

Kruijssen, J. M. D., Longmore, S. N., Elmegreen, B. G., et al. 2014, MNRAS, 440, 3370

Ladd, N., Purcell, C., Wong, T., & Robertson, S. 2005, PASA, 22, 62

Lang, C. C., Cyganowski, C., Goss, W. M., & Zhao, J.-H. 2004, in Galactic Center Workshop 2002, The Central 300 Parsecs of the Milky Way, ed. A. Cotera et al. (Weinheim: Wiley), 1

Lang, C. C., Figer, D. F., Goss, W. M., & Morris, M. 1999, Astron. J., 118, 2327

Lang, C. C., Goss, W. M., Cyganowski, C., & Clubb, K. I. 2010, ApJS, 191, 275

Lang, C. C., Goss, W. M., & Morris, M. 2001, Astron. J., 121, 2681

Lang, C. C., Goss, W. M., & Morris, M. 2002, Astron. J., 124, 2677

Lang, C. C., Goss, W. M., & Wood, D. O. S. 1997, ApJ, 474, 275

Lang, C. C., Morris, M., & Echevarria, L. 1999, ApJ, 526, 727

Langer, W. D., Goldsmith, P. F., Pineda, J. L., et al. 2015, A&A, 576, A1

Langer, W. D., Velusamy, T., Pineda, J. L., Willacy, K., & Goldsmith, P. F. 2014, A&A, 561, AA122

Larson, K. A., & Whittet, D. C. B. 2005, ApJ, 623, 897

Larson, K. A., Whittet, D. C. B., & Hough, J. H. 1996, ApJ, 472, 755

Lau, R. M., Herter, T. L., Morris, M. R., & Adams, J. D. 2014, ApJ, 794, 108

Lau, R. M., Herter, T. L., Morris, M. R., Li, Z., & Adams, J. D. 2015, arXiv:1503.07173

Launhardt, R., Zylka, R., & Mezger, P. G. 2002, A&A, 384, 112

Law, C. J., Yusef-Zadeh, F., & Cotton, W. D. 2008, ApJS, 177, 515

Lee, H.-H., Bettens, R. P. A., & Herbst, E. 1996, A&AS, 119, 111

Linke, R. A., Stark, A. A., & Frerking, M. A. 1981, ApJ, 243, 147

Liu, H. B., Ho, P. T. P., Wright, M. C. H., et al. 2014, Massive Young Star Clusters Near and Far: From the Milky Way to Reionization, 39

Longmore, S. N., Kruijssen, J. M. D., Bally, J., et al. 2013, MNRAS, 433, L15

Maloney, P. R., Hollenbach, D. J., & Tielens, A. G. G. M. 1996, ApJ, 466, 561

Martin, H. M., Hills, R. E., & Sanders, D. B. 1984, MNRAS, 208, 35

Martin, C. L., Walsh, W. M., Xiao, K., et al. 2004, ApJS, 150, 239

Mauerhan, J. C., Cotera, A., Dong, H., et al. 2010, ApJ, 725, 188

McElroy, D., Walsh, C., Markwick, A. J., et al. 2013, A&A, 550, AA36

McGary, R. S., Coil, A. L., & Ho, P. T. P. 2001, ApJ, 559, 326

Mezger, P. G., Duschl, W. J., & Zylka, R. 1996, A&A Rev., 7, 289

Mezger, P. G., Pankonin, V., Schmid-Burgk, J., Thum, C., & Wink, J. 1979, A&A, 80, L3

Mezger, P. G., Zylka, R., Salter, C. J., et al. 1989, A&A, 209, 337

Mihalas, D. 1978, San Francisco, W. H. Freeman and Co., 1978. 650 p.,

Minh, Y. C., Irvine, W. M., & Friberg, P. 1992, A&A, 258, 489

Minh, Y. C., Kim, S.-J., Pak, S., et al. 2005, New Astronomy, 10, 425

Mizutani, K., Maihara, T., Matsuhara, H., et al. 1994, ApJS, 91, 613

Molinari, S., Bally, J., Noriega-Crespo, A., et al. 2011, ApJL, 735, L33

Mott, A., Spitoni, E., & Matteucci, F. 2013, MNRAS, 435, 2918

Morris, M., & Serabyn, E. 1996, ARA&A, 34, 645

Müller, M., & Jellema, W.,"The HIFI Beam: Release #1, Release Note for Astronomers", 19 Sept 2014

Müller, H. S. P., Schlöder, F., Stutzki, J., & Winnewisser, G. 2005, Journal of Molecular Structure, 742, 215

Müller, H. S. P., Thorwirth, S., Roth, D. A., & Winnewisser, G. 2001, A&A, 370, L49

Nagayama, T., Omodaka, T., Handa, T., et al. 2007, PASJ, 59, 869

Nishiyama, S., Nagata, T., Kusakabe, N., et al. 2006, ApJ, 638, 839

Nishiyama, S., Nagata, T., Tamura, M., et al. 2008, ApJ, 680, 1174

Nishiyama, S., Tamura, M., Hatano, H., et al. 2009, ApJ, 696, 1407

Oka, T., Geballe, T. R., Goto, M., Usuda, T., & McCall, B. J. 2005, ApJ, 632, 882

Oka, T., Hasegawa, T., Sato, F., et al. 2001, ApJ, 562, 348

Oka, T., Hasegawa, T., Sato, F., Tsuboi, M., & Miyazaki, A. 1998, ApJS, 118, 455

Oka, T., Hasegawa, T., White, G. J., et al. 2008, PASJ, 60, 429

Oka, T., Nagai, M., Kamegai, K., Tanaka, K., & Kuboi, N. 2007, PASJ, 59, 15

Oka, T., Onodera, Y., Nagai, M., et al. 2012, ApJS, 201, 14

Oka, T., Tanaka, K., Matsumura, S., et al. 2011, The Galactic Center: a Window to the Nuclear Environment of Disk Galaxies, 439, 3

Okumura, S. K., Ishiguro, M., Fomalont, E. B., et al. 1991, ApJ, 378, 127

Ossenkopf, V., Röllig, M., Neufeld, D. A., et al. 2013, A&A, 550, A57

Ott, J., Weiß, A., Staveley-Smith, L., Henkel, C., & Meier, D. S. 2014, ApJ, 785, 55

Pardo, J. R., Cernicharo, J. & Serabyn, E., 2001, IEEE Trans. on Antennas and Propagation, 49/12, 1683

Pauls, T., Downes, D., Mezger, P. G., & Churchwell, E. 1976, A&A, 46, 407

Pierce-Price, D., Richer, J. S., Greaves, J. S., et al. 2000, ApJL, 545, L121

Pilbratt, G. L., Riedinger, J. R., Passvogel, T., et al. 2010, A&A, 518, LL1

Pineda, J. L., Langer, W. D., & Goldsmith, P. F. 2014, A&A, 570, AA121

Pineda, J. L., Mizuno, N., Röllig, M., et al. 2012, A&A, 544, A84

Pineda, J. L., Mizuno, N., Stutzki, J., et al. 2008, A&A, 482, 197

Poglitsch, A., Stacey, G. J., Geis, N., et al. 1991, ApJL, 374, L33

Porquet, D., Rodriguez, J., Corbel, S., et al. 2003, A&A, 406, 299

Portegies Zwart, S. F., Makino, J., McMillan, S. L. W., & Hut, P. 2002, ApJ, 565, 265

Price, S. D., Egan, M. P., Carey, S. J., Mizuno, D. R., & Kuchar, T. A. 2001, Astron. J., 121, 2819

Reid, M. J., Menten, K. M., Brunthaler, A., et al. 2014, ApJ, 783, 130

Requena-Torres, M. A., Güsten, R., Weiß, A., et al. 2012, A&A, 542, L21

Rieke, G. H., & Lebofsky, M. J. 1985, ApJ, 288, 618

Riquelme, D., Amo-Baladrón, M. A., Martín-Pintado, J., et al. 2010, A&A, 523, AA51

Riquelme, D., Amo-Baladrón, M. A., Martín-Pintado, J., et al. 2013, A&A, 549, AA36

Rodríguez-Fernández, N. J., Martín-Pintado, J., & de Vicente, P. 2001, A&A, 377, 631

Rodríguez-Fernández, N. J., Martín-Pintado, J., Fuente, A., & Wilson, T. L. 2004, A&A, 427, 217

Roelfsema, P. R., Helmich, F. P., Teyssier, D., et al. 2012, A&A, 537, A17

Röllig, M., & Ossenkopf, V. 2013, A&A, 550, AA56

Röllig, M., Ossenkopf, V., Jeyakumar, S., Stutzki, J., & Sternberg, A. 2006, A&A, 451, 917

Röllig, M., Szczerba, R., Ossenkopf, V., Glück, C. 2013. Astronomy and Astrophysics 549, AA85.

Romero-Gómez, M., Athanassoula, E., Antoja, T., & Figueras, F. 2011, MNRAS, 418, 1176

Rybicki, G. B., & Lightman, A. P. 1979, New York, Wiley-Interscience, 1979. 393 p.

Sawada, T., Hasegawa, T., Handa, T., et al. 2001, ApJS, 136, 189

Sawada, T., Hasegawa, T., Handa, T., & Cohen, R. J. 2004, MNRAS, 349, 1167

Schöier, F. L., van der Tak, F. F. S., van Dishoeck, E. F., & Black, J. H. 2005, A&A, 432, 369

Schuller, F., Menten, K. M., Contreras, Y., et al. 2009, A&A, 504, 415

Serabyn, E., & Guesten, R. 1987, A&A, 184, 133

Serabyn, E., Lacy, J. H., & Achtermann, J. M. 1992, ApJ, 395, 166

Shields, J. C., & Ferland, G. J. 1994, ApJ, 430, 236

Sidoli, L., Belloni, T., & Mereghetti, S. 2001, A&A, 368, 835

Simon, R. 1997, PhD thesis, University of Cologne

Simon, R., Graf, U., Kramer, C., Stutzki, J., Onishi, T., Report on beam efficiency measurements at NANTEN after surface adjustment, Version of February 13th, 2007

Simón-Díaz, S., & Stasińska, G. 2011, A&A, 526, A48

Simpson, J. P., Colgan, S. W. J., Cotera, A. S., et al. 2007, ApJ, 670, 1115

Sodroski, T. J., Odegard, N., Dwek, E., et al. 1995, ApJ, 452, 262

Stark, A. A., Bally, J., Balm, S. P., et al. 2001, PASP, 113, 567

Stark, A. A., & Bania, T. M. 1986, ApJL, 306, L17

Sternberg, A., & Dalgarno, A. 1989, ApJ, 338, 197

Sternberg, A., & Dalgarno, A. 1995, ApJS, 99, 565

Stoerzer, H., Stutzki, J., & Sternberg, A. 1996, A&A, 310, 592

Stolovy, S., Ramirez, S., Arendt, R. G., et al. 2006, Journal of Physics Conference Series, 54, 176

Stolte, A., Ghez, A. M., Morris, M., et al. 2008, ApJ, 675, 1278

Stutzki, J., Bensch, F., Heithausen, A., Ossenkopf, V., & Zielinsky, M. 1998, A&A, 336, 697

Tanaka, K., Oka, T., Matsumura, S., Nagai, M., & Kamegai, K. 2011, ApJL, 743, L39

Tielens, A. G. G. M. 2005, The Physics and Chemistry of the Interstellar Medium, by A. G. G. M. Tielens, pp. . ISBN 0521826349. Cambridge, UK: Cambridge University Press, 2005.

Timmermann, R., Genzel, R., Poglitsch, A., et al. 1996, ApJ, 466, 242

Tsuboi, M., Handa, T., & Ukita, N. 1999, ApJS, 120, 1

Tsuboi, M., Ukita, N., & Handa, T. 1997, ApJ, 481, 263

van der Tak, F. F. S., Black, J. H., Schöier, F. L., Jansen, D. J., & van Dishoeck, E. F. 2007, A&A, 468, 627

van Dishoeck, E. F. 2014, arXiv:1411.5280

van Dishoeck, E. F., & Black, J. H. 1986, ApJS, 62, 109

van Dishoeck, E. F., Jansen, D. J., & Phillips, T. G. 1993, A&A, 279, 541

Watson, M. G., Willingale, R., Hertz, P., & Grindlay, J. E. 1981, ApJ, 250, 142

Weingartner, J. C., & Draine, B. T. 2001, ApJ, 548, 296

Whittet, D. C. B. 2003, Dust in the galactic environment, 2nd ed. by D.C.B. Whittet. Bristol: Institute

Wilson, T. L., Rohlfs, K., Hüttemeister, S. 2009, Tools of Radio Astronomy, by Thomas L. Wilson; Kristen Rohlfs and Susanne Hüttemeister. ISBN 978-3-540-85121-9. Published by Springer-Verlag, Berlin, Germany, 2009.

Yusef-Zadeh, F., & Morris, M. 1987a, ApJ, 320, 545

Yusef-Zadeh, F., & Morris, M. 1987b, Astron. J., 94, 1178

Yusef-Zadeh, F., Morris, M., & Chance, D. 1984, Nature, 310, 557

Yusef-Zadeh, F., Muno, M., Wardle, M., & Lis, D. C. 2007, ApJ, 656, 847

Yusef-Zadeh, F., Roberts, D. A., Goss, W. M., Frail, D. A., & Green, A. J. 1996, ApJL, 466, L25

Yusef-Zadeh, F., Roberts, D. A., Goss, W. M., Frail, D. A., & Green, A. J. 1999, ApJ, 512, 230

Zhao, J.-H., Desai, K., Goss, W. M., & Yusef-Zadeh, F. 1993, ApJ, 418, 235

Zhao, J.-H., Morris, M. R., & Goss, W. M. 2013, ApJ, 777, 146

Zylka, R., Philipp, S., Duschl, W. J., et al. 1998, The Central Regions of the Galaxy and Galaxies, 184, 291

Zylka, R., Mezger, P. G., & Wink, J. E. 1990, A&A, 234, 133

Appendix A

Antenna Temperature Scale of the Observations

A common antenna temperature scale must be chosen when comparing observations taken with different telescopes. This is the case for the present work since the data acquired with the Herschel-HIFI satellite and the NANTEN2/SMART ground based telescope are used for characterizing the physical conditions of the warm gas in the Sgr A Complex.

In general, the large number of physical quantities (and their respective uncertainties) involved in the data calibration process make the conversion of the measured intensities into antenna temperatures not trivial. Since the measured intensities are in fact a convolution of the antenna pattern with the intrinsic intensity distribution of the astronomical source, different antenna temperature scales can be adopted base on the different telescope efficiencies. Therefore, in adopting a particular scale, aspects such as the spatial extent of the source emission and shape of the antenna pattern need to be considered. Once a temperature scale is adopted, a cross-check of the measurements taken with both telescopes can be used to assess their inherent differences, and how much observations for the same position on the sky, measured with both telescopes, differ systematically from each other. Ideally, once the measurements have been corrected by the inherent construction and performance differences between telescopes, the measured spectra under the same spatial resolution should be similar within error uncertainties.

In section A.1, I briefly summarize the calibration process used to convert the measured intensities into the antenna temperature scale for the case of the NANTEN2 telescope and its double sideband heterodyne receiver SMART. The process for the HIFI heterodyne receiver onboard the Herschel Satellite is similar, but without the correction for atmospheric effects. In section A.2, an antenna temperature scale is chosen to compare the data measured with both telescopes.

Finally, in section A.3, using measurements of the [CI](1-0) line, the antenna temperatures measured with both telescopes of the same target and on a common angular resolution are cross-checked.

A.1 The Data Calibration Process

In the following, the data acquisition and calibration process, from the sky signal detection to its conversion into an antenna temperature scale for the NANTEN2 telescope and its heterodyne receiver SMART are briefly described. A few examples of the detection process with heterodyne instruments and the calibration procedure of the recorded data can be found in Gundlach & Schicke (2000), Stark et al. (2001), and Guan et al. (2012).

A.1.1 Down-Conversion of the Sky Signal

In the sub-mm spectral range, from 300 GHz up to a few THz, the down-conversion of the sky signal into lower frequencies is necessary because current electronics are not able to process such high frequency signals. One way to down-convert them succeeds through the heterodyne principle in a SIS mixing device. The absorption by the quasi-particles (dissociated Cooper pairs in the SIS) of the sky photons together with the photons of a monochromatic external signal, produces a photon-assisted tunneling of the quasi-particles through the isolator material, causing a lower frequency current (much lower than the sky signal frequency) that can be processed afterwards (Gundlach & Schicke , 2000). The signal fed to the SIS consists of a very week sky signal of frequency ν_{Sky} and much stronger monochromatic reference signal of frequency ν_{LO}, the so called Local Oscillator signal (LO). This mixing process down-converts the sky signal frequency to the so called *intermediate frequency* $\nu_{IF} = |\nu_{Sky} - \nu_{LO}|$, giving rise to two sidebands: the Upper Sideband (USB[1]) with $\nu_{SKY} = \nu_{LO} + \nu_{IF}$ and the Lower Sideband (LSB[2]) with $\nu_{SKY} = \nu_{LO} - \nu_{IF}$. In the case of the SMART DBS heterodyne receiver, both bands are transmitted by the mixers devices. In radio astronomy, the sideband containing the sky signal of interest is often referred to as the *signal sideband* and the other as the *image sideband*.

The 1 GHz bandwidth around the ν_{IF} signal, typically 1.5 GHz or 4 GHz for SMART, can be further processed and amplified with low noise amplifiers

[1] Upper SideBand
[2] Lower SideBand

available with the state-of-the-art technology. Finally, the 1 GHz bandwidth around the ν_{IF} signal is fed into a backend and converted into "counts rates" (or just "counts" for simplicity) per frequency channel, where the counts are particles proportional to the incoming radiation intensity (e.g., charge carriers in a CCD). In this way, the photon flux that carries the sky signal is recorded by the system.

A.1.2 Conversion of Counts into Antenna Temperature

After the sky signal was down-converted and expressed into counts per channel, the recorded data are transformed into a physical scale. This happens through the conversion of the counts into the so called *antenna temperature* scale through a HOT/COLD measurement. The process consist in using the measured counts produced by two BB[3] emitters, for which the physical temperatures are known, to relate both quantities. In radio astronomy, the antenna temperature is defined as:

$$T_{A,\nu} = \frac{c^2}{2k_B\nu^2} I_\nu, \tag{A.1}$$

where I_ν is the specific intensity of the emitting source (see Section 2.3), ν is the observed frequency, and k_B is the Boltzmann constant. In the case of BB emitters, $I_\nu = B_\nu(T)$, where $B_\nu(T)$ refers to the the Planck function, yielding the so called *radiation temperature* T_R (see Equations 2.10 and 2.11). In the sub-mm range of the electromagnetic spectrum, where $\epsilon = h\nu/kT \ll 1$, the Taylor expansion of $T_{R,\nu}$ in Equation 2.12 includes the so called *Rayleigh-Jeans correction* which is frequency and temperature dependent. In the case of the Rayleigh-Jeans approximation, the Rayleigh-Jeans correction term is simply $h\nu/2k_B$, independent of temperature. For two BB emitters, a proportionality between measured counts in each spectrometer channel and antenna temperature can be established. By knowing the physical temperature of the BB emitters, and assuming that this temperature does not vary significantly over the frequency range from the signal- to the image-sideband, a HOT-COLD antenna temperature difference can be expressed as:

$$T_{R,\nu}^{HOT} - T_{R,\nu}^{COLD} = (T_{HOT} - T_{COLD})\Big[1 - \frac{1}{6}\Big(\frac{h\nu}{k_B T_{HOT}}\Big)\Big(\frac{h\nu_{LO}}{k_B T_{COLD}}\Big)\Big]. \tag{A.2}$$

In this way, the spectrometer gain γ_ν can be evaluated for each frequency channel ν as:

$$\gamma_\nu = \frac{C_\nu^{HOT} - C_\nu^{COLD}}{G_s x_s (T_{R,\nu_s}^{HOT} - T_{R,\nu_s}^{COLD}) + G_i x_i (T_{R,\nu_i}^{HOT} - T_{R,\nu_i}^{COLD})} \left[\frac{counts}{K}\right], \tag{A.3}$$

where the C_ν values are the measured counts at the frequency channel ν within the 1 GHz bandpass of the receiver. A reasonable frequency to evaluate the T_R^{HOT}

[3] Black-Body

and T_R^{COLD} terms under the previous assumption is the LO frequency ν_{LO}. Is this way, the measured photon flux, expressed in counts detected by the receiver, can be translated into an antenna temperature scale.

In a more general way, since we are interested in detecting emission lines, which by definition are not produced by BB emitters, the measured antenna temperature can be expressed as the sum of the contributions of all emitters from both sidebands that are detected by the receiver. This is shown in Guan et al. (2012) as:

$$\begin{aligned} T_{A,\nu} \quad = \quad & \eta_{MB} t_{a,\nu_s} G_s x_s T_{MB,\nu_s} + \eta_{MB} t_{a,\nu_i} G_i x_i T_{MB,\nu_i} + \\ & (1 - f_{amb}) \left[(1 - t_{a,\nu_s}) G_s x_s \tilde{T}_{sky,\nu_s} + (1 - t_{a,\nu_i}) G_i x_i \tilde{T}_{sky,\nu_i} \right] + \\ & f_{amb} \left[G_s x_s J_{\nu_s}(T_{amb}) + G_i x_i J_{\nu_i}(T_{amb}) \right] + \\ & (1 - x_s) G_s J_{\nu_s}(T_{term}) + (1 - x_i) G_i J_{\nu_i}(T_{term}), \end{aligned} \tag{A.4}$$

where f_{amb} is the fraction of ambient material in the sky beam, η_{MB} is the main beam efficiency, $T_{MB,s,i}$ is the source main antenna temperature in the signal(image) sideband, $\tilde{T}_{sky,\nu_{i,s}}$ is the effective sky antenna temperature at frequency ν in the signal(image) sideband defined as $\tilde{T}_{sky,\nu_{i,s}} = T_{sky,\nu_{i,s}}/(1 - t_{a,\nu_{s,i}})$, where $t_{a,\nu_{s,i}}$ is the atmospheric transmission at frequency ν in the signal(image) sideband, $G_{s,i}$ is the signal(image) sideband gain ($G_s + G_i = 1$), $x_{s,i}$ is the signal(image) fraction of the beam that looks at the sky, $(1 - x_{s,i})$ is the coupling to the sideband filter termination at antenna temperature T_{term}, and $J_{\nu_{i,s}}(T)$ is the radiation temperature as shown in Equation 2.11. The NANTEN2/SMART instrument is a DBS receiver, but has no cold termination of the image sideband, so in Equation A.4, $x_s = x_i = 1$ can be set.

A.1.3 Correction for Atmospheric Transmission

For ground based telescopes, such as NANTEN2, the attenuation of the sky signal due to the presence of the Earth's atmosphere has to be corrected. In order to do so, the transmissions $t_{a,\nu_{s,i}}$ in Equation A.4 have to be determined. These are defined as:

$$t_{a,\nu_{s,i}} = exp\left(-\frac{\tau_{\nu_{s,i}}}{\sin\zeta}\right), \tag{A.5}$$

where $\tau_{\nu_{s,i}}$ is the Zenith opacity in the signal- and image-sideband and $1/\sin\zeta$ is the airmass at the current source elevation ζ.

In order to estimate $t_{a,\nu_{s,i}}$, a reference position (SKY) and a HOT load measurements are carried out. In this way, the transmission of the atmosphere in both

sidebands can be expressed as a function of the calibrated SKY-HOT difference as:

$$t_{a,\nu_s} + \Gamma\omega t_{a,\nu_i} = \frac{(C_\nu^{HOT} - C_\nu^{SKY})/\gamma_\nu}{(1 - f_{amb})\tilde{T}_{SKY,\nu_s} G_s x_s} - \frac{1 - a_s}{a_s}(1 + \Gamma\Omega), \tag{A.6}$$

where $\tilde{T}_{SKY,\nu_s} = (J_{\nu_s}(T_{SKY,\nu_s}) - f_{amb} J_{\nu_s}(T_{amb}))/(1 - f_{amb})$ is the effective SKY temperature, $\Gamma = G_i x_i / G_s x_s$, $\Omega = (\tilde{T}_{HOT,\nu_i} - \tilde{T}_{SKY,\nu_i})/(\tilde{T}_{HOT,\nu_S} - \tilde{T}_{SKY,\nu_s})$, $\omega = (\tilde{T}_{SKY,\nu_i})/(\tilde{T}_{SKY,\nu_s})$, and $a_s = (\tilde{T}_{SKY,\nu_s})/(\tilde{T}_{HOT,\nu_s})$ as defined in Guan et al. (2012).

A.1.4 The Atmospheric Model (ATM)

Since the receiver detects simultaneously the emission from the signal- and image sidebands and they can not be disentangled, in order to determine the transmissions $t_{a,\nu_{s,i}}$ from Equation A.6, additional information of the atmosphere's behavior in both sidebands is needed. To overcome this difficulty, an atmospheric model is applied. In the case of the NANTEN2/SMART telescope, the ATM model of Pardo et al. (2001) is used. The model assumes that the opacity τ_ν in Equation A.5 scales linearly with the amount of precipitable water in the atmosphere (m_{H_2O} or *pwv*) plus and additional term as follows:

$$\tau_\nu = b_\nu m_{H_2O} + c_\nu, \tag{A.7}$$

where the b_ν and c_ν coefficients are called the *wet* and *dry* air parts of the atmospheric absorption, respectively, that take into account contributions from line and continuum atmospheric emission. These coefficients are stored in a look-up table, which was produced for the atmospheric conditions at the NANTEN2 site. Since m_{H_2O} depends mostly on local weather conditions, the parametrization of the opacities is split into the b_ν wet component, i.e., related to the water induced absorption, and the c_ν dry component for other species.

Using the parametrization of the opacity, as defined by the atmospheric model, the only unknown in Equation A.6 is the water vapor m_{H_2O}. All other parameters are either previously determined (such as the sideband gains $G_{s,i}$) or can be measured during the observations. In this way, the m_{H_2O} is obtained from the simultaneous fit of the LSB and USB sideband to the observed SKY-HOT difference so the transmissions in each sideband can be determined. The atmospheric transmission calculated from the ATM model for a set of precipitable water vapor values is shown in Figure A.1 in the frequency range from 445 GHz to 508 GHz. The vertical dashed lines indicate the position of the CO(4-3) and [CI](1-0) lines.

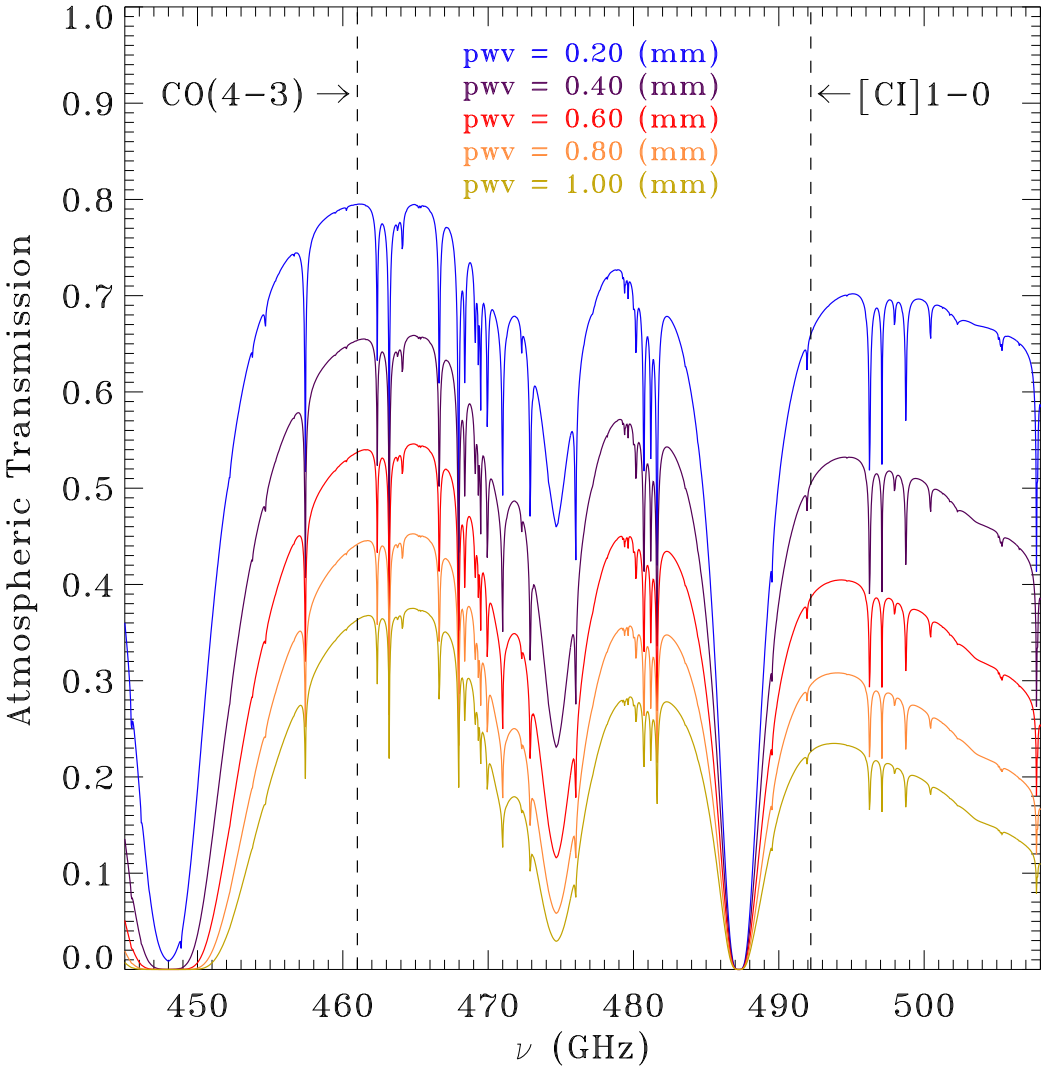

Figure. A.1: *Atmospheric transmission in the range from 445 GHz to 508 GHz from the ATM model of Pardo et al. (2001). Each color represents a different precipitable water vapor value.*

A.1.5 Antenna Temperature Scale

Finally, to produce the observed spectrum of the source outside the atmosphere, the SKY measurement is subtracted from the on source (ON) measurement. This allows to remove all remaining atmospheric effects, such as atmospheric lines, leaving only the spectrum (continuum and line) produced by the astronomical source. This process yields:

$$\begin{aligned} T_{A,\nu}^{ON} - T_{A,\nu}^{SKY} &= \frac{C_\nu^{ON} - C_\nu^{SKY}}{\gamma_\nu} \\ &= \eta_{MB} t_{a,\nu_s} G_s x_s T_{MB,\nu_s} + \eta_{MB} t_{a,\nu_i} G_i x_i T_{MB,\nu_i}, \end{aligned} \tag{A.8}$$

so the measured main beam antenna temperature $\Delta T_{MB,\nu_s}(SSB)$ is:

$$\begin{aligned}\Delta T_{MB,\nu}(SSB)|_{meas} &= \frac{C_\nu^{ON} - C_\nu^{OFF}}{\gamma_\nu} \times \frac{1}{\eta_{MB} t_{a,\nu_s} G_s x_s} \\ &= T_{MB,\nu_s} + \frac{t_{a,\nu_i} G_i x_i}{t_{a,\nu_s} G_s x_s} T_{MB,\nu_i}.\end{aligned} \tag{A.9}$$

For the NANTEN2/SMART receiver $G_i x_i = G_s x_s$, and assuming that there is no emission line of the source in the image-sideband, we set $T_{MB,\nu_i} = 0$, yielding:

$$\Delta T_{MB,\nu}(SSB)|_{meas} = \frac{C_\nu^{ON} - C_\nu^{SKY}}{\gamma_\nu G_s x_s t_{a,\nu_s} \eta_{MB}}. \tag{A.10}$$

The $\Delta T_{MB,\nu}(SSB)|_{meas}$ quantity is the measured spectrum in the main beam antenna temperature scale (correction for η_{MB}, see Equation A.11). For the forward beam antenna temperature scale T^*_{A,ν_s}, since $\eta_{MB} T_{MB,\nu_s} = \eta_{feff} T^*_{A,\nu_s}$, where η_{feff} is the forward efficiency, Equation A.10 can be scaled accordingly to change from one antenna temperature scale to the other.

The η_{feff} and η_{MB} efficiencies characterize the amount of power detected by the antenna pattern of the telescope's dish. This radiation pattern (or antenna pattern or far-field pattern) refers to the directional (angular) dependence of the strength of the detected emission produced by a source. For a given radio telescope shape, the strength of the detected radiation has a preferred direction along which most of the power is detected. This is the so called "main lobe" (or main beam), which can be identified from the normalized (to the peak value) power pattern of the telescope as a function of angular offsets on the sky, being the full-width at half-power of the largest lobe, the size of the main beam . Other "side lobes" can also detect radiation simultaneously, but usually their contribution to the total power is rather small, around a few percents.

The measured antenna temperature is always the convolution of the antenna pattern of the telescope with the true brightness distribution of the source. This implies that the measured antenna temperature will approach the *true* brightness temperature of the source depending on how the antenna pattern of the telescope couples to the brightness distribution (direction of the main and side lobes, and their corresponding relative strengths) and on how extended the brightness distribution of the source on the sky is. The combination of these factors allows the definition of two extreme temperature scales:

- *Main Beam Antenna Temperature* T_{Mb}: describes the equivalent antenna temperature of a source that fills the main beam of the antenna pattern completely and does not go beyond. Its associated main beam efficiency η_{MB}

(also known as B_{eff} as defined in Kramer (1997)) is:

$$B_{eff} = \frac{\iint_{MB} P(\Omega)\, d\Omega}{\iint_{4\pi} P(\Omega)\, d\Omega}, \tag{A.11}$$

where the $P(\Omega)$ function describes the antenna pattern of the telescope. The main beam efficiency B_{eff} represents the fraction of power that is detected/emitted through the main lobe of the antenna pattern.

- *Forward Beam Antenna Temperature* T_A^*: describes the equivalent antenna temperature of a source that fills completely the forward side of the antenna pattern. Its associated forward efficiency η_{feff} (also known as F_{eff} as defined in Kramer (1997)) is:

$$F_{eff} = \frac{\iint_{2\pi} P(\Omega)\, d\Omega}{\iint_{4\pi} P(\Omega)\, d\Omega}. \tag{A.12}$$

  The forward efficiency represents the fraction of power that is detected/emitted through the part of the antenna pattern inside the 2π solid angle measured from the telescope toward the sky.

Given the different values of B_{eff} and F_{eff}, choosing a common temperature scale for observations taken with different telescopes has to take into account the angular extent of the source's brightness distribution and the individual antenna pattern of each telescope. For the former, this would need an a priori knowledge of the source which is not always possible. Nonetheless, from data of similar transitions already observed, a rough estimation of the extent of such a distribution can be made.

In the following, we select a common temperature scale for the Herschel-HIFI and NANTEN2/SMART observations and cross-check the antenna temperatures measured with both telescopes, using the [CI](1-0) emission around the peak intensity of the Sgr A Complex.

A.2 A Common Antenna Temperature Scale

In order to choose a common antenna temperature scale to compare the NANTEN2/SMART and Herschel-HIFI observations, we examine the brightness distribution of the Sgr A Complex and some aspects of the antenna patterns of both

telescopes. Table A.1 contains all relevant parameters to define the absolute temperature scales shown in section A.1.5. The Herschel-HIFI beams are calculated using the formula described in Roelfsema et al. (2012):

$$\Theta = \frac{2}{\pi}(1.6 + 0.021 \times T_e(dB))\frac{\lambda}{D}\ [rad], \tag{A.13}$$

where T_e = 7.94 ± 0.82 dB is the edge taper (assumed common for all frequencies) and D = 3.28 m is the diameter of Herschel's dish. Recently, Müller & Jellema (2014) performed a new analysis of the Herschel's beam pattern, and derived better estimates for the beam sizes (HPBW), main beam efficiencies (B_{eff}), and aperture efficiencies, (η_A) values based on all Mars observations performed during Herschel's operations, together with an optical model of the telescope, which includes obscuration, truncation, and measured wave-front errors. These estimates represent the best values for the telescope parameters up to the date of the present work. The values are shown in the last four columns of Table A.1 in which the new main beam efficiencies B^*_{eff} and percentage difference with the previous estimates of Roelfsema et al. (2012) ΔB^*_{eff}, $\Delta\eta_A$, and ΔHPBW, are listed. Since Müller & Jellema (2014) obtained estimates for each polarization individually, the numbers quoted in Table A.1 are the averaged values between the derived parameters for each polarization. The new values in Müller & Jellema (2014) are still not part of the standard HIFI calibration pipeline and are intended to be included only in the forthcoming version of the data reduction package HIPE-13. For the NANTEN2/SMART telescope, the beam size values (HPBW) are extrapolated from the HPBW = 37.1" value at 465 GHz derived by U. Graf in September 2006. On the other hand, using Equation A.13 for the NANTEN2/SMART telescope, the measured edge taper T_e = 7.8 dB at 460 GHz and its 4 meter dish yield a beam size of 37.7" at 461 GHz, which is fully consistent with the value shown in Table A.1.

				Roelfsema et al. (2012)			Müller & Jellema (2014)			
Telescope	Line	ν (GHz)	λ (μm)	HPBW (")	F_{eff}	B_{eff}	B^*_{eff}	ΔB^*_{eff} (%)	$\Delta\eta_A$ (%)	ΔHPBW (%)
NANTEN2/SMART	CO(4-3)	461.0	650.3	37.4	0.86	0.50	...	...	...	...
NANTEN2/SMART	[CI](1-0)	492.2	609.1	35.1	0.86	0.50	...	...	...	...
Herschel-HIFI	[CI](1-0)	492.2	609.1	43.1	0.96	0.76	0.62	−18.4	−5.9	−2.1
Herschel-HIFI	[CI](2-1)	809.3	370.4	26.2	0.96	0.75	0.63	−16.7	−3.8	−1.7
Herschel-HIFI	[NII]	1461.1	205.2	14.5	0.96	0.72	0.58	−19.4	−8.5	−1.4
Herschel-HIFI	[CII]	1900.5	157.7	11.2	0.96	0.69	0.59	−15.2	−7.3	0.0

Table. A.1: *Forward and Main Beam efficiencies of the NANTEN2/SMART and Herschel-HIFI telescopes.*

The spatial extent of the sub-mm emission in the Sgr A Complex is very wide in all lines included in the present work. As examples, Figures A.2 and A.3 show the [CI](1-0) and CO(4-3) integrated emission from the Herschel-HIFI and NAN-

TEN2/SMART observations, respectively. The intensity map was created by integrating the emission between +57 kms^{-1} and +58 kms^{-1}. This narrow integration range contains the [CI](1-0) peak antenna temperature of the source, but only a small fraction of the total emission along the line-of-sight, given the very broad (> 100 kms^{-1}) lines seen in this region. The 600"× 600" maps show the peak emission at the center of the maps. The contours go from black to white as the emission level decreases. The first contour of both images is located at ~ $10\sigma_{map}$. From the figures, the emission above the significant detection level $3\sigma_{map}$ is very extended, even for spatial scales larger than eight arcminutes.

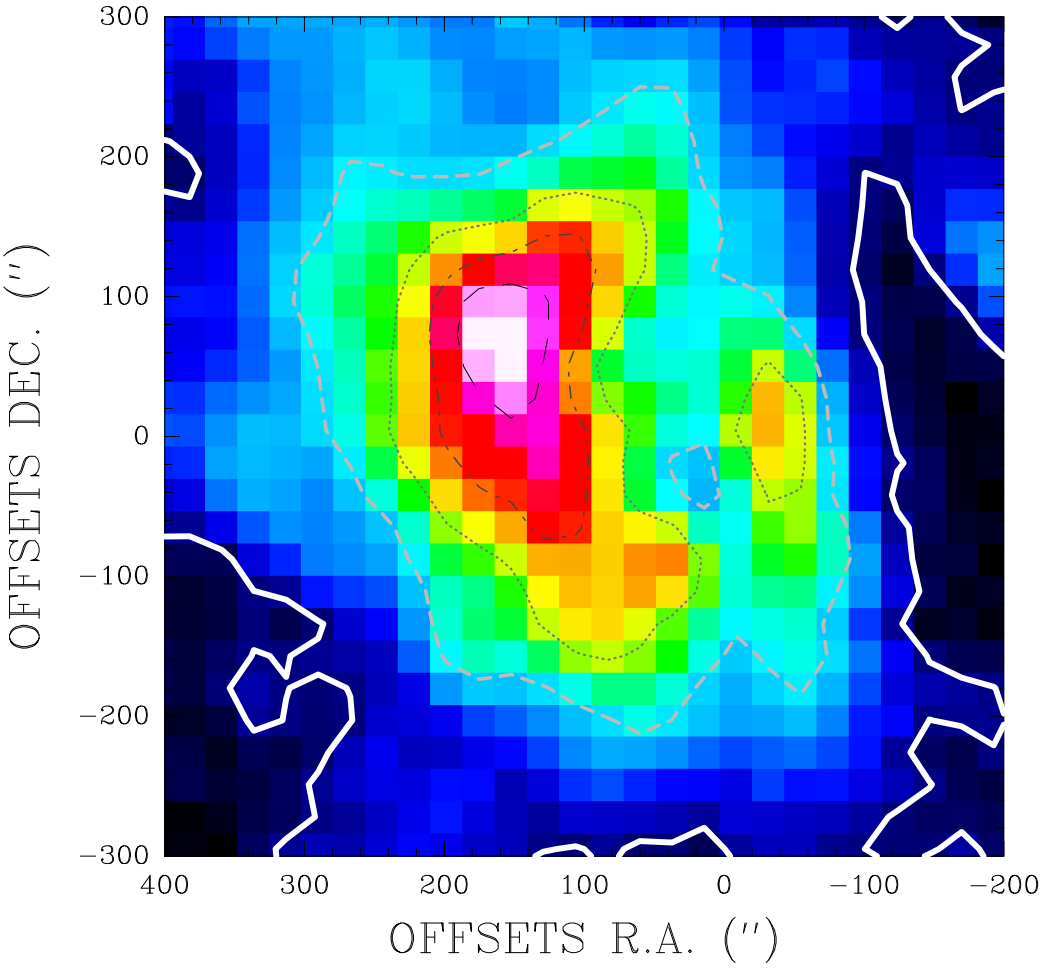

Figure. A.2: *Central area of the Herschel-HIFI [CI](1-0) observations of the Sgr A Complex. The emission was integrated between +57 kms^{-1} and +58 kms^{-1} to create the intensity map. The first contour is located at ~ $10\sigma_{map}$ level, where σ_{map} ~ 0.1 K kms^{-1} is the typical noise of the map.*

The measured beam patterns, power distributions, and encircled energy fraction (EEF) from Müller & Jellema (2014) in the H-polarization for the four Herschel-

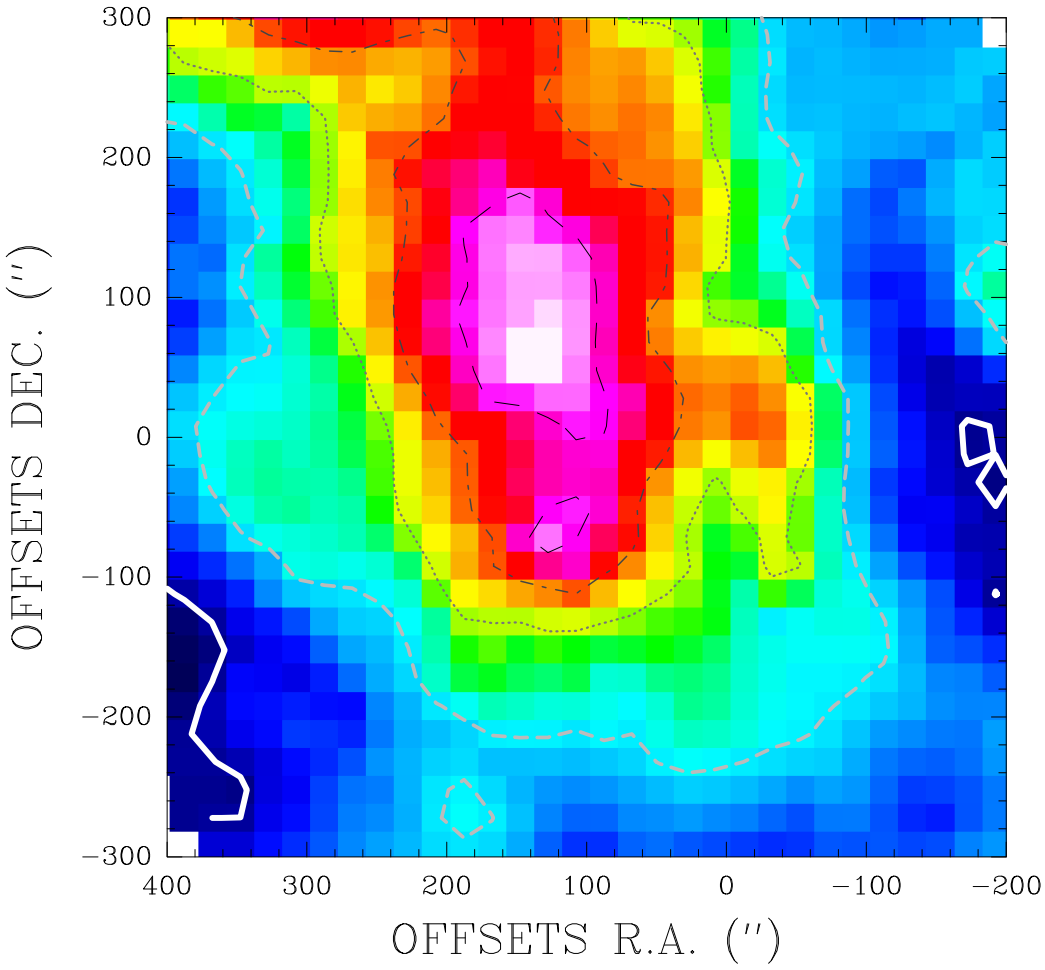

Figure. A.3: *Central area of the NANTEN2/SMART CO(4-3) observations of the Sgr A Complex. The emission was integrated between +57 kms^{-1} and +58 kms^{-1} to create the intensity map. The first contour is located at ~ 10σ_{map} level, where σ_{map} ~ 0.27 K kms^{-1} is the typical noise of the map.*

HIFI observed lines in the present work are shown in Figure A.4. There is an extended error beam (or sidelobes) due to the panel roughness of the telescope's dish. A substantial fraction of the power is in the sidelobes and it varies with frequency. This is shown by the slow convergence of the EEF at large radii (>20×HPWB). Also, there is a large azimuthal asymmetry seen at all beam models that increases with frequency, specially at large radii. The main beam is round at low frequencies, with increasing asymmetry at higher frequencies. Ossenkopf et al. (2013) used the T_A^* antenna temperature scale for C$^+$ observations arguing a large contribution from the sidelobes to their extended measured emission. The changes in $\Delta\eta_A$ and B_{eff}^* affect only the flux density conversion (K-to-Jy factor) and main beam antenna temperatures, leaving the T_A^* antenna temperature scale unaffected. For the NANTEN2/SMART telescope, the error beam at 461.1 GHz is expected to be within 7-10 times the main lobe size (Simon et al., 2007, Internal

NANTEN2 Report), i.e., at radii less than 3'. The the error beam pickup is expected to be around 20% of the detected power (Urs Graf, private communication)

Given the extended emission of the source, the location of the error beams for both telescopes, and the fraction of power contained in the error beam in each case, it can be considered that the most representative temperature scale of the true convolved antenna temperatures within the Sgr A Complex is the *Forward Beam Antenna Temperature* T_A^* . We apply this temperature scale to all datasets used in the present work. Given the contribution of the error beam pickup, the T_A^* scale represents a lower limit to the true convolved antenna temperature. The *Main Beam Antenna Temperature* would imply a negligible contribution of the error beam pickup to the measured antenna temperatures, increasing the line strength by $\frac{F_{eff}}{B_{mb}}$. The calibration error in the antenna temperatures for the Herschel-HIFI observations, described in Roelfsema et al. (2012), ranges from 15% in band 1a up to 25% for band 7b. In the case of the NANTEN2/SMART observations, the calibration error for the 460 - 490 GHz range, including uncertainties in beam efficiencies, is around 20% (Pineda et al., 2008, 2012).

A.3 Cross-Check of the Antenna Temperatures

The [CI](1-0) line was used to cross-check the antenna temperatures measured with both telescopes. A small area around the peak intensity, shown by the Herschel-HIFI observations, was selected and re-observed with the NANTEN2/SMART telescope. The $\sim$ 100"×100" map is shown in Figure A.5. The spatial resolution of the map is 46" (smoothed to the Herschel-HIFI resolution) with a spacing of 23"×23". The spectral resolution of the data is 1 kms^{-1} and the rms noise temperature ranges from 0.044 K up to 0.071 K. The pointing is very stable for both telescopes as can be seen in the very similar line shape of the spectra.

In order to compare the antenna temperatures measured with both telescopes at the same positions on the sky, we explore the behavior of the integrated intensity ratio with integration velocity interval. To minimize the influence of the noise temperature in our results, we select only the emission that is above a 10σ detection level, where σ = 0.071 K is the maximum rms noise temperature among all spectra in Figure A.5. This threshold defines a velocity range ΔV from +23 kms^{-1} to +83 kms^{-1} common for all spectra.

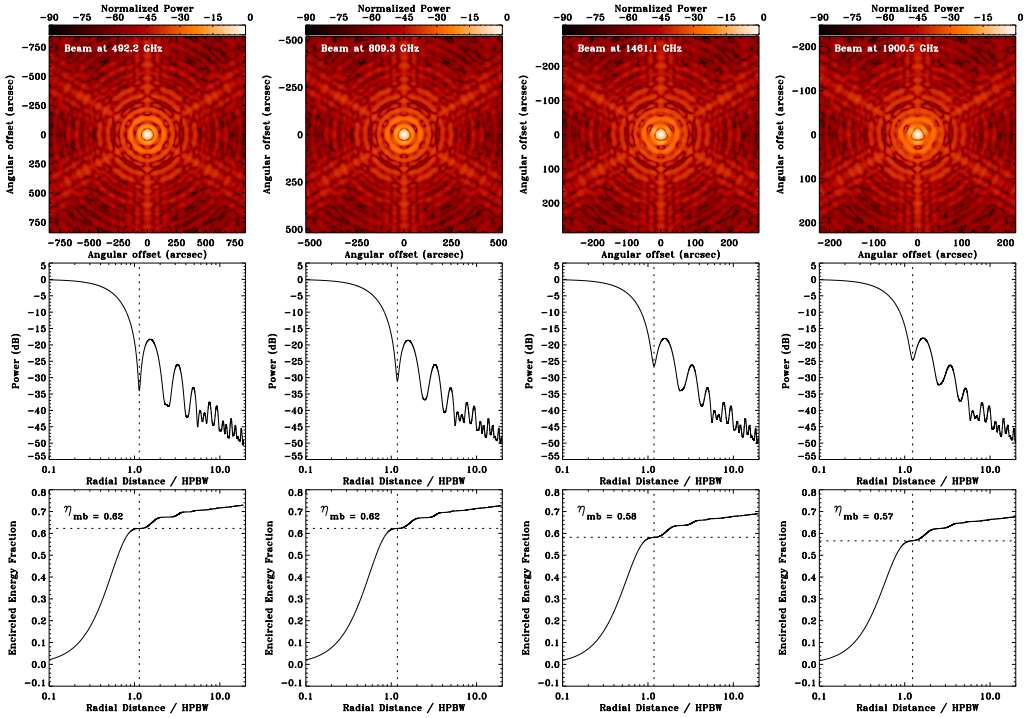

Figure. A.4: *Top panels: Herschel-HIFI horizontal polarization beam fit models for bands 1a, 3a, 6a, and 7b. Middle panels: logarithm of the normalized intensity as a function of HPBW. Bottom panels: encircled energy fraction as a function of the HPBW as shown in Müller & Jellema (2014). The plots show a large azimuthal asymmetry and a large contribution from sidelobes to the measured emission.*

For each pair of spectra in Figure A.5, we divide ΔV into velocity intervals (ΔV_i) in order to calculate the total intensity contained within them. The following values are used for ΔV_i: 1, 2, 3, 4, 5, 6, 10, 15, 20, 30, and 60 kms^{-1}. The division of ΔV by a given ΔV_i value yields $n = \frac{\Delta V}{\Delta V_i}$ sub-intervals for each spectrum. With these definitions, the integrated intensity ratio $R(\Delta V_i)_j$ in the j sub-interval for the given ΔV_i value is calculated from the Herschel-HIFI $I(\Delta V_i)^H_j$ and the NANTEN2/SMART $I(\Delta V_i)^N_j$ integrated intensities as $R(\Delta V_i)_j = I(\Delta V_i)^N_j / I(\Delta V_i)^H_j$. Then, the average integrated intensity ratio $R(\Delta V_i)$ for the given ΔV_i interval is calculated as $R(\Delta V_i) = \frac{1}{n}\sum_{j=1}^{n} R(\Delta V_i)_j$ for each pair of spectra observed at position "k" in Figure A.5.

Then, the integrated intensity ratios $R(\Delta V_i)_k$ and ΔV_i information of all 20 spectra pairs can be combined. First, I calculated the averaged integrated intensity ratio for all spectra pairs at ΔV_i as $R(\Delta V_i) = \frac{1}{N}\sum_{k=1}^{N} R(\Delta V_i)_k$, with $N = 20$. From this, I obtained one $R(\Delta V_i)$ value for a given ΔV_i interval. The results are shown in Figure A.6. The error bars correspond to the root-mean-square variation of each point and vary from 6% of $R(\Delta V_i)$ at $\Delta V_i = 1$ kms^{-1} to 4% at $\Delta V_i = 60$ kms^{-1}.

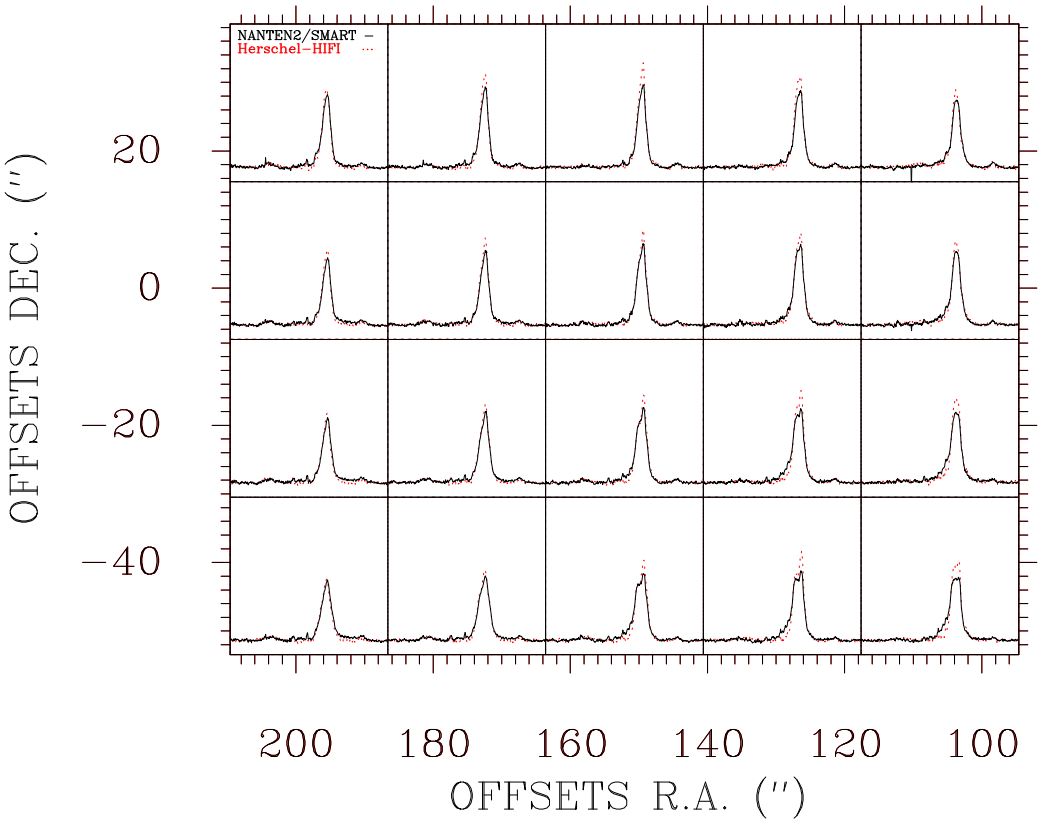

Figure. A.5: *Observations around the [CI](1-0) peak emission measured with the Herschel-HIFI (dotted red lines) and NANTEN2/SMART (solid black lines) telescopes. The observations are used to cross-check the antenna temperatures measured with both telescopes.*

From Figure A.6, R(ΔV_i) is constant at 1.0 (red line) for $\Delta V_i \leq 6$ kms^{-1}. For larger ΔV_i values, there is a small decrease to 0.94. From Figure A.5, it is clear that the largest difference between the spectra measured with NANTEN2/SMART and Herschel-HIFI occurs at the peak antenna temperatures. Since integrated intensities are proportional to $\Delta V \times T_{peak}$, this difference has an impact on the calculated ratios R(ΔV_i). This behavior could be due to several effects coming together: (a) atmospheric turbulence can cause fluctuations in the intensity and phase of the received signal by affecting the refractive index of different atmospheric layers. This effect is not present in the Herschel-HIFI observations; (b) deviation of the fit transmission and hence, opacities at the line center; (c) slightly different baseline subtraction from the measured spectra; and (d) interpolation effects when resampling the spatial resolution of the NANTEN2/SMART data to the Herschel-HIFI resolution at the observed frequency. By increasing the ΔV_i size, the difference in antenna temperature peaks becomes more relevant given the smaller number of intervals used to calculate the average values.

The measured NANTEN2/SMART antenna temperatures are ∼ 2% lower (on average over the whole ΔV interval) than the measured antenna temperatures in the Herschel-HIFI observations. For comparison, assuming a calibration error of 20% in the antenna temperature measured with both telescopes and an integrated intensity ratio of 0.98, the corresponding error is ∼ 30%, much larger than the 2% systematic underestimation of the Herschel-HIFI measured antenna temperatures by the NANTEN2/SMART observations. **Therefore, I am confident that both telescopes measure basically the same antenna temperatures on the T_A^* scale, which I thus consider a fair representation of the true convolved antenna temperature of the source**.

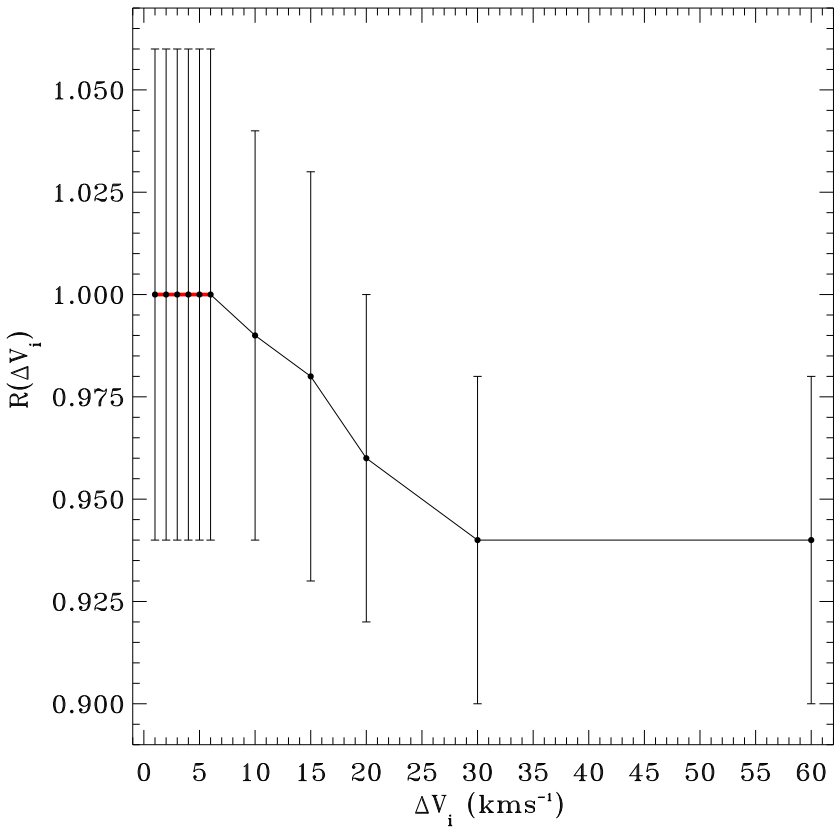

Figure. A.6: *Averaged Integrated Intensity Ratio $R(\Delta V_i)$ of the [CI](1-0) emission measured with the Herschel-HIFI and NANTEN2/SMART telescopes as a function of velocity integration interval ΔV_i as explained in the text. The intensity ratios are on average ∼ 2% lower (within error uncertainties) than unity over the whole range of ΔV_i values, showing that the measured NANTEN2/SMART antenna temperatures are systematically lower than the ones measured with the Herschel-HIFI telescope by the same amount. The red line delimits the ΔV_i range where the $R(\Delta V_i)$ values are closest to unity.*

Appendix B

Recovery of the Emission in the Reference Position

I investigated the presence of emission at the observed reference position used in the calibration process of each data set measured with the Herschel-HIFI and NANTEN2/SMART telescopes. If line emission is present at the reference position, it will be subtracted from the observations ON source measurements producing artificial absorption features in the final spectra. Given the very extended emission for all observed lines around the Sgr A Complex, such an emission contamination is very likely. In the following, I describe the process I implemented for recovering such emission contamination at the reference position used for the Herschel-HIFI observations. Also, I checked for emission contamination at the reference position of the NANTEN2/SMART observations.

B.1 Herschel-HIFI Observed Reference Position

The reference position of the Herschel-HIFI observations is located at $\alpha(J2000) = 17^h\ 44'\ 33''$, $\delta(J2000) = -28^\circ\ 52'\ 08''$ in Equatorial Coordinates, for all four lines observed: [CI](1-0), [CI](2-1), [NII], and [CII]. The selection of this position was based on a compromise between the absence of dust emission detected by the SPIRIT III infrared telescope at 8.3 μm as part of the Midcourse Space Experiment (MSX) Galactic Plane Survey, and a reference position not far away from the astronomical target. Figure B.1 shows the average spectrum of the [NII] and [CII] lines over the entire observed region. From the figure, a massive absorption feature around 0 kms^{-1} can be seen in both spectra, going well below the 0 K temperature level.

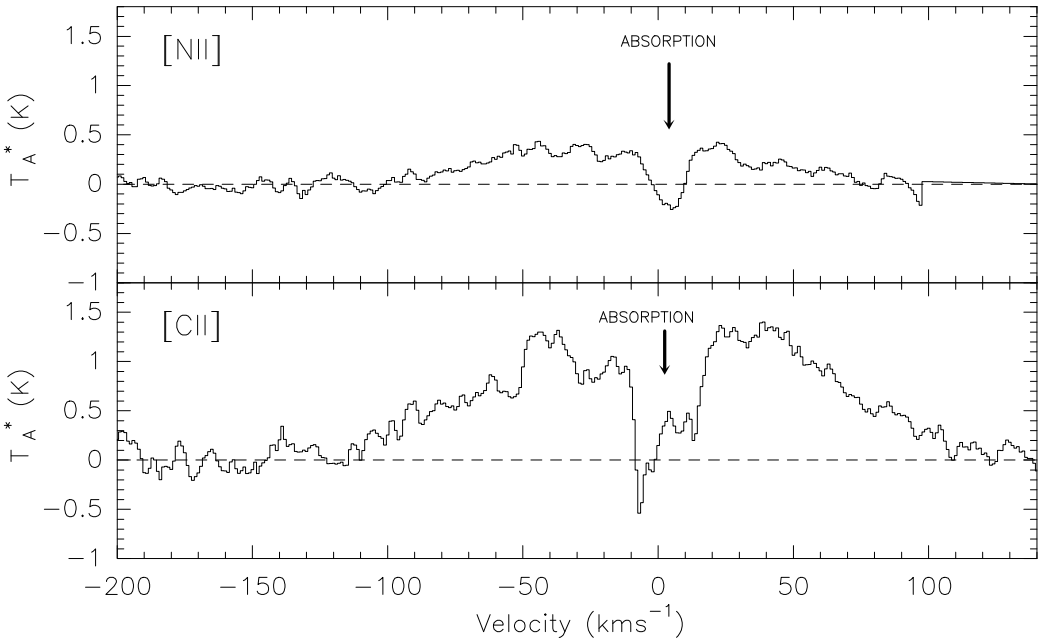

Figure. B.1: *Average spectra of the Herschel-HIFI [NII] and [CII] observations. The arrows show the position of the absorption features present in the data due to the contamination of the reference position (SKY) with line emission.*

Absorption features are expected to be found when observing toward the Galactic Center due to the presence of foreground material (such as spiral arms) along the l.o.s. (Linke et al., 1981). In order to identify whether the absorption features seen in Figure B.1 are the product of a contaminated reference position or of the foreground absorbing material, I looked for emission in the reference position. In the following, I describe the method used to produce the calibrated spectrum towards the reference position (SKY) and the modeling of the emission.

B.1.1 Calibrated Reference Position Spectra

The most common way to recover the emission of a contaminated reference position is by selecting an area on the observed region that contains no emission. From the selected spectra, an average spectrum with lower noise temperature than the rest of the map can be created. After that, the observed absorption features can be inverted and added to all the spectra in the map. It is desirable that the average spectrum has the lowest possible noise temperature to minimize the increase of noise when adding it to the spectra in the map.

Unfortunately, this approach can not be used in the case of the Herschel-HIFI observations. The emission distribution is very extended in all lines, so there

is no position free of emission in the map. Therefore, a different approach must be used. Given the observing mode used in some of the Herschel-HIFI observed data sets, it is possible to reconstruct the reference position spectrum for each of the OTF lines observed. The calibration of the measured reference position is possible for all lines observed in the *"OTF Map With Load Chop And Position-Switch Reference"* observing mode such as [CI](2-1), [NII], and [CII]. The case of the [CI](1-0) line detected using the *"OTF Map With Position-Switch Reference"* observing mode is treated in Section B.1.4.

The *"OTF Map With Load Chop And Position-Switch Reference"* observing mode chops to internal loads (HOT and COLD) immediately before taking a spectrum. The use of this observing mode is related to the short stability time of the receiver in the used bands as shown in Roelfsema et al. (2012). The chop to internal loads is used to determine the bandpass of the receiver and is done for the ON source position as well as for the reference position. In this way, the standard data reduction pipeline of the Herschel-HIFI observations can be applied to convert the measured counts at the reference position into fully calibrated reference spectra in the T_A^* temperature scale. This is possible because there is no atmosphere, and consequently, no transmission needs to be determined from the SKY-HOT difference (see appendix A). Nonetheless, there are telescope related artifacts such as standing waves, produced by the difference in light path when chopping to the internals loads, that are not removed from the SKY spectra during the standard calibration process. In this sense, the reference spectra are calibrated properly in temperature scale but may contain standing waves, whose shape depends on the utilized spectral band, that have to be removed in order to recover the line emission. The corresponding amplitudes of these standing waves are of the order of ~ 0.5 K for the [CII] and [NII] lines, and ~ 1 K for the [CI](2-1) line.

B.1.2 Model of the Reference Position Emission

In order to model the emission detected in the reference spectra, an average reference spectrum was produced doing the following steps: (a) each observed reference position was calibrated with the HIPE pipeline, producing a spectrum in T_A^* temperature scale; (b) I fit a 0-order polynomial to the spectra and selected only the ones with the lowest noise temperature. Thus, an average spectrum with very low noise temperature, in comparison to the spectra in the map, was created. The selected spectra used to create the average spectrum are ~ 100 for the [CI](2-1) line, and around ~ 200 for the [CII] and [NII] lines; (c) I removed only well defined standing waves by doing a Fourier transform of the average spectrum. This is possible because all standing waves have a consistent structure in all spectra, so adding them only increase the signal-to-noise ration but preserves

its structure. Well defined standing waves appear as very narrow intensity spikes in the time domain, so it is possible to remove them by interpolating the intensity just before and after the intensity spike without affecting the true emission structure of the spectrum; (d) a low order baseline was fitted and subtracted from the resulting average spectrum, where the emission is already clearly visible; (e) I modeled the emission by fitting up to five independent Gaussians to the average spectrum creating an **emission model** that was added to each spectrum in the observed map. This procedure avoids adding extra noise to the data apart from the uncertainties in the fitted Gaussian parameters.

It is important to emphasize that I controlled that no artificial emission was created during the removal of the standing waves by trying different interpolations and checking the variations in the results. Only when the standing wave was very well defined as a narrow intensity peak in the time domain and its radial velocity coincided with the radial velocity corresponding to the absorption features (as shown in Figure B.1), the resulting spectrum was used to create the emission model. The difference in the measured positions of the reference spectra is of the order of the Absolute Pointing Error (APE) of the telescope ~ 2" (Roelfsema et al., 2012), so it is assumed that all reference spectra were measured at the same position on the sky.

B.1.3 Results of the Emission Recovery

The results of the procedure are shown in Figure B.2. The black line in panels (a), (b), and (c) represent the average reference spectrum for the [NII], [CII] and [CI](2-1) lines, respectively. The noise in each spectrum is $\sigma = 0.196$ K for the [NII] line, $\sigma = 0.173$ K for the [CII] line, and $\sigma = 0.022$ K for the [CI](2-1) line. In all three cases, the noise of the average reference spectrum is more than 10 times lower than the typical noise of the map. The green line is the emission model constructed from the fitting of up to five independent Gaussians to the spectrum. I reproduce all observed emission above $\sim 2.5\sigma$ noise level. The quality of the model can be assessed from the residual spectra (red line) showing pure noise across the whole velocity range. All three models reproduce very well the emission contained in the average reference spectrum.

As a final check, I compared the average spectrum before and after adding the emission model to each individual spectrum. This is shown in Figure B.3 where the red line is the original average spectrum, the green line is the emission model, and the black line is the average spectrum after adding the model to each spectrum. The models of the [NII] and [CII] emission in the reference position recover all major absorption features shown in Figure B.1. In the case

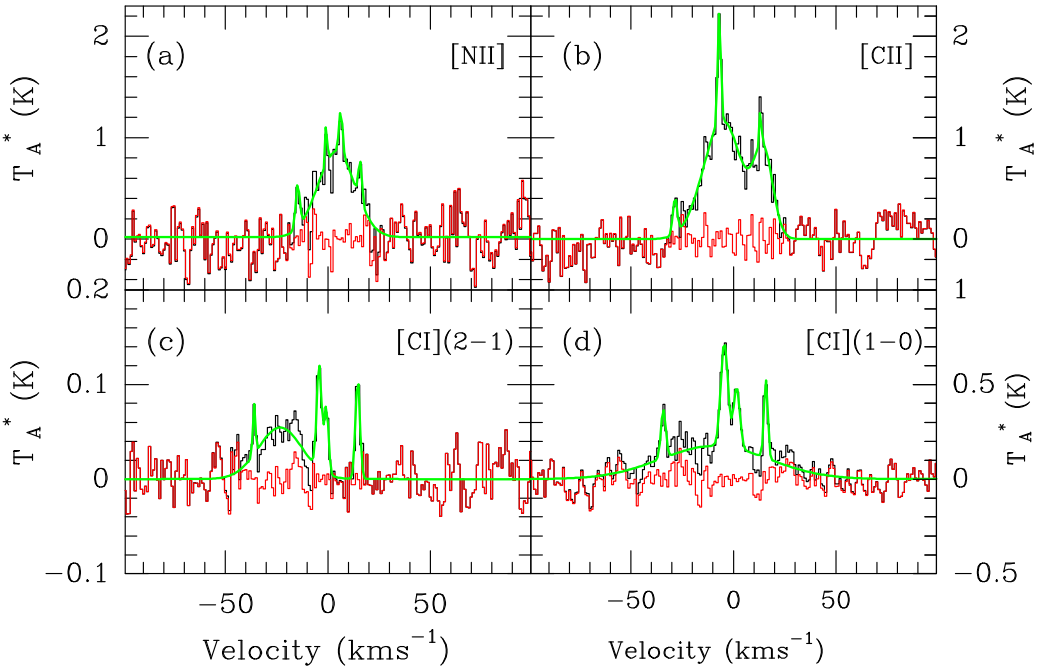

Figure. B.2: *Panels (a), (b), (c), and (d) show the reference position calibrated average spectrum (black), the fitted emission model (green), and the residual after the subtraction of the fitted model from the reference position emission (red), for the [NII], [CII], [CI](2-1), and [CI](1-0) observations, respectively. The emission in the reference position of the high frequency lines [NII] and [CII], and in the low frequency line [CI](1-0), is much brighter than the emission in the intermediate frequency line [CI](2-1).*

of the [NII] line, the emission in the reference position is much stronger than the average emission over the map, so the model shape stands out more clearly than in the other lines, as seen in the intensity peak around +5 kms^{-1}. In this way, I successfully recovered the emission artificially subtracted from the observed maps due to the contamination of the reference position for lines observed in the *"OTF Map With Load Chop And Position-Switch Reference"* observing mode.

B.1.4 The [CI](1-0) Reference Emission

In the case of the [CI](1-0) line, the *"OTF Map With Position-Switch Reference"* observing mode was used to carry out the observations. In this observing mode, given the stability of the receiver, no chop to the internal loads is needed before each ON read out. Instead, a load measurement were done after each OTF line. In principle, it is possible to obtain as many full calibrated reference spectra as there are OTF lines, using the load measurement and reference position integration closest in time. Nonetheless, this approach requires a major modification of the standard HIFI data reduction pipeline. I rather adopted a different and much

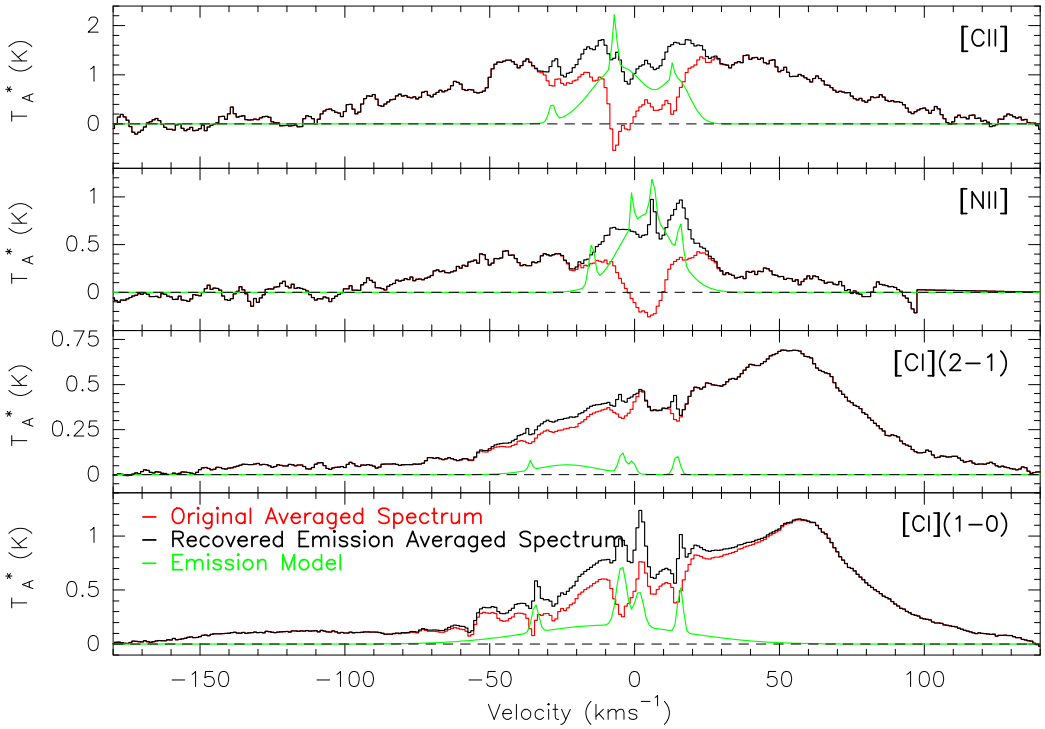

Figure. B.3: *From top to bottom, the [CII], [NII], and [CI](2-1), and [CI](1-0) average spectra before (red) and after (black) the addition of the reference position emission model (green) to each individual spectrum are shown. The absorption features due to the contamination of the reference position in all four lines are fully recovered.*

easier approach to check for emission contamination in the reference position.

In order to determine if the reference position was contaminated with emission in this case, I used the NANTEN2/SMART telescope to re-observed the Herschel-HIFI reference position. I observed a 30"×30" square map, centered at the reference position, with 10" spacing in both directions, making a total of nine spectra per map. Given the better spatial resolution of the 4 m NANTEN2/SMART telescope, I smoothed the map to a resolution equivalent to the beam size (FWHM) of the Herschel-HIFI telescope at this frequency (43.1"). The average spectrum of the map, shown in Figure B.2, panel (d), has a rms noise of σ = 0.064 K in the T_A^* antenna temperature scale, which is lower than the rms noise of all Herschel-HIFI spectra. The emission model (green line) reproduces very well the main features in the spectrum, yielding a residual spectrum (red line) consistent with pure noise.

In order to recover the emission artificially subtracted from the ON spectra, I added the modeled emission channel by channel to the Herschel-HIFI [CI](1-0) spectra. I assumed by this procedure that both telescopes measure the same

antenna temperatures in the T_A^* scale, assumption that is fully supported by the analysis in appendix A, where I have shown that, for integration velocity intervals $\Delta V \leq 6$ kms^{-1}, there is, on average, no difference between the measurements from both telescopes in this temperature scale. In Figure B.3, a comparison between the average spectrum, before and after recovering the emission artificially subtracted from the ON spectra, is shown. The remaining absorption features in the average spectrum are now truly due to foreground material along the l.o.s..

B.2 NANTEN2/SMART Observed Reference Position

The reference position of the NANTEN2/SMART CO(4-3) observations is $l = +0°.497$, $b = +0°.980$ in Galactic Coordinates. This position was selected based on the CO(2-1) maps of Sawada et al. (2001) of the Galactic Center. The reference position lays outside the lowest contour of the CO(2-1) emission, far enough from the Galactic Center, so that none of the eight pixels of the SMART array falls into regions where the CO(2-1) emission is significant. In Figure B.4, the average spectrum of the NANTEN2/SMART CO(4-3) emission shows a ~ 2 K absorption feature around -5 kms^{-1} and less deep absorption features at LSR velocities -55 kms^{-1} and -30 kms^{-1}. These absorption features are associated with the loci of the local, 3 kpc, and 4.5 kpc spiral arms, respectively (Oka et al., 1998; Jones et al., 2012). No absorption features below the 0 K level are present in the average spectrum.

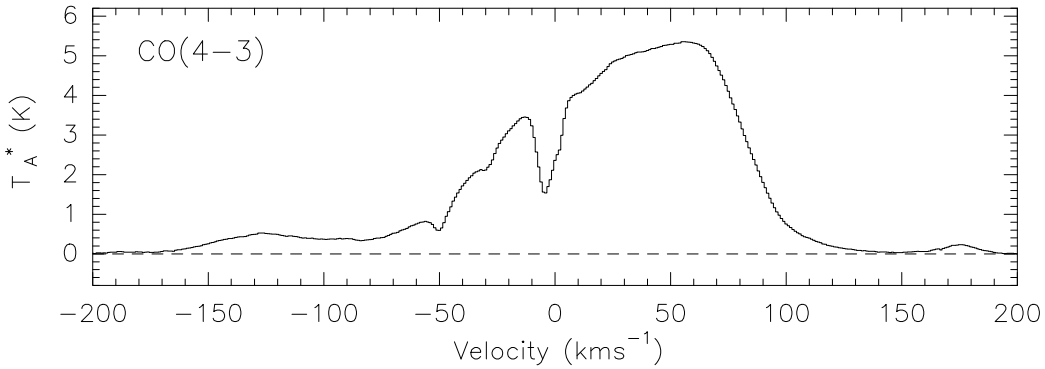

Figure. B.4: *NANTEN2/SMART CO(4-3) average spectrum after baseline subtraction. No absorption feature is present below the 0 K emission level. The absorption feature around -5 kms^{-1} is produced by foreground material along the l.o.s..*

In order to check the selected reference position (OFF) for emission contamination, I observed a 170"×340" map centered at the reference position of the

NANTEN2/SMART observations. Figure B.5 shows the results of the measurements with an array angle of 180°. As reference position for these observations I used another, further away OFF, at $l = -0°.068$, $b = +1°.385$. This second reference position was tested in previous observations showing no emission in the CO(4-3) line. Each panel in Figure B.5 shows the average OFF spectrum of a 85"×85" area in the measured map. The map coordinate system is shown for orientation. The dotted lines represent the $\pm 3\sigma$ noise level of each average OFF spectrum. The average CO(4-3) spectrum in Figure B.4 is also shown in each panel for comparison with the LSR velocities of the absorption features. The $T^*_{A,rms}$ noise level of the average OFF spectra is σ = 0.024 K, 0.020 K, 0.022 K, 0.025 K, 0.028 K, 0.023 K, 0.023 K, and 0.023 K, for the eight average positions on the map, from pixels 0 to 7, respectively.

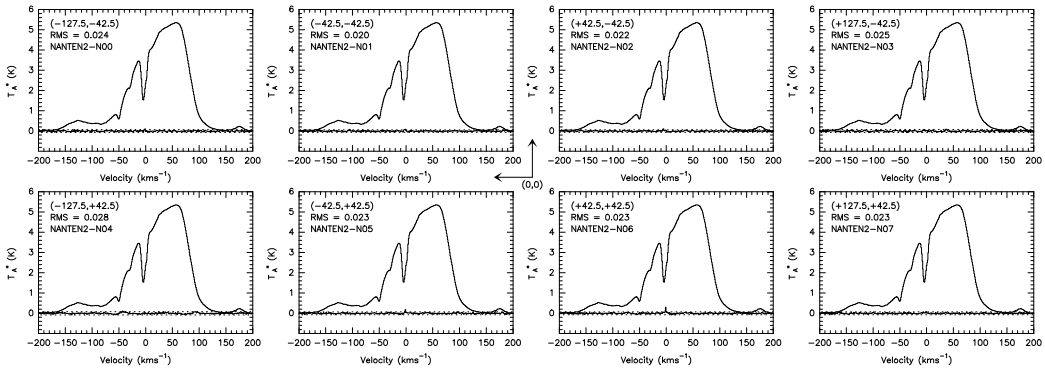

Figure. B.5: *Average spectra of the measured 170"×340" map containing the reference position used for the NANTEN2/SMART CO(4-3) observations. No emission is detected above the 3σ noise level.*

No emission was found above a 3σ significance level for most of the average OFF spectra except for pixels 5 and 6, where a very weak (< 0.3 K) and narrow ($\Delta V < 2$ kms^{-1}) emission feature at 0 kms^{-1} is seen. If all positions in the map are averaged, the noise level decreases to 0.01 K with no detection above the 3σ significance outside the ± 2 kms^{-1} range. Since The typical noise level of the NANTEN2/SMART CO(4-3) data is $\sim$ 0.14 K, the very weak emission in the reference position is negligible with respect to the typical noise of the data so I added no emission model to the ON spectra to correct for it.

Appendix C

Comparison Between AOS Backends and the new XFFTS Backends

During September of 2013, a major upgrade of the backend instrumentation of the NANTEN2/SMART telescope was performed. The AOSs (Horn et al., 1999) installed as backends were replaced by the new XFFTSs. Their broad 2.5 GHz instantaneous bandwidth (broader than the 1 GHz bandwidth of the AOSs) and high 88.5 KHz frequency resolution (higher than the 1.04 MHz of the AOSs) allow a better coverage of the very broad ($\sim$ 400 kms^{-1}) emission lines observed towards the Sgr A Complex, and a higher signal-to-noise ratio per measured spectrum after the LSR velocity resampling of the data to 1 kms^{-1}, as used in the present work for all observed lines. A full description of the XFFTSs performance and technical aspects is described by Klein et al. (2012, and references therein).

After the XFFTSs were operational, I performed [CI](1-0) observations around the peak emission within the Sgr A Complex to cross-check the measured antenna temperatures with both backends. The measured spectra are shown in Figure C.1. In the figure, all spectra share a common spectral and spatial resolution. **The measurements show that both spectrometers measure the same antenna temperatures within calibration errors**. The small differences in the peak antenna temperatures are due to slightly different baseline subtraction between both datasets. In this way, it is safe to combine the measured antenna temperatures obtained with both spectrometers and produce the final CO(4-3) dataset as described in Chapter 3.

The spatial extent covered by each spectrometer during the data acquisition campaign is divided as follows: with the AOSs as backends, the area between Galactic

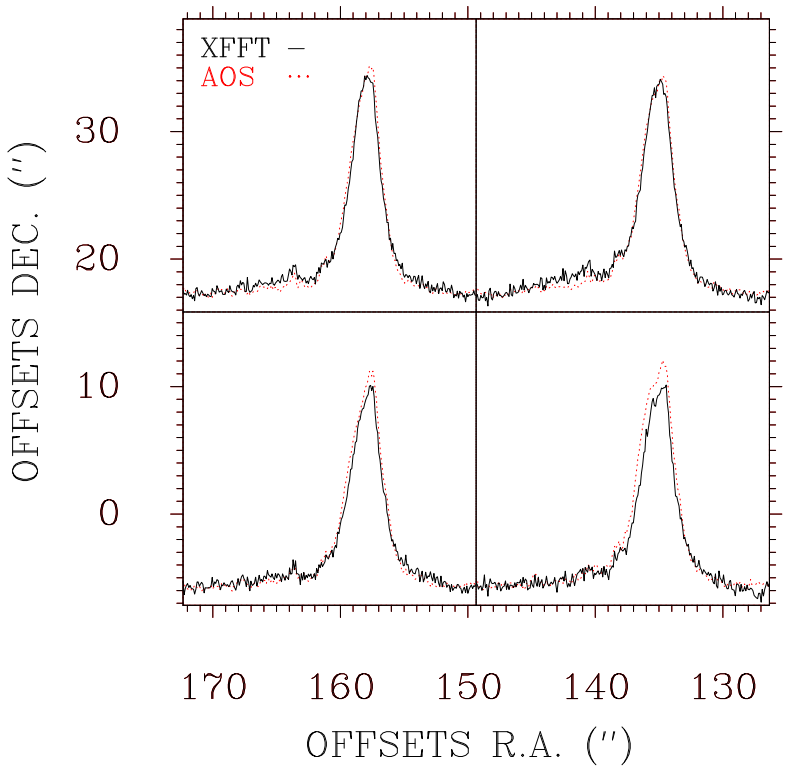

Figure. C.1: *Observations around the [CI](1-0) peak emission measured with the NANTEN2/SMART telescope using AOSs (dotted red lines) and the new XFFTSs (solid black line) as backends.*

longitude $l = \pm 0°.250$ and Galactic latitude from $b = -0°.180$ to $b = +0°.028$, was observed. After the swap to the XFFTSs, the region between Galactic longitude $l = -0°.153$ and $l = +0°.250$, and Galactic latitude $b = +0°.028$ and $b = +0°.125$, was observed.

Appendix D

Gaussian Fitting Results

In this Appendix, the results of the Gaussian (and high order Polynomial in some cases) fits performed to the spectra for the analyzed sources in the present work are shown. The Gaussian fits are performed in order to determine the radial velocity (V_{lsr}), velocity width ($\Delta V(FWHM)$), peak antenna temperature (T_{peak}), and total integrated intensity (I) in units of K kms^{-1} for each source. Usually, multiple Gaussians components are needed in order to properly reproduce the observed profiles, given the large velocity blending between sources along the l.o.s.. It can be argued that, in some cases, the observed spectra deviate from a single (or multiple) Gaussian profile(s). Such deviations can be due to several physical processes, for instance: absorption features along the l.o.s. due to foreground (spiral arms) and in-situ material (self-absorption due to large column densities), strong shocks affecting the velocity structure of the gas (specially likely in the very crowded velocity field of the GC), or the influence of the gravitational potential compressing/expanding the gas depending on their 3-D position in the GC gravitational potential. Nonetheless, Gaussian fits are still a good first-order approximation to determine the parameters previously mentioned. Individual cases where this does not apply are discussed in the text. In such cases, high order polynomials are used to obtain the total integrated intensity of the source.

Critical densities and upper energies levels (E_u) of the relevant species for the present work are shown in Table D.1. They were calculated using Equation 2.54, neglecting radiative trapping and induced emission depopulation ($n_\gamma \ll 1$ for frequencies higher than the 21 cm atomic hydrogen transition). The collisional rates coefficients γ_{ul} and Einstein spontaneous emission coefficients A_{ul} were taken from the LAMBDA (Schöier et al. (2005), http://home.strw.leidenuniv.nl/~moldata/) and CDMS[1] (Müller et al. (2001, 2005), http://www.astro.uni-koeln.de/cdms) databases.

[1]The Cologne Database for Molecular Spectroscopy

Line	E_u (K)	T_{kin} 50 (K)	100 (K)	200 (K)	Coll. Partners
$H^{13}CO^+$(1-0)	4.2	1.9E+05	2.1E+05	1.8E+05	H_2
HCO^+(1-0)	4.3	2.1E+05	2.4E+05	1.9E+05	H_2
^{13}CO(1-0)	5.3	9.5E+02	9.0E+02	8.7E+02	p-H_2, o-H_2
CO(1-0)	5.5	1.1E+03	1.0E+03	1.0E+03	p-H_2, o-H_2
CO(4-3)	55.3	4.0E+05	3.0E+05	2.3E+05	p-H_2, o-H_2
[CI](1-0)	23.6	6.9E+01	5.8E+01	4.3E+01	H, H^+, e^-, He, p-H_2, o-H_2
[CI](2-1)	62.5	4.0E+02	3.2E+02	2.3E+02	H, H^+, e^-, He, p-H_2, o-H_2
[CII]	91.2	9.6E+02	9.1E+02	8.5E+02	p-H_2, o-H_2, H, e^-

Table. D.1: *Critical densities for relevant species in the present work for characteristic kinetic temperatures (T_{kin}) in the GC. Radiative trapping and induced emission are neglected in the calculation. The critical densities of the [NII] line are similar to those of [CII] (Abel, 2006).*

D.1 Arched Filaments Positions

Gaussian(s) and high order polynomial fit results for selected positions in the Arches Filaments in Chapter 5: E1, E2-N, E2-S, G0.10+0.02, G0.07+0.04, P1, P2, W1, and W2. For each measured spectrum two plots are shown: the left panel shows the Gaussian(s) component(s) containing the source (solid red line), other Gaussian components necessary for the fit (black dashed lines), and the total Gaussian fit (blue solid line). In some cases, the fitted profile of other species (pink solid line) is shown for comparison; the right panel shows a high order polynomial fit, where vertical dotted lines indicate the radial velocity integration range from which the total integrated intensity was calculated. In both panels, the black dotted lines represent the residual from the fits while the vertical dashed lines indicate the position of spiral arms along the l.o.s.. The boxes at the bottom of each spectrum indicate the region excluded for the fitting procedure.

D.2 High Velocity Gas CO(4-3) Positions

Gaussian fit results for HVG sources in Chapter 6. In each spectrum, the Gaussian component containing the source (solid red line), other Gaussian components necessary for the fit (black dashed lines), and the total Gaussian fit (blue solid line) are displayed. In some cases, the fitted profile of other species (pink solid line) is shown for comparison. The black dotted lines represent the residual from the Gaussian fit. Vertical dashed lines indicate the position of spiral arms along the l.o.s. while the box at the bottom of each spectrum indicates the region

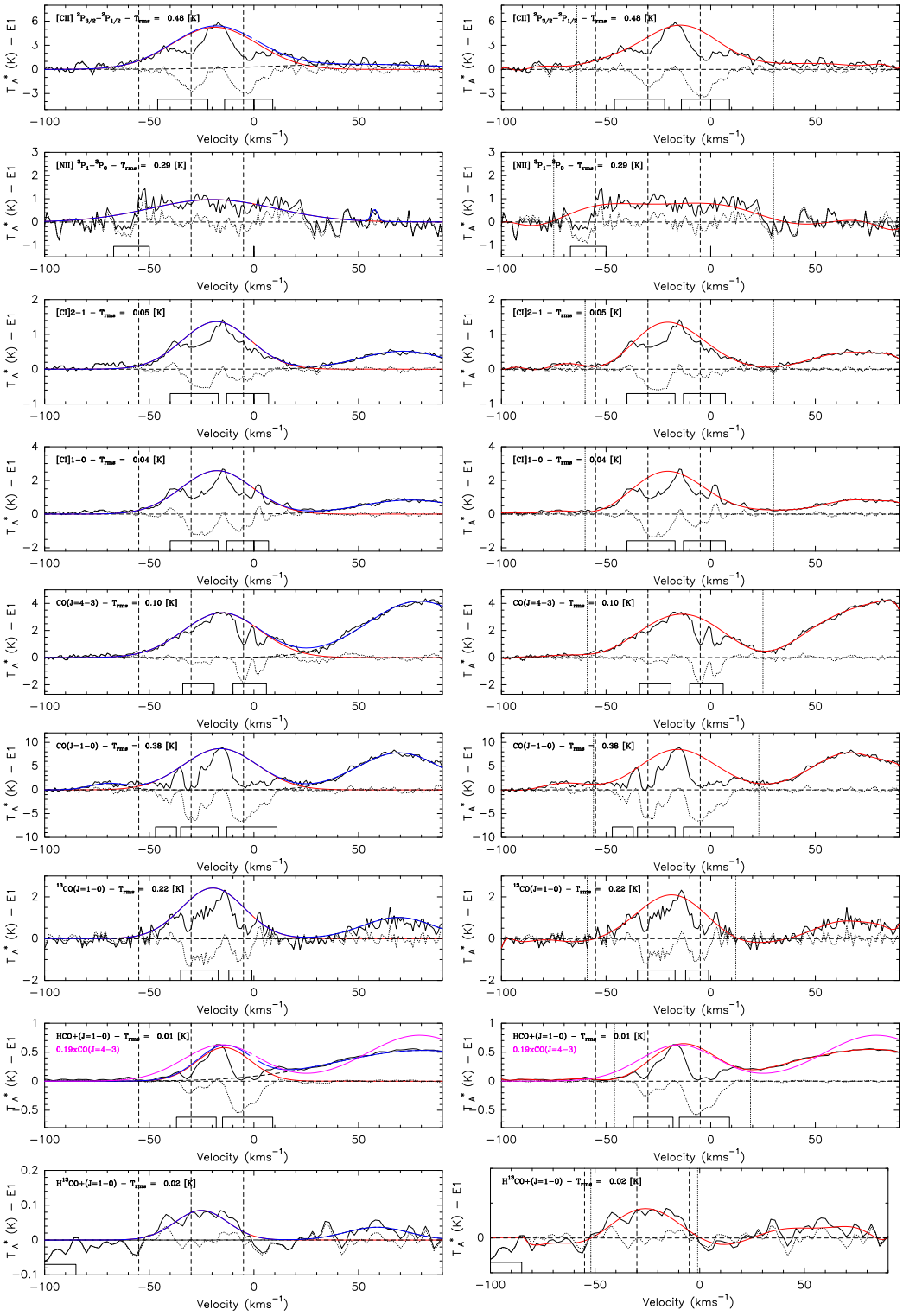

Figure. D.1: *Gaussian (left) and polinomial (right) fit results for position E1.*

excluded for the fitting procedure.

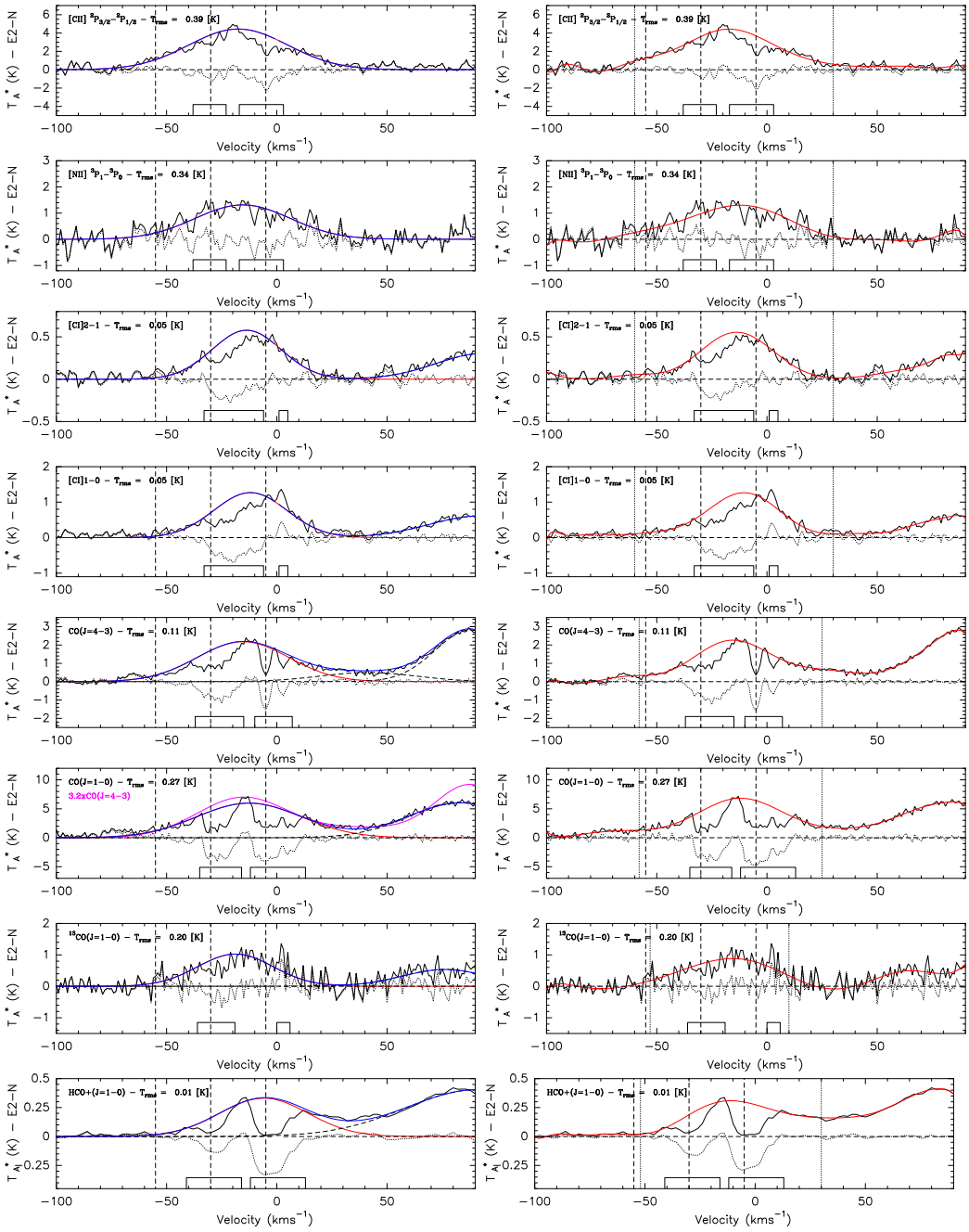

Figure. D.2: *Gaussian (left) and polinomial (right) fit results for position E2-N.*

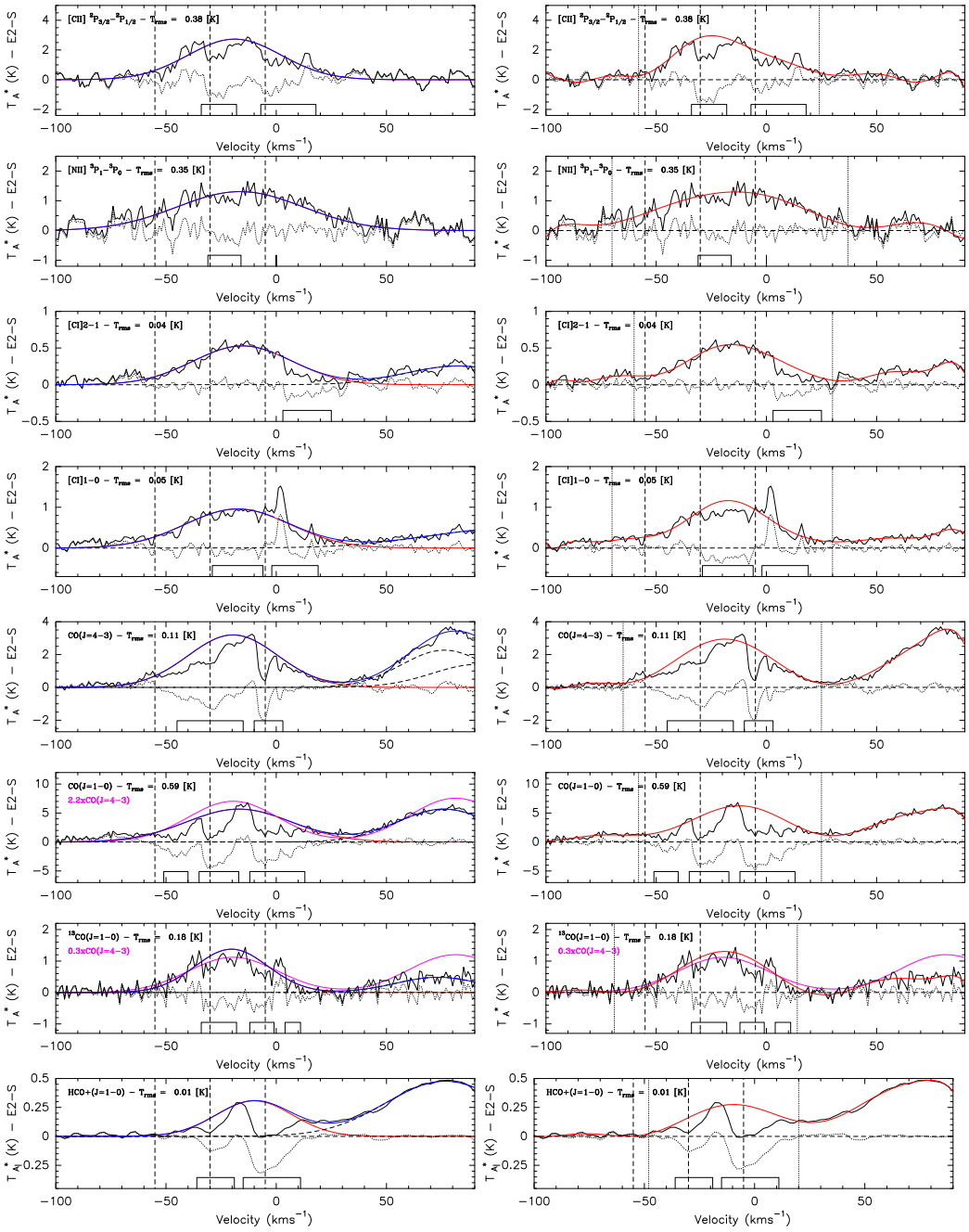

Figure. D.3: *Gaussian (left) and polinomial (right) fit results for position E2-S.*

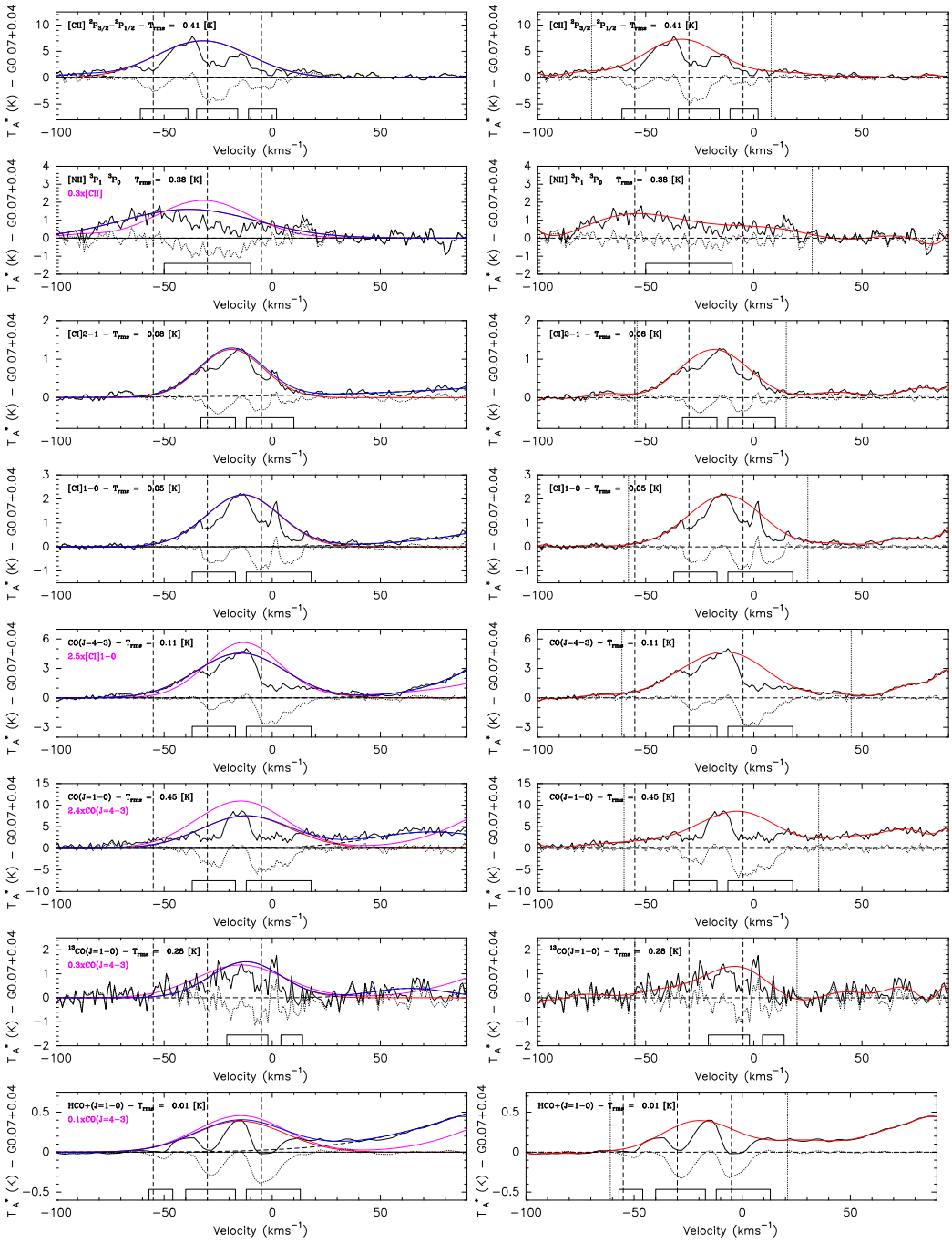

Figure. D.4: *Gaussian (left) and polinomial (right) fit results for position G0.07+0.04.*

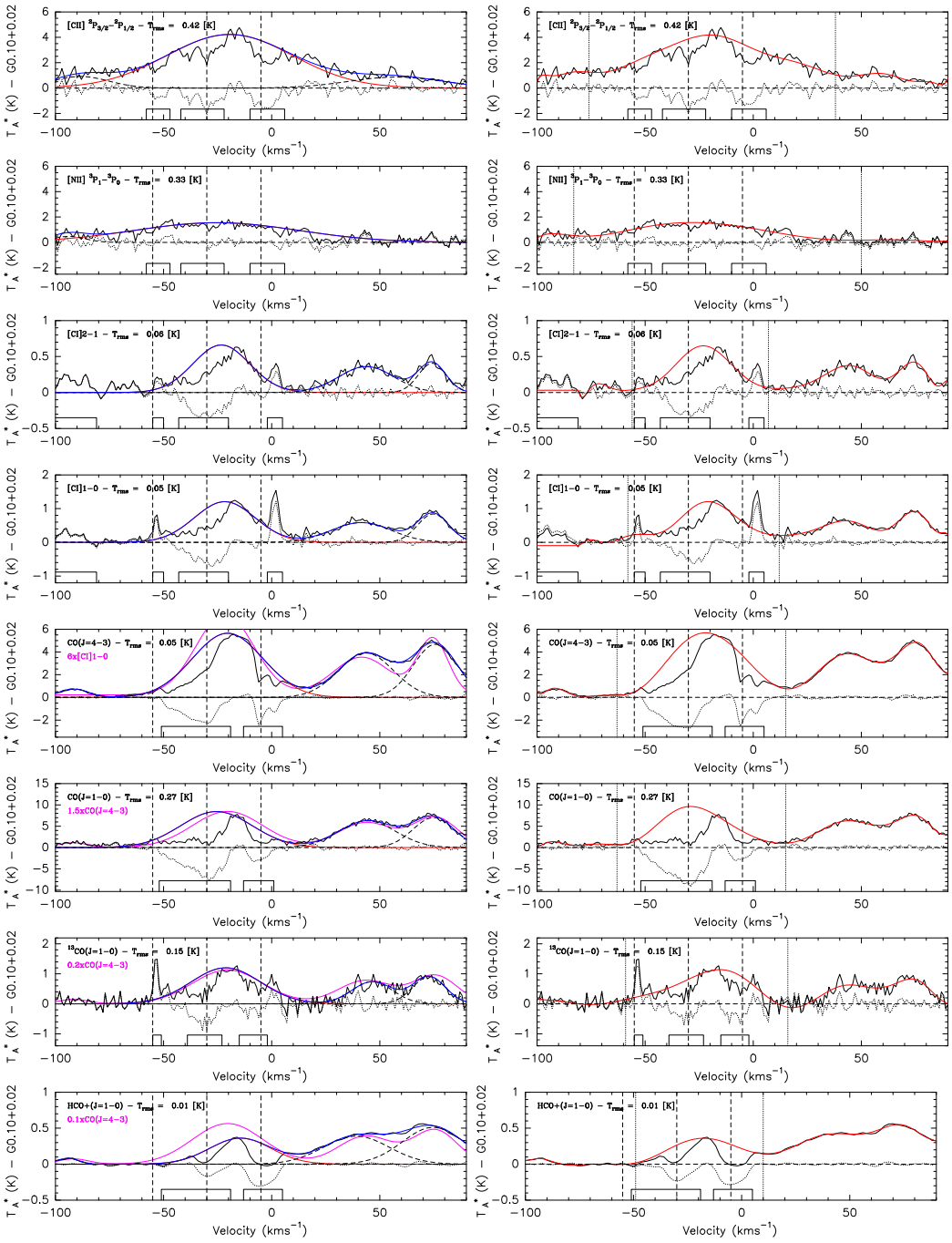

Figure. D.5: *Gaussian (left) and polinomial (right) fit results for position G0.10+0.02.*

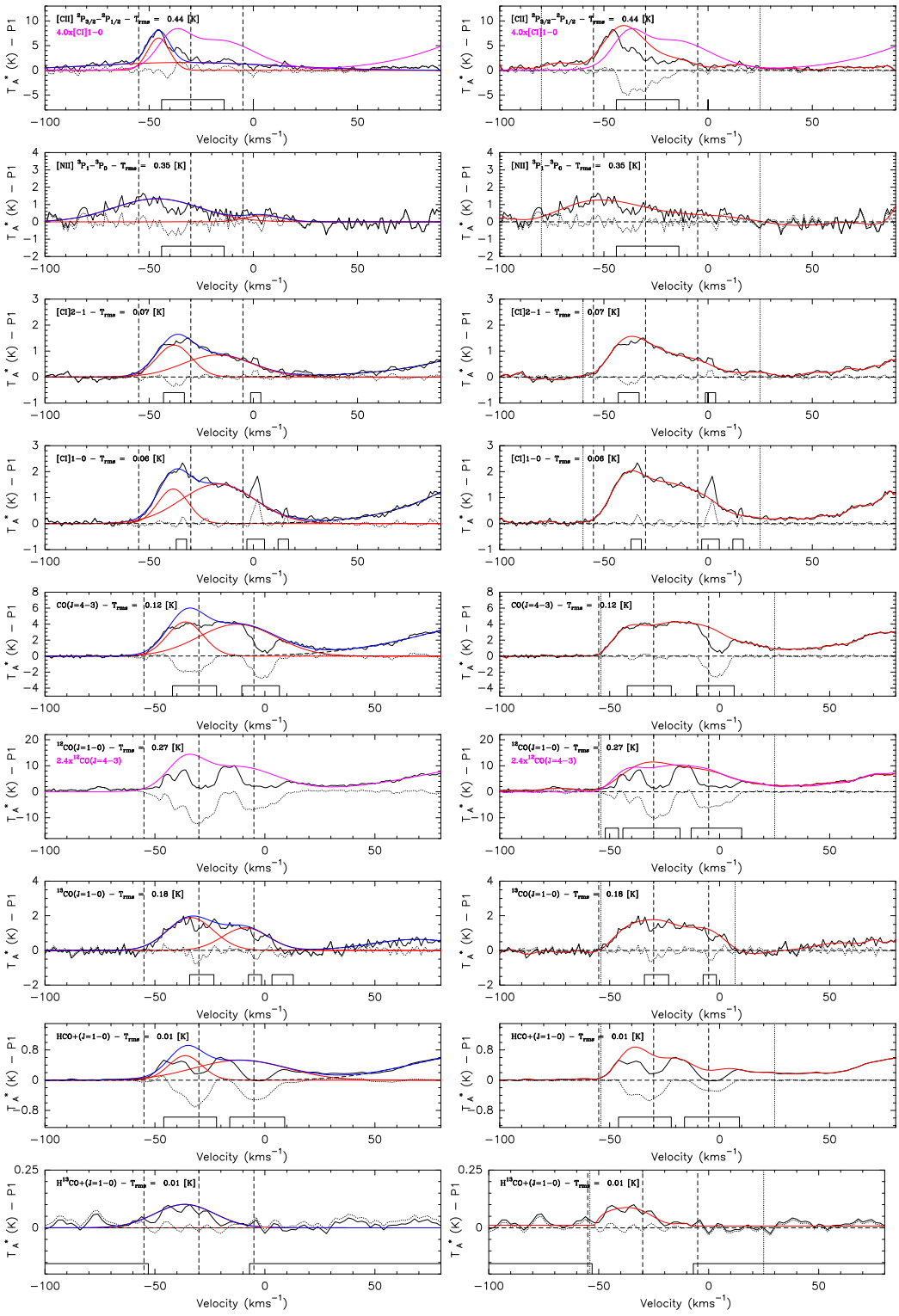

Figure. D.6: *Gaussian (left) and polinomial (right) fit results for position P1.*

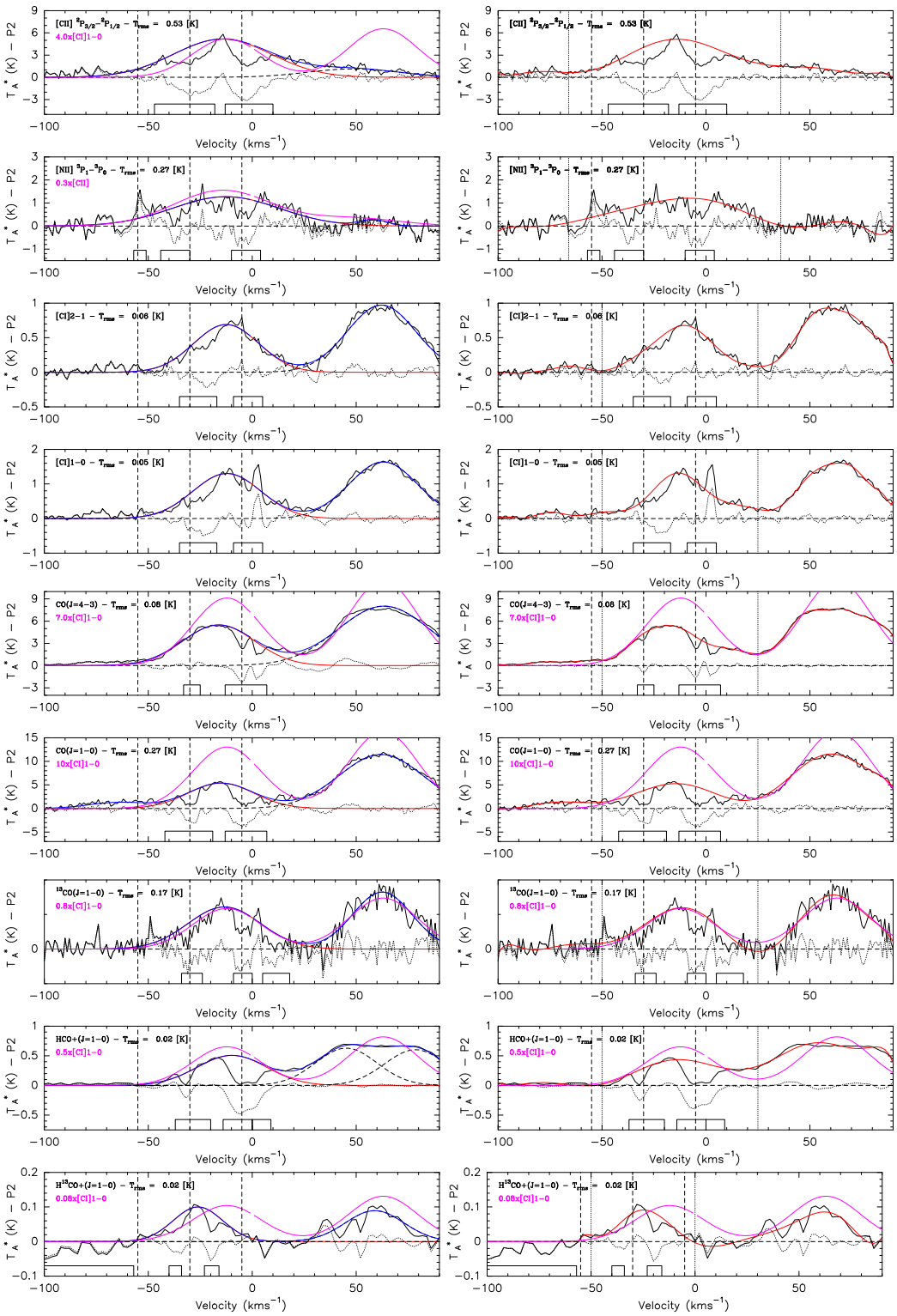

Figure. D.7: *Gaussian (left) and polinomial (right) fit results for position P2.*

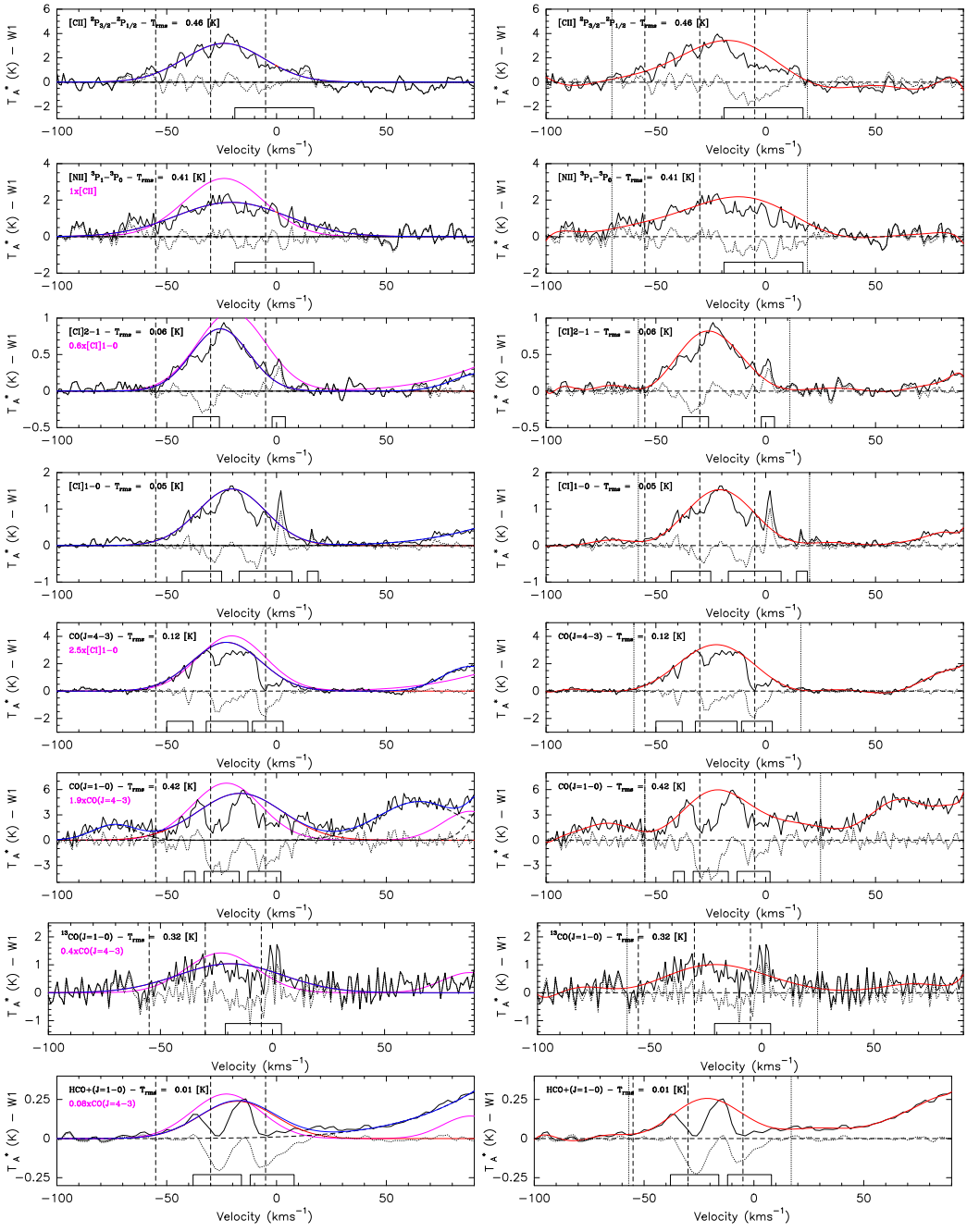

Figure. D.8: *Gaussian (left) and polinomial (right) fit results for position W1.*

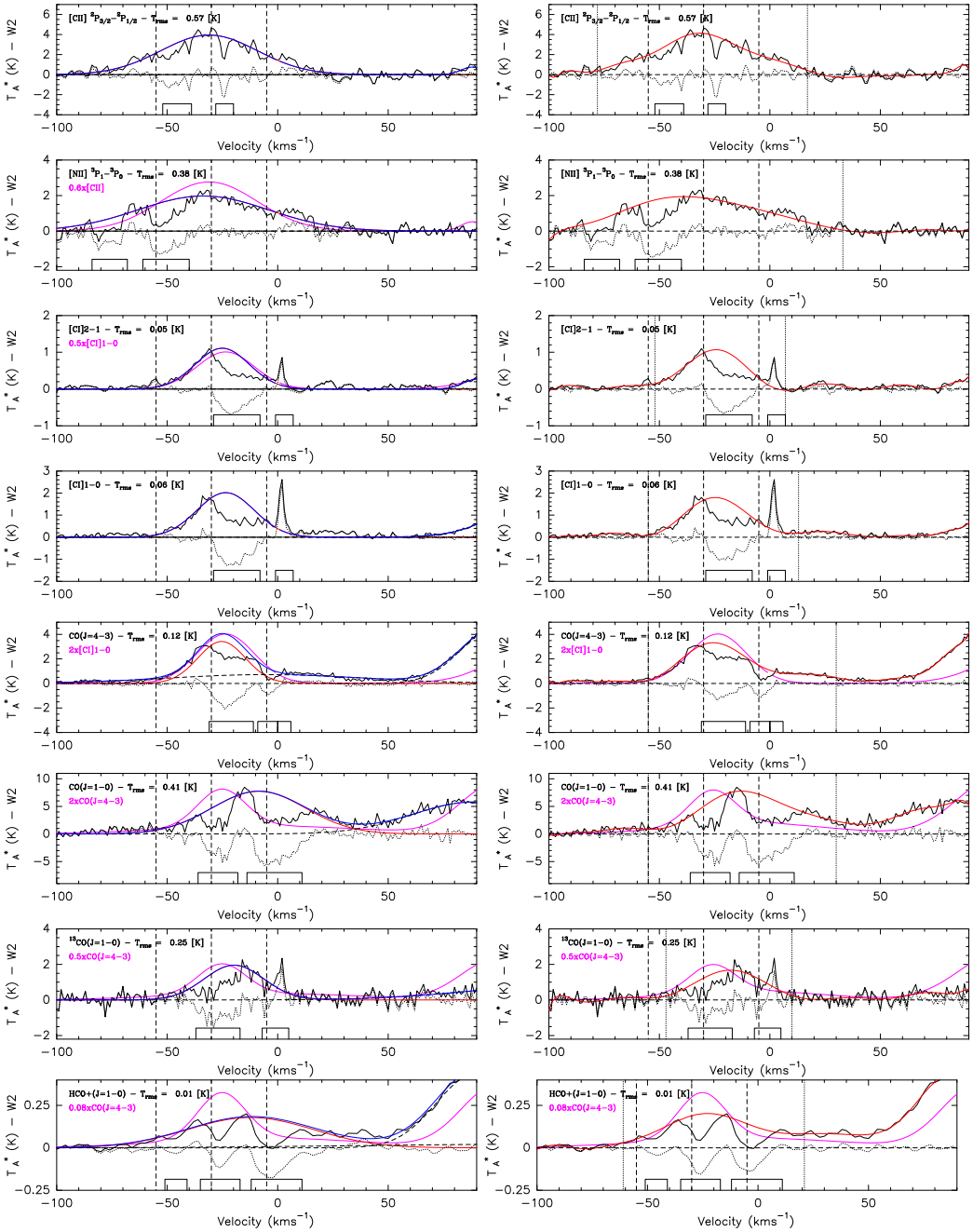

Figure. D.9: *Gaussian (left) and polinomial (right) fit results for position W2.*

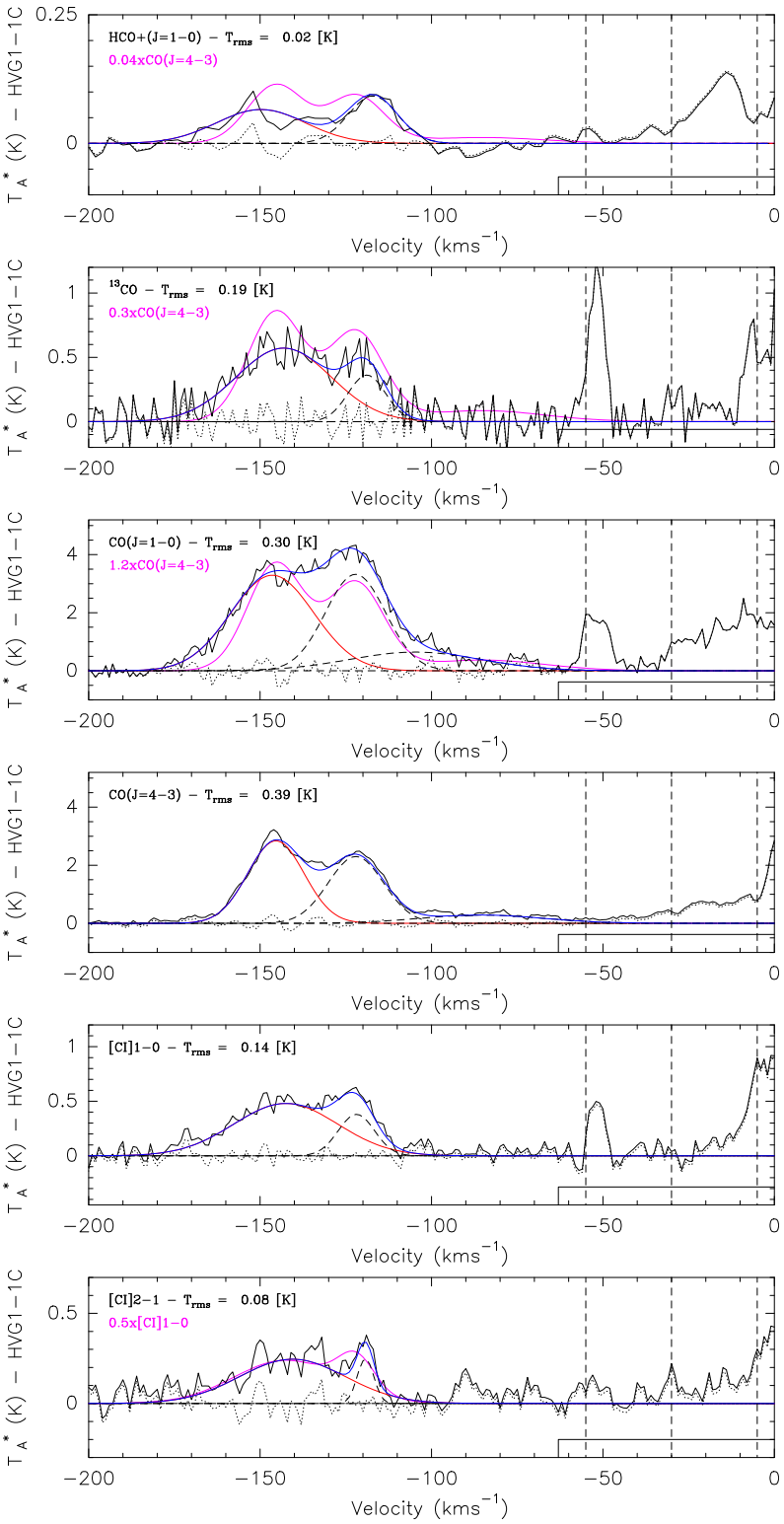

Figure. D.10: *Gaussian fit results for HVG1-1C.*

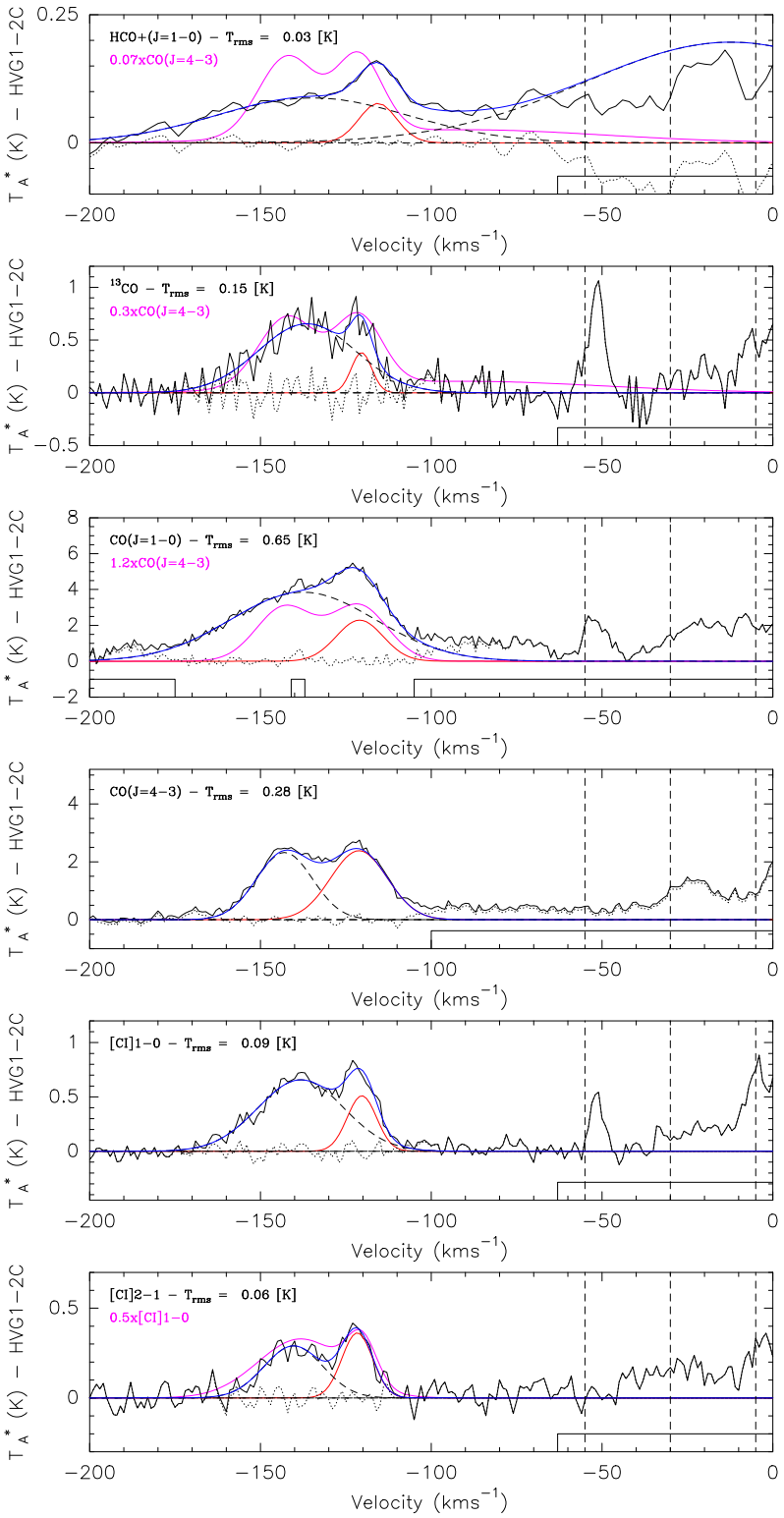

Figure. D.11: *Gaussian fit results for HVG1-2C.*

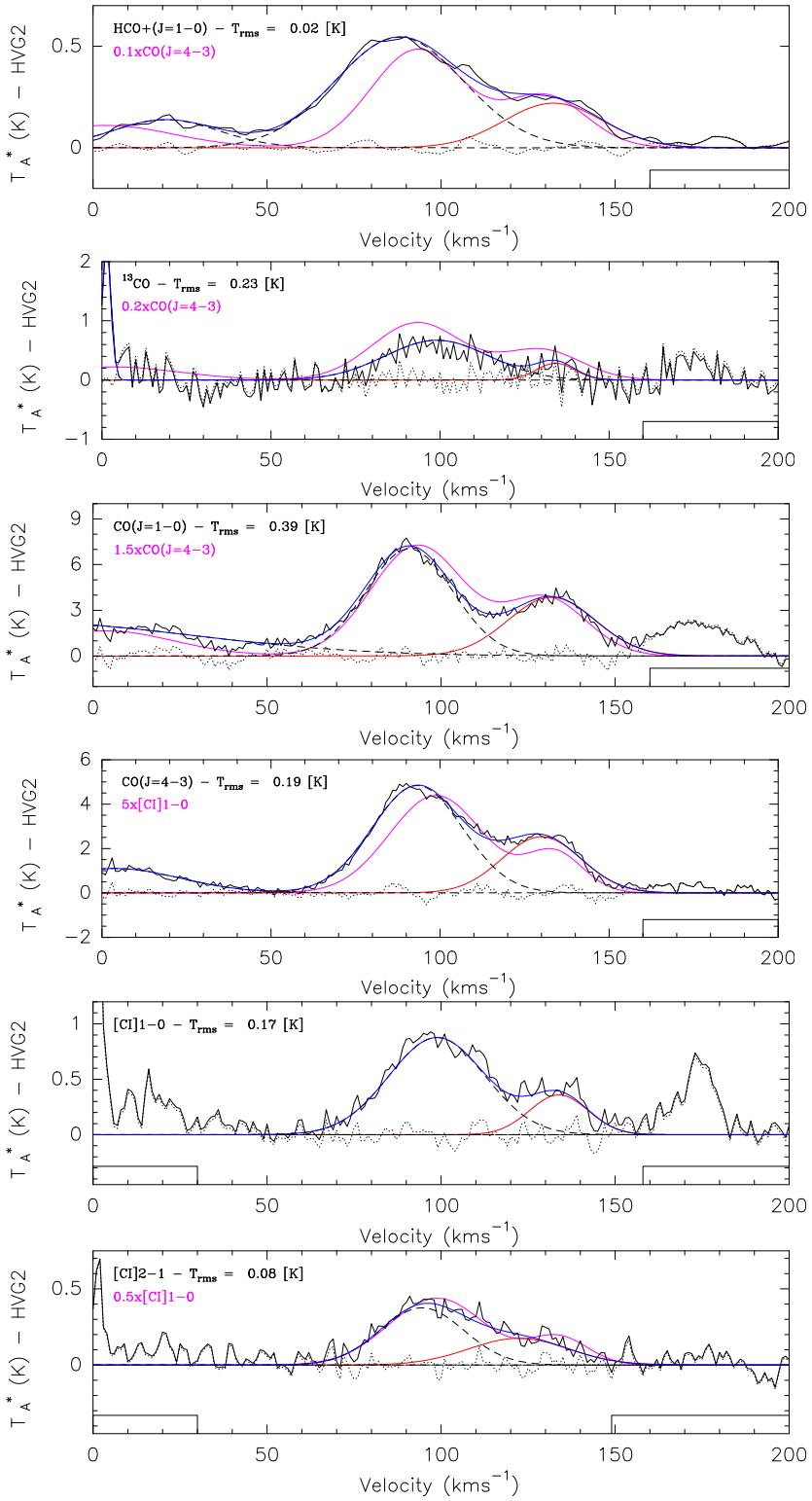

Figure. D.12: *Gaussian fit results for HVG2.*

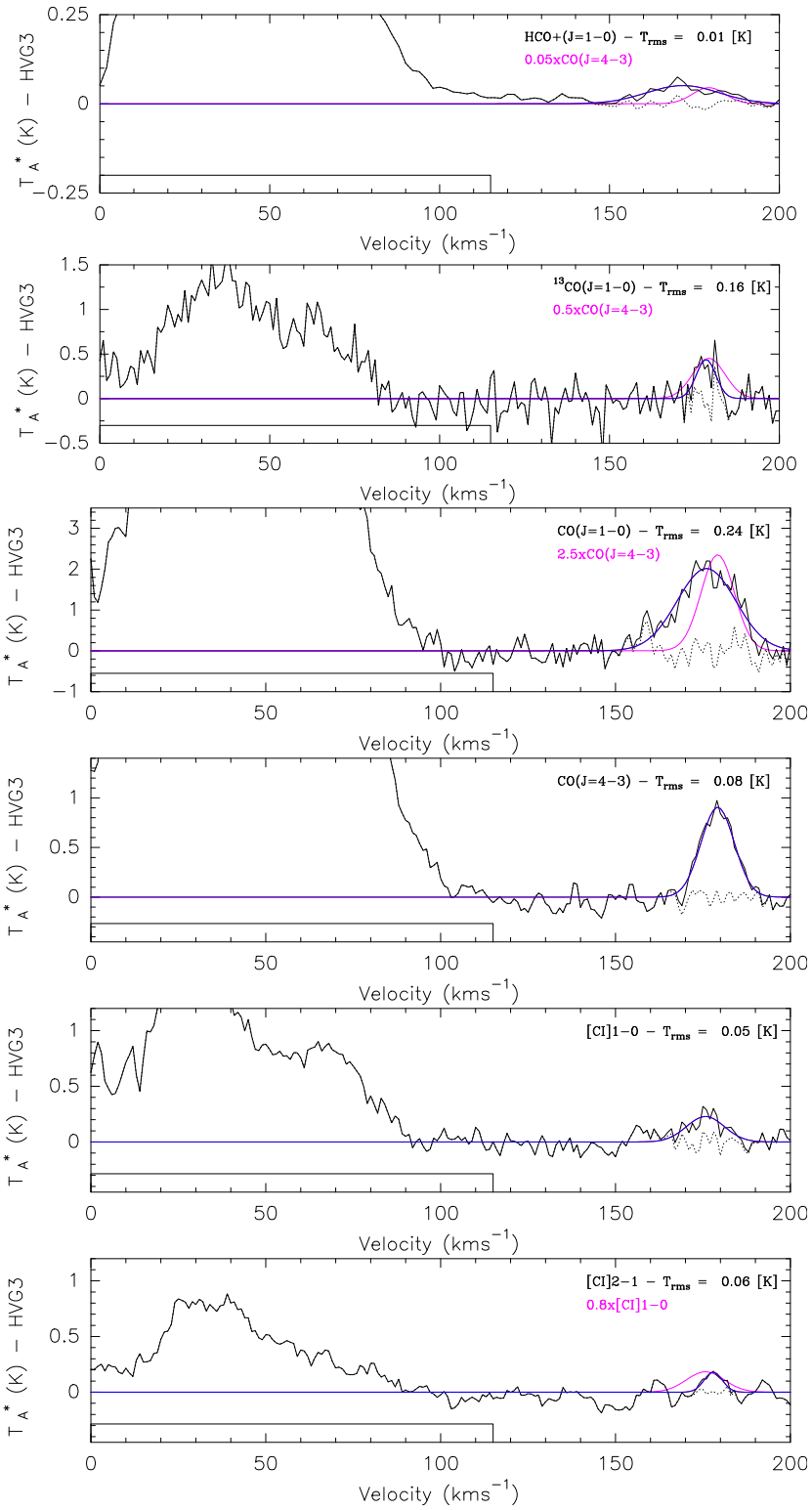

Figure. D.13: *Gaussian fit results for HVG3.*

Appendix E

RADEX Results

In this Appendix, the results of the non-LTE RADEX models for the HVG clouds are shown. Each plot contains the column density N of the observed species as a function of H_2 volume densities n(H_2), for five different kinetic temperatures (T_{kin}): 50 K, 100 K, 200, K, 300 K, and 500 K. Solid black lines represent the measured peak antenna temperatures in Table 6.2, while the gray dashed area accounts for the uncertainty in T_{peak} given by the $T^*_{A,rms}$ values. The dashed gray area spans between $T_{peak} + T^*_{A,rms}$ and $T_{peak} - T^*_{A,rms}$. For carbon and carbon monoxide observations, where two lines have been observed, the blue and red circles show the grid points of the models. Dashed lines show the solutions (intersection of two lines) for each species. In the cases where there is only one transition available (^{13}CO(1-0) and HCO^+(1-0)), the solutions in column densities are obtained from the volume densities solutions of the carbon monoxide observations. The filling factor f is assumed to be 1 for all lines. The impact of different filling factors on the solutions for N and n(H_2) are discussed in the next Section E.1.

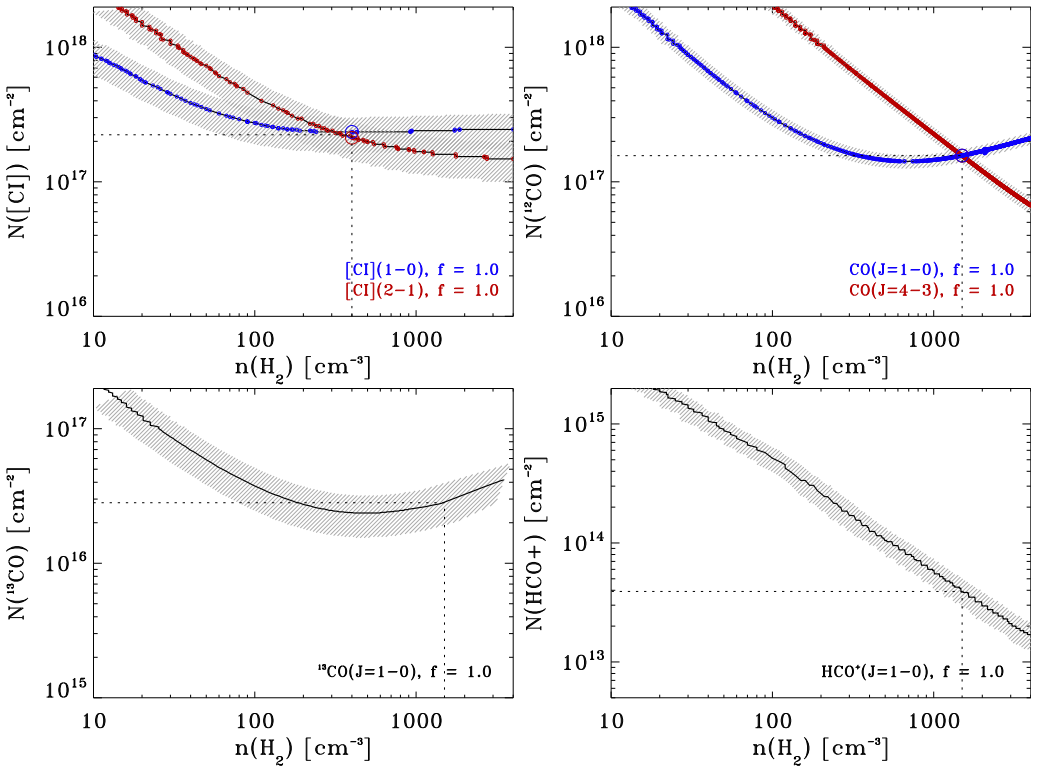

Figure. E.1: *HVG1-1C: RADEX Results for 50 K kinetic temperature.*

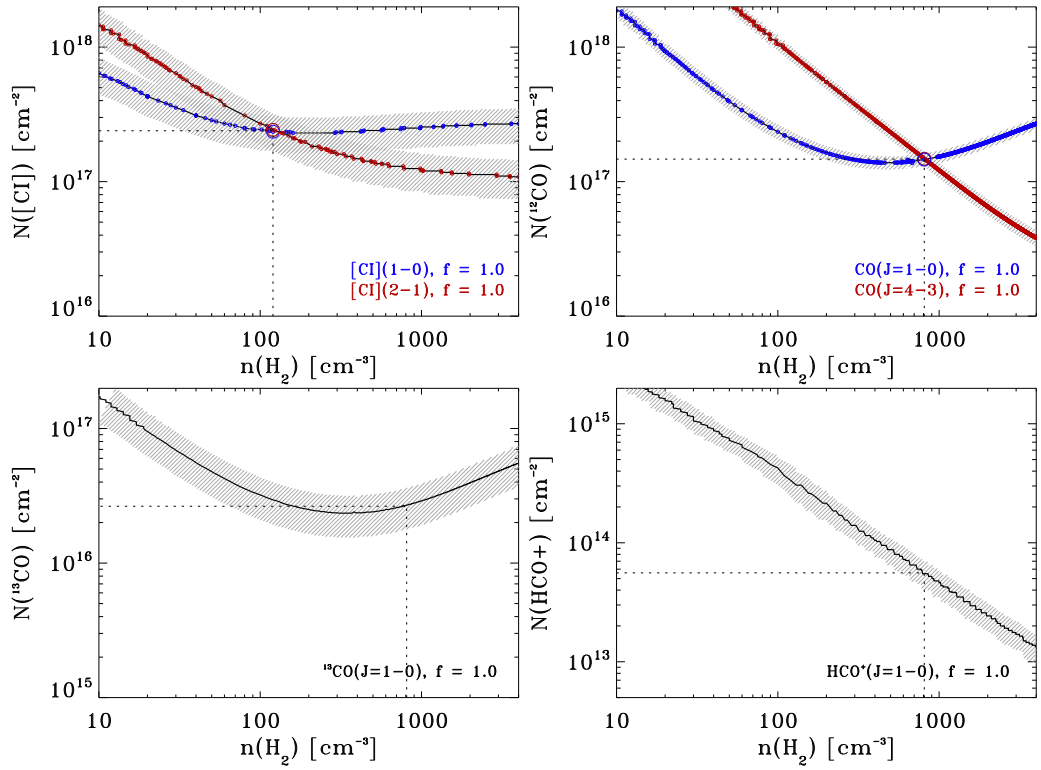

Figure. E.2: *HVG1-1C: RADEX Results for 100 K kinetic temperature.*

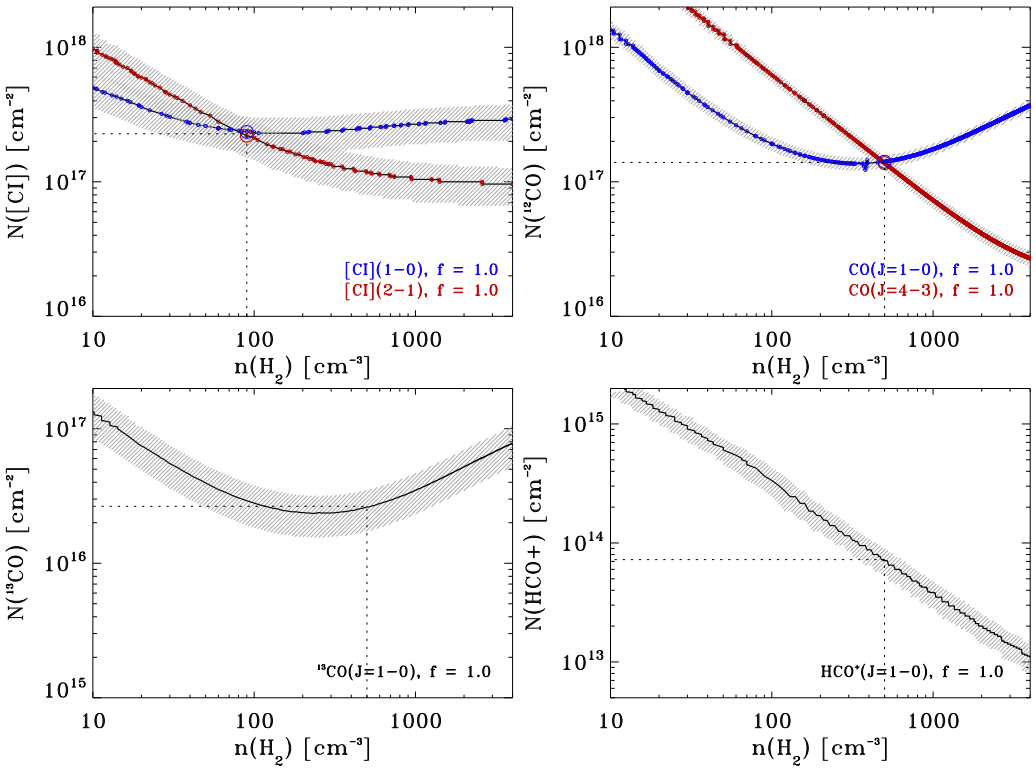

Figure. E.3: *HVG1-1C: RADEX Results for 200 K kinetic temperature.*

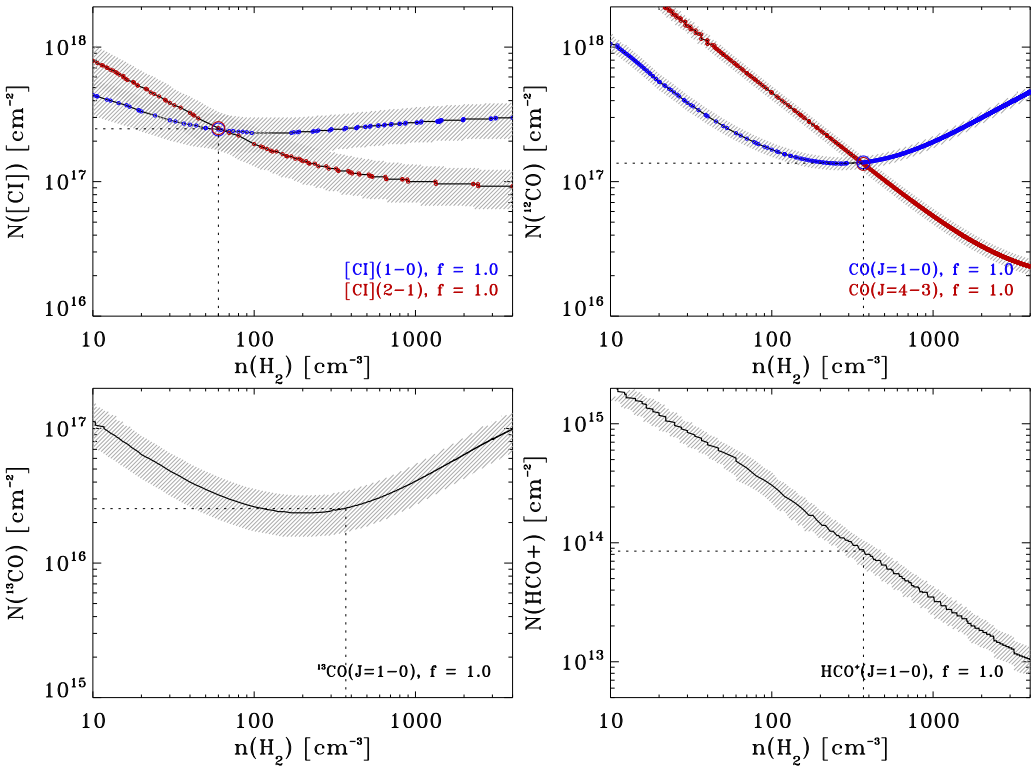

Figure. E.4: *HVG1-1C: RADEX Results for 300 K kinetic temperature.*

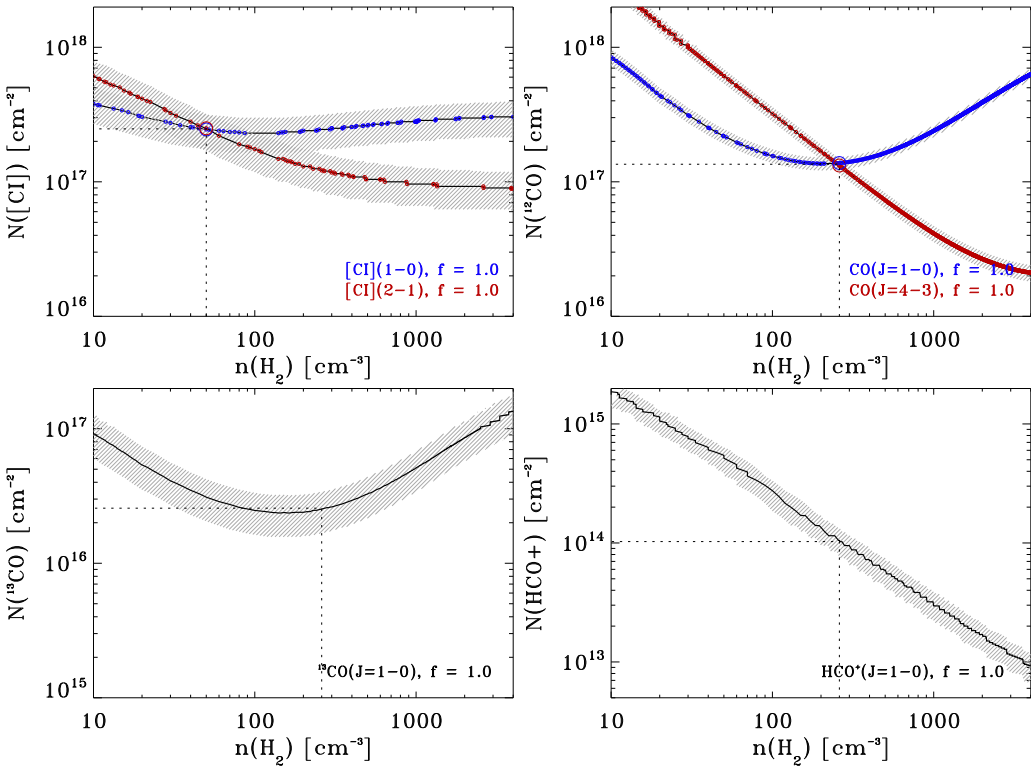

Figure. E.5: *HVG1-1C: RADEX Results for 500 K kinetic temperature.*

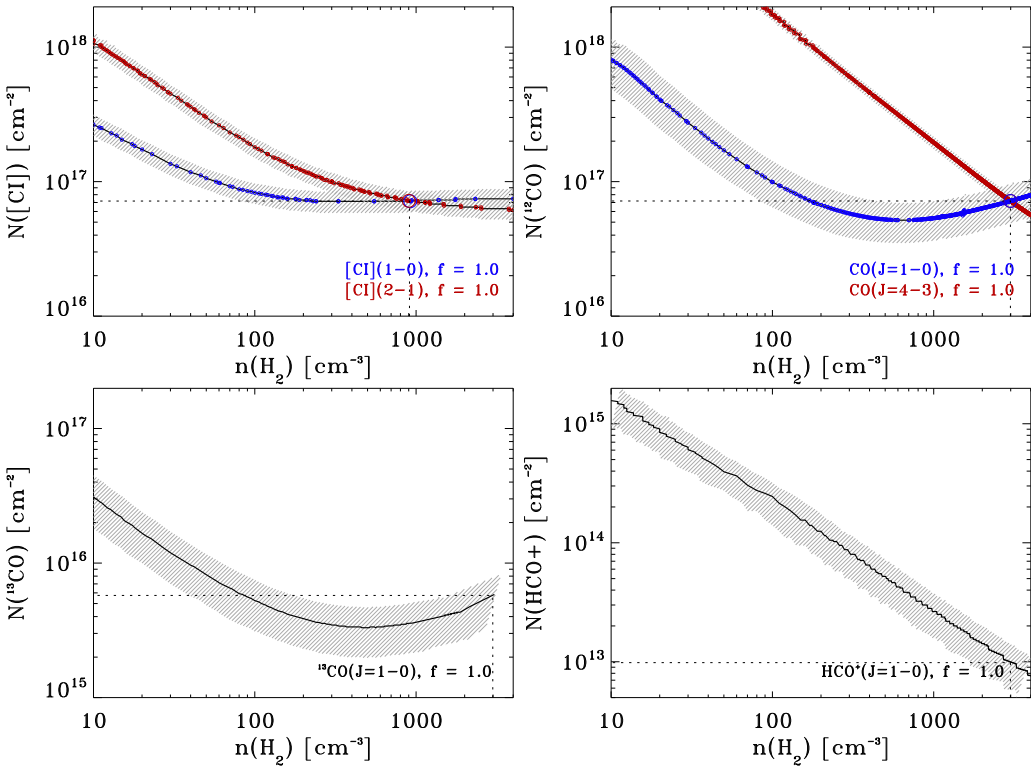

Figure. E.6: *HVG1-2C: RADEX Results for 50 K kinetic temperature.*

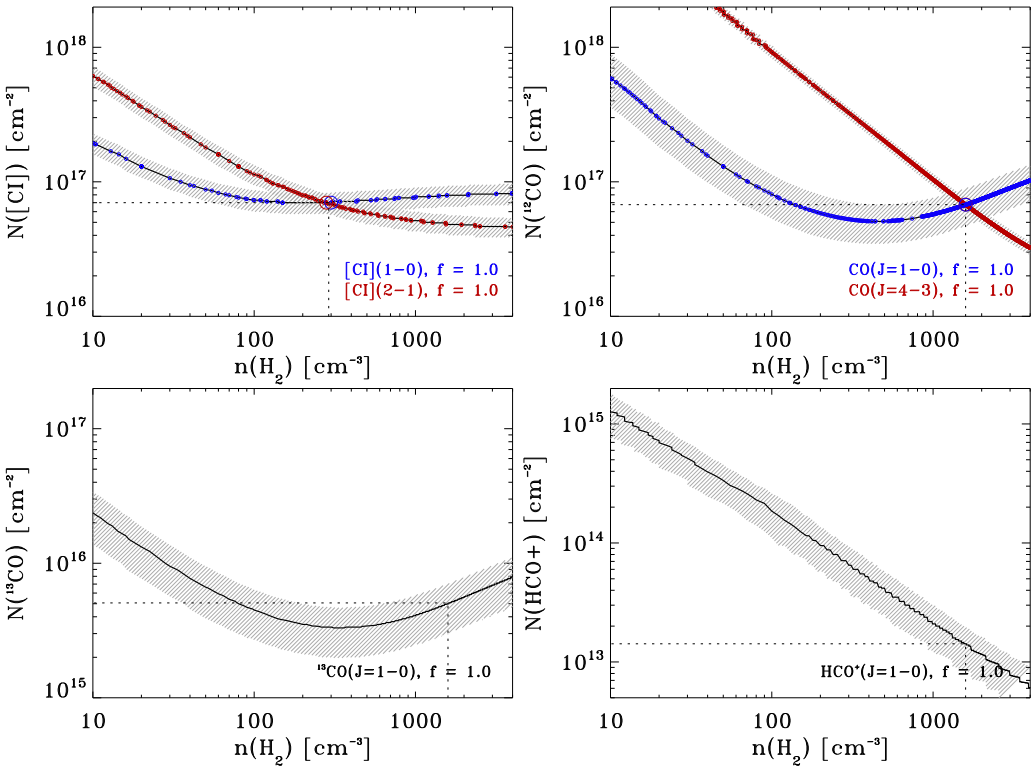

Figure. E.7: *HVG1-2C: RADEX Results for 100 K kinetic temperature.*

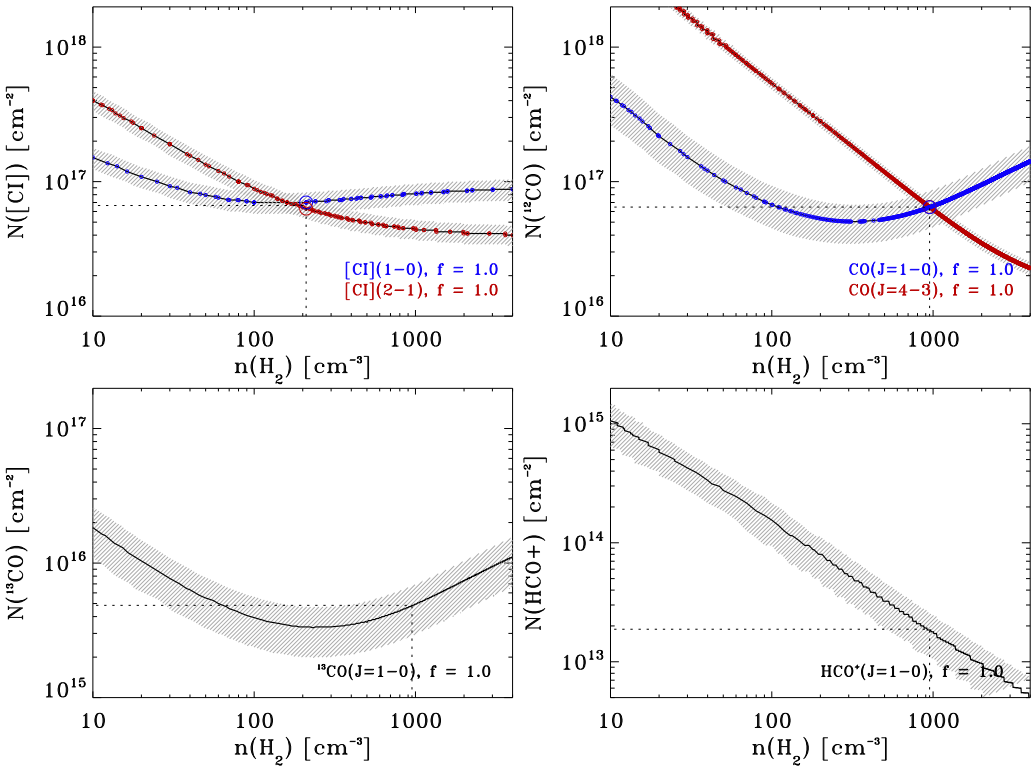

Figure. E.8: *HVG1-2C: RADEX Results for 200 K kinetic temperature.*

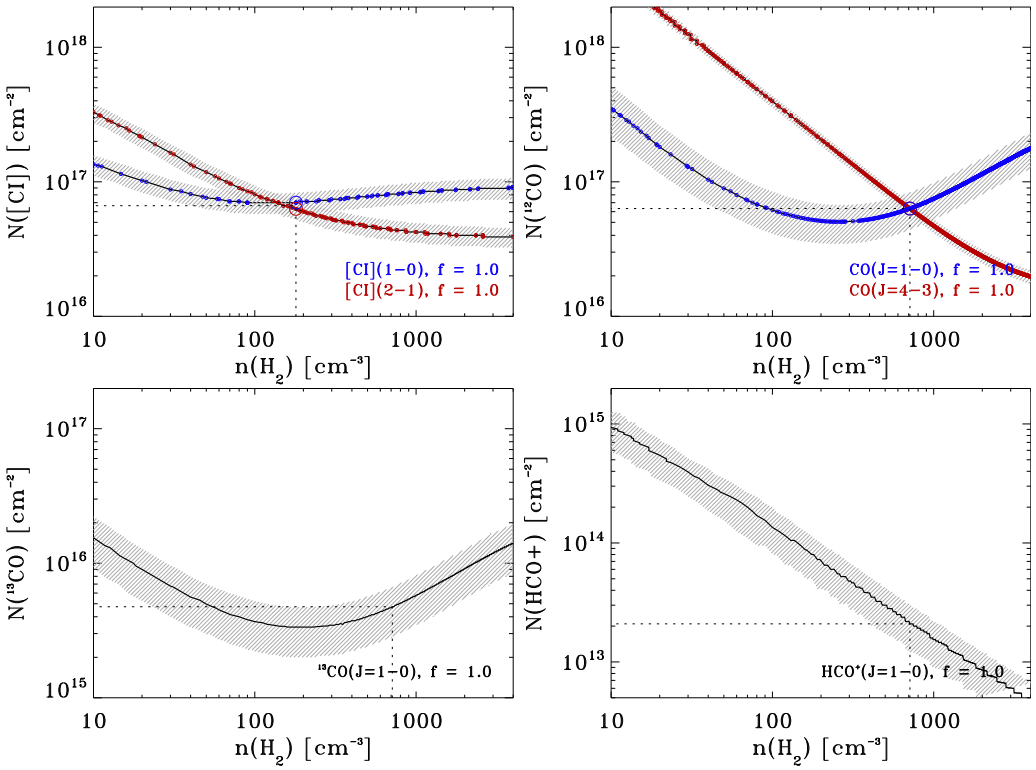

Figure. E.9: *HVG1-2C: RADEX Results for 300 K kinetic temperature.*

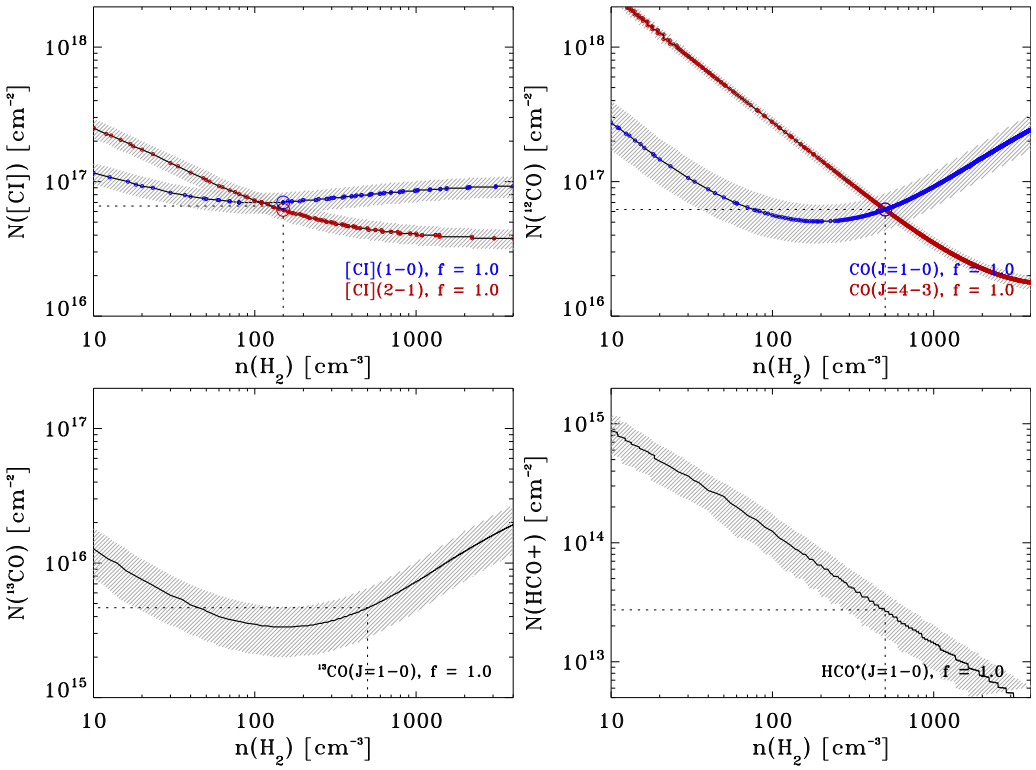

Figure. E.10: *HVG1-2C: RADEX Results for 500 K kinetic temperature.*

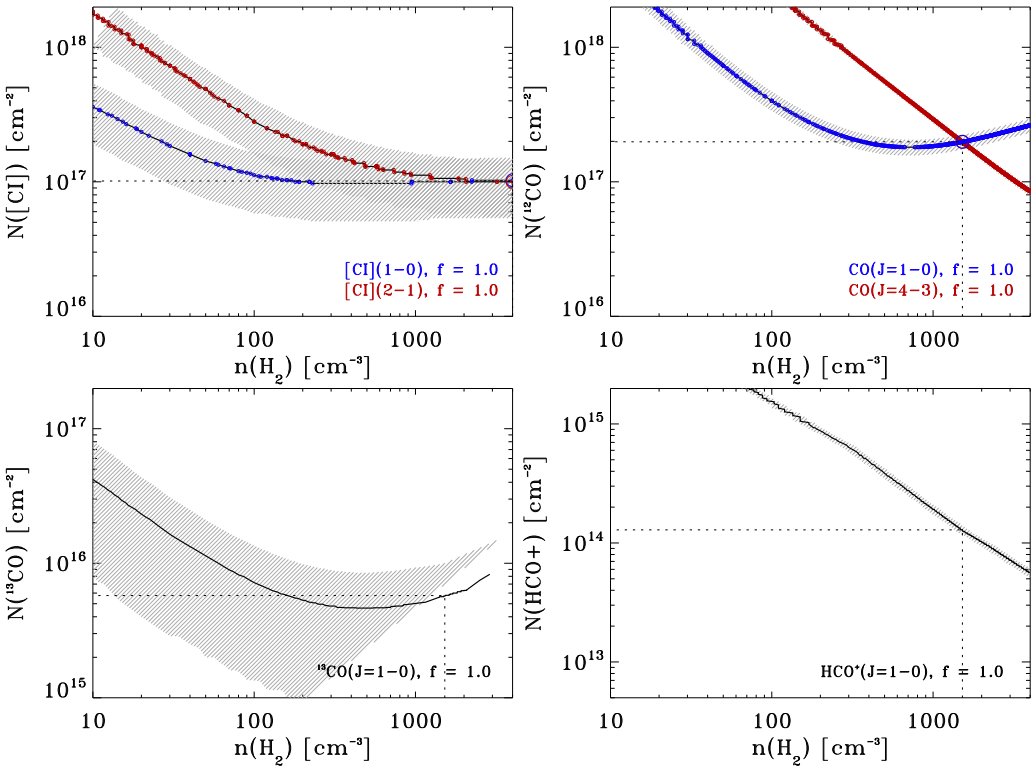

Figure. E.11: *HVG2: RADEX Results for 50 K kinetic temperature.*

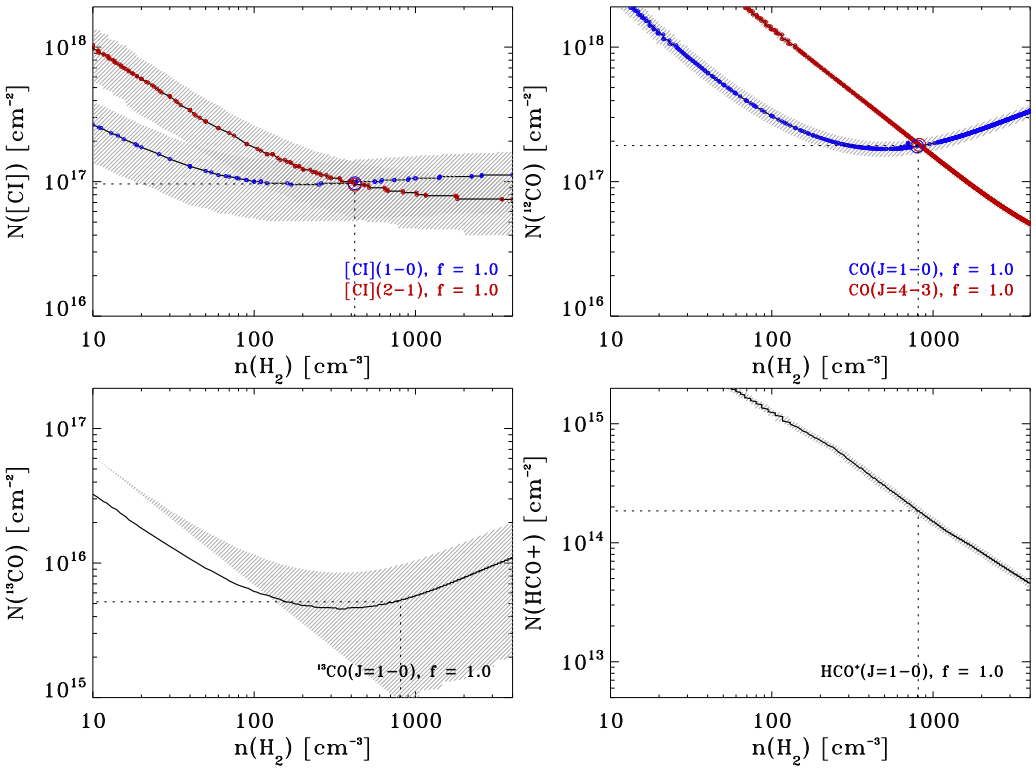

Figure. E.12: *HVG2: RADEX Results for 100 K kinetic temperature.*

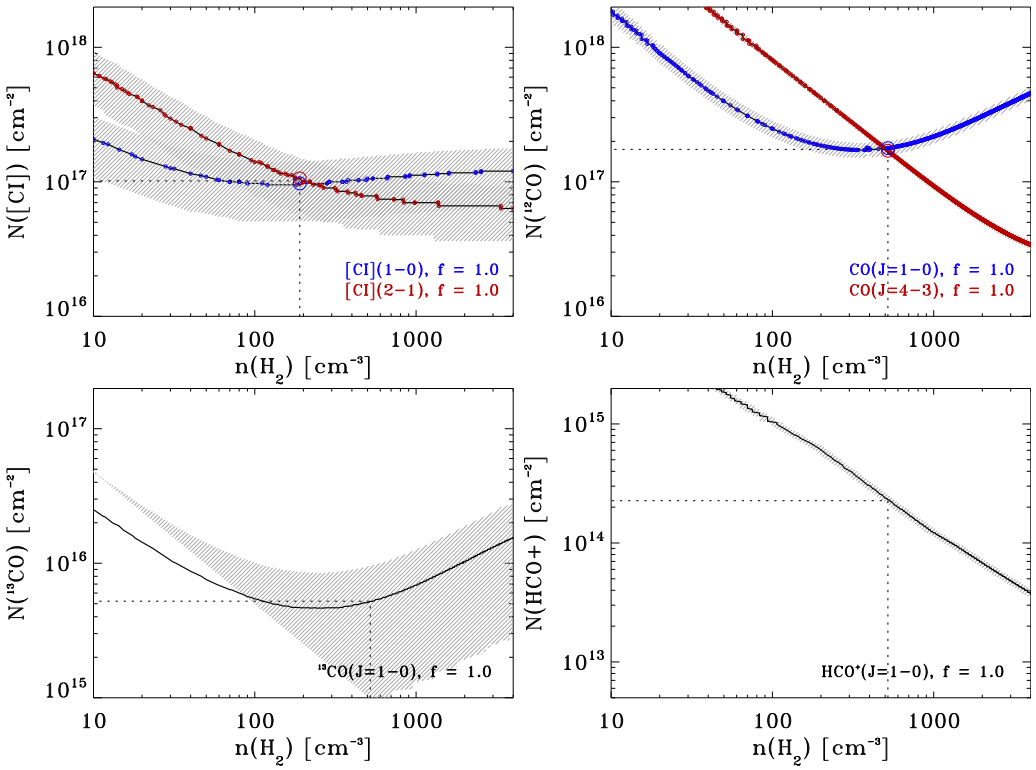

Figure. E.13: *HVG2: RADEX Results for 200 K kinetic temperature.*

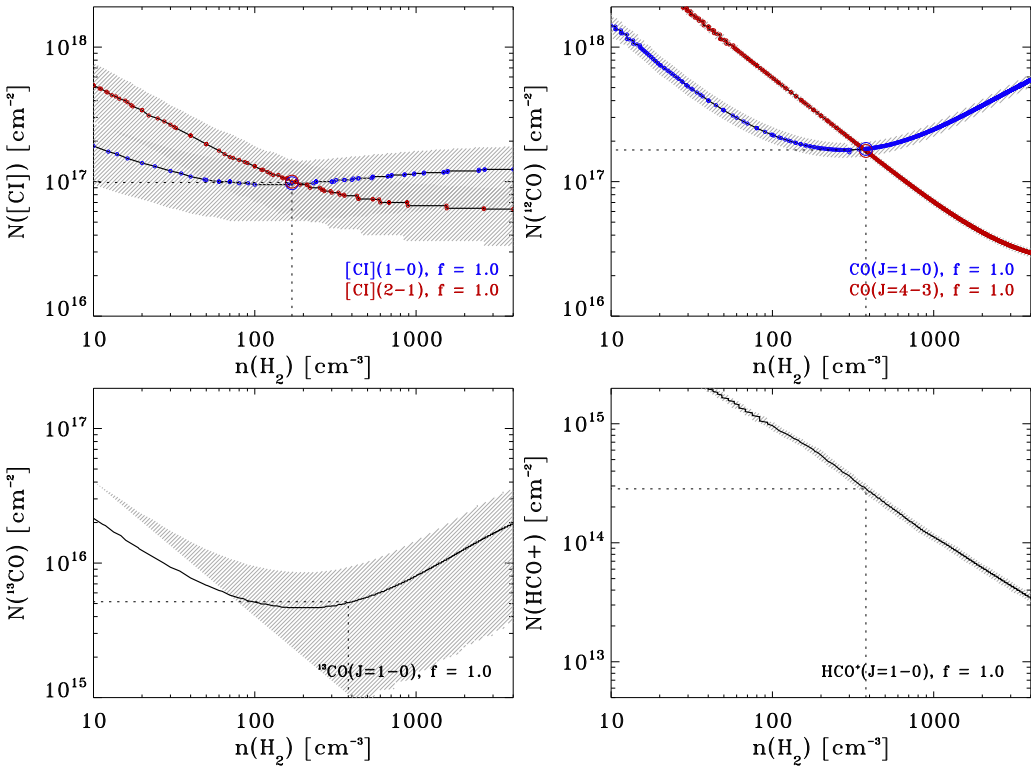

Figure. E.14: *HVG2: RADEX Results for 300 K kinetic temperature.*

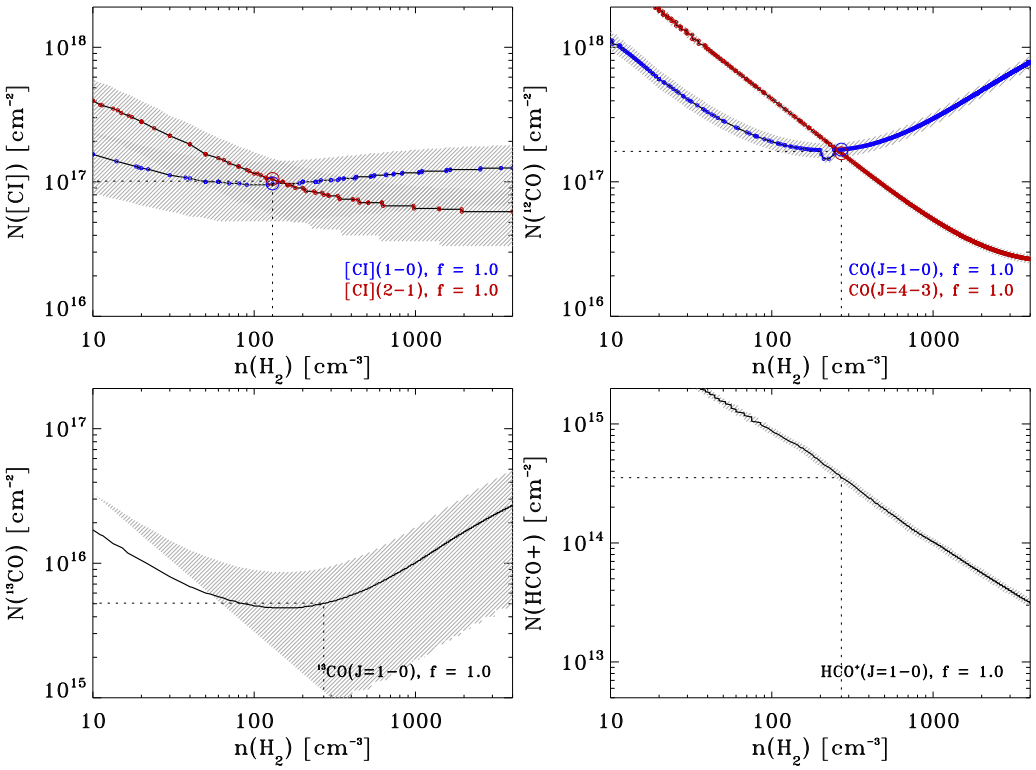

Figure. E.15: *HVG2: RADEX Results for 500 K kinetic temperature.*

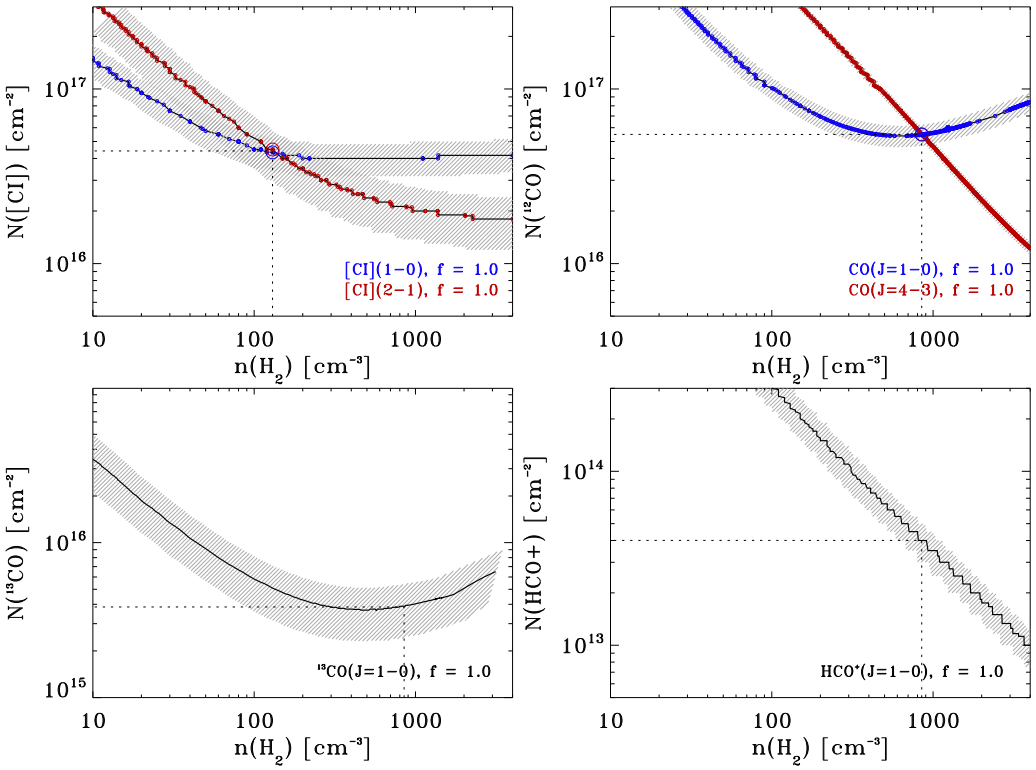

Figure. E.16: *HVG3: RADEX Results for 50 K kinetic temperature.*

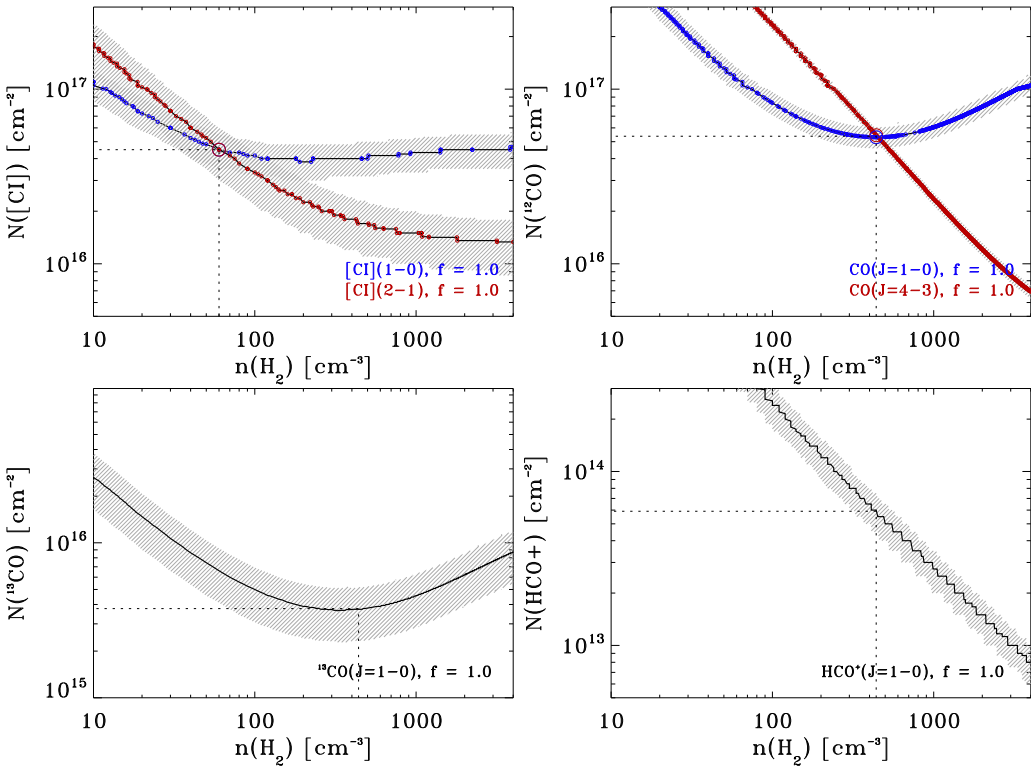

Figure. E.17: *HVG3: RADEX Results for 100 K kinetic temperature.*

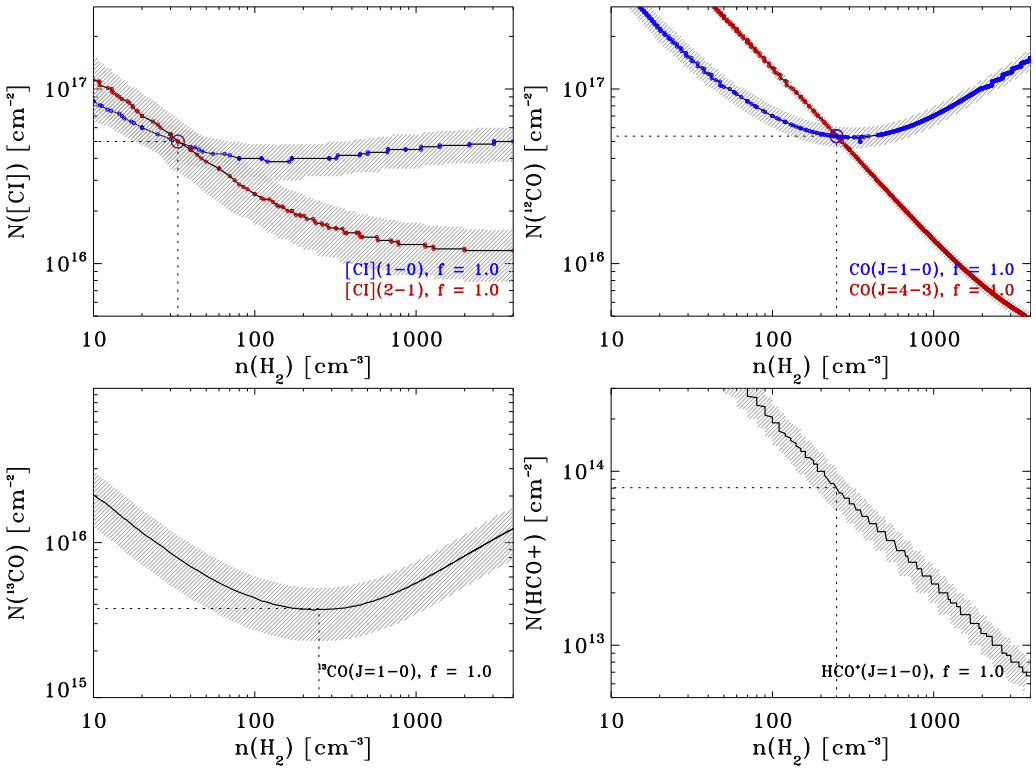

Figure. E.18: *HVG3: RADEX Results for 200 K kinetic temperature.*

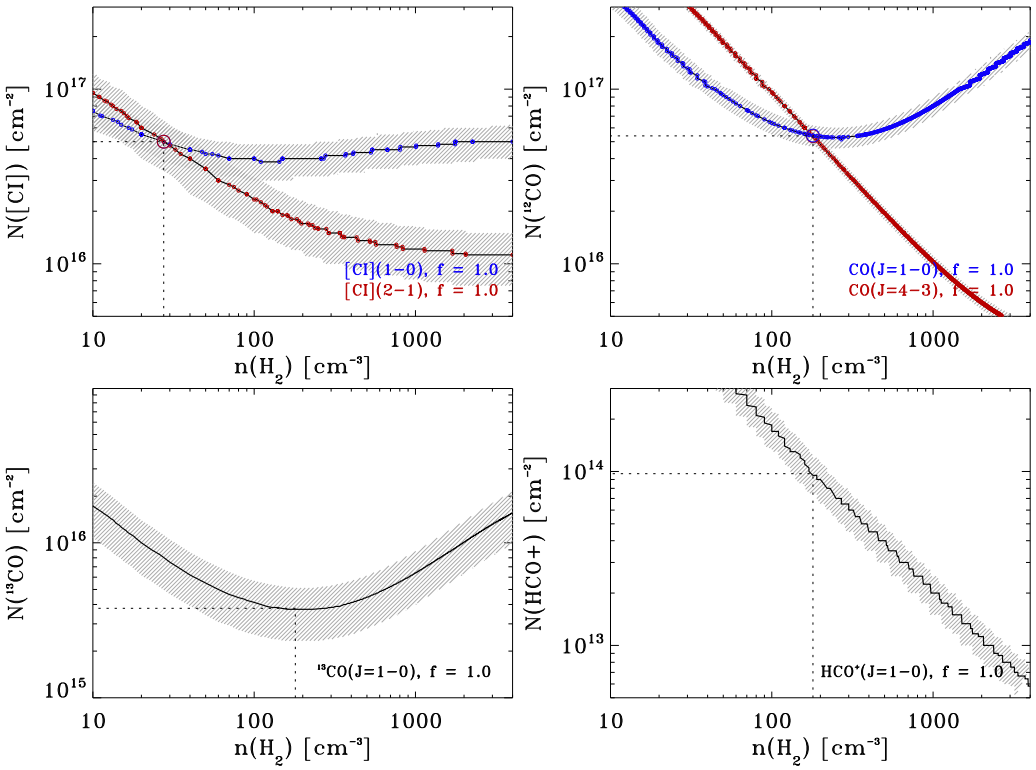

Figure. E.19: *HVG3: RADEX Results for 300 K kinetic temperature.*

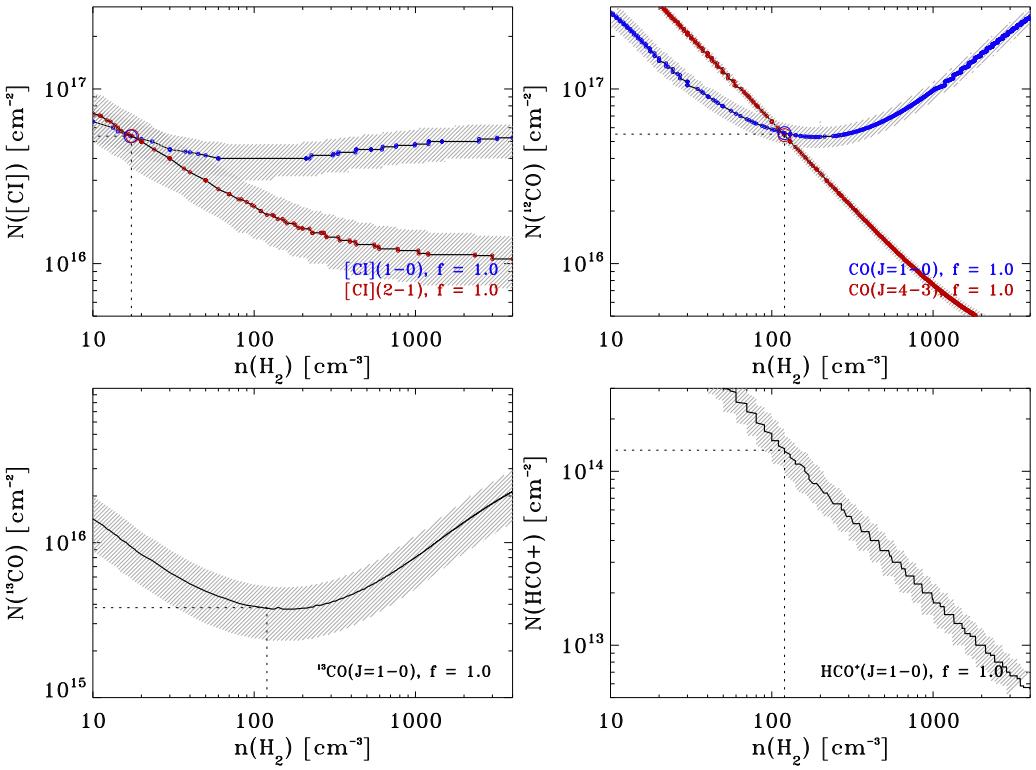

Figure. E.20: *HVG3: RADEX Results for 500 K kinetic temperature.*

E.1 RADEX Results: Filling Factor Impact

I explored the impact of different filling factors on the obtained column and volume densities as solutions of the RADEX models, for the measured carbon (left panels) and carbon monoxide (right panels) transitions in Figure E.21. The T_{peak} values used for the comparison are those measured for HVG1-1C. In the first three panels of the figure, the filling factors of the low and high frequency lines (in blue and red) were set to f = 1.0, 0.5, and 0.2. For equal f values, the lower the filling factor is, the lower the volume densities n(H_2), and the higher the column densities N are. Therefore, for f = 1.0, the obtained n(H_2) and N represent strict upper and lower limits, respectively. In the bottom two panels, different filling factors between the low and high frequency lines are used. The filling factors of the high frequency lines are set to f = 0.5 and f = 0.1 in the extreme case. From the panels, it can be seen that in the former case, the volume and column densities are increased and decreased, respectively, while in the latter, no solutions are found within the parameter grid. It can be noticed that in all cases, volume densities are less than a few times 10^3 cm^{-3}, with column densities between 10^{17} - 10^{18} cm^{-2}, approximately. The extreme case of f = 0.1 at the bottom panel gives no solutions within the parameter grid, though an order of magnitude difference between filling factors of the same species is rather unrealistic. Filling factors towards the dense molecular clouds in the CMZ (n(H_2) $\geq$ 10^4 cm^{-3}) have been reported to be $\geq$ 0.1 (Morris & Serabyn, 1996), though much lower values around 0.01 from H_3^+ observations have been reported (Oka et al., 2005). Also, optical depths and clumpiness effects would have an impact on the values of f by altering the observed extent of the source relative to the beam size. Therefore, a scenario with slightly different filling factors and lower than 1 for different lines of the same species seems to be more realistic.

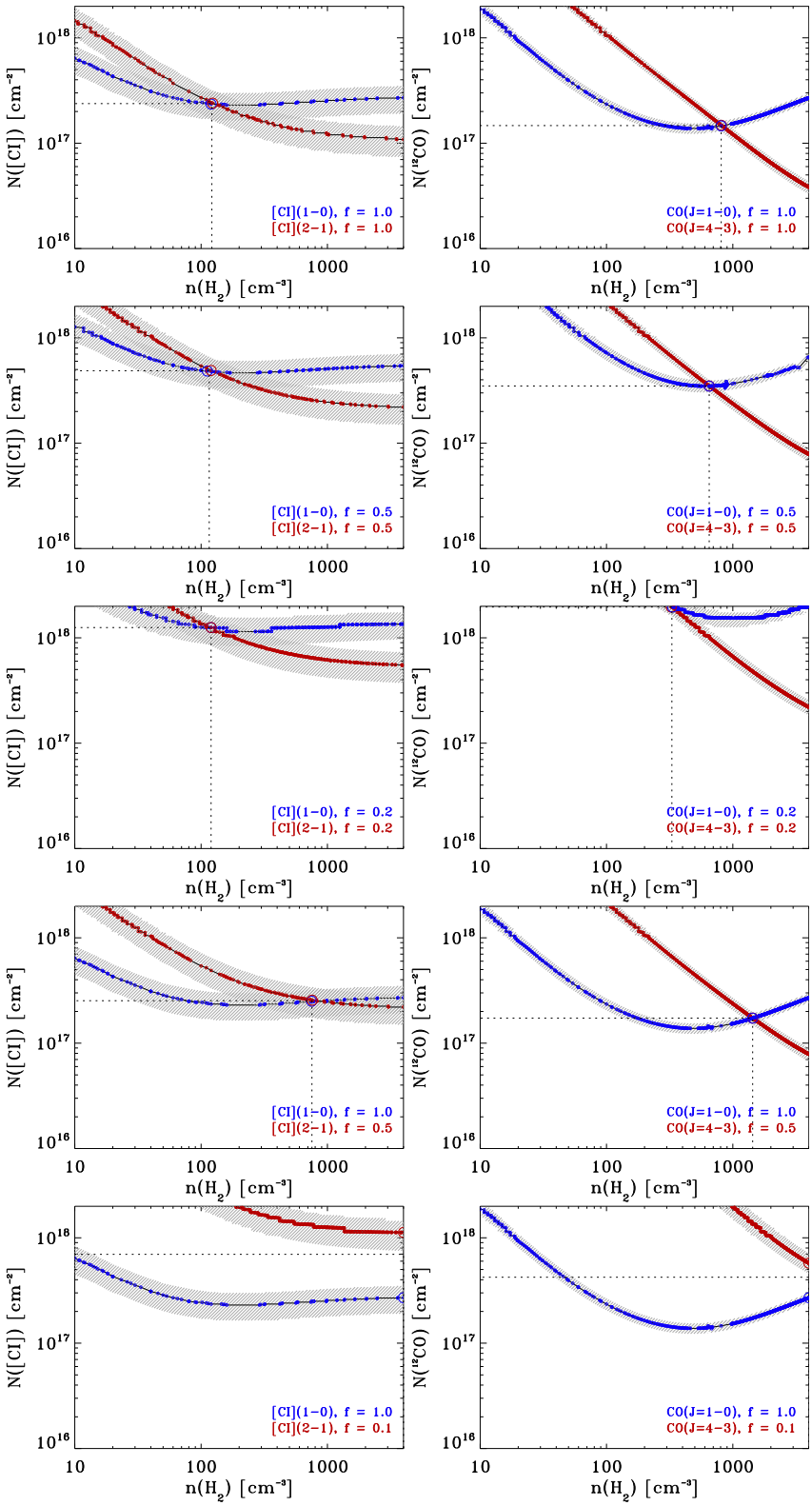

Figure. E.21: *HVG1-1C: RADEX Results for T_{kin} = 100 K with varying filling factor f: (a) keeping the same values for both transitions (top three panels) and (b) varying only the one for the high frequency transition (bottom two panels).*

Appendix F

Channel Maps of the Observed Sub-mm Lines

In this appendix, the channel maps of all sub-mm lines observed in the present work are shown. The maps spacing is 1 kms^{-1} equivalent to the spectral resolution of the data. The spatial axes of the maps correspond to angular offsets in arcseconds with respect to the astronomical coordinates of the observed source, located at the (0,0) position. The CO(4-3) NANTEN/SMART dataset observed in the Galactic coordinates frame are centered at $l = 0°.000$, $b = 0°.000$, while the Herschel-HIFI [CI](1-0), [CI](2-1), [NII], and [CII] datasets, observed in Equatorial(J2000) coordinates are centered at $\alpha(J2000) = 17^h$ 45' 39.9", $\delta(J2000) = -29°$ 00' 28.1". The LSR velocity of each map is indicated in each panel as well as the spatial resolution described in Table 3.1 shown as a black filled circle. The peak position within each dataset is shown as a filled black star on the map.

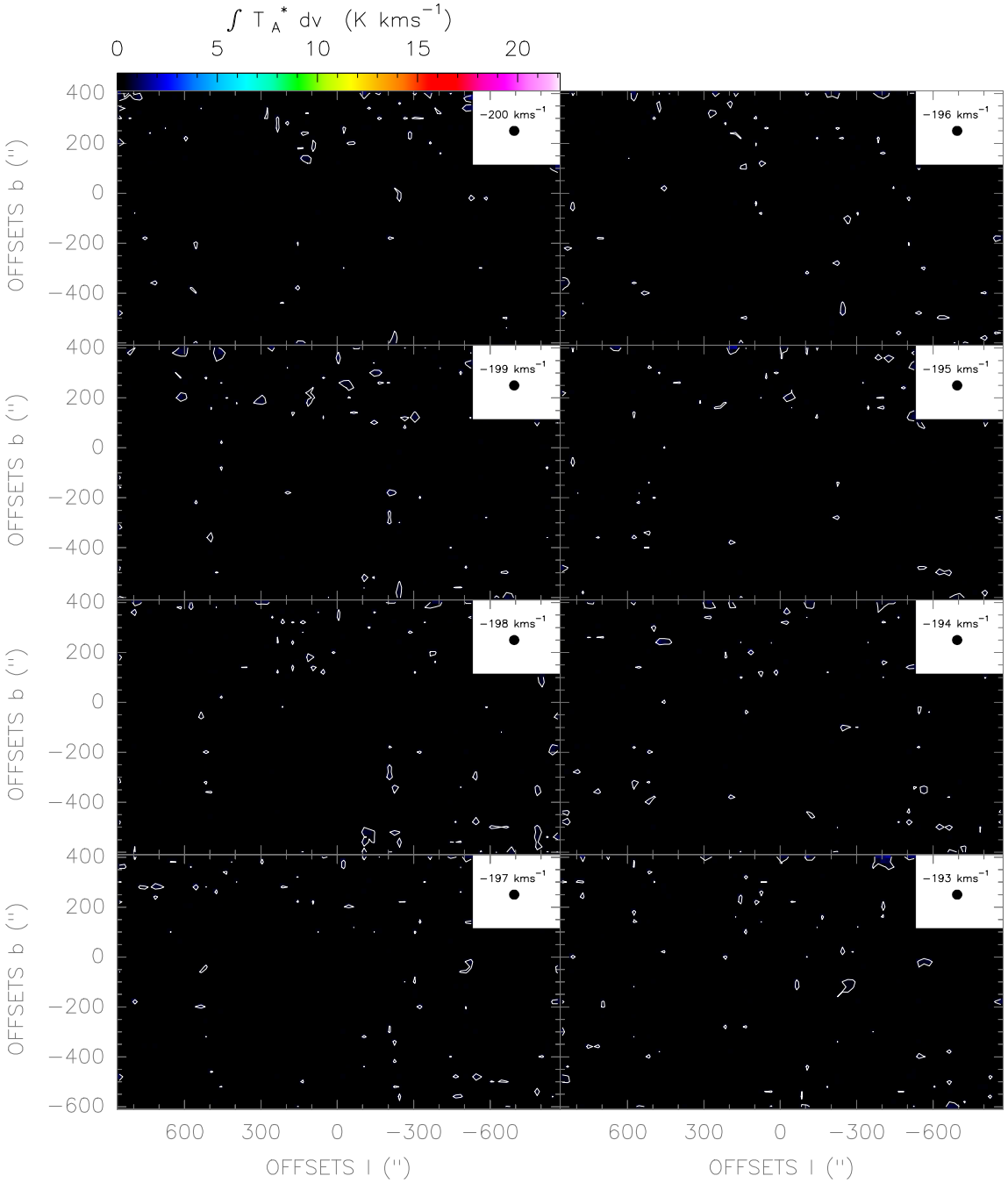

Figure. F.1: *CO(4-3) line observed with the NANTEN2/SMART telescope in Galactic coordinates. The spatial resolution of the maps is 40".*

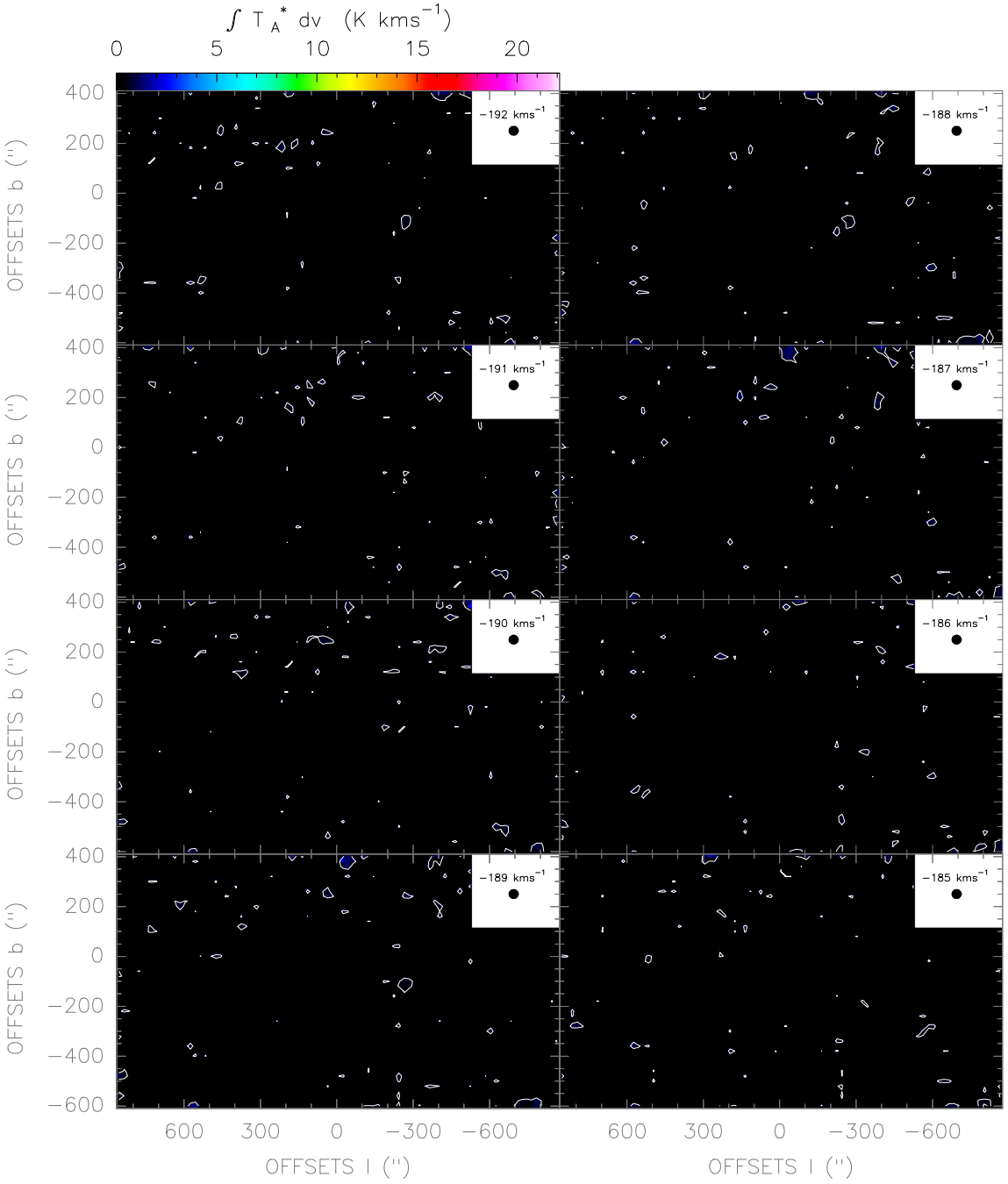

Figure. F.2: *CO(4-3) line observed with the NANTEN2/SMART telescope in Galactic coordinates. The spatial resolution of the maps is 40".*

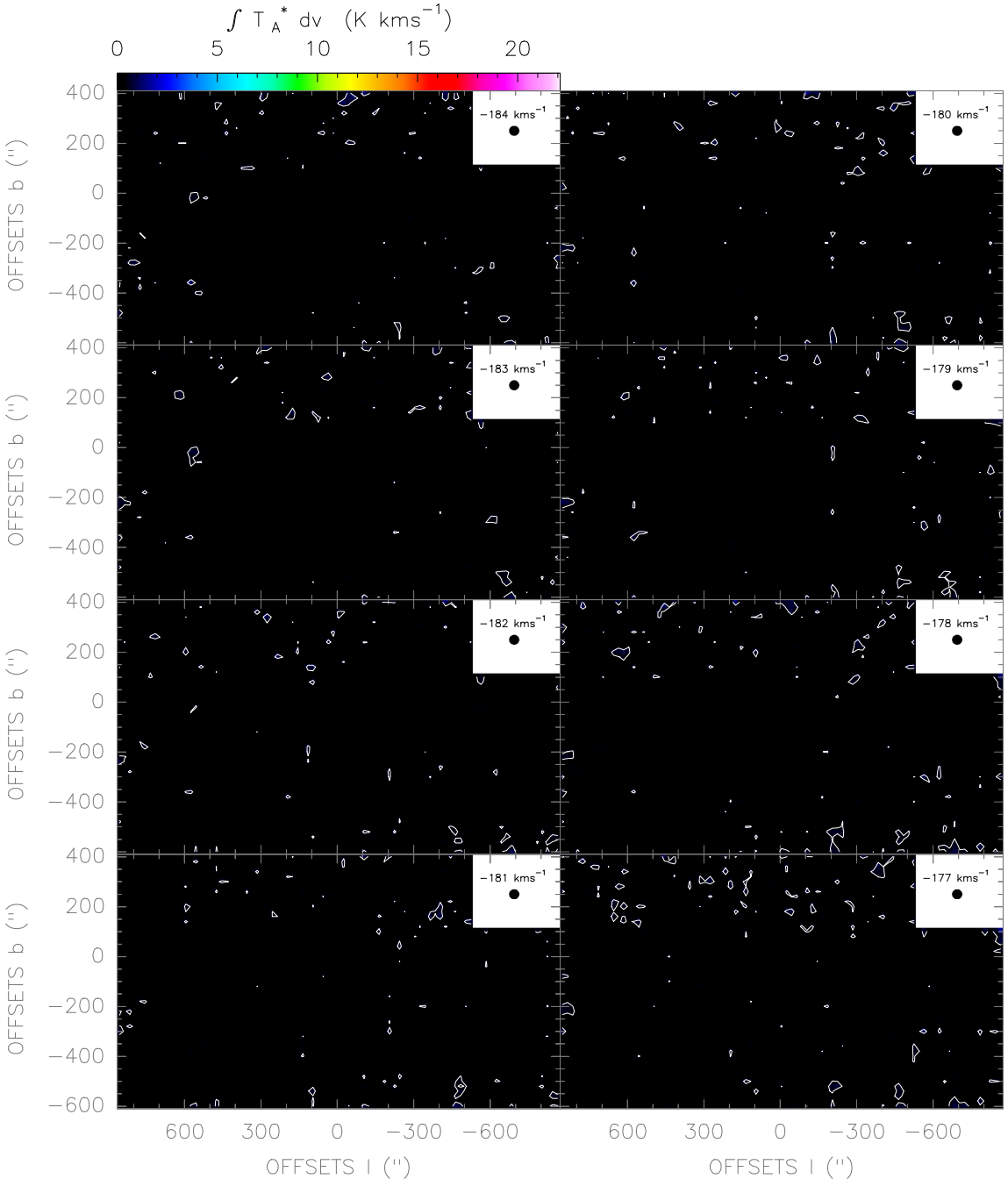

Figure. F.3: *CO(4-3) line observed with the NANTEN2/SMART telescope in Galactic coordinates. The spatial resolution of the maps is 40".*

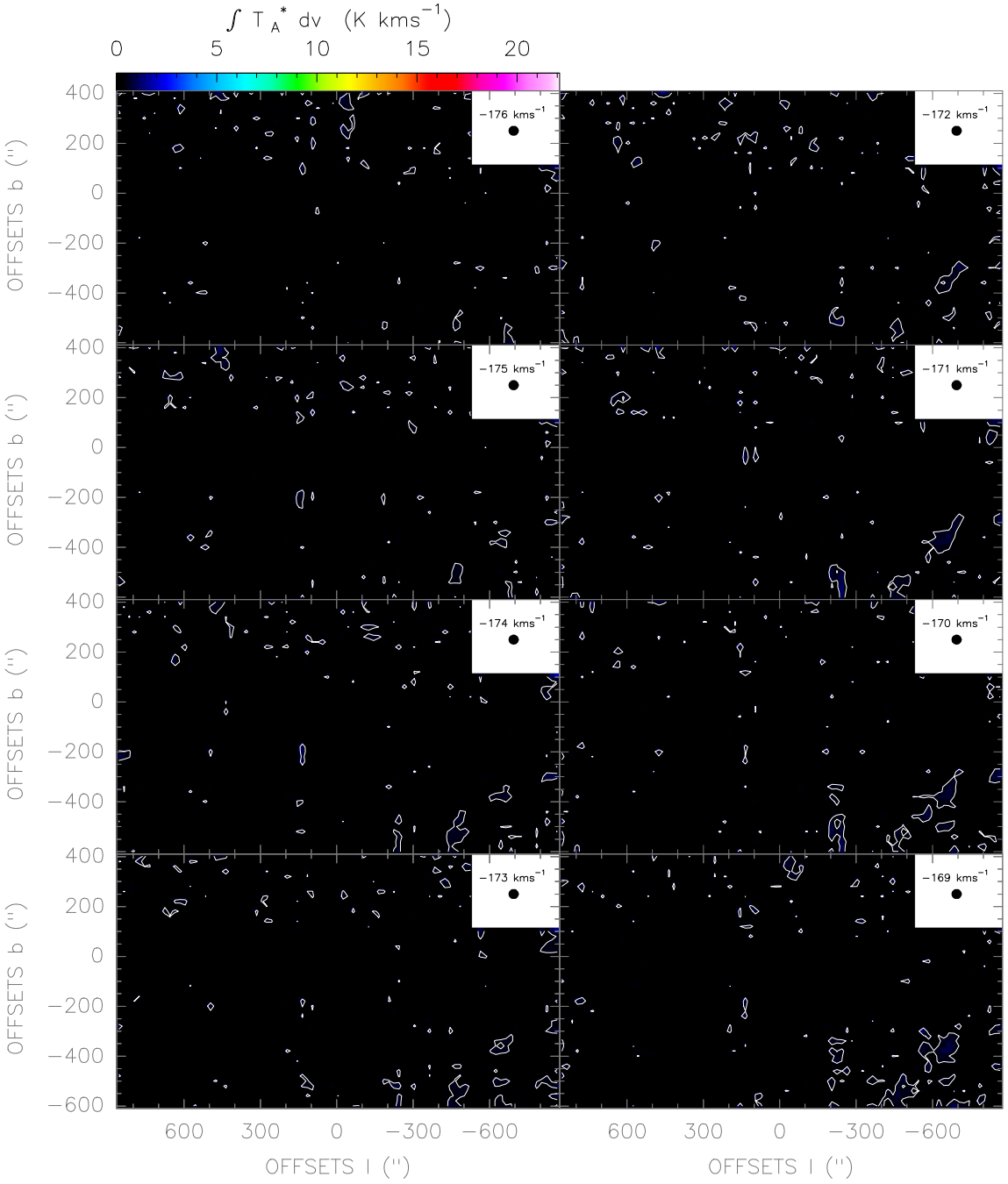

Figure. F.4: *CO(4-3) line observed with the NANTEN2/SMART telescope in Galactic coordinates. The spatial resolution of the maps is 40".*

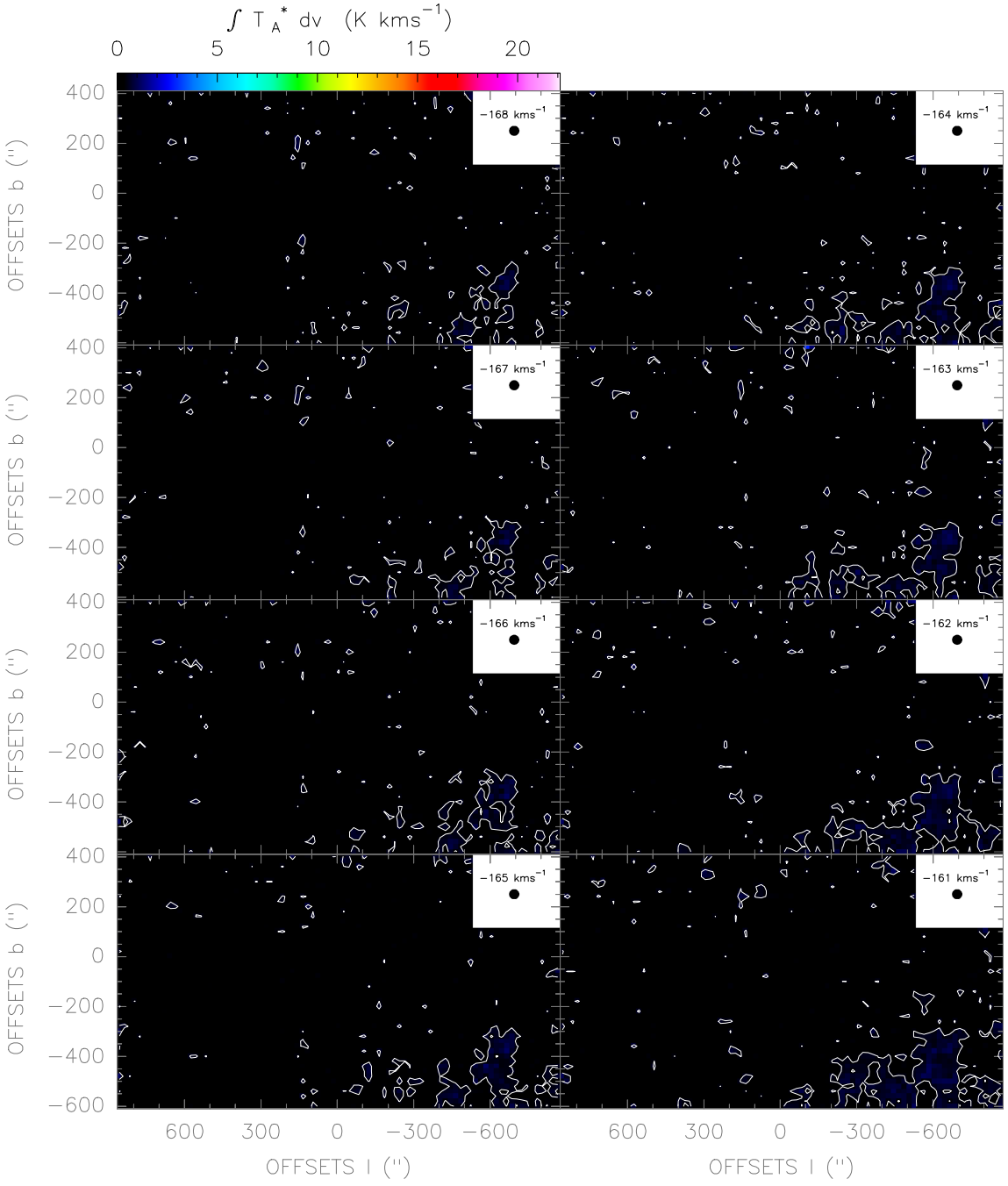

Figure. F.5: *CO(4-3) line observed with the NANTEN2/SMART telescope in Galactic coordinates. The spatial resolution of the maps is 40".*

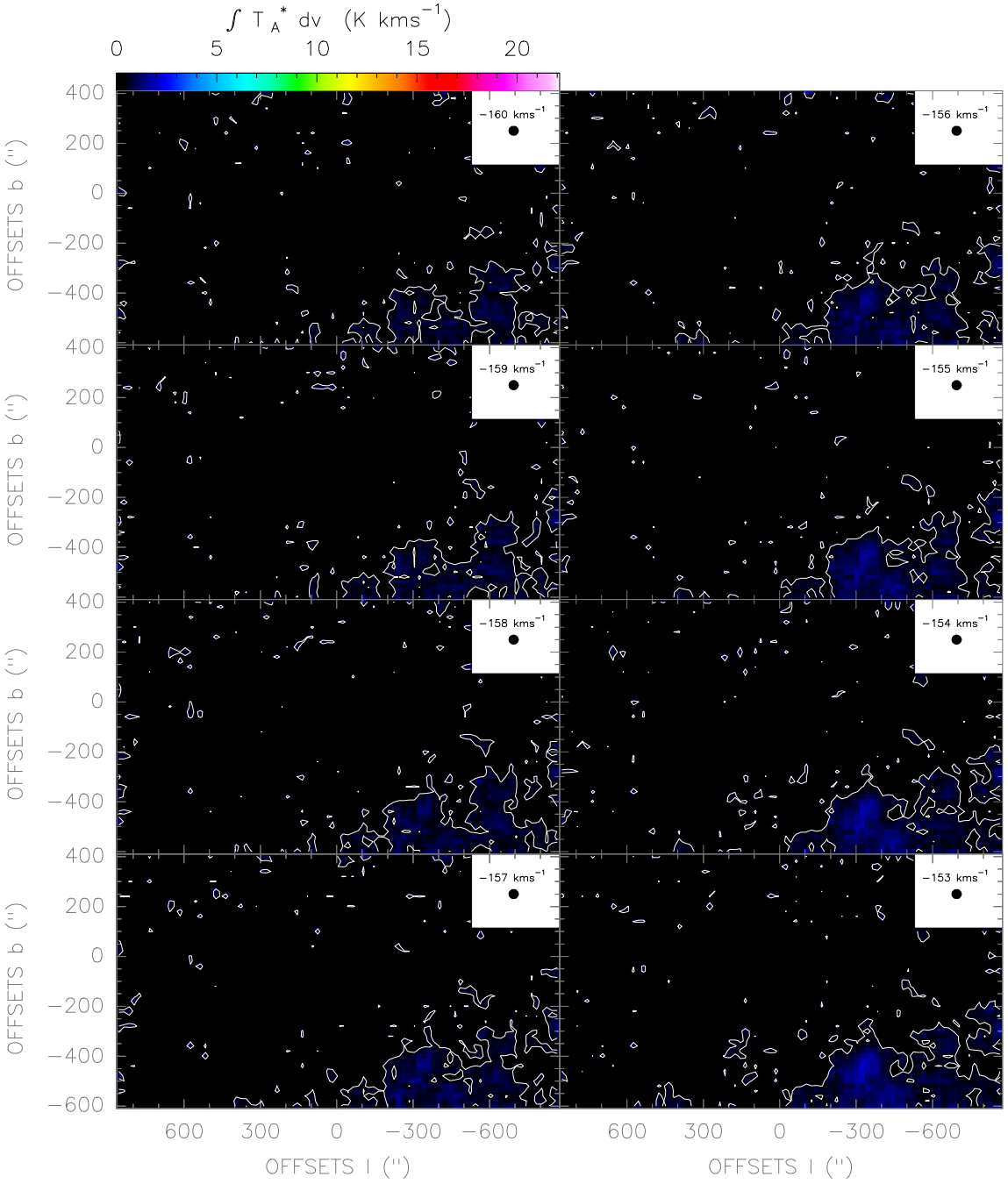

Figure. F.6: *CO(4-3) line observed with the NANTEN2/SMART telescope in Galactic coordinates. The spatial resolution of the maps is 40".*

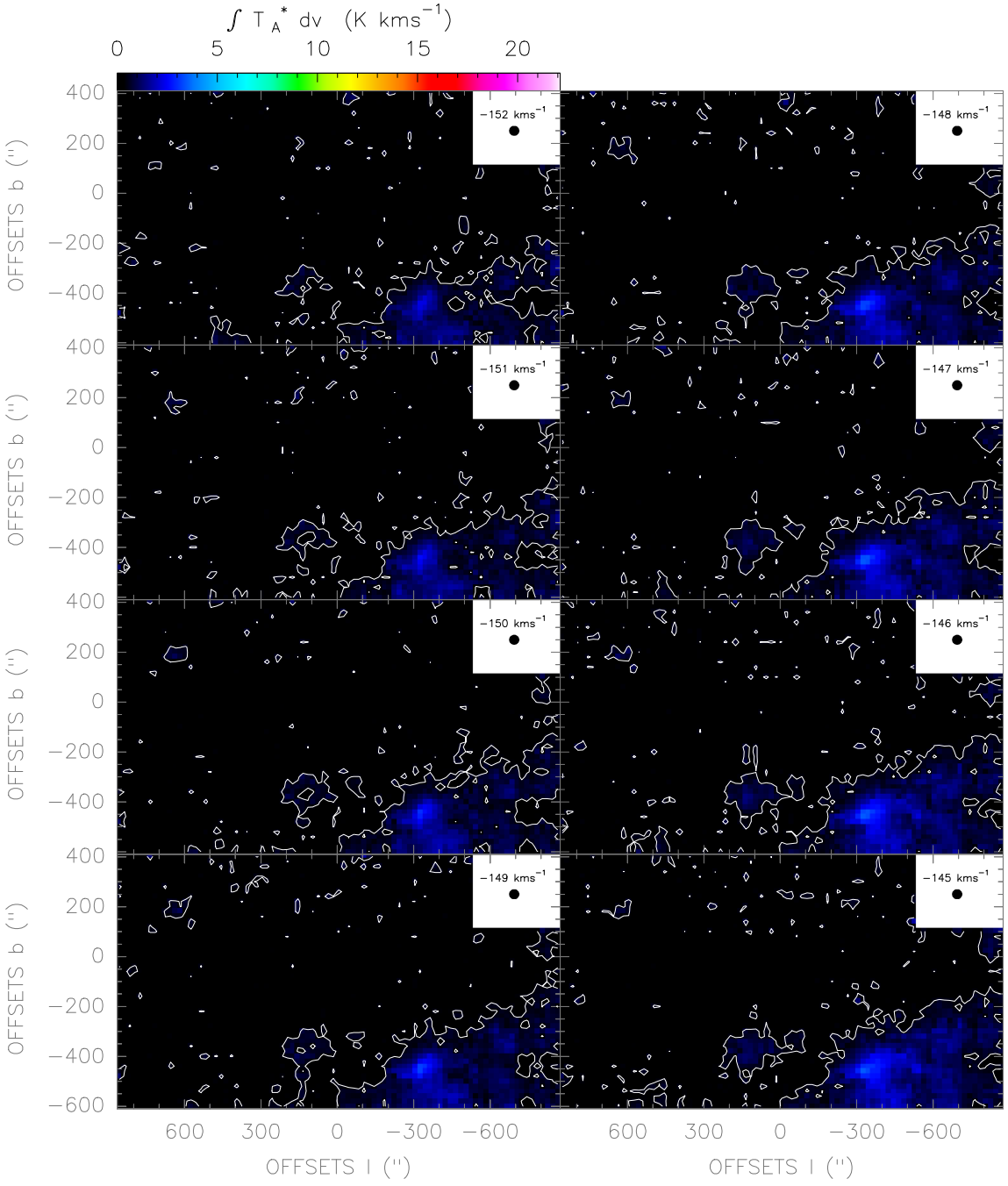

Figure. F.7: *CO(4-3) line observed with the NANTEN2/SMART telescope in Galactic coordinates. The spatial resolution of the maps is 40".*

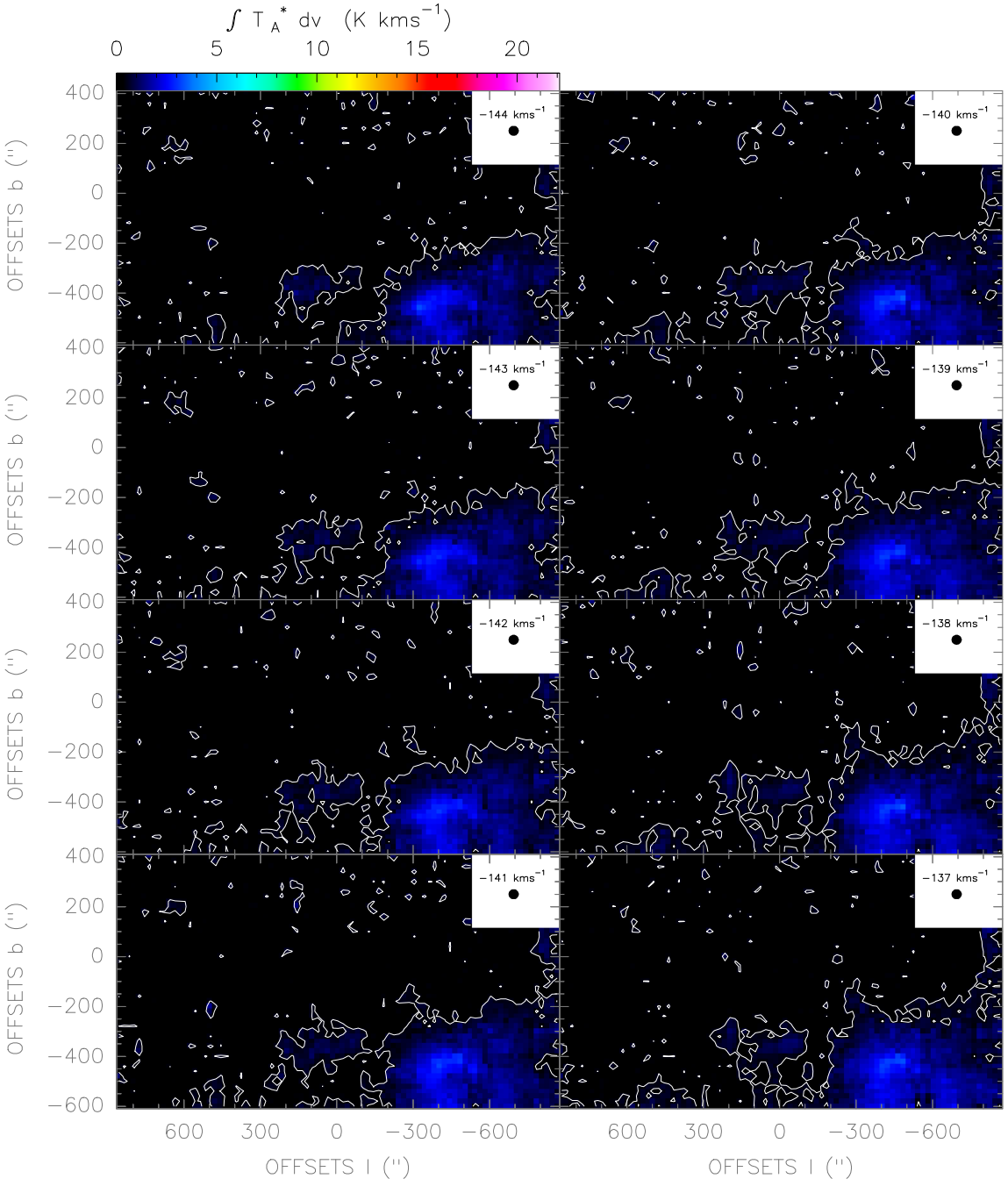

Figure. F.8: *CO(4-3) line observed with the NANTEN2/SMART telescope in Galactic coordinates. The spatial resolution of the maps is 40".*

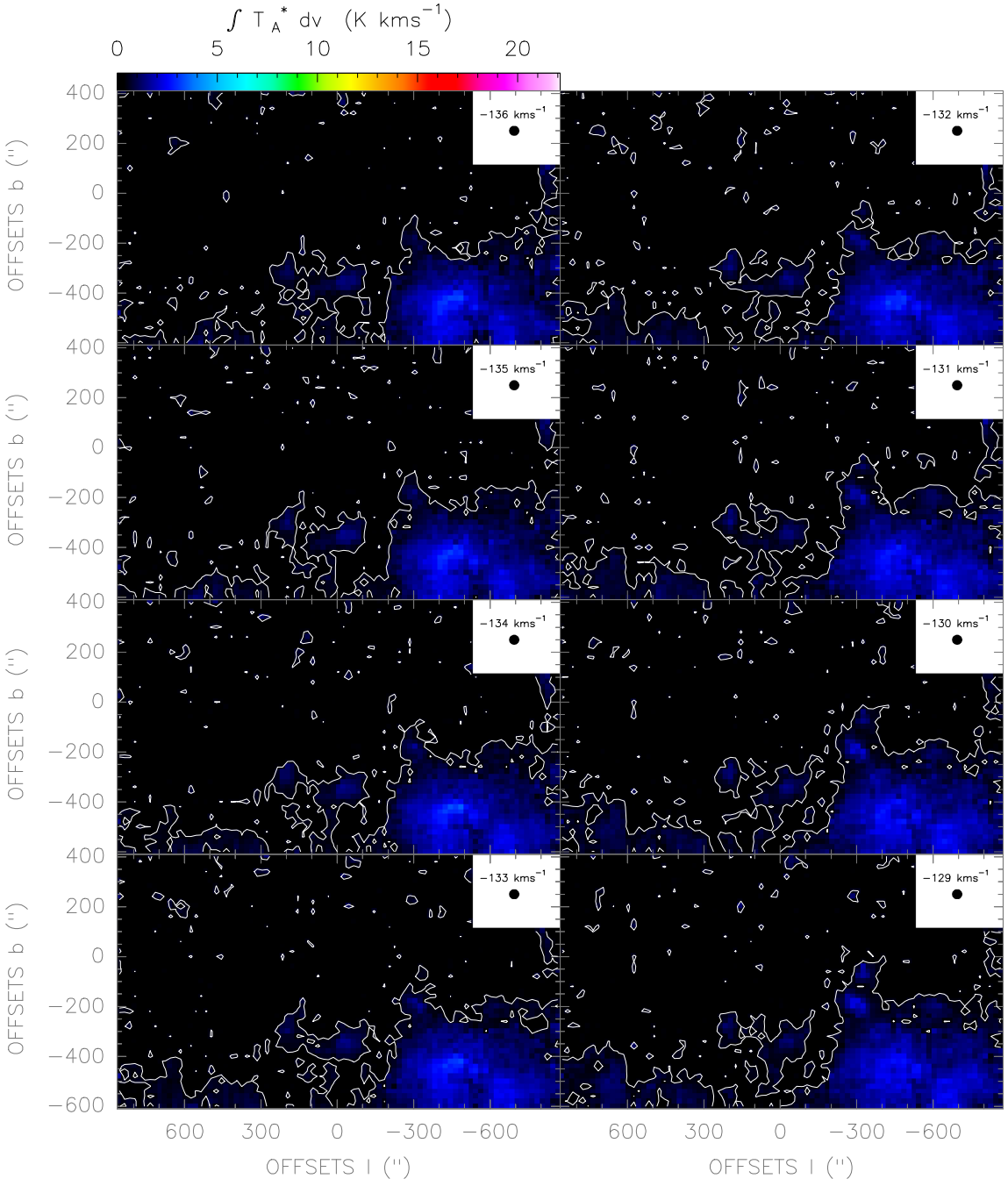

Figure. F.9: *CO(4-3) line observed with the NANTEN2/SMART telescope in Galactic coordinates. The spatial resolution of the maps is 40".*

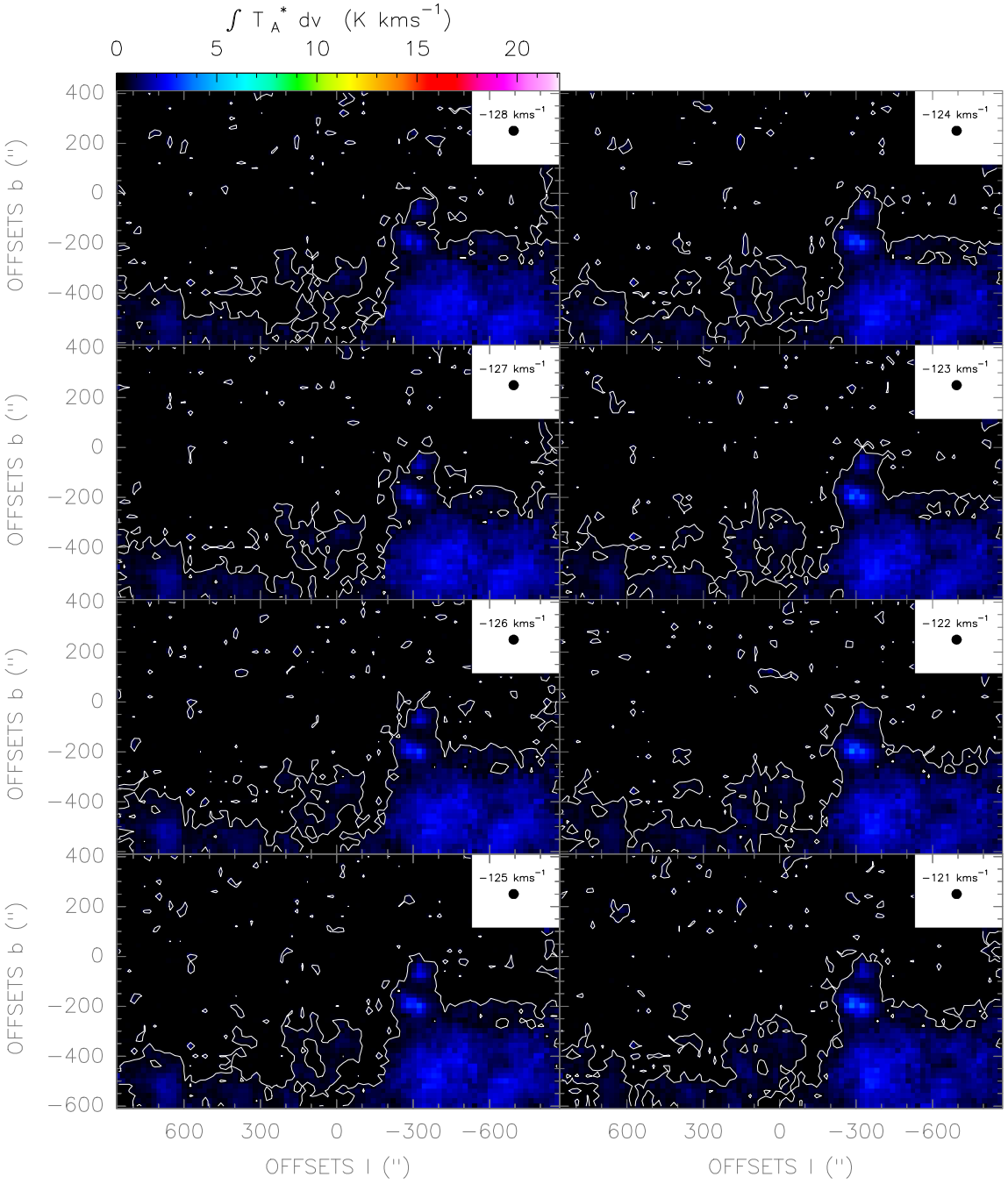

Figure. F.10: *CO(4-3) line observed with the NANTEN2/SMART telescope in Galactic coordinates. The spatial resolution of the maps is 40".*

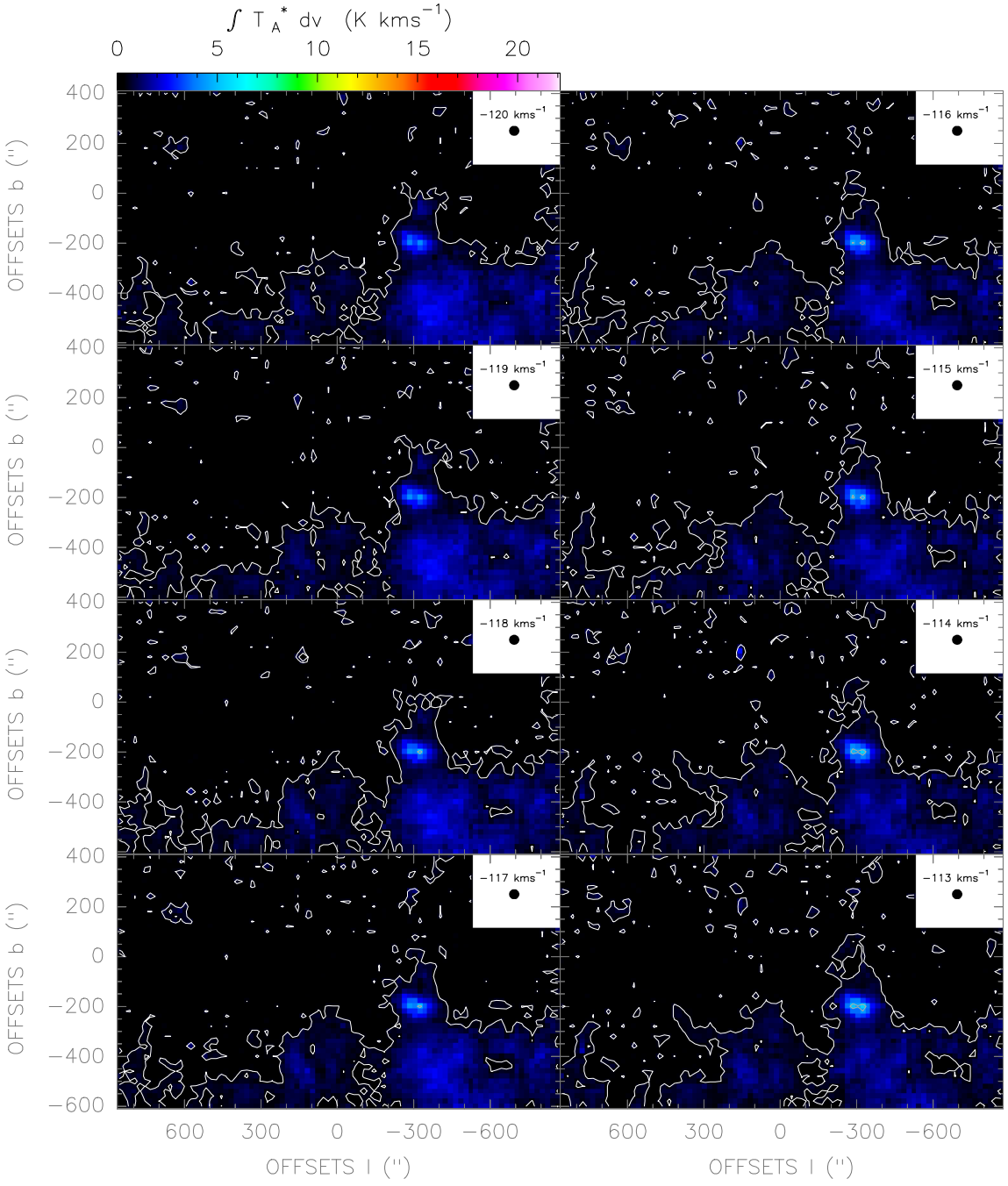

Figure. F.11: *CO(4-3) line observed with the NANTEN2/SMART telescope in Galactic coordinates. The spatial resolution of the maps is 40".*

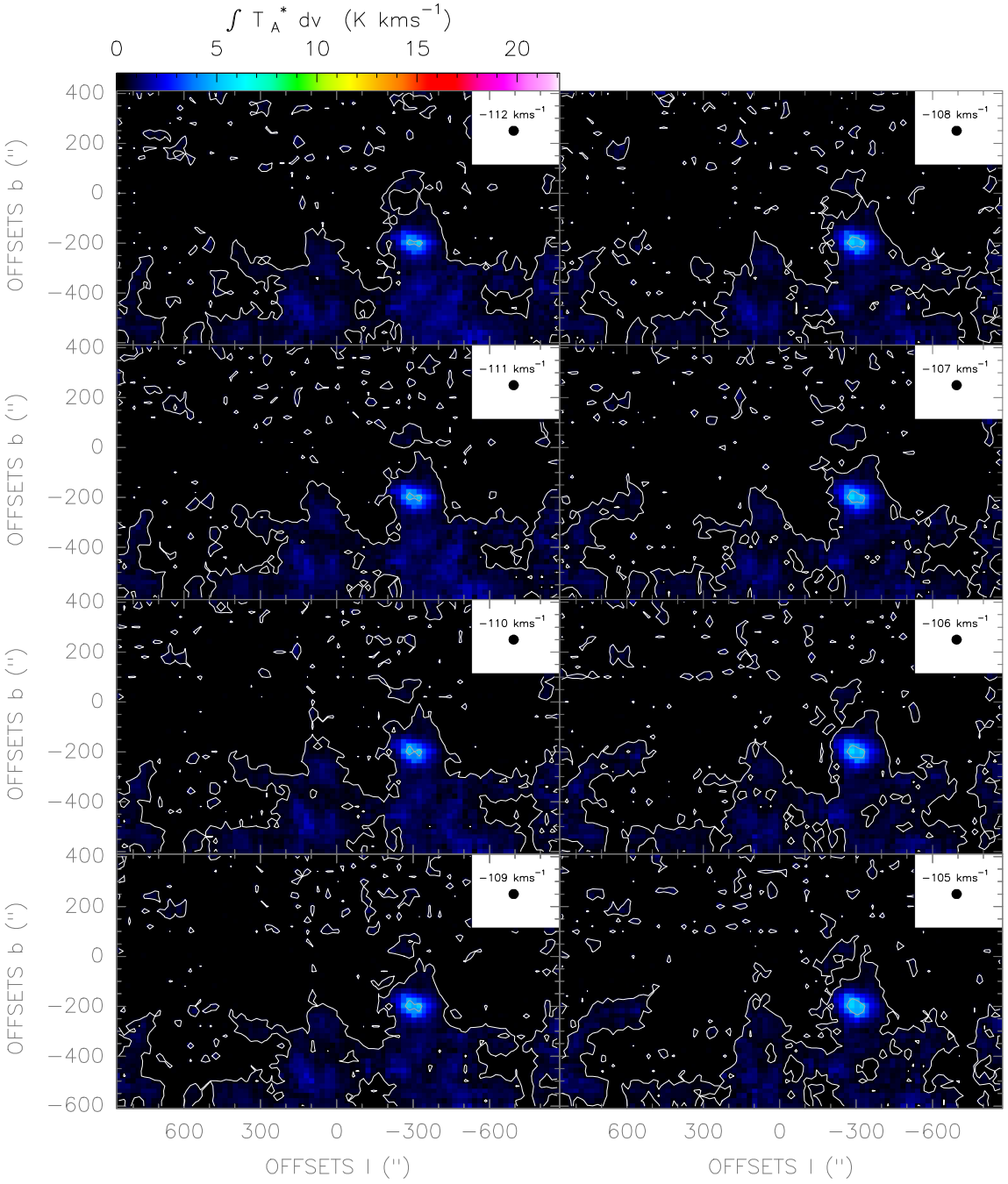

Figure. F.12: *CO(4-3) line observed with the NANTEN2/SMART telescope in Galactic coordinates. The spatial resolution of the maps is 40".*

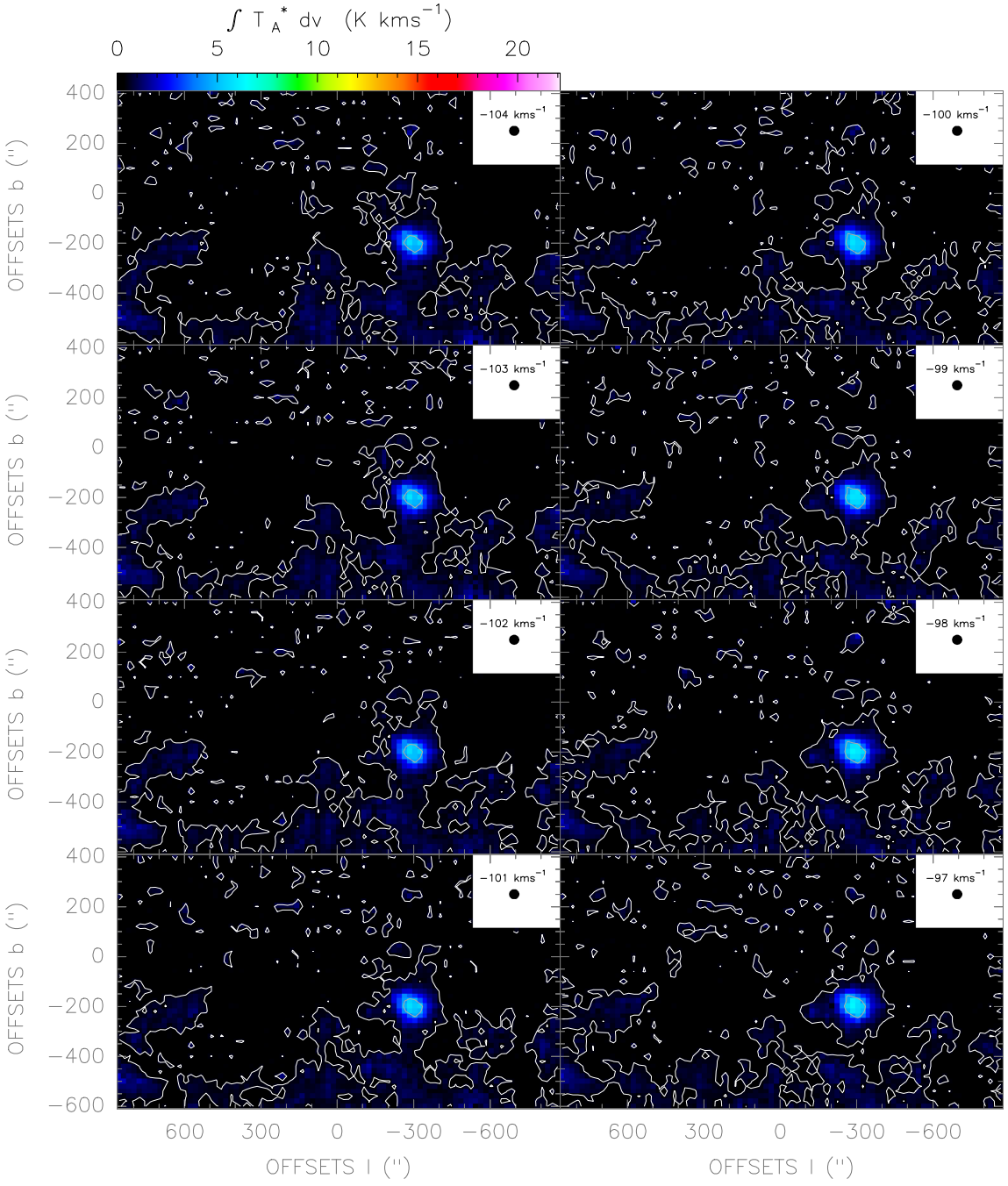

Figure. F.13: *CO(4-3) line observed with the NANTEN2/SMART telescope in Galactic coordinates. The spatial resolution of the maps is 40".*

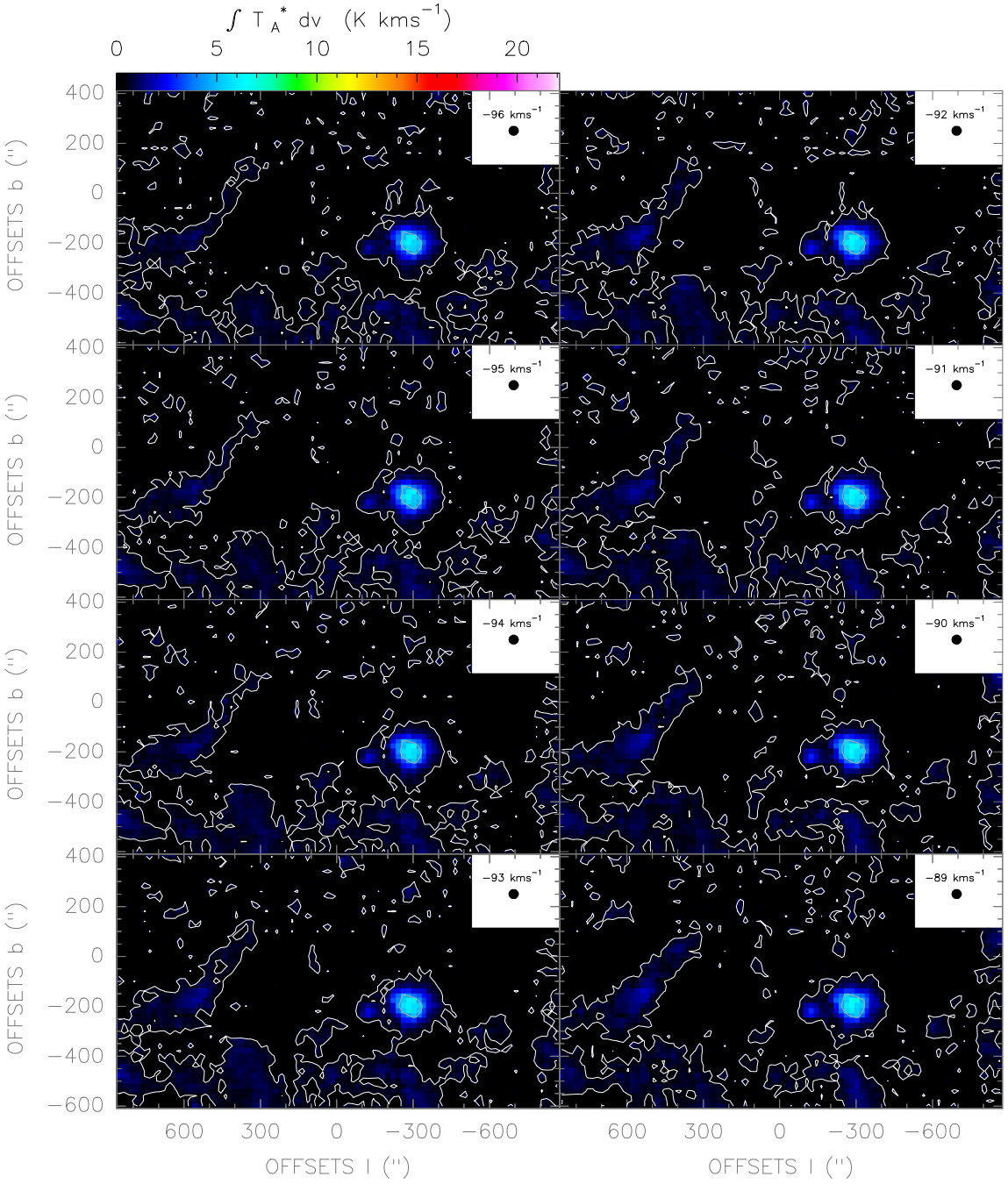

Figure. F.14: *CO(4-3) line observed with the NANTEN2/SMART telescope in Galactic coordinates. The spatial resolution of the maps is 40".*

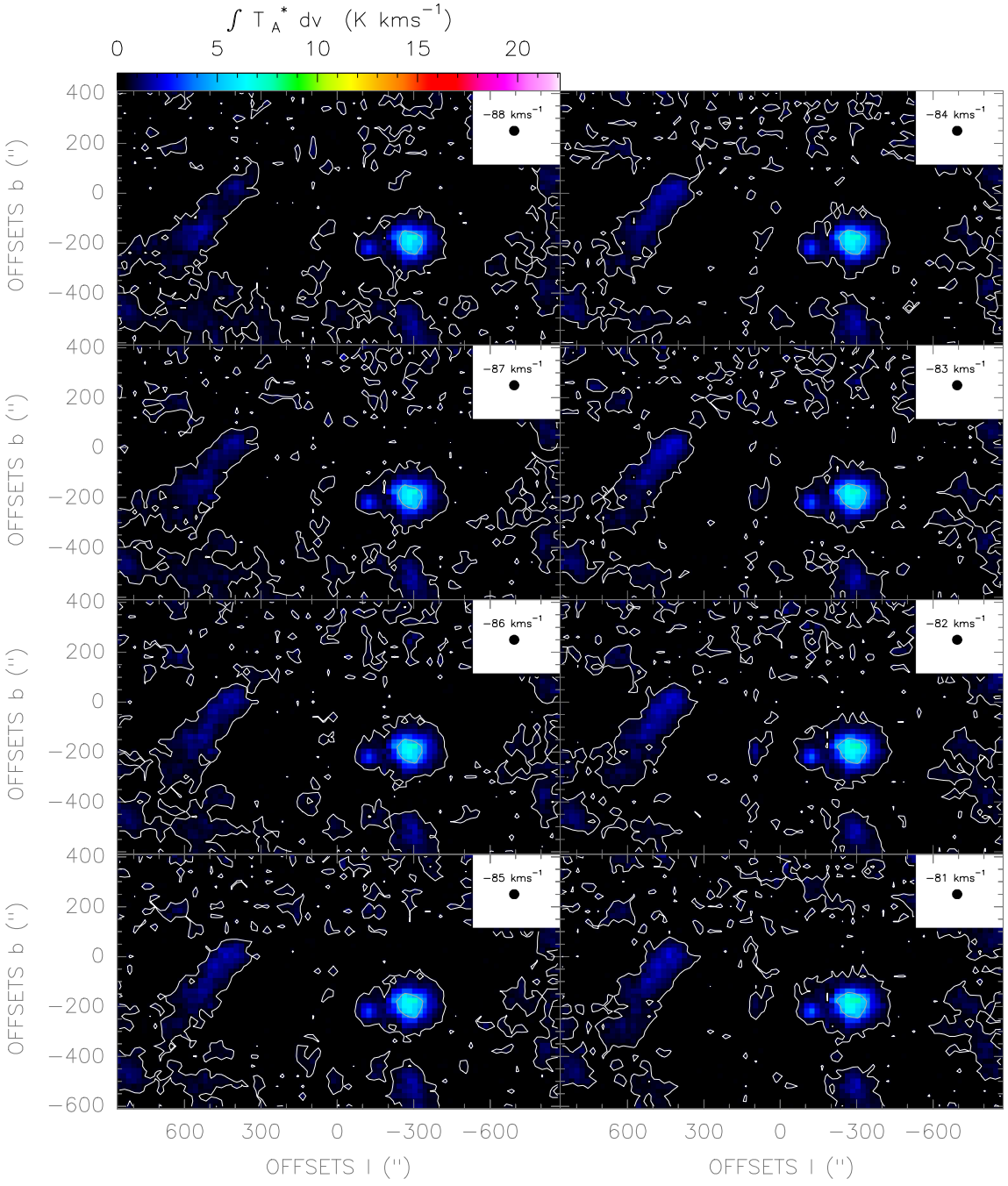

Figure. F.15: *CO(4-3) line observed with the NANTEN2/SMART telescope in Galactic coordinates. The spatial resolution of the maps is 40".*

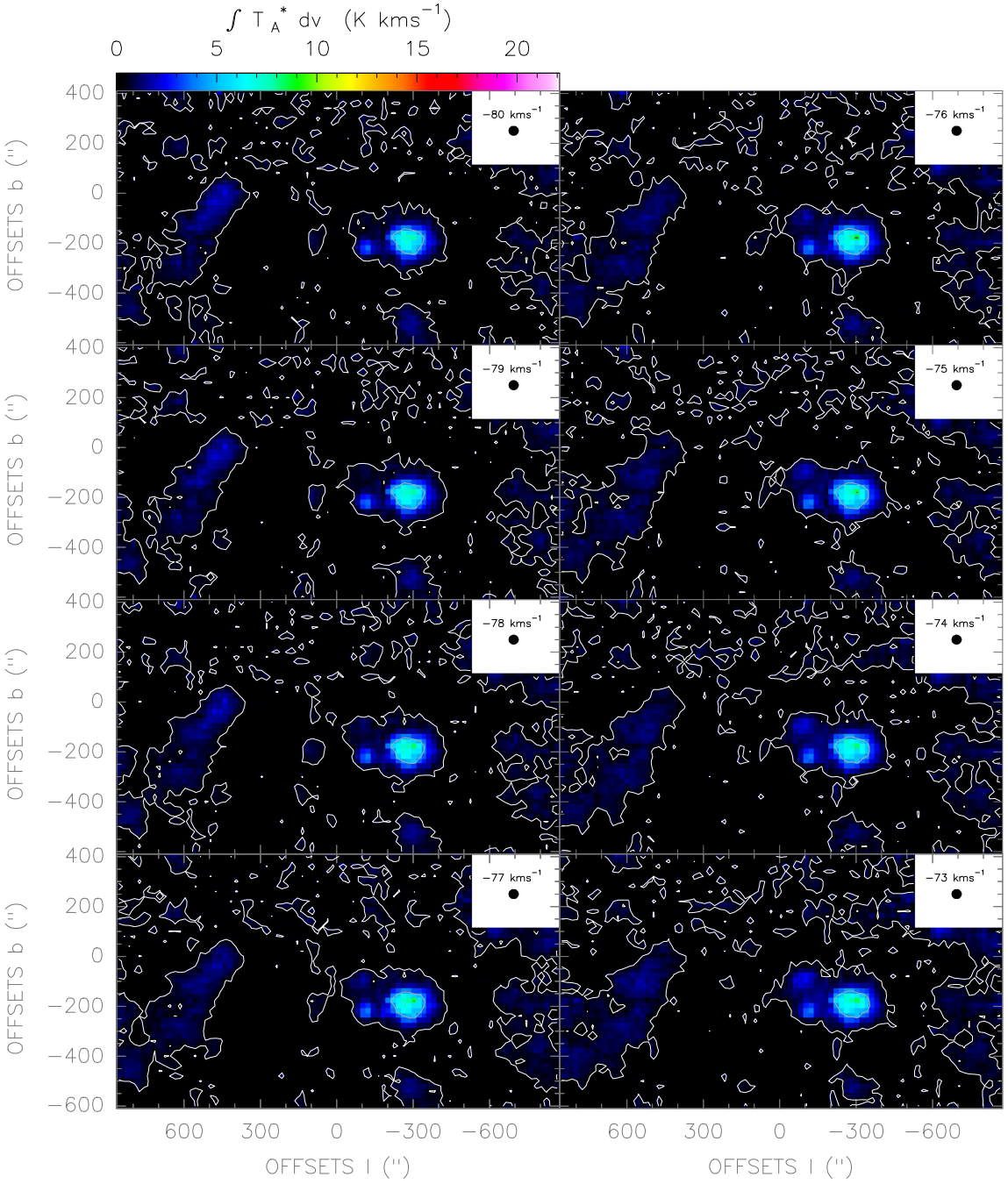

Figure. F.16: *CO(4-3) line observed with the NANTEN2/SMART telescope in Galactic coordinates. The spatial resolution of the maps is 40".*

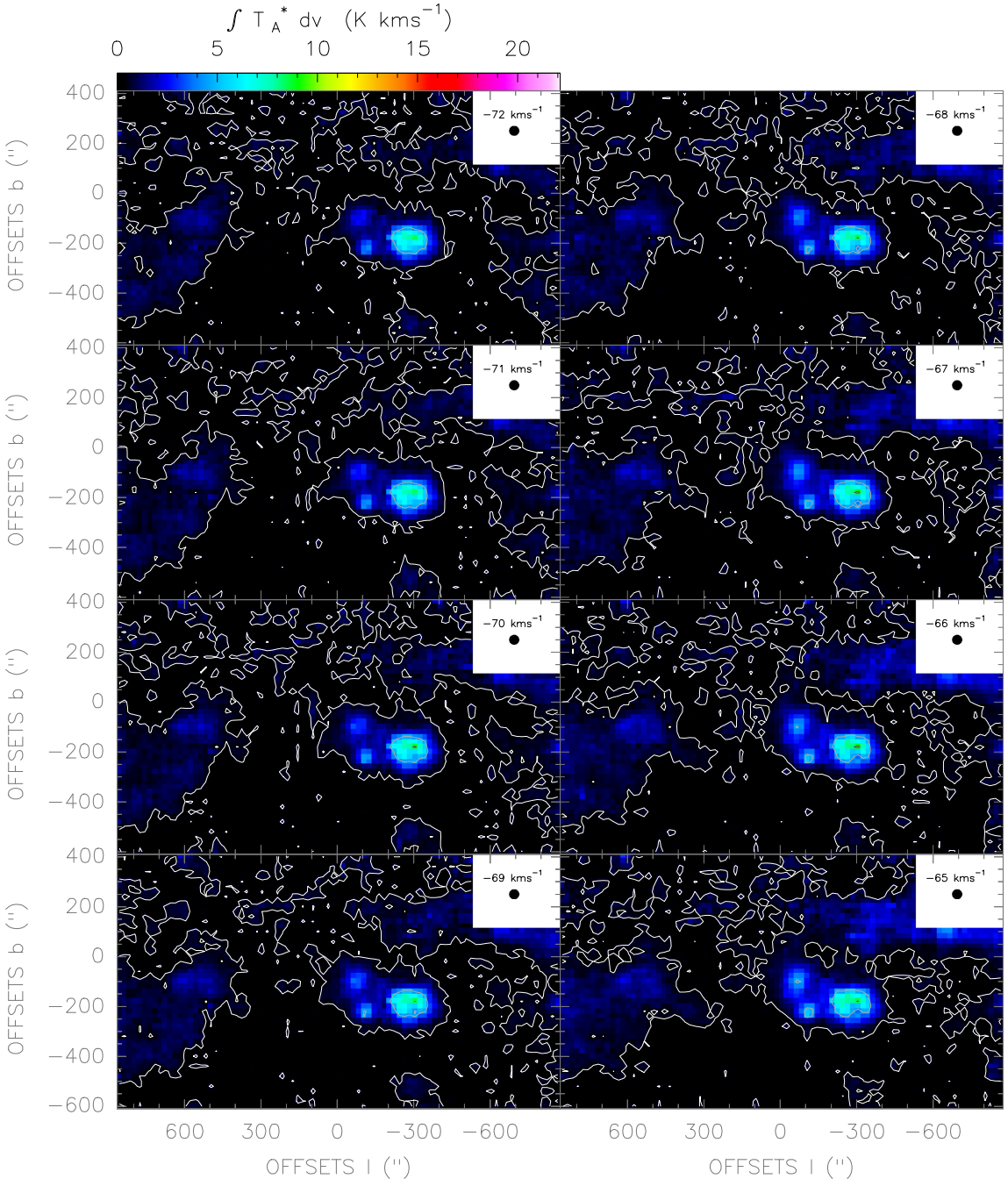

Figure. F.17: *CO(4-3) line observed with the NANTEN2/SMART telescope in Galactic coordinates. The spatial resolution of the maps is 40".*

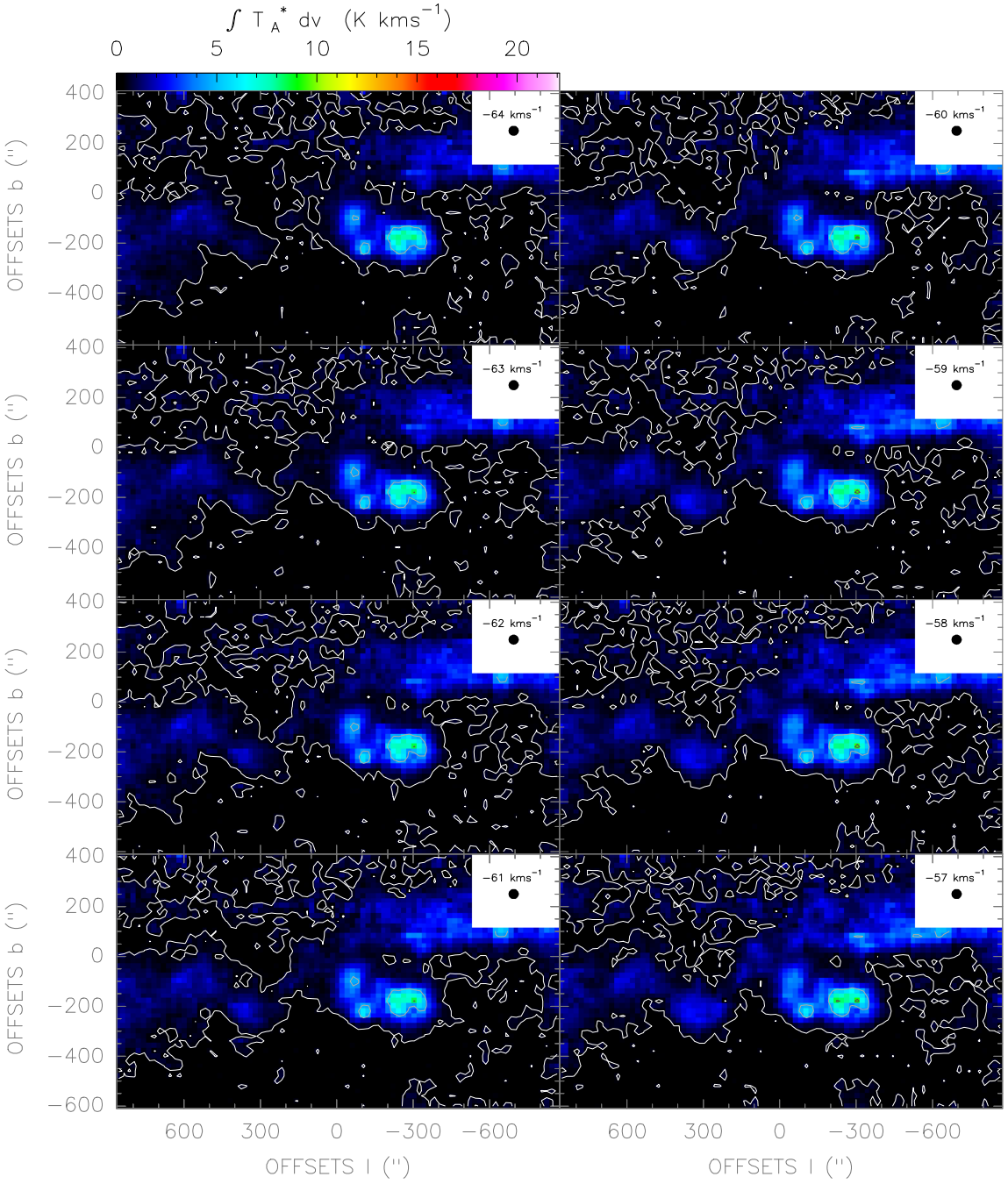

Figure. F.18: *CO(4-3) line observed with the NANTEN2/SMART telescope in Galactic coordinates. The spatial resolution of the maps is 40".*

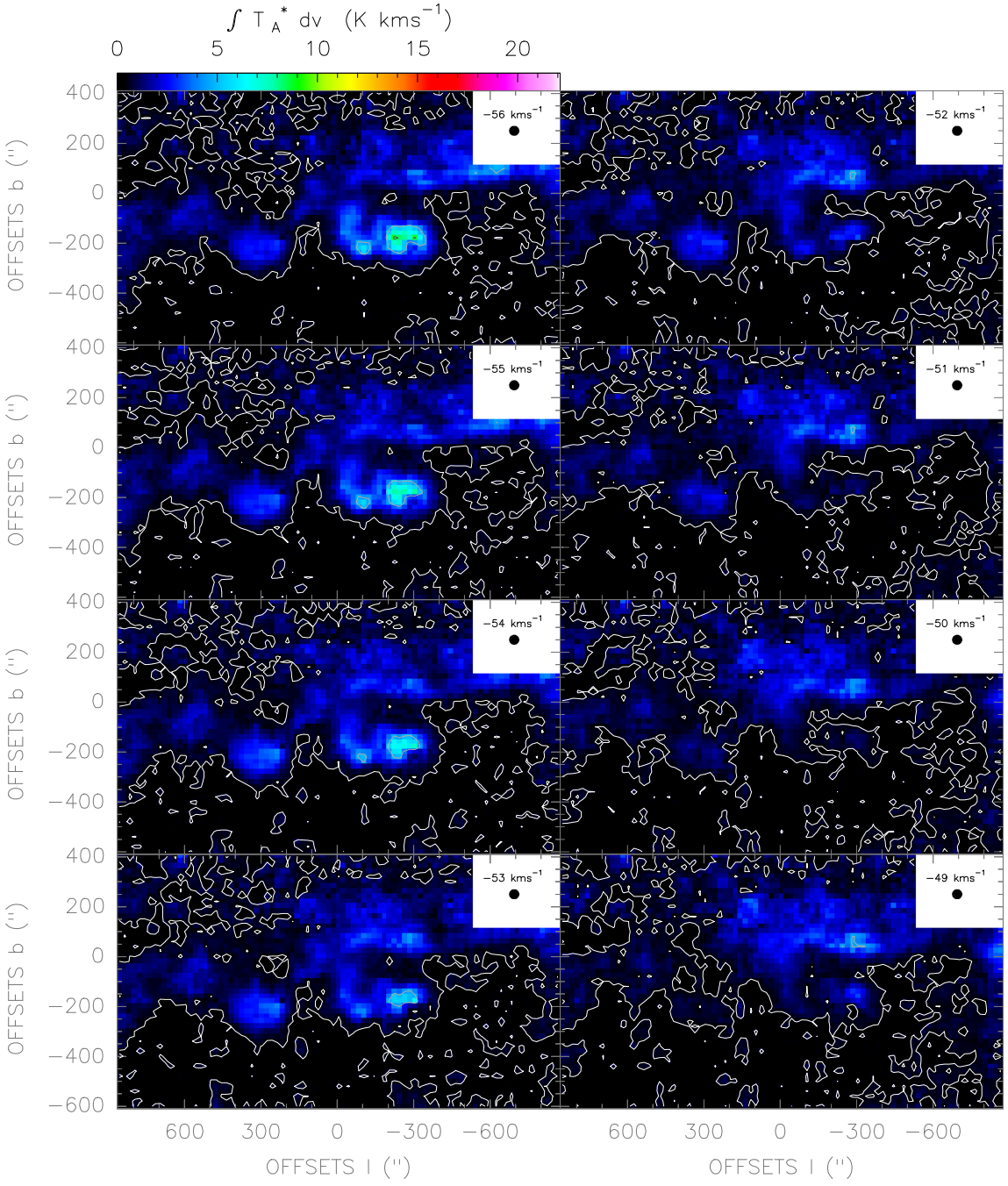

Figure. F.19: *CO(4-3) line observed with the NANTEN2/SMART telescope in Galactic coordinates. The spatial resolution of the maps is 40".*

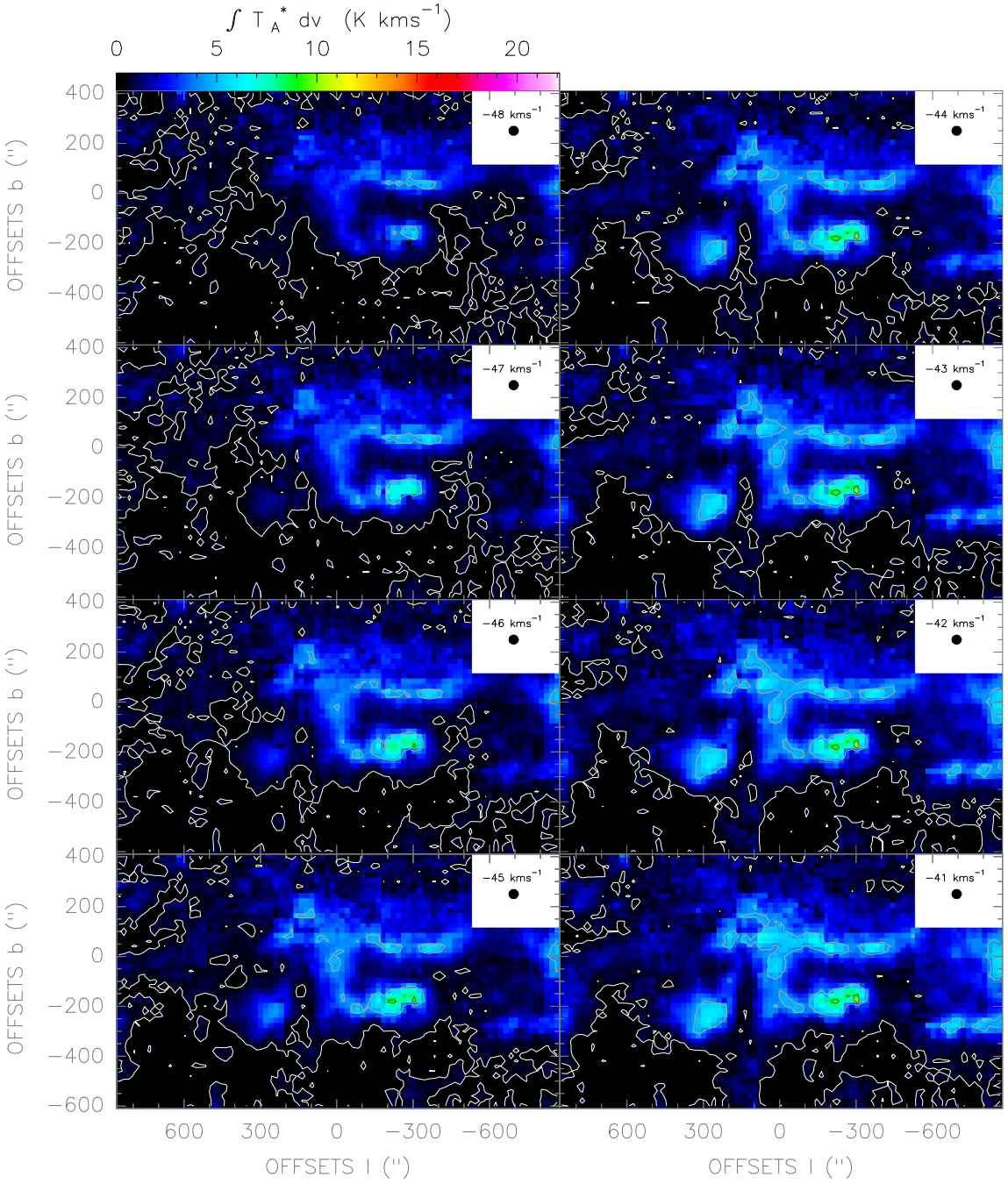

Figure. F.20: *CO(4-3) line observed with the NANTEN2/SMART telescope in Galactic coordinates. The spatial resolution of the maps is 40".*

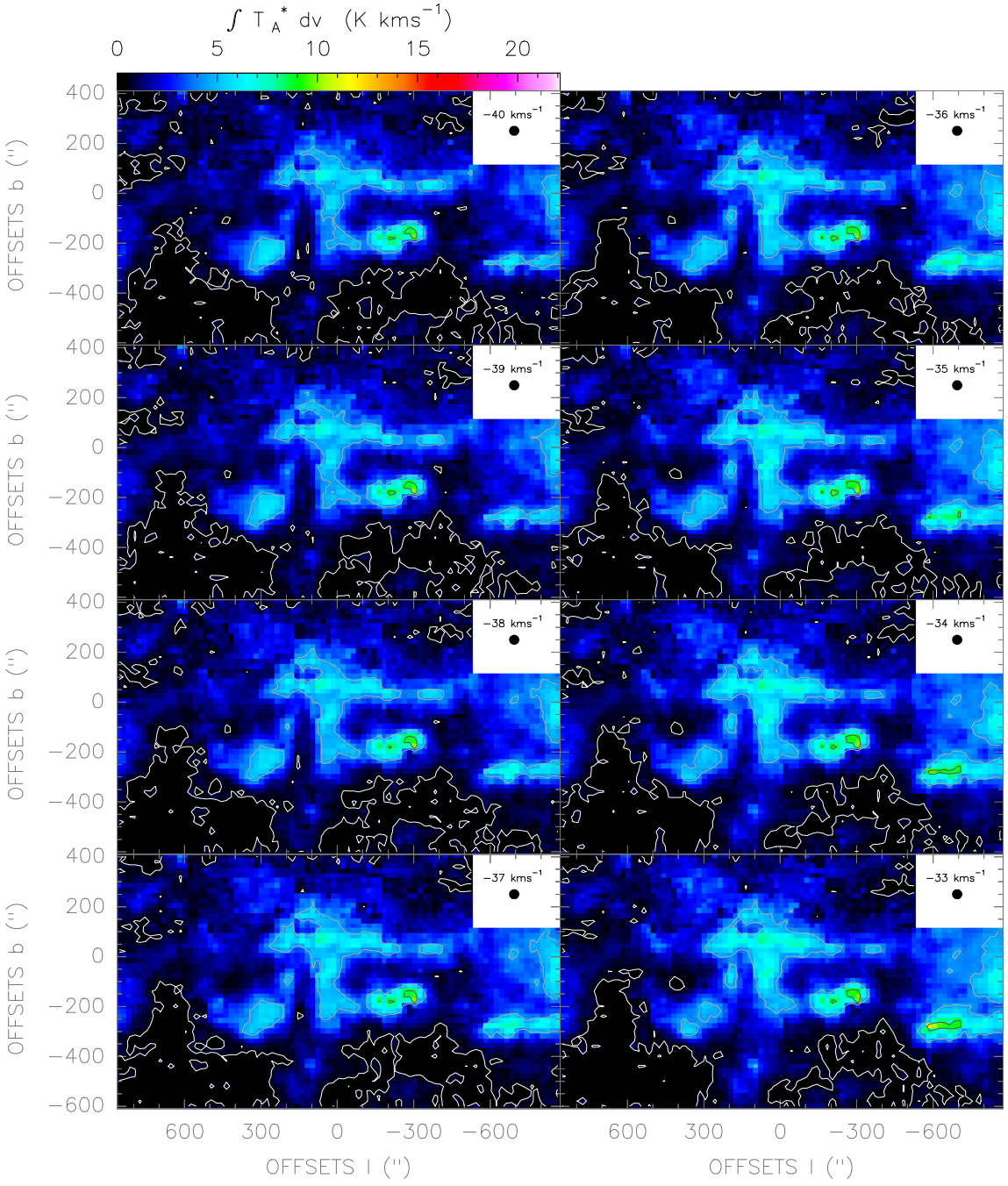

Figure. F.21: *CO(4-3) line observed with the NANTEN2/SMART telescope in Galactic coordinates. The spatial resolution of the maps is 40".*

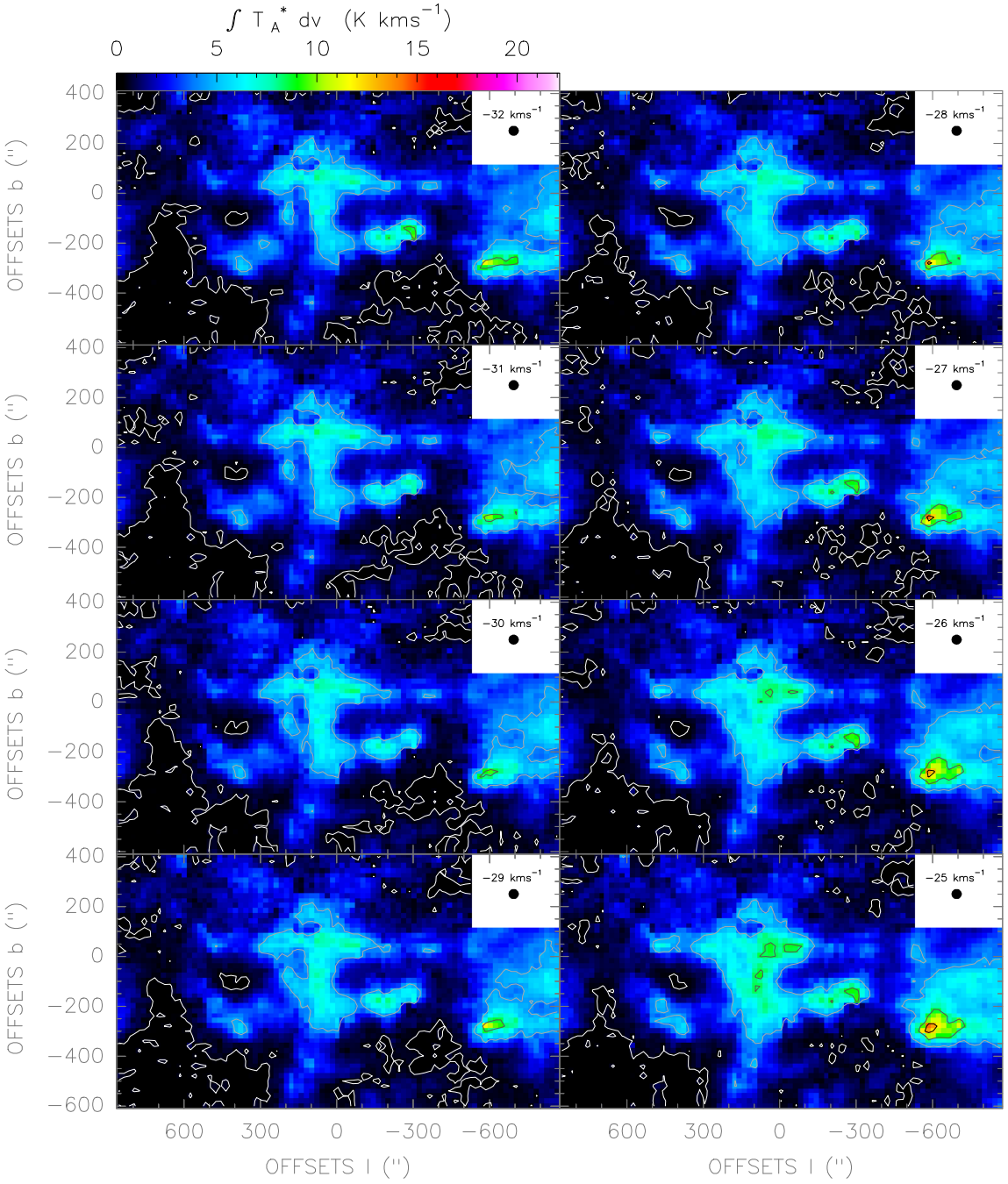

Figure. F.22: *CO(4-3) line observed with the NANTEN2/SMART telescope in Galactic coordinates. The spatial resolution of the maps is 40".*

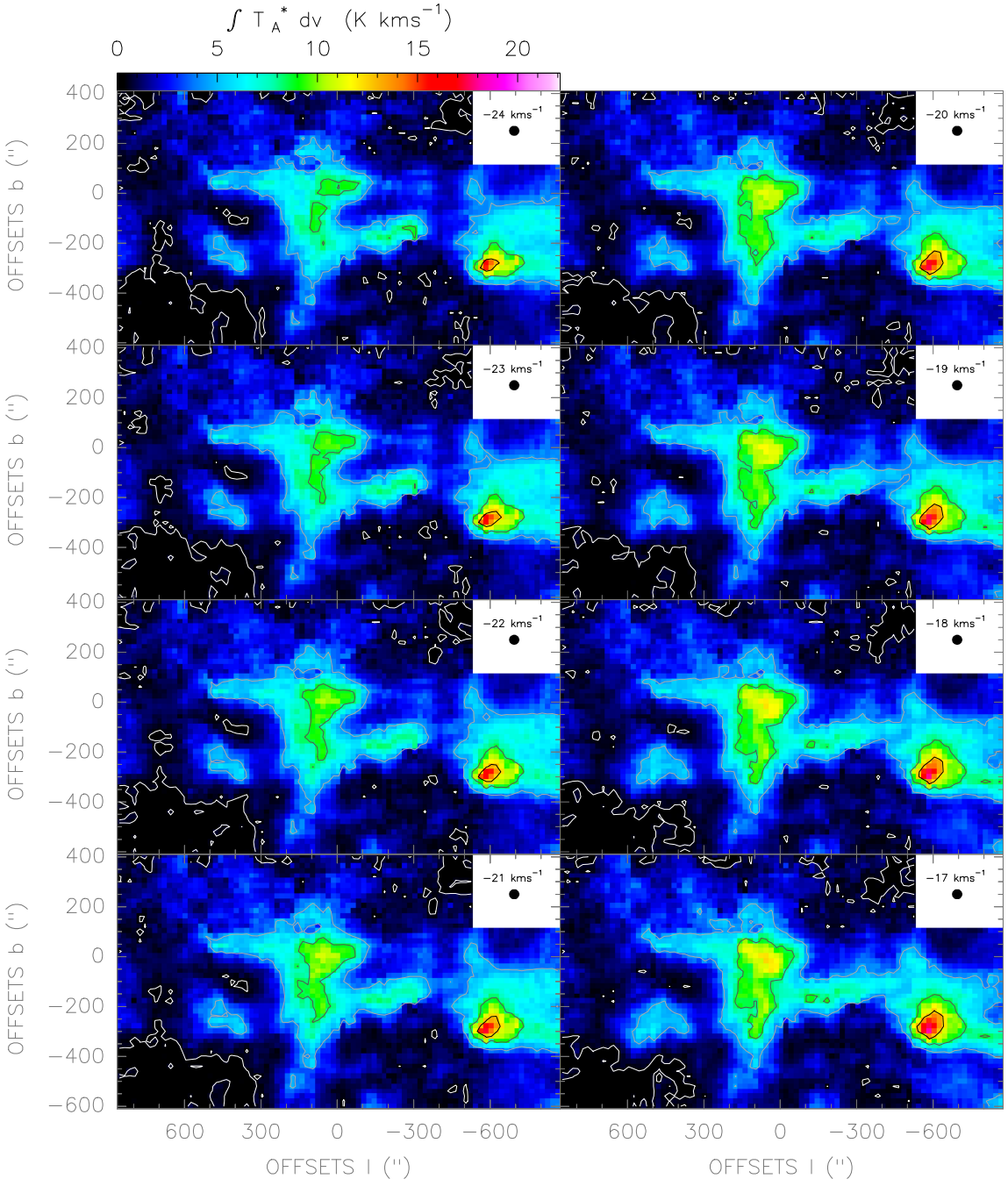

Figure. F.23: *CO(4-3) line observed with the NANTEN2/SMART telescope in Galactic coordinates. The spatial resolution of the maps is 40".*

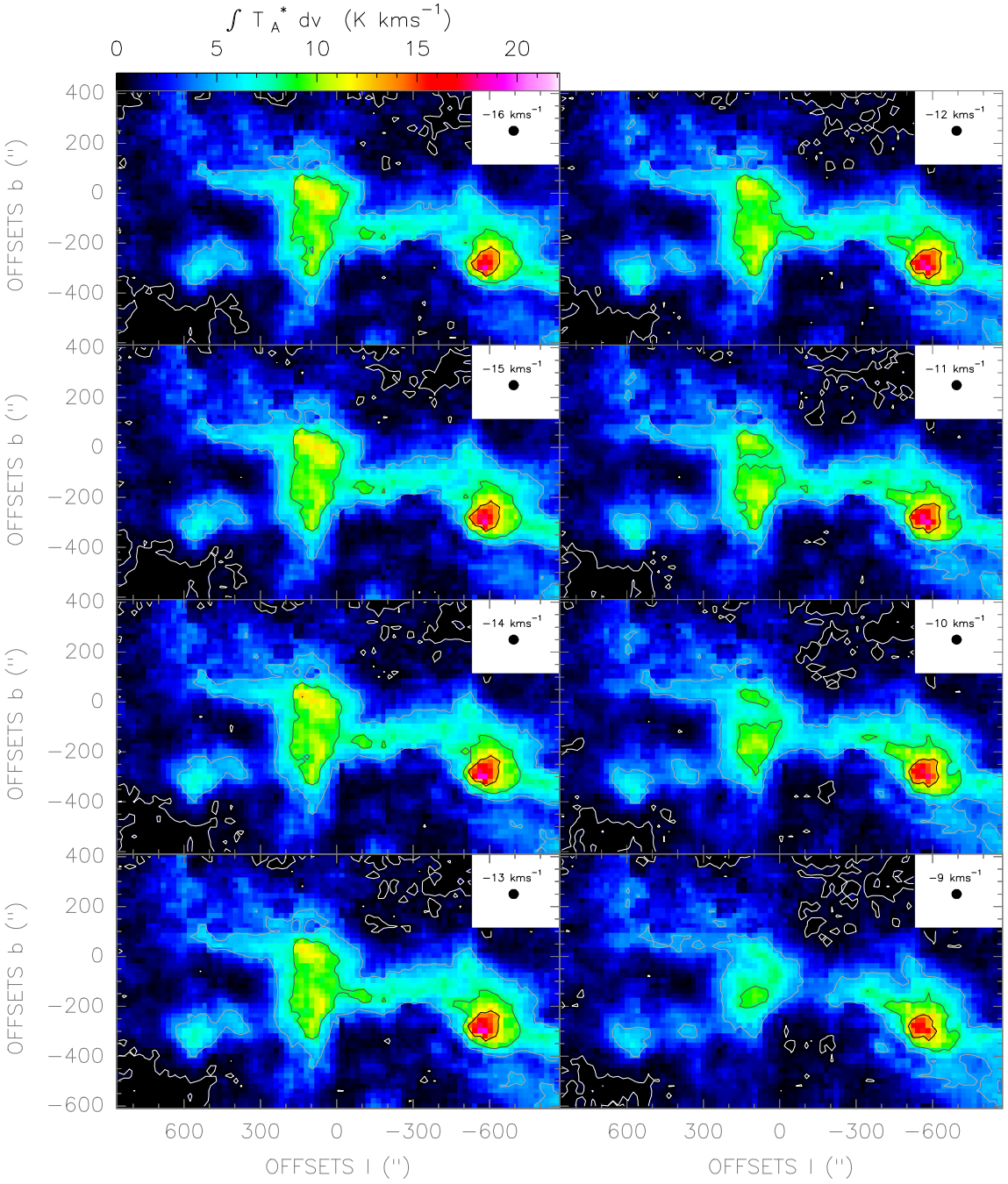

Figure. F.24: *CO(4-3) line observed with the NANTEN2/SMART telescope in Galactic coordinates. The spatial resolution of the maps is 40".*

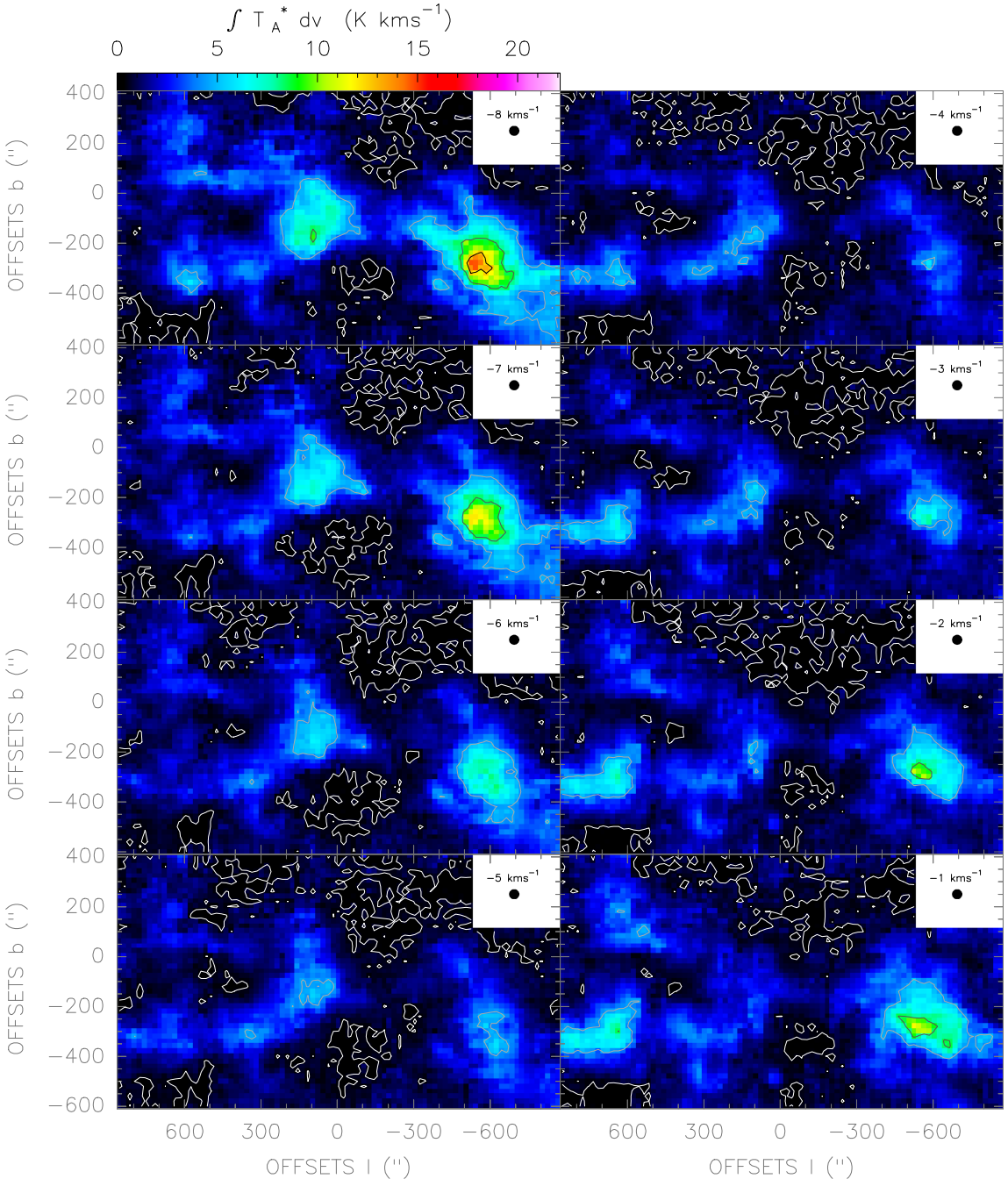

Figure. F.25: *CO(4-3) line observed with the NANTEN2/SMART telescope in Galactic coordinates. The spatial resolution of the maps is 40".*

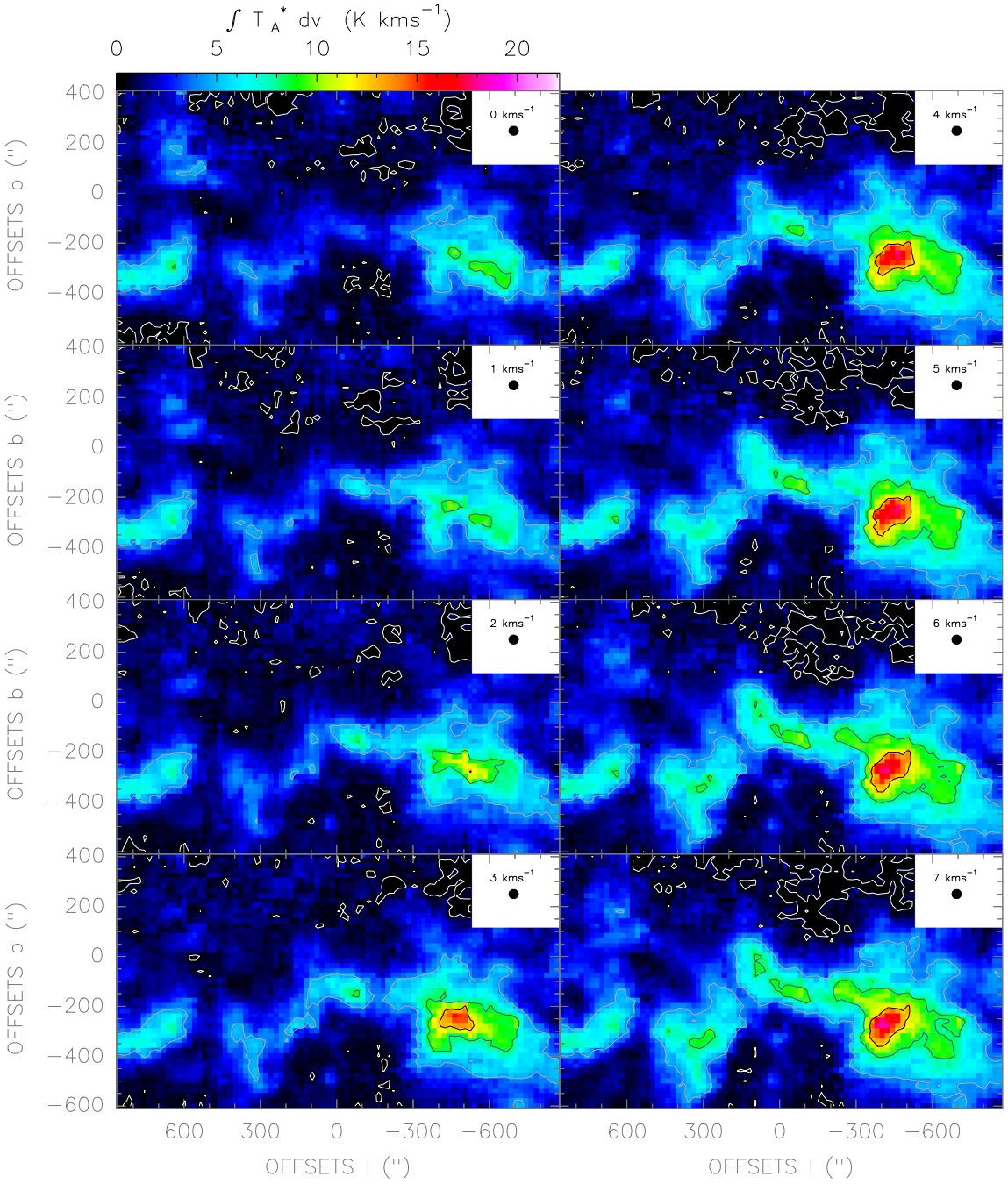

Figure. F.26: *CO(4-3) line observed with the NANTEN2/SMART telescope in Galactic coordinates. The spatial resolution of the maps is 40".*

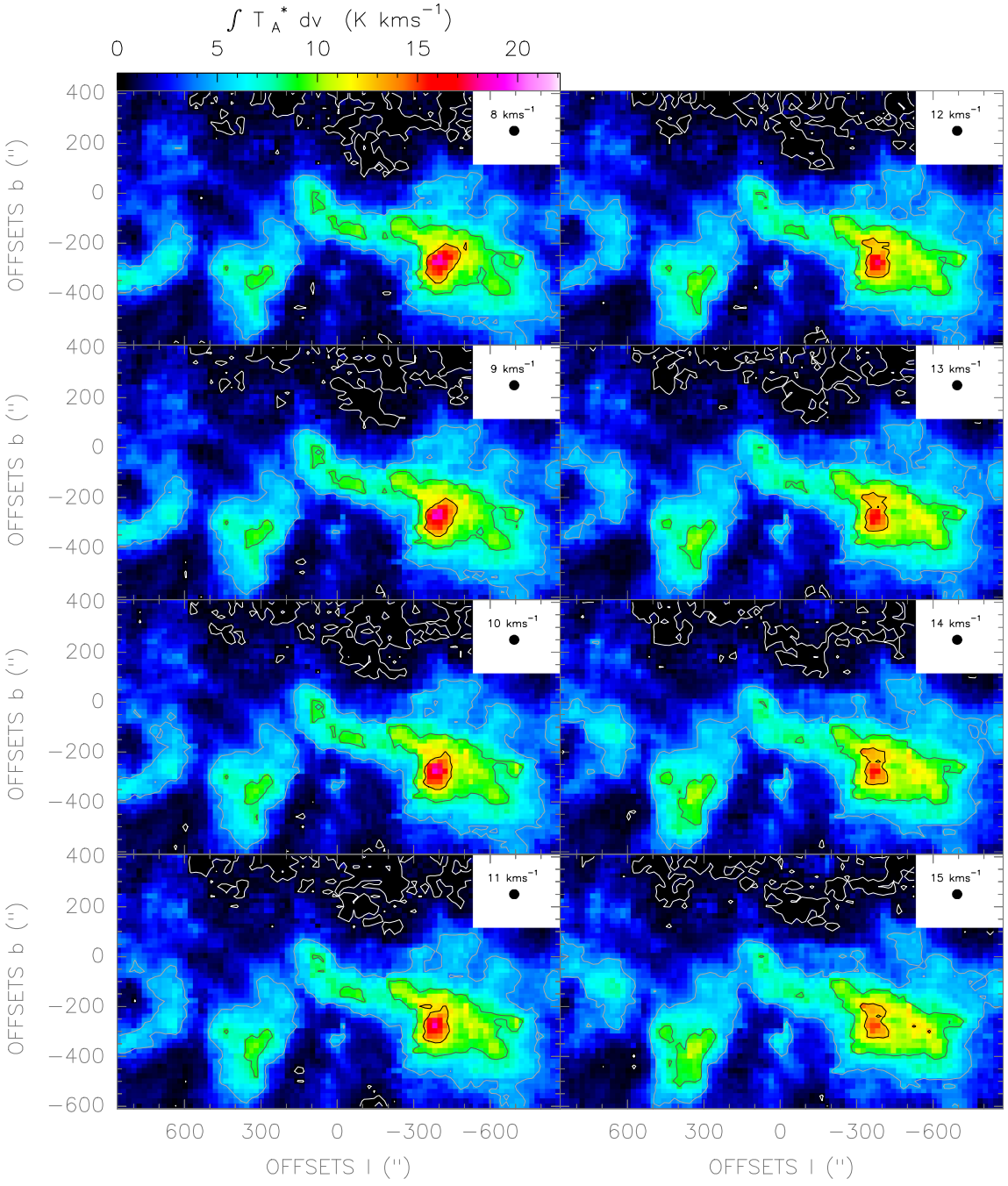

Figure. F.27: *CO(4-3) line observed with the NANTEN2/SMART telescope in Galactic coordinates. The spatial resolution of the maps is 40".*

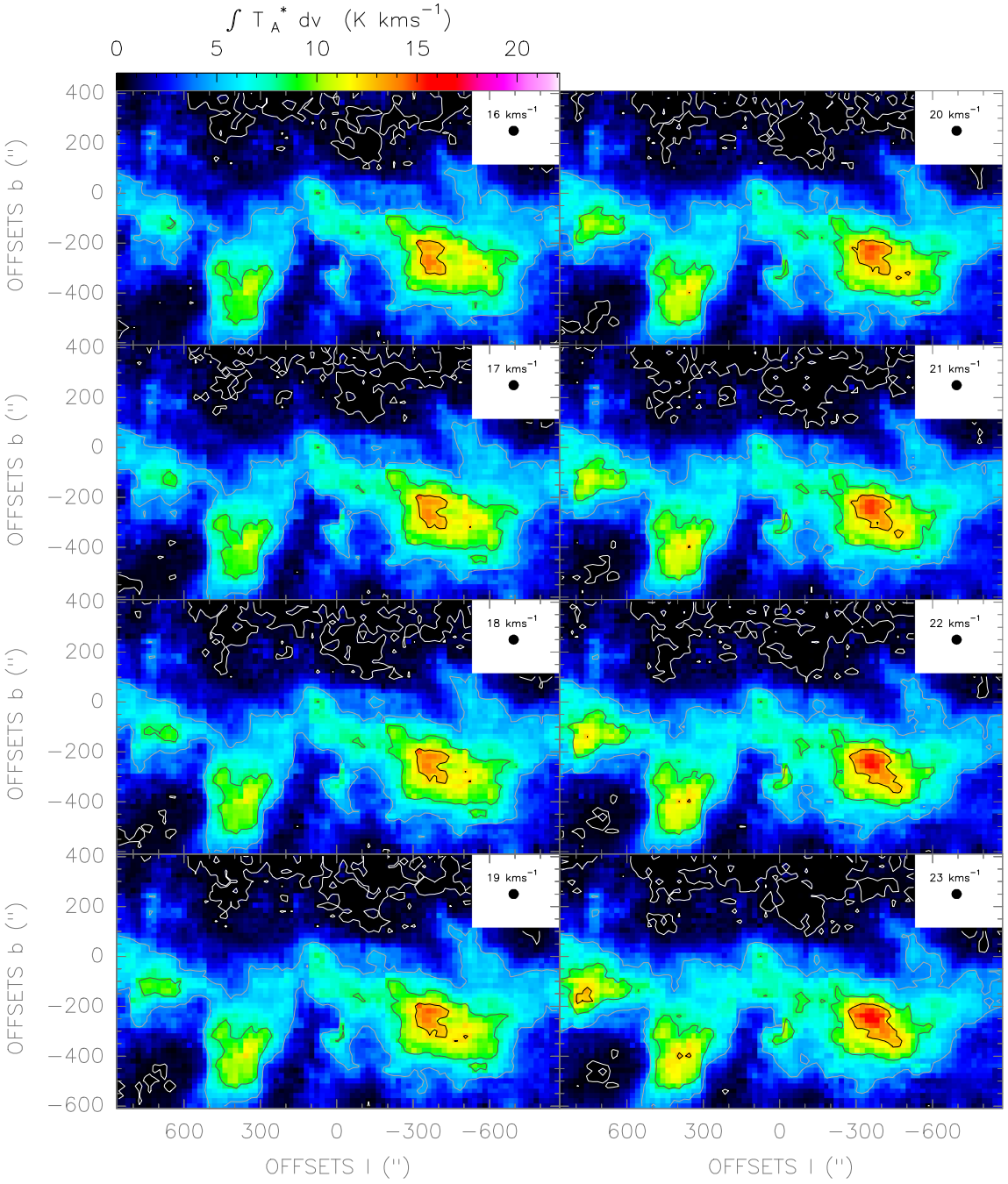

Figure. F.28: *CO(4-3) line observed with the NANTEN2/SMART telescope in Galactic coordinates. The spatial resolution of the maps is 40".*

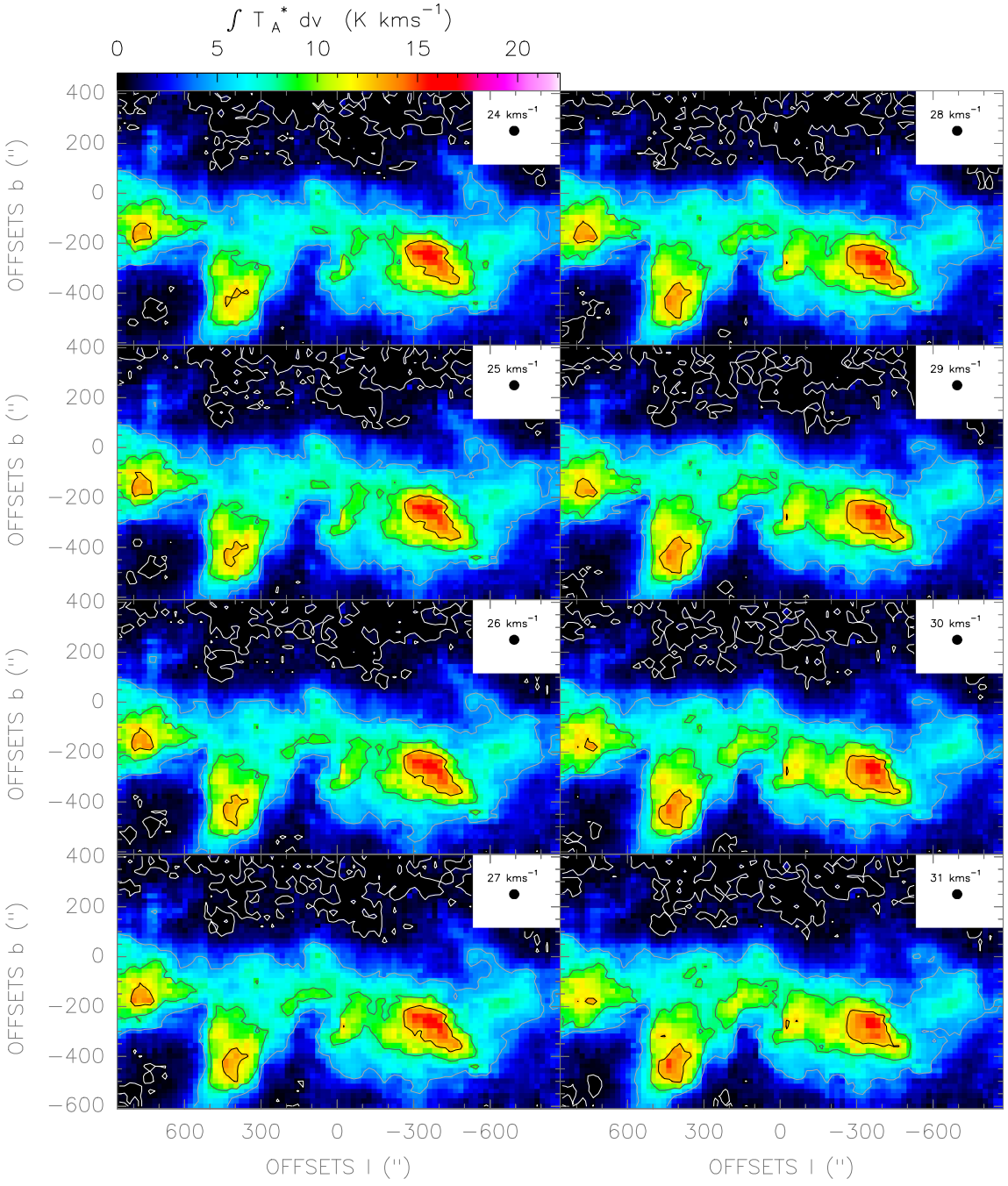

Figure. F.29: *CO(4-3) line observed with the NANTEN2/SMART telescope in Galactic coordinates. The spatial resolution of the maps is 40".*

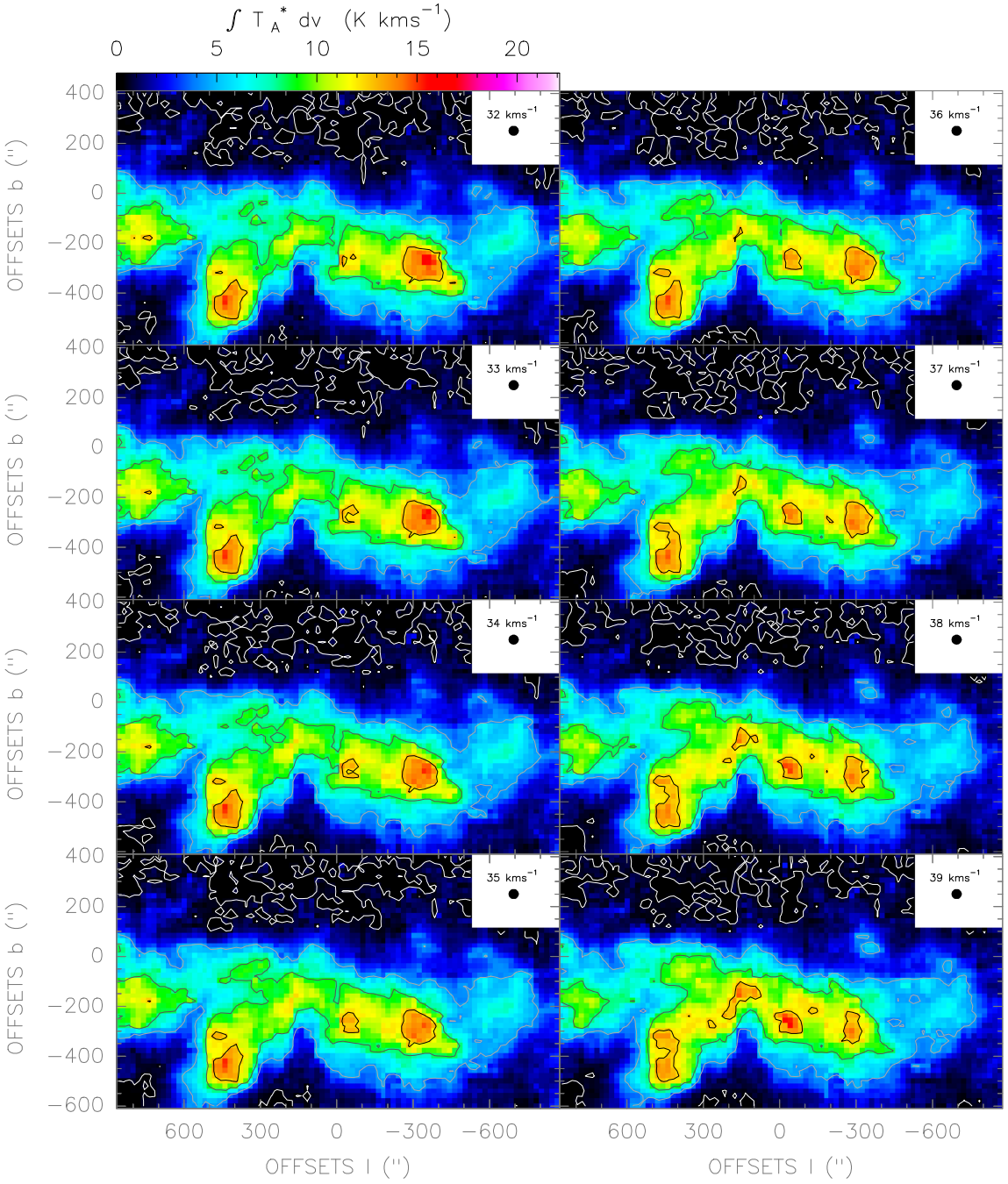

Figure. F.30: *CO(4-3) line observed with the NANTEN2/SMART telescope in Galactic coordinates. The spatial resolution of the maps is 40".*

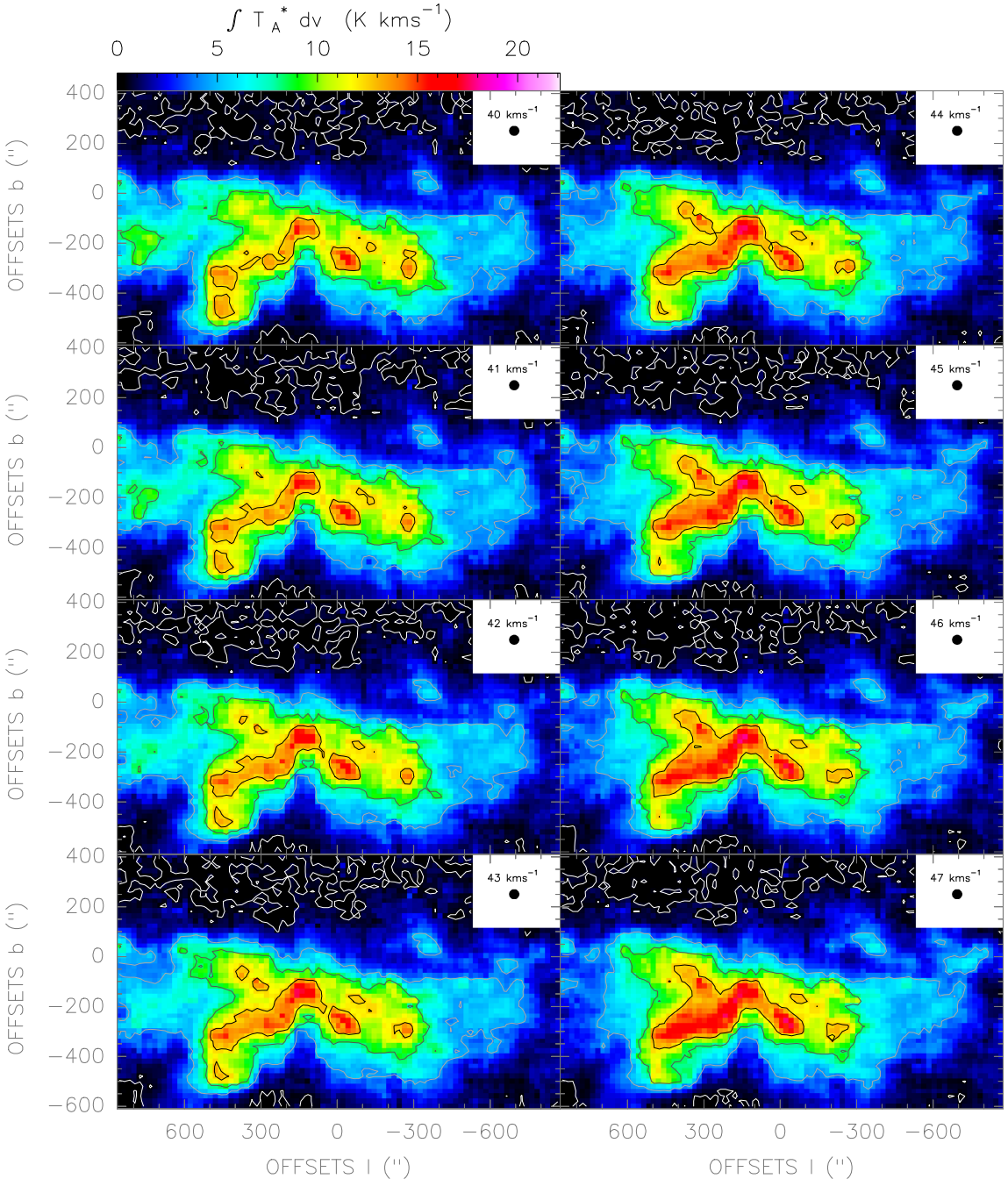

Figure. F.31: *CO(4-3) line observed with the NANTEN2/SMART telescope in Galactic coordinates. The spatial resolution of the maps is 40".*

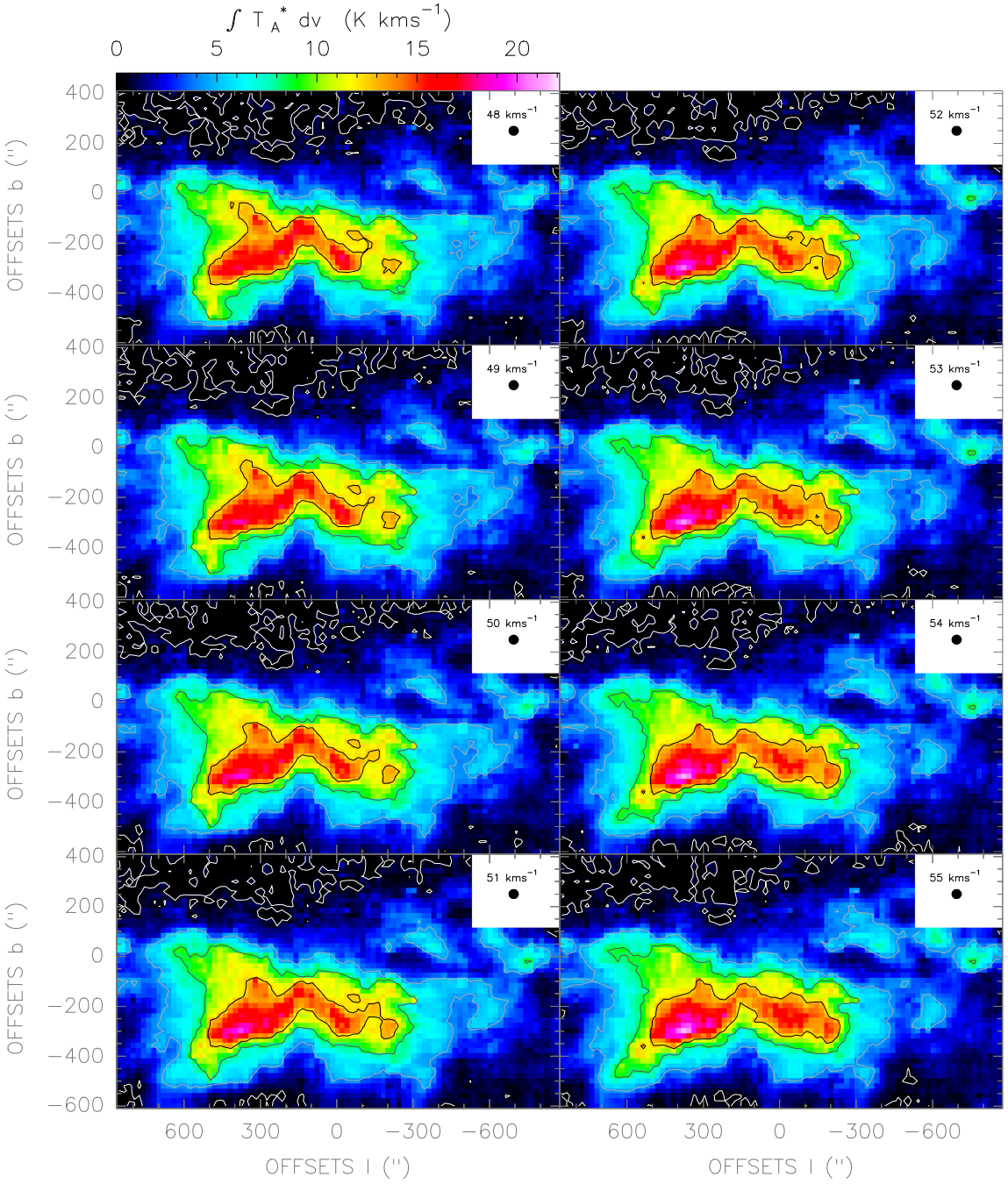

Figure. F.32: *CO(4-3) line observed with the NANTEN2/SMART telescope in Galactic coordinates. The spatial resolution of the maps is 40".*

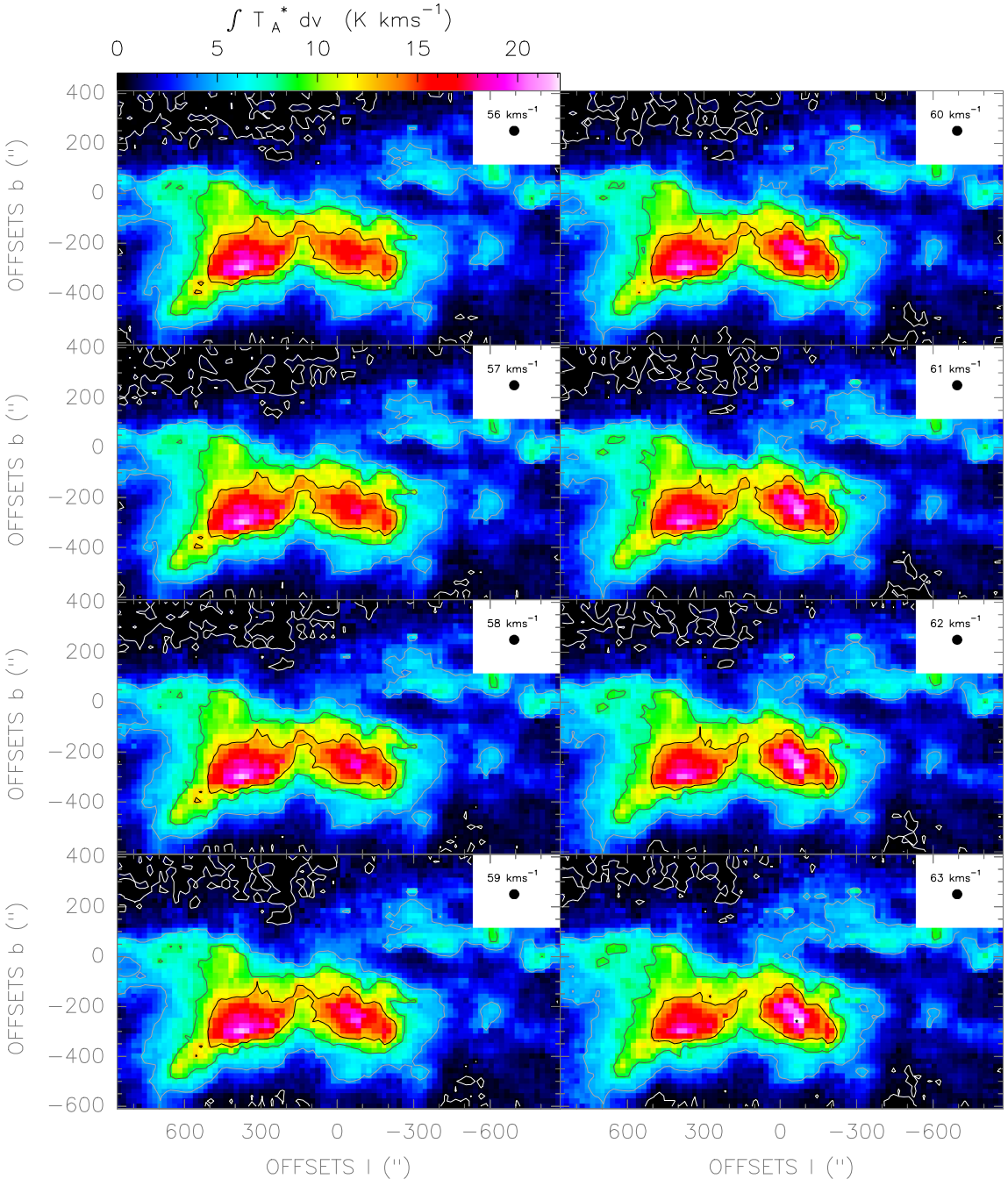

Figure. F.33: *CO(4-3) line observed with the NANTEN2/SMART telescope in Galactic coordinates. The spatial resolution of the maps is 40".*

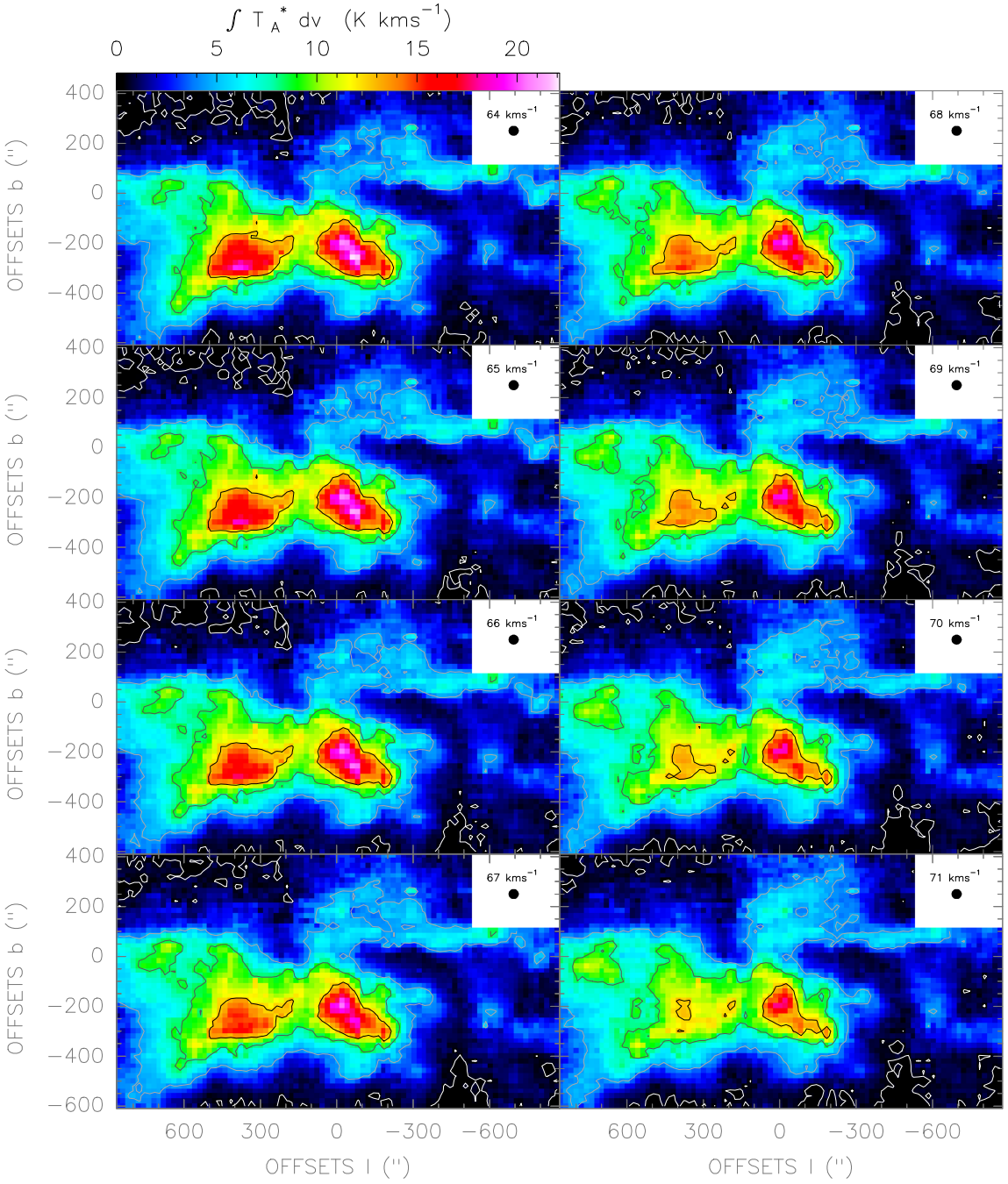

Figure. F.34: *CO(4-3) line observed with the NANTEN2/SMART telescope in Galactic coordinates. The spatial resolution of the maps is 40".*

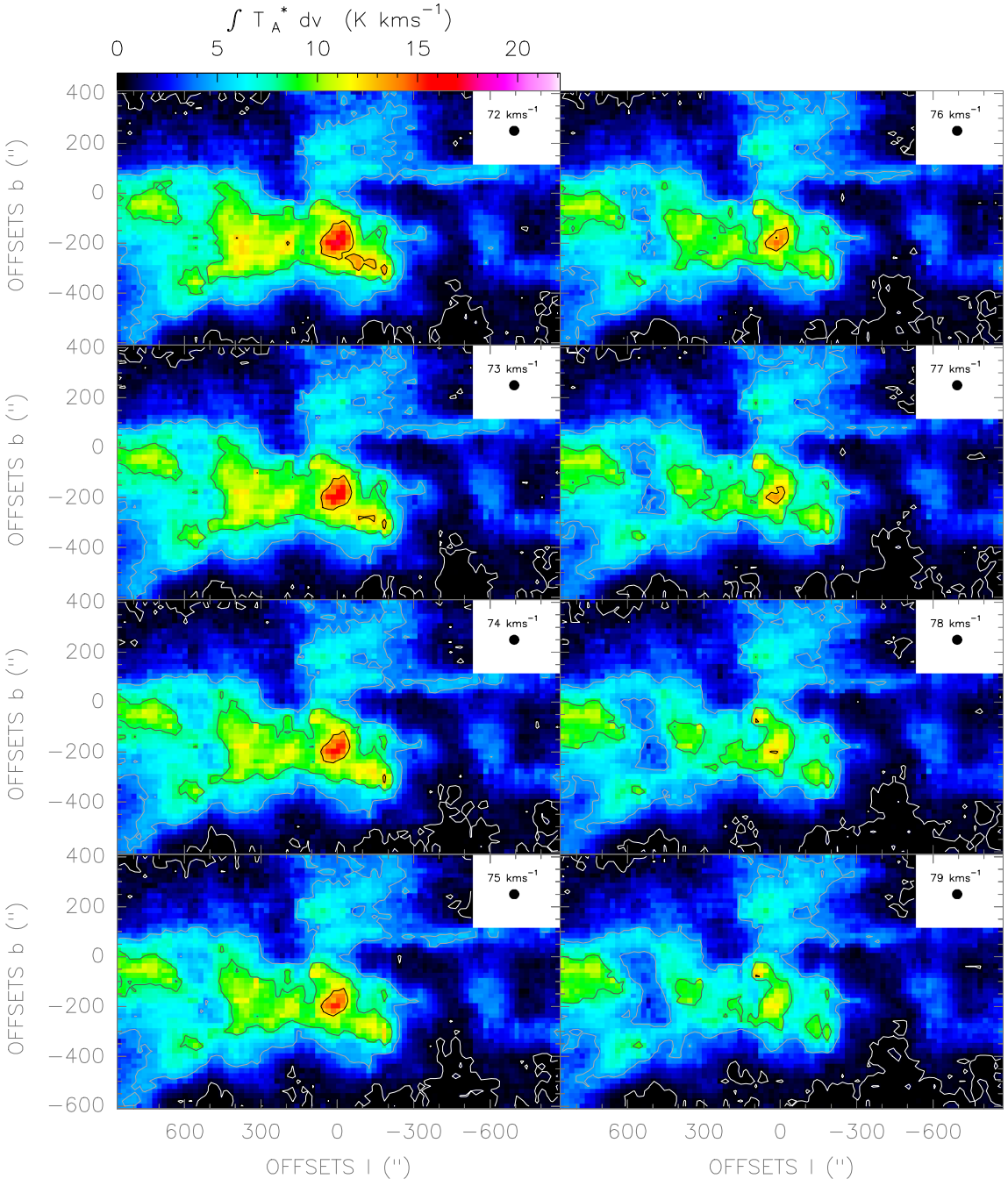

Figure. F.35: *CO(4-3) line observed with the NANTEN2/SMART telescope in Galactic coordinates. The spatial resolution of the maps is 40".*

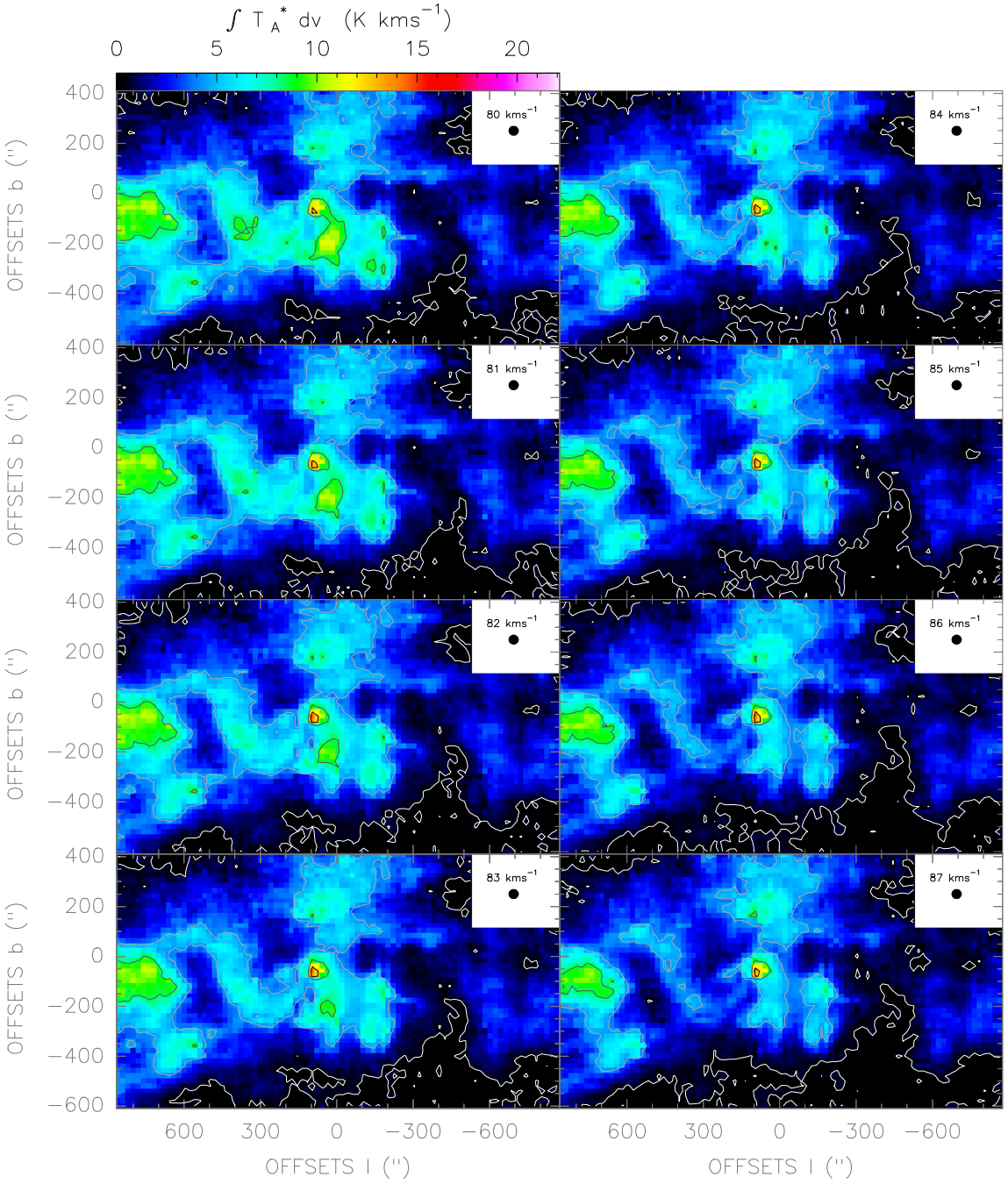

Figure. F.36: *CO(4-3) line observed with the NANTEN2/SMART telescope in Galactic coordinates. The spatial resolution of the maps is 40".*

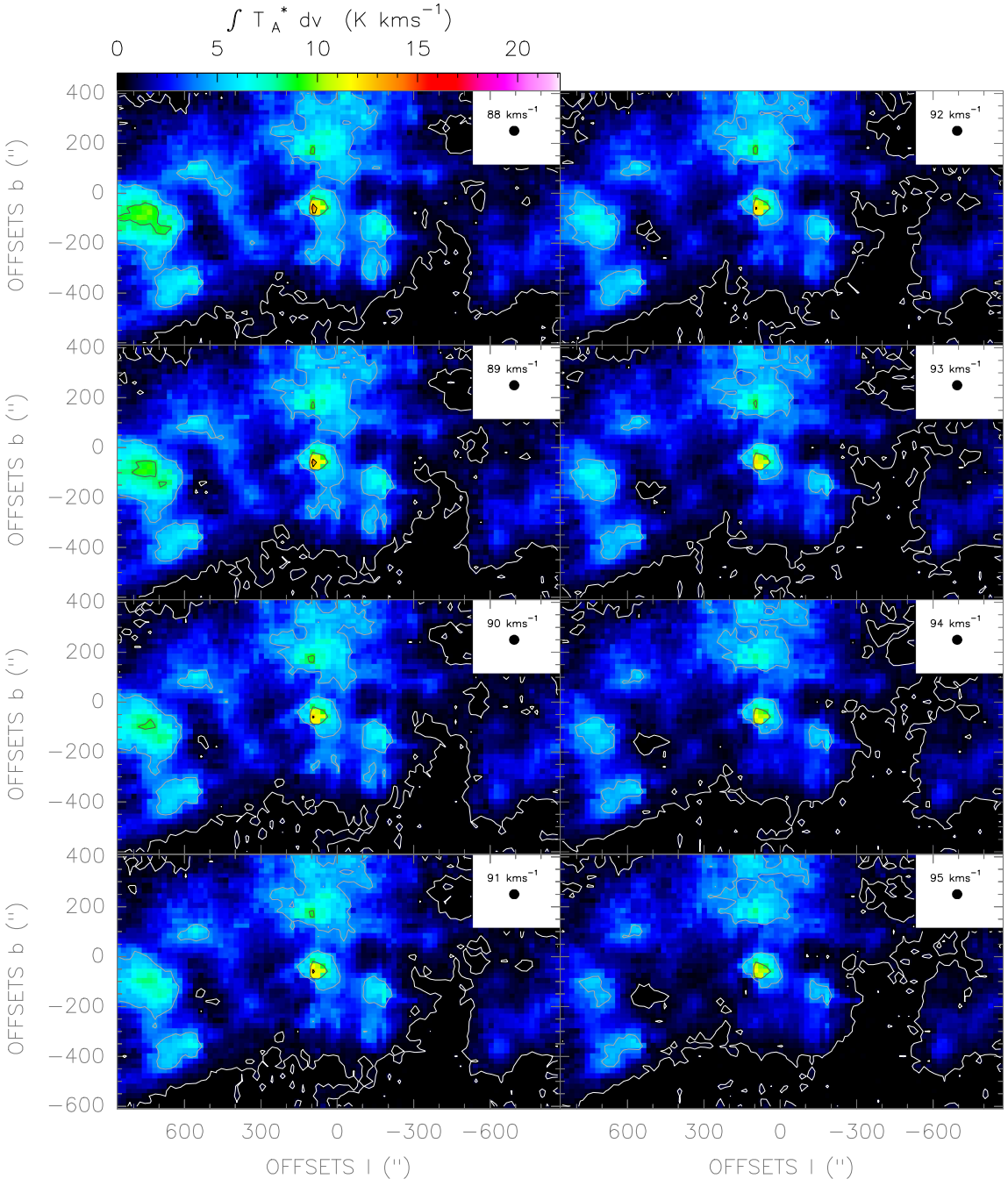

Figure. F.37: *CO(4-3) line observed with the NANTEN2/SMART telescope in Galactic coordinates. The spatial resolution of the maps is 40".*

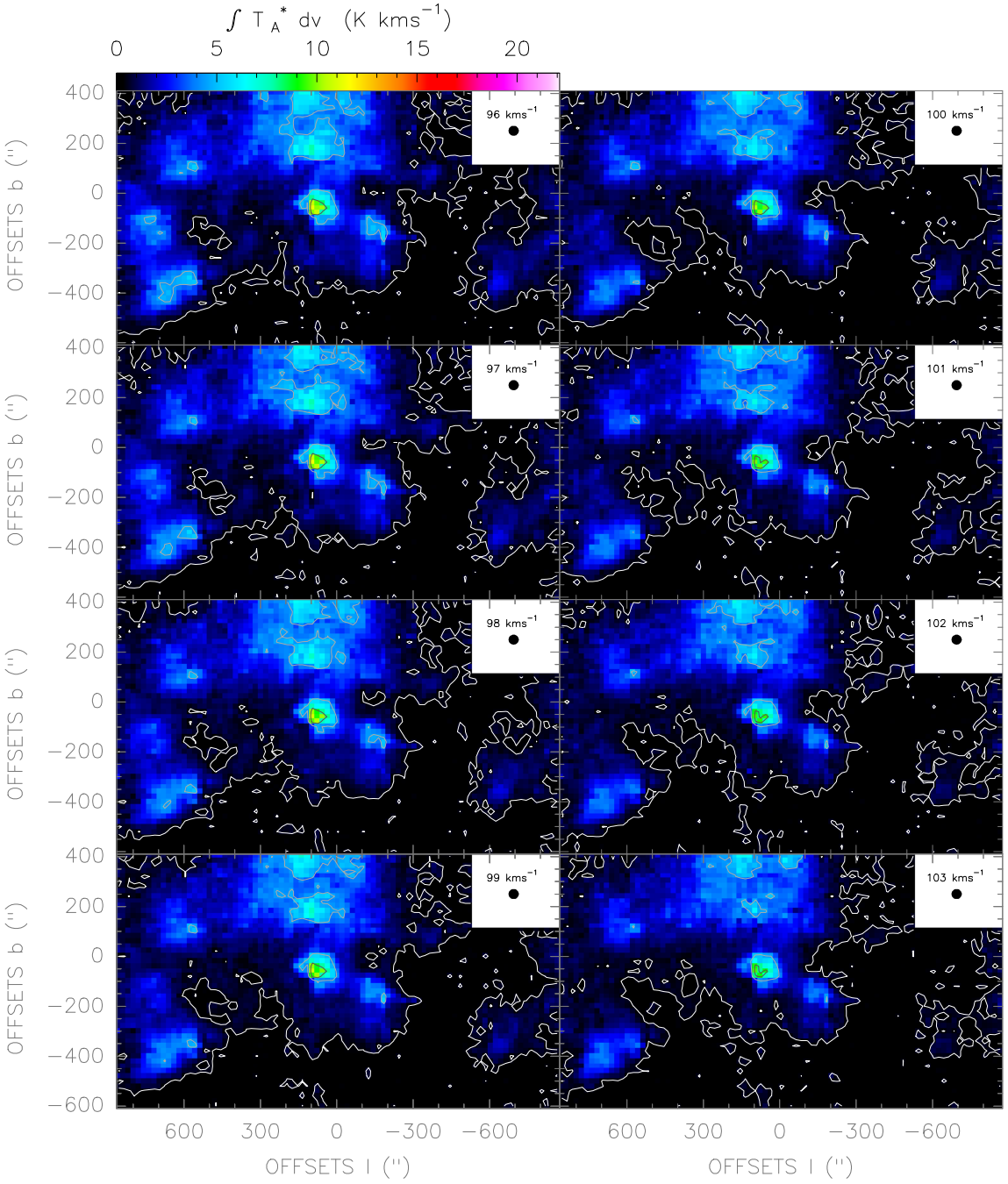

Figure. F.38: *CO(4-3) line observed with the NANTEN2/SMART telescope in Galactic coordinates. The spatial resolution of the maps is 40".*

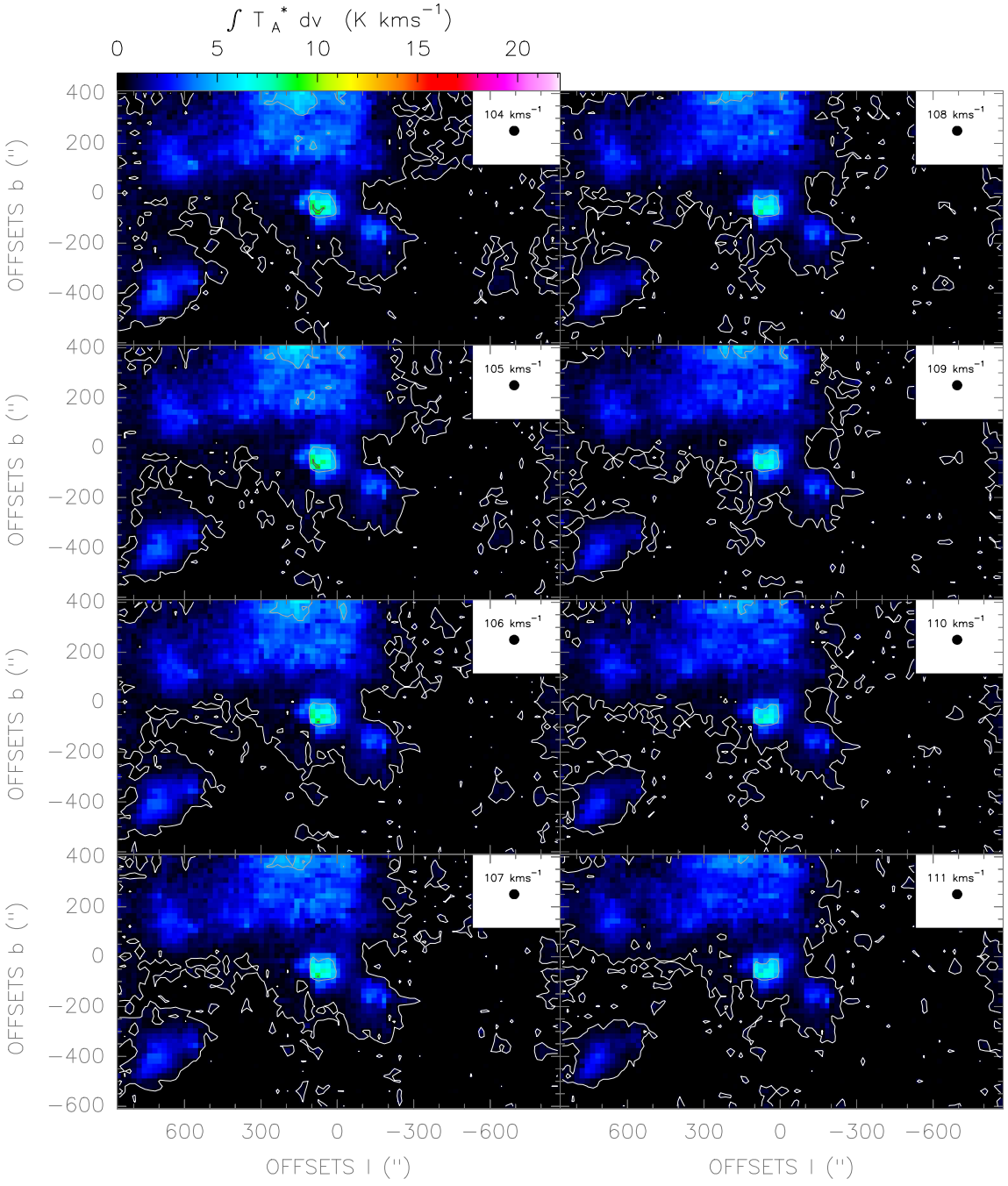

Figure. F.39: *CO(4-3) line observed with the NANTEN2/SMART telescope in Galactic coordinates. The spatial resolution of the maps is 40".*

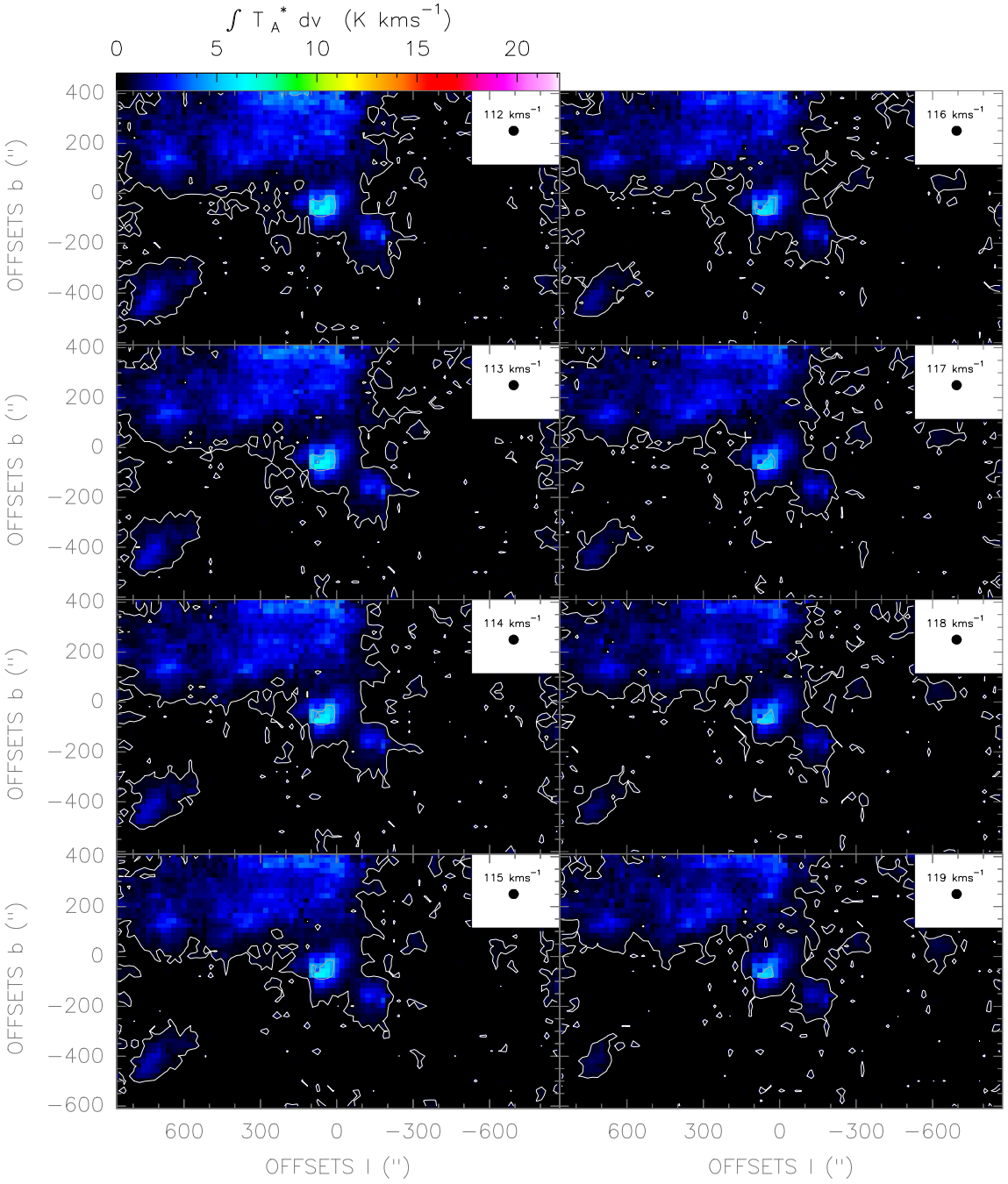

Figure. F.40: *CO(4-3) line observed with the NANTEN2/SMART telescope in Galactic coordinates. The spatial resolution of the maps is 40".*

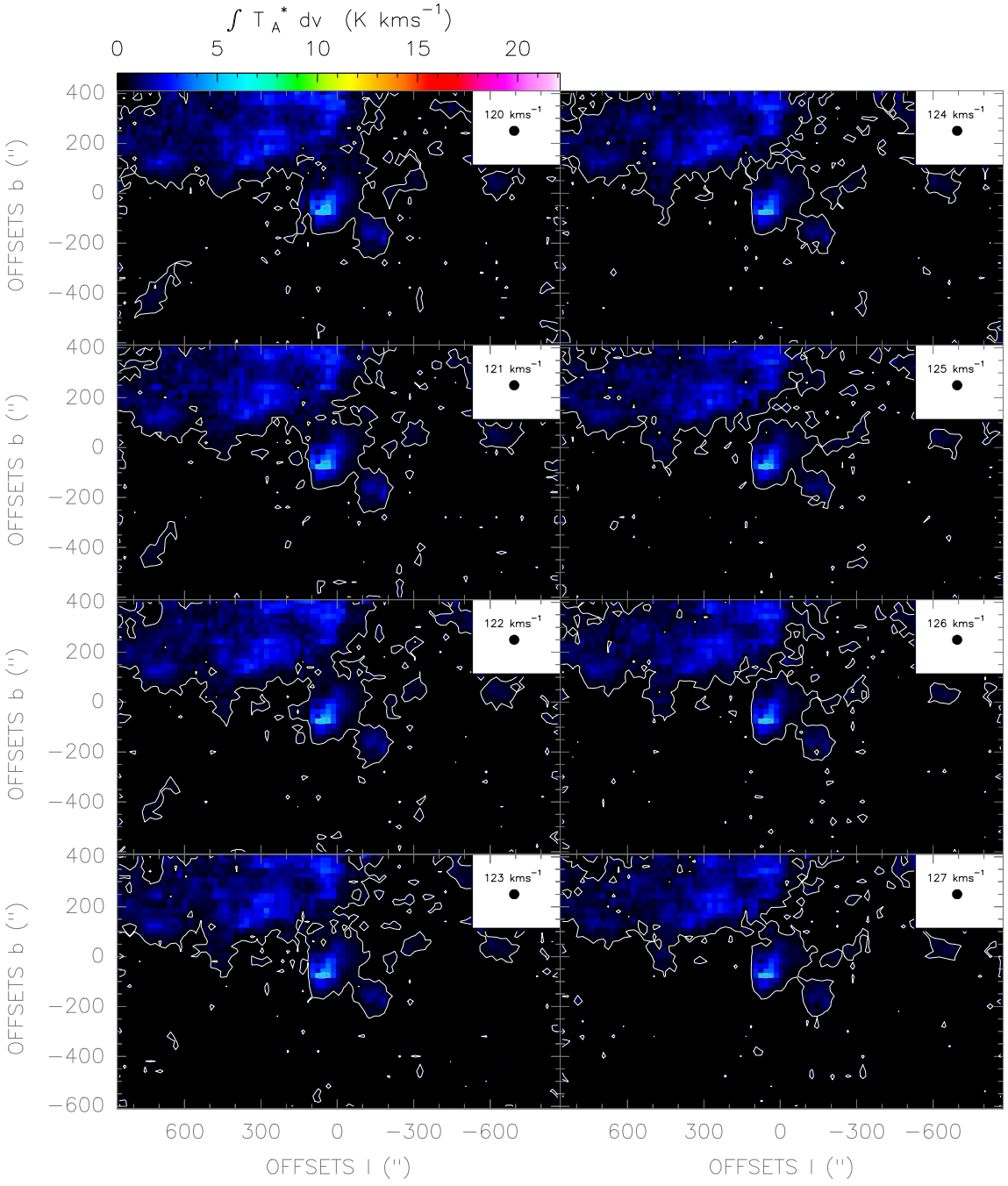

Figure. F.41: *CO(4-3) line observed with the NANTEN2/SMART telescope in Galactic coordinates. The spatial resolution of the maps is 40".*

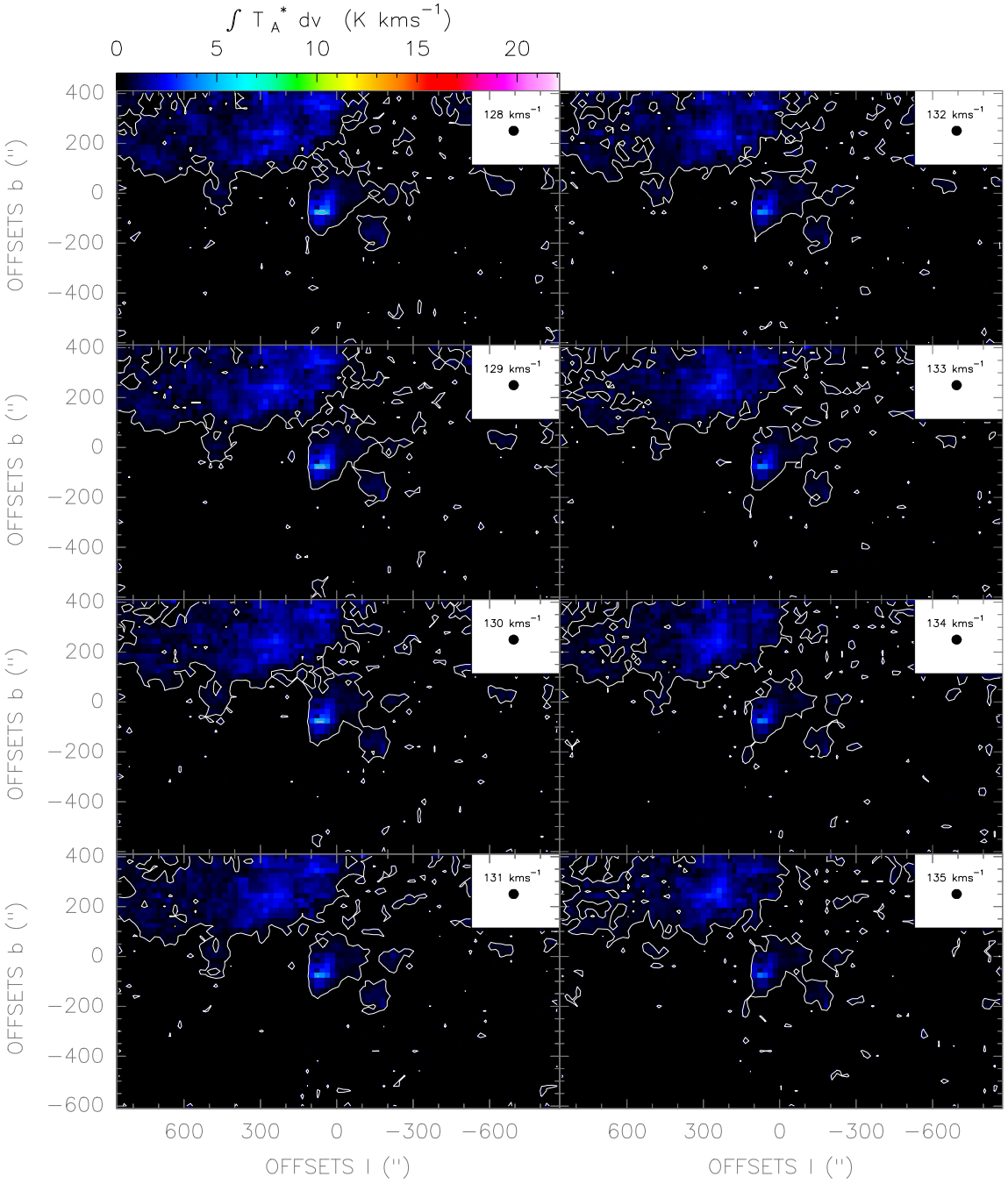

Figure. F.42: *CO(4-3) line observed with the NANTEN2/SMART telescope in Galactic coordinates. The spatial resolution of the maps is 40".*

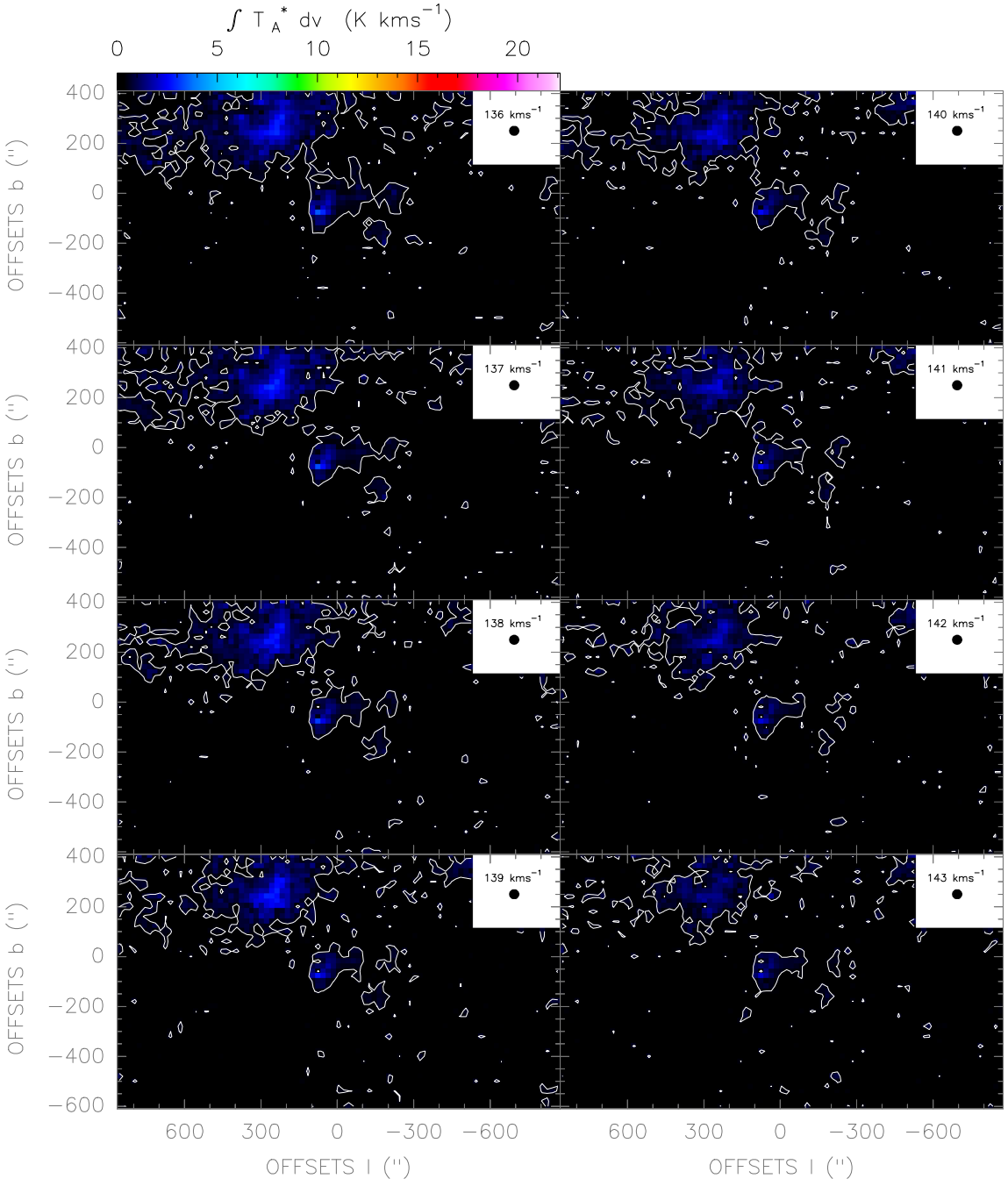

Figure. F.43: *CO(4-3) line observed with the NANTEN2/SMART telescope in Galactic coordinates. The spatial resolution of the maps is 40".*

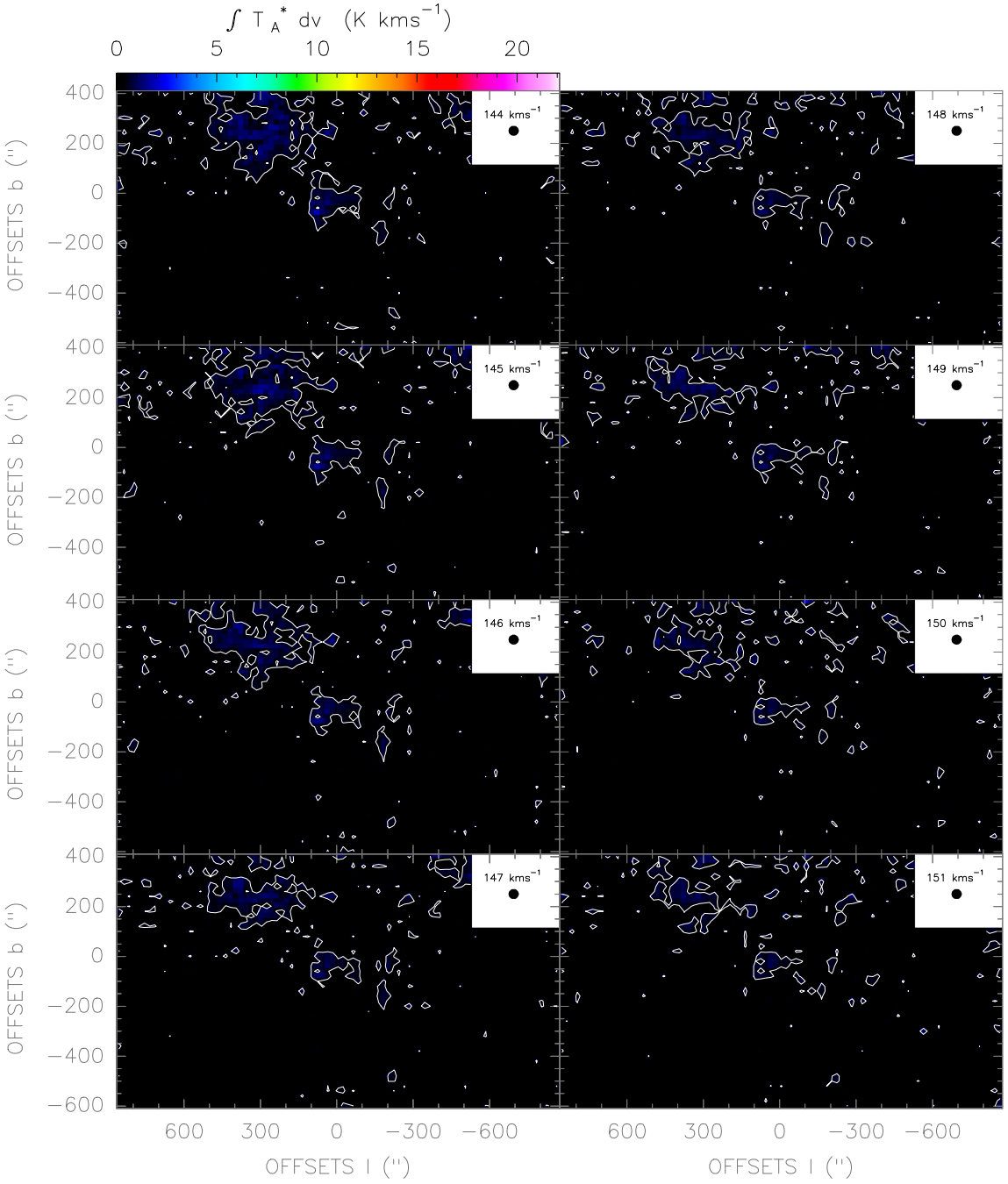

Figure. F.44: *CO(4-3) line observed with the NANTEN2/SMART telescope in Galactic coordinates. The spatial resolution of the maps is 40".*

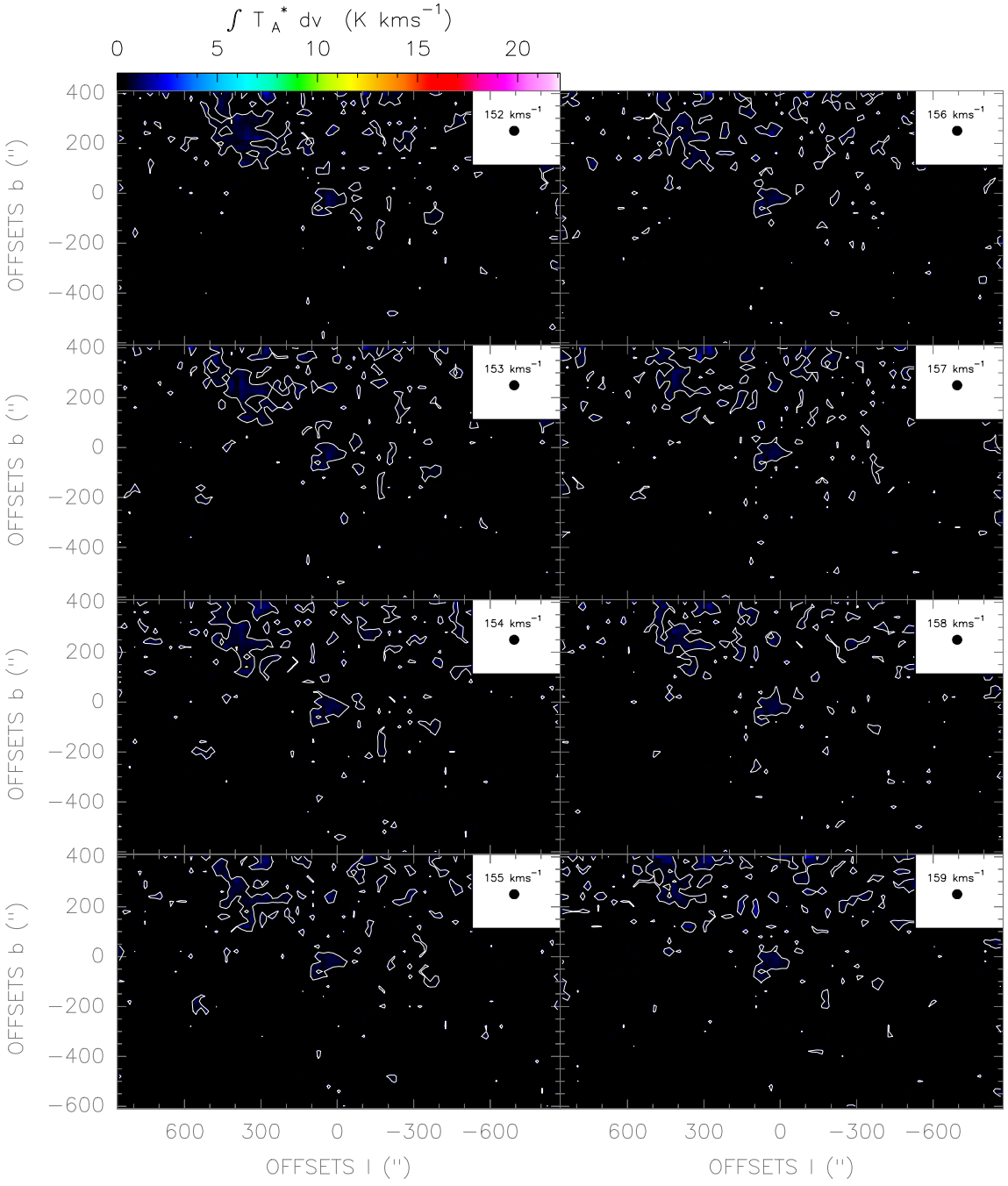

Figure. F.45: *CO(4-3) line observed with the NANTEN2/SMART telescope in Galactic coordinates. The spatial resolution of the maps is 40".*

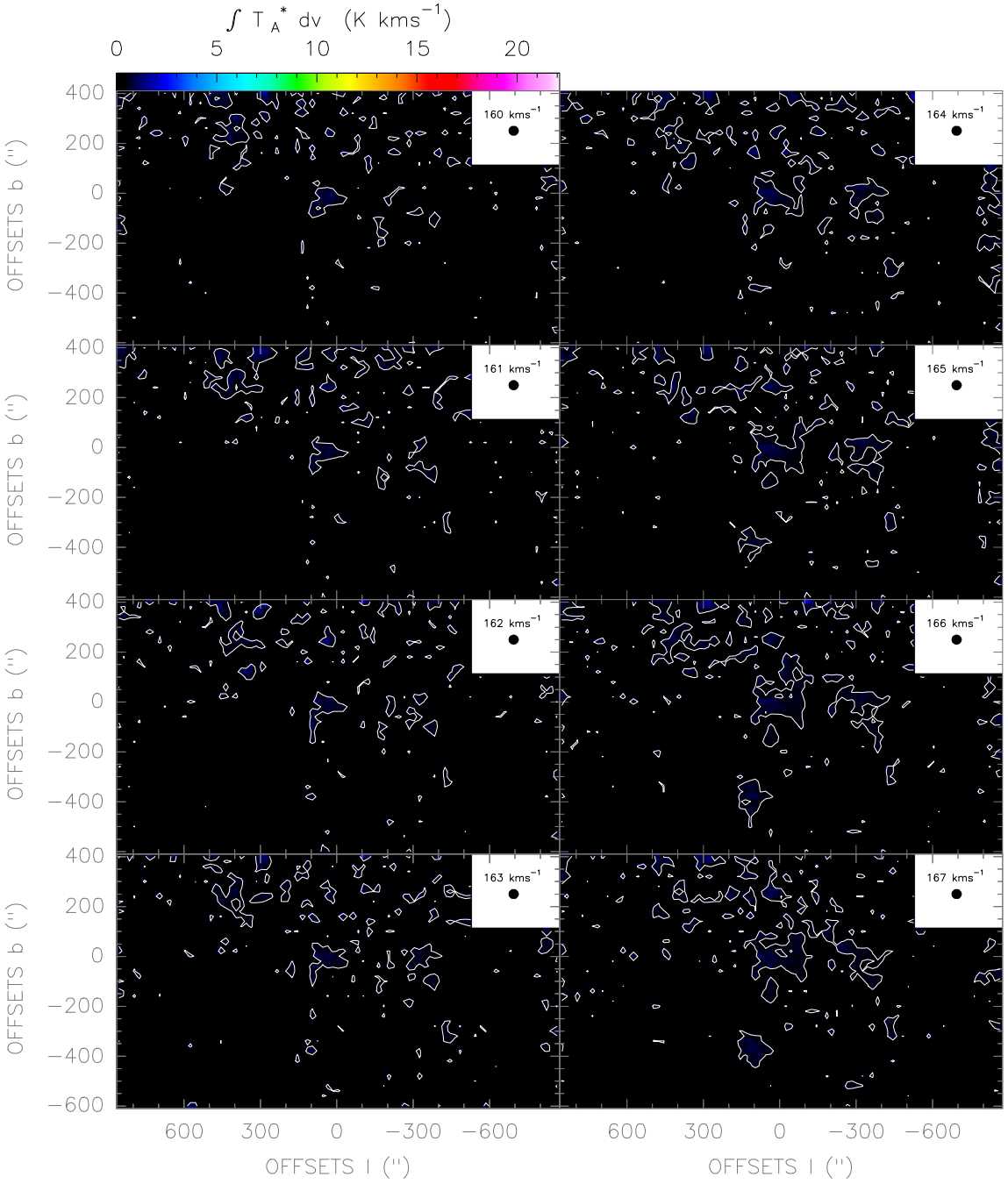

Figure. F.46: *CO(4-3) line observed with the NANTEN2/SMART telescope in Galactic coordinates. The spatial resolution of the maps is 40".*

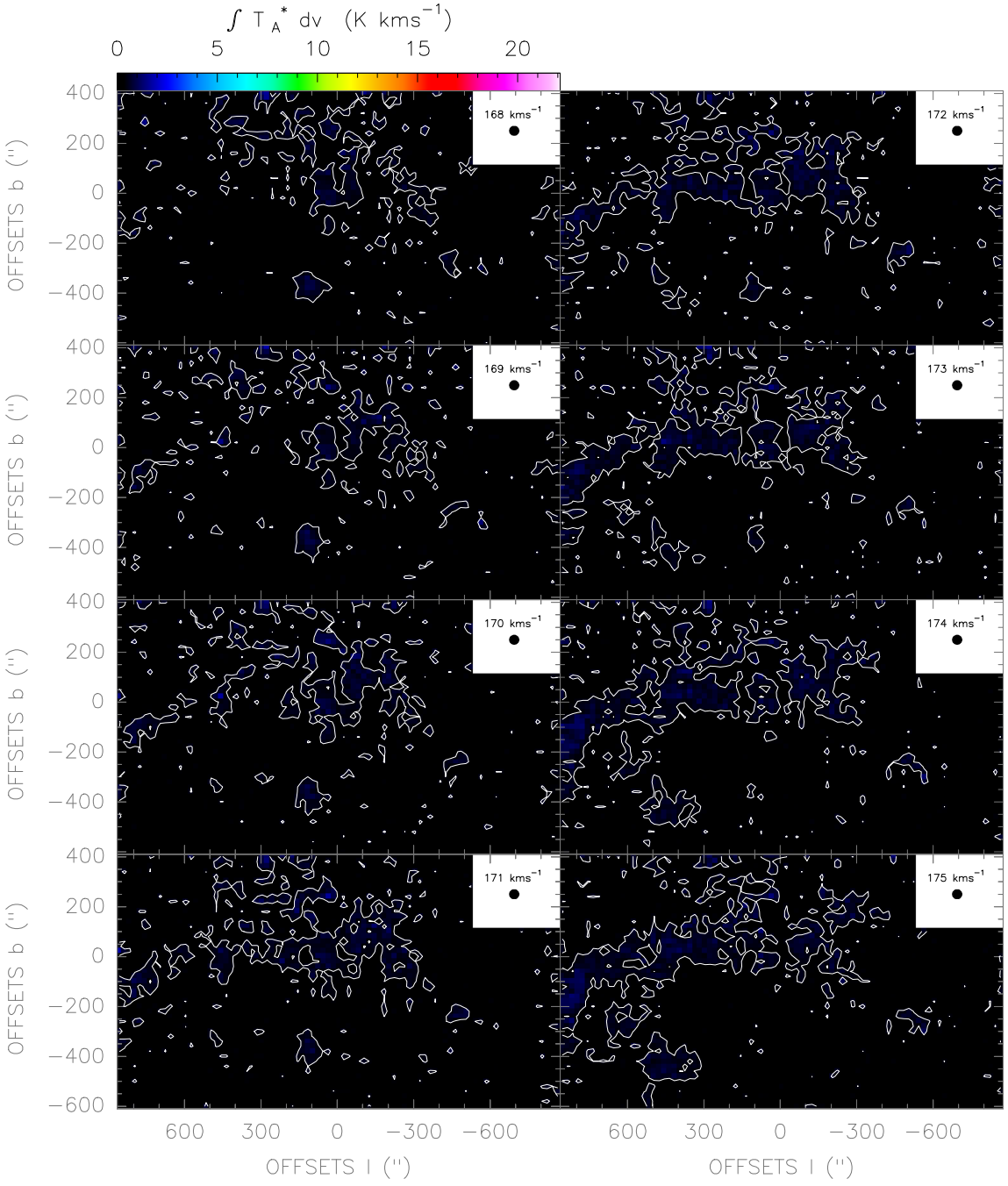

Figure. F.47: *CO(4-3) line observed with the NANTEN2/SMART telescope in Galactic coordinates. The spatial resolution of the maps is 40".*

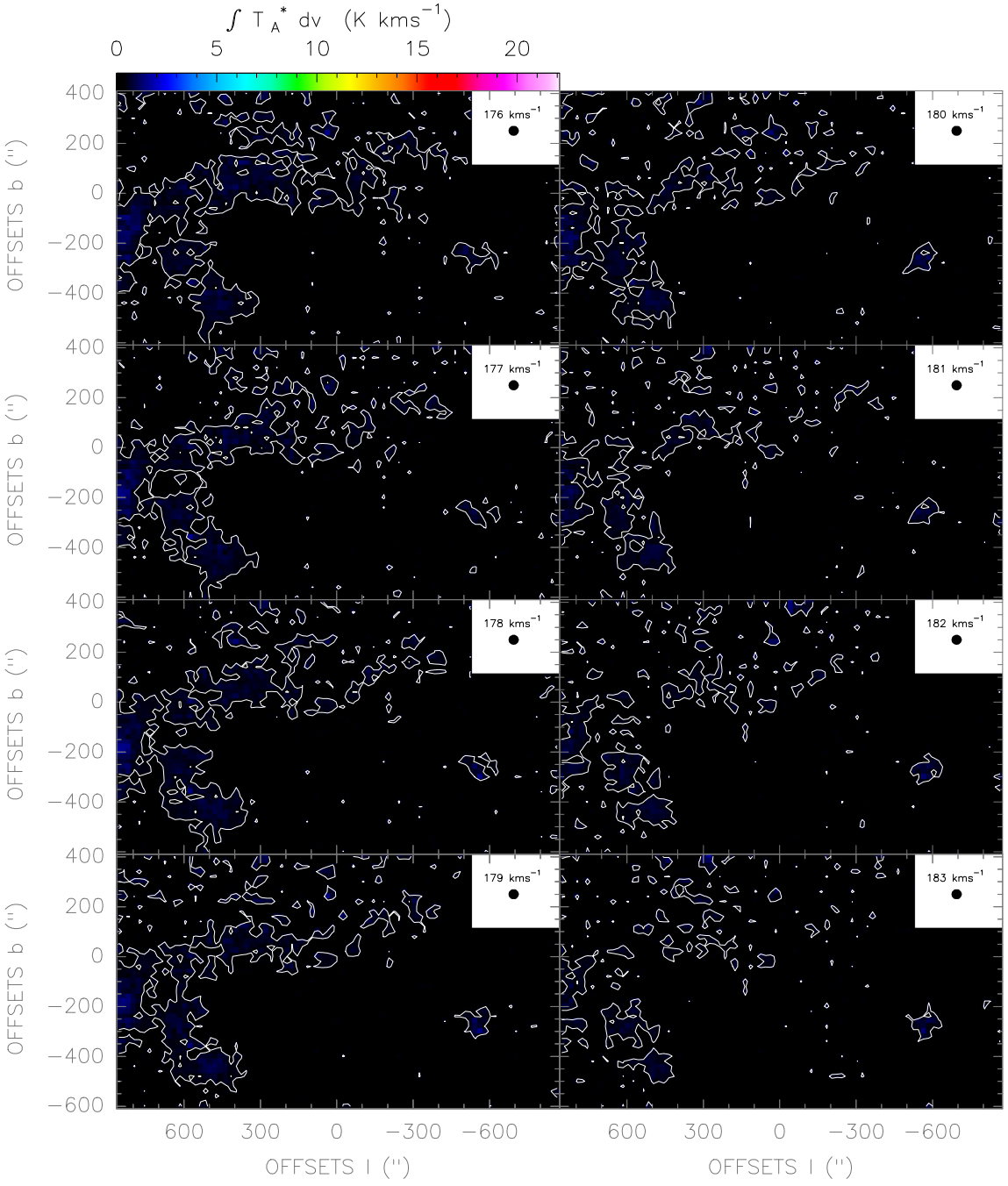

Figure. F.48: *CO(4-3) line observed with the NANTEN2/SMART telescope in Galactic coordinates. The spatial resolution of the maps is 40".*

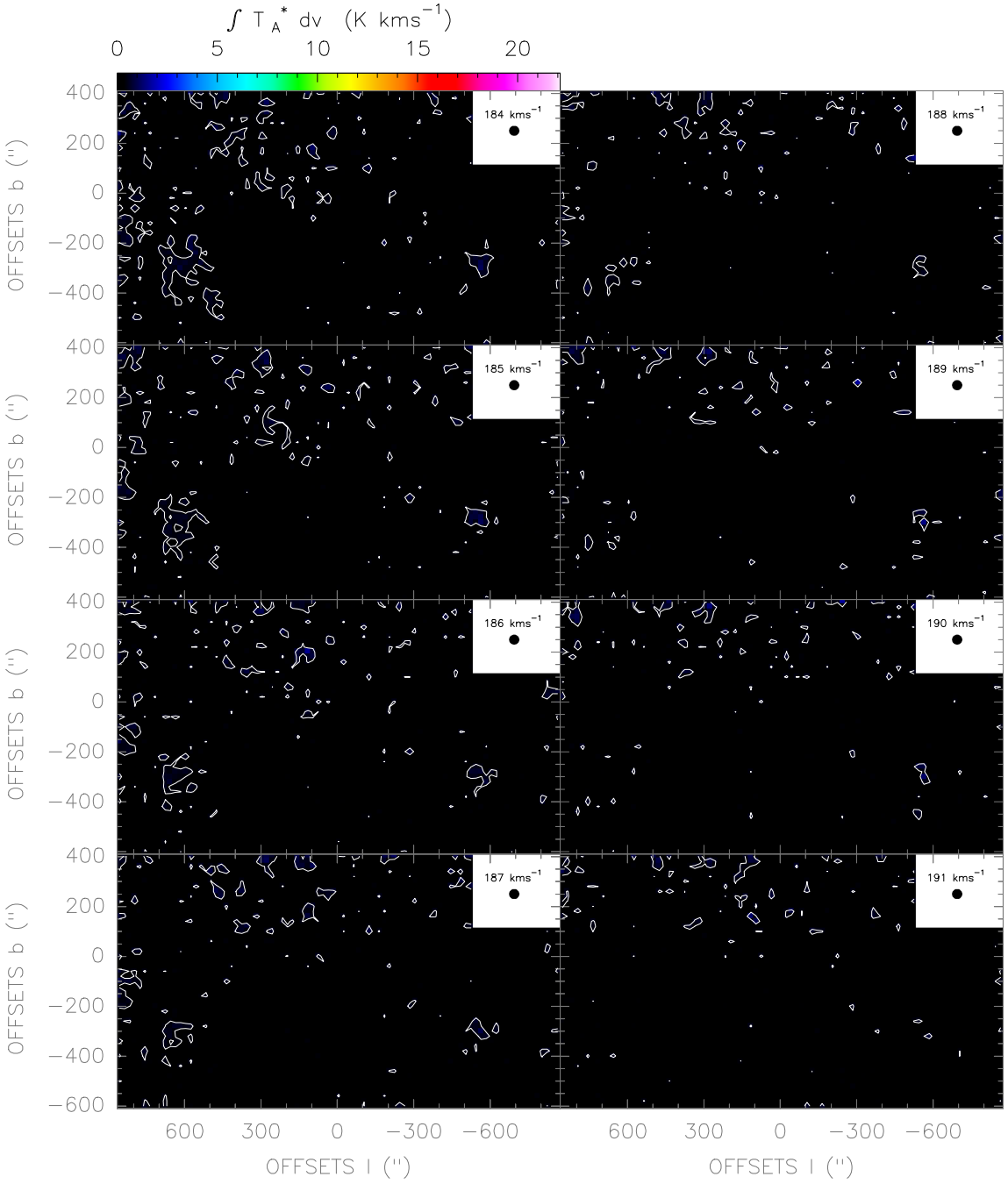

Figure. F.49: *CO(4-3) line observed with the NANTEN2/SMART telescope in Galactic coordinates. The spatial resolution of the maps is 40".*

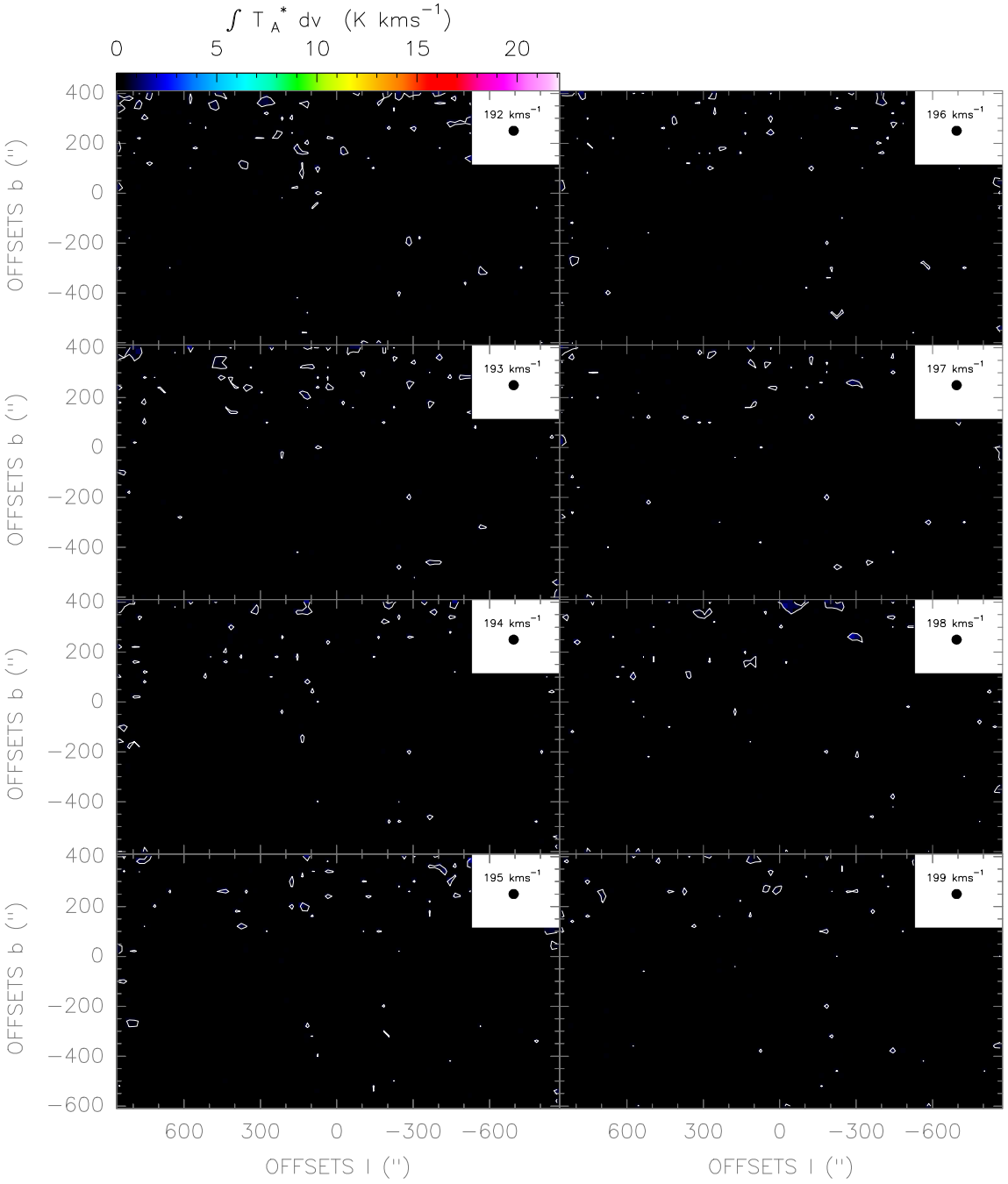

Figure. F.50: *CO(4-3) line observed with the NANTEN2/SMART telescope in Galactic coordinates. The spatial resolution of the maps is 40".*

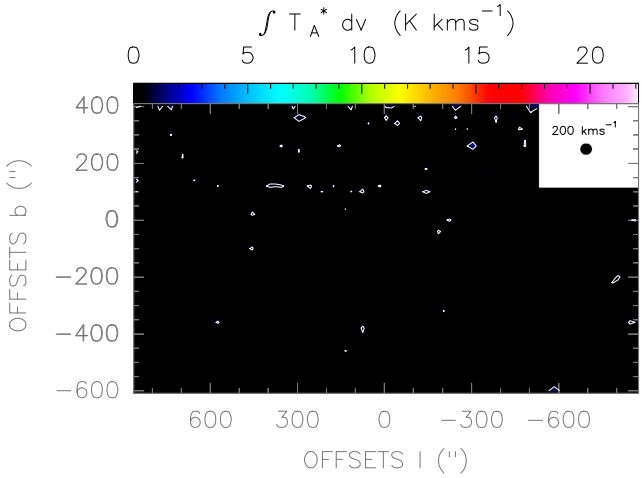

Figure. F.51: *CO(4-3) line observed with the NANTEN2/SMART telescope in Galactic coordinates. The spatial resolution of the maps is 40".*

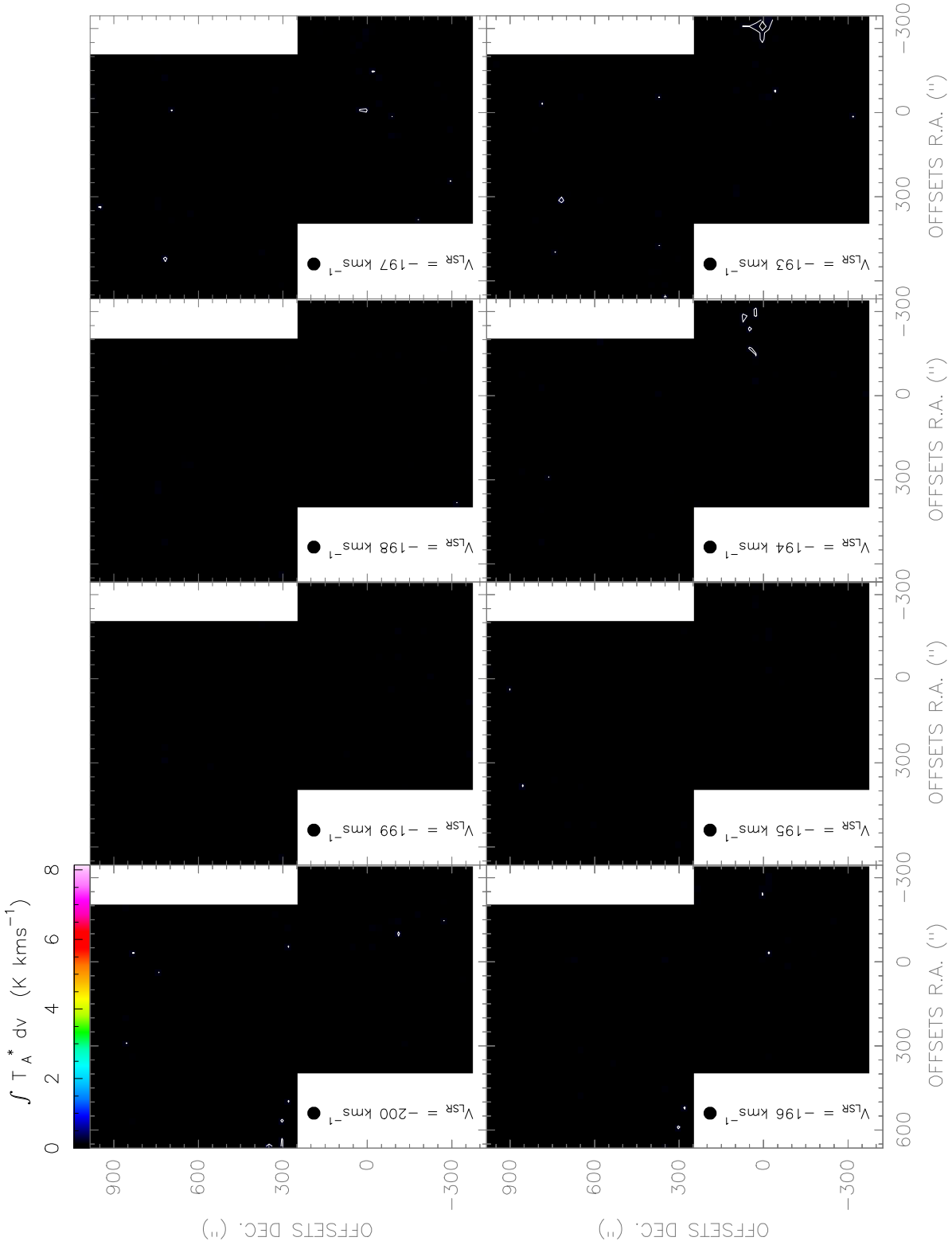

Figure. F.52: *[CI](1-0) line observed with the Herschel-HIFI satellite in Equatorial (J2000) coordinates. The spatial resolution of the maps is 46".*

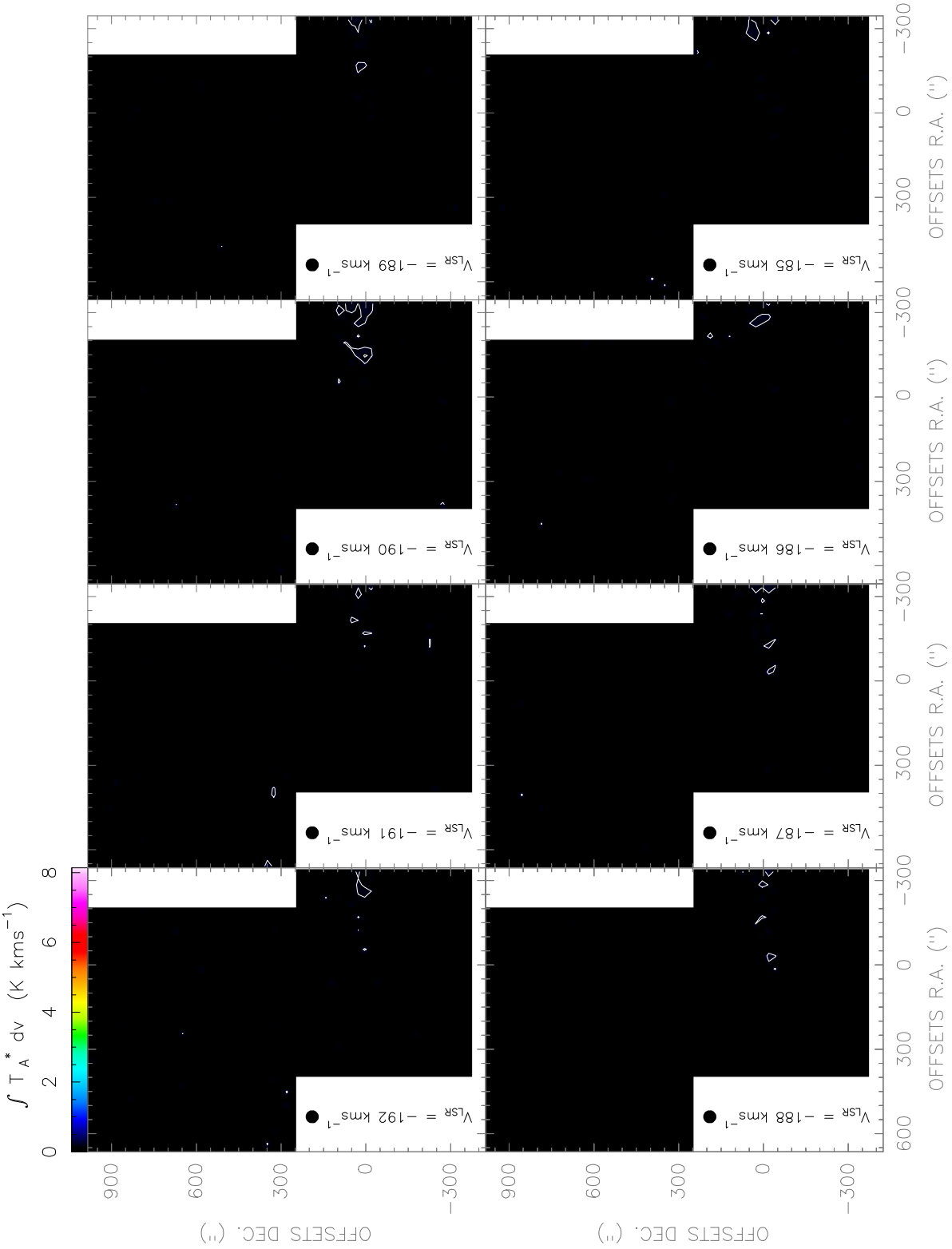

Figure. F.53: *[CI](1-0) line observed with the Herschel-HIFI satellite in Equatorial (J2000) coordinates. The spatial resolution of the maps is 46".*

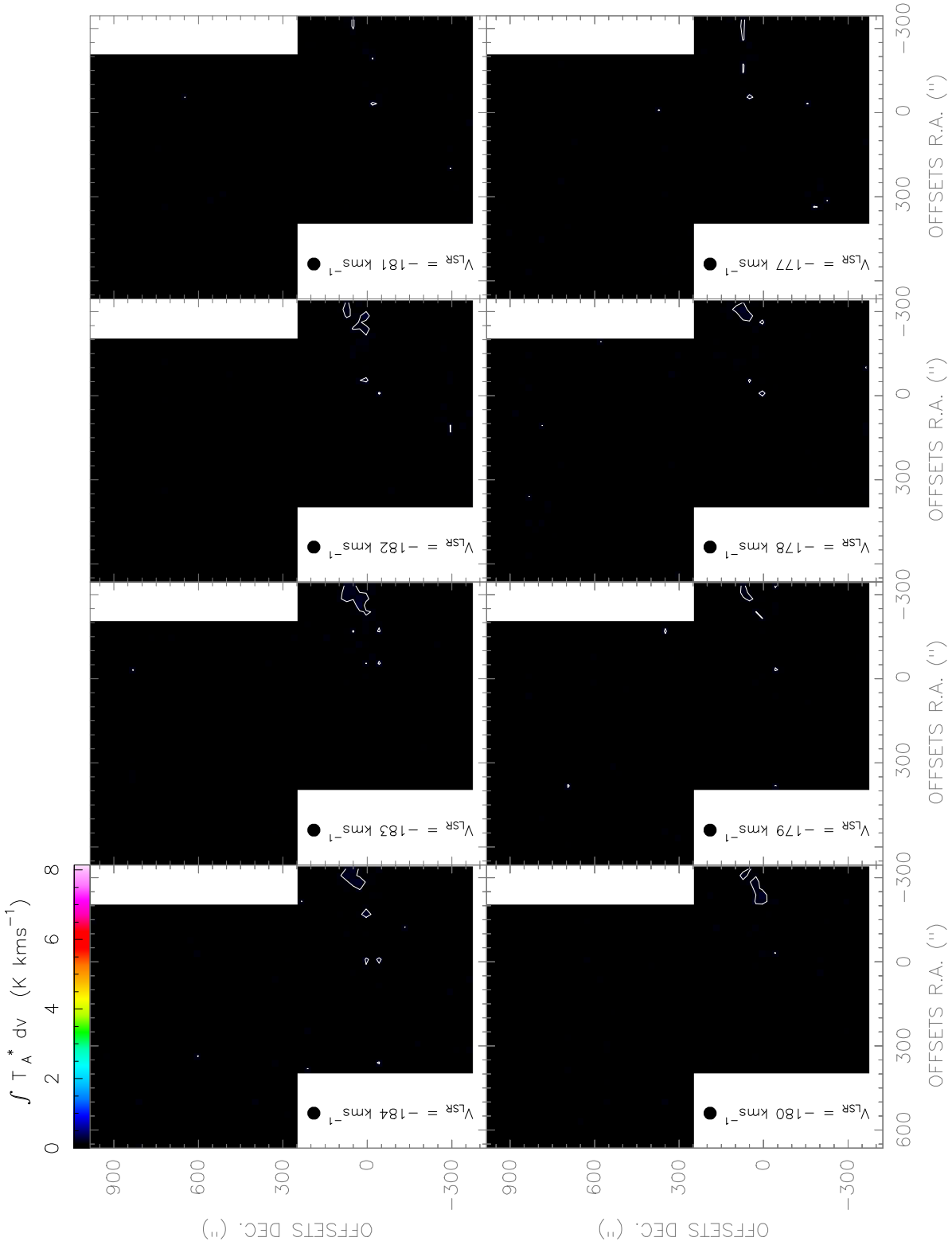

Figure. F.54: *[CI](1-0) line observed with the Herschel-HIFI satellite in Equatorial (J2000) coordinates. The spatial resolution of the maps is 46".*

Figure. F.55: *[CI](1-0) line observed with the Herschel-HIFI satellite in Equatorial (J2000) coordinates. The spatial resolution of the maps is 46".*

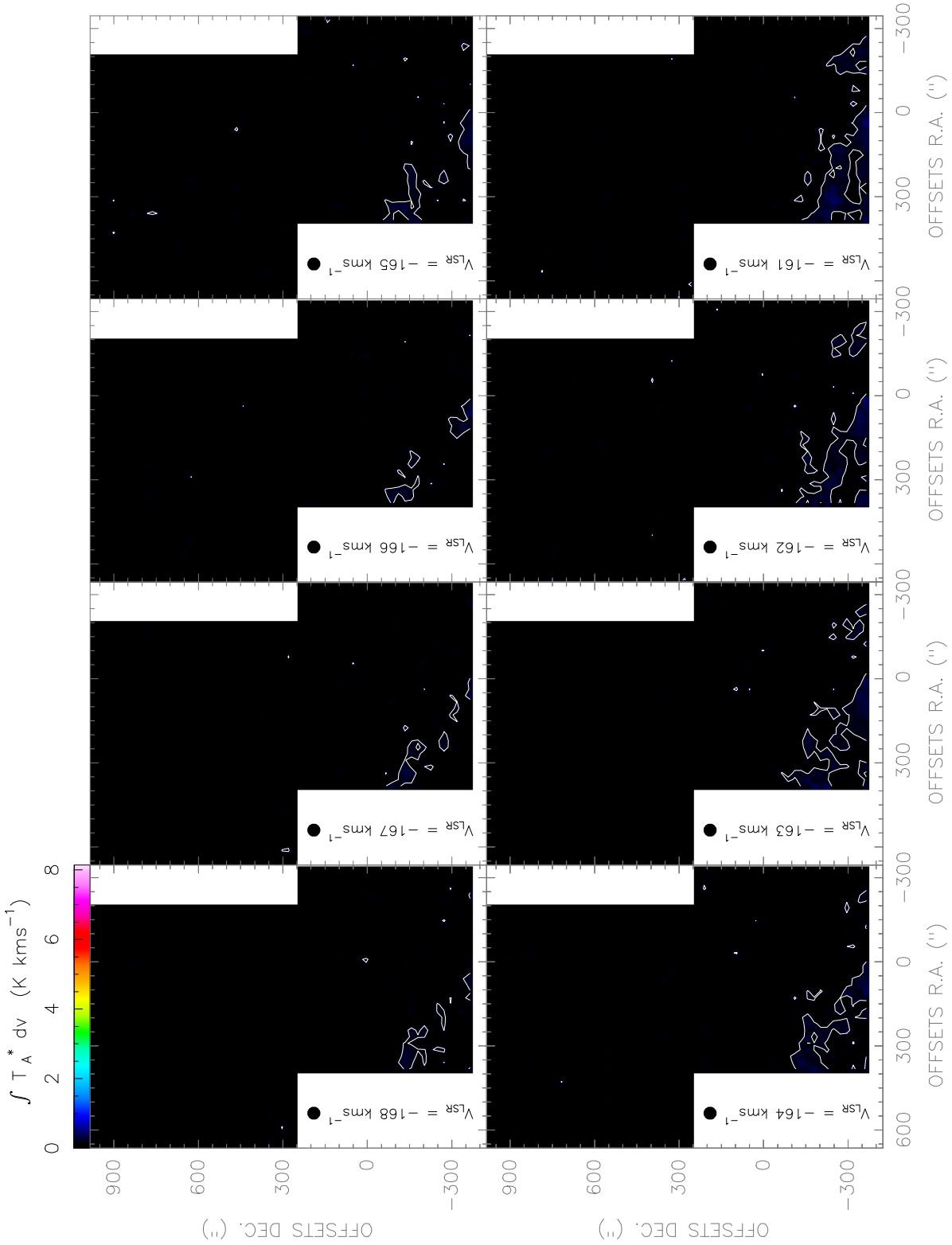

Figure. F.56: *[CI](1-0) line observed with the Herschel-HIFI satellite in Equatorial (J2000) coordinates. The spatial resolution of the maps is 46".*

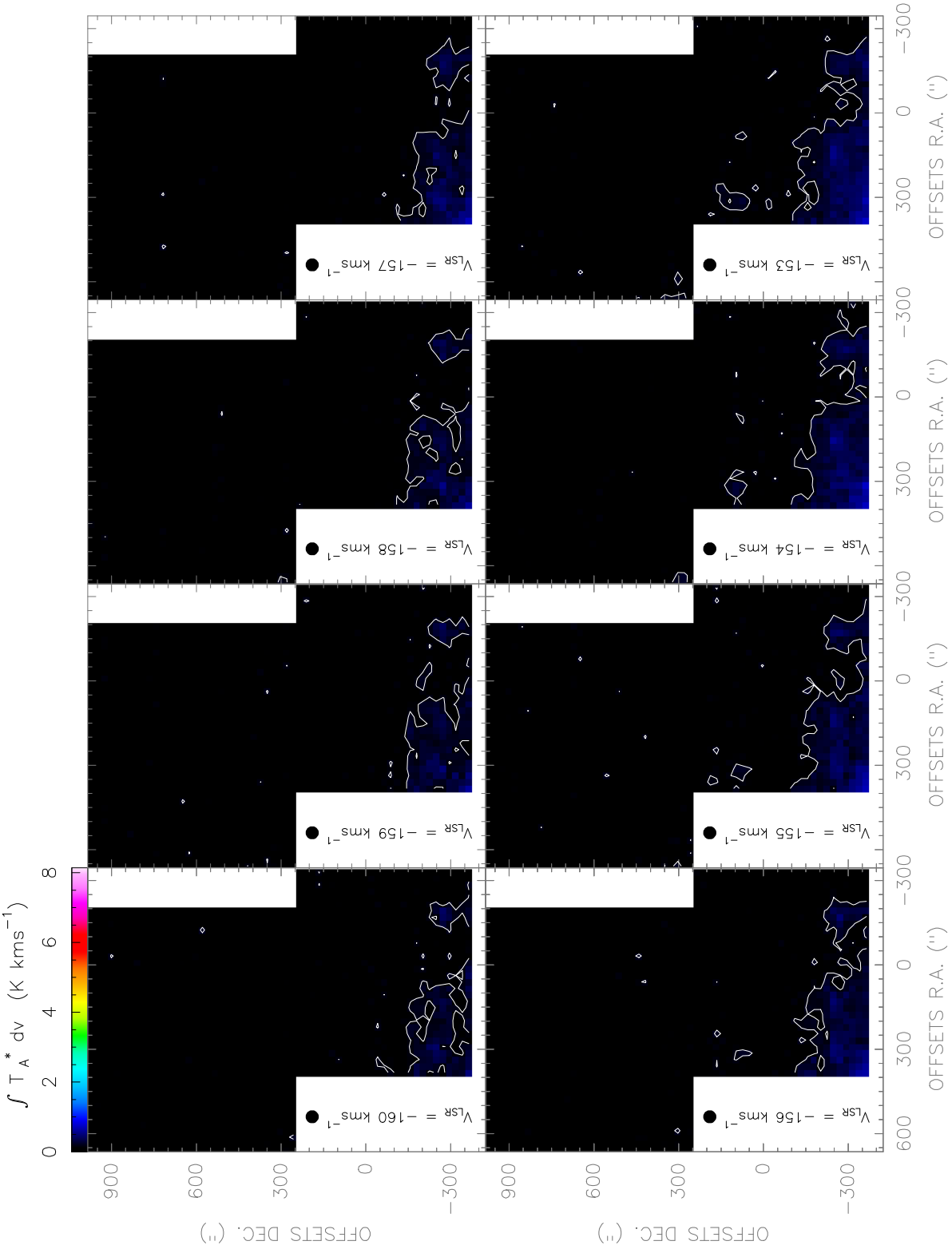

Figure. F.57: *[CI](1-0) line observed with the Herschel-HIFI satellite in Equatorial (J2000) coordinates. The spatial resolution of the maps is 46".*

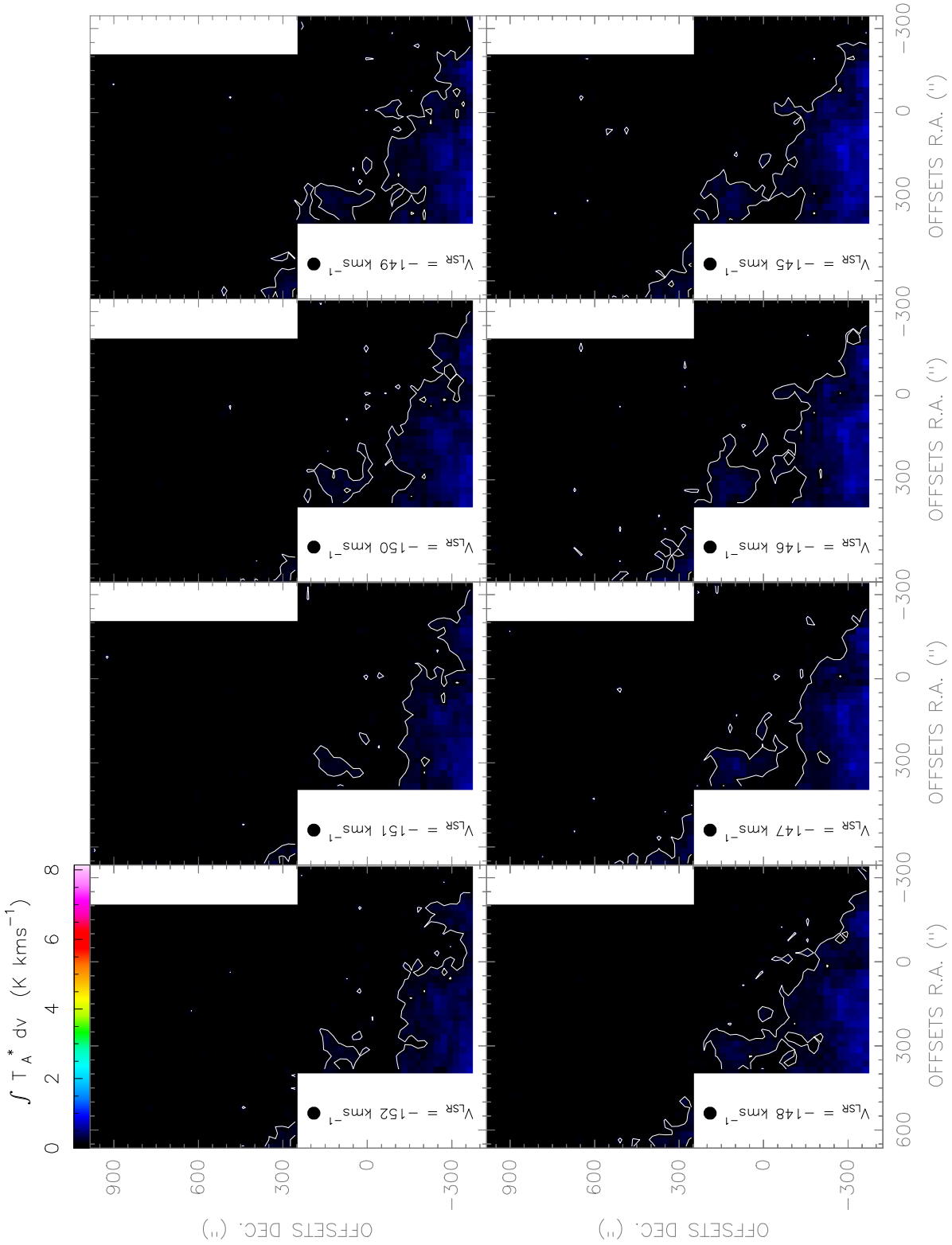

Figure. F.58: *[CI](1-0) line observed with the Herschel-HIFI satellite in Equatorial (J2000) coordinates. The spatial resolution of the maps is 46".*

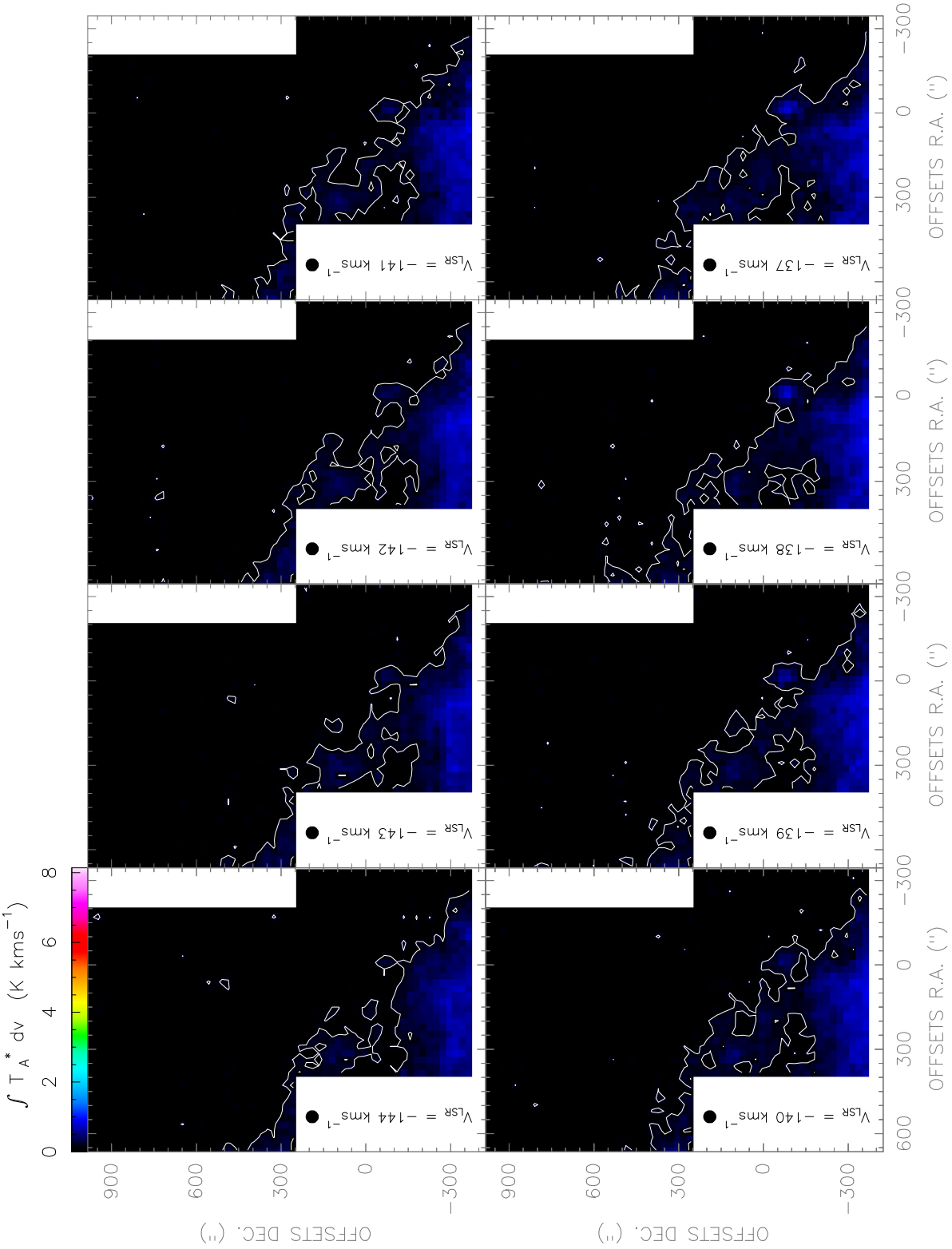

Figure. F.59: *[CI](1-0) line observed with the Herschel-HIFI satellite in Equatorial (J2000) coordinates. The spatial resolution of the maps is 46".*

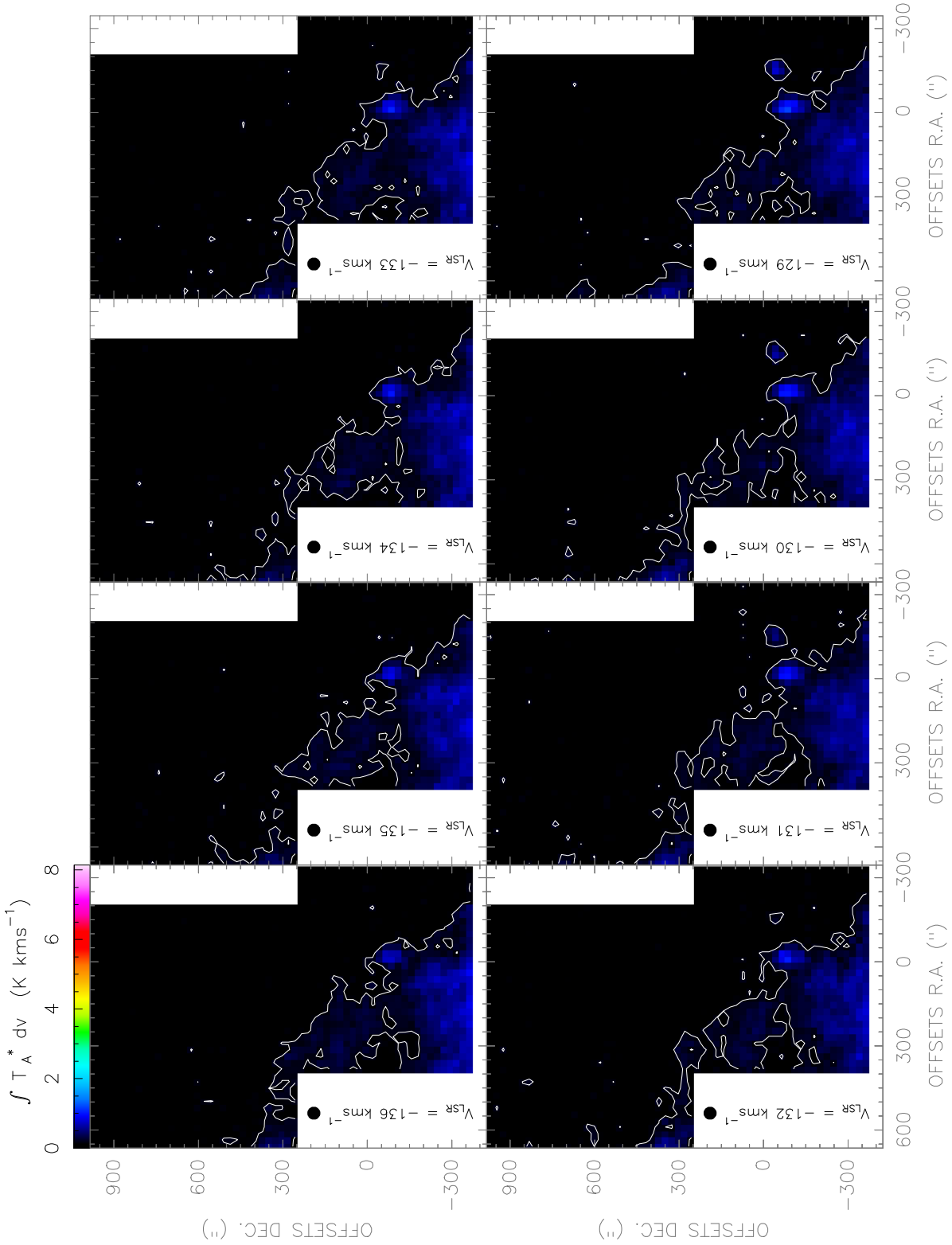

Figure. F.60: *[CI](1-0) line observed with the Herschel-HIFI satellite in Equatorial (J2000) coordinates. The spatial resolution of the maps is 46".*

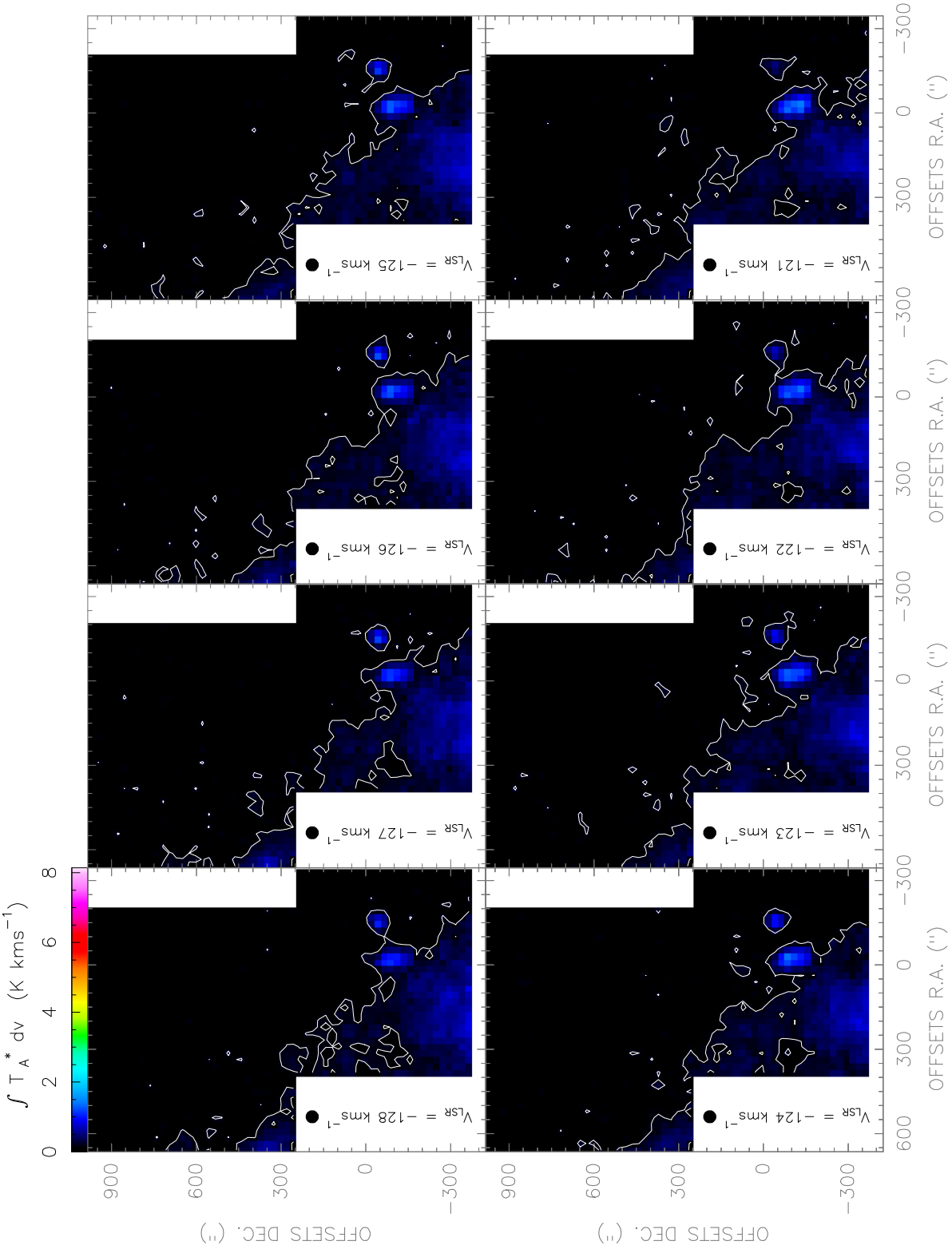

Figure. F.61: *[CI](1-0) line observed with the Herschel-HIFI satellite in Equatorial (J2000) coordinates. The spatial resolution of the maps is 46".*

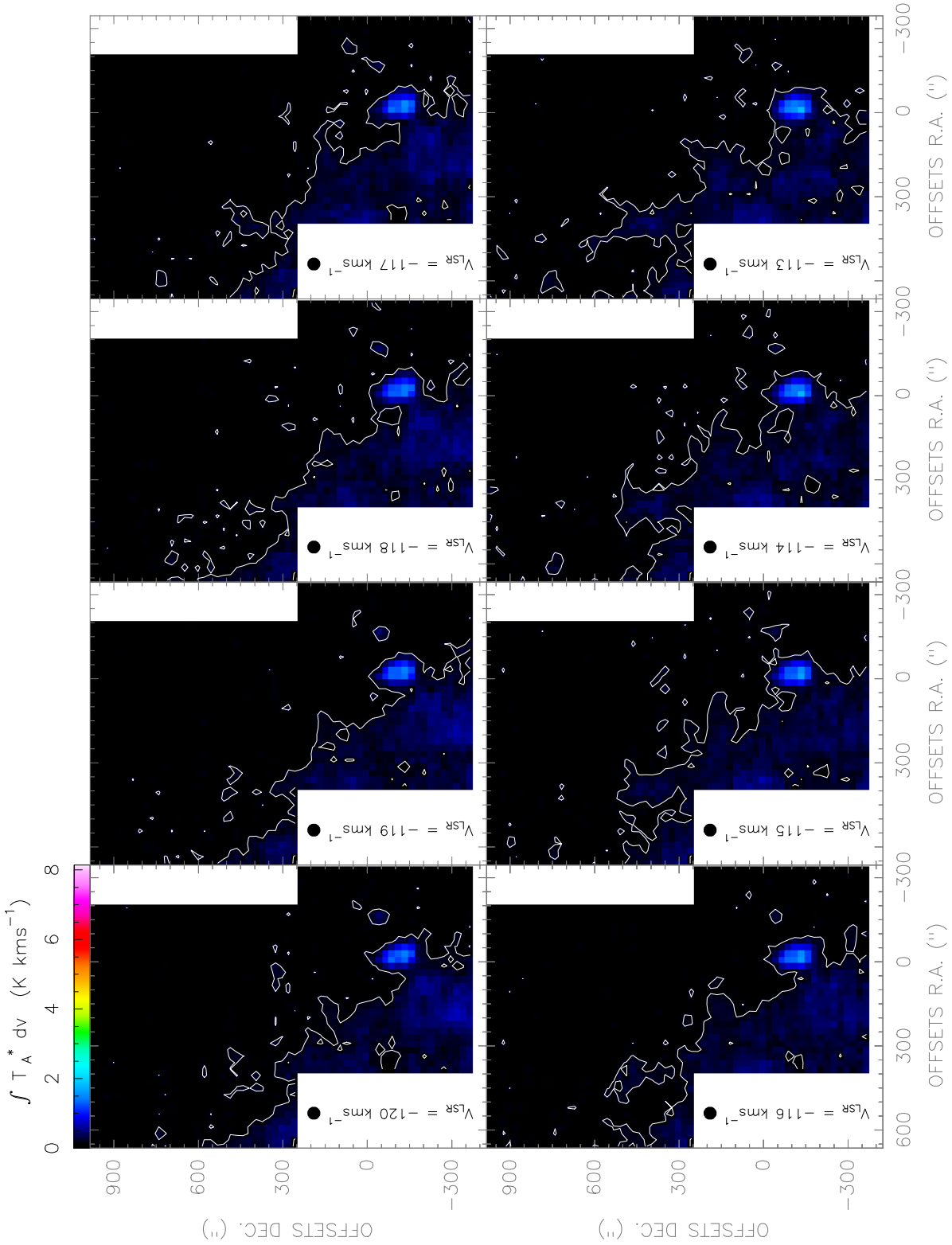

Figure. F.62: *[CI](1-0) line observed with the Herschel-HIFI satellite in Equatorial (J2000) coordinates. The spatial resolution of the maps is 46".*

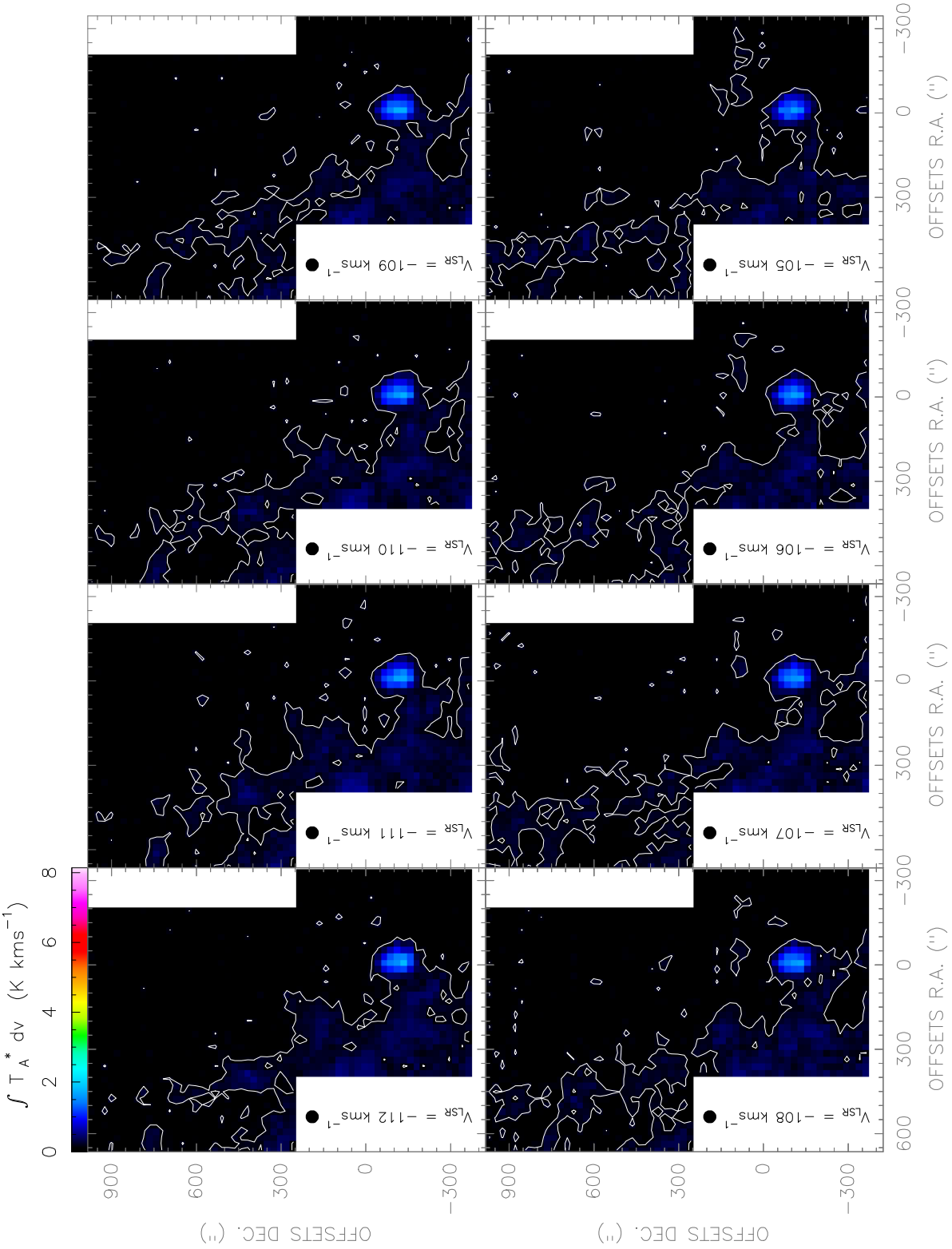

Figure. F.63: *[CI](1-0) line observed with the Herschel-HIFI satellite in Equatorial (J2000) coordinates. The spatial resolution of the maps is 46".*

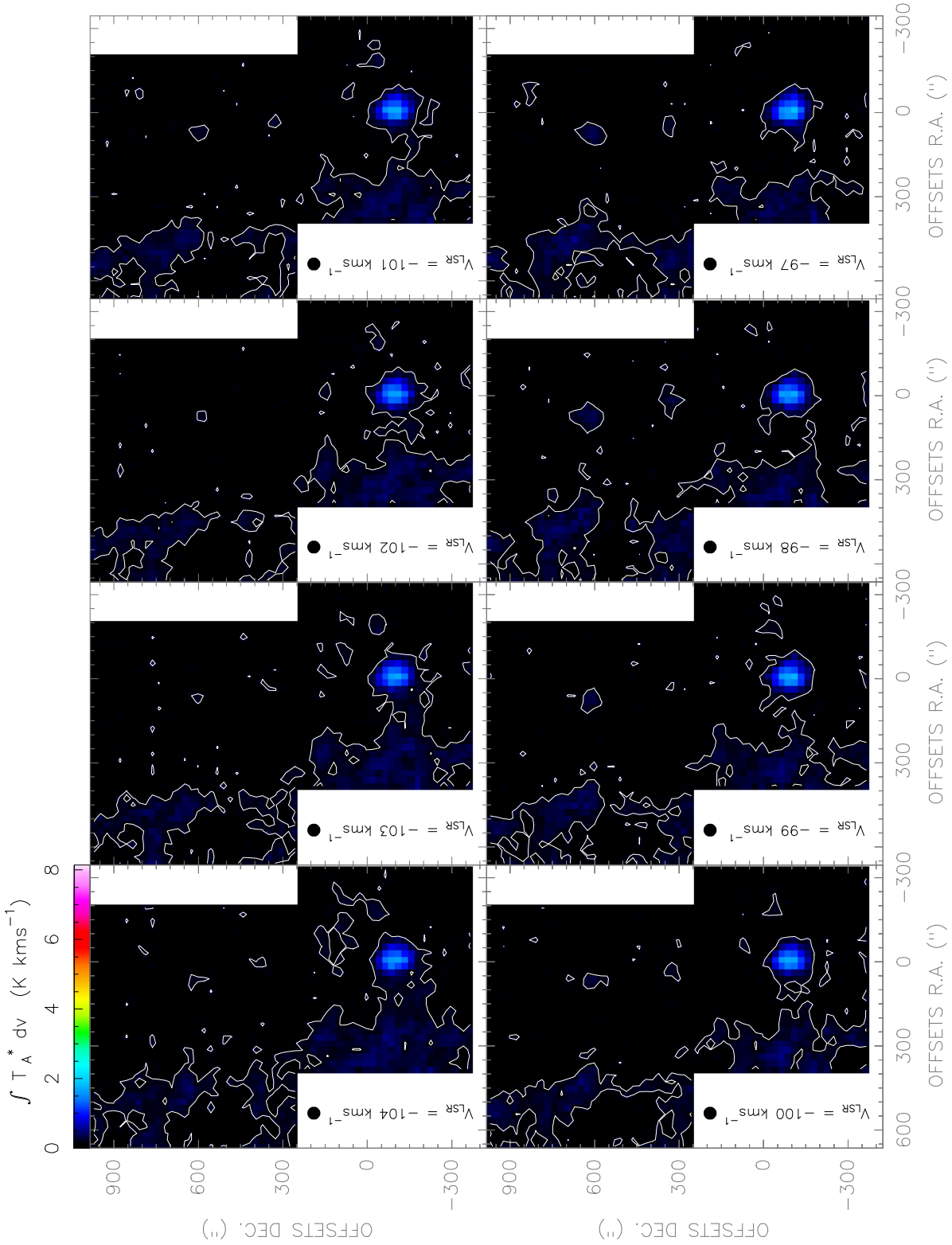

Figure. F.64: *[CI](1-0) line observed with the Herschel-HIFI satellite in Equatorial (J2000) coordinates. The spatial resolution of the maps is 46".*

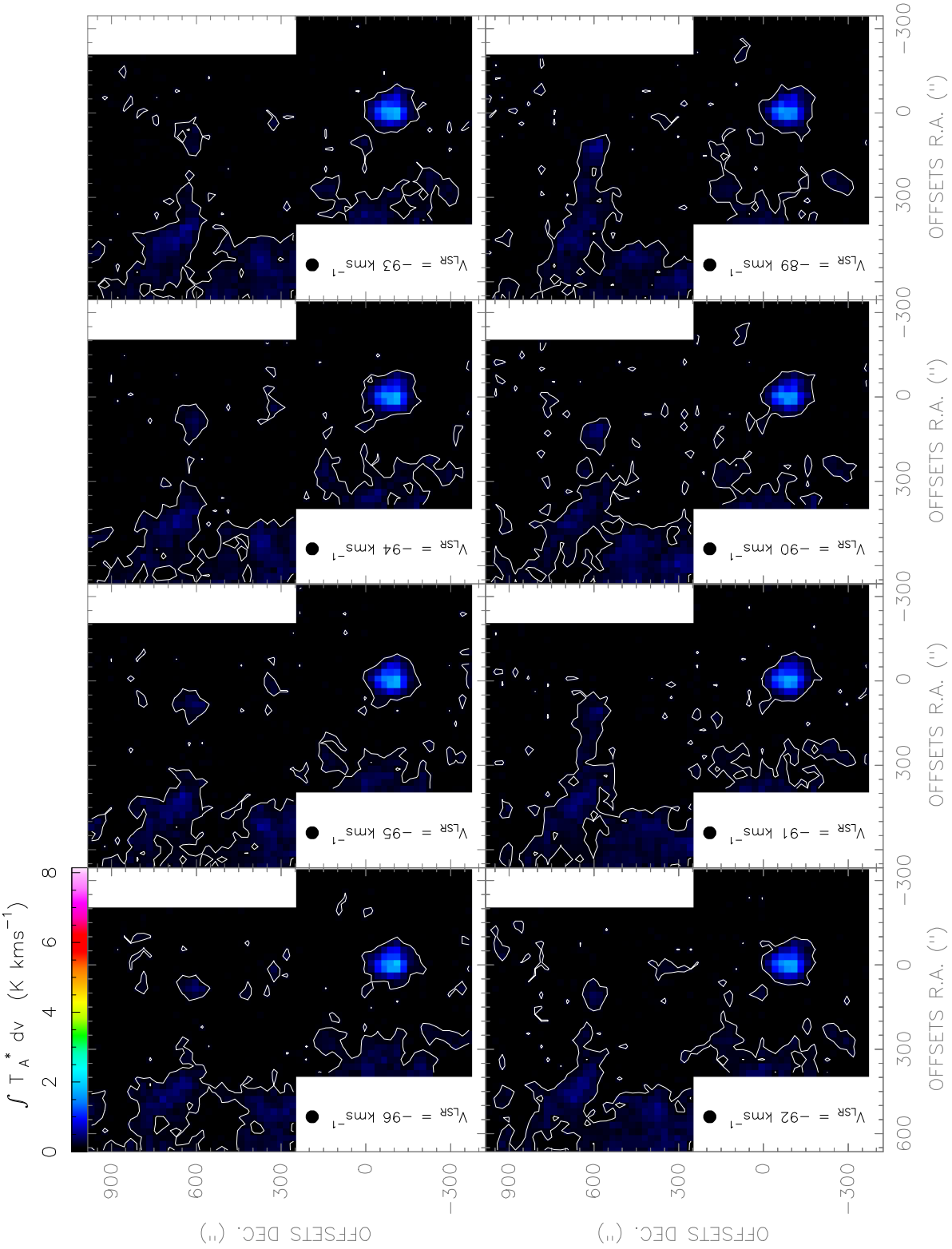

Figure. F.65: *[CI](1-0) line observed with the Herschel-HIFI satellite in Equatorial (J2000) coordinates. The spatial resolution of the maps is 46".*

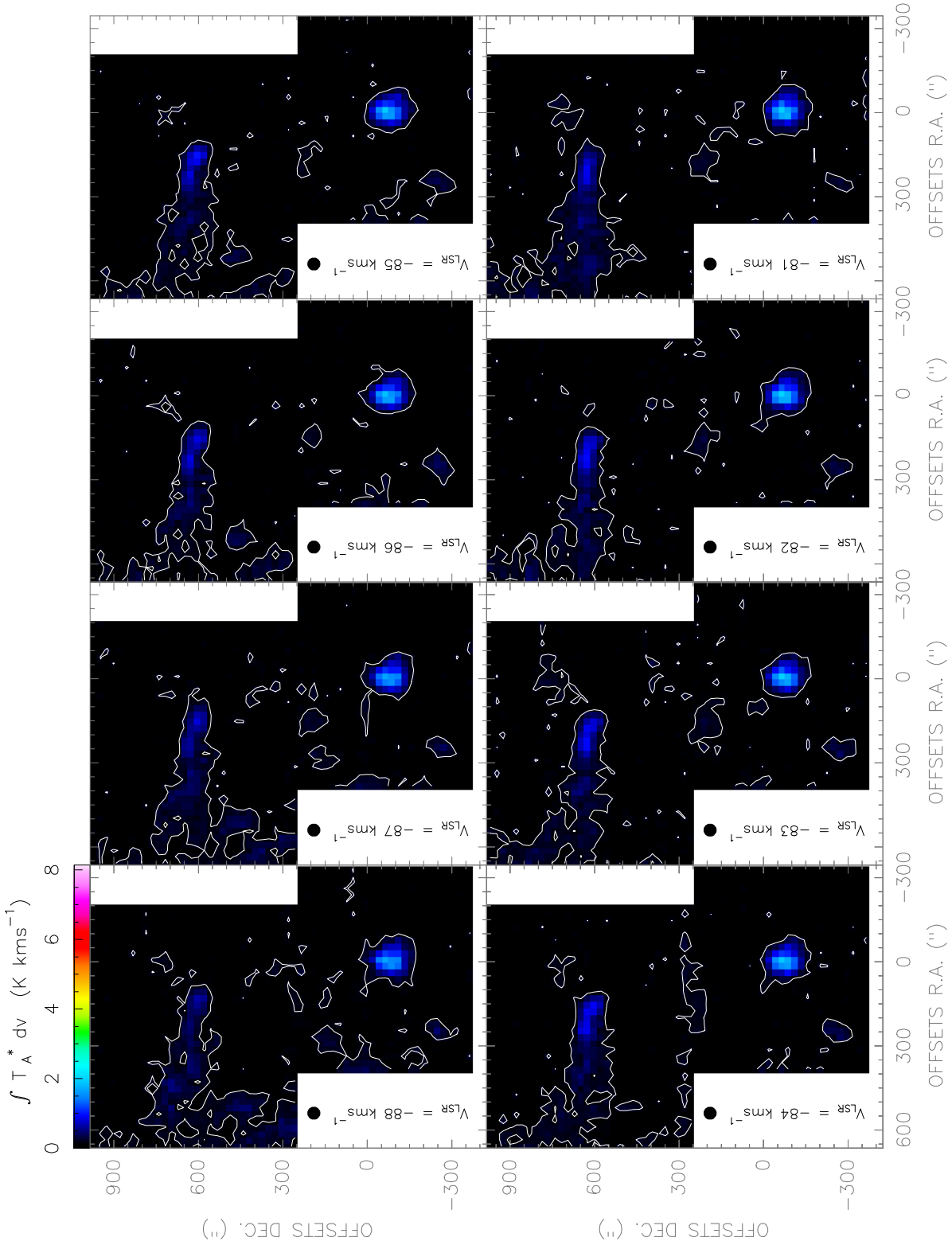

Figure. F.66: *[CI](1-0) line observed with the Herschel-HIFI satellite in Equatorial (J2000) coordinates. The spatial resolution of the maps is 46".*

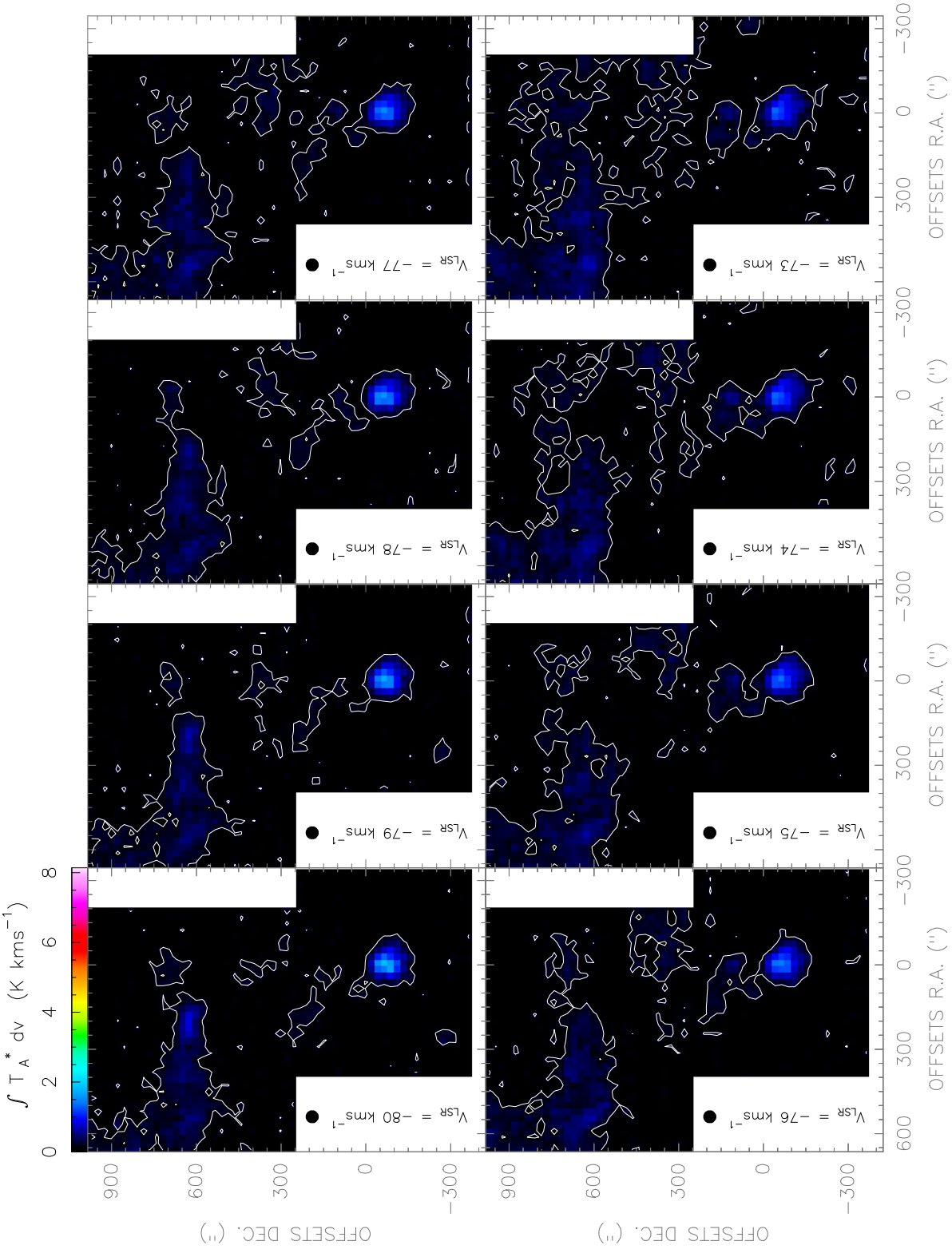

Figure. F.67: *[CI](1-0) line observed with the Herschel-HIFI satellite in Equatorial (J2000) coordinates. The spatial resolution of the maps is 46".*

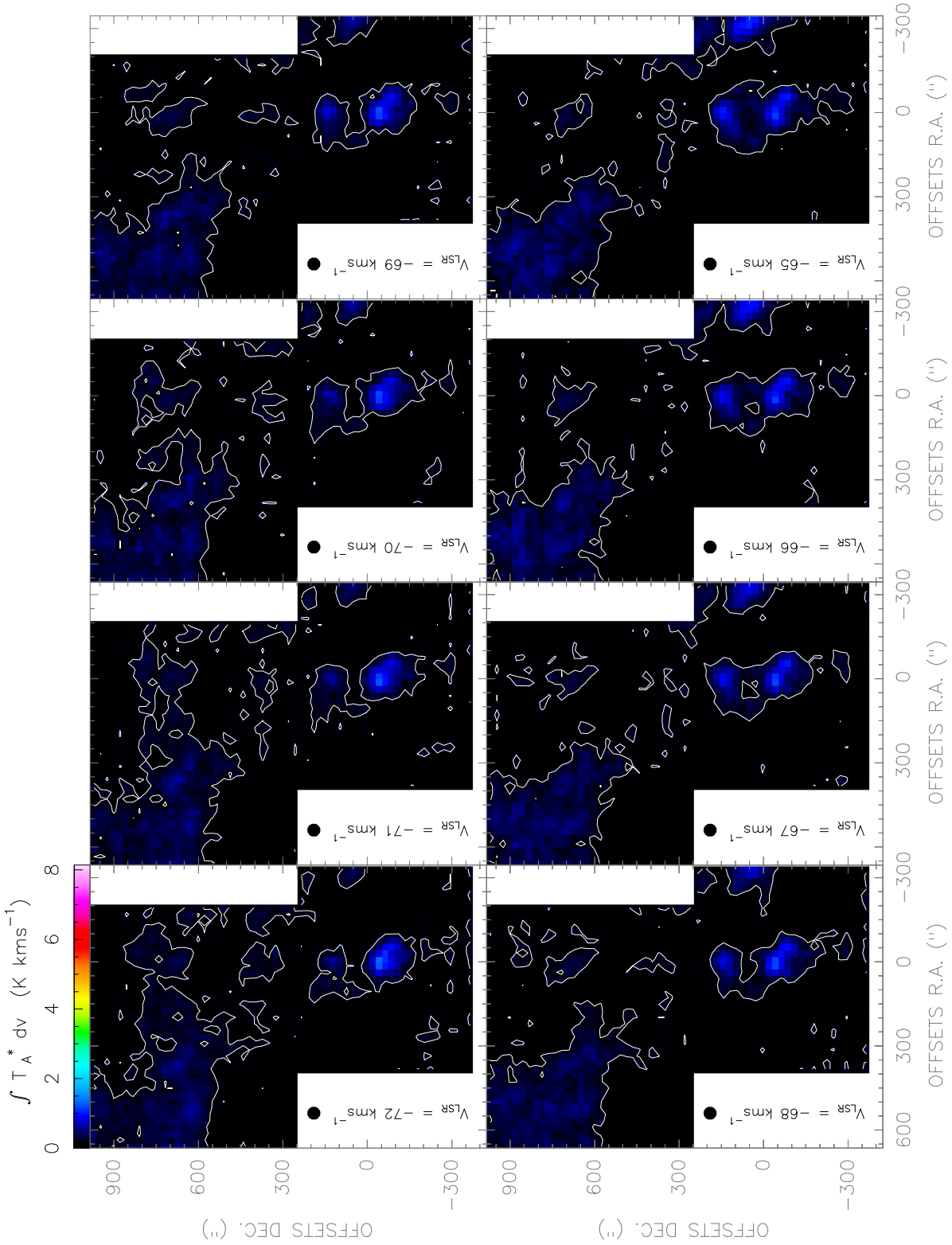

Figure. F.68: *[CI](1-0) line observed with the Herschel-HIFI satellite in Equatorial (J2000) coordinates. The spatial resolution of the maps is 46".*

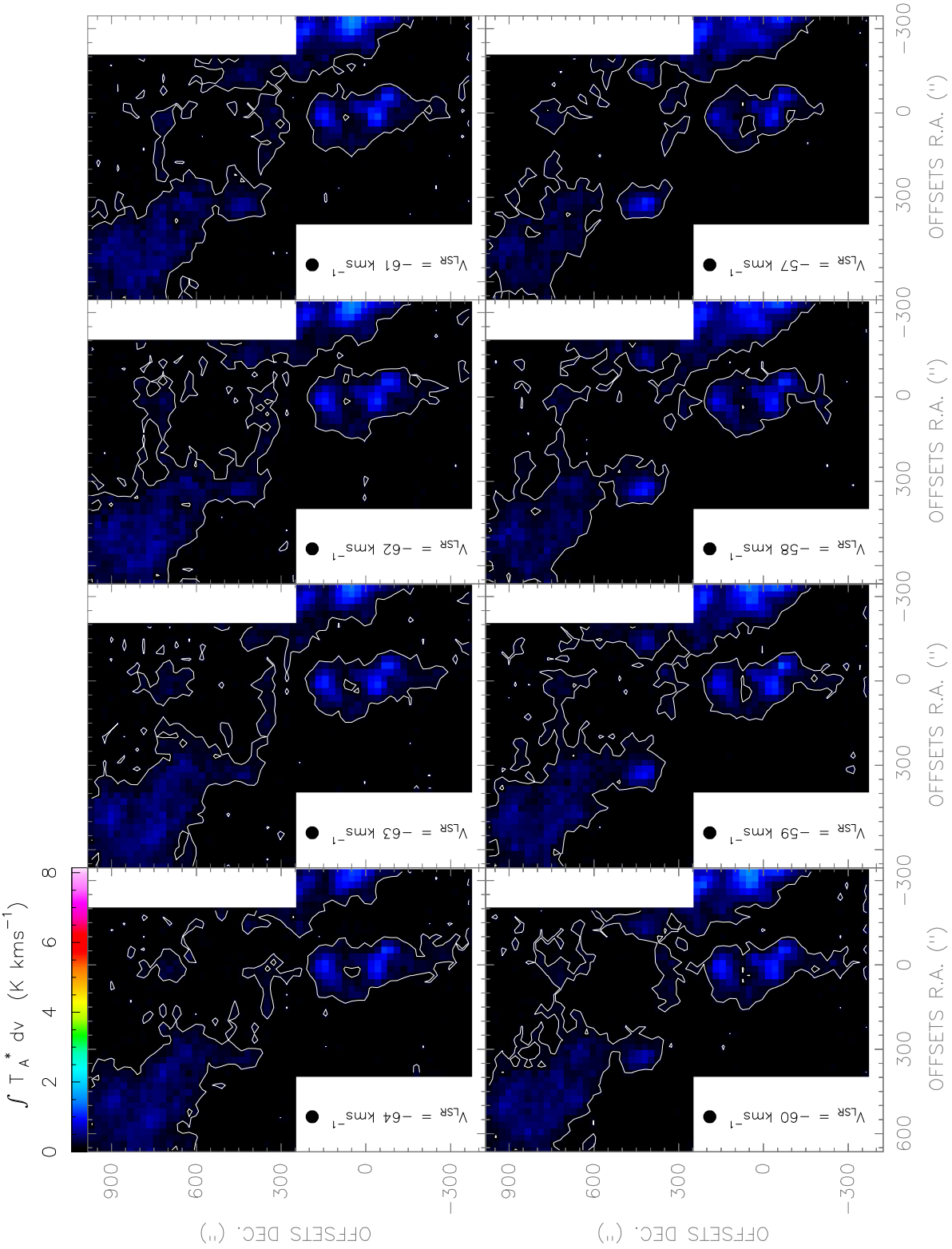

Figure. F.69: *[CI](1-0) line observed with the Herschel-HIFI satellite in Equatorial (J2000) coordinates. The spatial resolution of the maps is 46".*

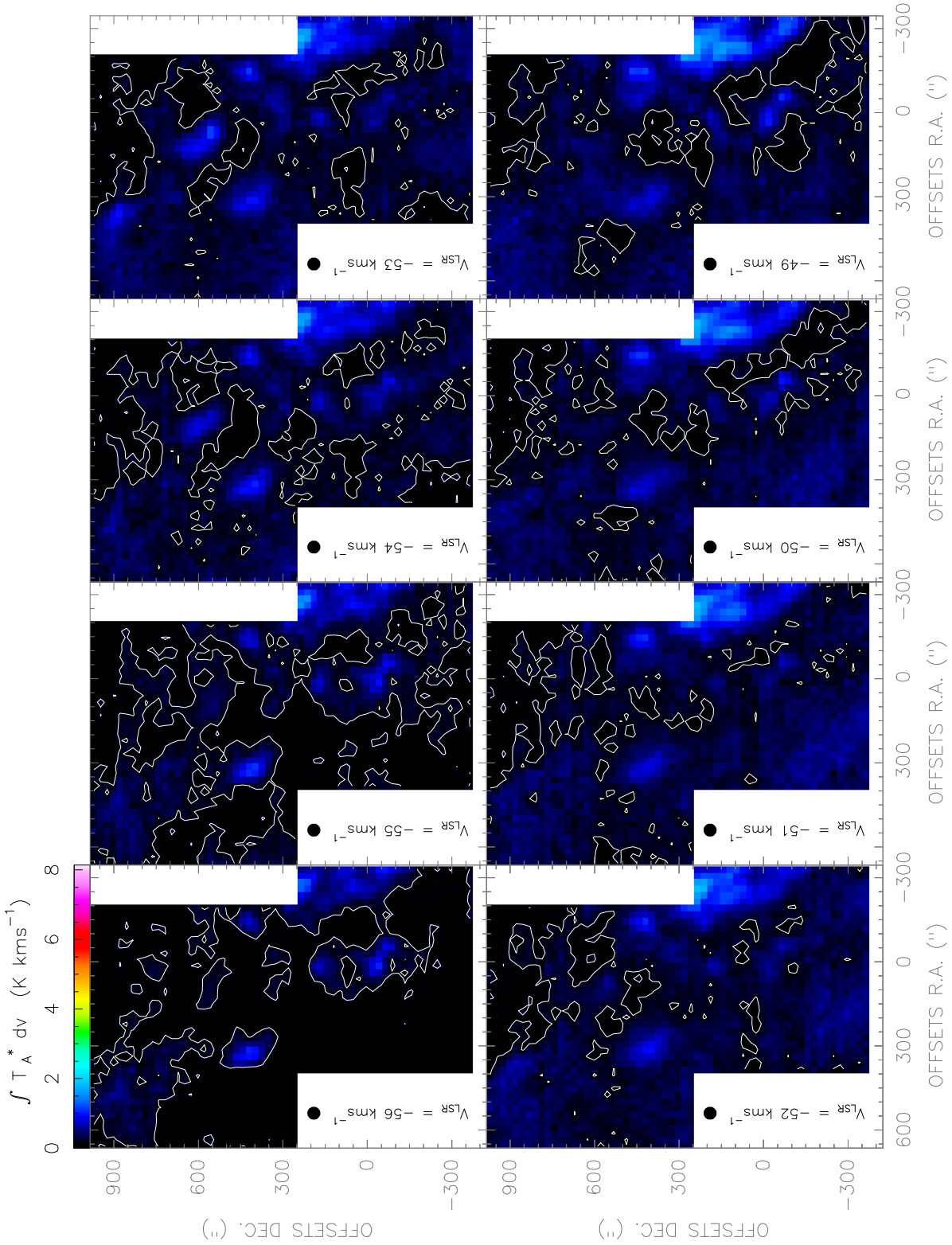

Figure. F.70: *[CI](1-0) line observed with the Herschel-HIFI satellite in Equatorial (J2000) coordinates. The spatial resolution of the maps is 46".*

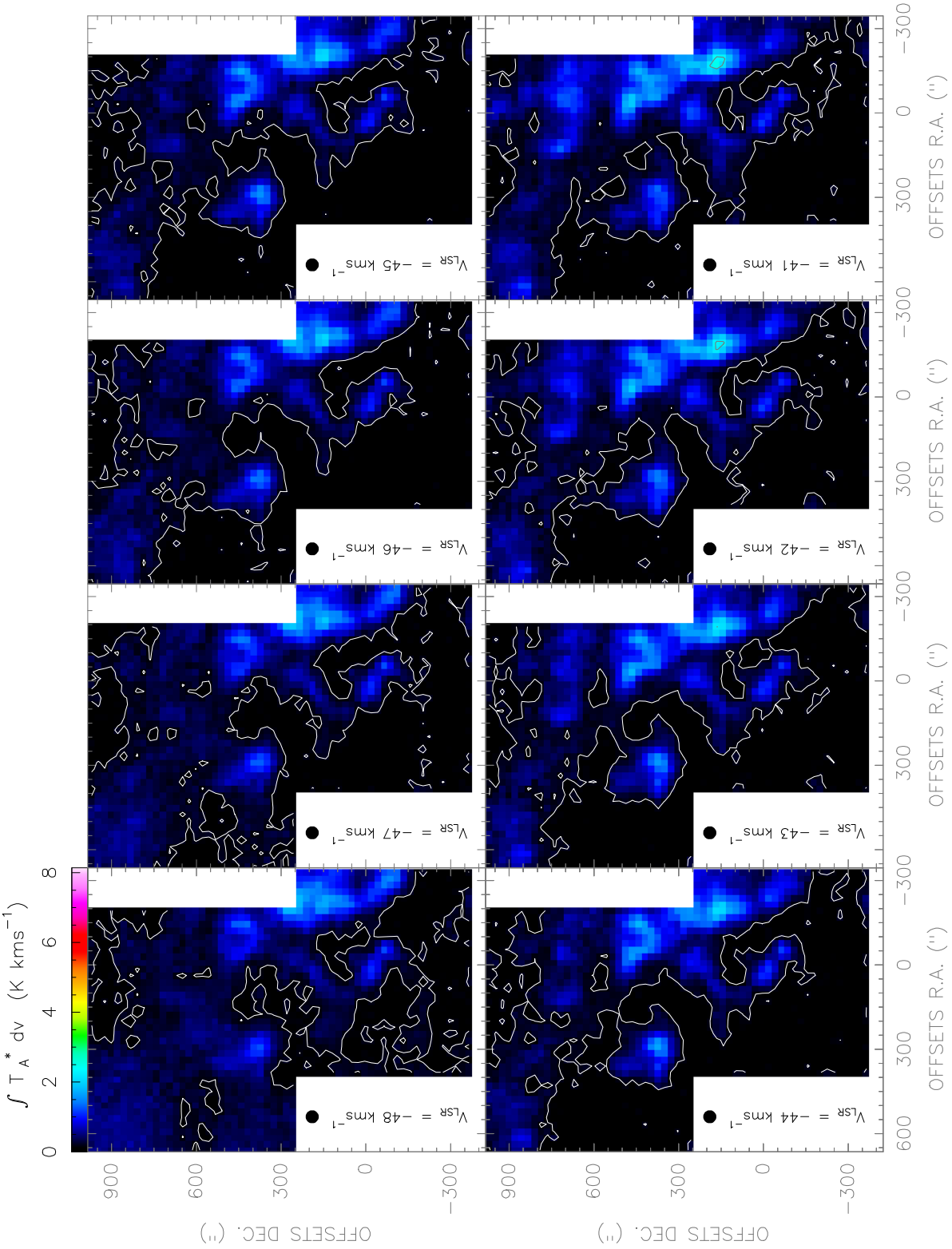

Figure. F.71: *[CI](1-0) line observed with the Herschel-HIFI satellite in Equatorial (J2000) coordinates. The spatial resolution of the maps is 46".*

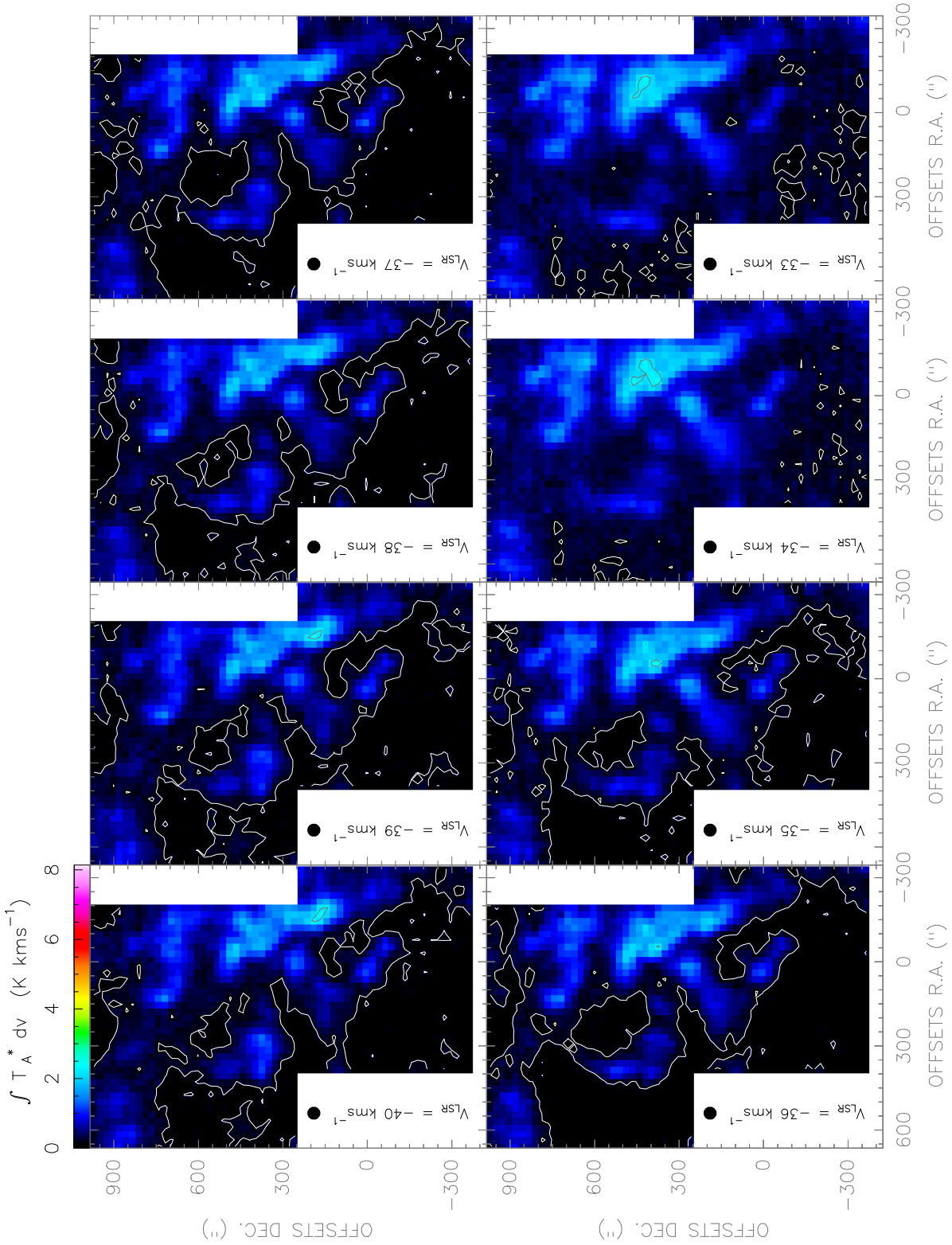

Figure. F.72: *[CI](1-0) line observed with the Herschel-HIFI satellite in Equatorial (J2000) coordinates. The spatial resolution of the maps is 46".*

Figure. F.73: *[CI](1-0) line observed with the Herschel-HIFI satellite in Equatorial (J2000) coordinates. The spatial resolution of the maps is 46".*

Figure. F.74: *[CI](1-0) line observed with the Herschel-HIFI satellite in Equatorial (J2000) coordinates. The spatial resolution of the maps is 46".*

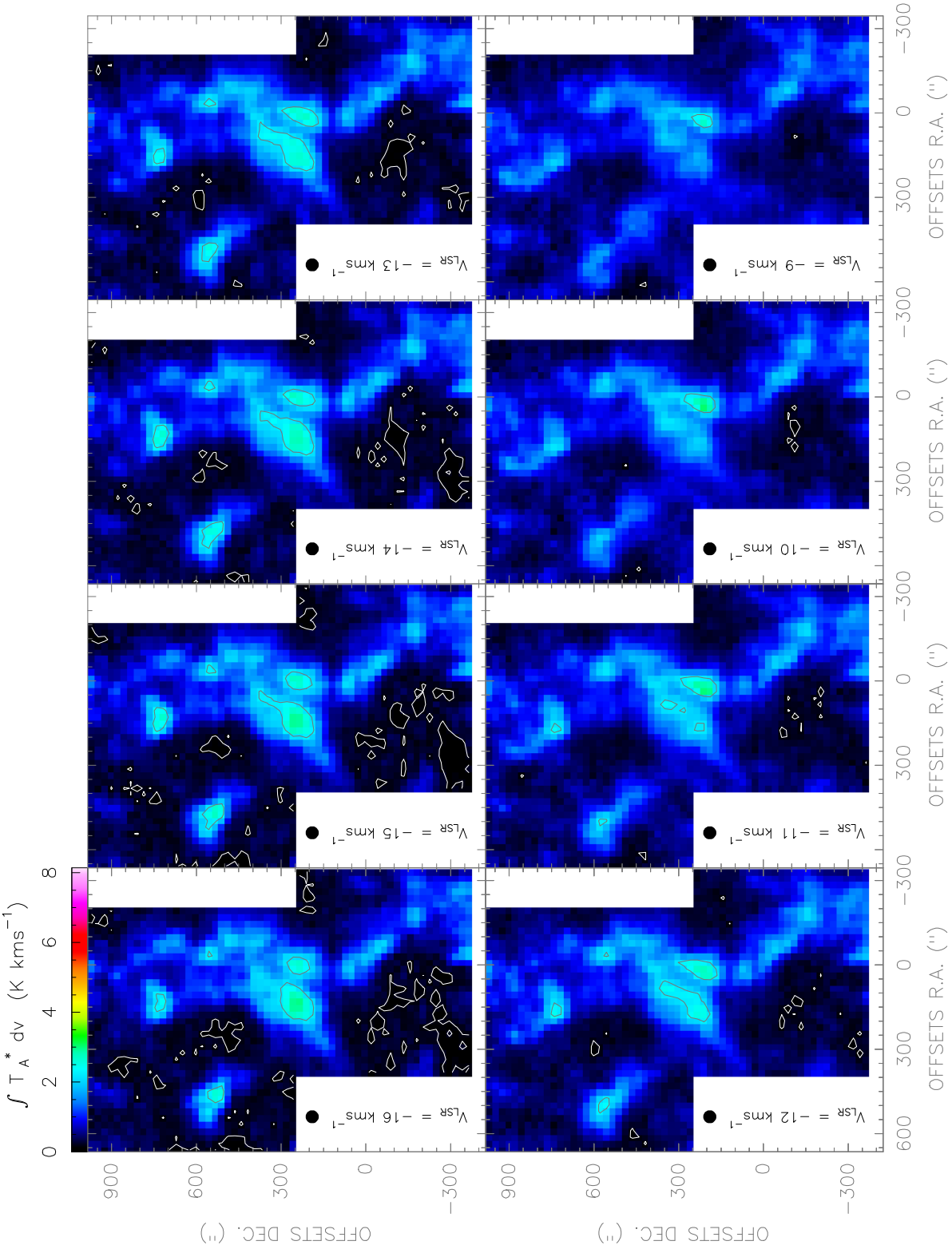

Figure. F.75: *[CI](1-0) line observed with the Herschel-HIFI satellite in Equatorial (J2000) coordinates. The spatial resolution of the maps is 46".*

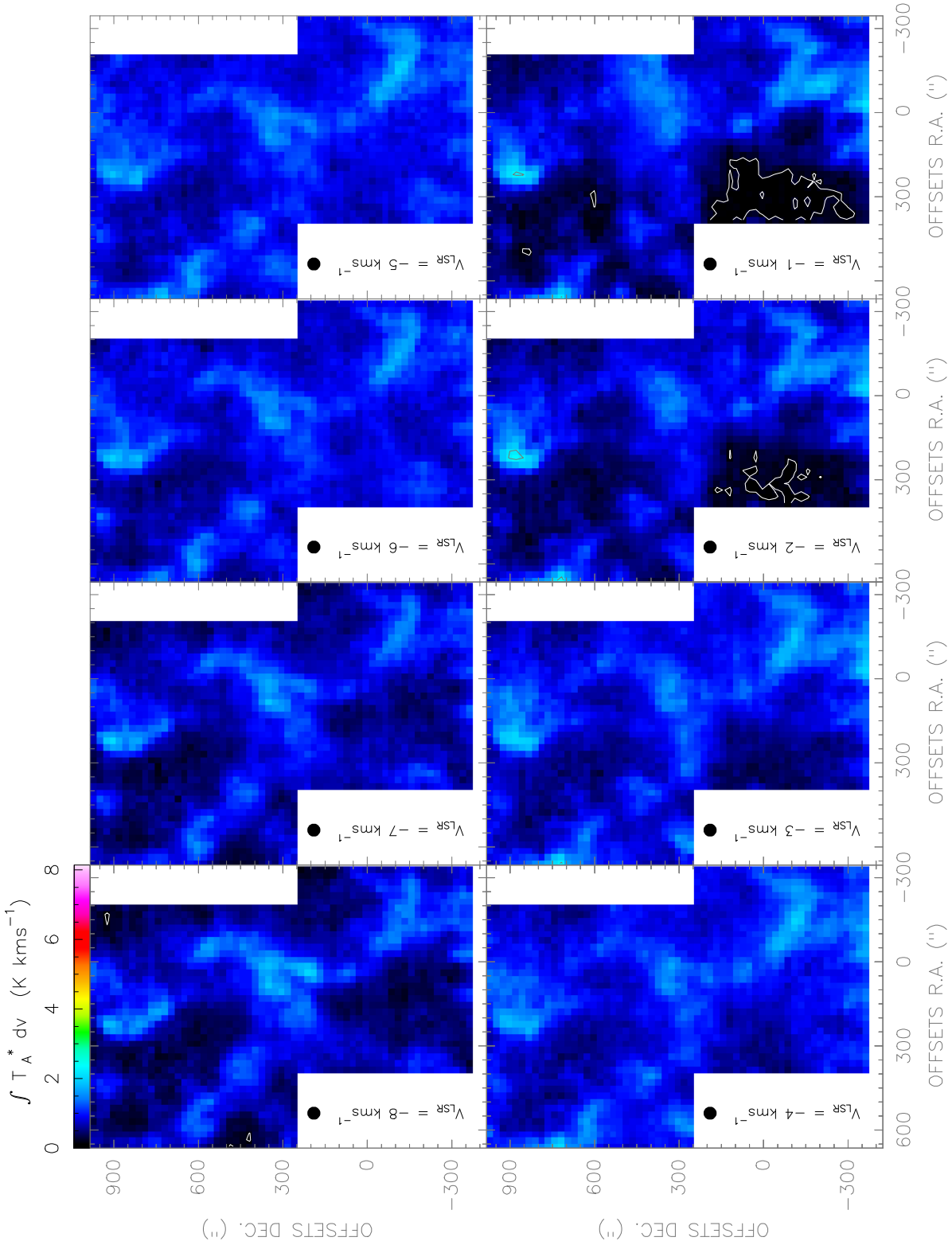

Figure. F.76: *[CI](1-0) line observed with the Herschel-HIFI satellite in Equatorial (J2000) coordinates. The spatial resolution of the maps is 46".*

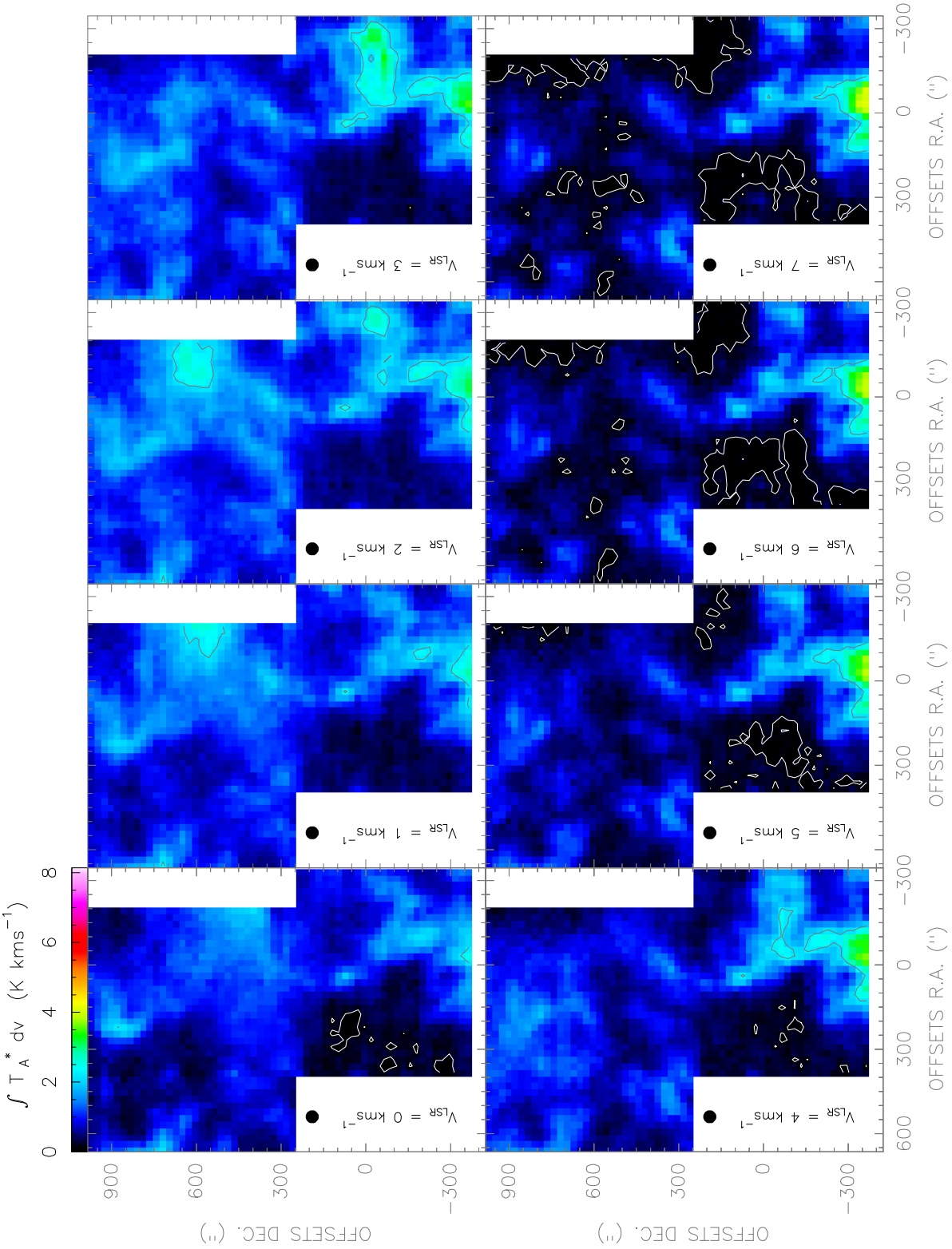

Figure. F.77: *[CI](1-0) line observed with the Herschel-HIFI satellite in Equatorial (J2000) coordinates. The spatial resolution of the maps is 46".*

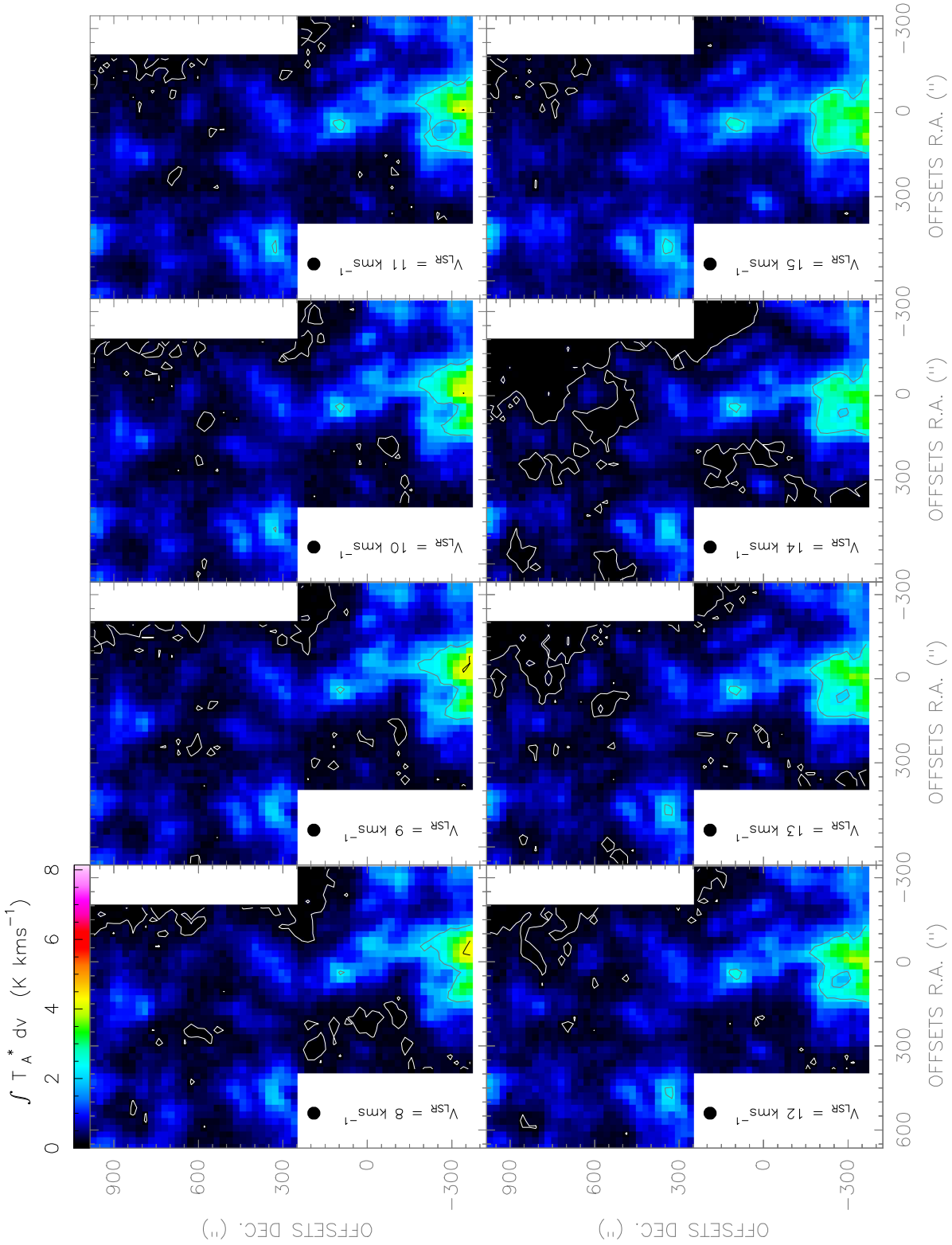

Figure. F.78: *[CI](1-0) line observed with the Herschel-HIFI satellite in Equatorial (J2000) coordinates. The spatial resolution of the maps is 46".*

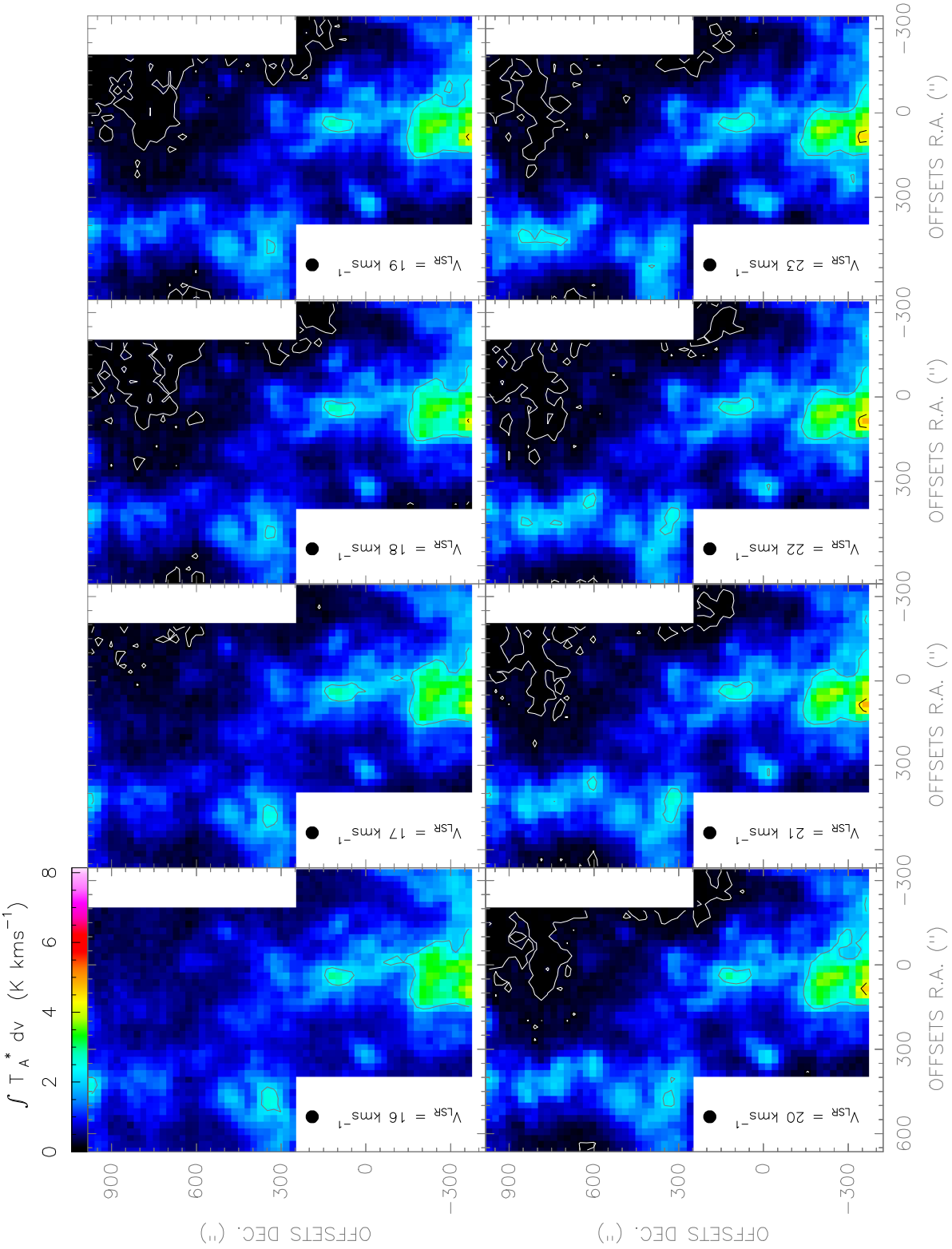

Figure. F.79: *[CI](1-0) line observed with the Herschel-HIFI satellite in Equatorial (J2000) coordinates. The spatial resolution of the maps is 46".*

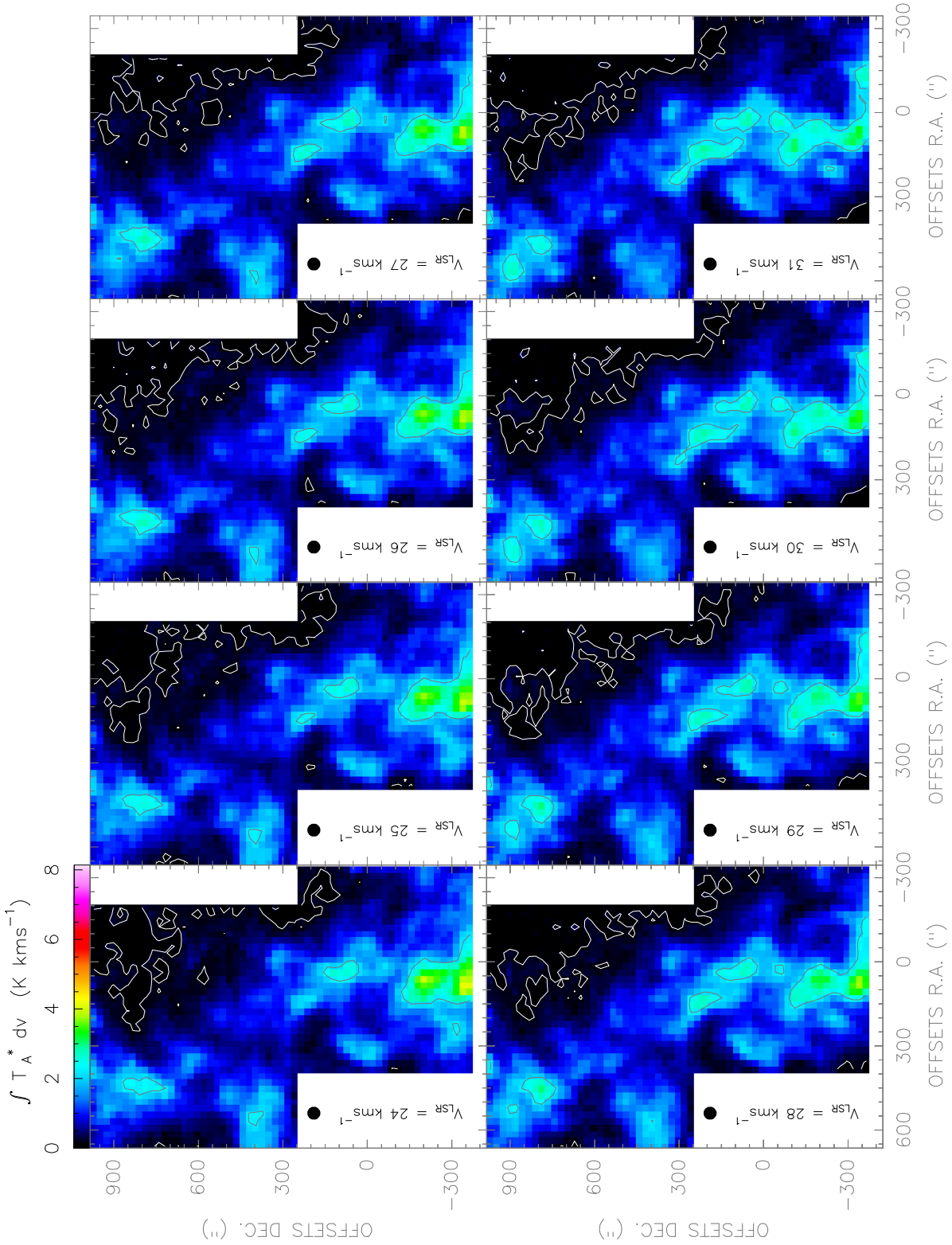

Figure. F.80: *[CI](1-0) line observed with the Herschel-HIFI satellite in Equatorial (J2000) coordinates. The spatial resolution of the maps is 46".*

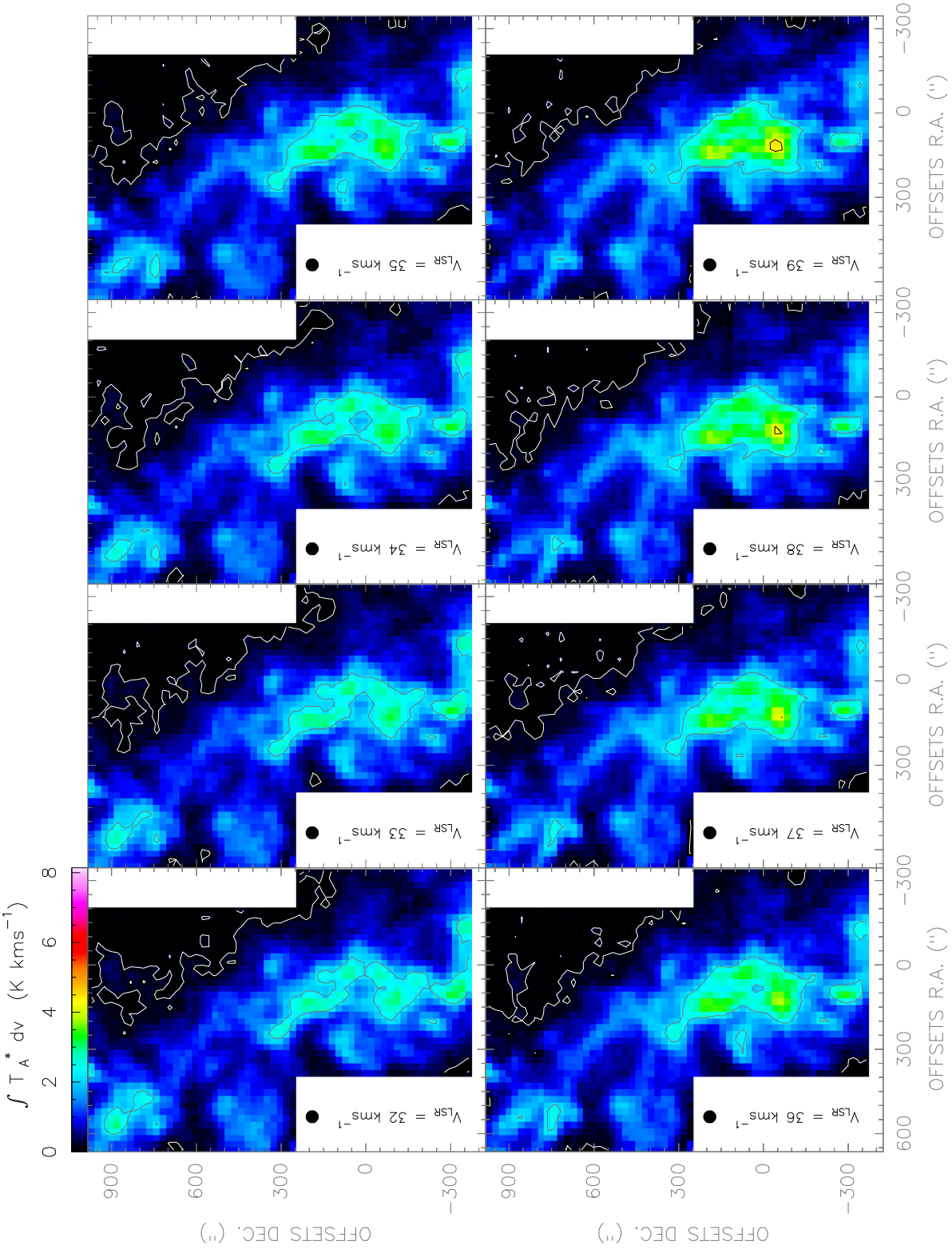

Figure. F.81: *[CI](1-0) line observed with the Herschel-HIFI satellite in Equatorial (J2000) coordinates. The spatial resolution of the maps is 46".*

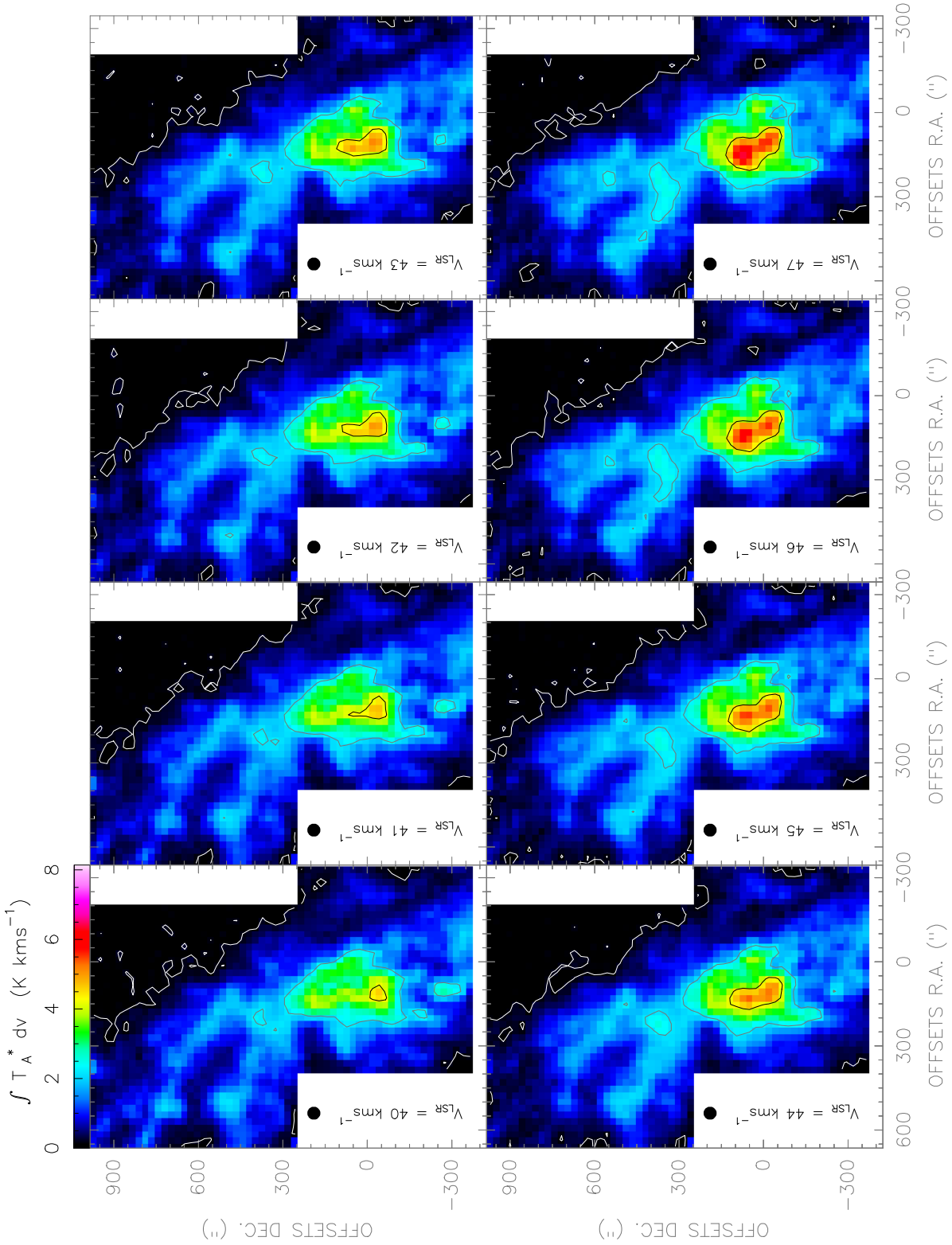

Figure. F.82: *[CI](1-0) line observed with the Herschel-HIFI satellite in Equatorial (J2000) coordinates. The spatial resolution of the maps is 46".*

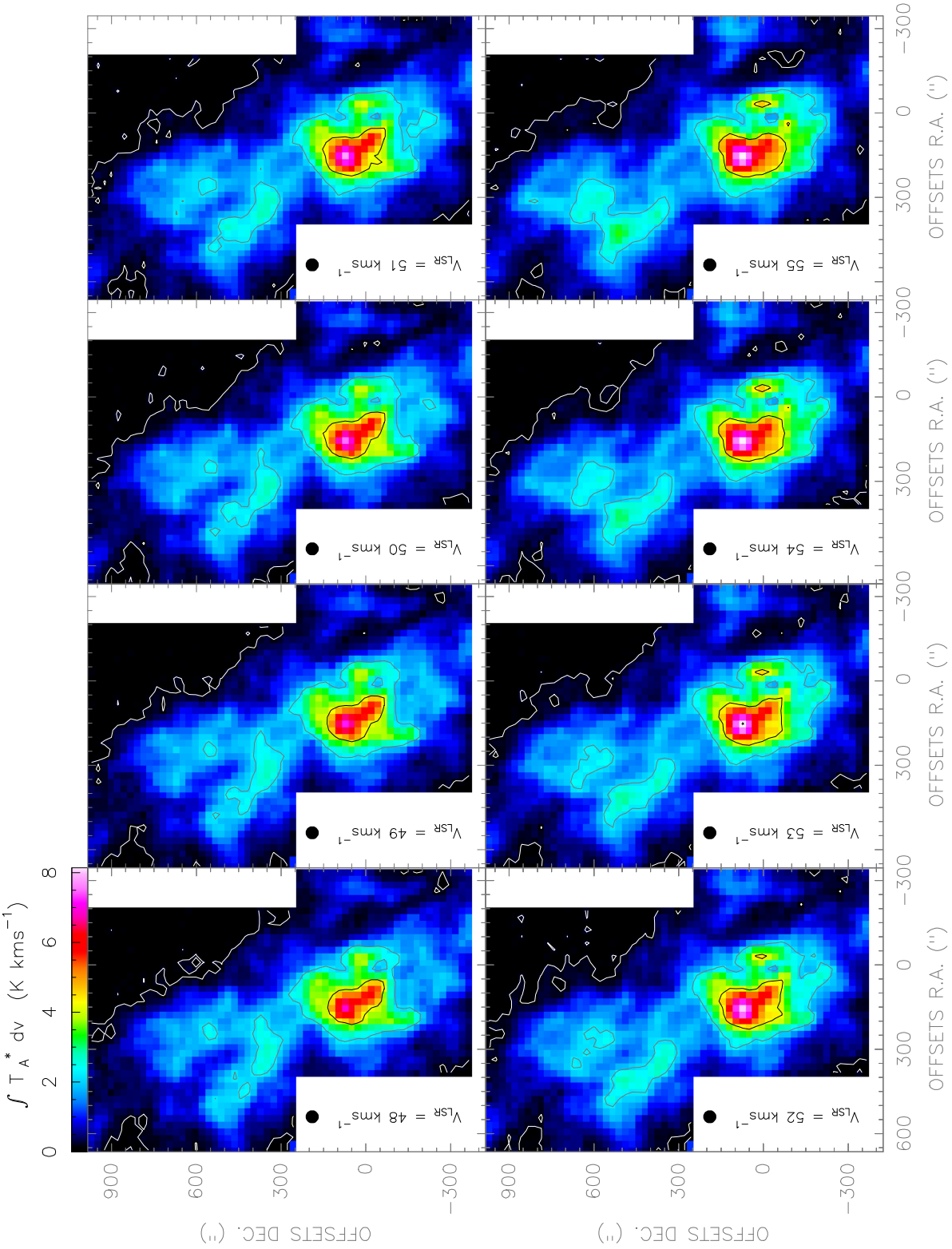

Figure. F.83: *[CI](1-0) line observed with the Herschel-HIFI satellite in Equatorial (J2000) coordinates. The spatial resolution of the maps is 46".*

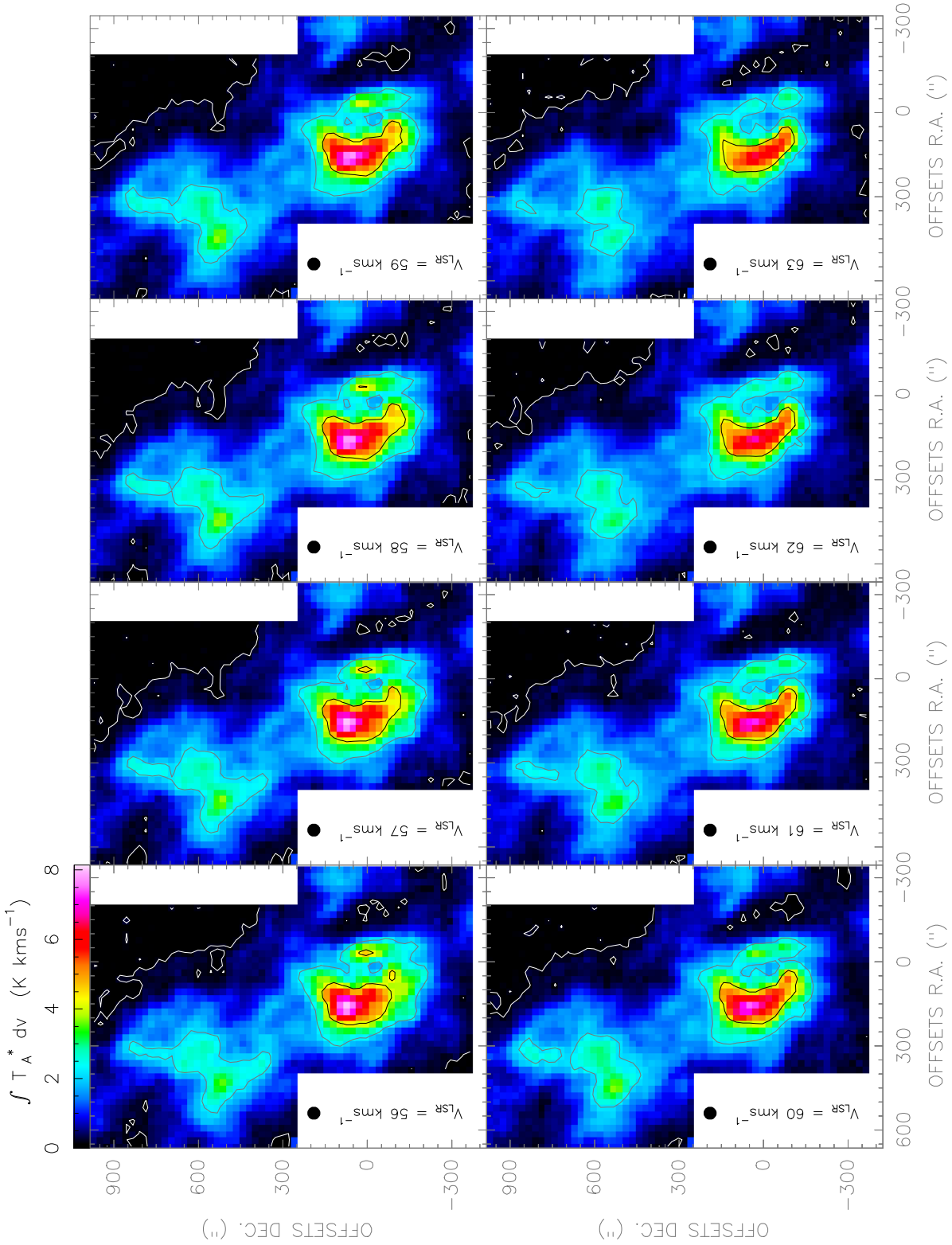

Figure. F.84: *[CI](1-0) line observed with the Herschel-HIFI satellite in Equatorial (J2000) coordinates. The spatial resolution of the maps is 46".*

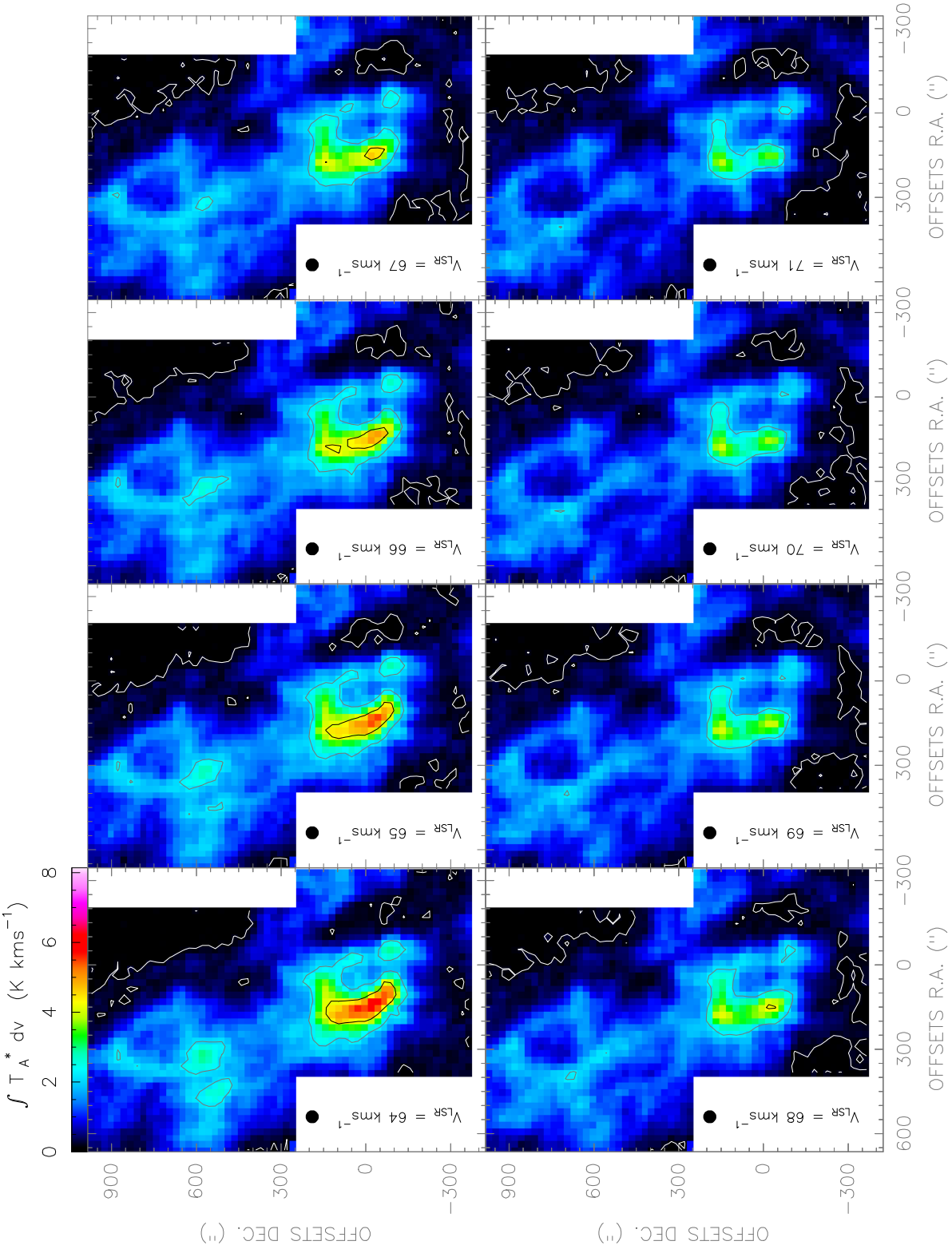

Figure. F.85: *[CI](1-0) line observed with the Herschel-HIFI satellite in Equatorial (J2000) coordinates. The spatial resolution of the maps is 46".*

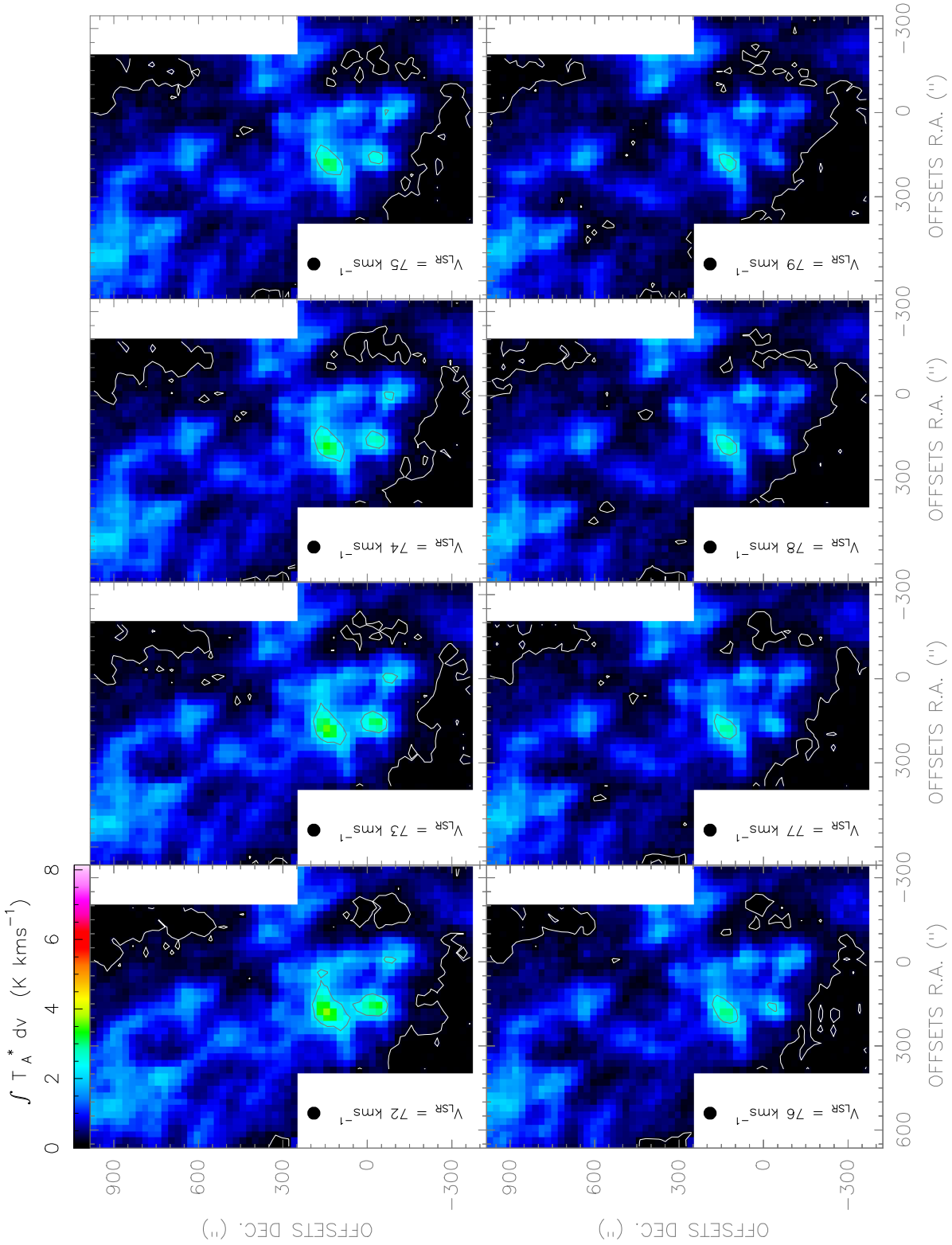

Figure. F.86: *[CI](1-0) line observed with the Herschel-HIFI satellite in Equatorial (J2000) coordinates. The spatial resolution of the maps is 46".*

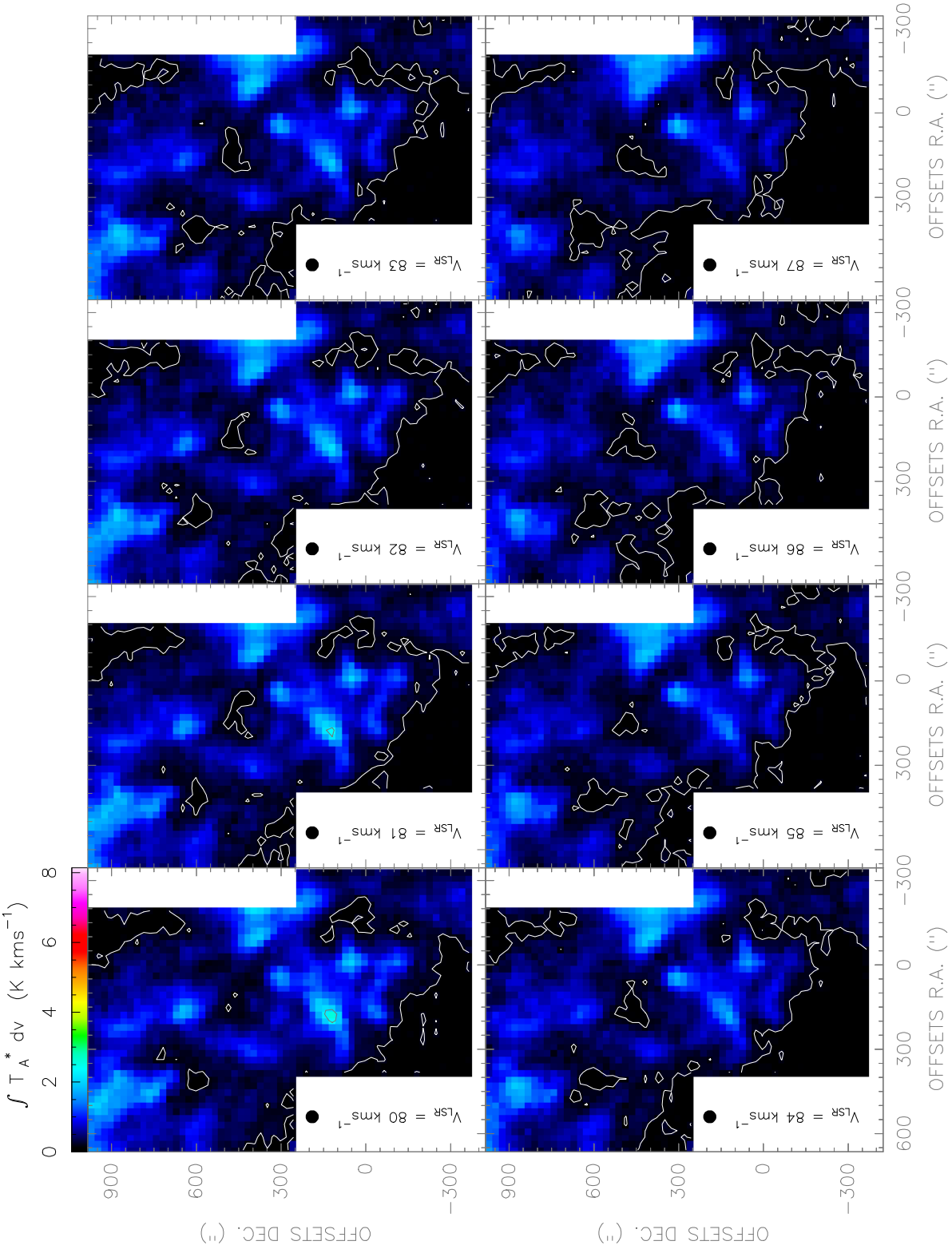

Figure. F.87: *[CI](1-0) line observed with the Herschel-HIFI satellite in Equatorial (J2000) coordinates. The spatial resolution of the maps is 46".*

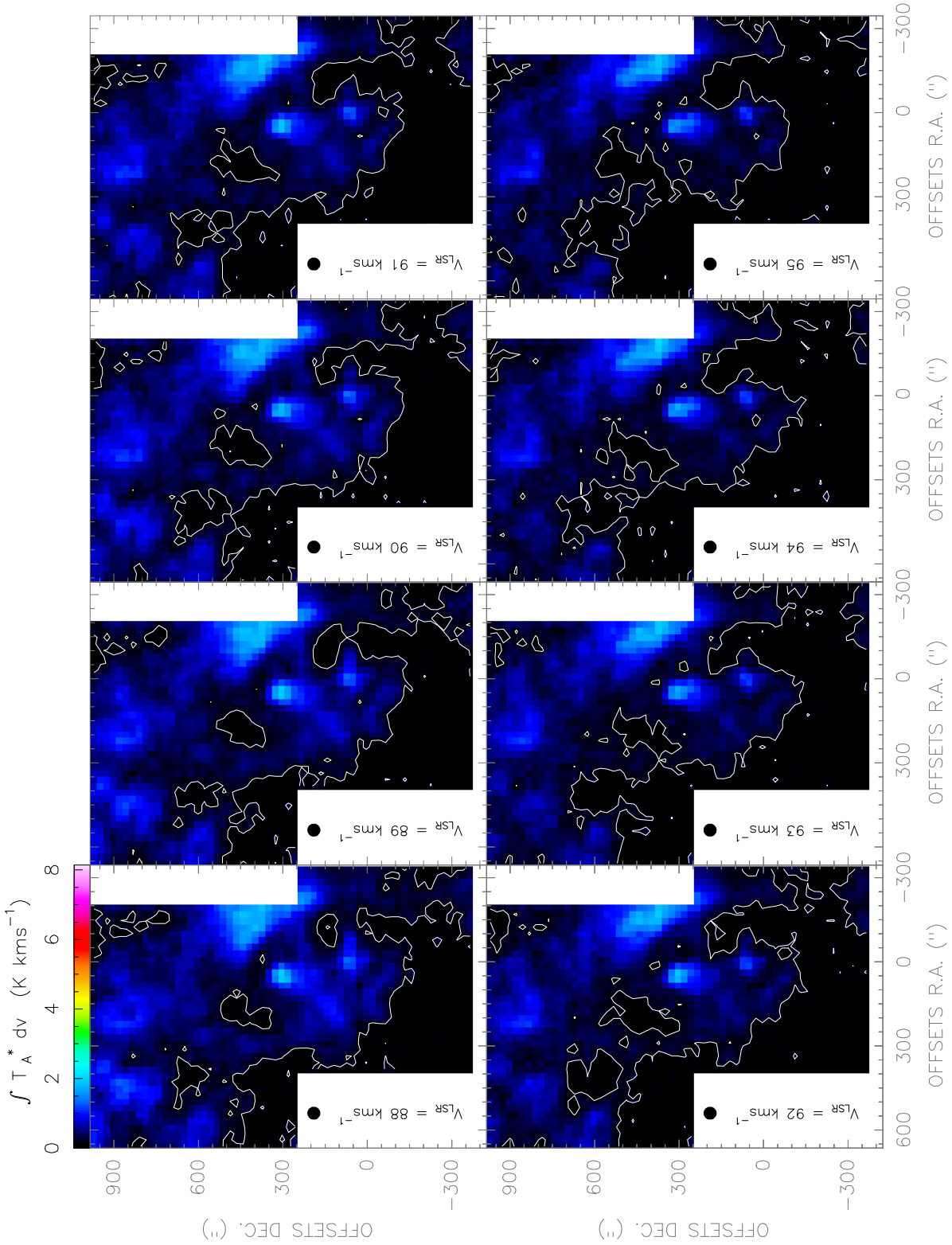

Figure. F.88: *[CI](1-0) line observed with the Herschel-HIFI satellite in Equatorial (J2000) coordinates. The spatial resolution of the maps is 46".*

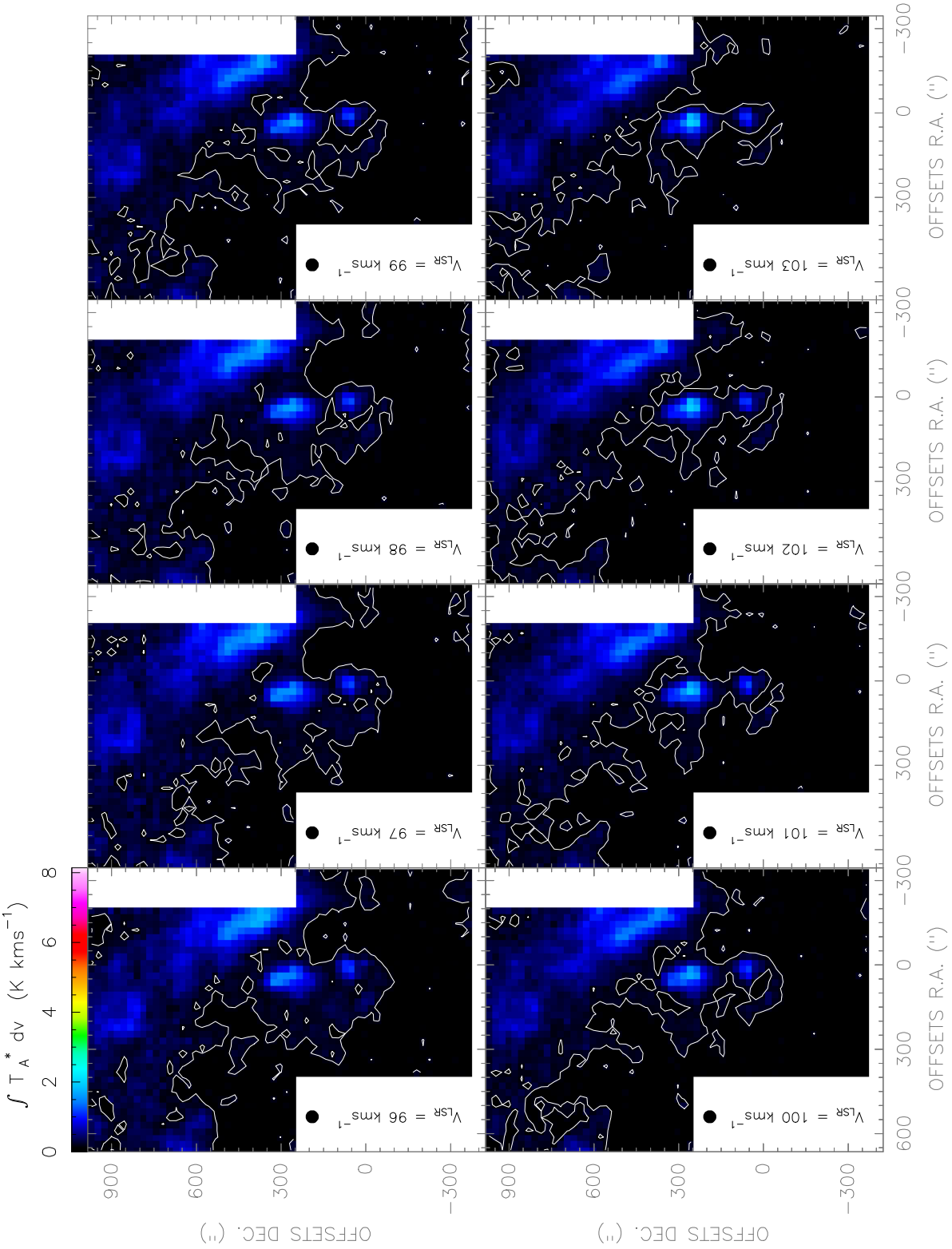

Figure. F.89: *[CI](1-0) line observed with the Herschel-HIFI satellite in Equatorial (J2000) coordinates. The spatial resolution of the maps is 46".*

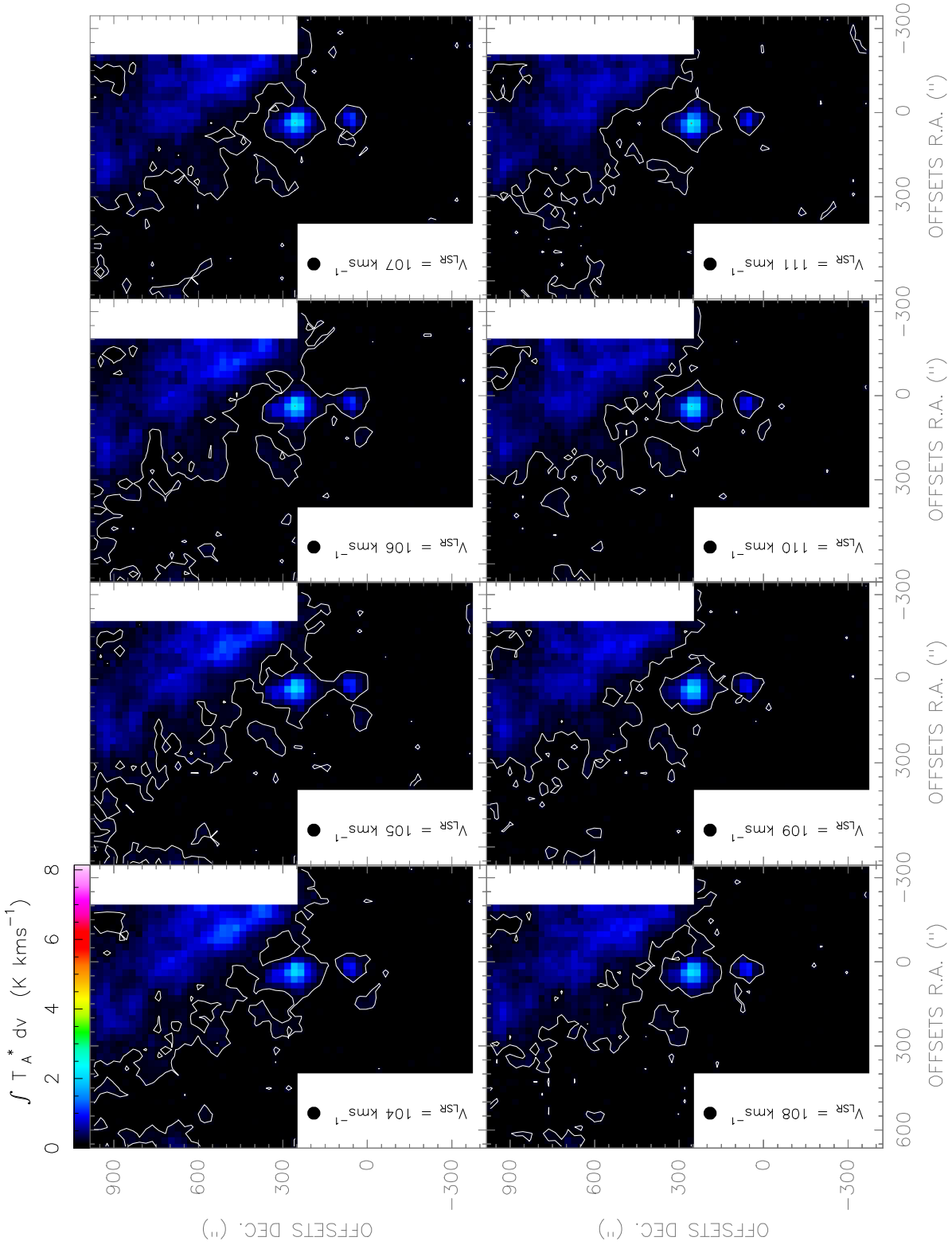

Figure. F.90: *[CI](1-0) line observed with the Herschel-HIFI satellite in Equatorial (J2000) coordinates. The spatial resolution of the maps is 46".*

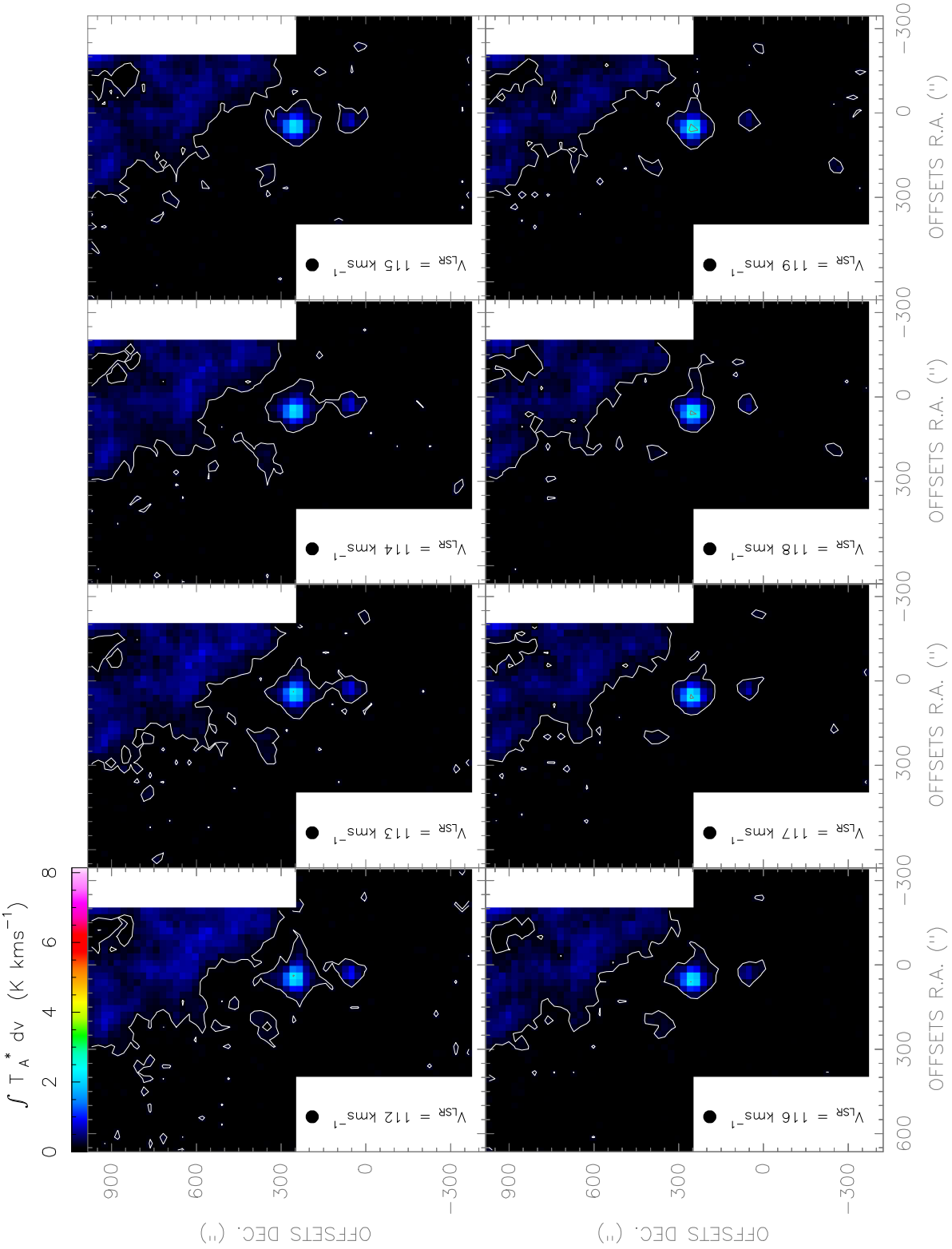

Figure. F.91: *[CI](1-0) line observed with the Herschel-HIFI satellite in Equatorial (J2000) coordinates. The spatial resolution of the maps is 46".*

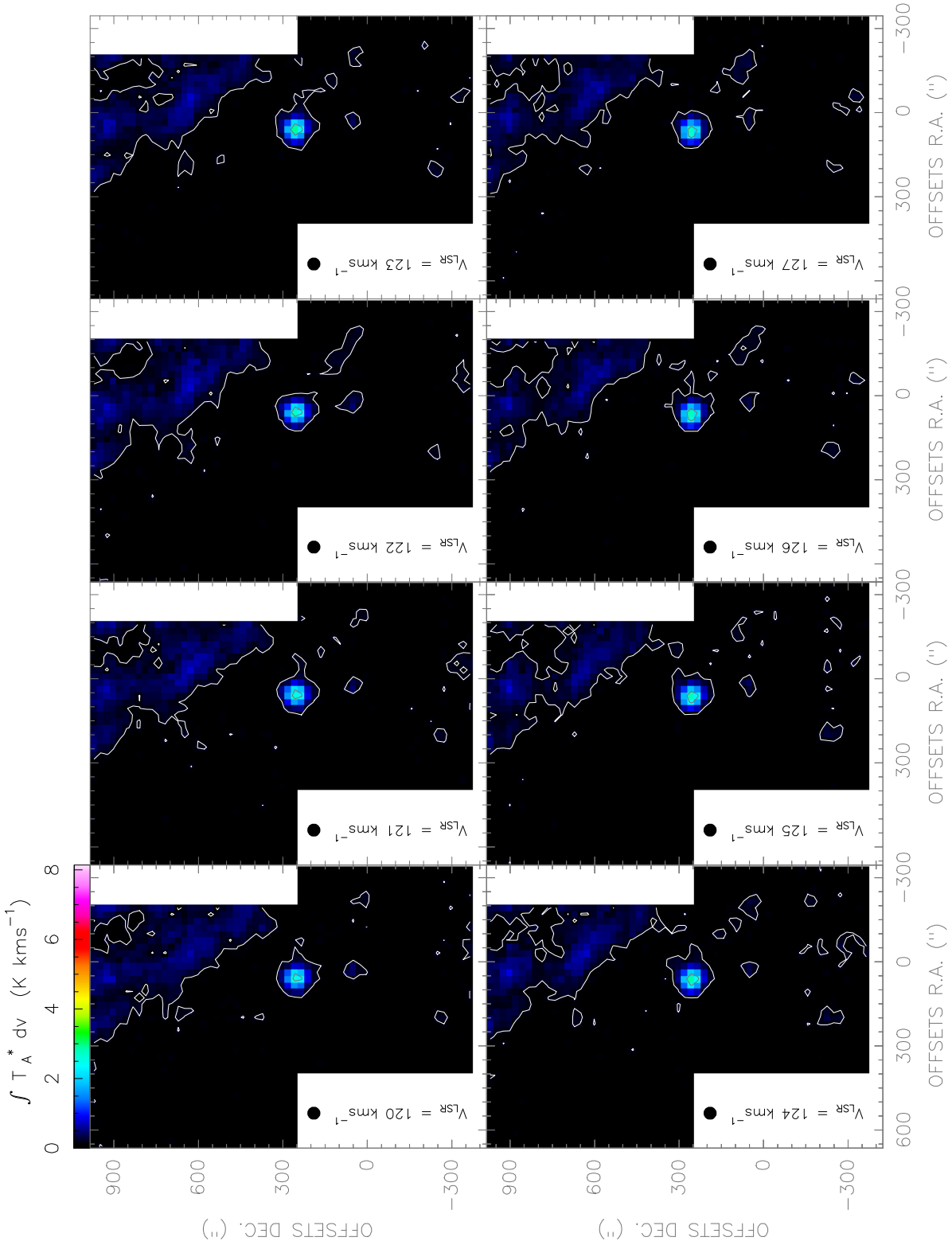

Figure. F.92: *[CI](1-0) line observed with the Herschel-HIFI satellite in Equatorial (J2000) coordinates. The spatial resolution of the maps is 46".*

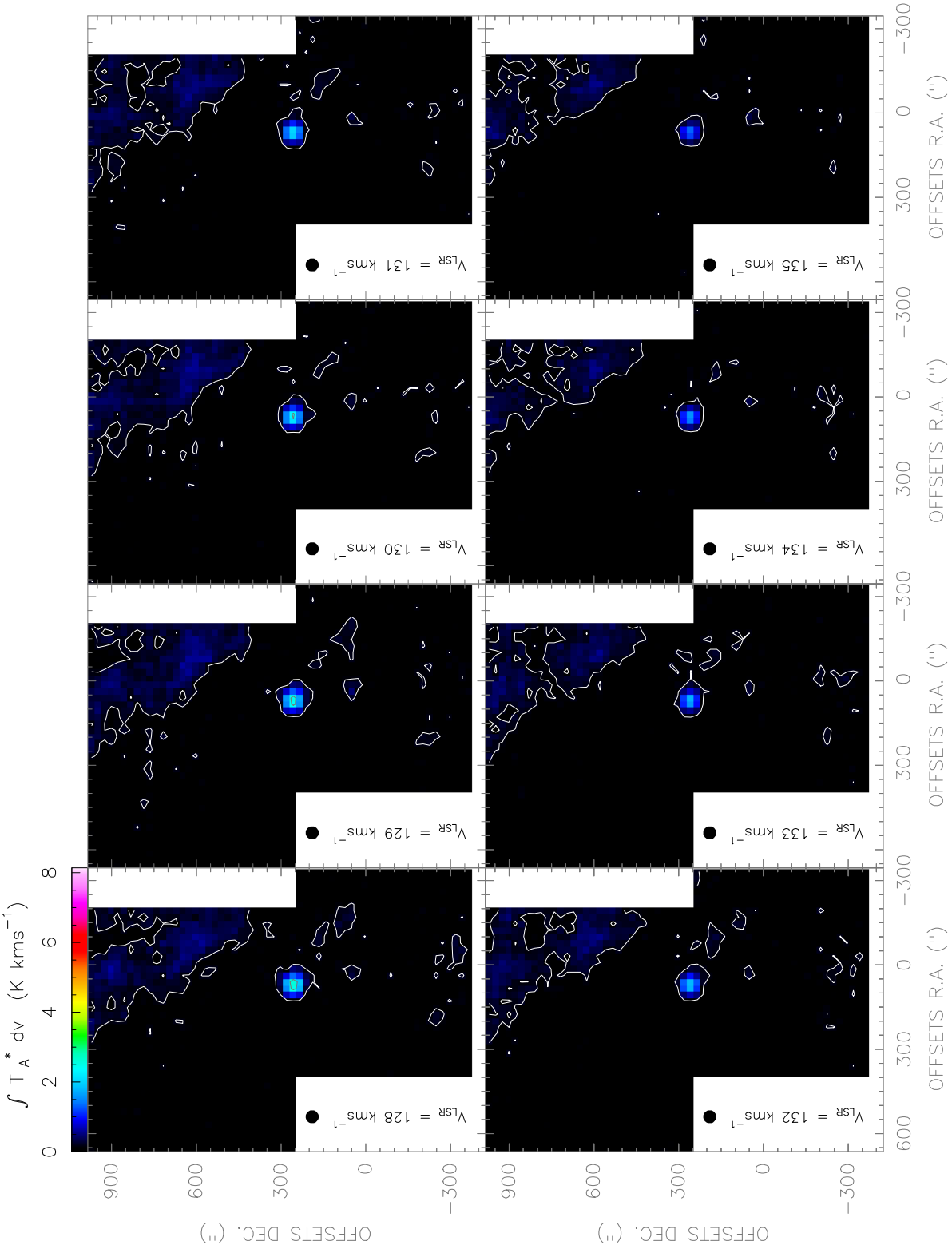

Figure. F.93: *[CI](1-0) line observed with the Herschel-HIFI satellite in Equatorial (J2000) coordinates. The spatial resolution of the maps is 46".*

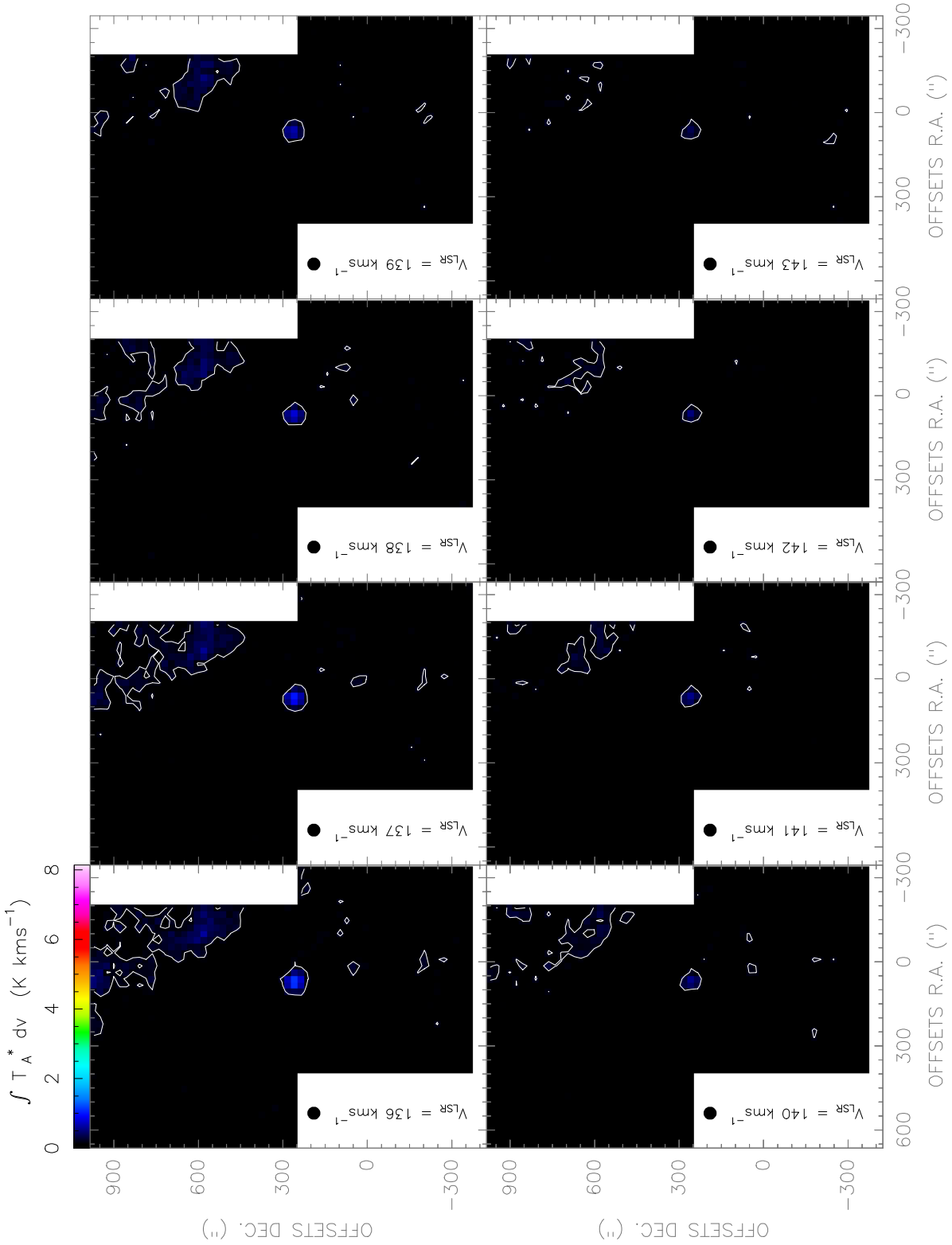

Figure. F.94: *[CI](1-0) line observed with the Herschel-HIFI satellite in Equatorial (J2000) coordinates. The spatial resolution of the maps is 46".*

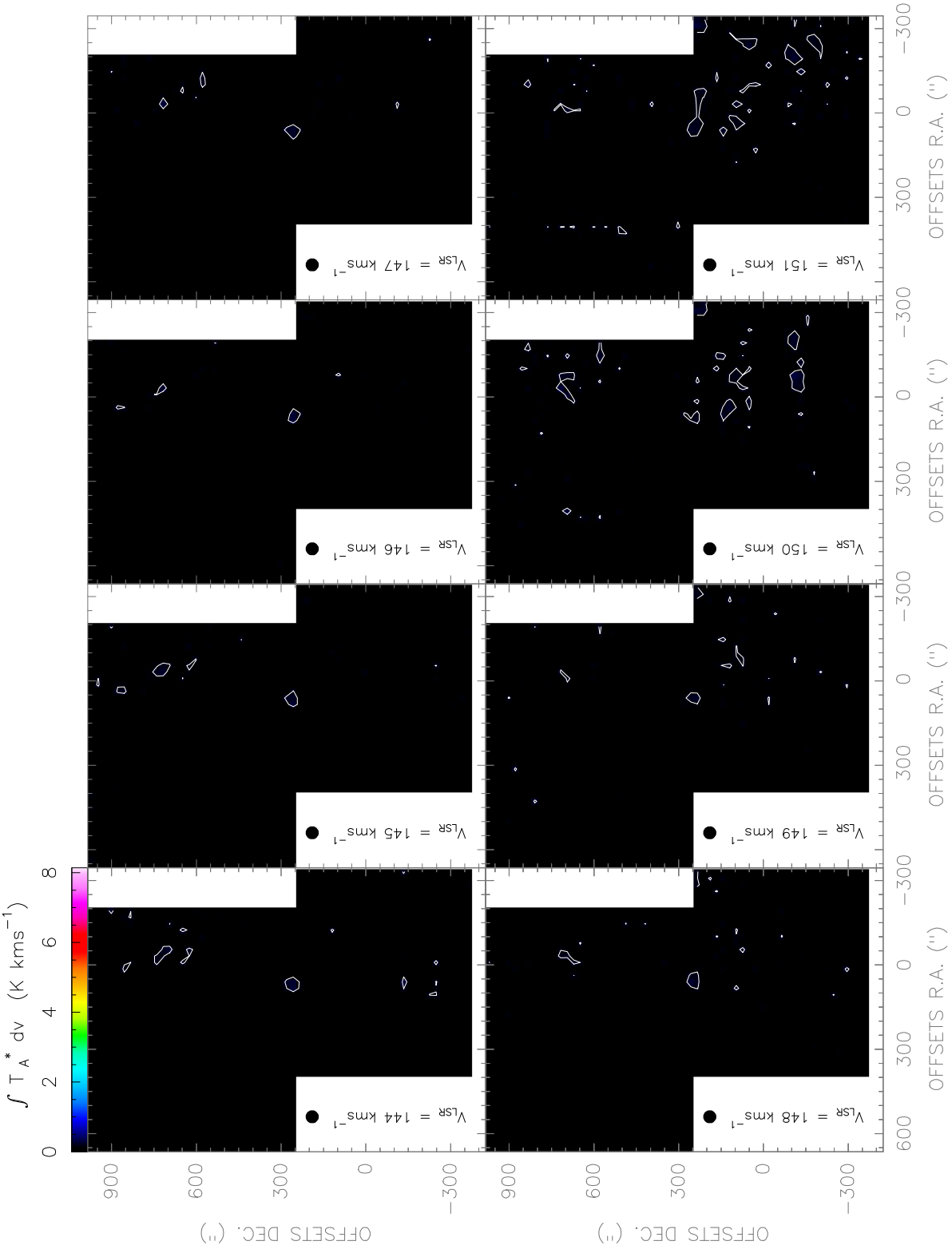

Figure. F.95: *[CI](1-0) line observed with the Herschel-HIFI satellite in Equatorial (J2000) coordinates. The spatial resolution of the maps is 46".*

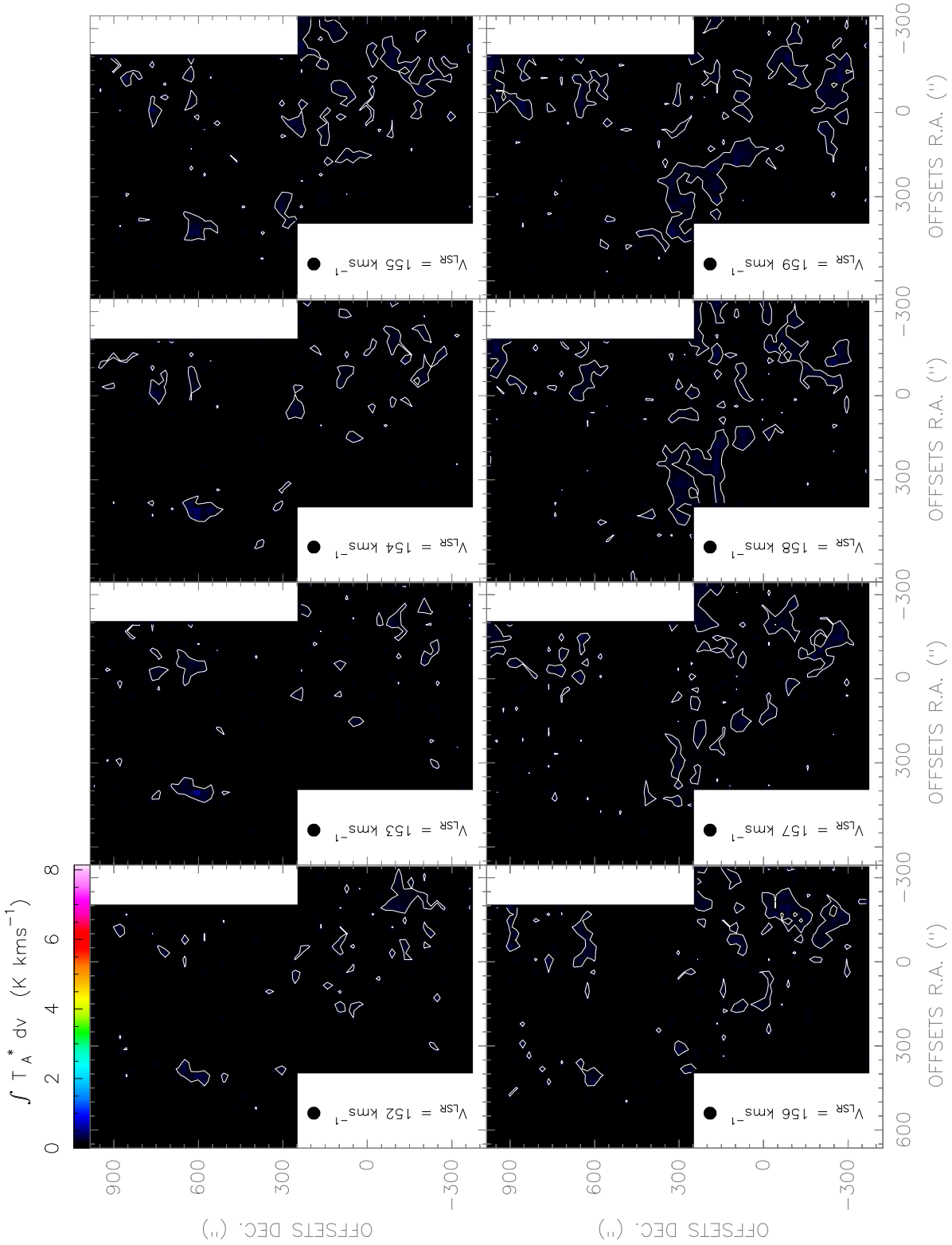

Figure. F.96: *[CI](1-0) line observed with the Herschel-HIFI satellite in Equatorial (J2000) coordinates. The spatial resolution of the maps is 46".*

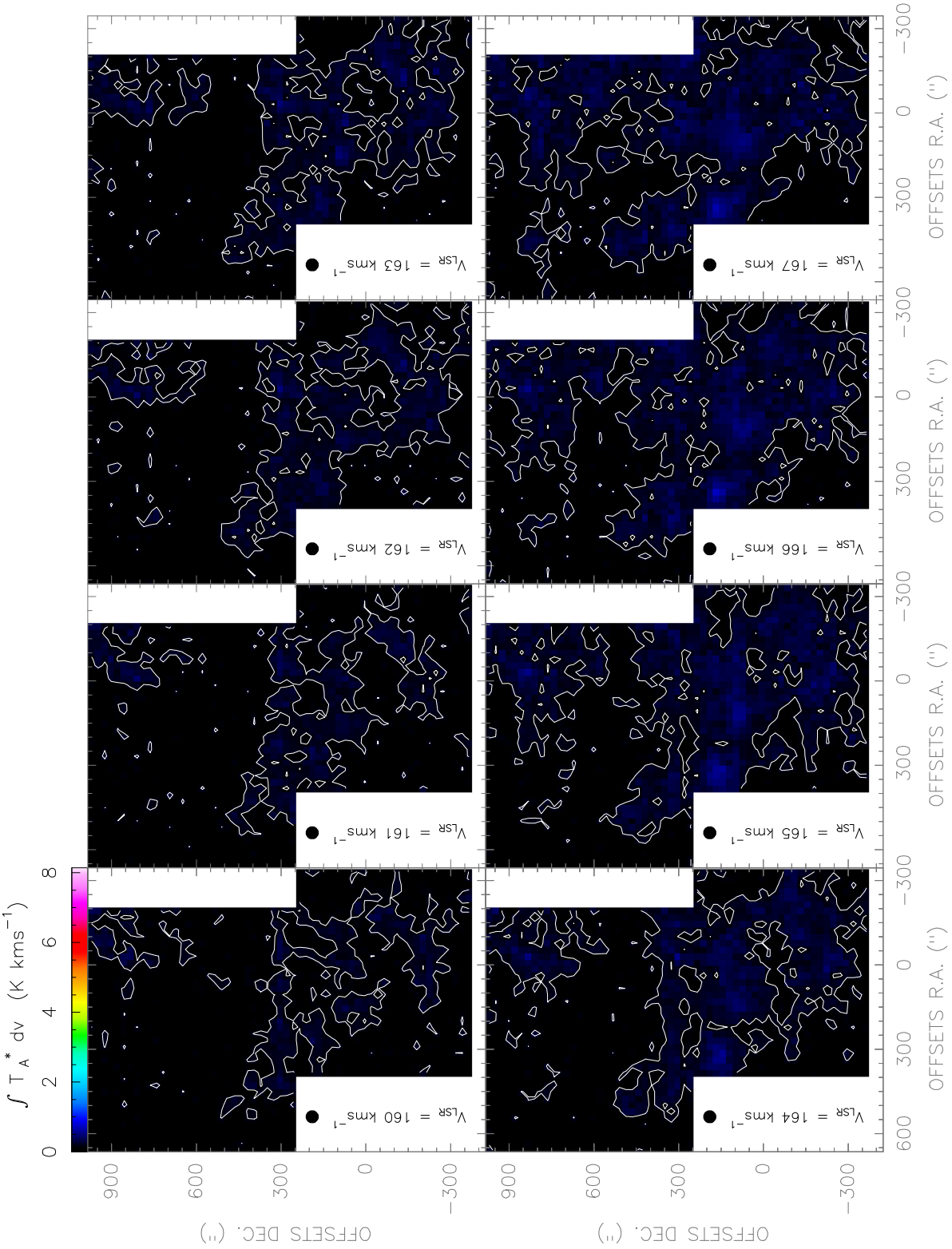

Figure. F.97: *[CI](1-0) line observed with the Herschel-HIFI satellite in Equatorial (J2000) coordinates. The spatial resolution of the maps is 46".*

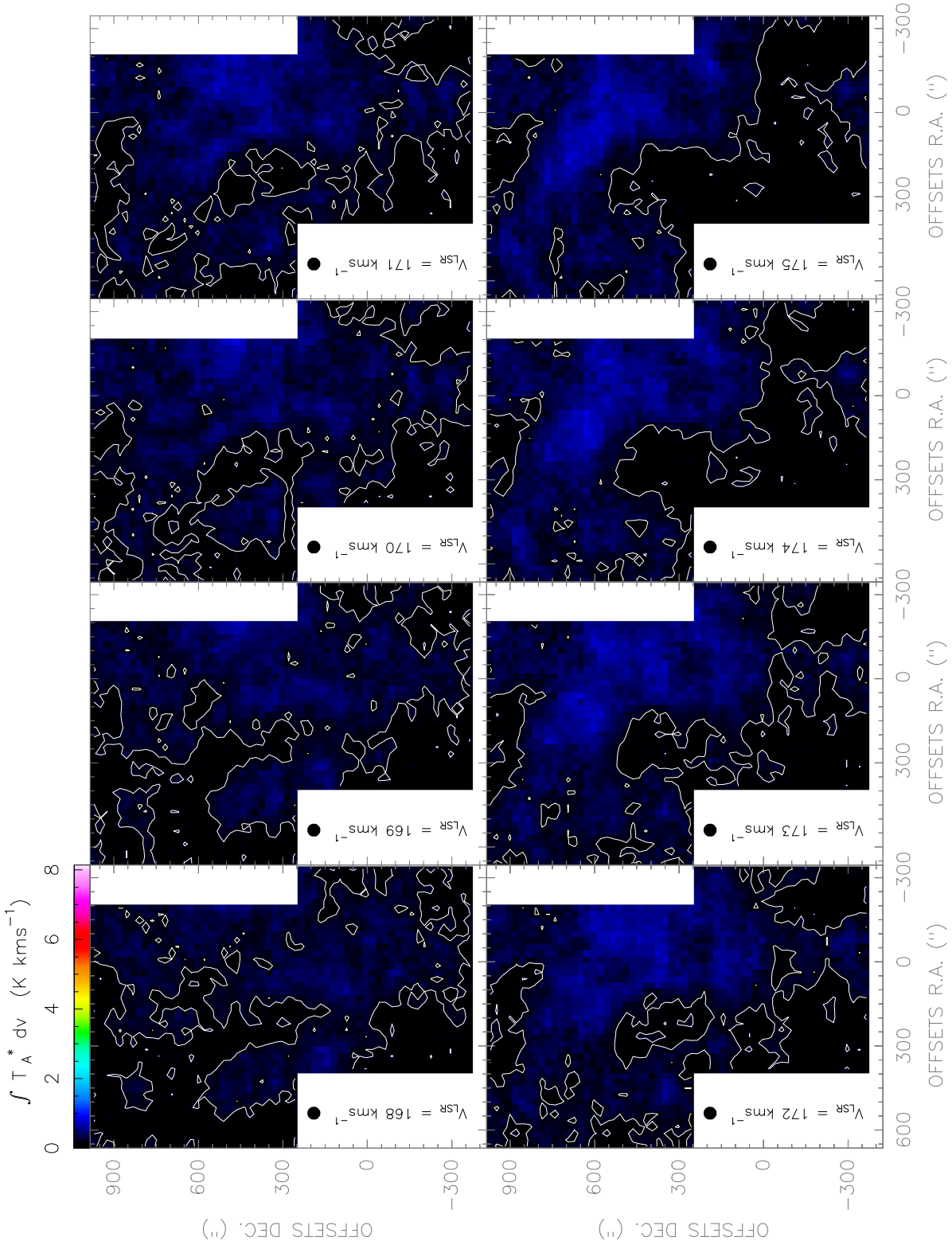

Figure. F.98: *[CI](1-0) line observed with the Herschel-HIFI satellite in Equatorial (J2000) coordinates. The spatial resolution of the maps is 46".*

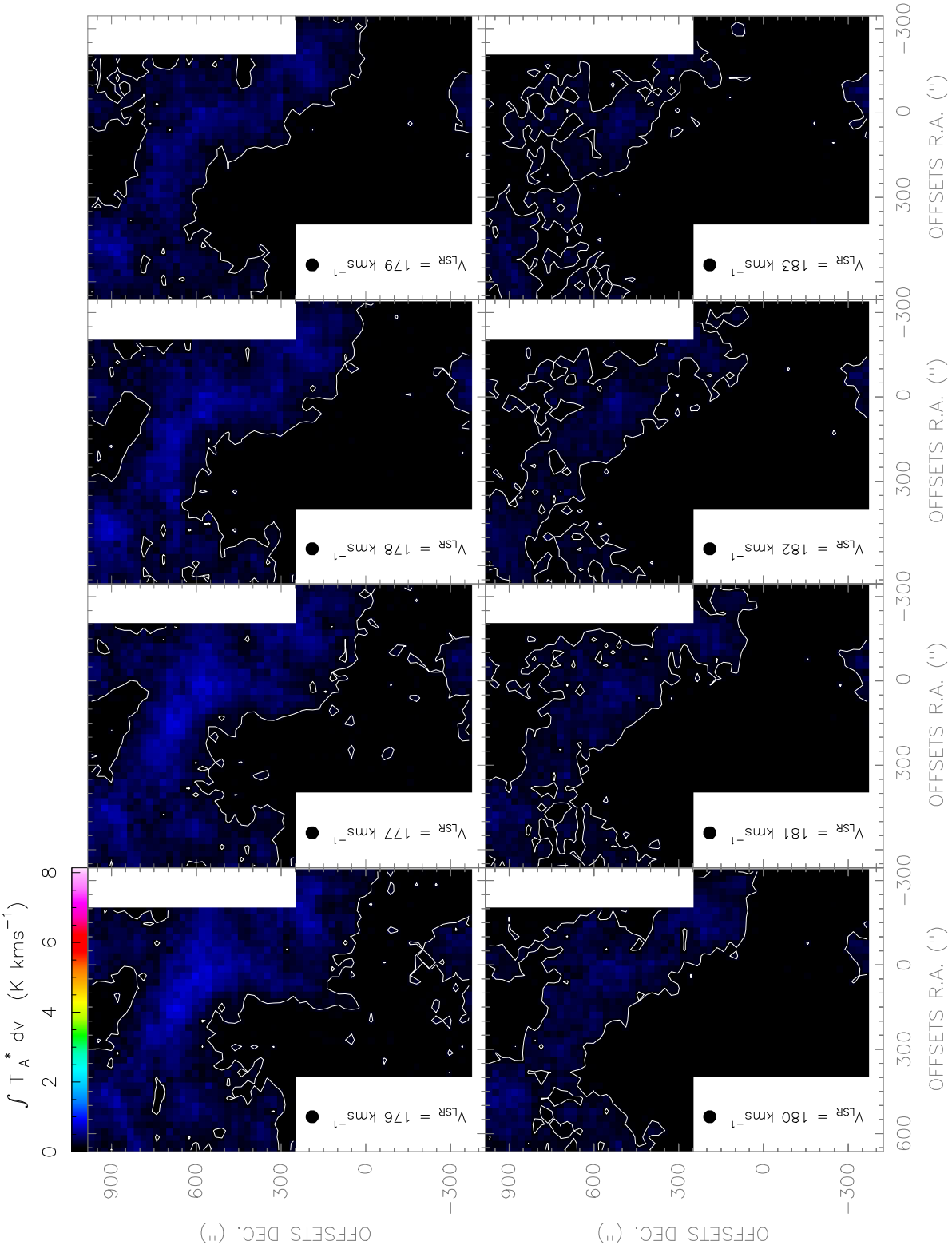

Figure. F.99: *[CI](1-0) line observed with the Herschel-HIFI satellite in Equatorial (J2000) coordinates. The spatial resolution of the maps is 46".*

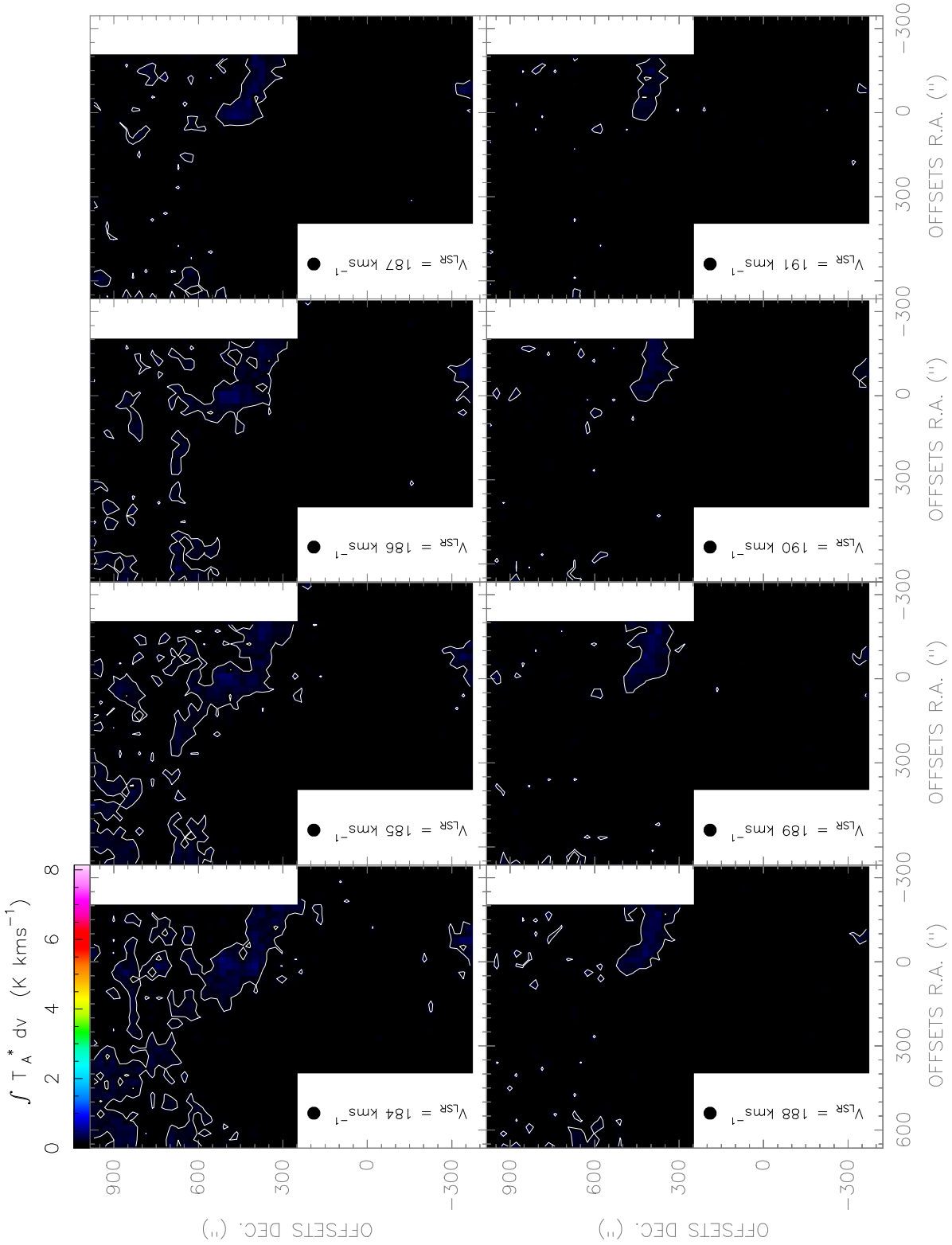

Figure. F.100: *[CI](1-0) line observed with the Herschel-HIFI satellite in Equatorial (J2000) coordinates. The spatial resolution of the maps is 46".*

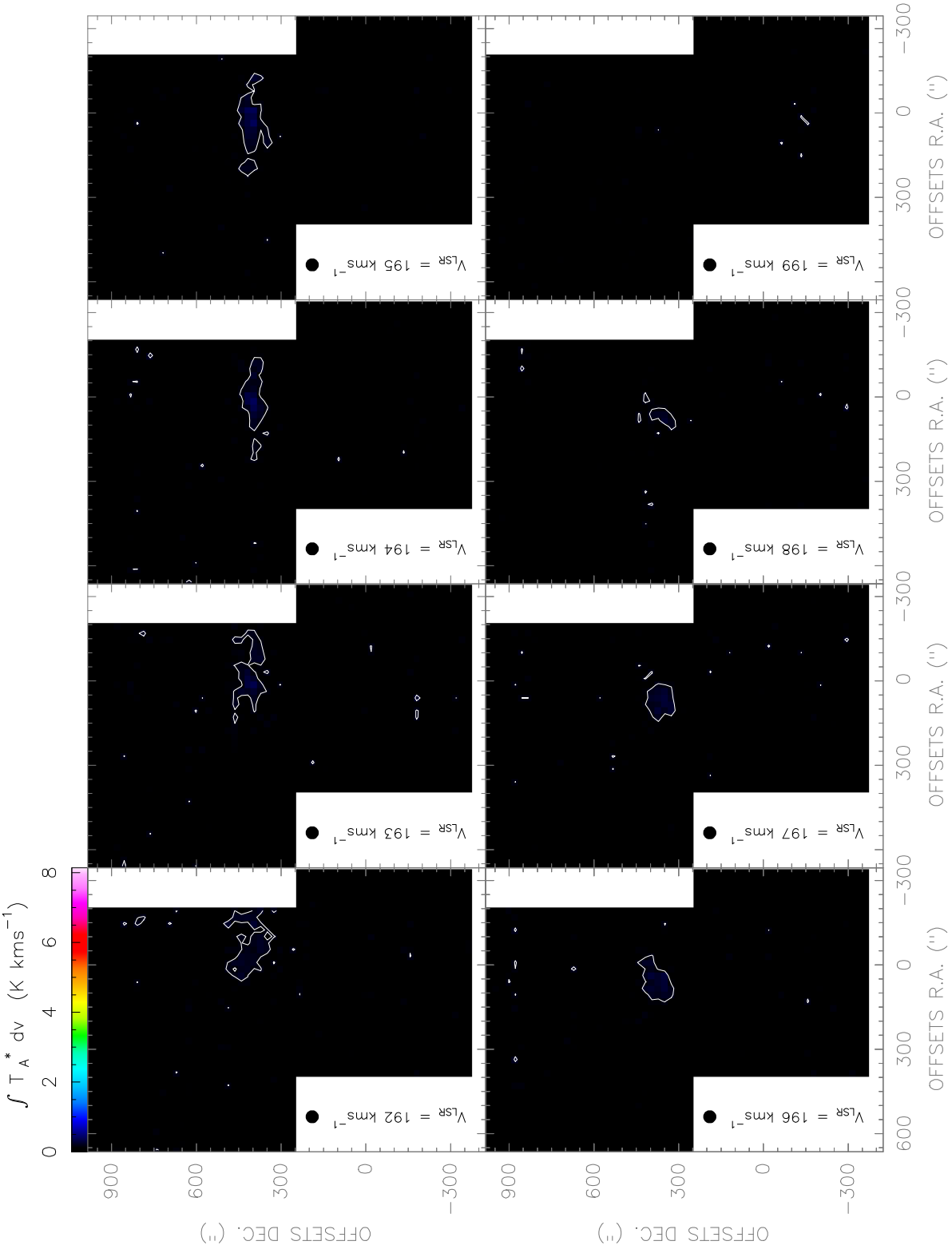

Figure. F.101: *[CI](1-0) line observed with the Herschel-HIFI satellite in Equatorial (J2000) coordinates. The spatial resolution of the maps is 46".*

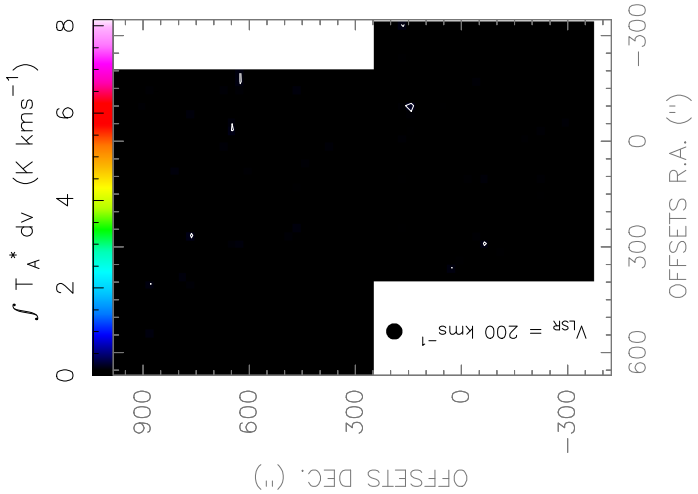

Figure. F.102: *[CI](1-0) line observed with the Herschel-HIFI satellite in Equatorial (J2000) coordinates. The spatial resolution of the maps is 46".*

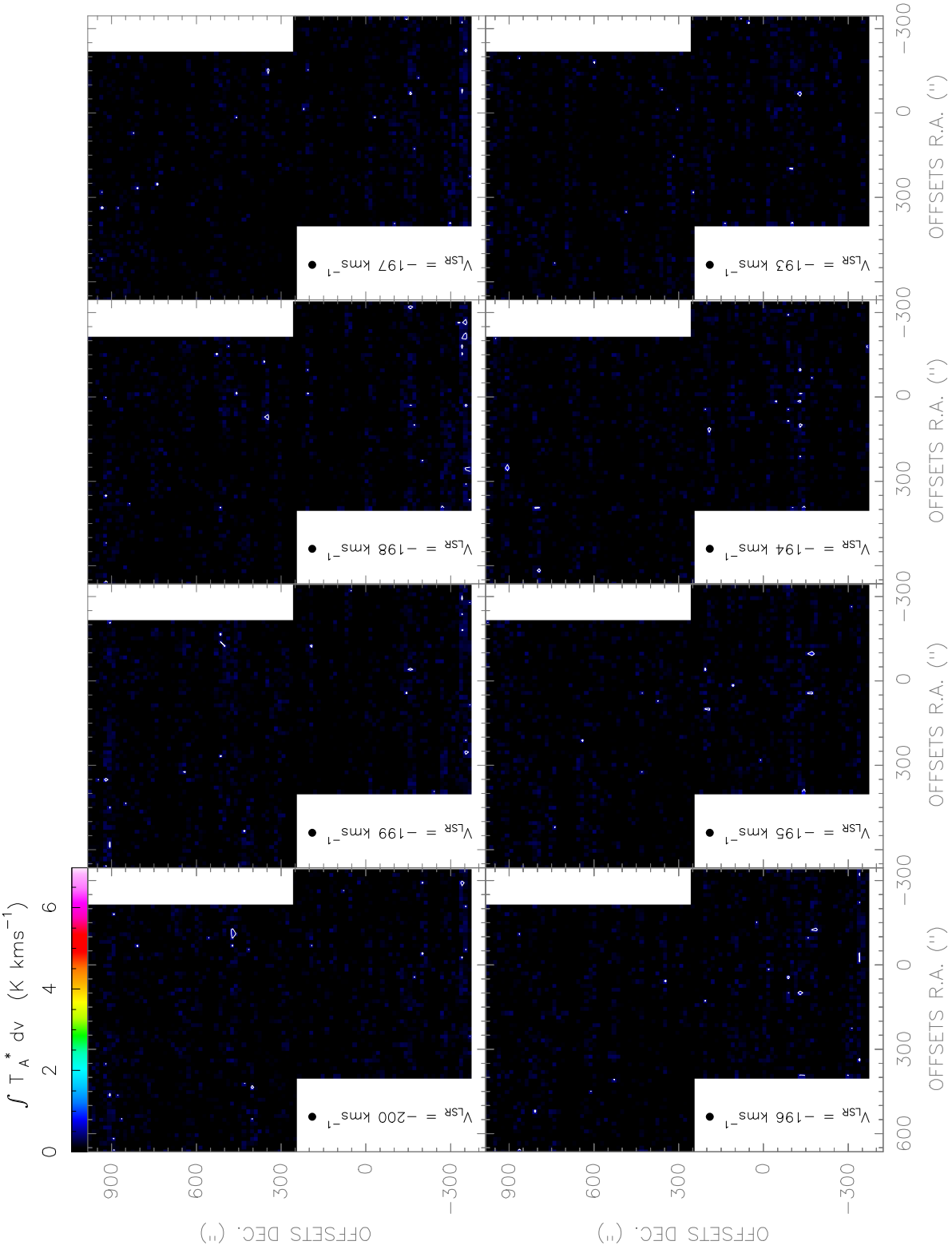

Figure. F.103: *[CI](2-1) line observed with the Herschel-HIFI satellite in Equatorial (J2000) coordinates. The spatial resolution of the maps is 28".*

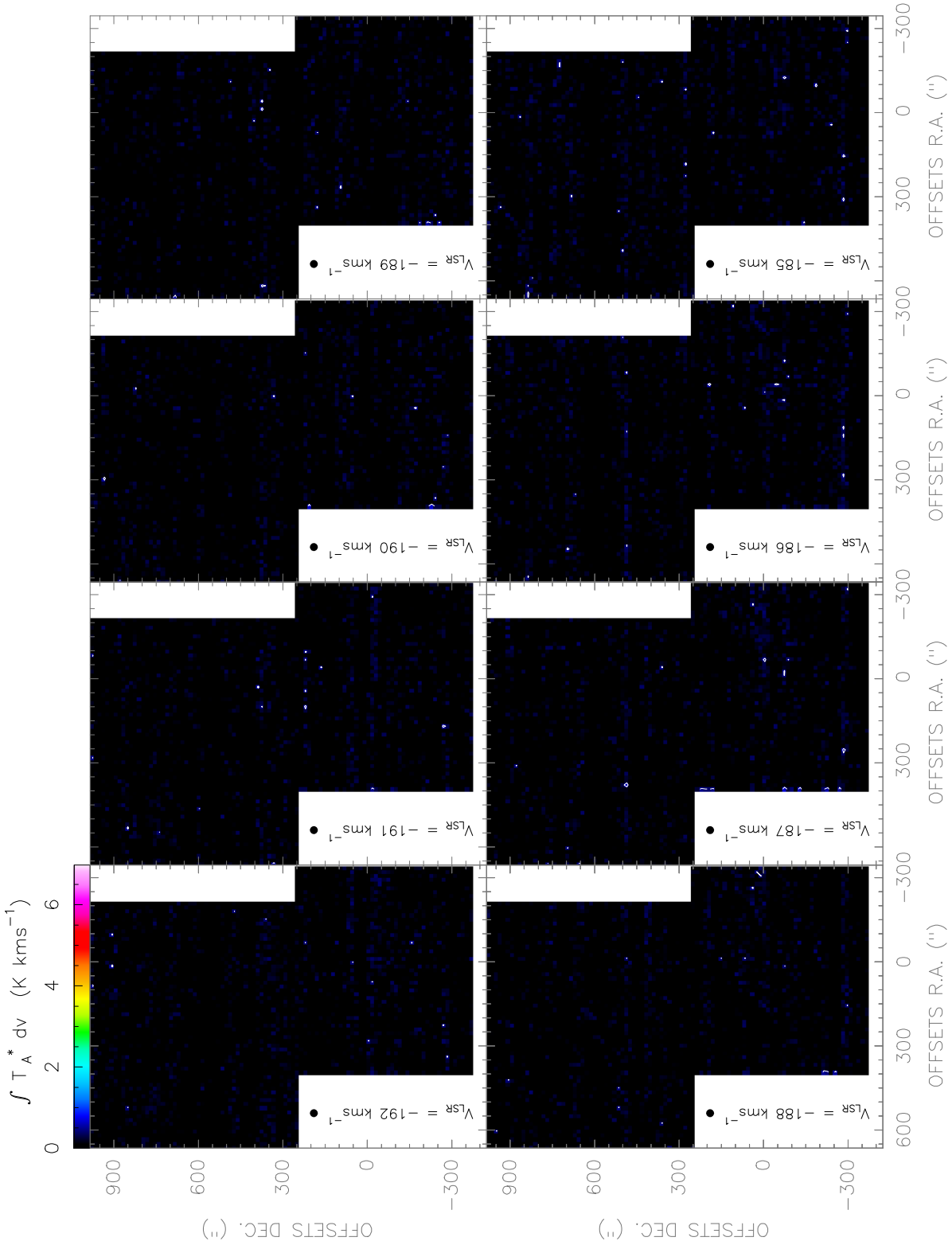

Figure. F.104: *[CI](2-1) line observed with the Herschel-HIFI satellite in Equatorial (J2000) coordinates. The spatial resolution of the maps is 28".*

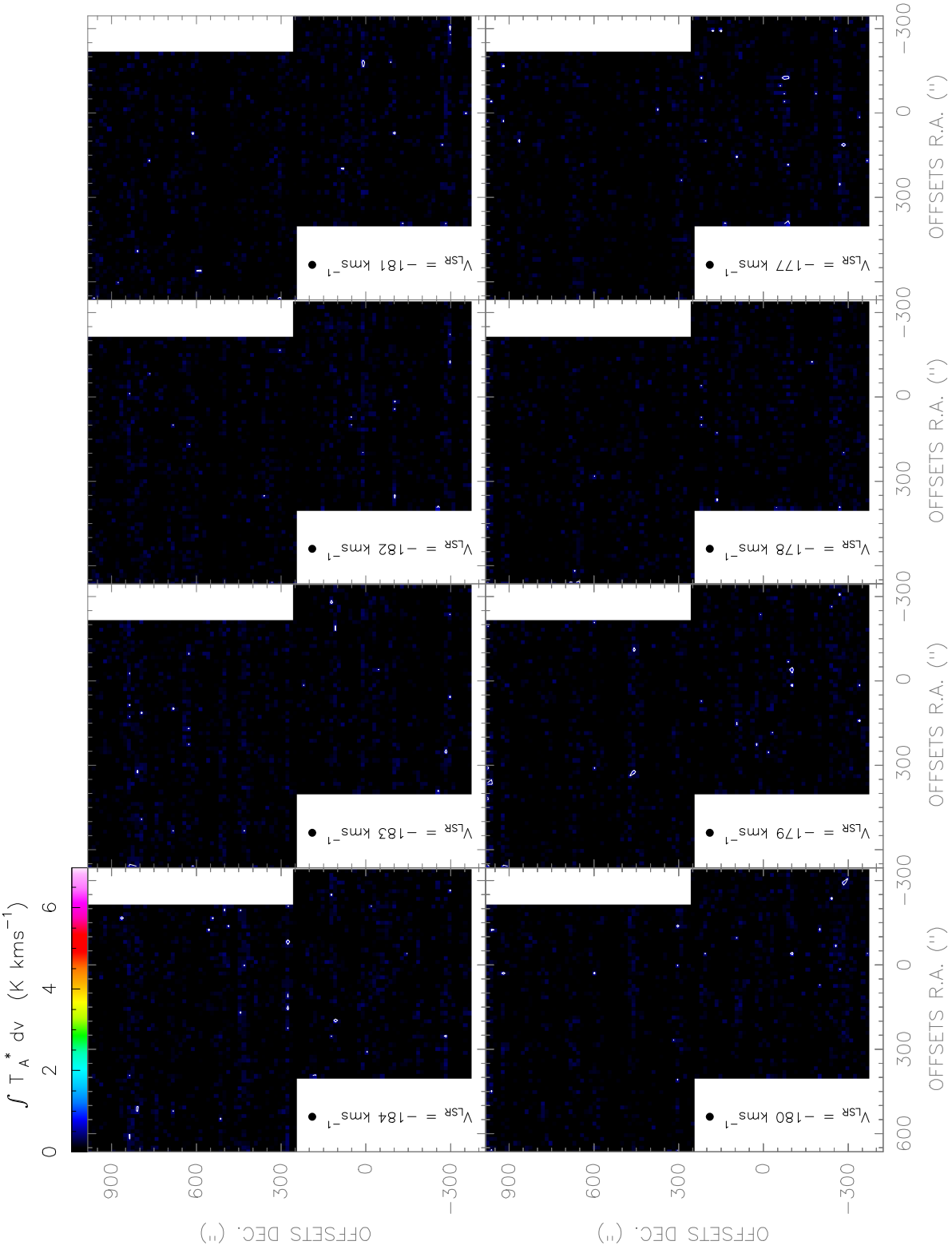

Figure. F.105: *[CI](2-1) line observed with the Herschel-HIFI satellite in Equatorial (J2000) coordinates. The spatial resolution of the maps is 28".*

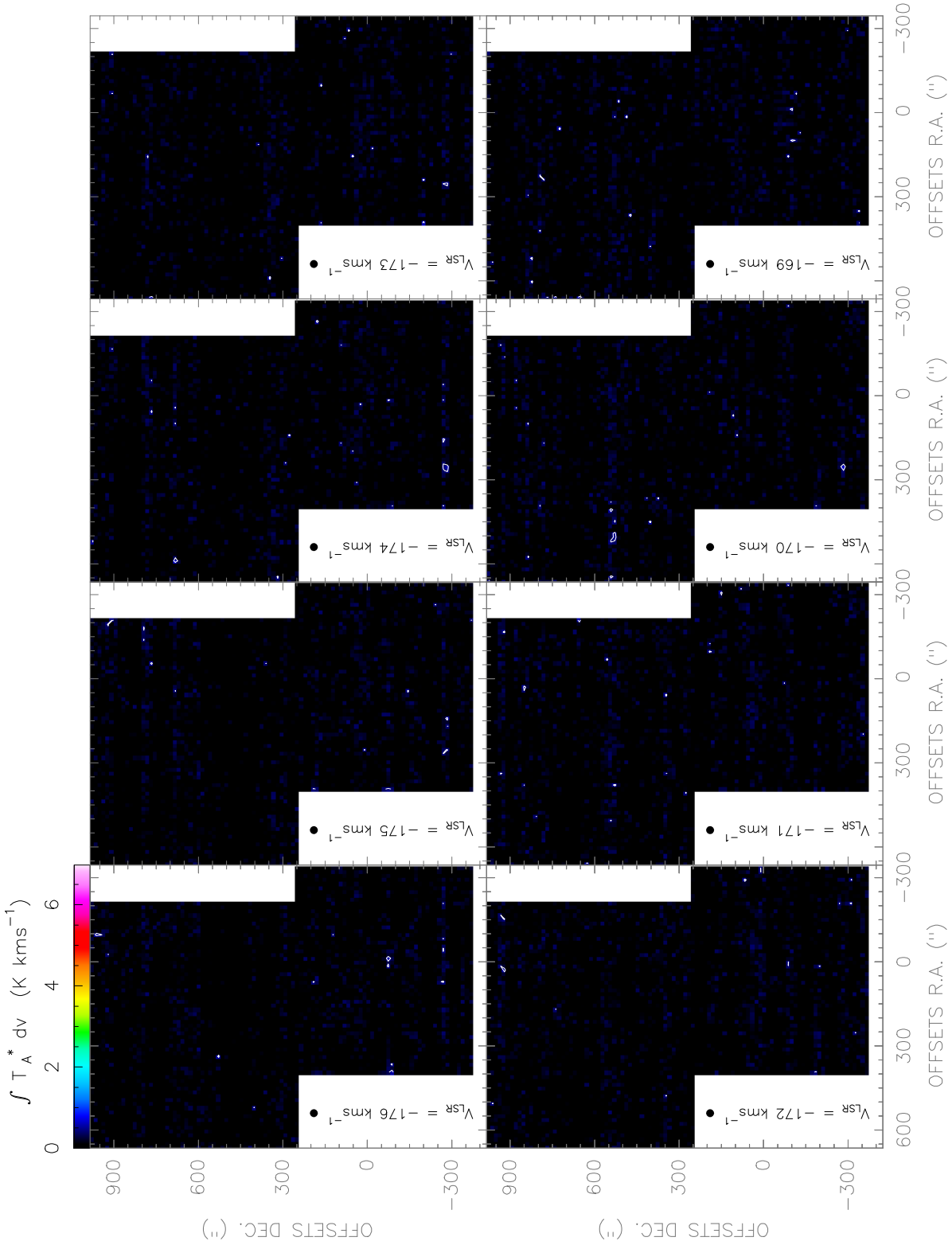

Figure. F.106: *[CI](2-1) line observed with the Herschel-HIFI satellite in Equatorial (J2000) coordinates. The spatial resolution of the maps is 28".*

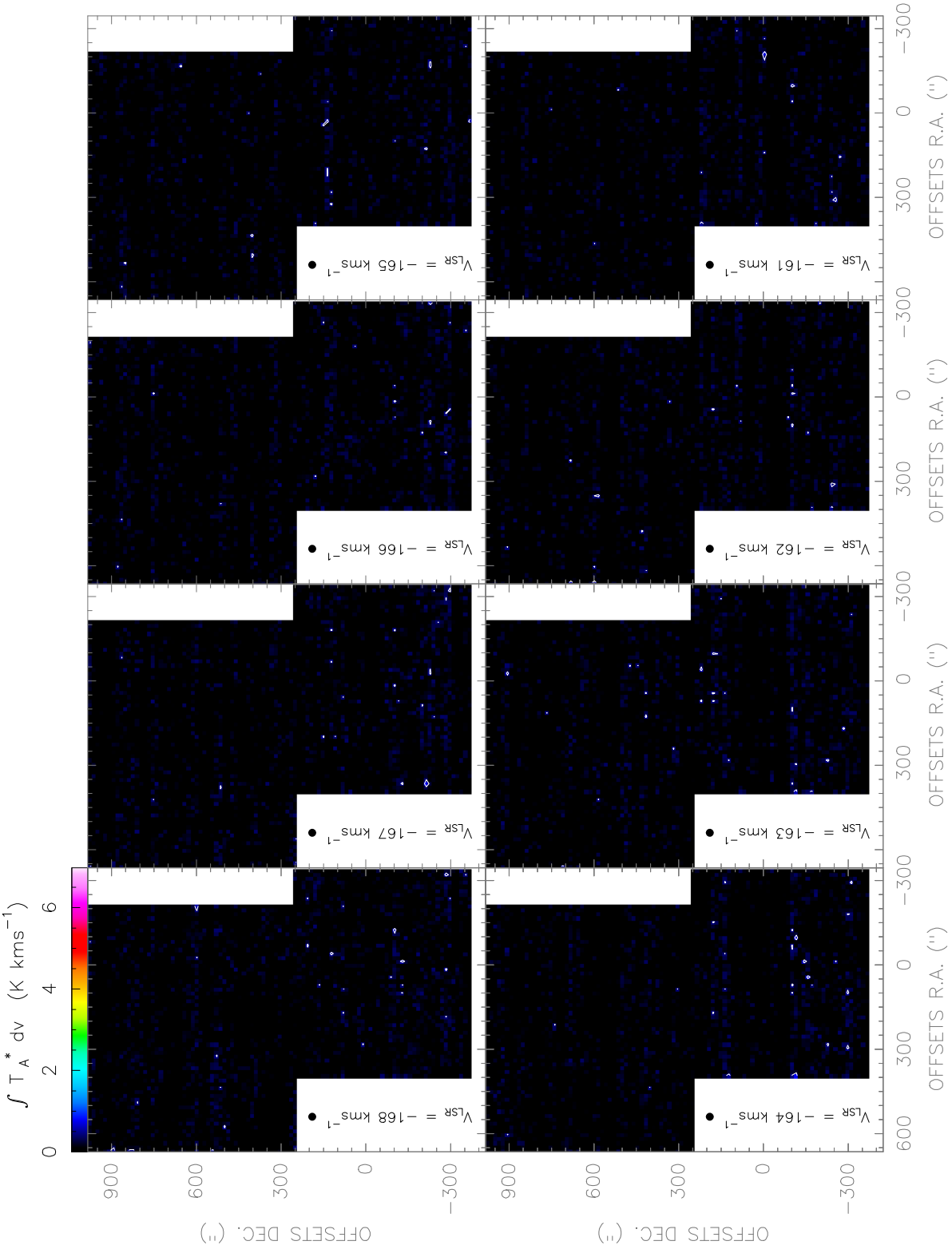

Figure. F.107: *[CI](2-1) line observed with the Herschel-HIFI satellite in Equatorial (J2000) coordinates. The spatial resolution of the maps is 28".*

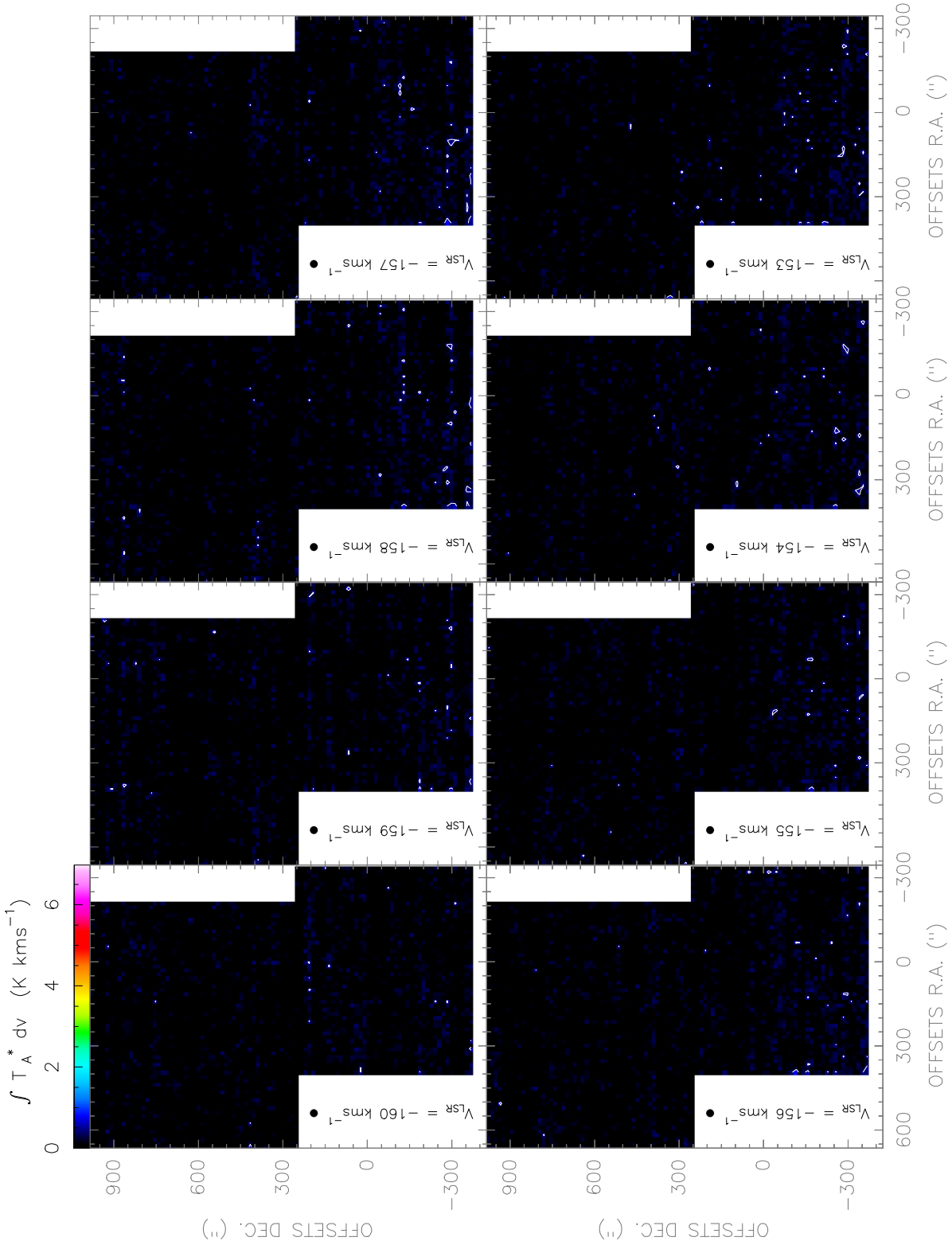

Figure. F.108: *[CI](2-1) line observed with the Herschel-HIFI satellite in Equatorial (J2000) coordinates. The spatial resolution of the maps is 28".*

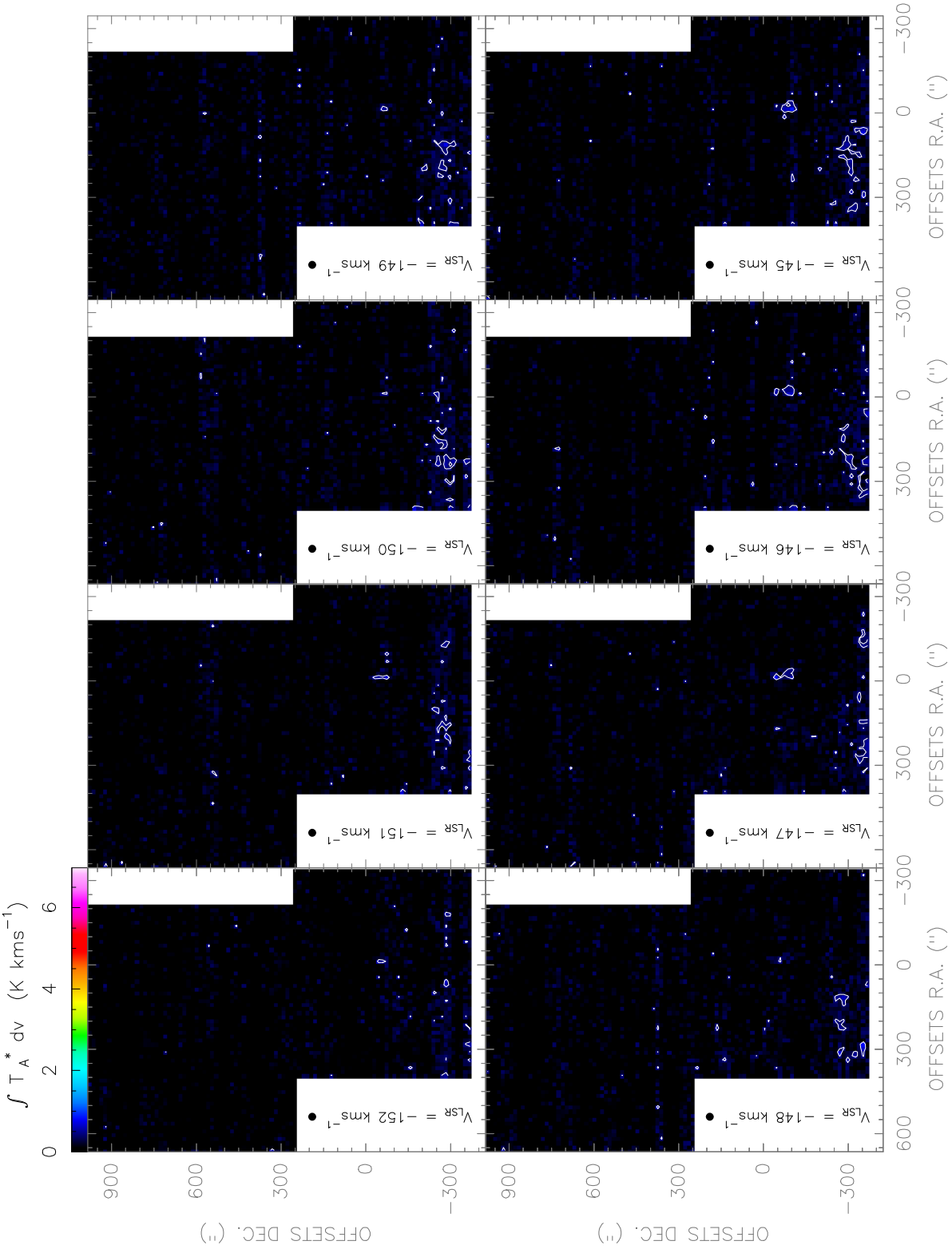

Figure. F.109: *[CI](2-1) line observed with the Herschel-HIFI satellite in Equatorial (J2000) coordinates. The spatial resolution of the maps is 28".*

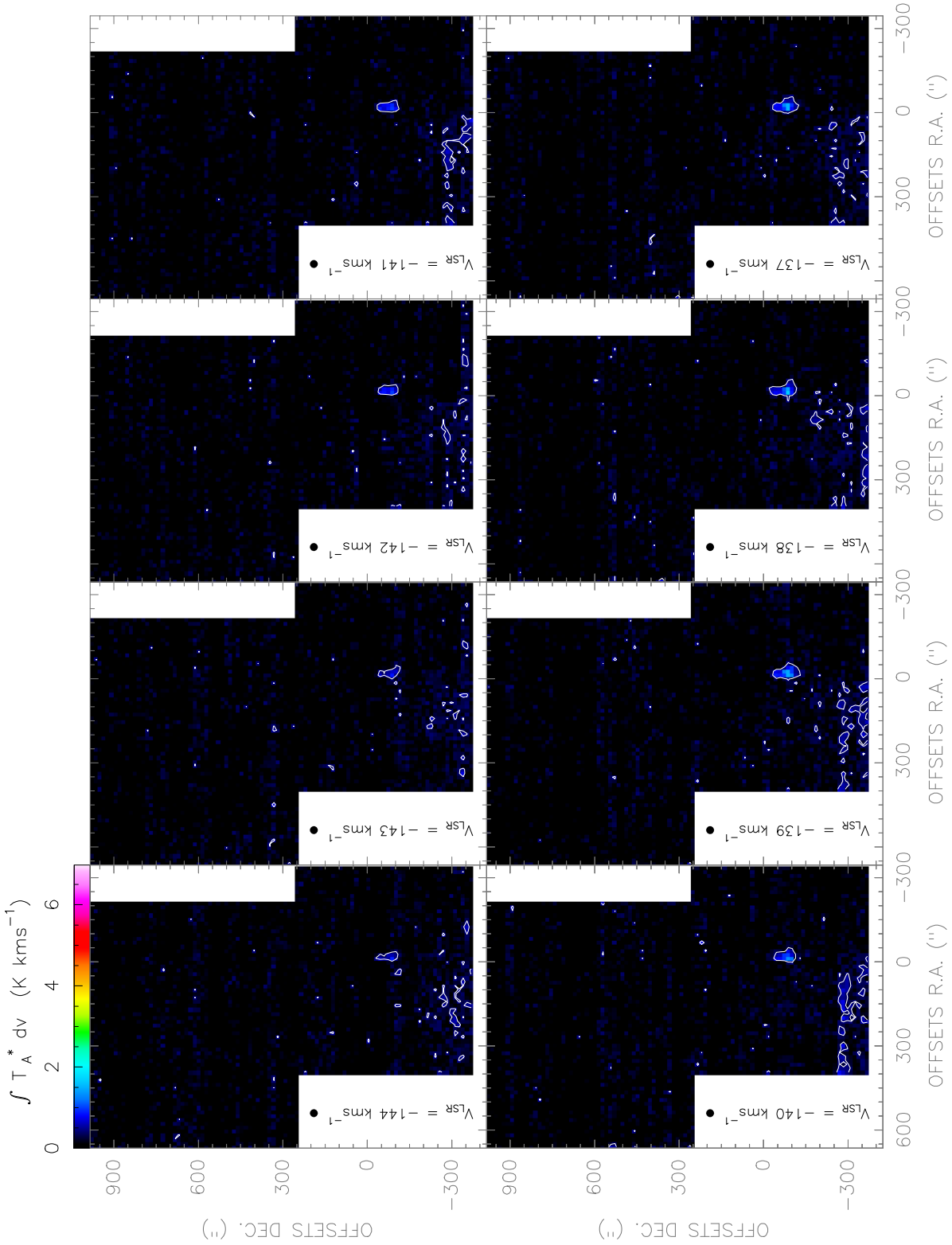

Figure. F.110: *[CI](2-1) line observed with the Herschel-HIFI satellite in Equatorial (J2000) coordinates. The spatial resolution of the maps is 28".*

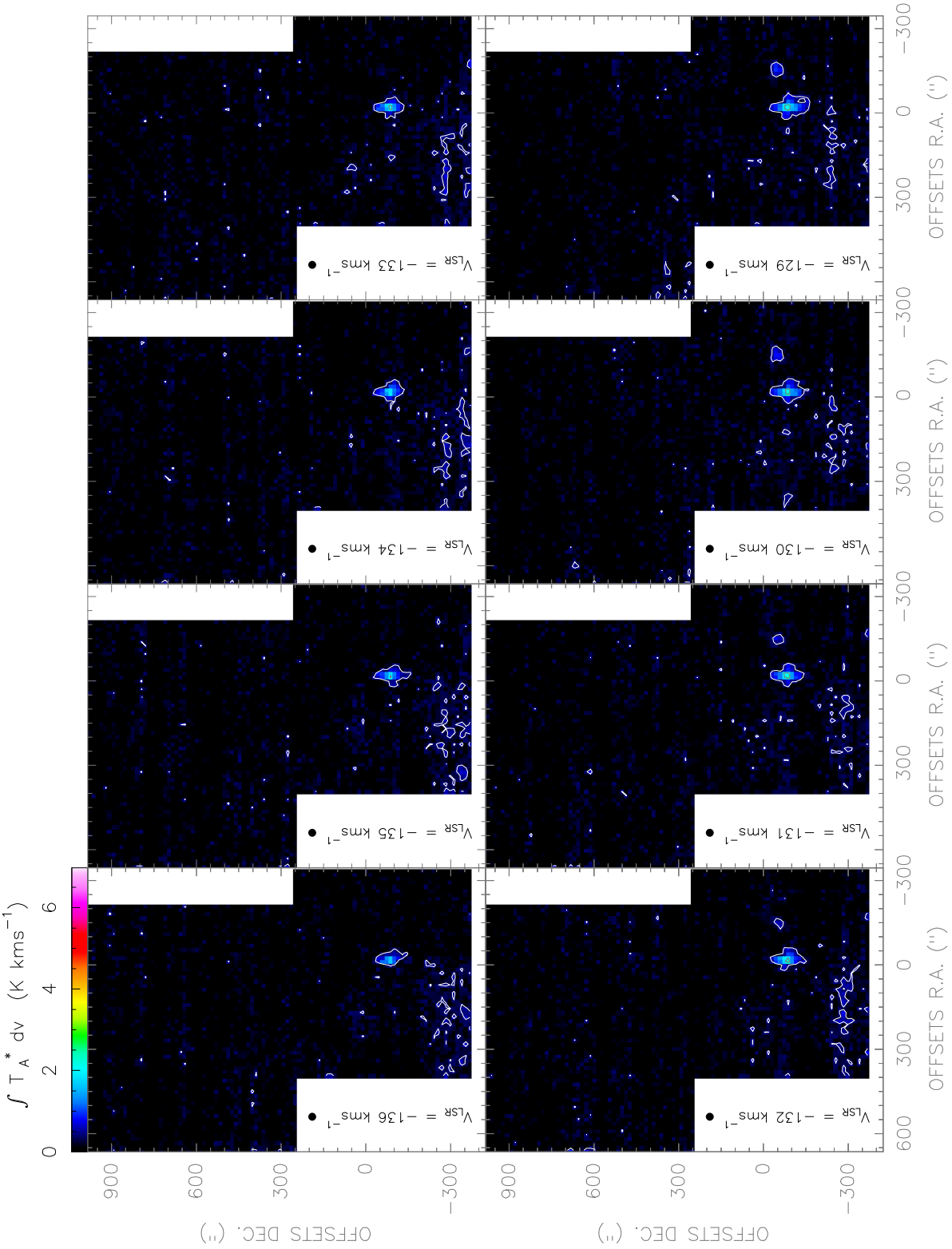

Figure. F.111: *[CI](2-1) line observed with the Herschel-HIFI satellite in Equatorial (J2000) coordinates. The spatial resolution of the maps is 28".*

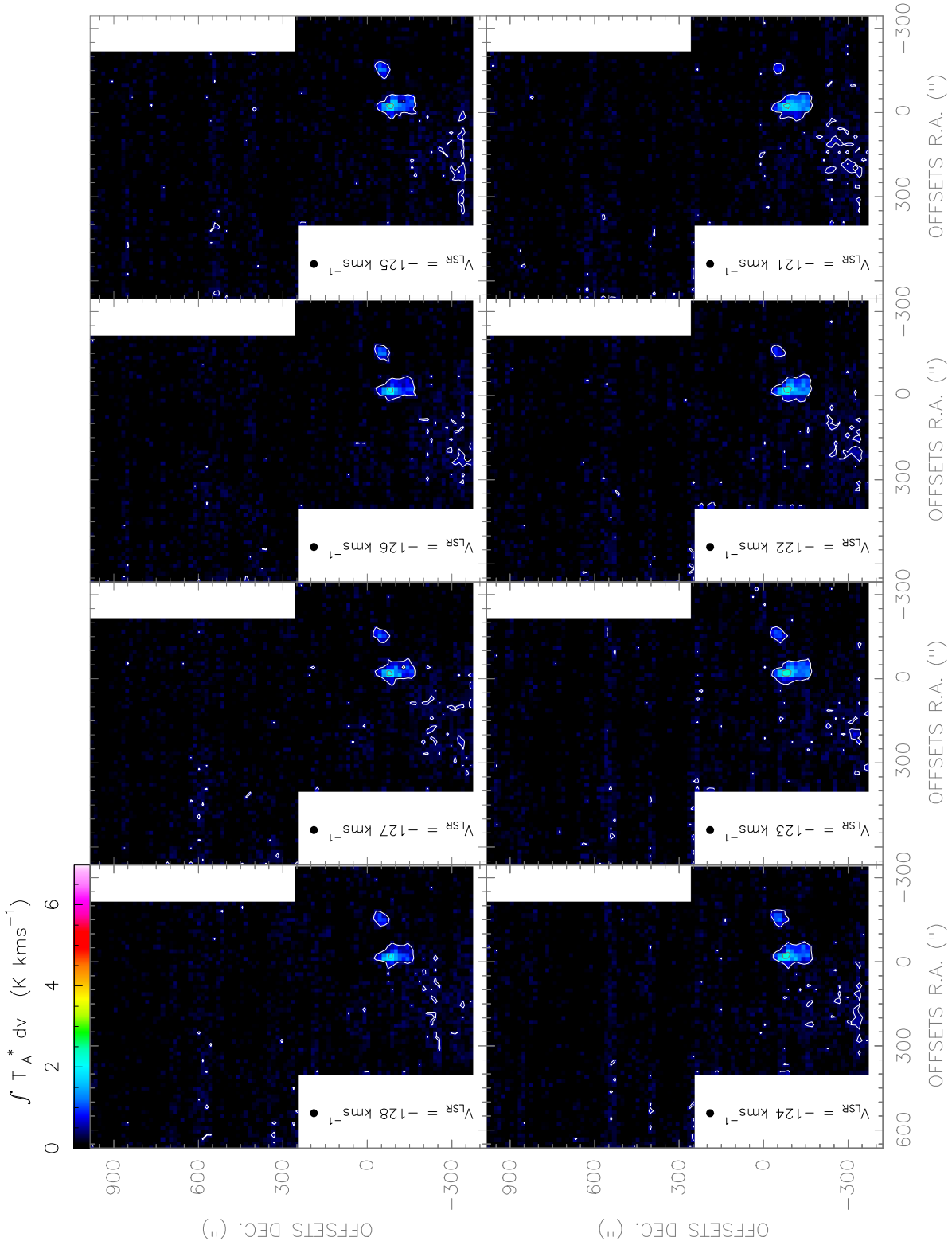

Figure. F.112: *[CI](2-1) line observed with the Herschel-HIFI satellite in Equatorial (J2000) coordinates. The spatial resolution of the maps is 28".*

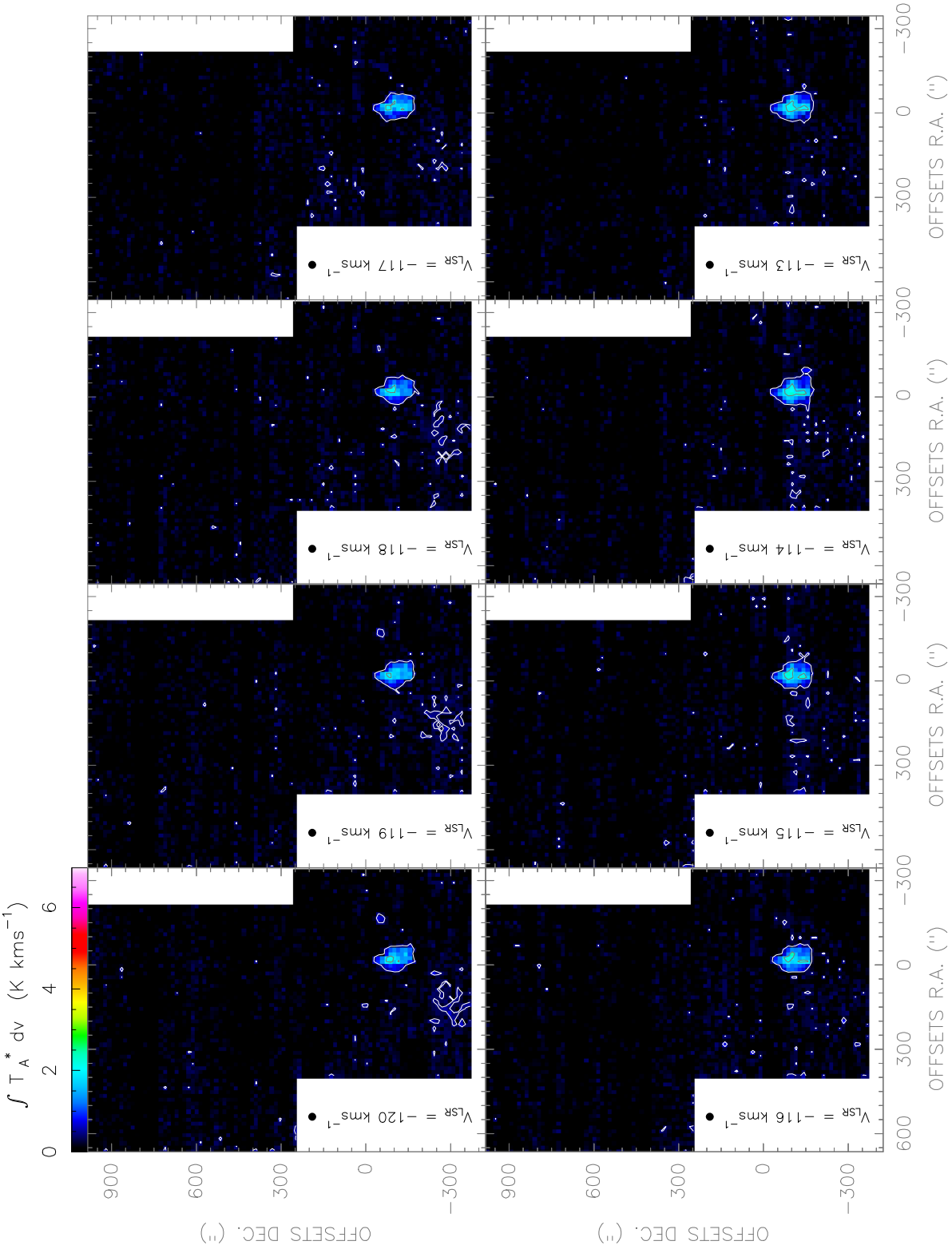

Figure. F.113: *[CI](2-1) line observed with the Herschel-HIFI satellite in Equatorial (J2000) coordinates. The spatial resolution of the maps is 28".*

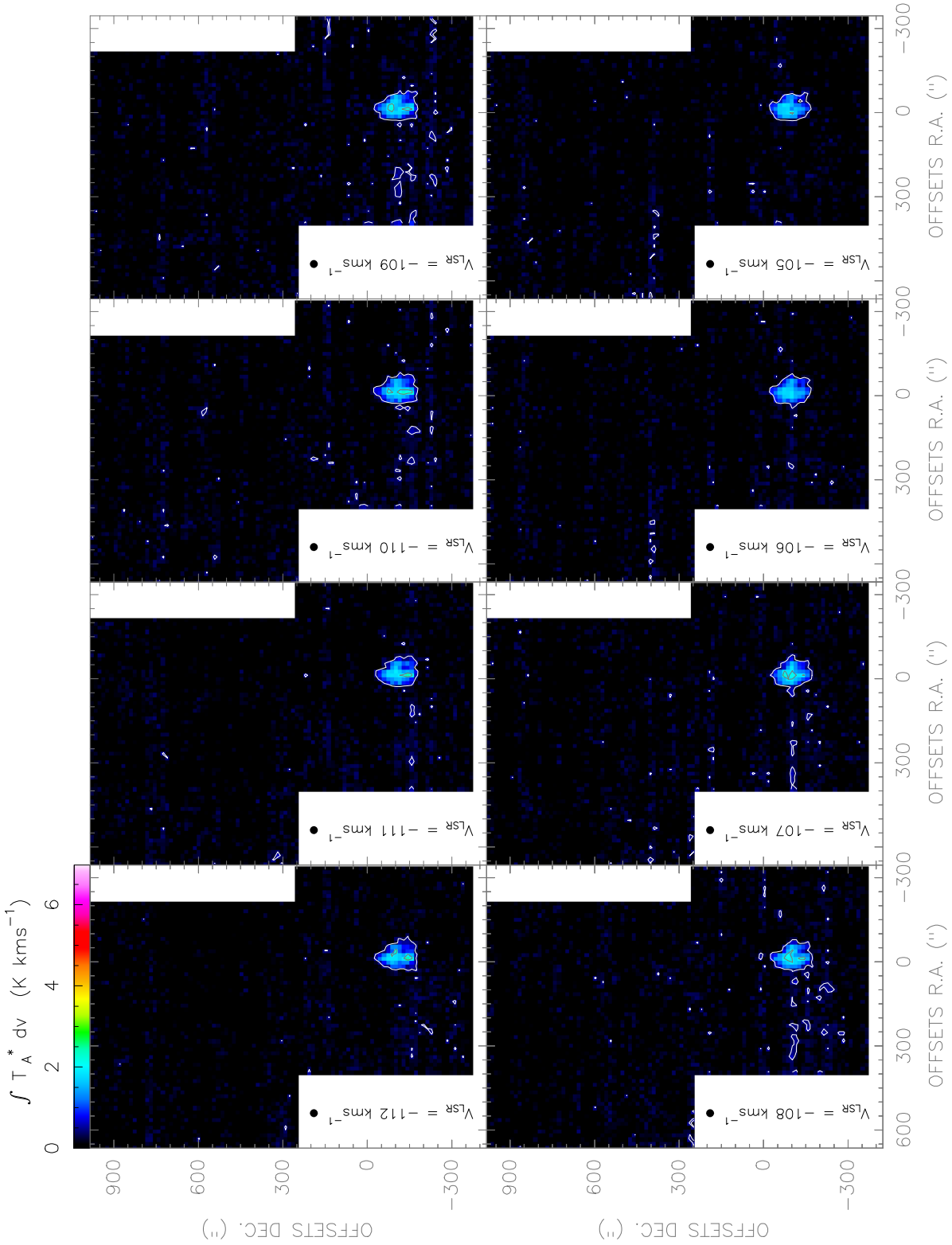

Figure. F.114: *[CI](2-1) line observed with the Herschel-HIFI satellite in Equatorial (J2000) coordinates. The spatial resolution of the maps is 28".*

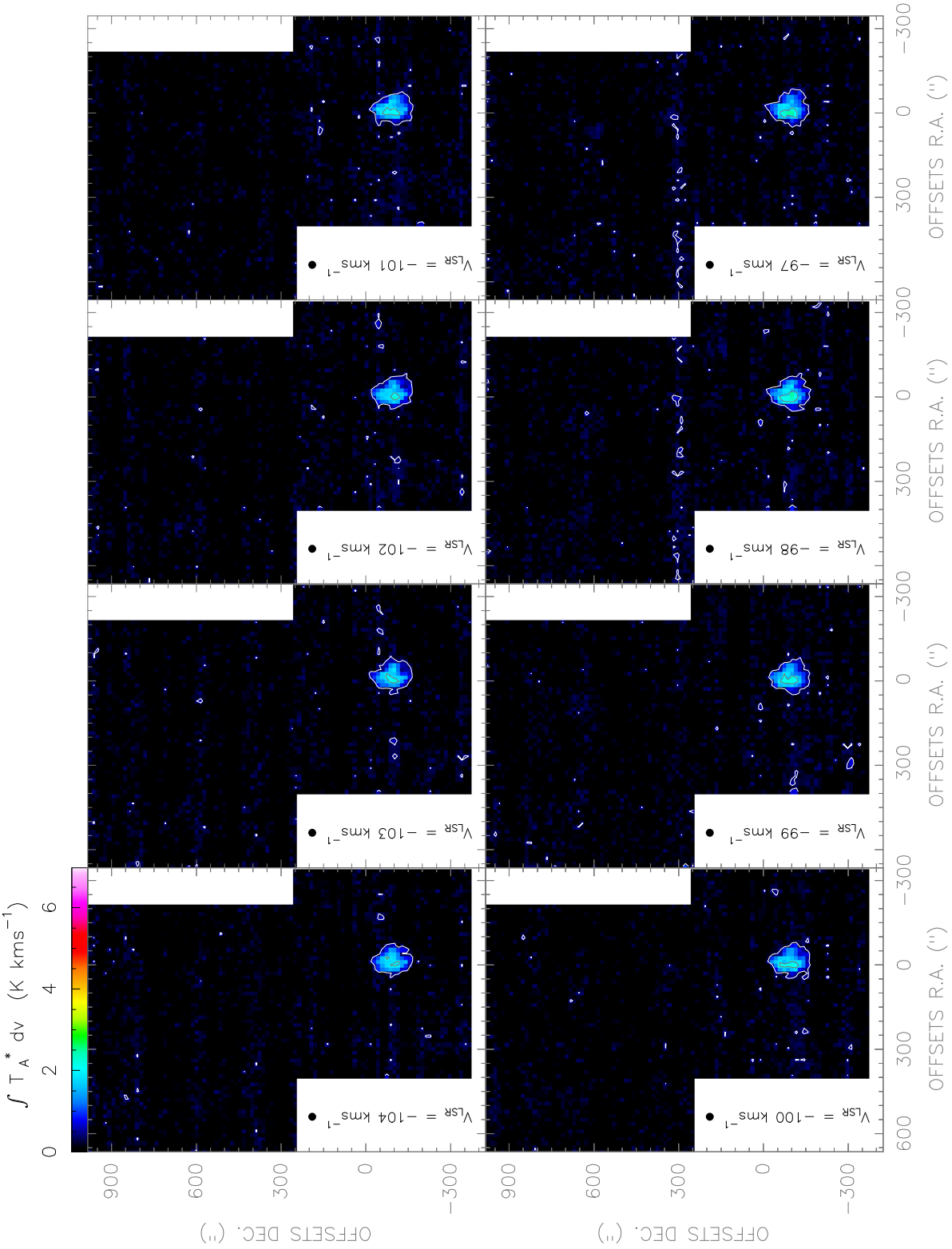

Figure. F.115: *[CI](2-1) line observed with the Herschel-HIFI satellite in Equatorial (J2000) coordinates. The spatial resolution of the maps is 28".*

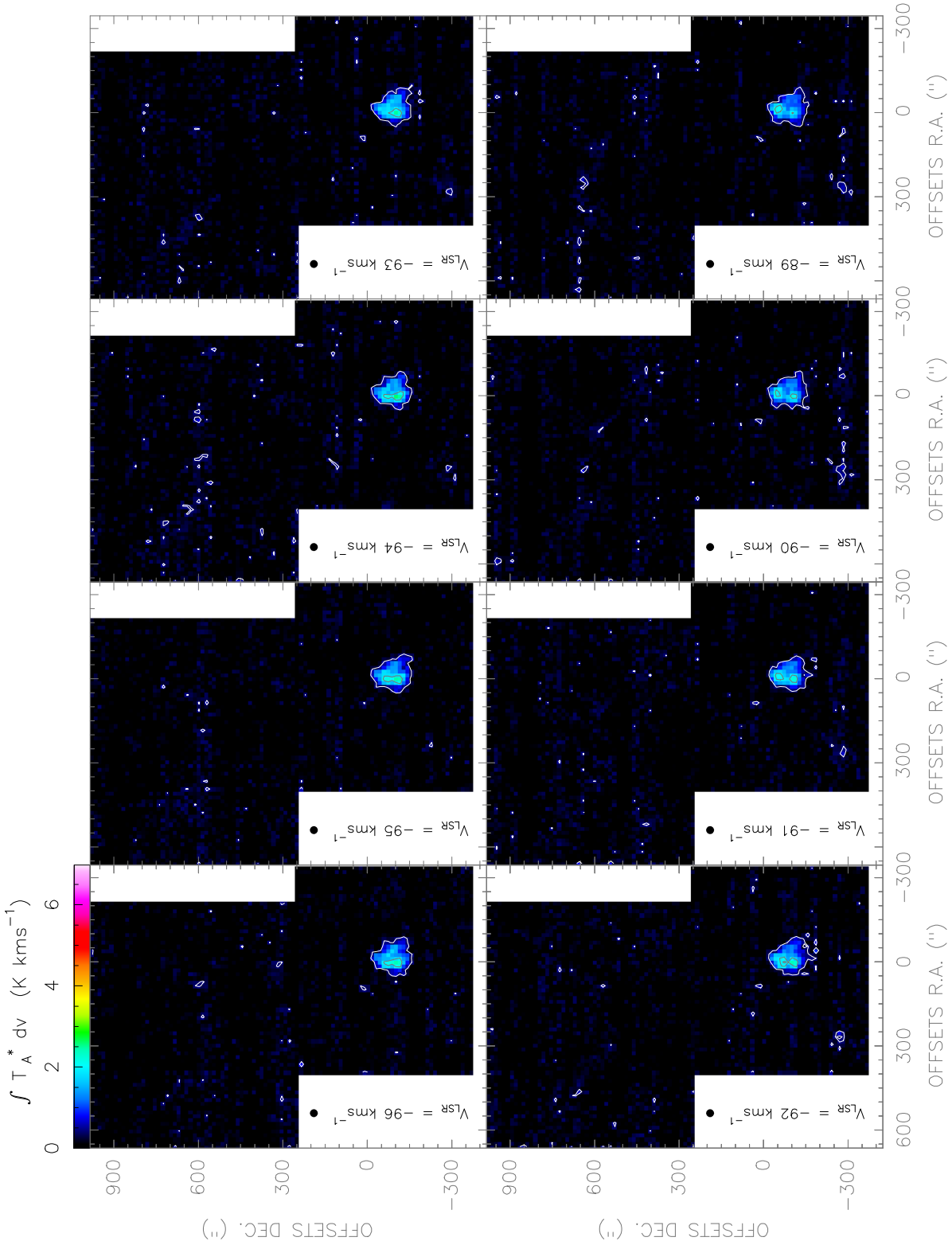

Figure. F.116: *[CI](2-1) line observed with the Herschel-HIFI satellite in Equatorial (J2000) coordinates. The spatial resolution of the maps is 28".*

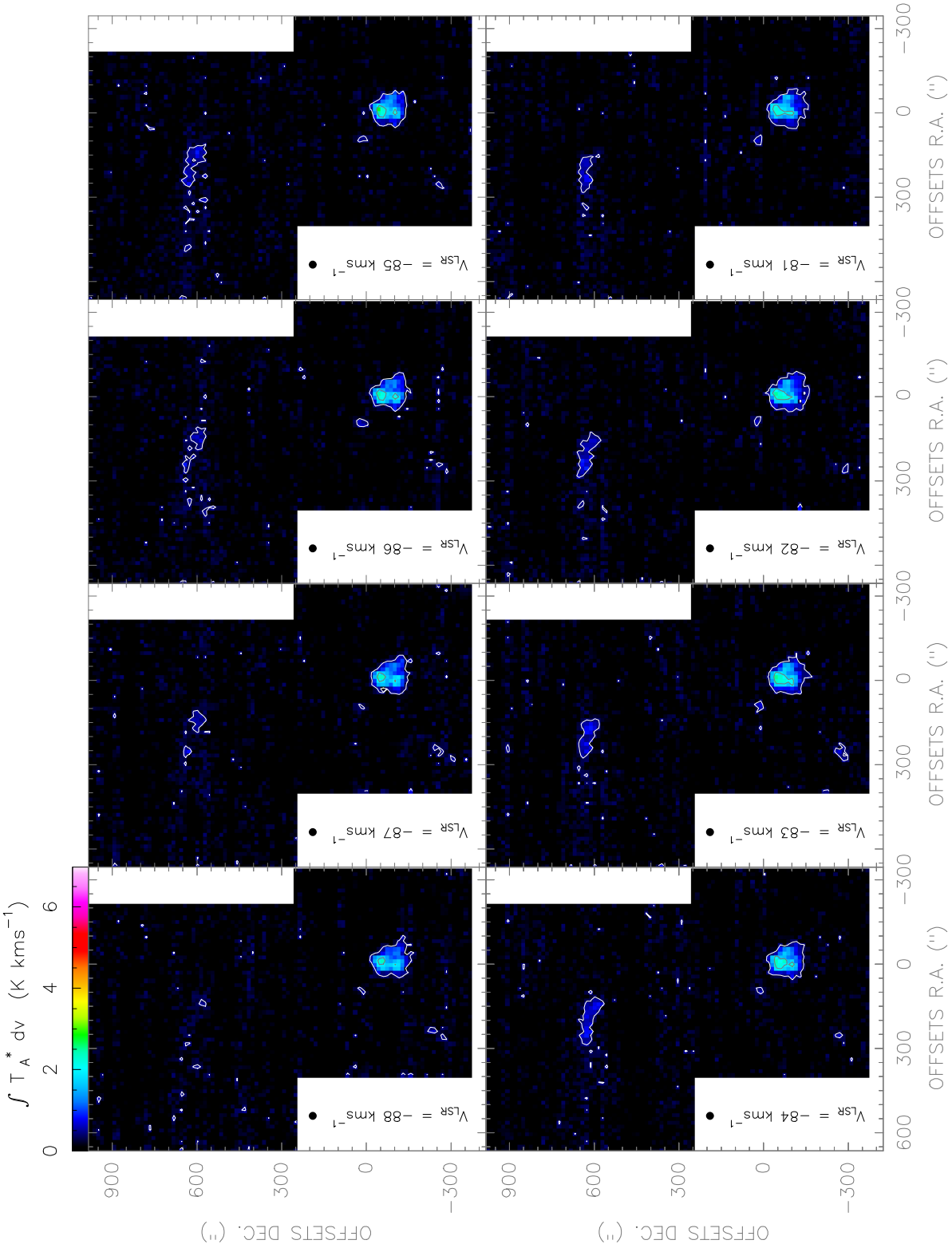

Figure. F.117: *[CI](2-1) line observed with the Herschel-HIFI satellite in Equatorial (J2000) coordinates. The spatial resolution of the maps is 28".*

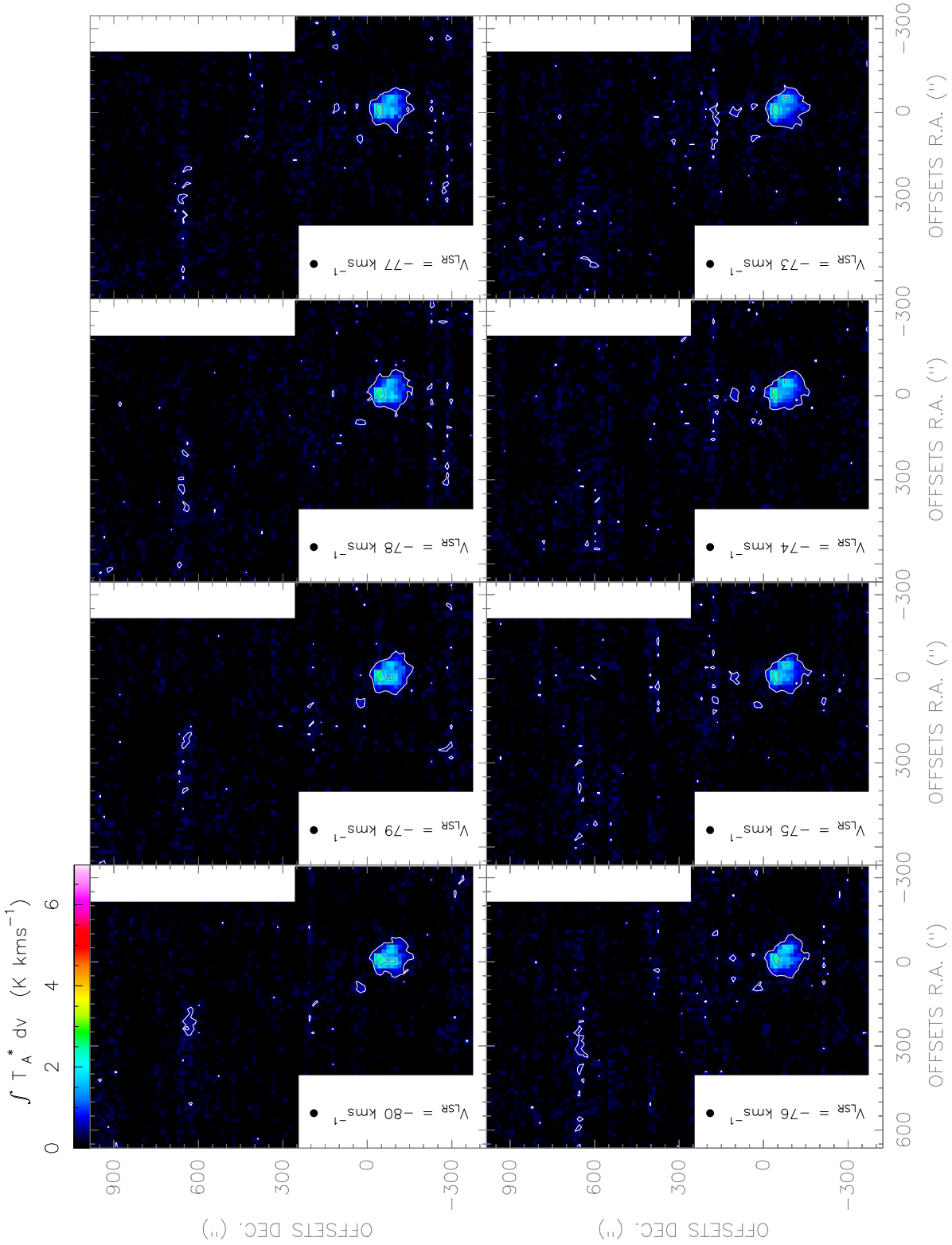

Figure. F.118: *[CI](2-1) line observed with the Herschel-HIFI satellite in Equatorial (J2000) coordinates. The spatial resolution of the maps is 28".*

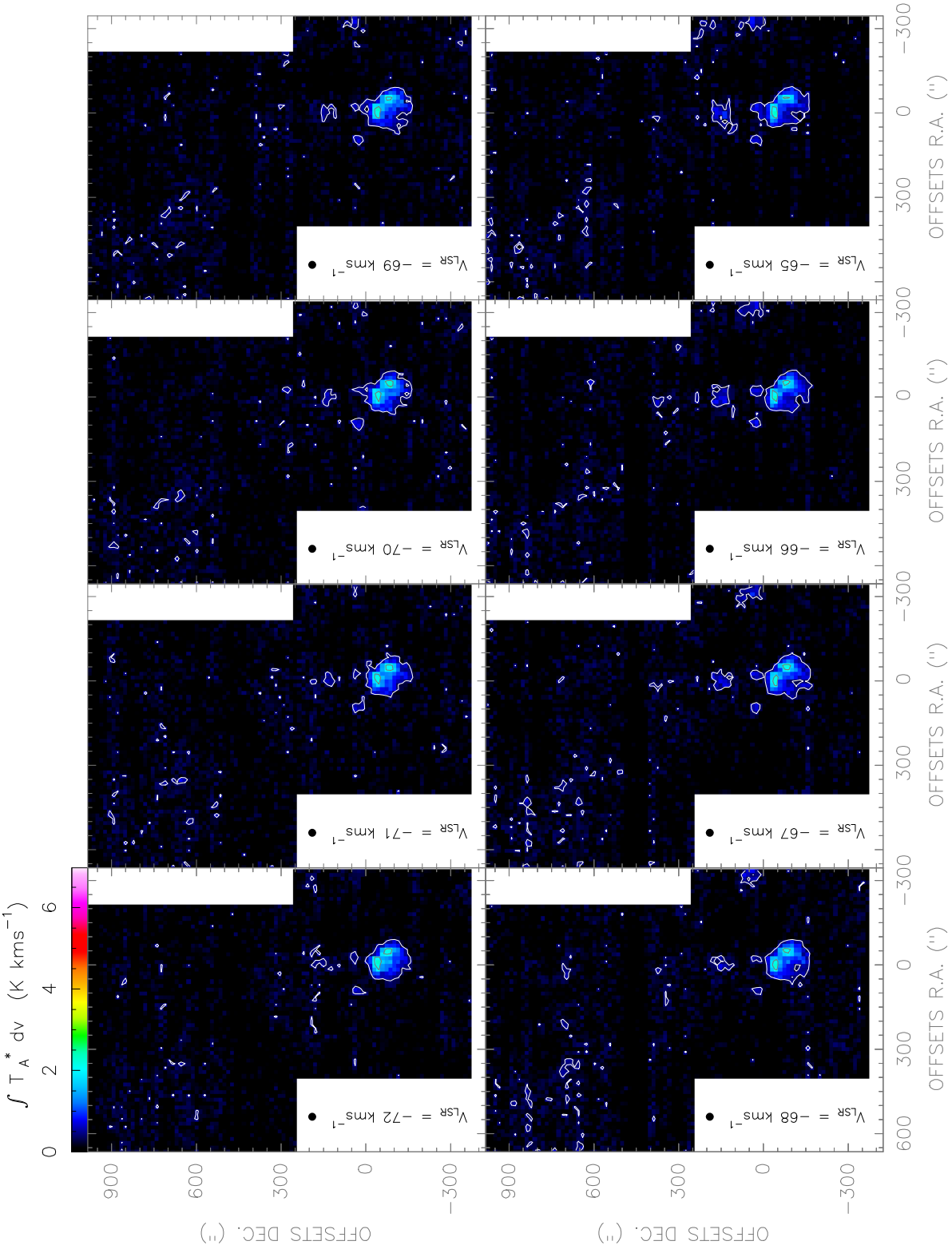

Figure. F.119: *[CI](2-1) line observed with the Herschel-HIFI satellite in Equatorial (J2000) coordinates. The spatial resolution of the maps is 28".*

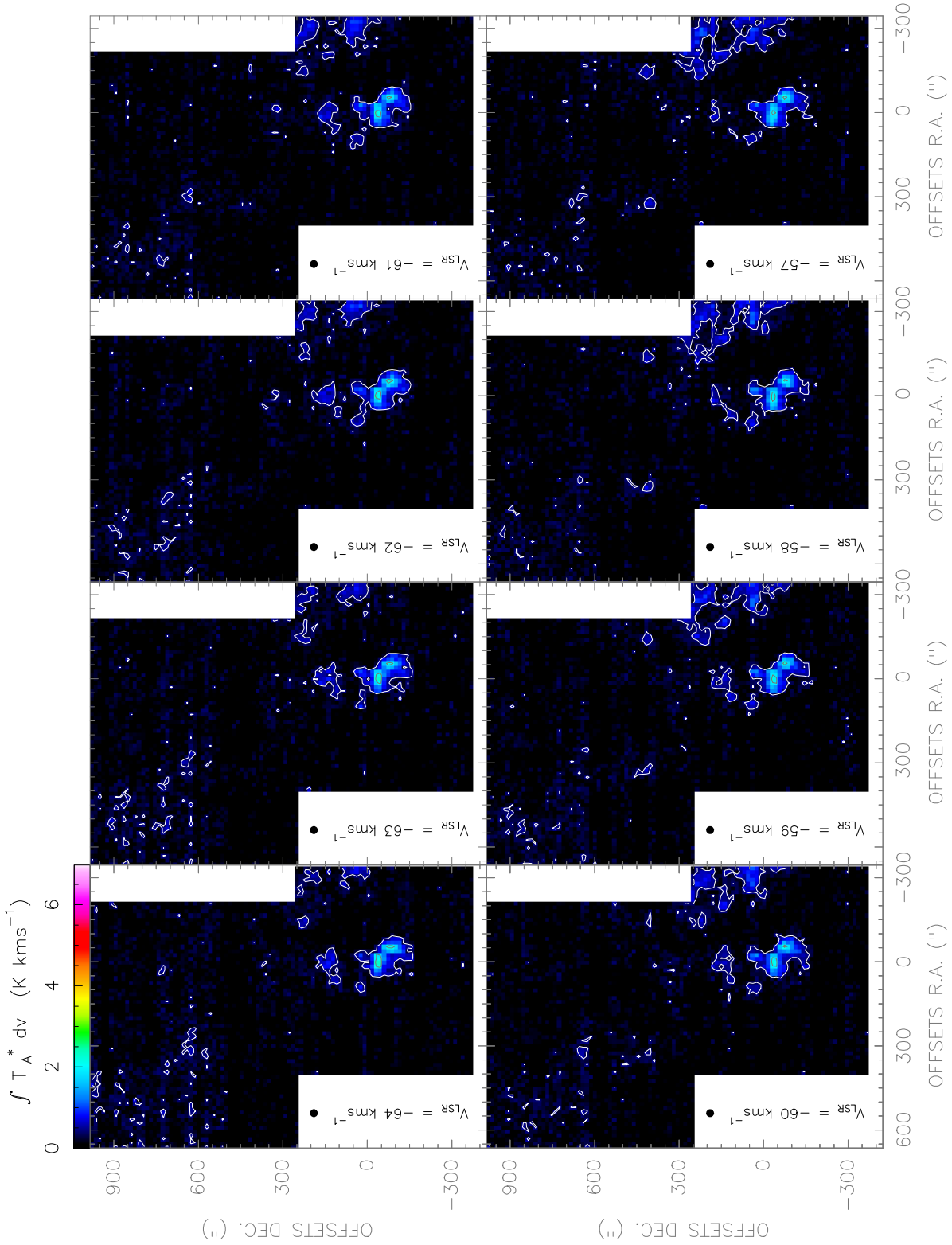

Figure. F.120: *[CI](2-1) line observed with the Herschel-HIFI satellite in Equatorial (J2000) coordinates. The spatial resolution of the maps is 28".*

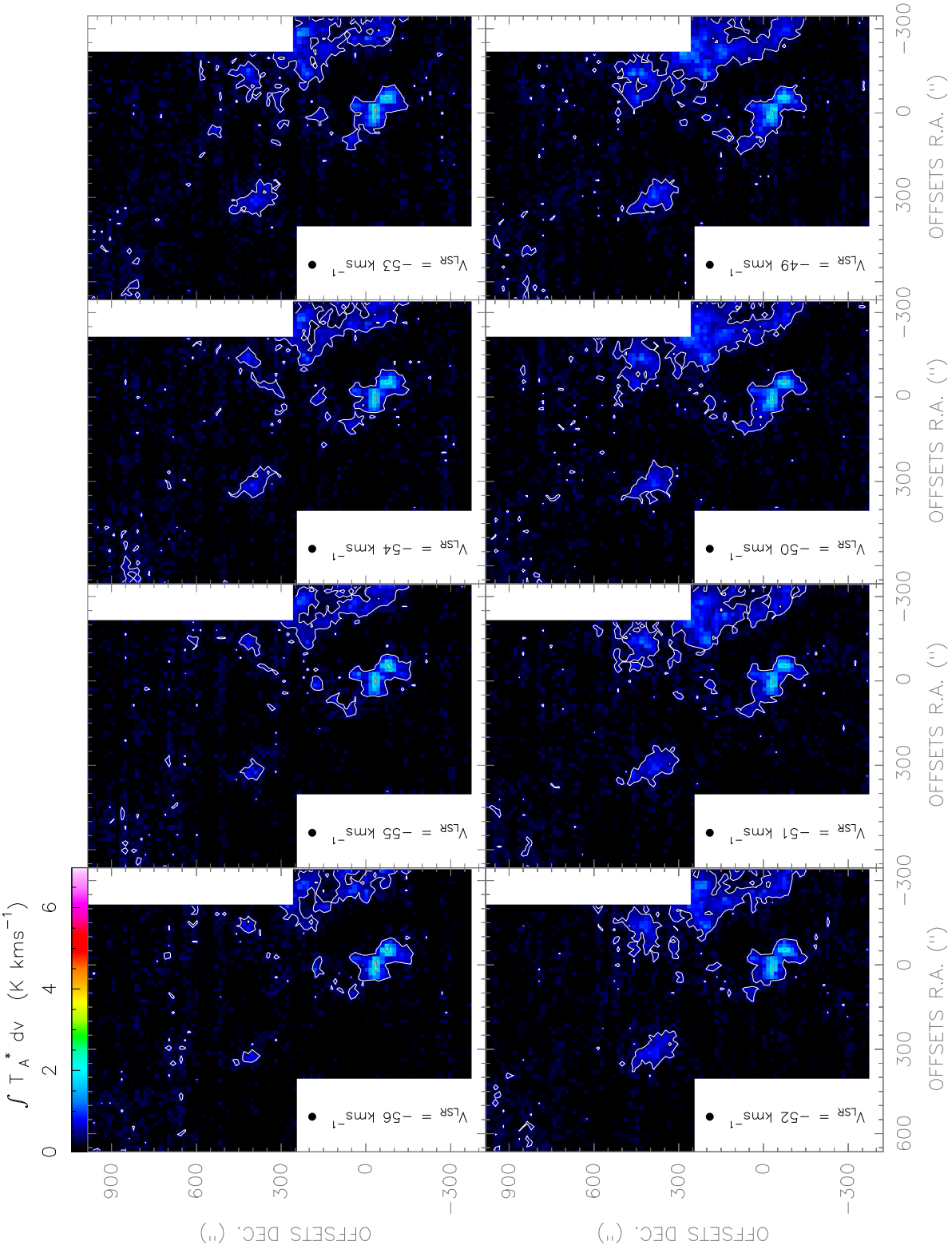

Figure. F.121: *[CI](2-1) line observed with the Herschel-HIFI satellite in Equatorial (J2000) coordinates. The spatial resolution of the maps is 28".*

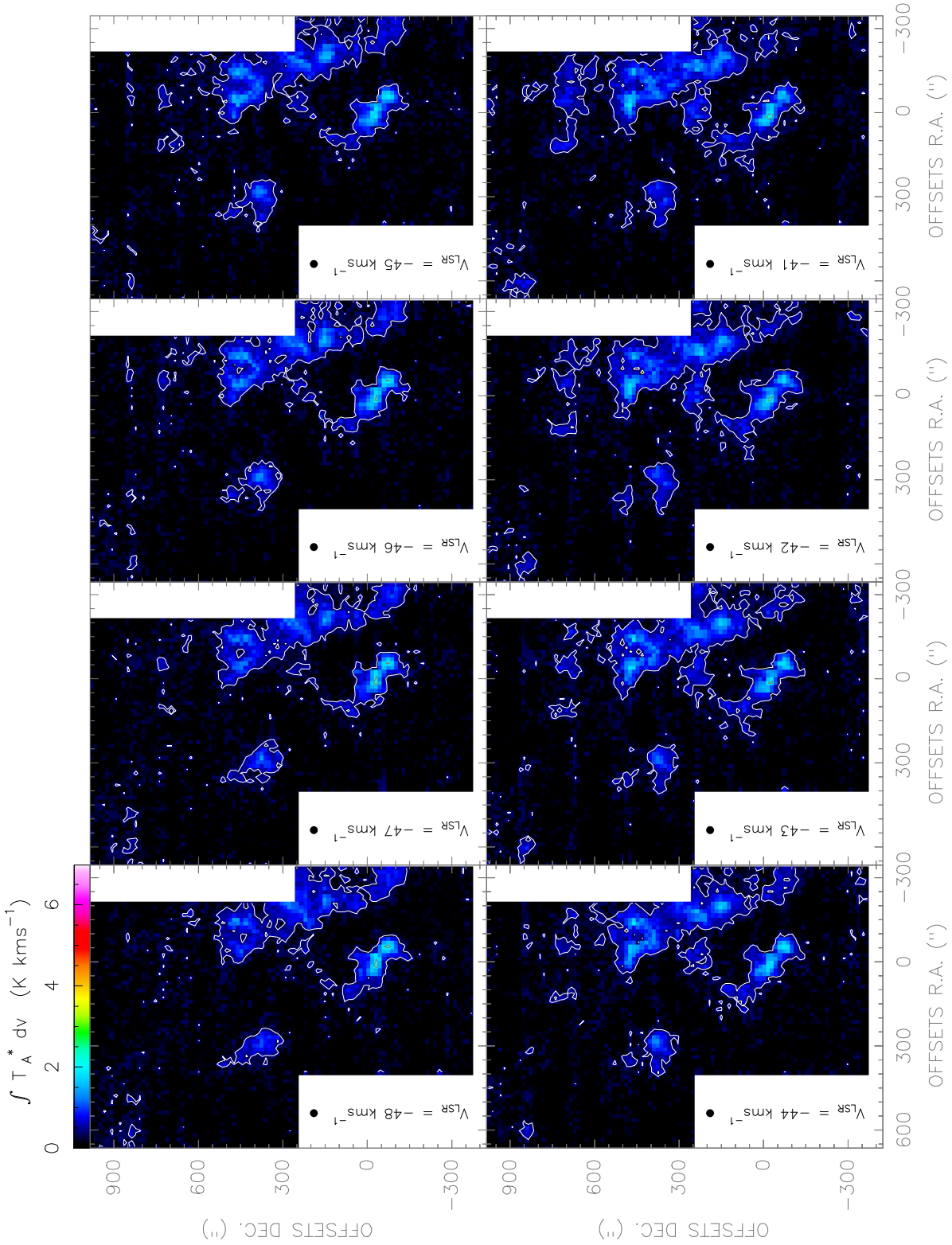

Figure. F.122: *[CI](2-1) line observed with the Herschel-HIFI satellite in Equatorial (J2000) coordinates. The spatial resolution of the maps is 28".*

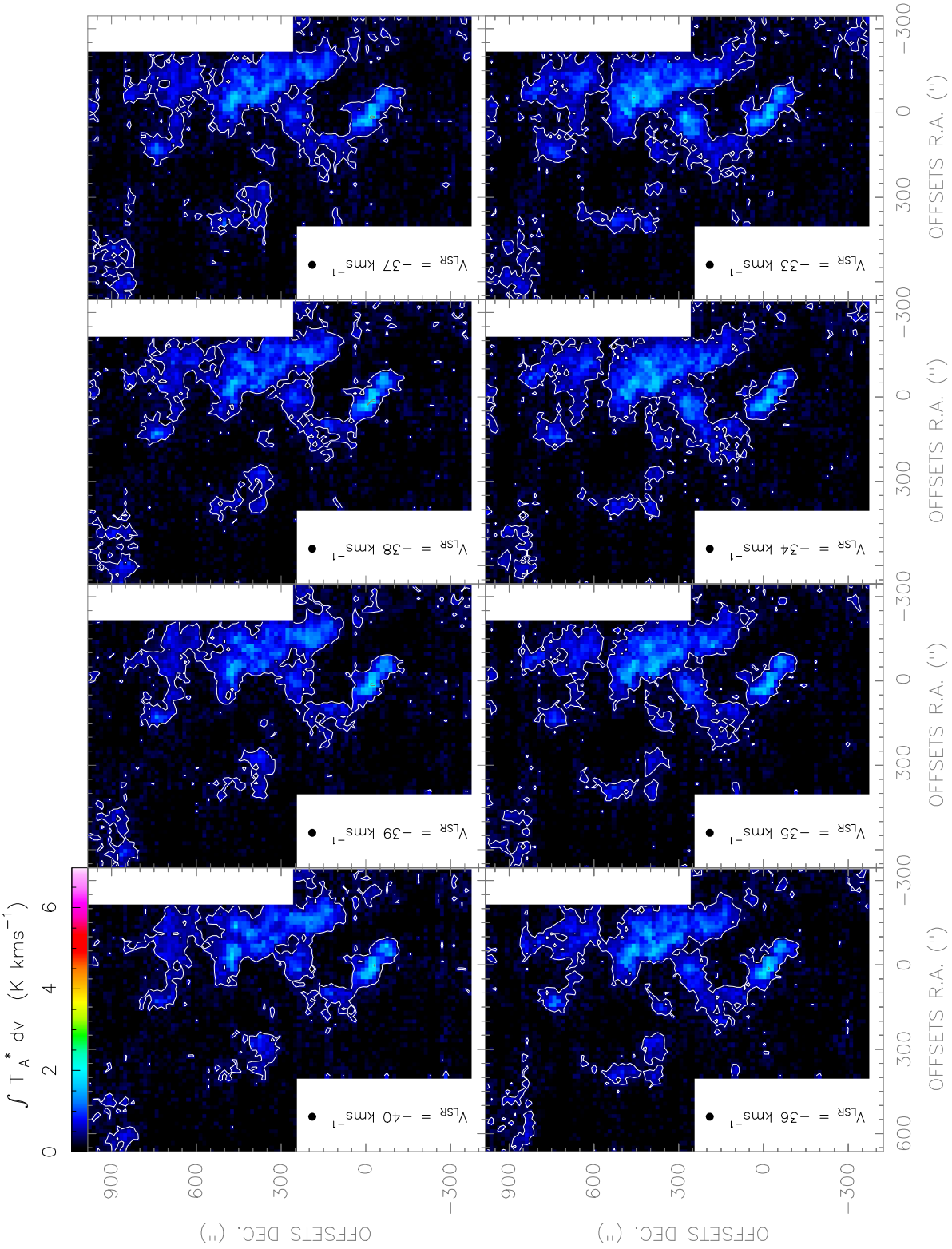

Figure. F.123: *[CI](2-1) line observed with the Herschel-HIFI satellite in Equatorial (J2000) coordinates. The spatial resolution of the maps is 28".*

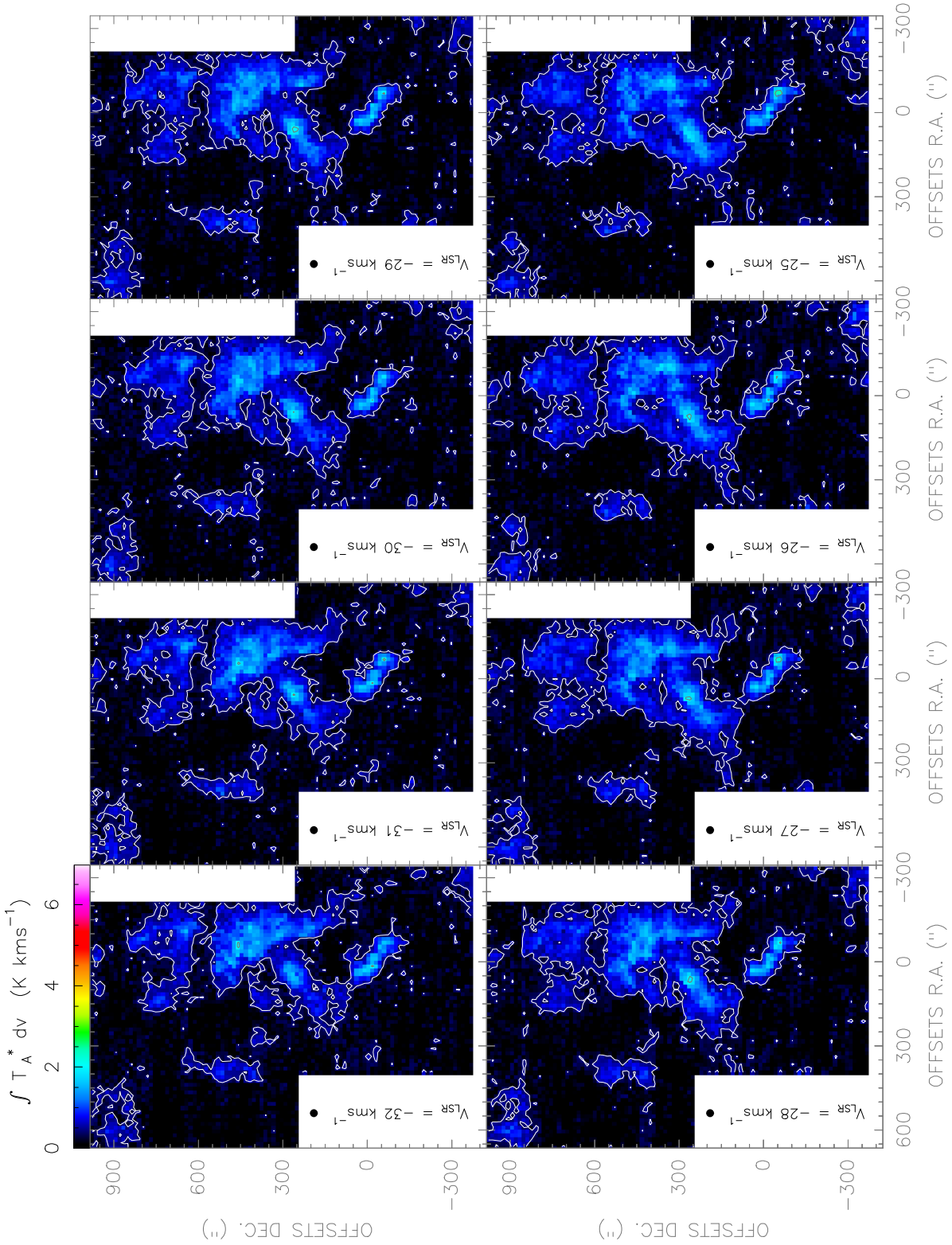

Figure. F.124: *[CI](2-1) line observed with the Herschel-HIFI satellite in Equatorial (J2000) coordinates. The spatial resolution of the maps is 28".*

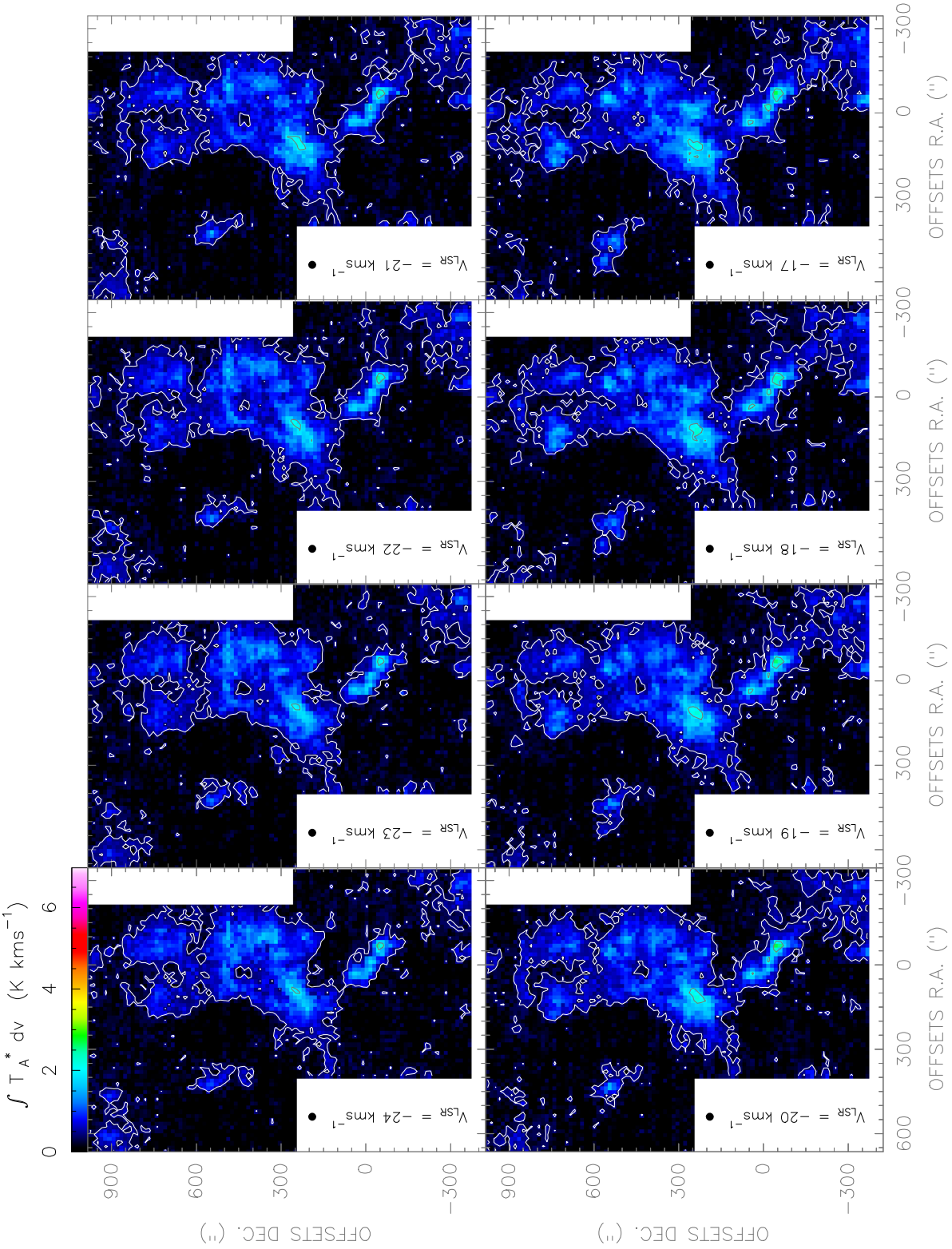

Figure. F.125: *[CI](2-1) line observed with the Herschel-HIFI satellite in Equatorial (J2000) coordinates. The spatial resolution of the maps is 28".*

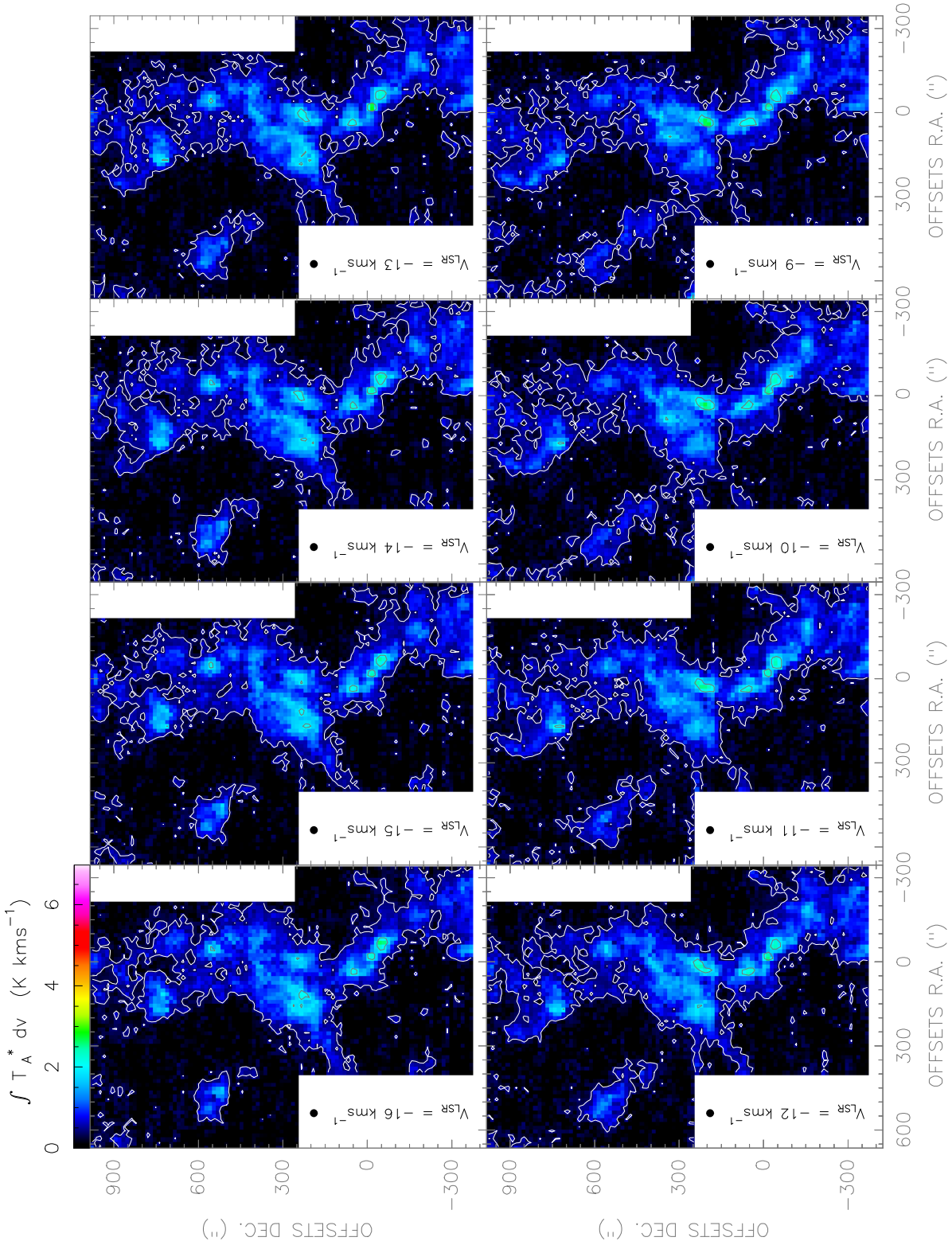

Figure. F.126: *[CI](2-1) line observed with the Herschel-HIFI satellite in Equatorial (J2000) coordinates. The spatial resolution of the maps is 28".*

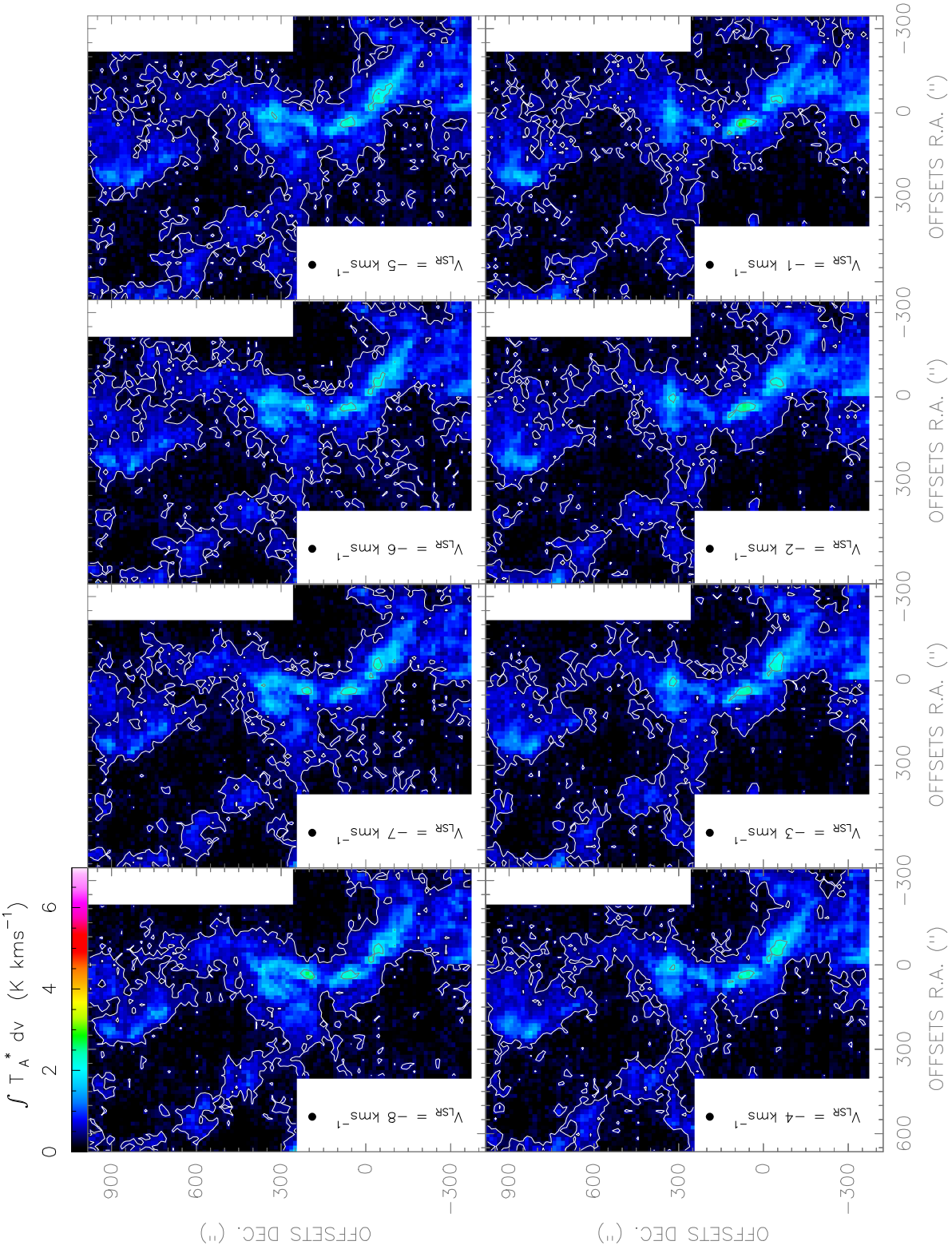

Figure. F.127: *[CI](2-1) line observed with the Herschel-HIFI satellite in Equatorial (J2000) coordinates. The spatial resolution of the maps is 28".*

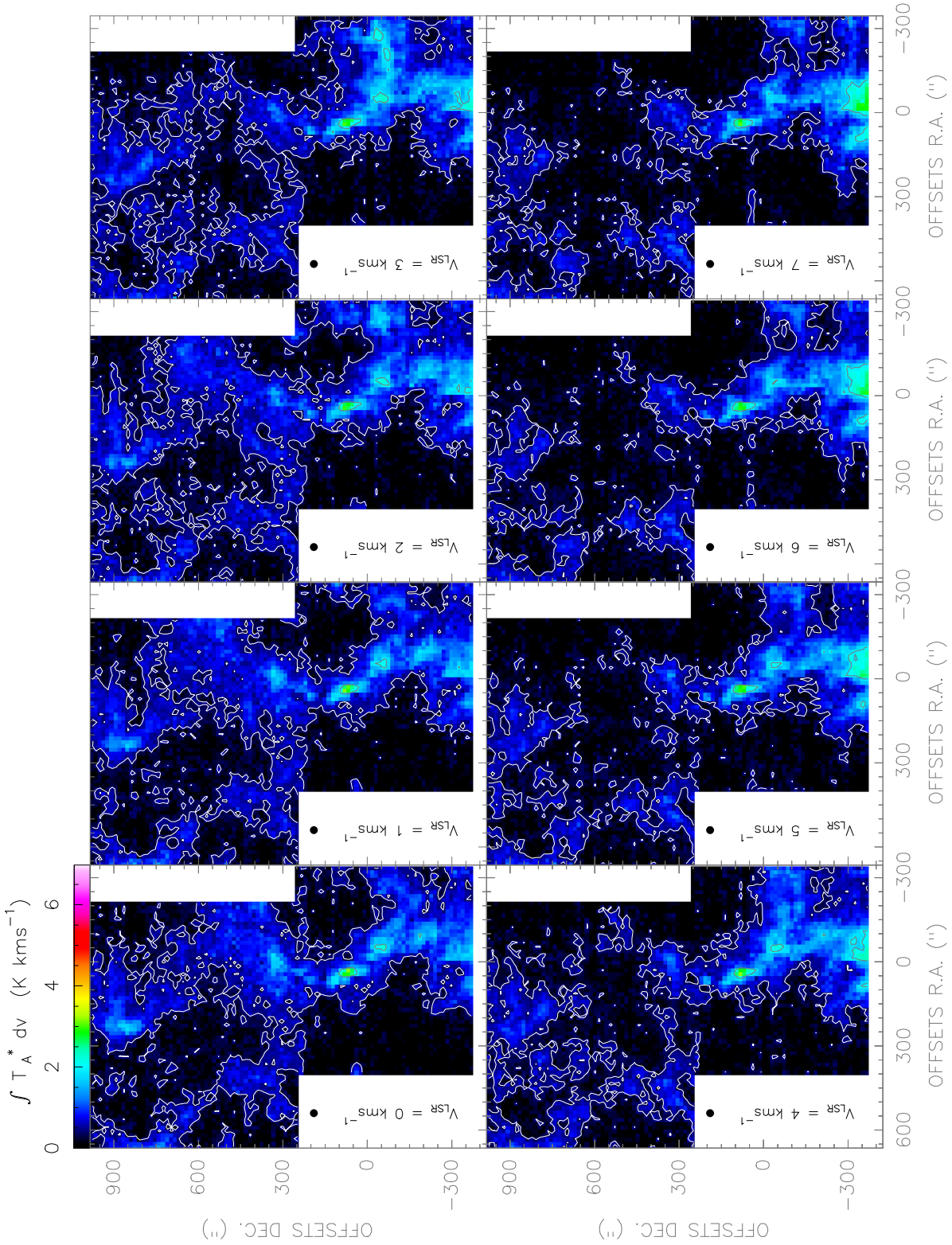

Figure. F.128: *[CI](2-1) line observed with the Herschel-HIFI satellite in Equatorial (J2000) coordinates. The spatial resolution of the maps is 28".*

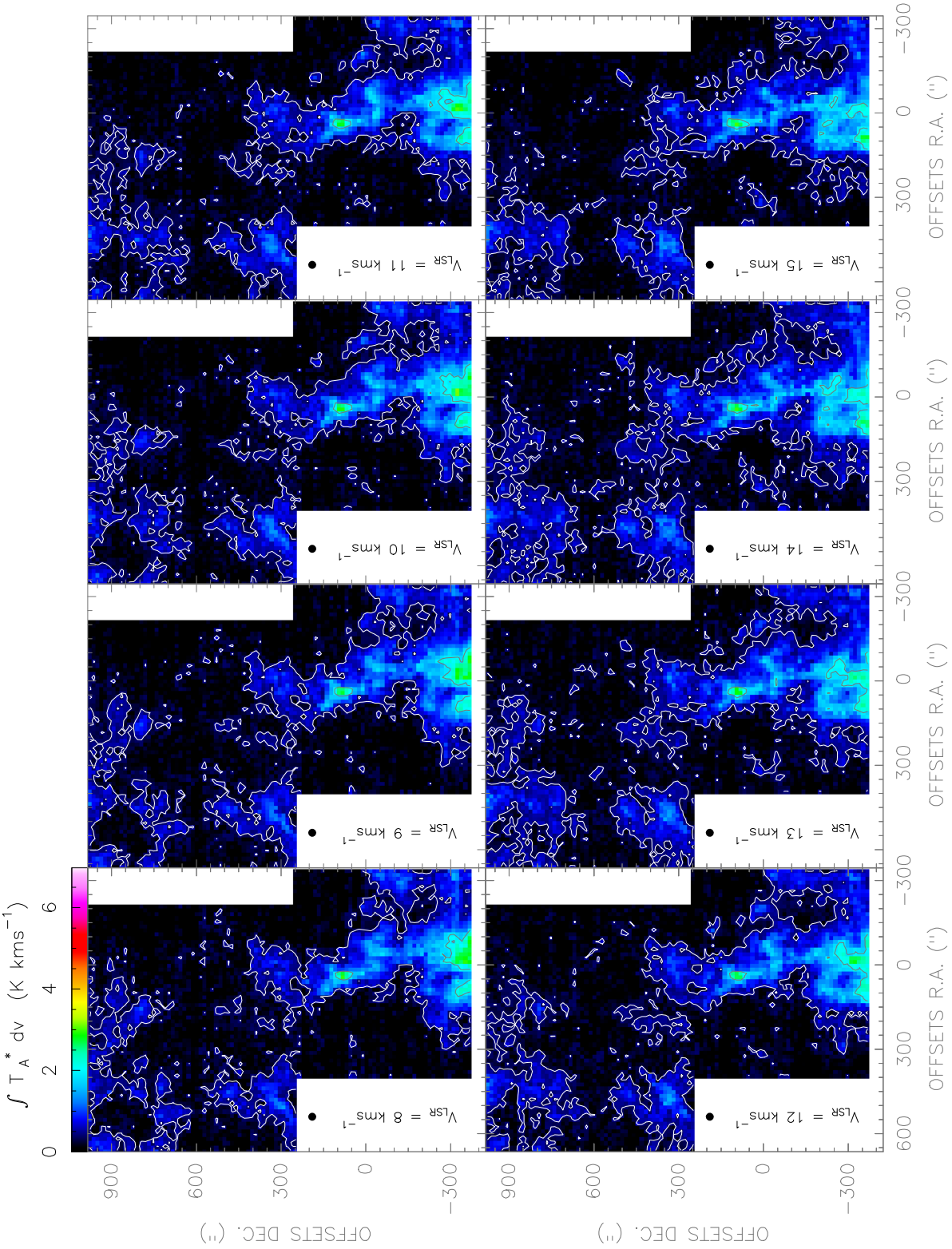

Figure. F.129: *[CI](2-1) line observed with the Herschel-HIFI satellite in Equatorial (J2000) coordinates. The spatial resolution of the maps is 28".*

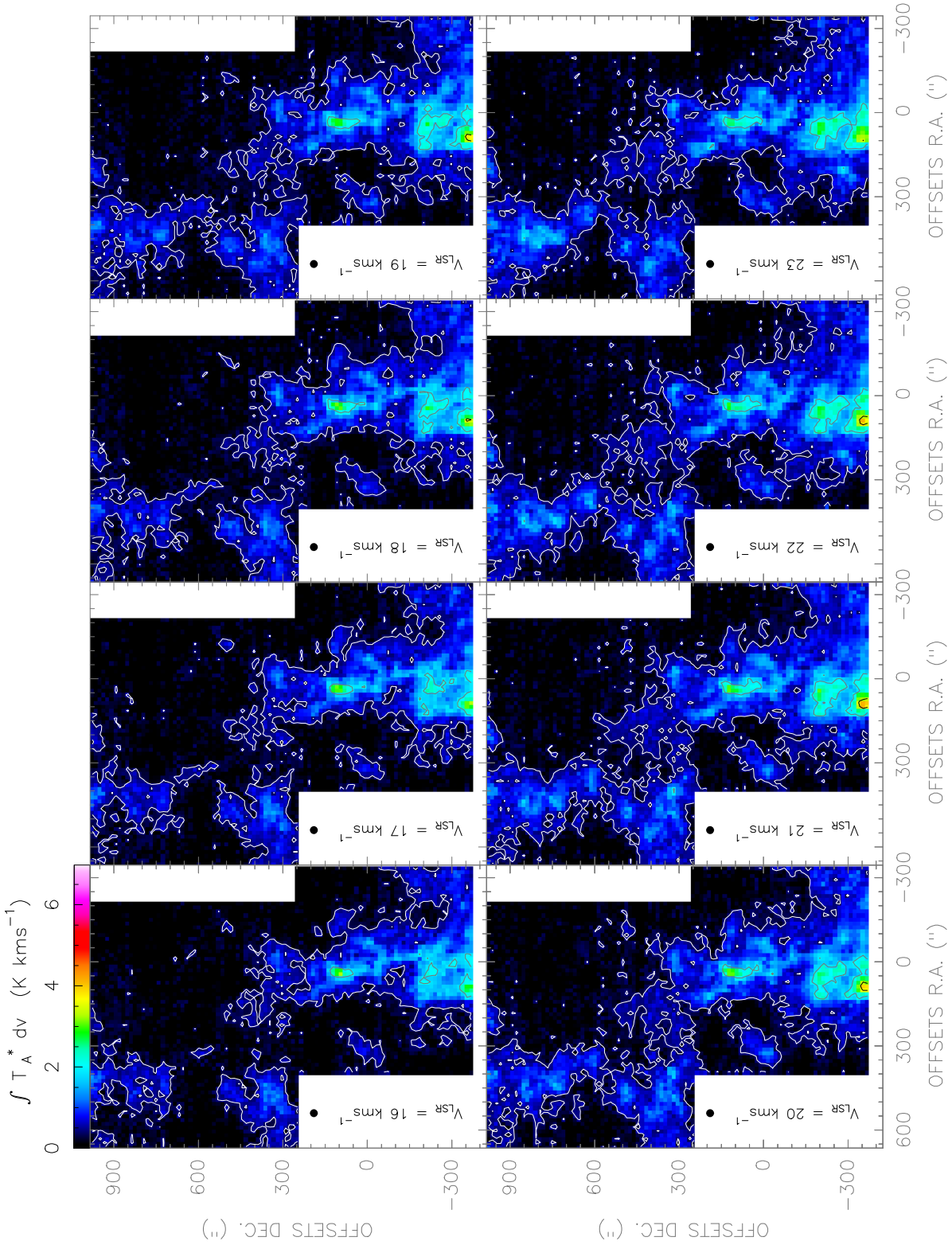

Figure. F.130: *[CI](2-1) line observed with the Herschel-HIFI satellite in Equatorial (J2000) coordinates. The spatial resolution of the maps is 28".*

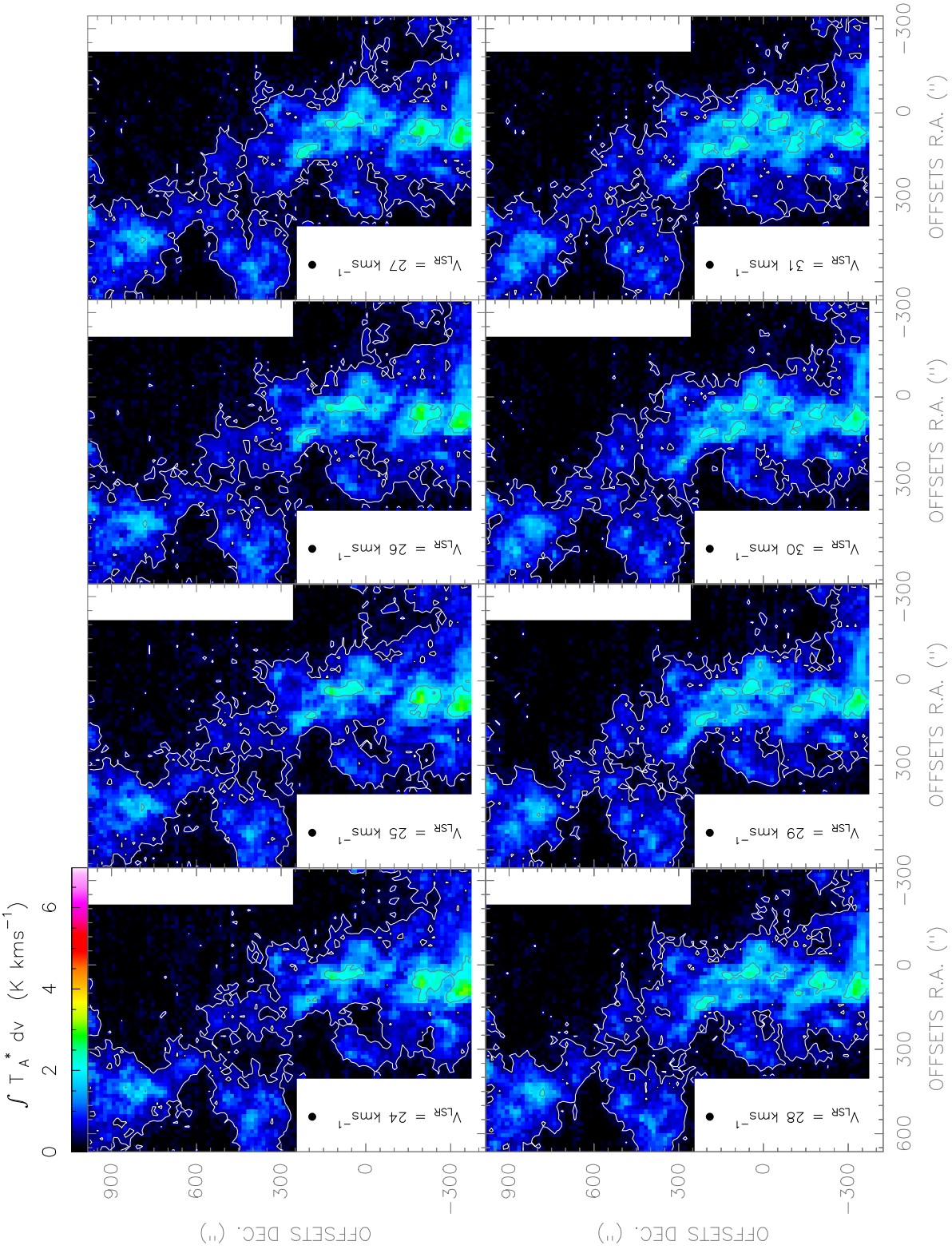

Figure. F.131: *[CI](2-1) line observed with the Herschel-HIFI satellite in Equatorial (J2000) coordinates. The spatial resolution of the maps is 28".*

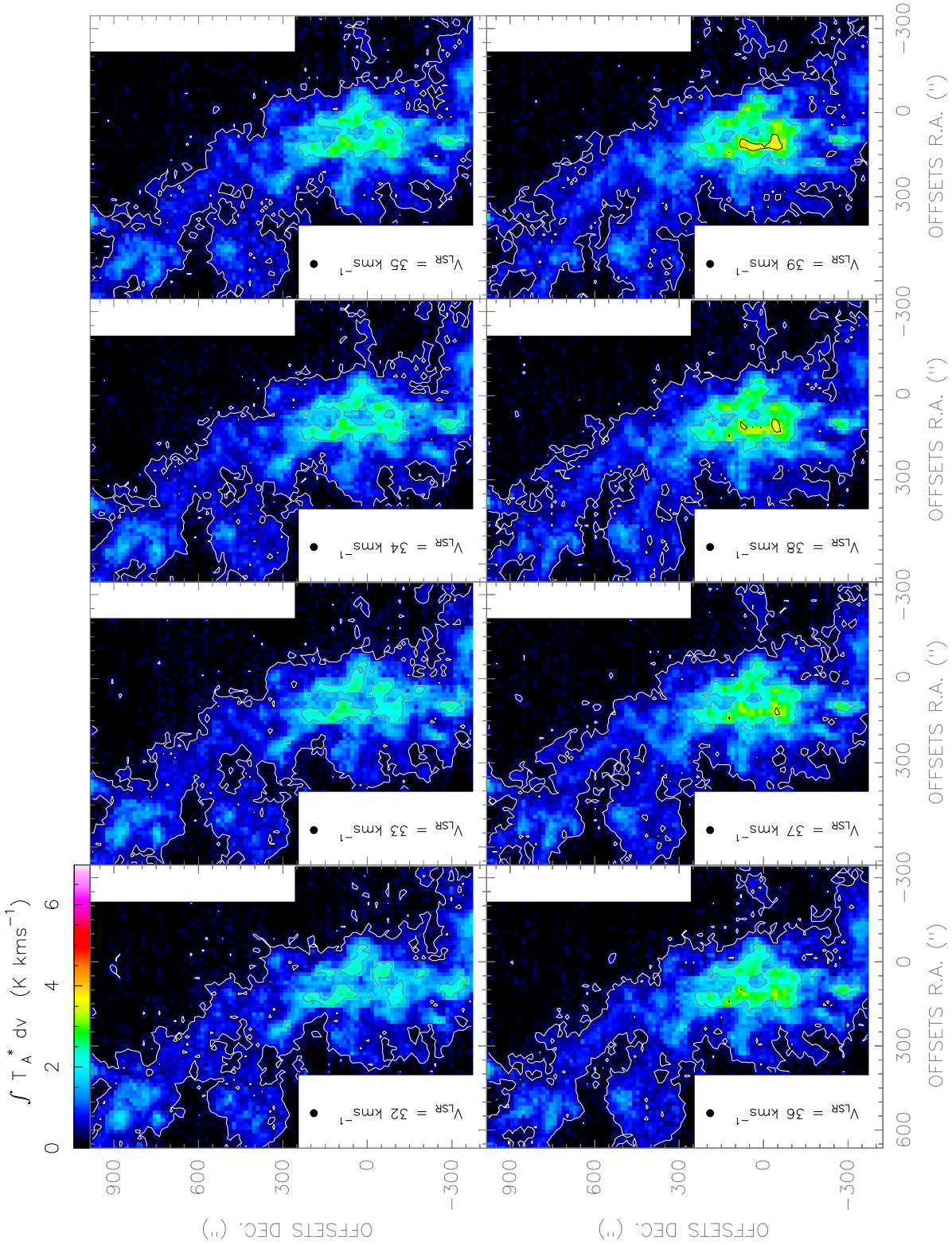

Figure. F.132: *[CI](2-1) line observed with the Herschel-HIFI satellite in Equatorial (J2000) coordinates. The spatial resolution of the maps is 28".*

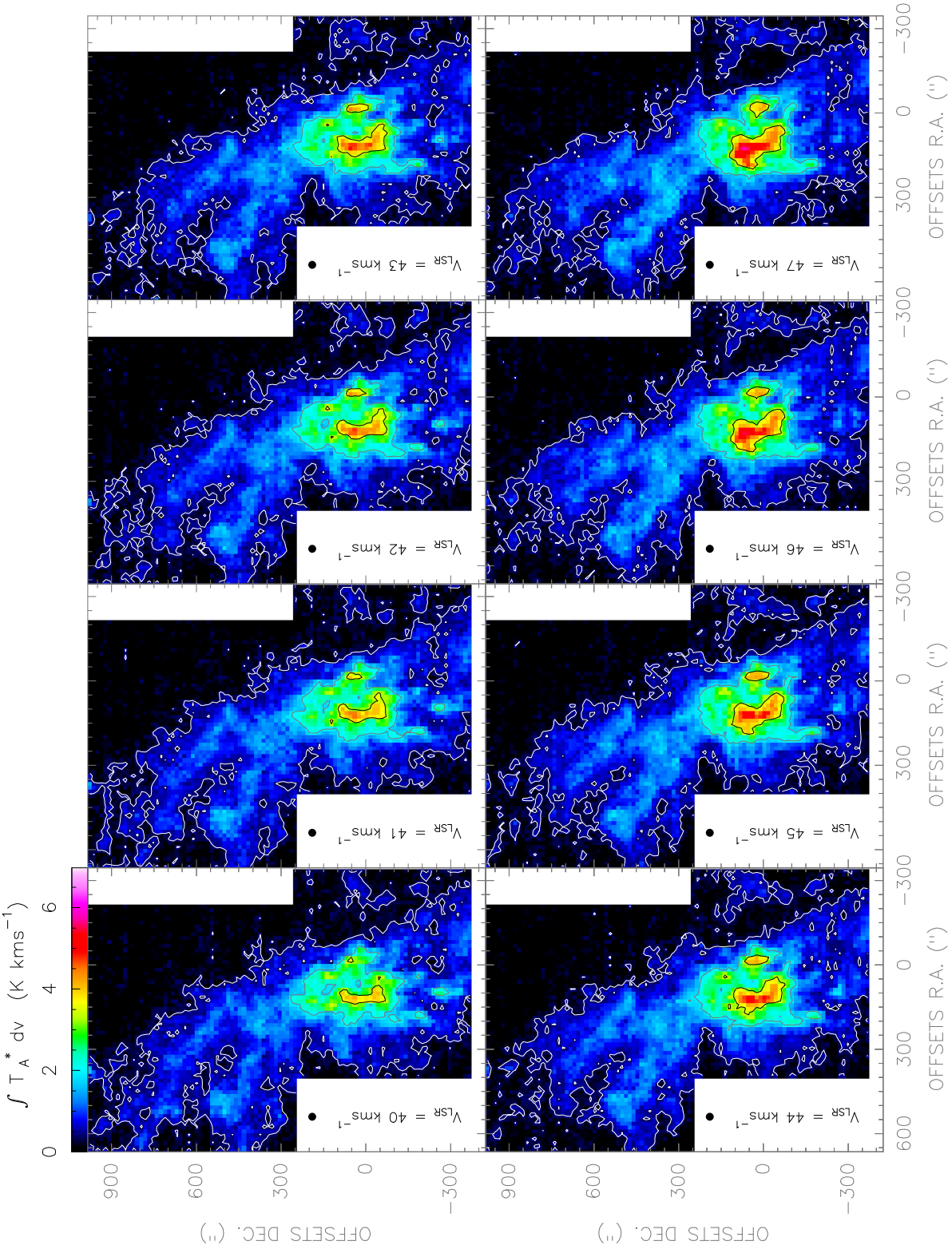

Figure. F.133: *[CI](2-1) line observed with the Herschel-HIFI satellite in Equatorial (J2000) coordinates. The spatial resolution of the maps is 28".*

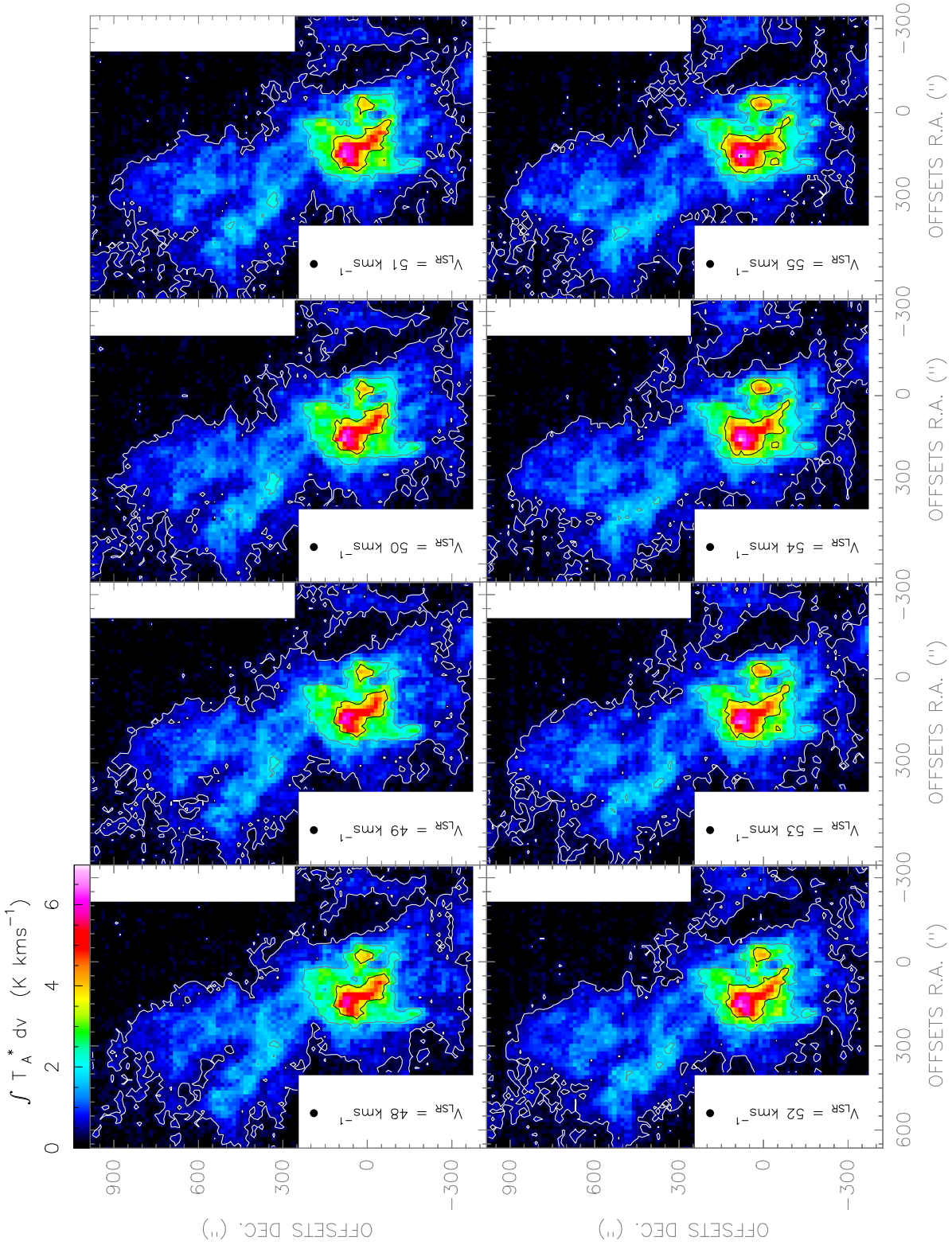

Figure. F.134: *[CI](2-1) line observed with the Herschel-HIFI satellite in Equatorial (J2000) coordinates. The spatial resolution of the maps is 28".*

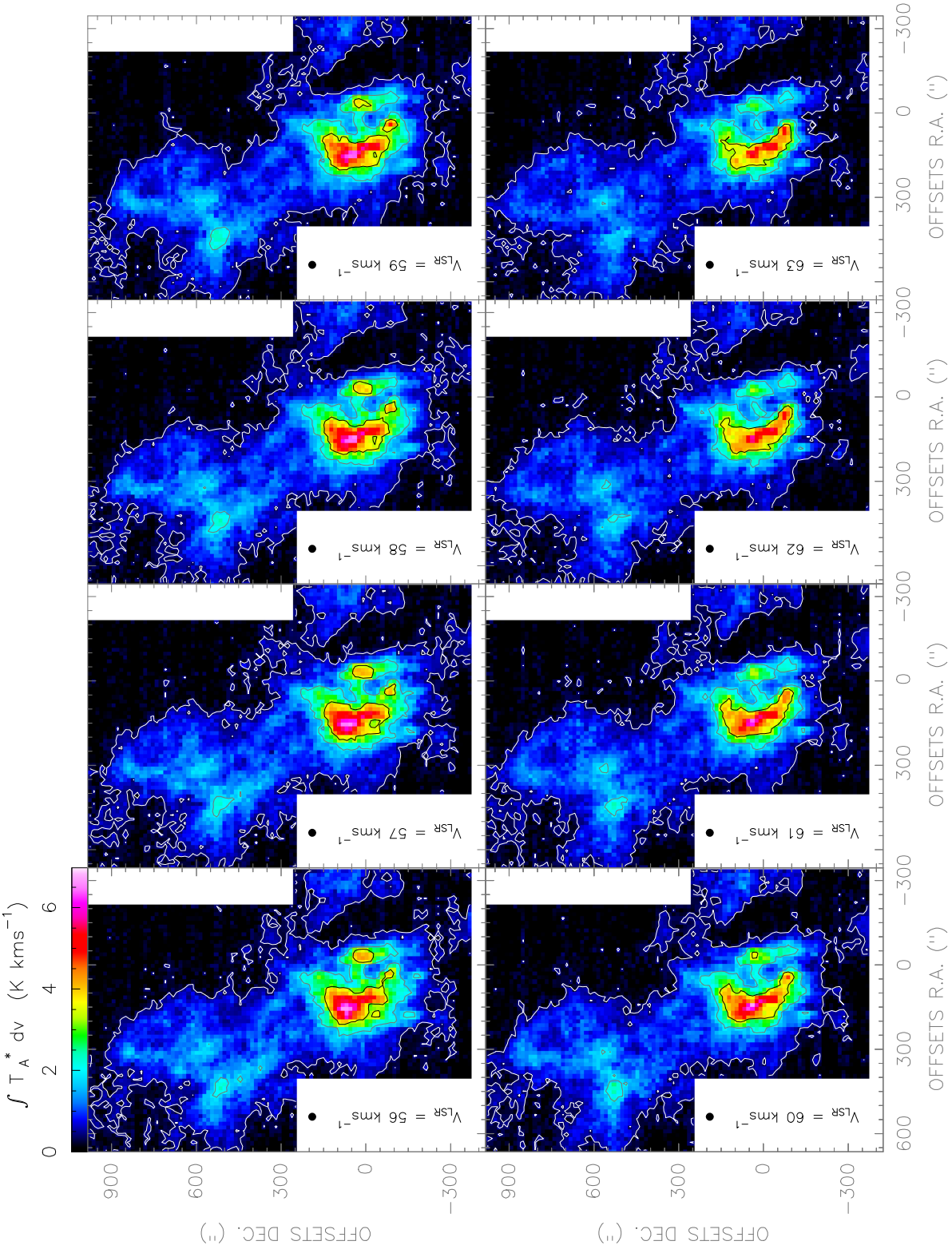

Figure. F.135: *[CI](2-1) line observed with the Herschel-HIFI satellite in Equatorial (J2000) coordinates. The spatial resolution of the maps is 28".*

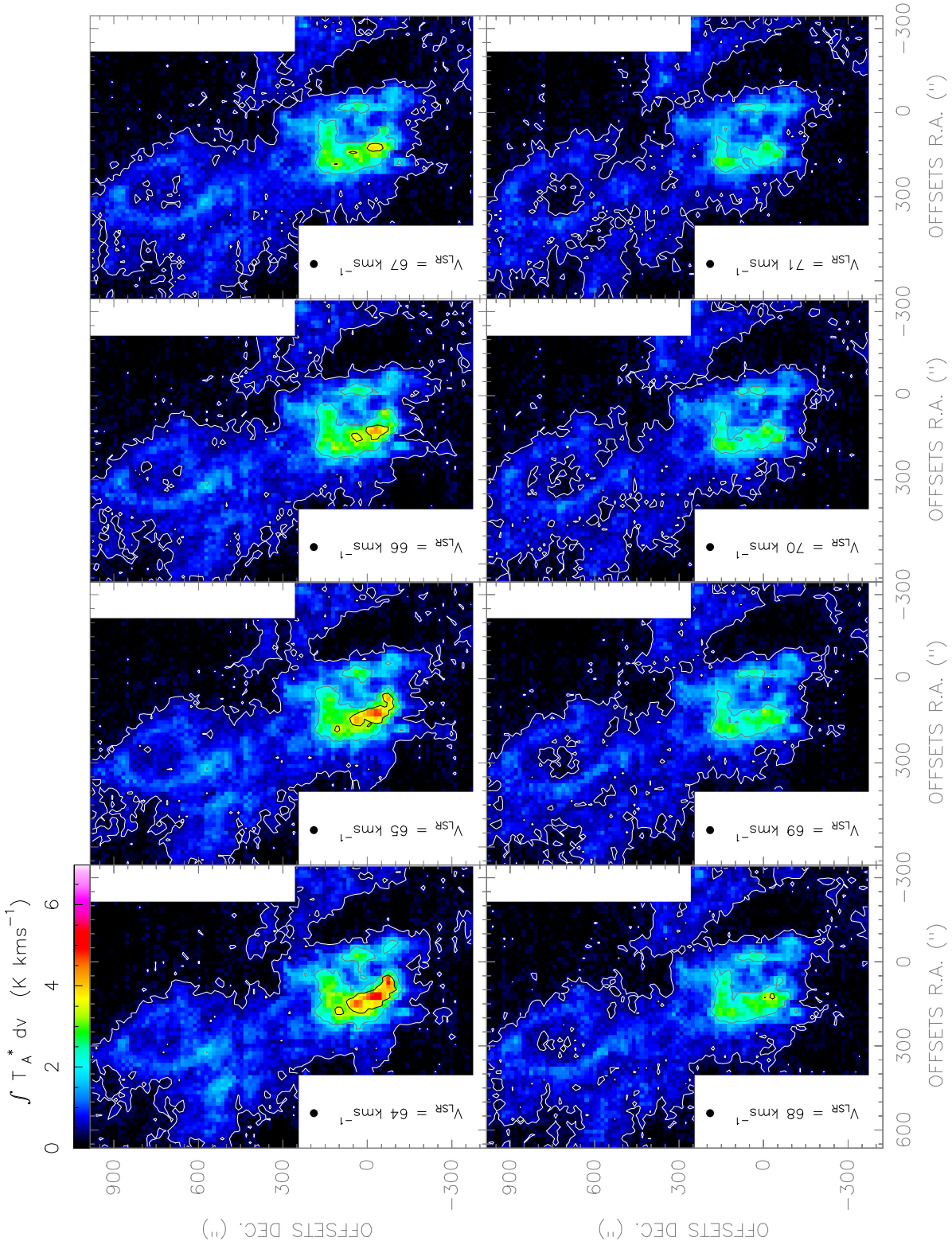

Figure. F.136: *[CI](2-1) line observed with the Herschel-HIFI satellite in Equatorial (J2000) coordinates. The spatial resolution of the maps is 28".*

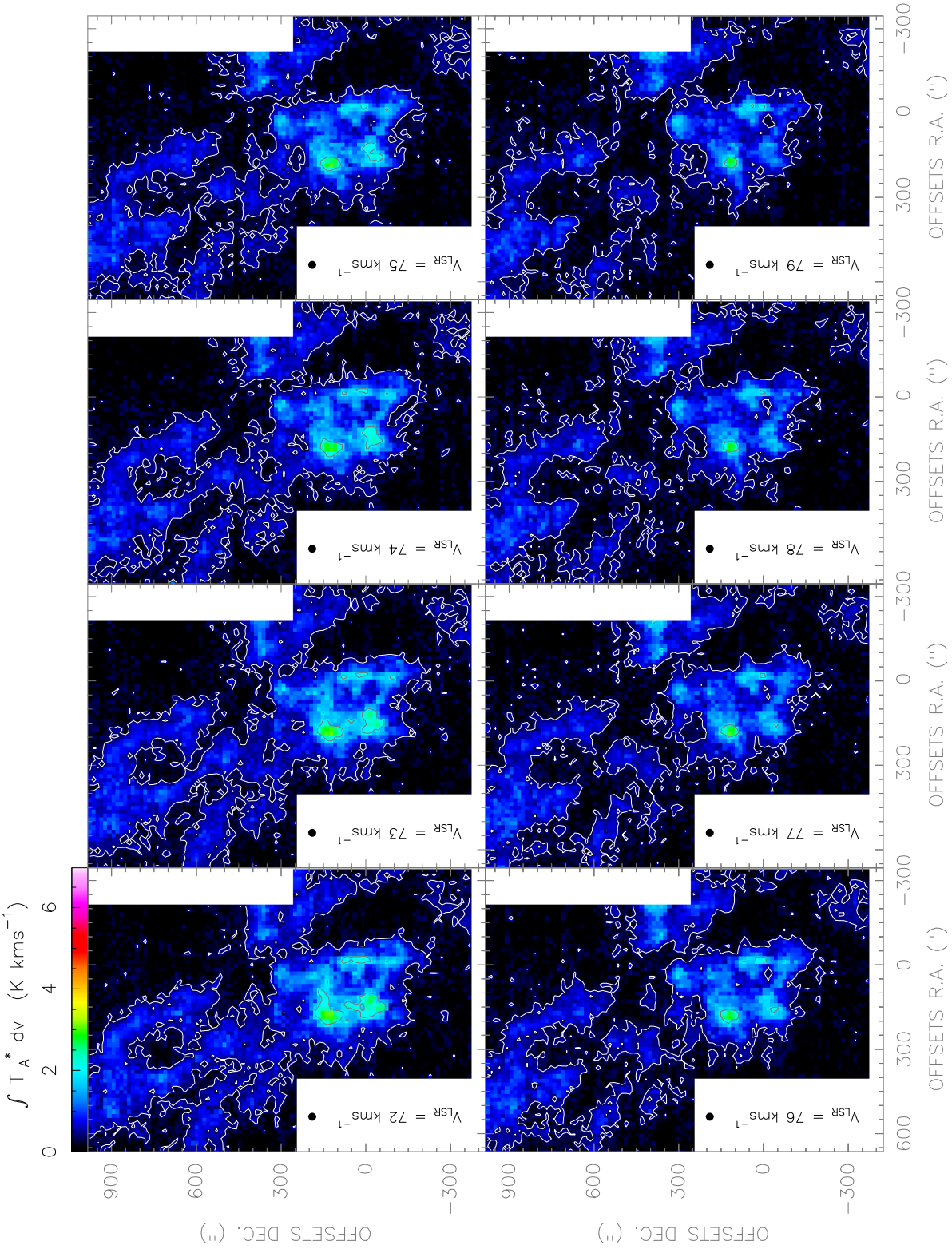

Figure. F.137: *[CI](2-1) line observed with the Herschel-HIFI satellite in Equatorial (J2000) coordinates. The spatial resolution of the maps is 28".*

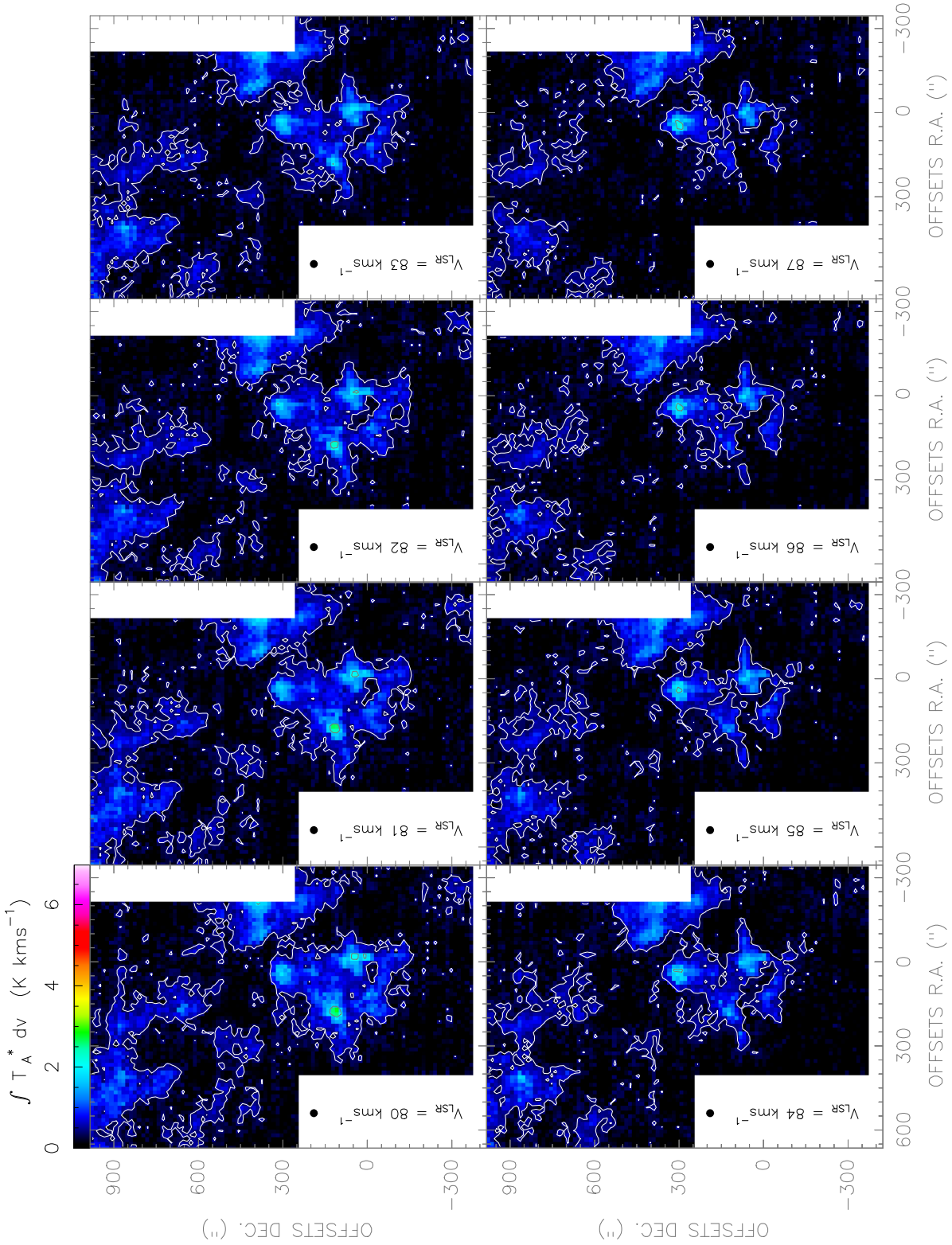

Figure. F.138: *[CI](2-1) line observed with the Herschel-HIFI satellite in Equatorial (J2000) coordinates. The spatial resolution of the maps is 28".*

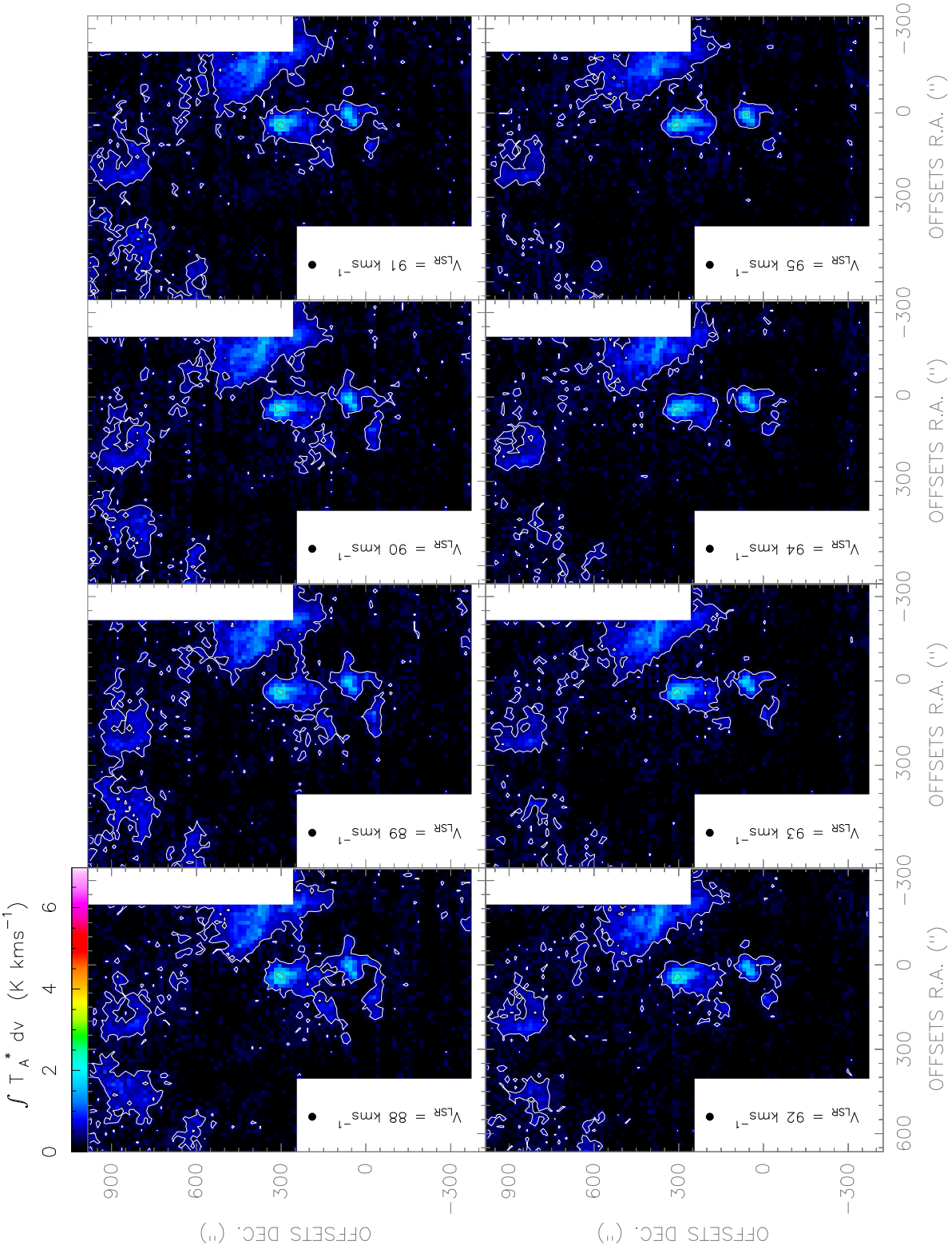

Figure. F.139: *[CI](2-1) line observed with the Herschel-HIFI satellite in Equatorial (J2000) coordinates. The spatial resolution of the maps is 28".*

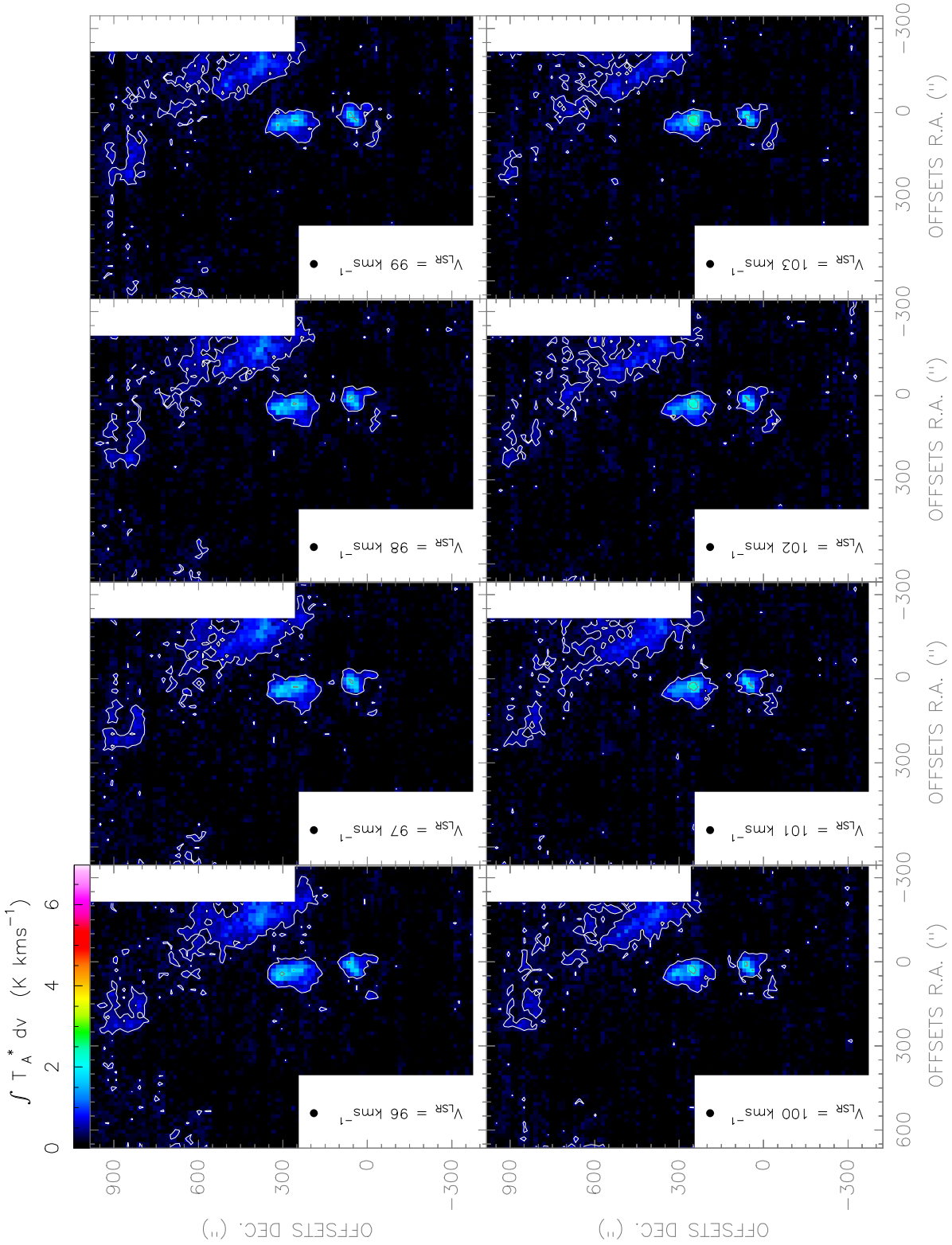

Figure. F.140: *[CI](2-1) line observed with the Herschel-HIFI satellite in Equatorial (J2000) coordinates. The spatial resolution of the maps is 28".*

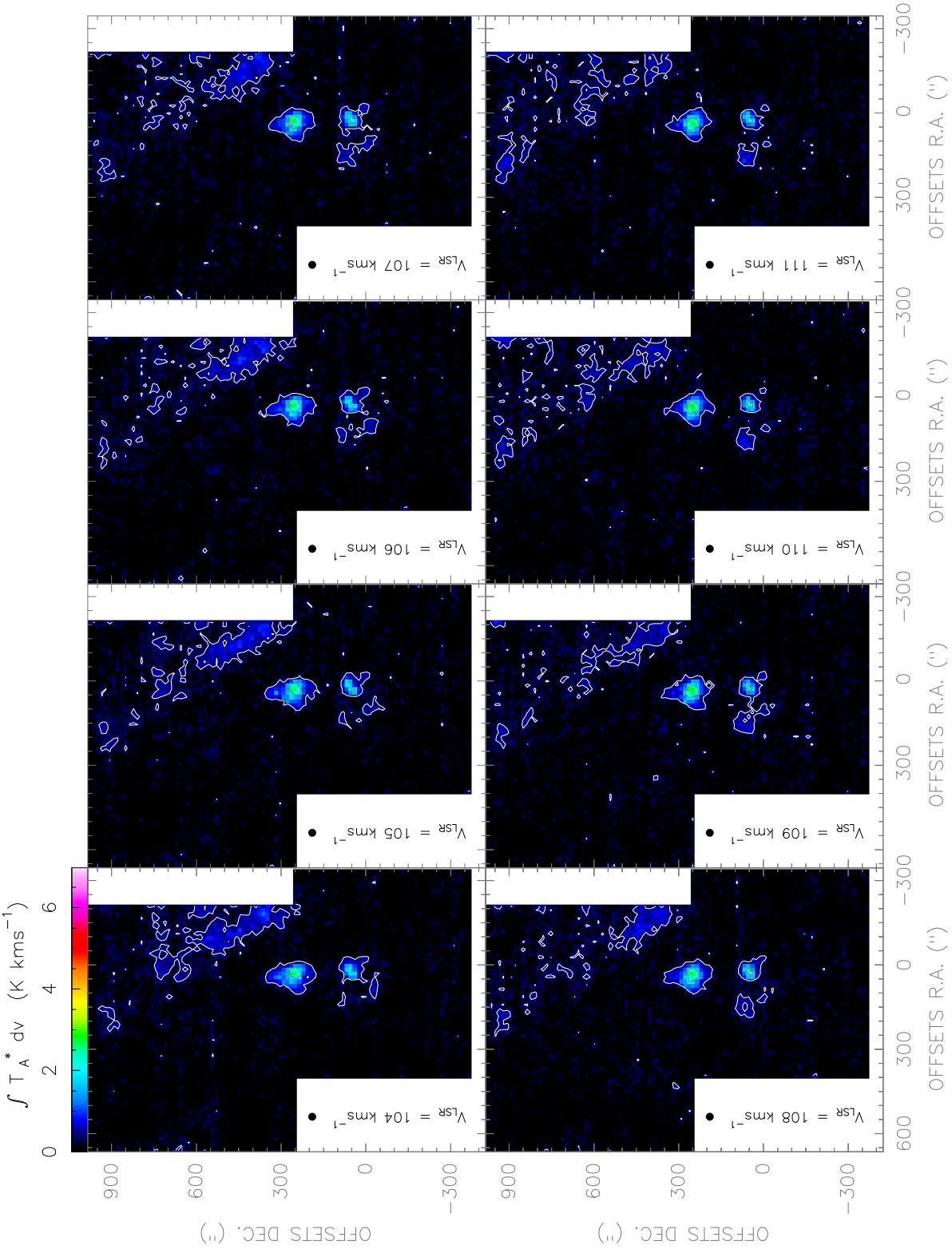

Figure. F.141: *[CI](2-1) line observed with the Herschel-HIFI satellite in Equatorial (J2000) coordinates. The spatial resolution of the maps is 28".*

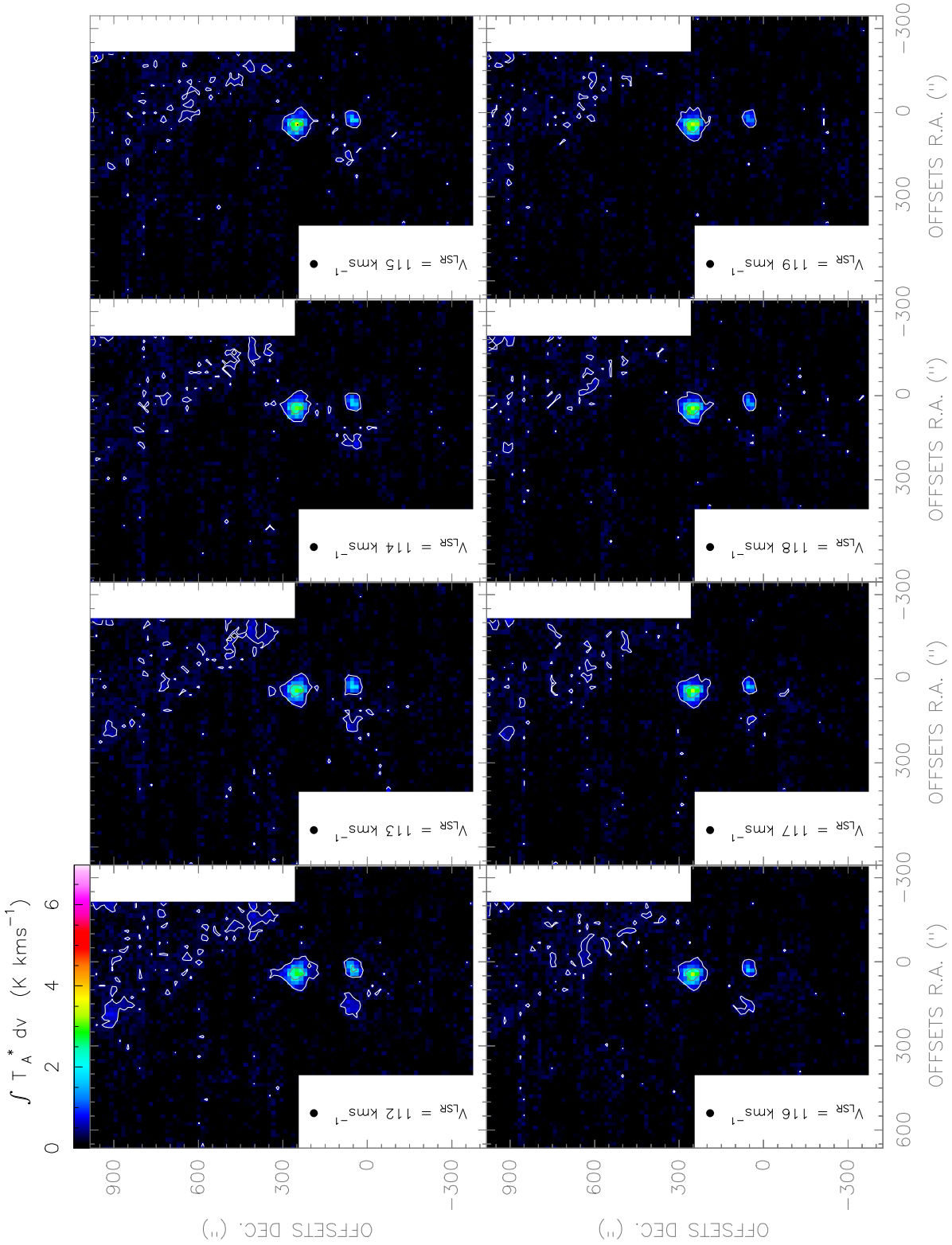

Figure. F.142: *[CI](2-1) line observed with the Herschel-HIFI satellite in Equatorial (J2000) coordinates. The spatial resolution of the maps is 28".*

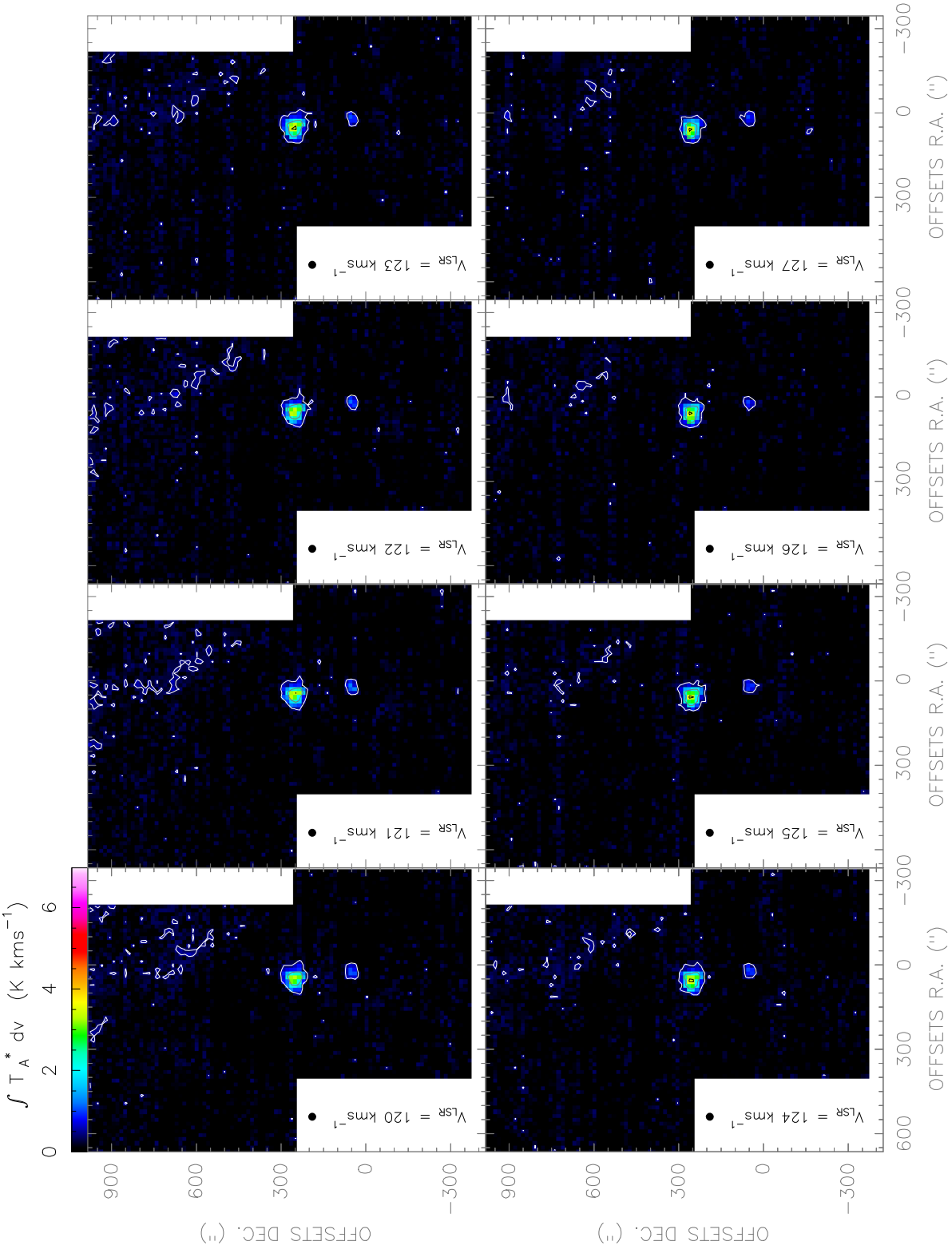

Figure. F.143: *[CI](2-1) line observed with the Herschel-HIFI satellite in Equatorial (J2000) coordinates. The spatial resolution of the maps is 28".*

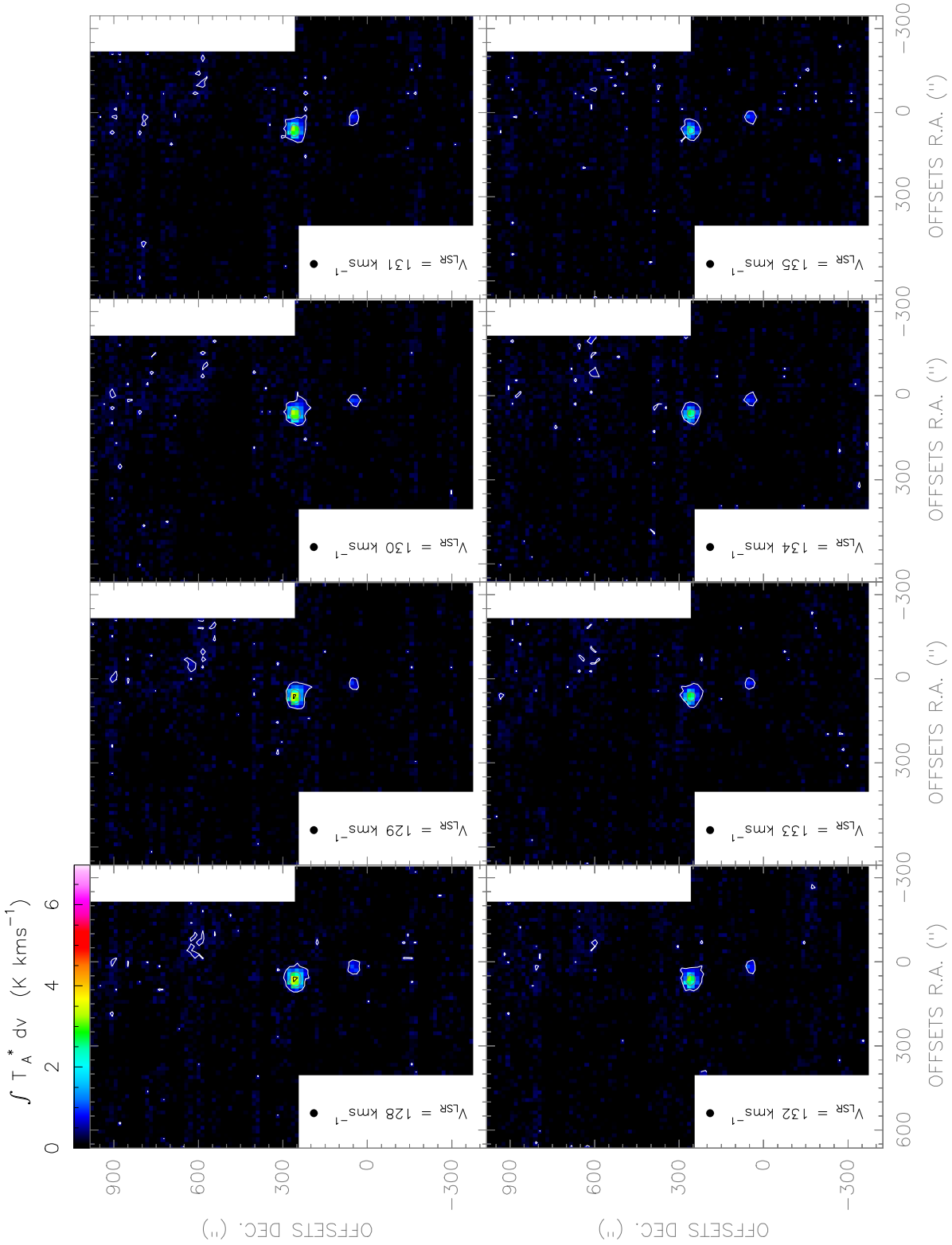

Figure. F.144: *[CI](2-1) line observed with the Herschel-HIFI satellite in Equatorial (J2000) coordinates. The spatial resolution of the maps is 28".*

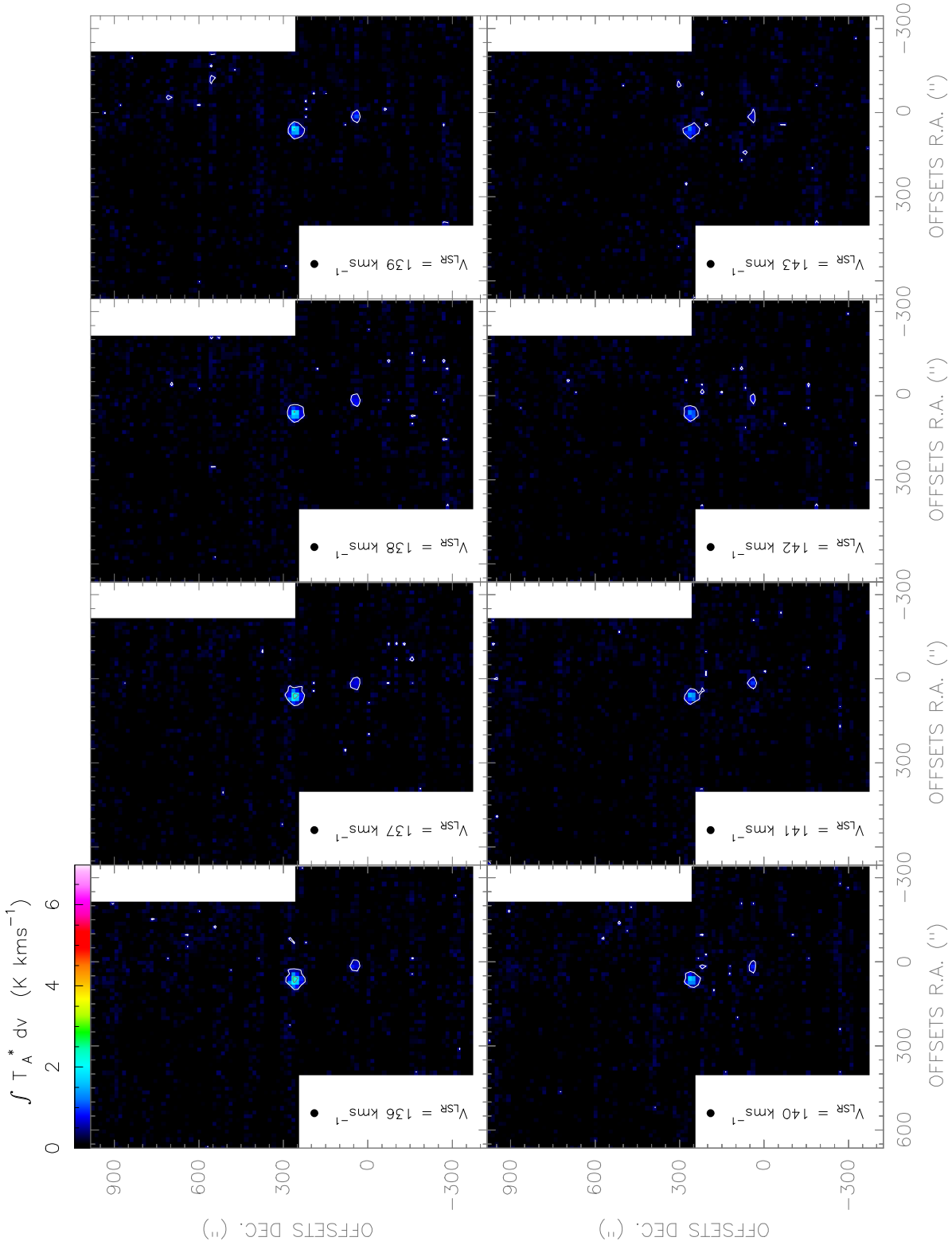

Figure. F.145: *[CI](2-1) line observed with the Herschel-HIFI satellite in Equatorial (J2000) coordinates. The spatial resolution of the maps is 28".*

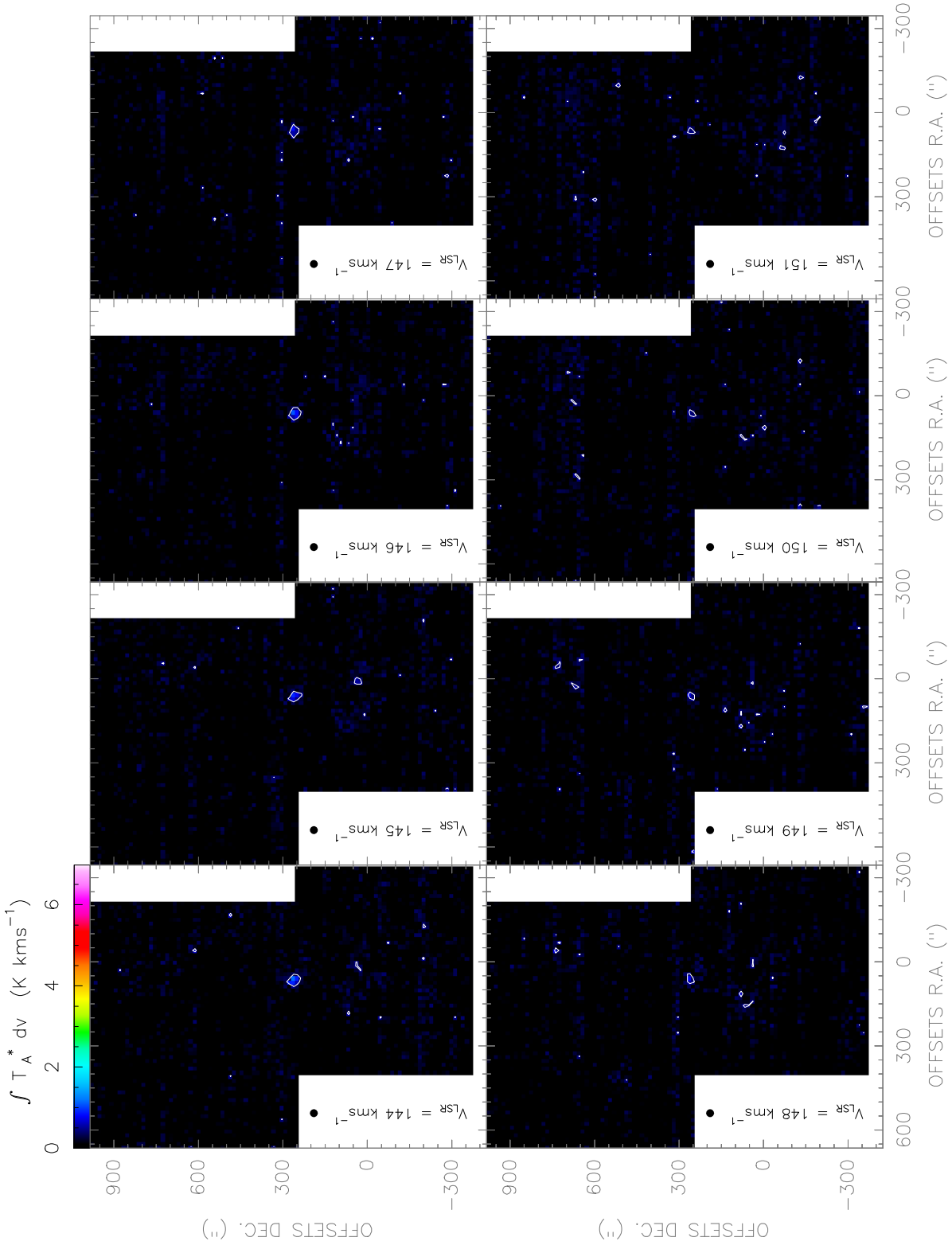

Figure. F.146: *[CI](2-1) line observed with the Herschel-HIFI satellite in Equatorial (J2000) coordinates. The spatial resolution of the maps is 28".*

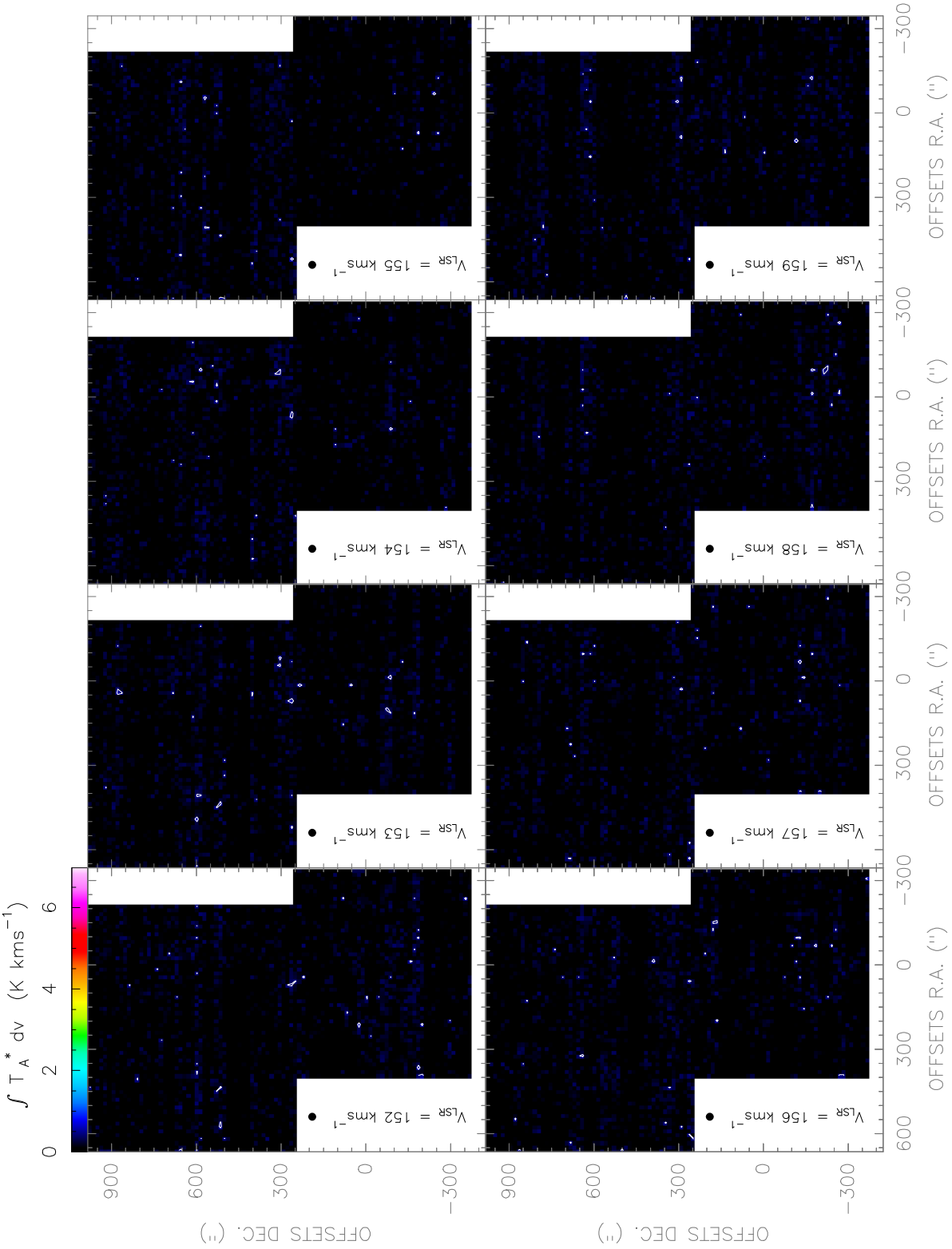

Figure. F.147: *[CI](2-1) line observed with the Herschel-HIFI satellite in Equatorial (J2000) coordinates. The spatial resolution of the maps is 28".*

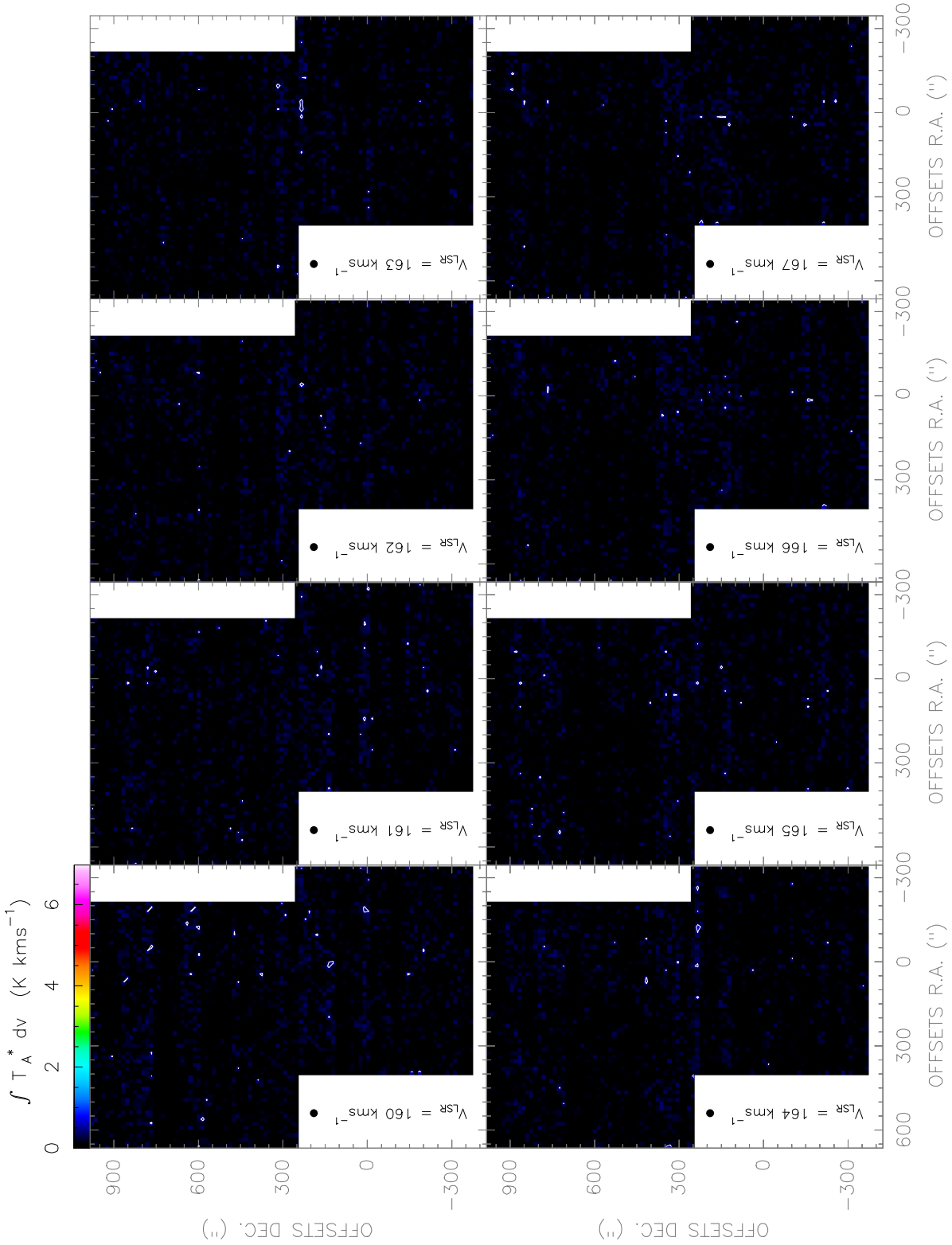

Figure. F.148: *[CI](2-1) line observed with the Herschel-HIFI satellite in Equatorial (J2000) coordinates. The spatial resolution of the maps is 28".*

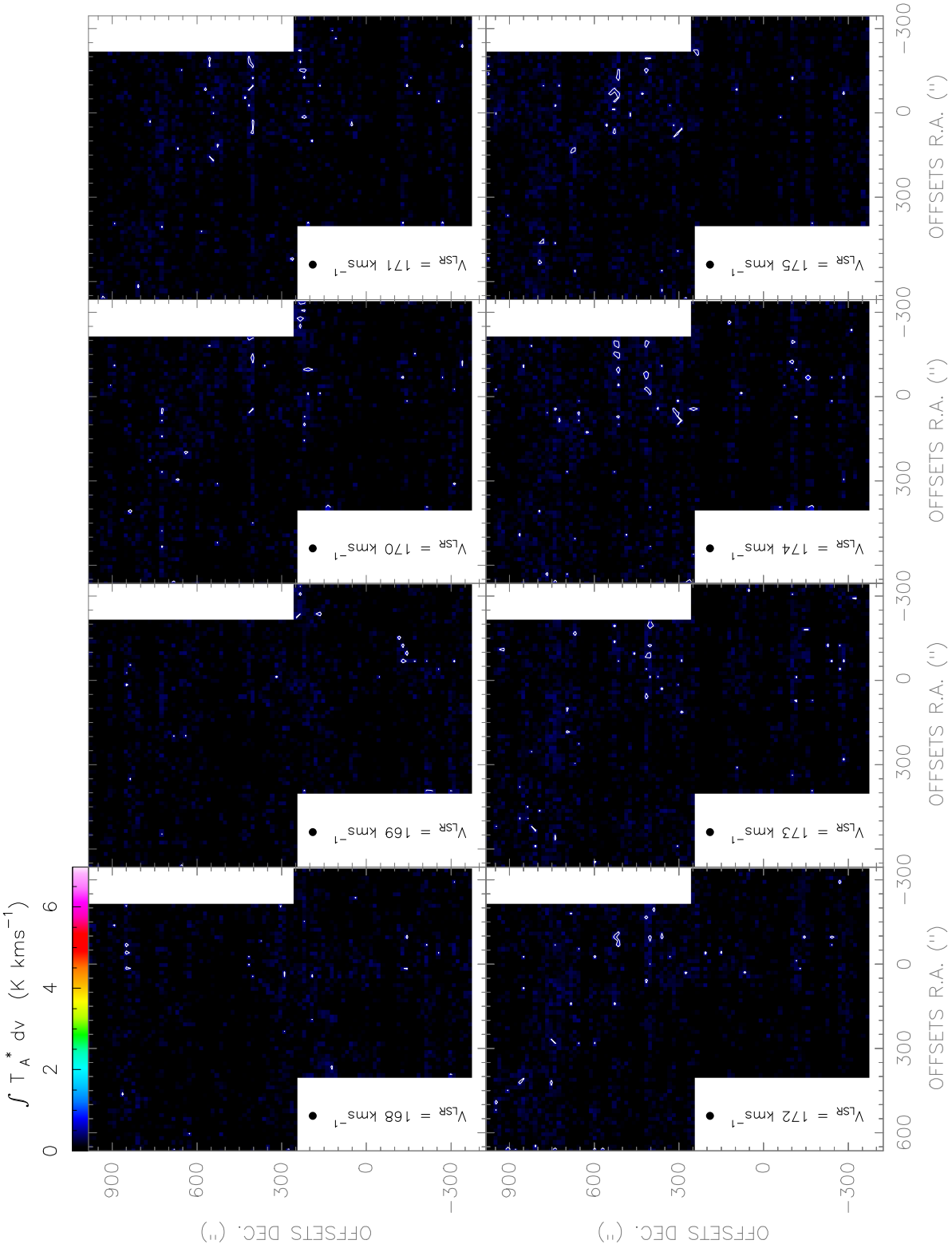

Figure. F.149: *[CI](2-1) line observed with the Herschel-HIFI satellite in Equatorial (J2000) coordinates. The spatial resolution of the maps is 28".*

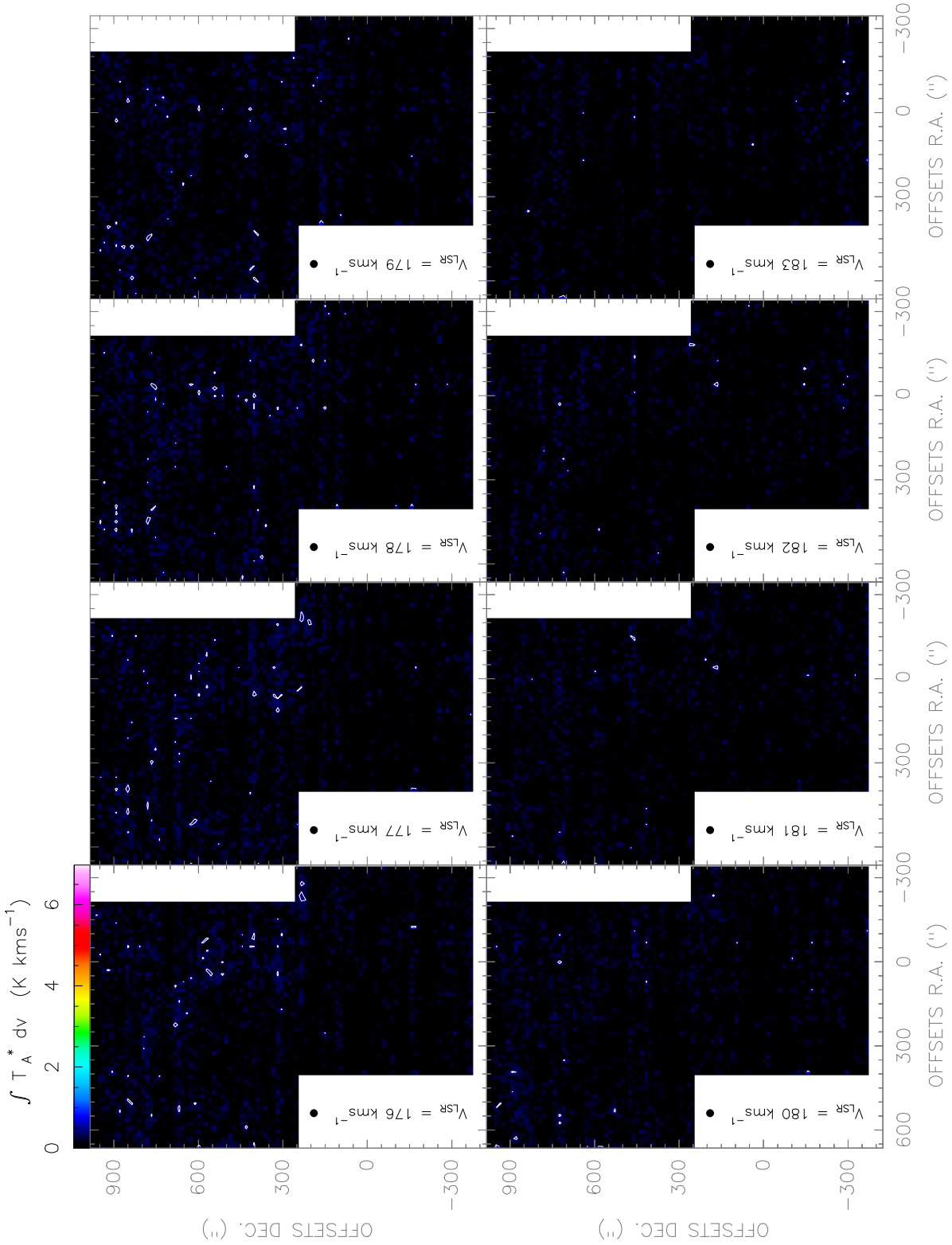

Figure. F.150: *[CI](2-1) line observed with the Herschel-HIFI satellite in Equatorial (J2000) coordinates. The spatial resolution of the maps is 28".*

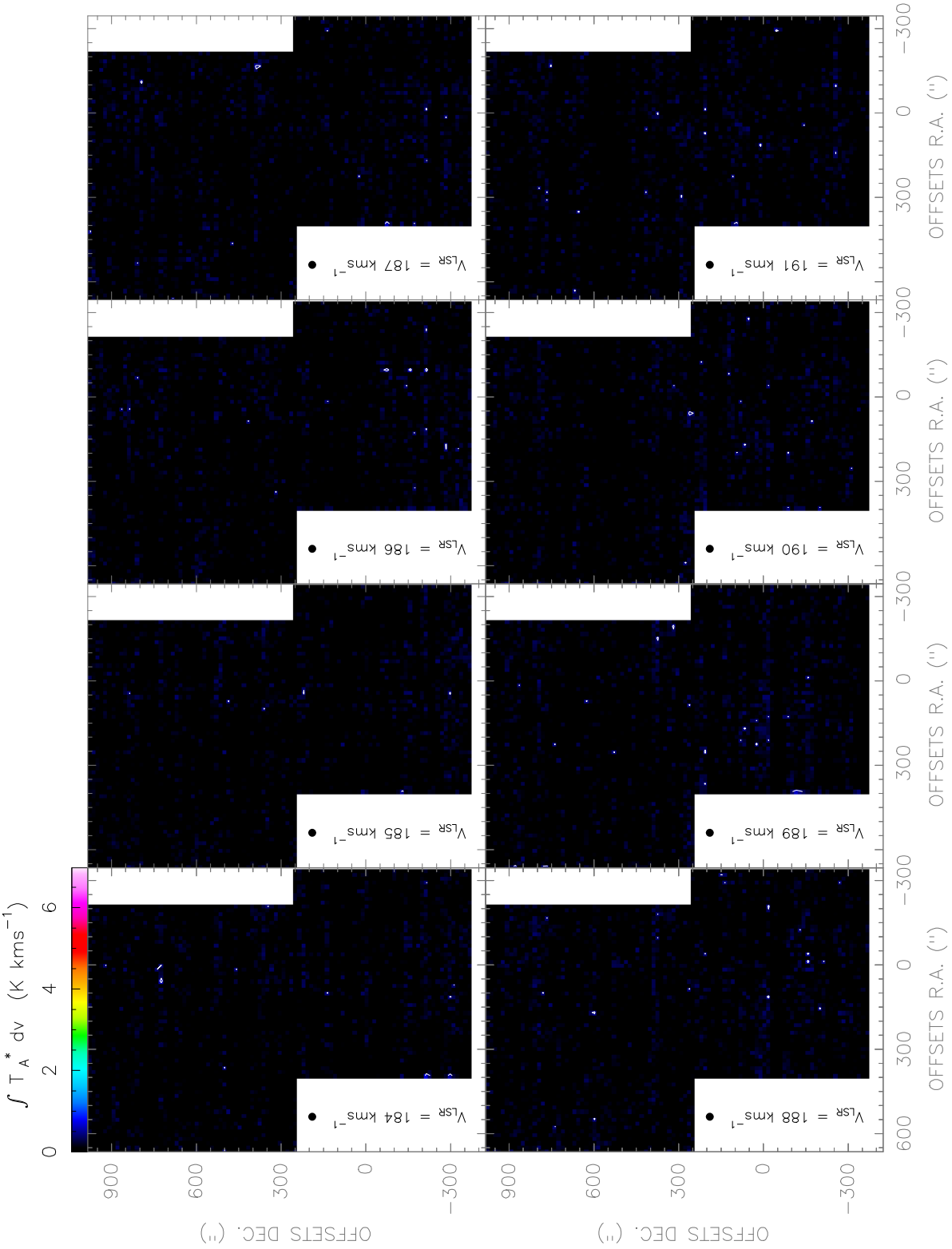

Figure. F.151: *[CI](2-1) line observed with the Herschel-HIFI satellite in Equatorial (J2000) coordinates. The spatial resolution of the maps is 28".*

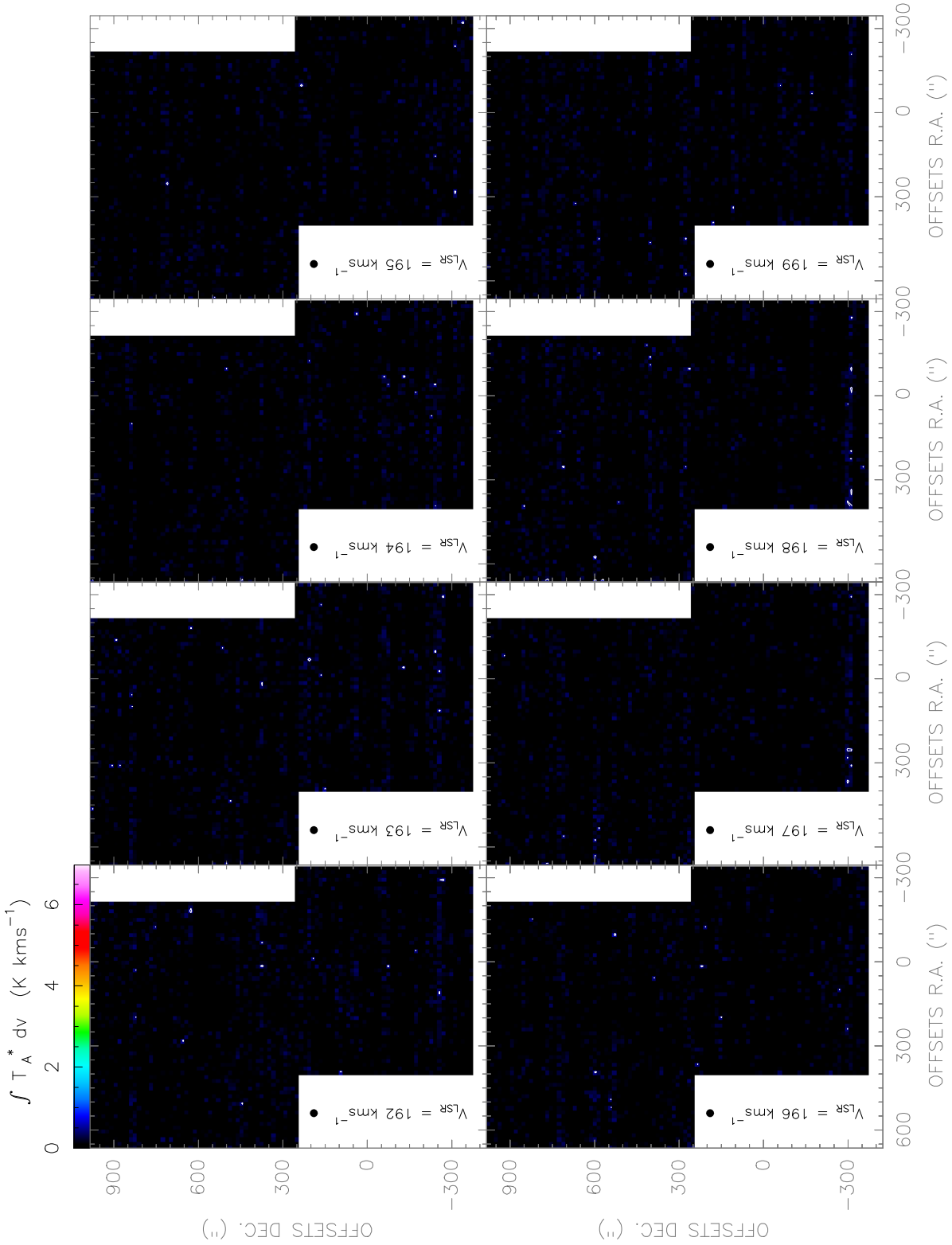

Figure. F.152: *[CI](2-1) line observed with the Herschel-HIFI satellite in Equatorial (J2000) coordinates. The spatial resolution of the maps is 28".*

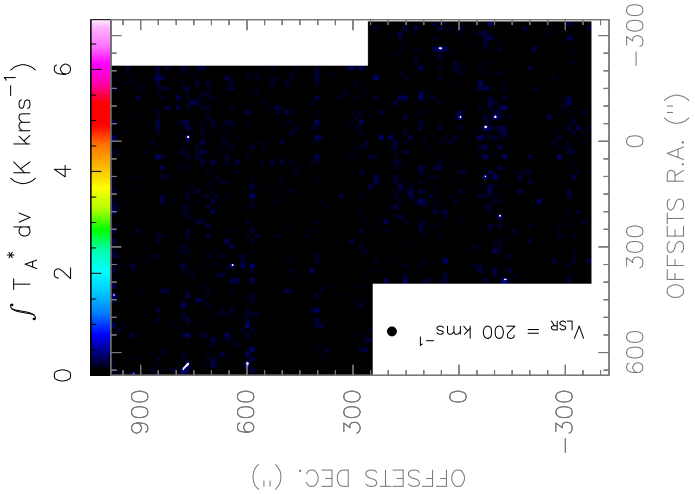

Figure. F.153: *[CI](2-1) line observed with the Herschel-HIFI satellite in Equatorial (J2000) coordinates. The spatial resolution of the maps is 28".*

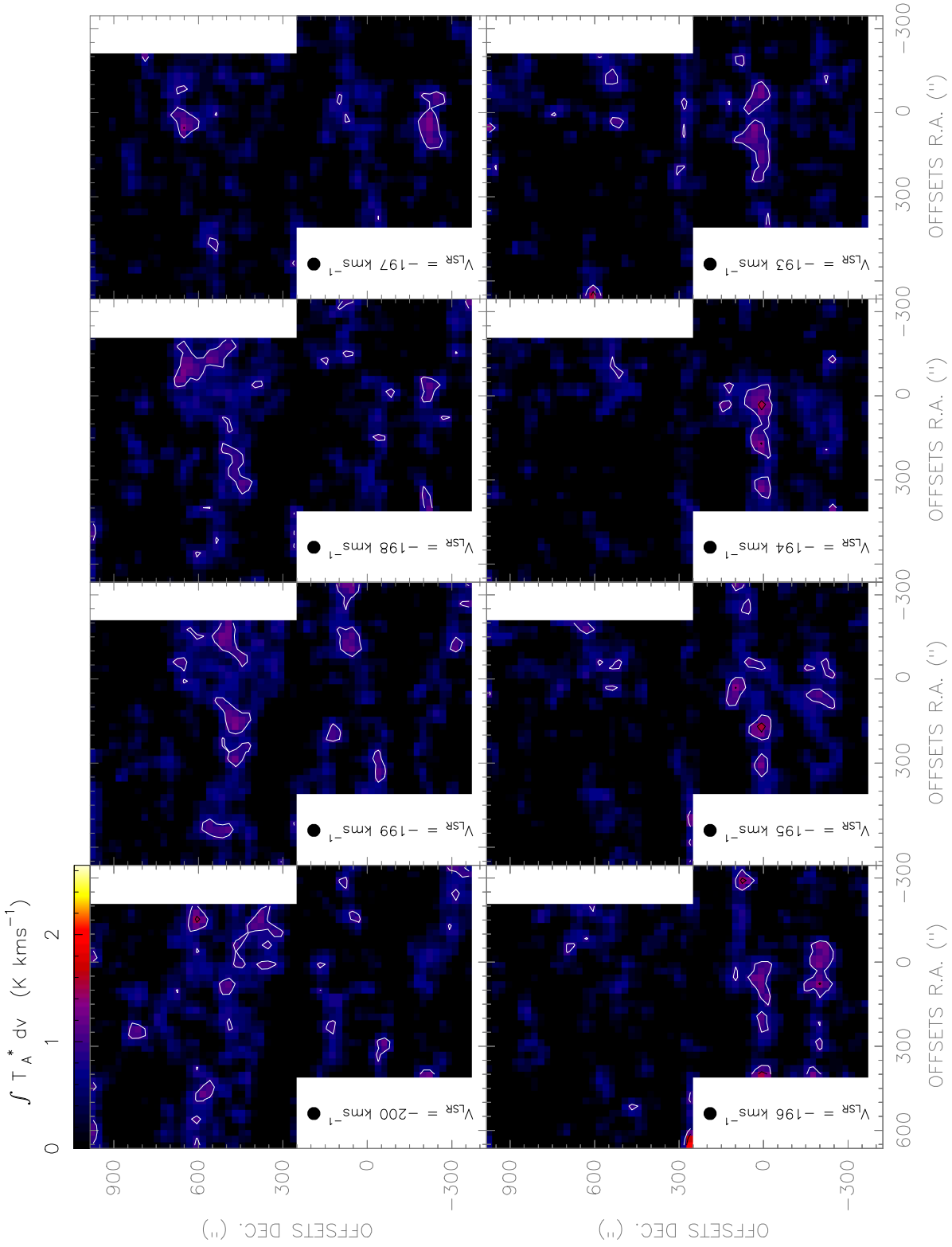

Figure. F.154: *[NII] line observed with the Herschel-HIFI satellite in Equatorial (J2000) coordinates. The spatial resolution of the maps is 46".*

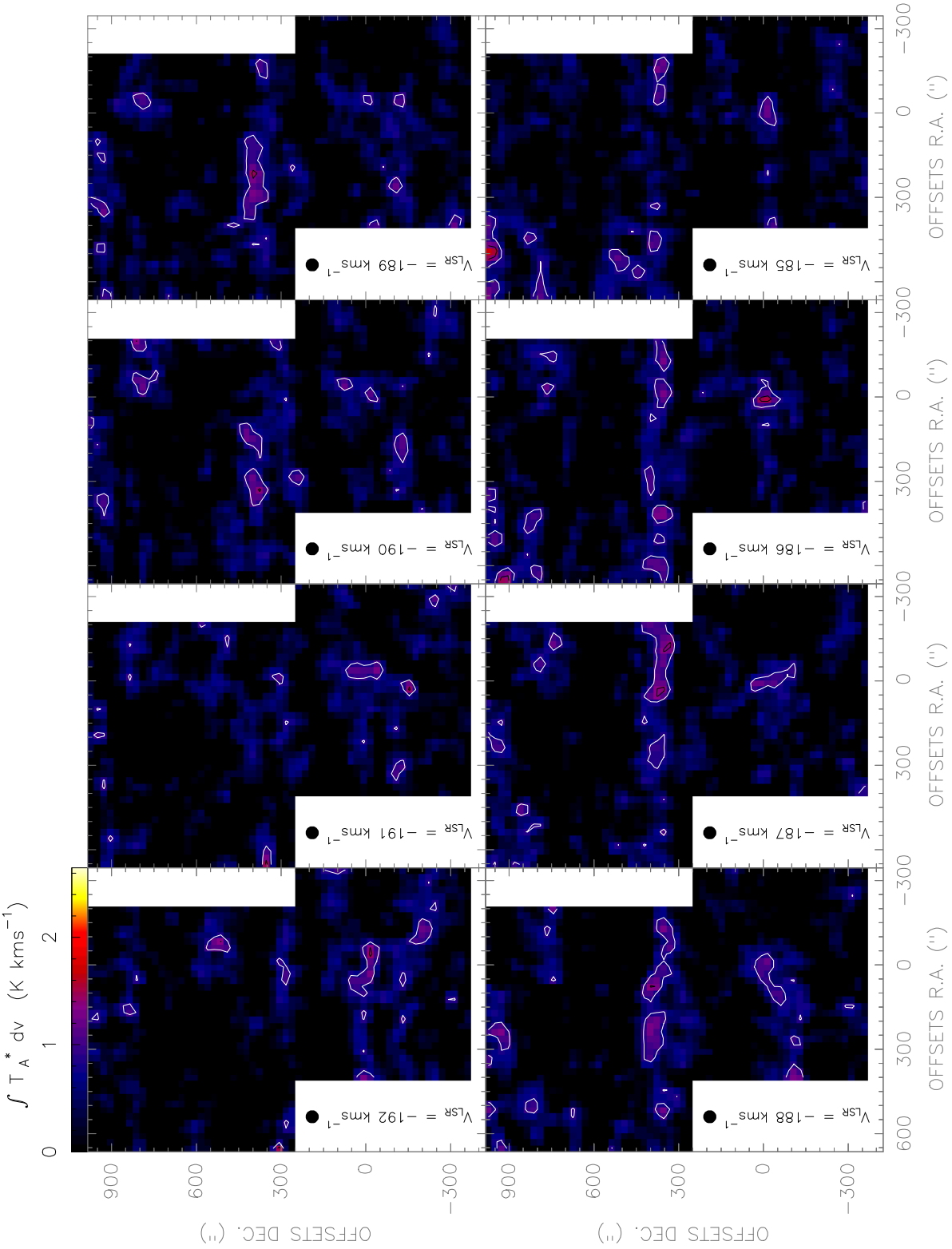

Figure. F.155: *[NII] line observed with the Herschel-HIFI satellite in Equatorial (J2000) coordinates. The spatial resolution of the maps is 46".*

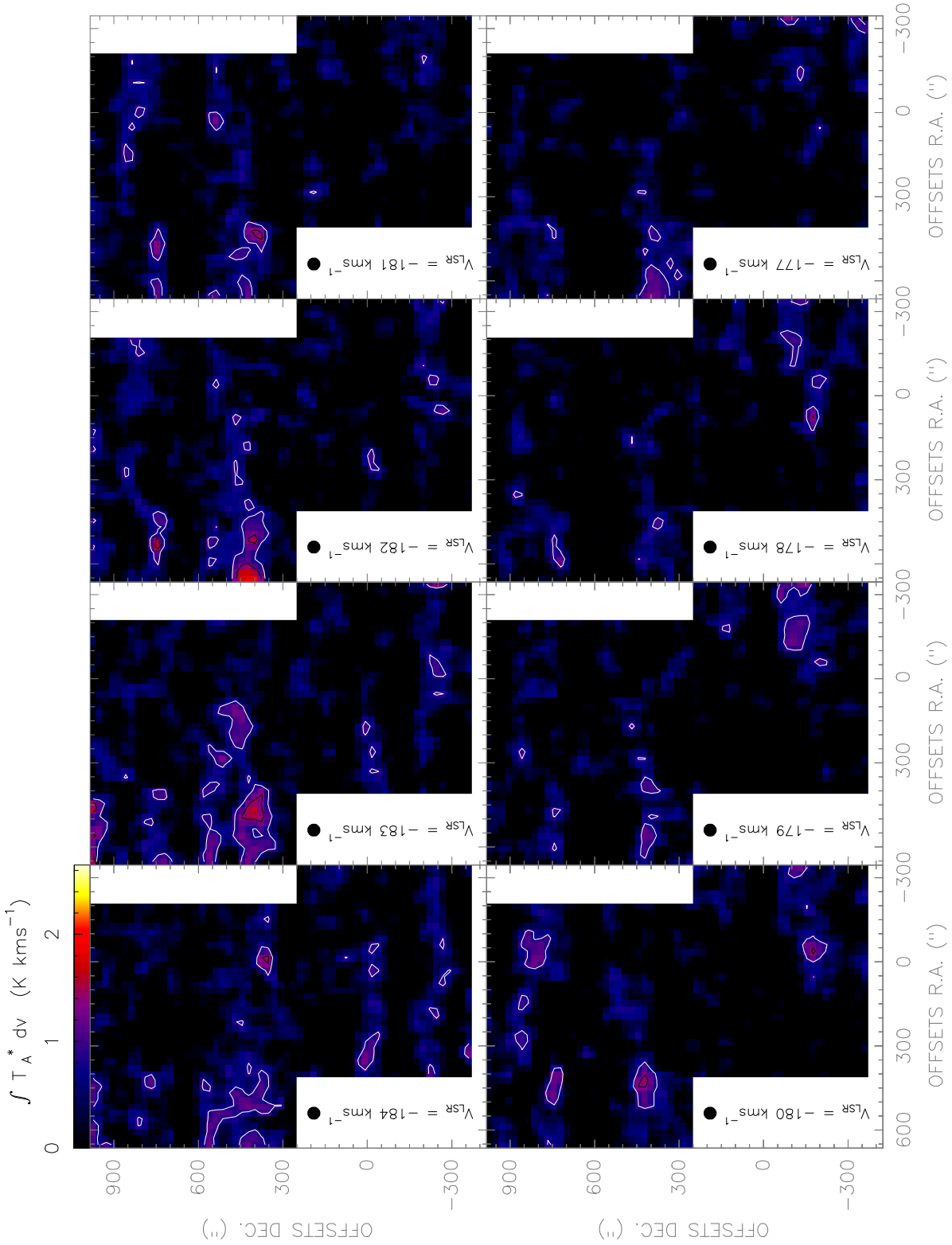

Figure. F.156: *[NII] line observed with the Herschel-HIFI satellite in Equatorial (J2000) coordinates. The spatial resolution of the maps is 46".*

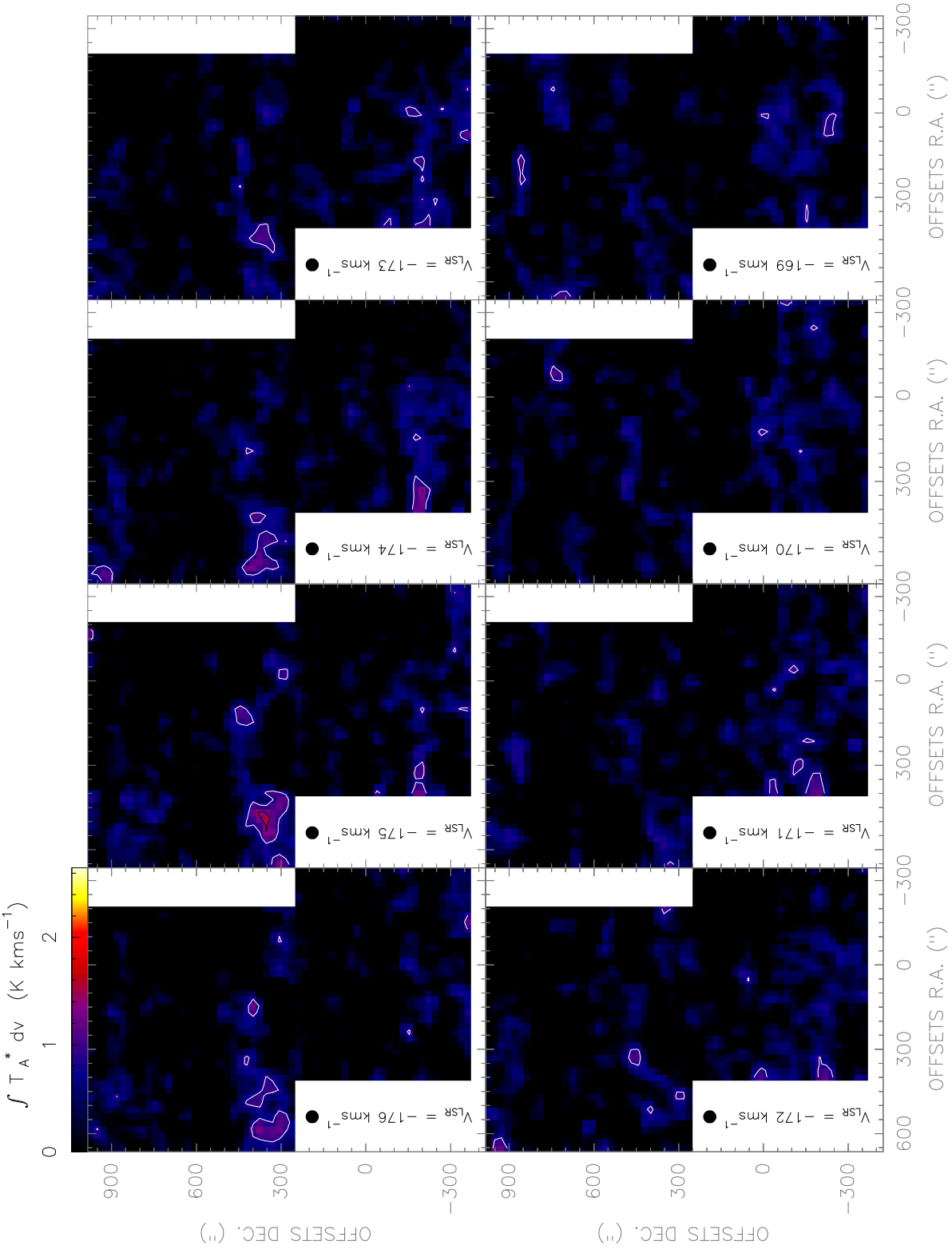

Figure. F.157: *[NII] line observed with the Herschel-HIFI satellite in Equatorial (J2000) coordinates. The spatial resolution of the maps is 46".*

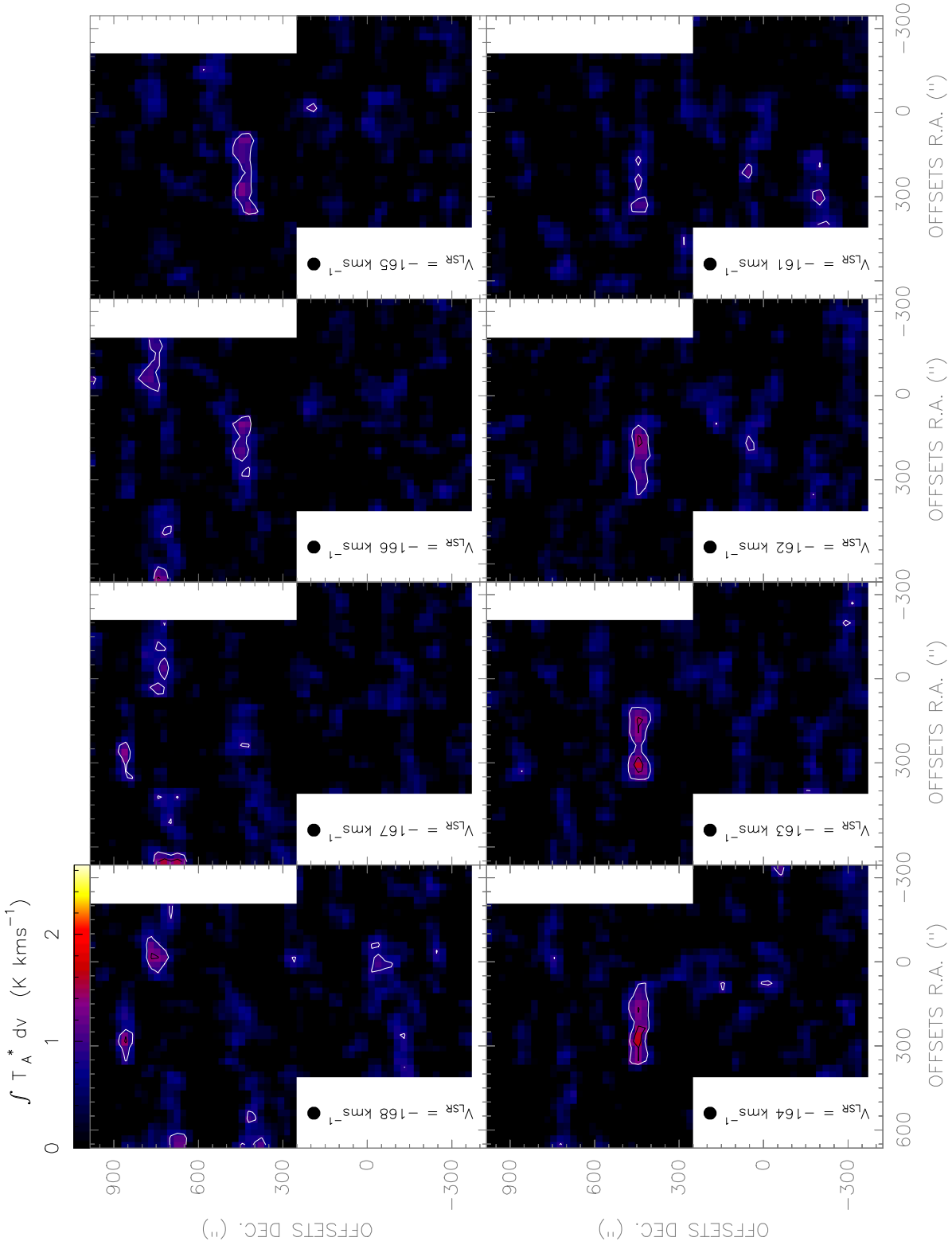

Figure. F.158: *[NII] line observed with the Herschel-HIFI satellite in Equatorial (J2000) coordinates. The spatial resolution of the maps is 46".*

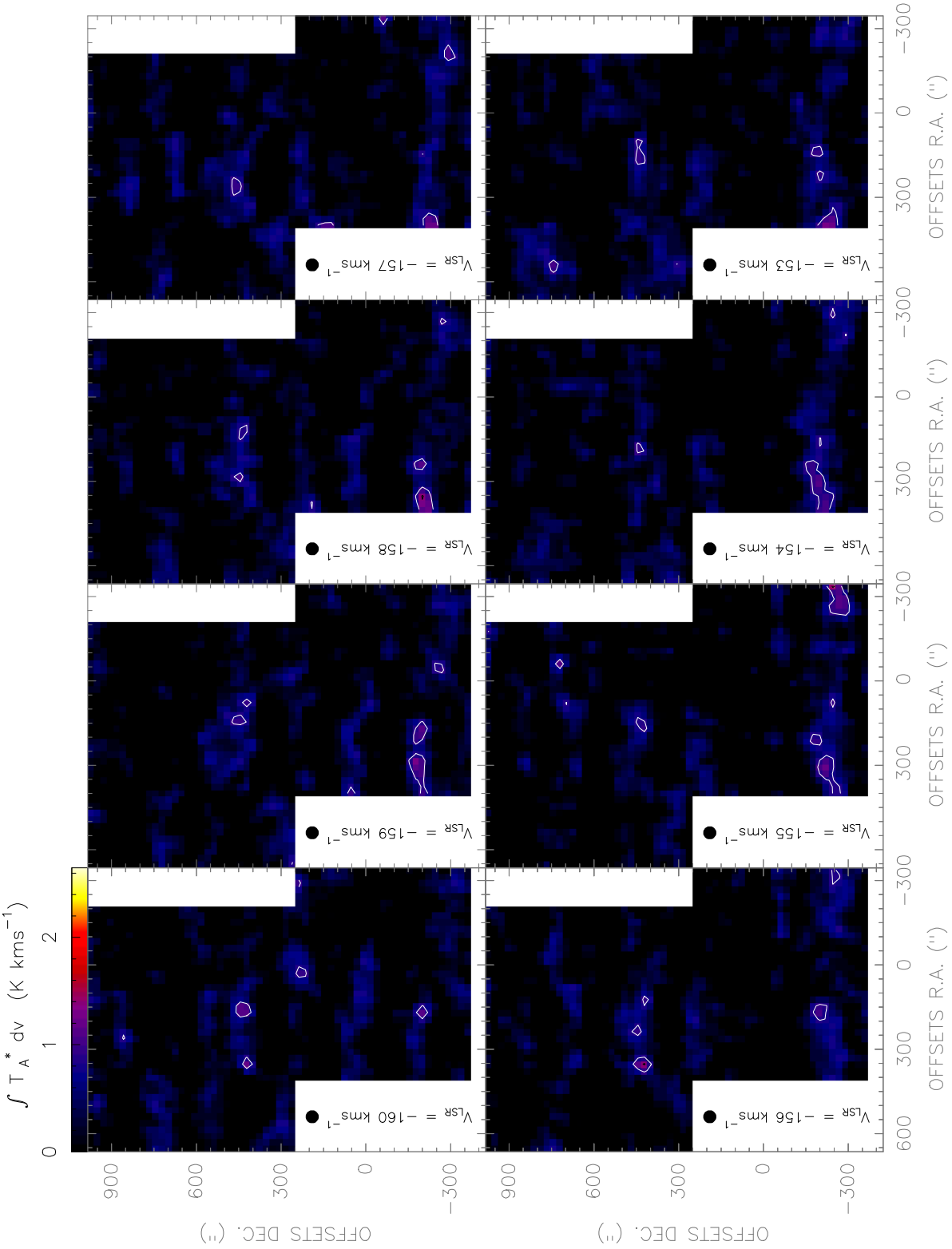

Figure. F.159: *[NII] line observed with the Herschel-HIFI satellite in Equatorial (J2000) coordinates. The spatial resolution of the maps is 46".*

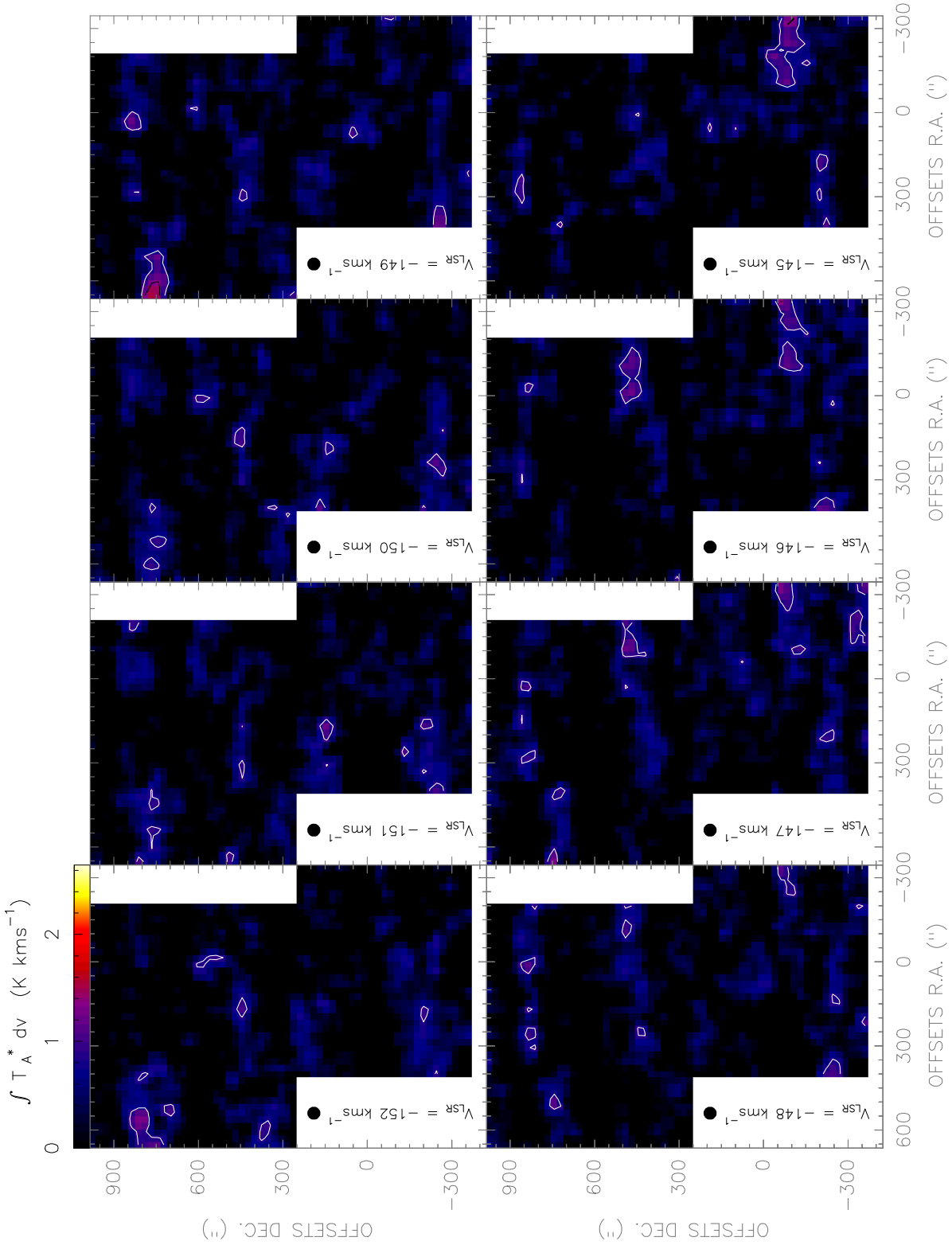

Figure. F.160: *[NII] line observed with the Herschel-HIFI satellite in Equatorial (J2000) coordinates. The spatial resolution of the maps is 46".*

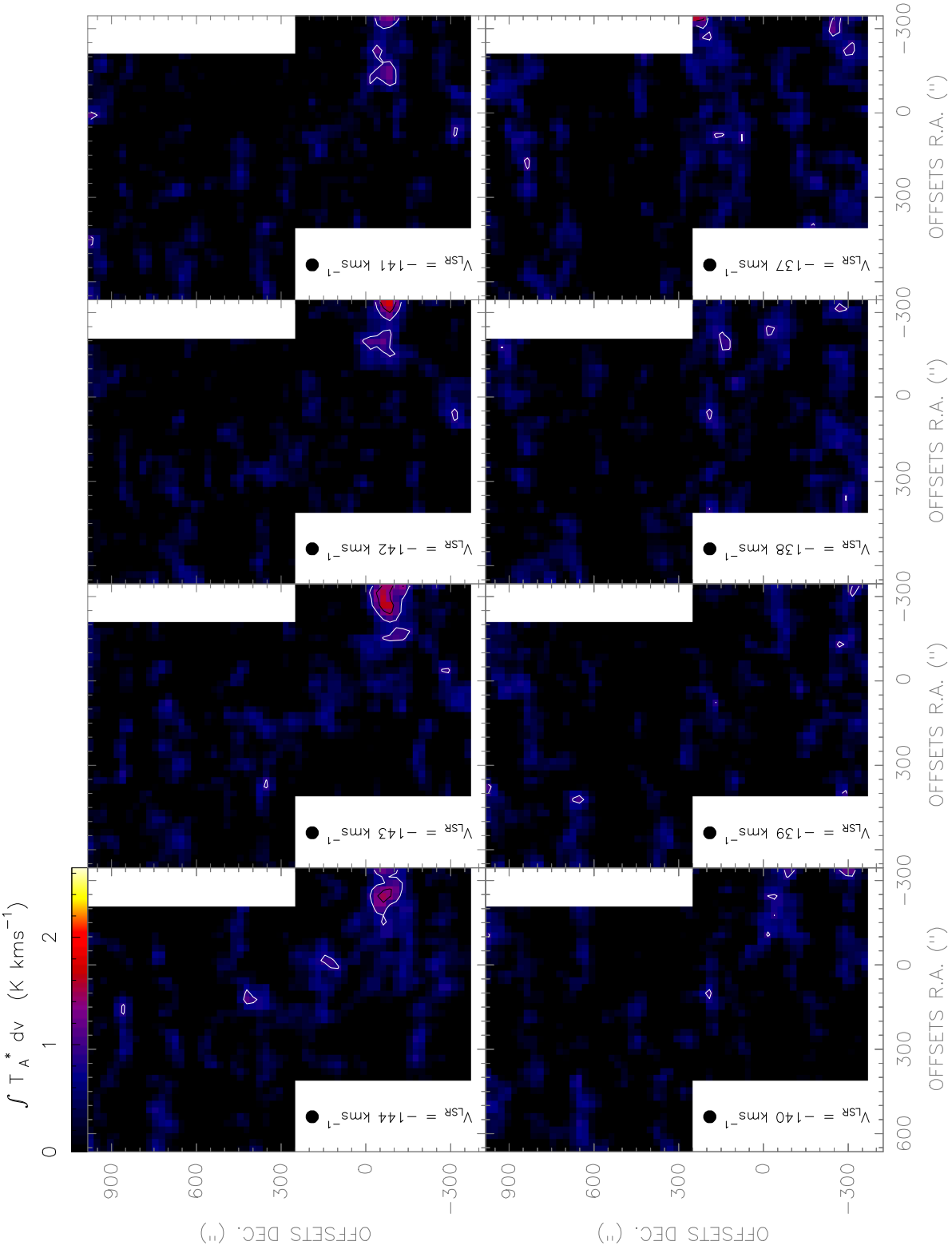

Figure. F.161: *[NII] line observed with the Herschel-HIFI satellite in Equatorial (J2000) coordinates. The spatial resolution of the maps is 46".*

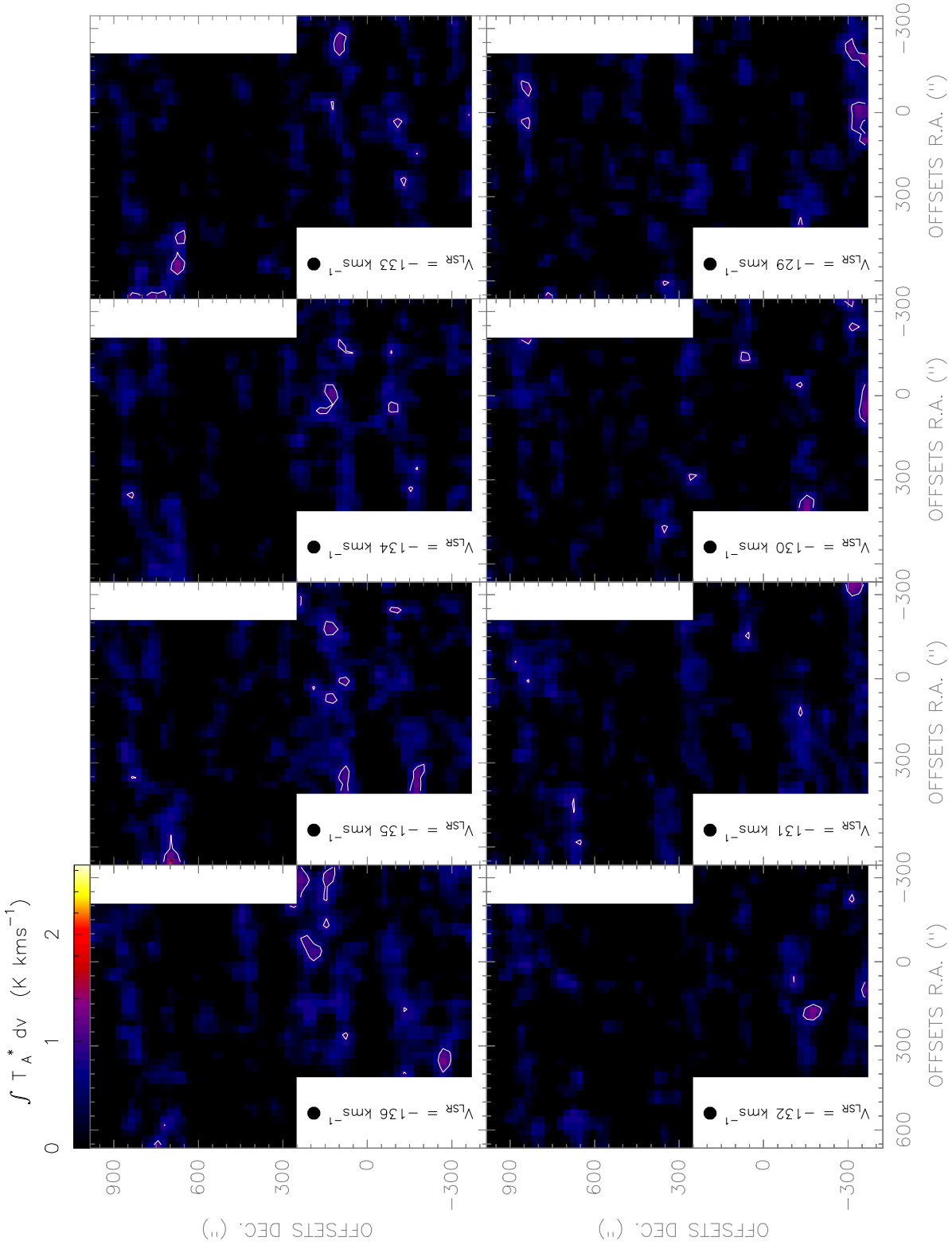

Figure. F.162: *[NII] line observed with the Herschel-HIFI satellite in Equatorial (J2000) coordinates. The spatial resolution of the maps is 46".*

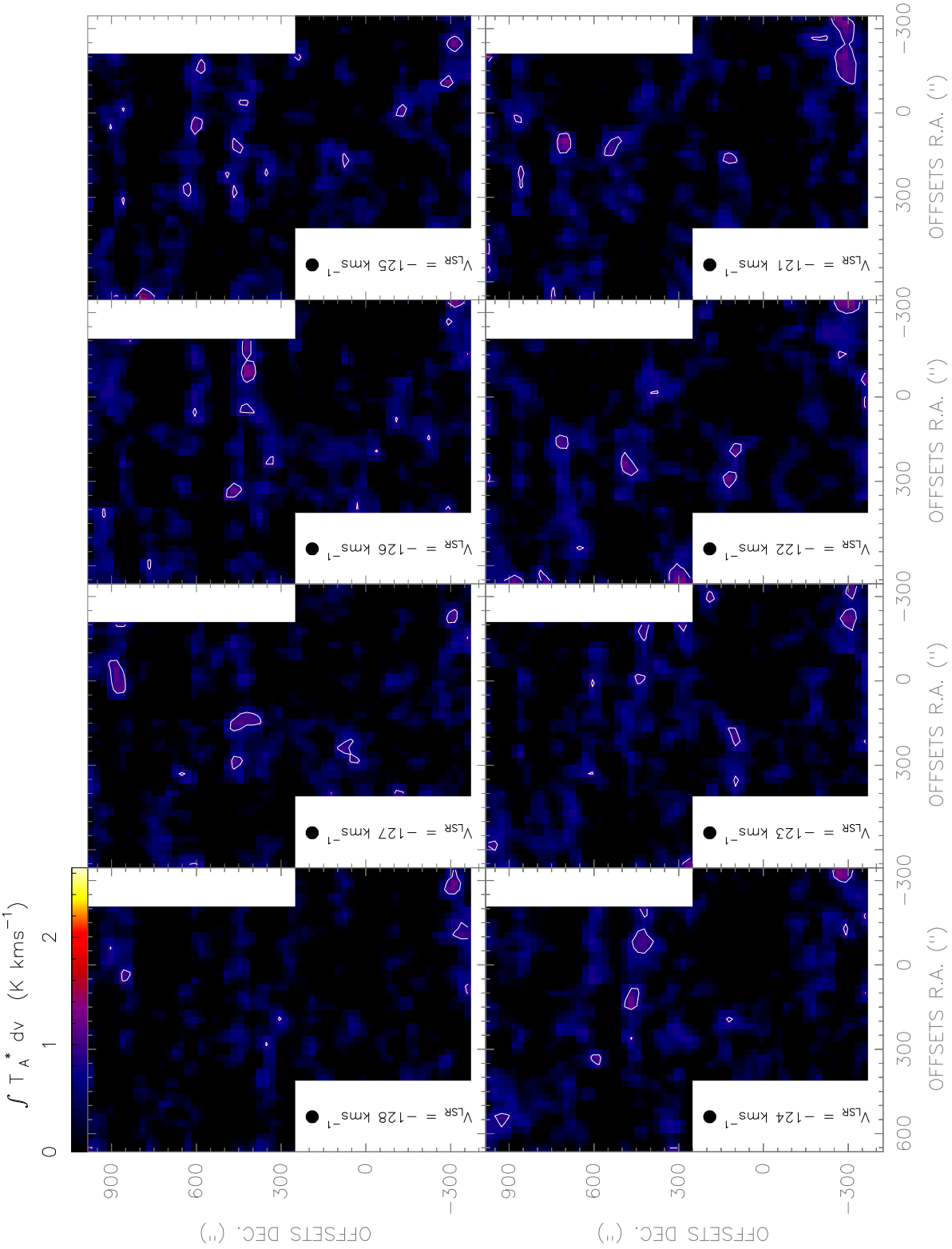

Figure. F.163: *[NII] line observed with the Herschel-HIFI satellite in Equatorial (J2000) coordinates. The spatial resolution of the maps is 46".*

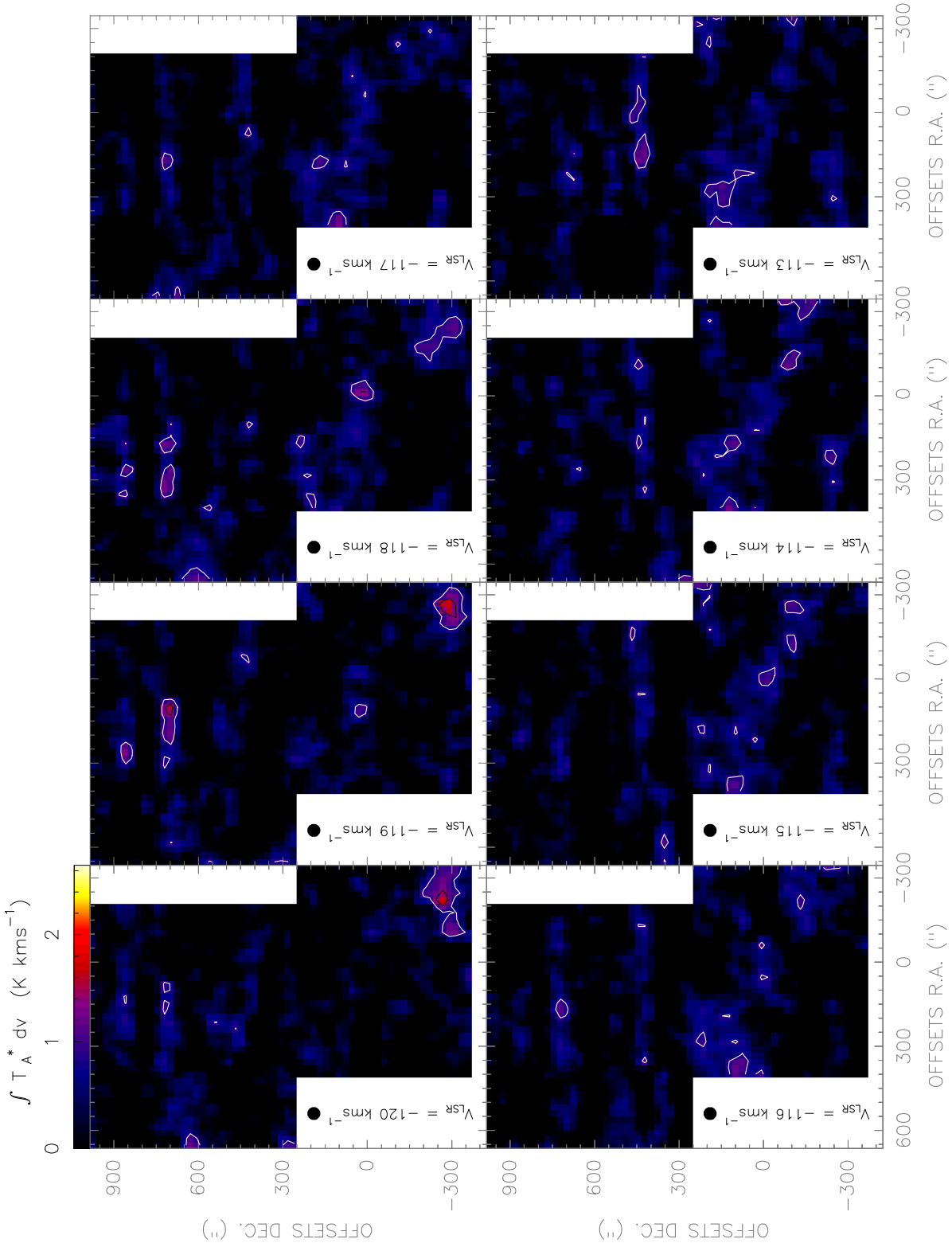

Figure. F.164: *[NII] line observed with the Herschel-HIFI satellite in Equatorial (J2000) coordinates. The spatial resolution of the maps is 46".*

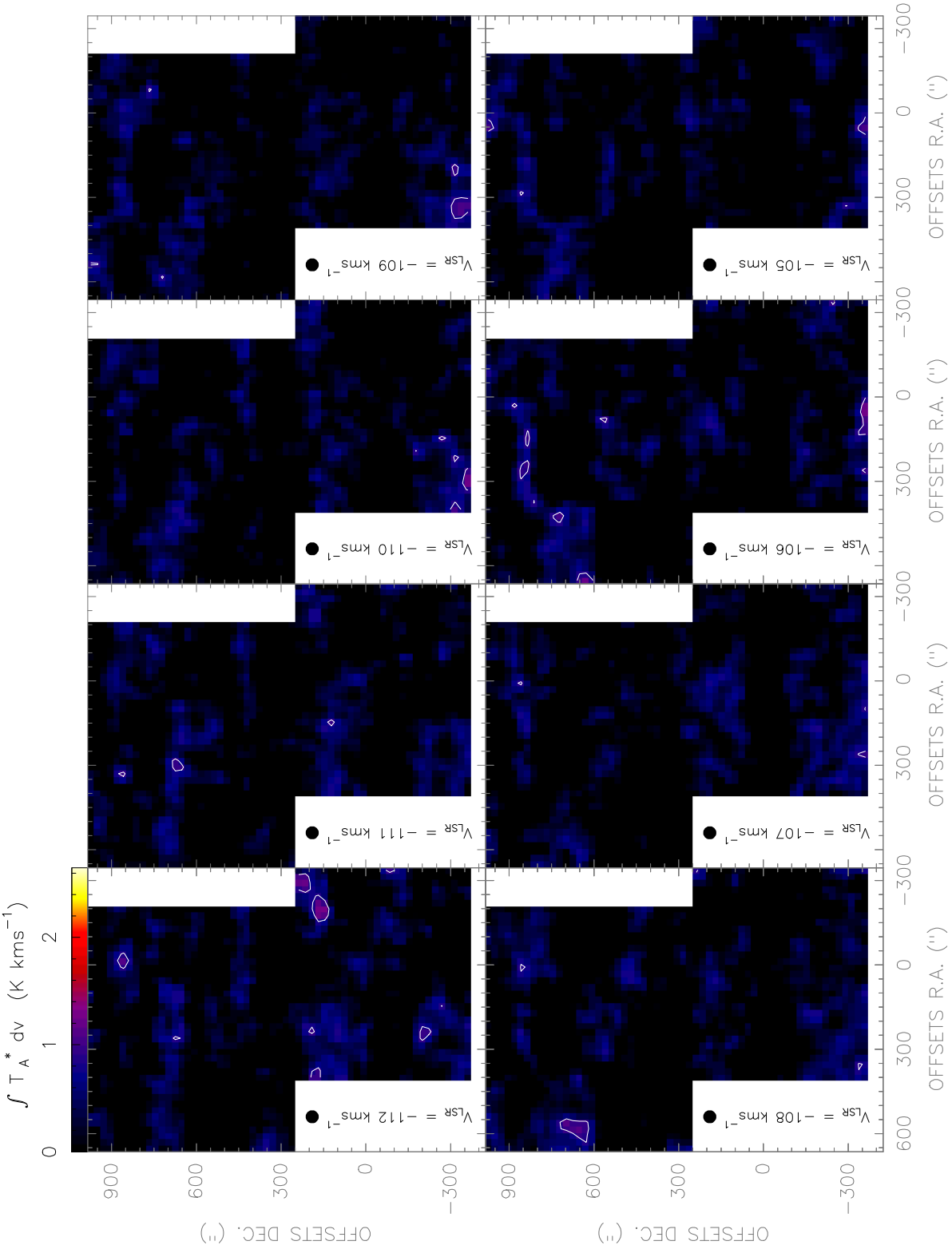

Figure. F.165: *[NII] line observed with the Herschel-HIFI satellite in Equatorial (J2000) coordinates. The spatial resolution of the maps is 46".*

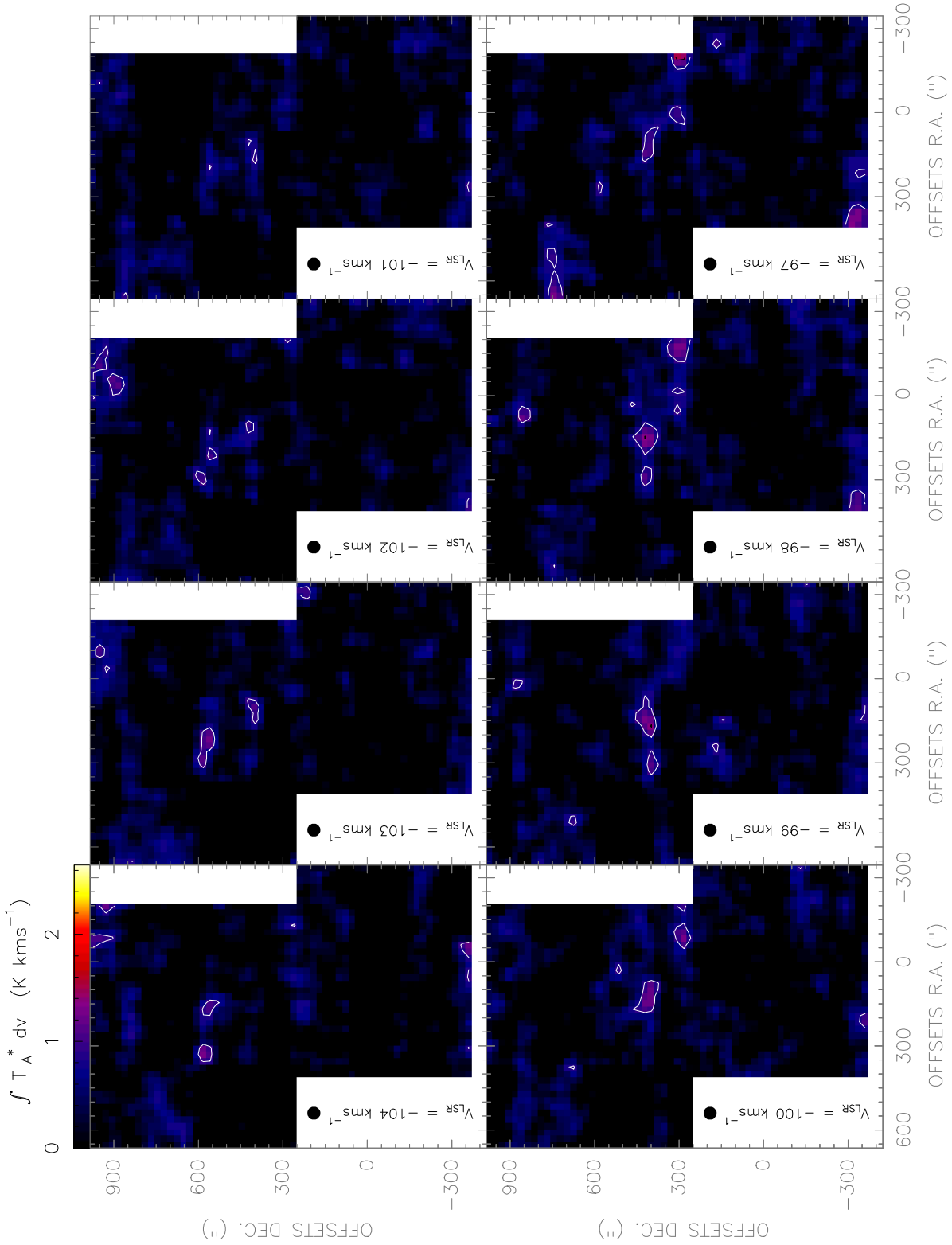

Figure. F.166: *[NII] line observed with the Herschel-HIFI satellite in Equatorial (J2000) coordinates. The spatial resolution of the maps is 46".*

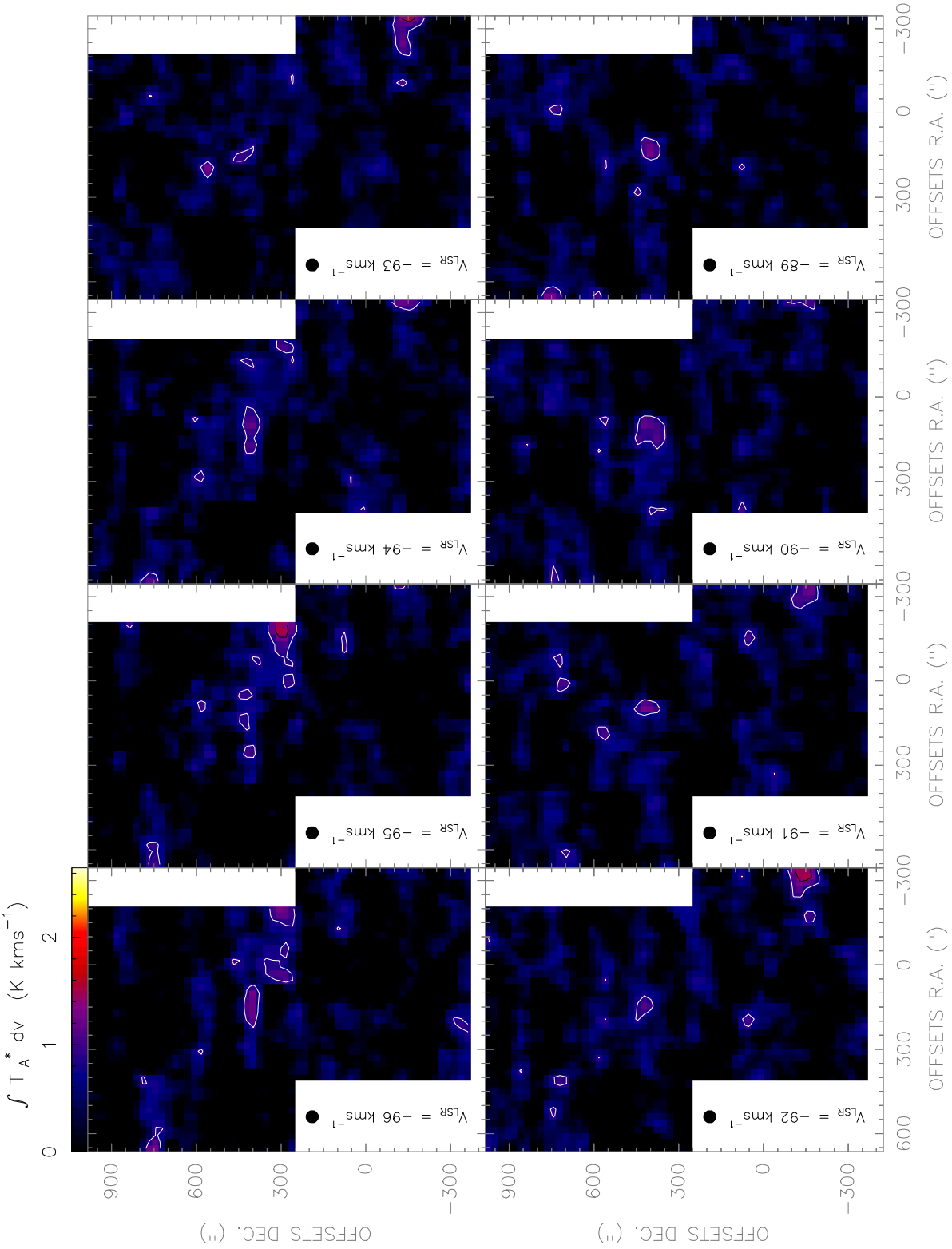

Figure. F.167: *[NII] line observed with the Herschel-HIFI satellite in Equatorial (J2000) coordinates. The spatial resolution of the maps is 46".*

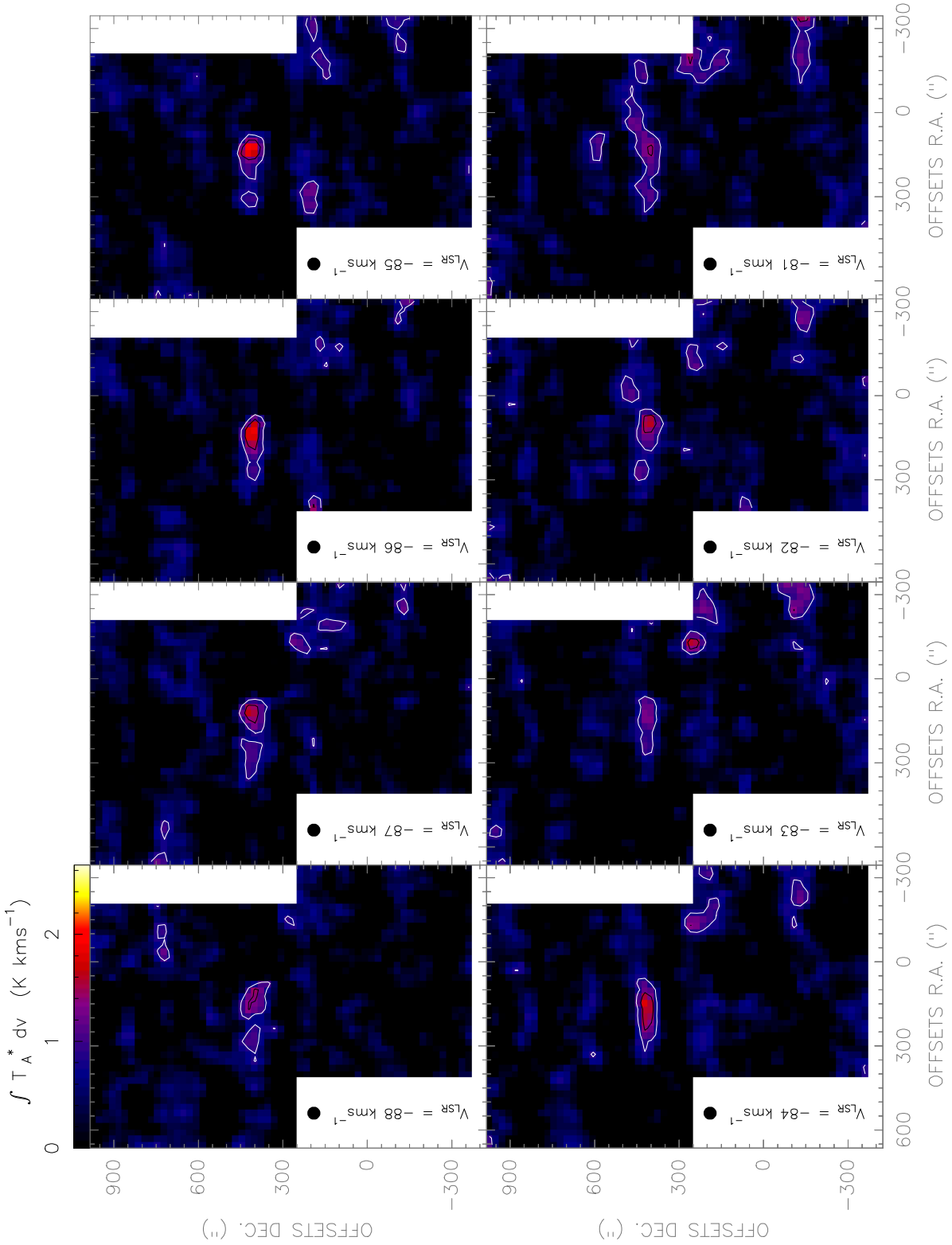

Figure. F.168: *[NII] line observed with the Herschel-HIFI satellite in Equatorial (J2000) coordinates. The spatial resolution of the maps is 46".*

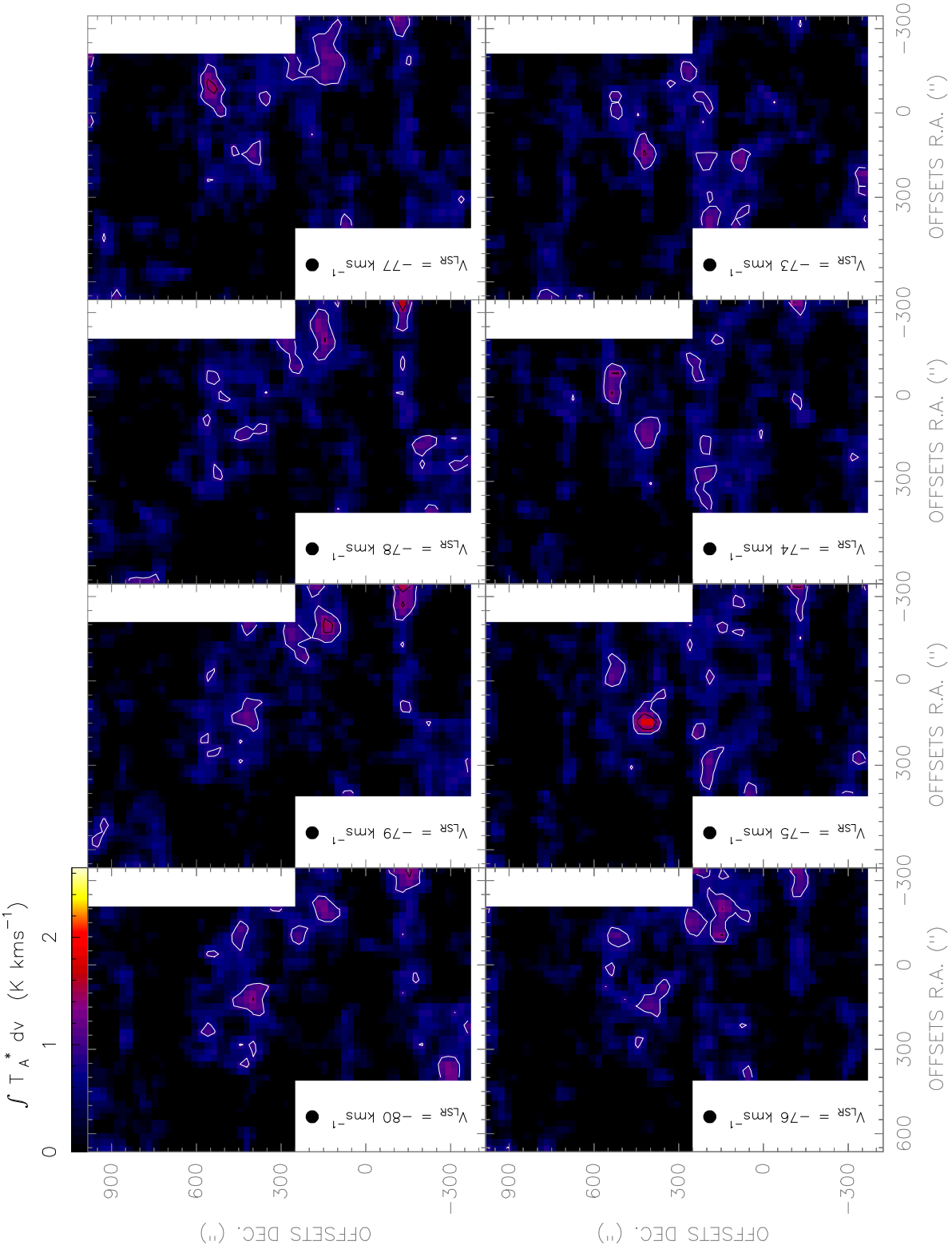

Figure. F.169: *[NII] line observed with the Herschel-HIFI satellite in Equatorial (J2000) coordinates. The spatial resolution of the maps is 46".*

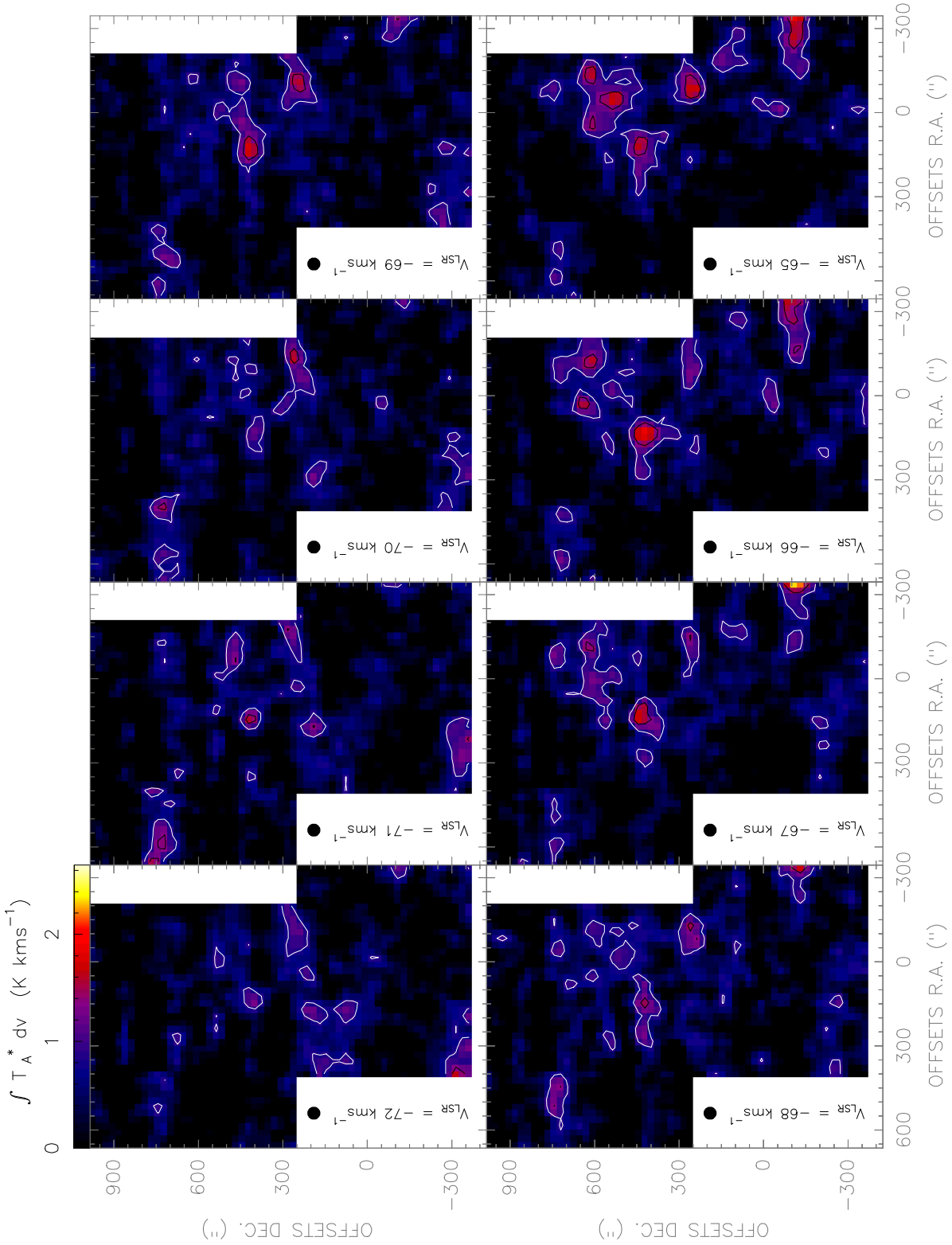

Figure. F.170: *[NII] line observed with the Herschel-HIFI satellite in Equatorial (J2000) coordinates. The spatial resolution of the maps is 46".*

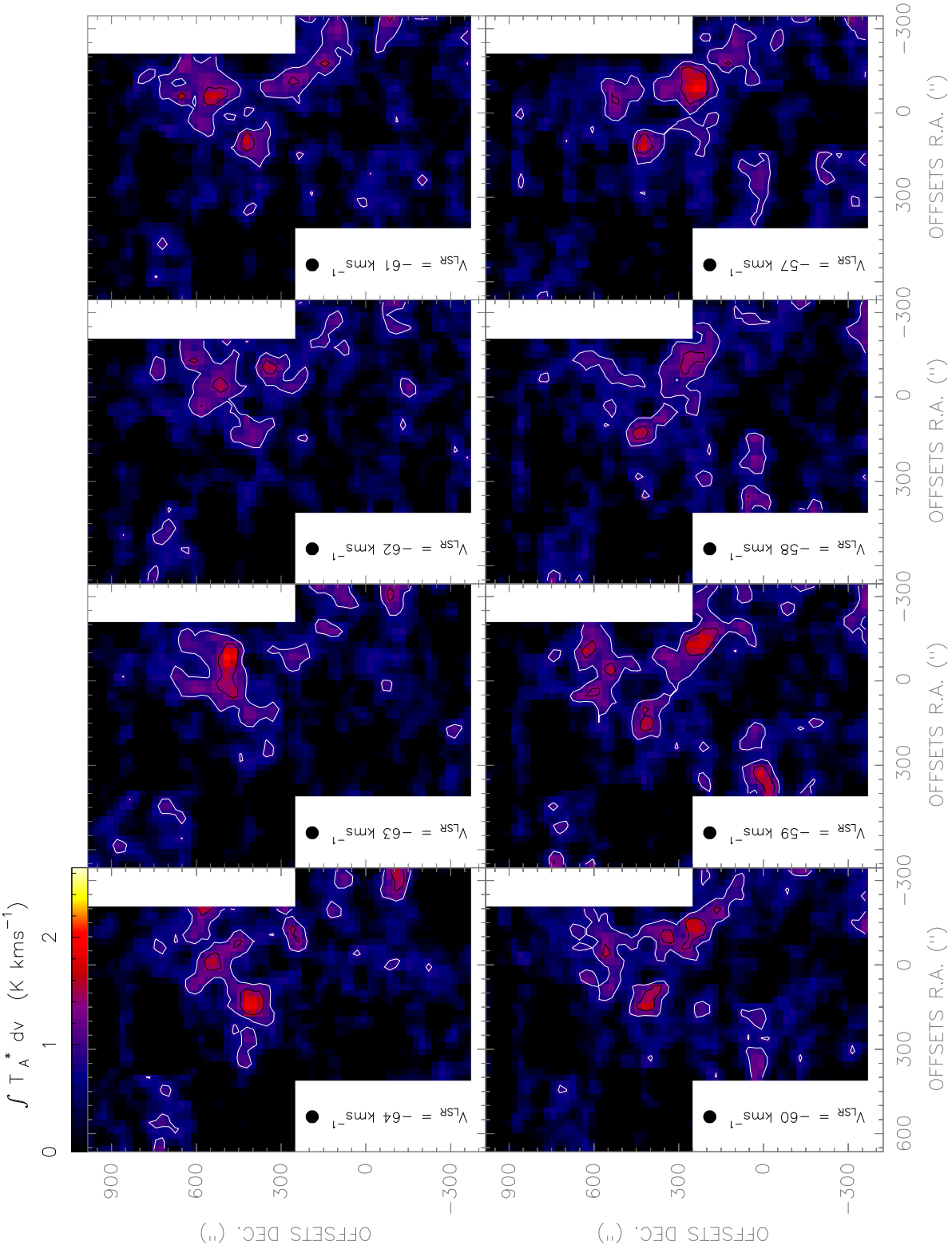

Figure. F.171: *[NII] line observed with the Herschel-HIFI satellite in Equatorial (J2000) coordinates. The spatial resolution of the maps is 46".*

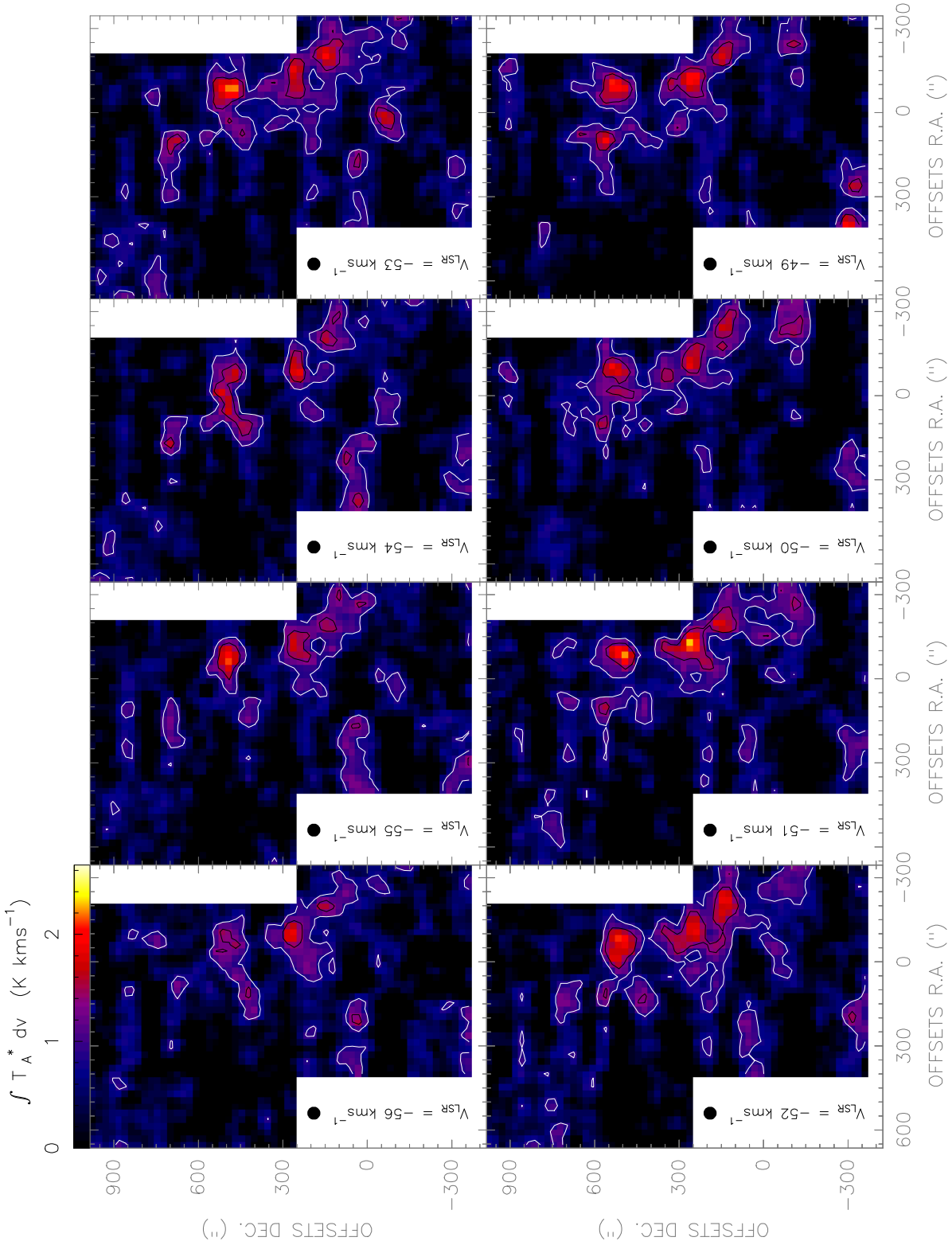

Figure. F.172: *[NII] line observed with the Herschel-HIFI satellite in Equatorial (J2000) coordinates. The spatial resolution of the maps is 46".*

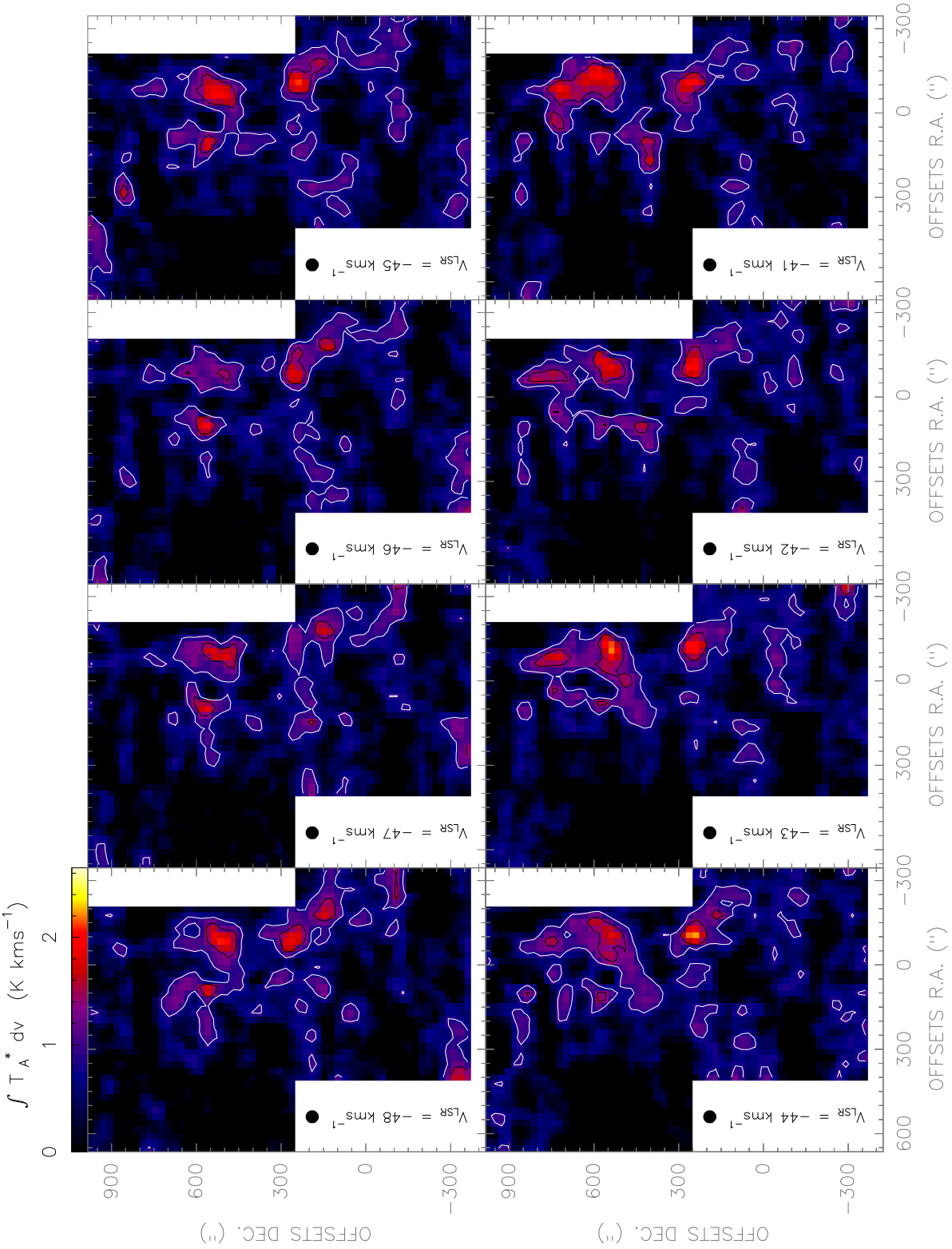

Figure. F.173: *[NII] line observed with the Herschel-HIFI satellite in Equatorial (J2000) coordinates. The spatial resolution of the maps is 46".*

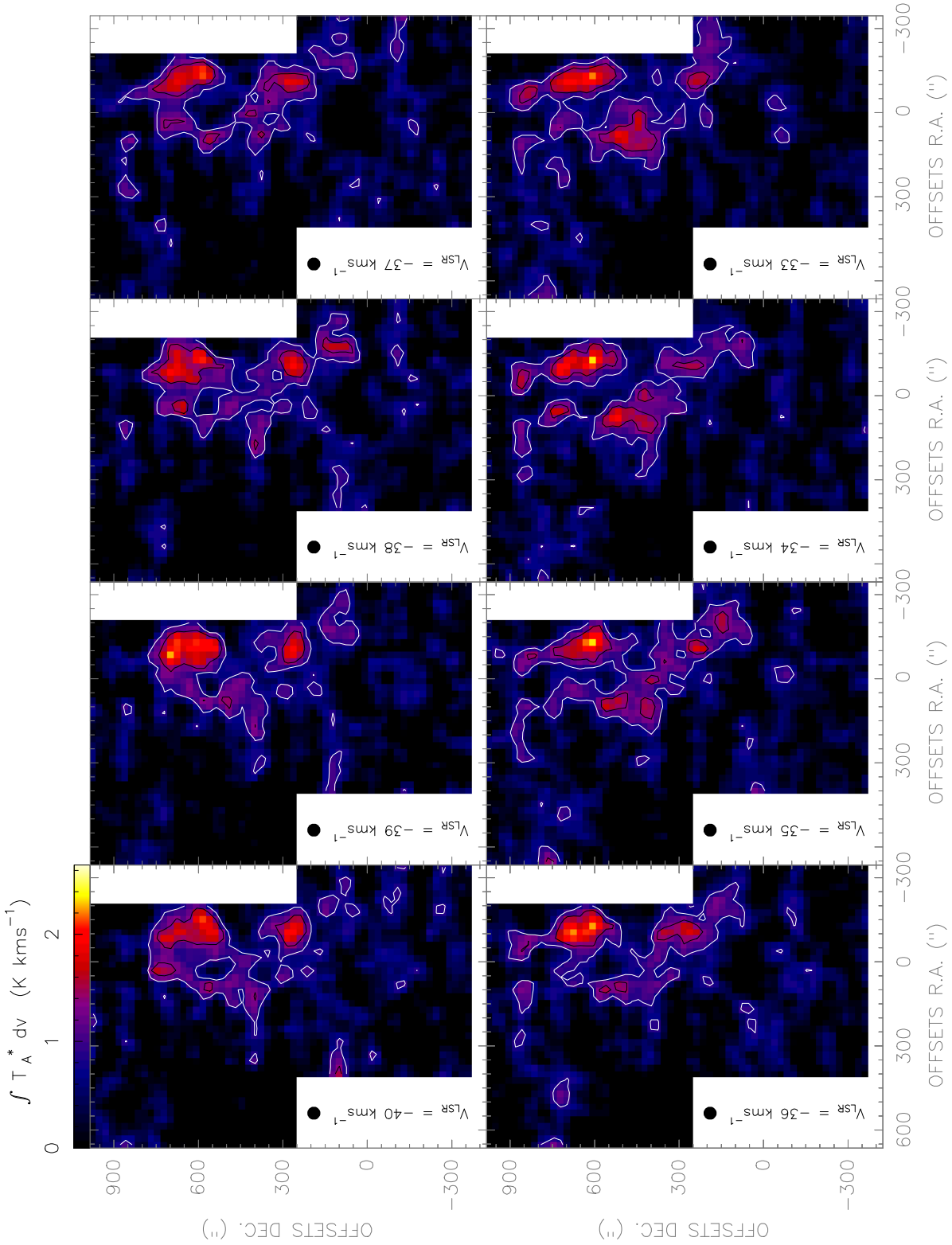

Figure. F.174: *[NII] line observed with the Herschel-HIFI satellite in Equatorial (J2000) coordinates. The spatial resolution of the maps is 46".*

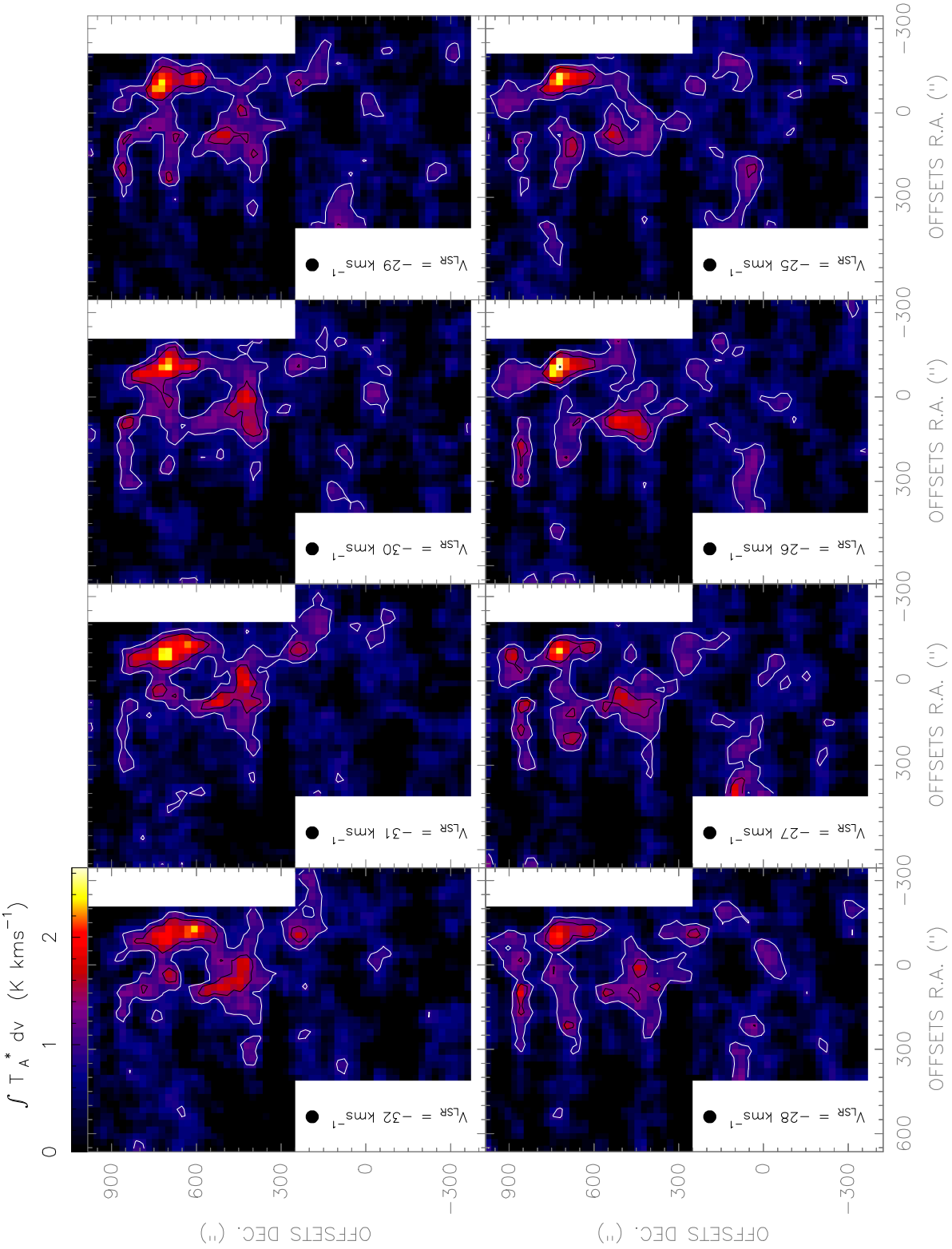

Figure. F.175: *[NII] line observed with the Herschel-HIFI satellite in Equatorial (J2000) coordinates. The spatial resolution of the maps is 46".*

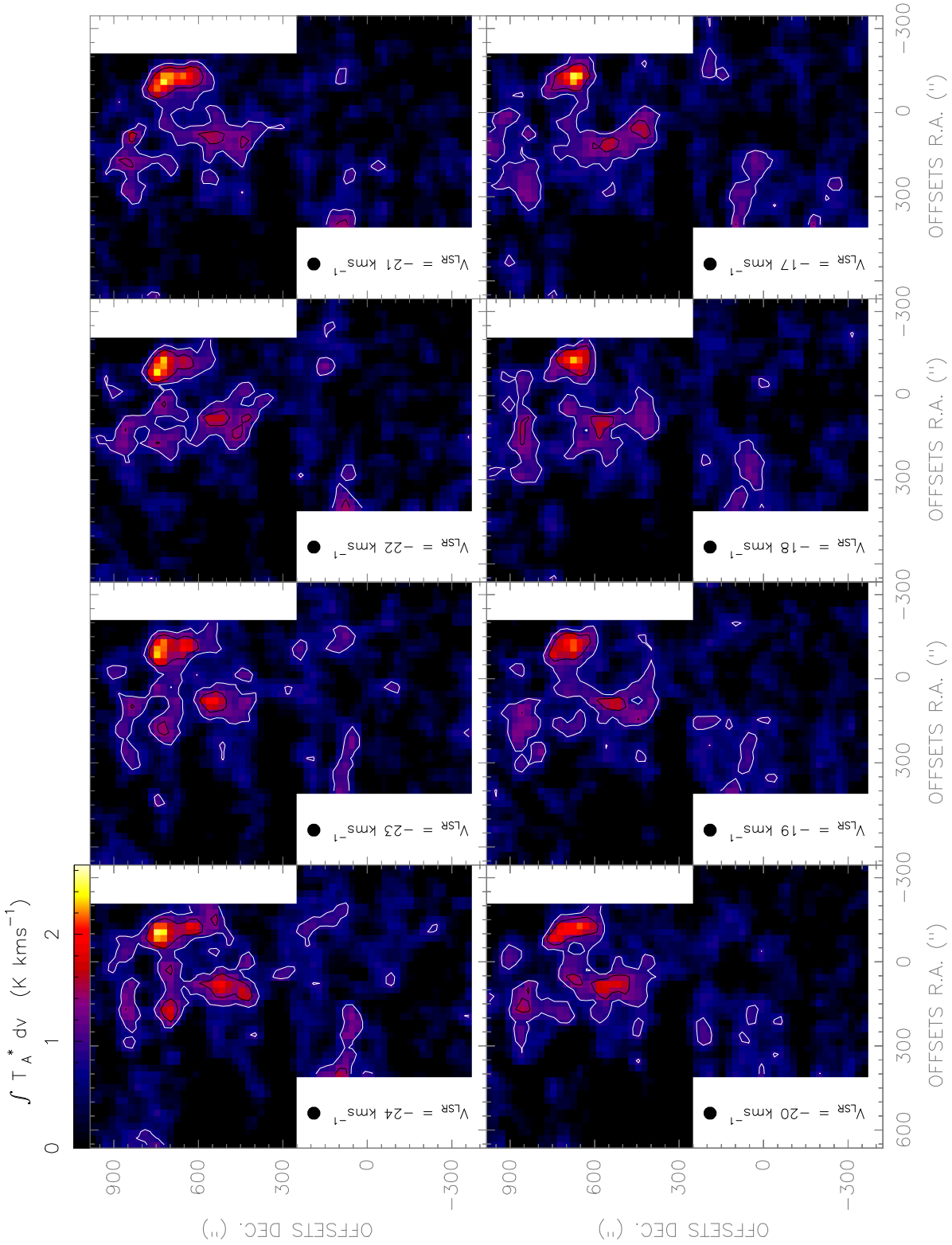

Figure. F.176: *[NII] line observed with the Herschel-HIFI satellite in Equatorial (J2000) coordinates. The spatial resolution of the maps is 46".*

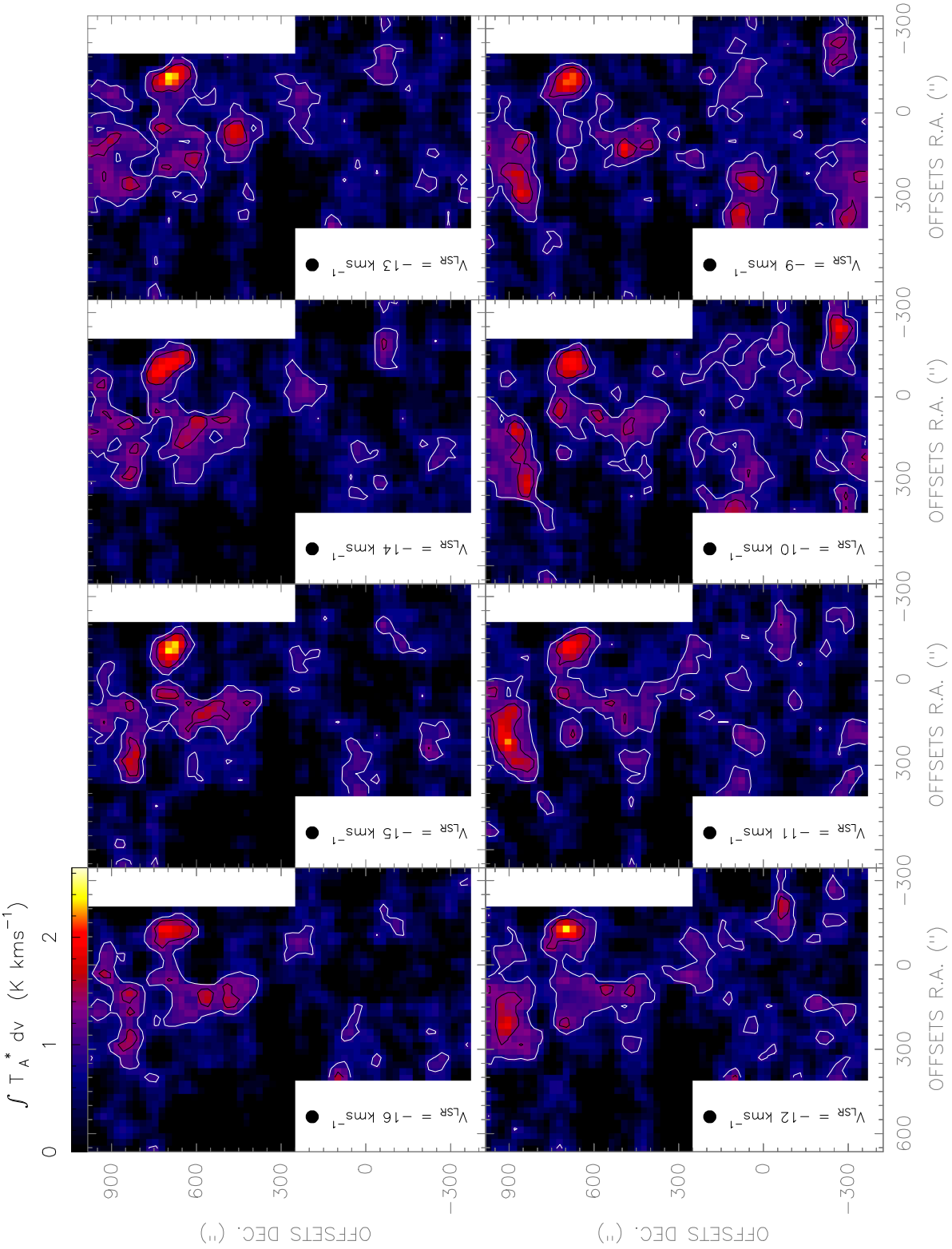

Figure. F.177: *[NII] line observed with the Herschel-HIFI satellite in Equatorial (J2000) coordinates. The spatial resolution of the maps is 46".*

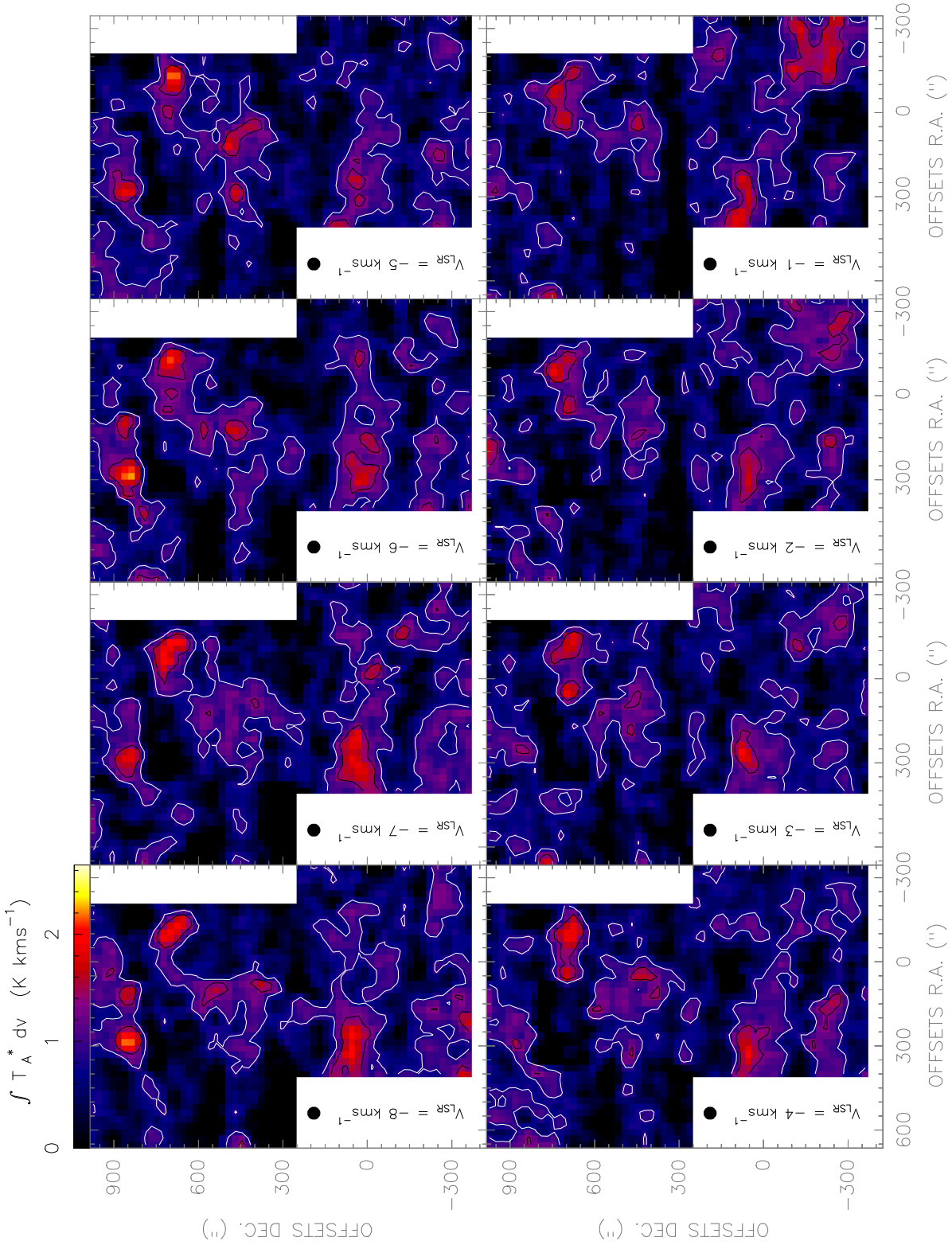

Figure. F.178: *[NII] line observed with the Herschel-HIFI satellite in Equatorial (J2000) coordinates. The spatial resolution of the maps is 46".*

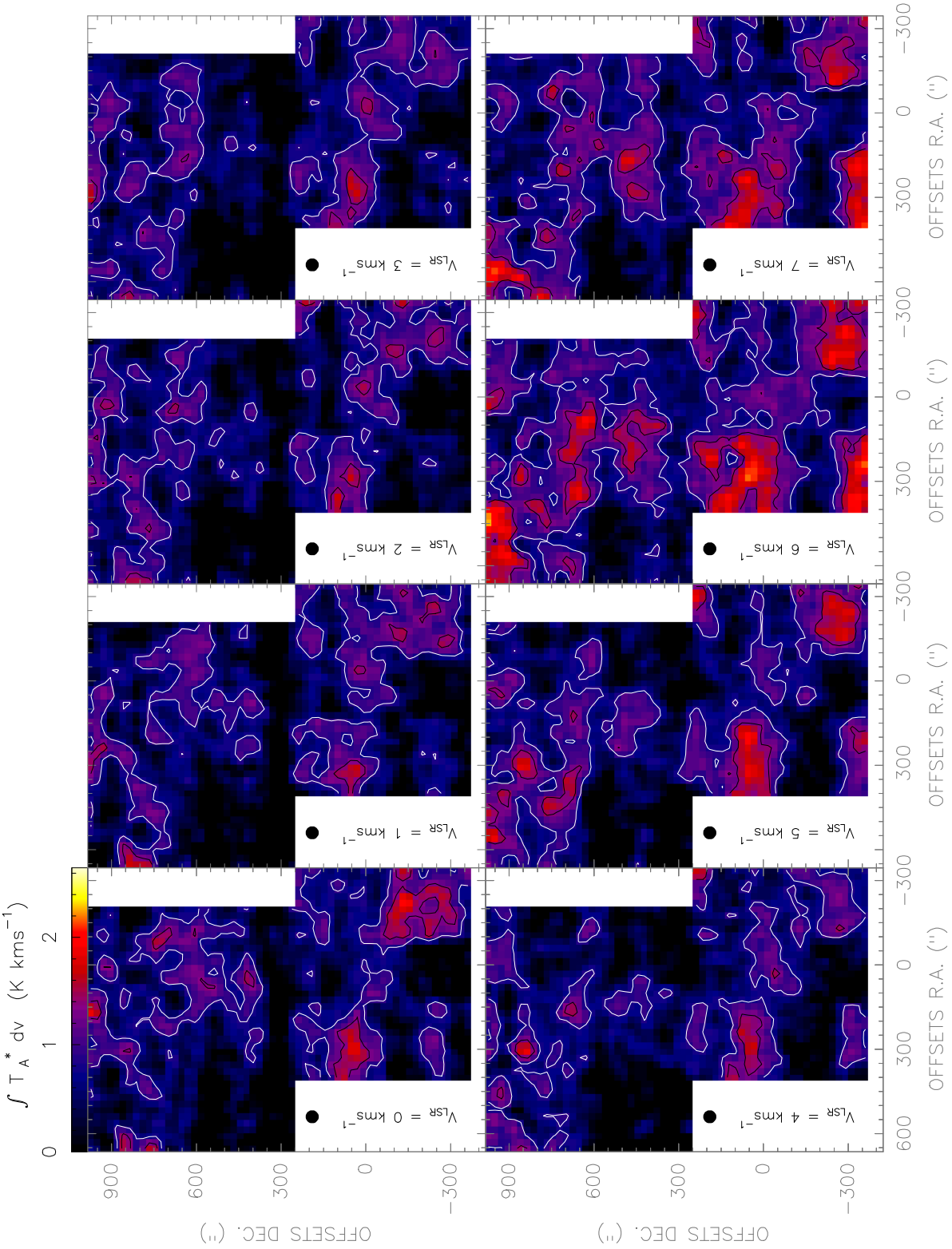

Figure. F.179: *[NII] line observed with the Herschel-HIFI satellite in Equatorial (J2000) coordinates. The spatial resolution of the maps is 46".*

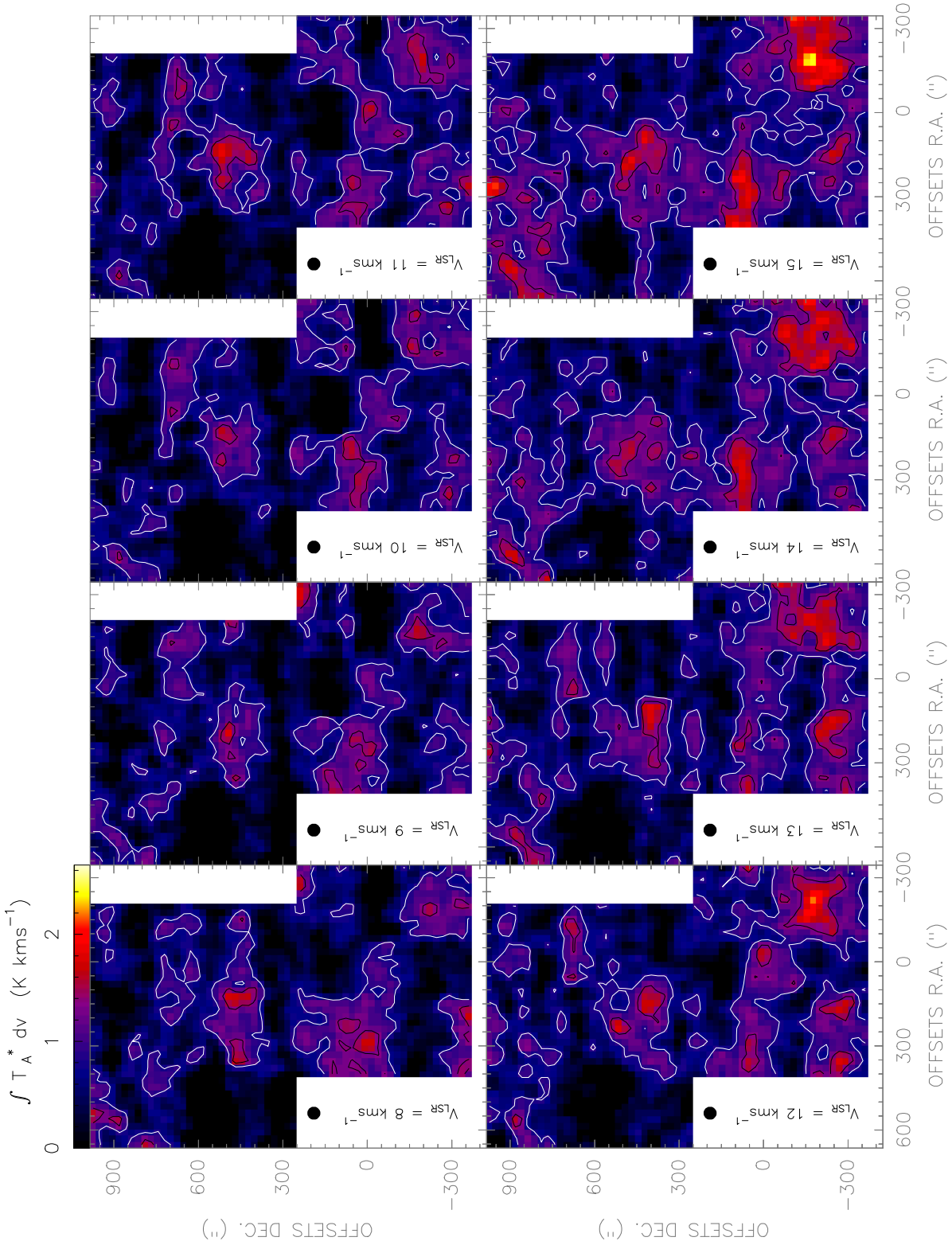

Figure. F.180: *[NII] line observed with the Herschel-HIFI satellite in Equatorial (J2000) coordinates. The spatial resolution of the maps is 46".*

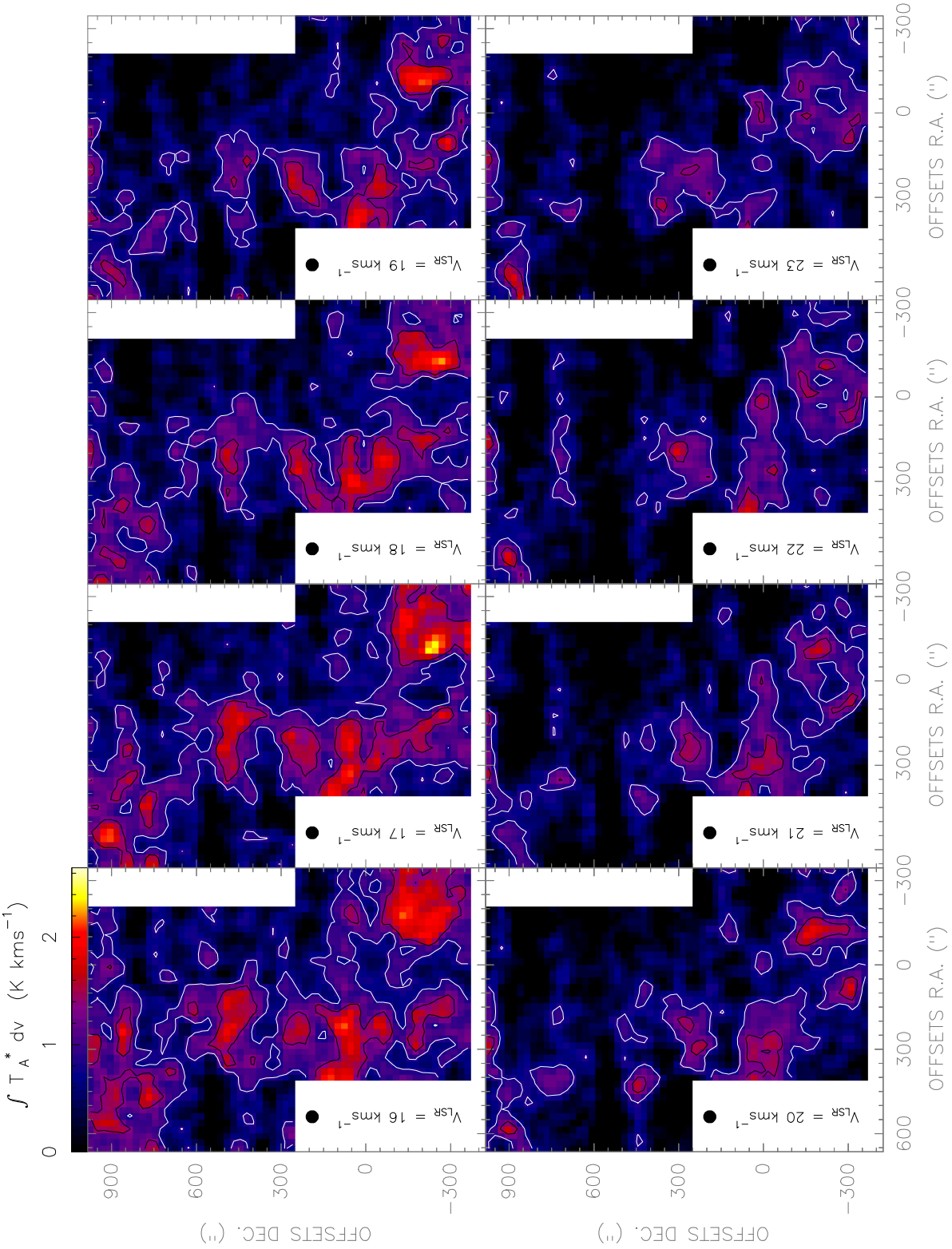

Figure. F.181: *[NII] line observed with the Herschel-HIFI satellite in Equatorial (J2000) coordinates. The spatial resolution of the maps is 46".*

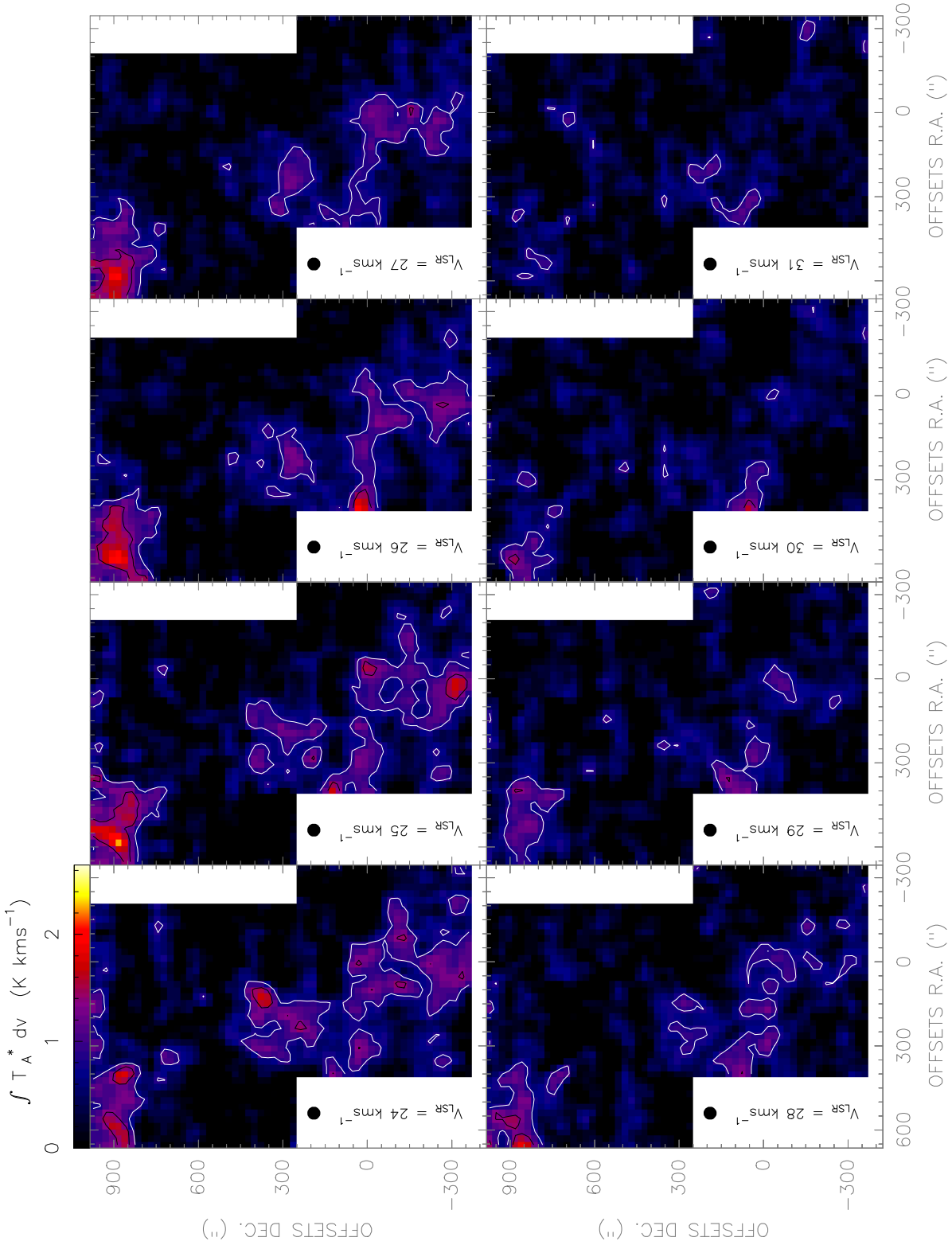

Figure. F.182: *[NII] line observed with the Herschel-HIFI satellite in Equatorial (J2000) coordinates. The spatial resolution of the maps is 46".*

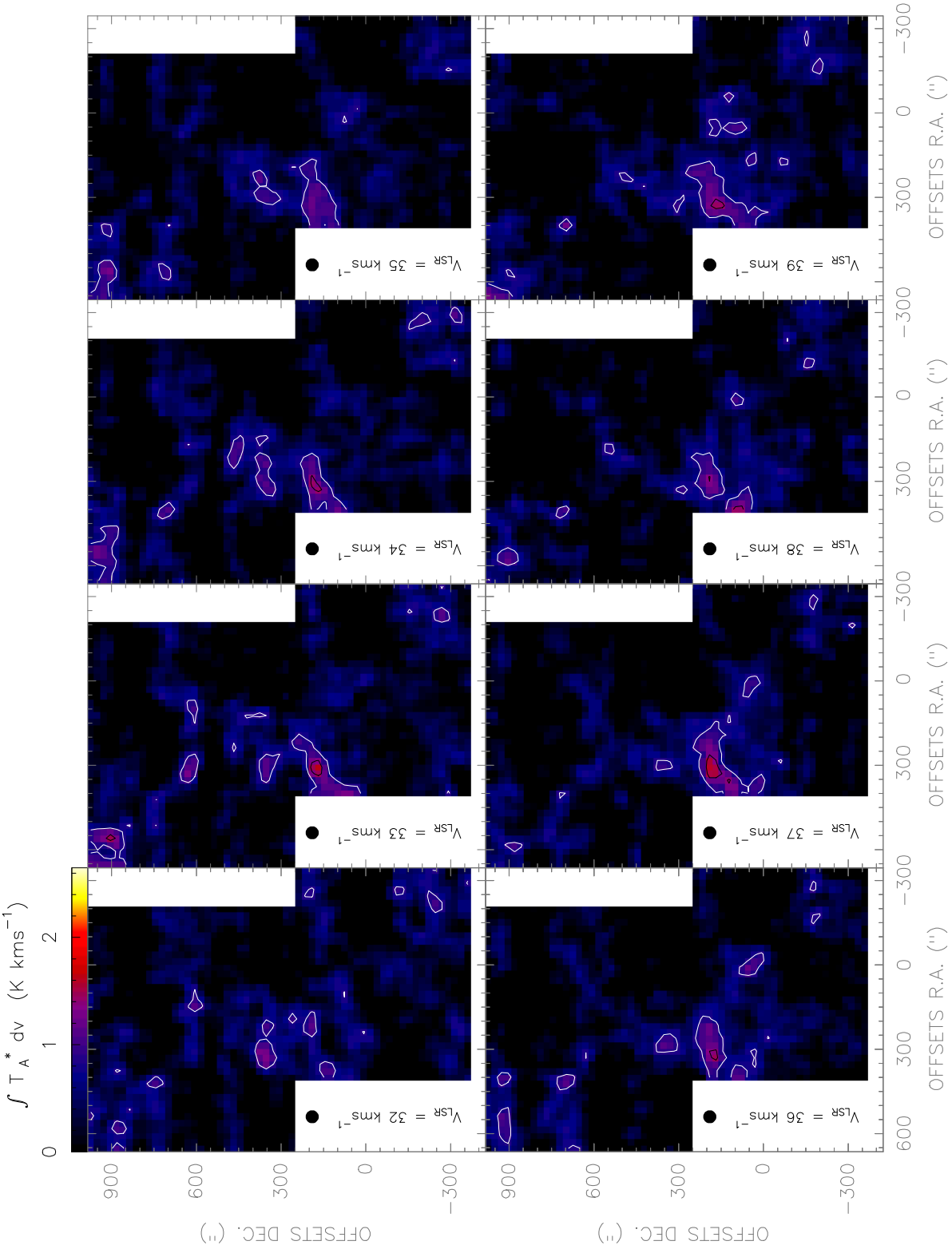

Figure. F.183: *[NII] line observed with the Herschel-HIFI satellite in Equatorial (J2000) coordinates. The spatial resolution of the maps is 46".*

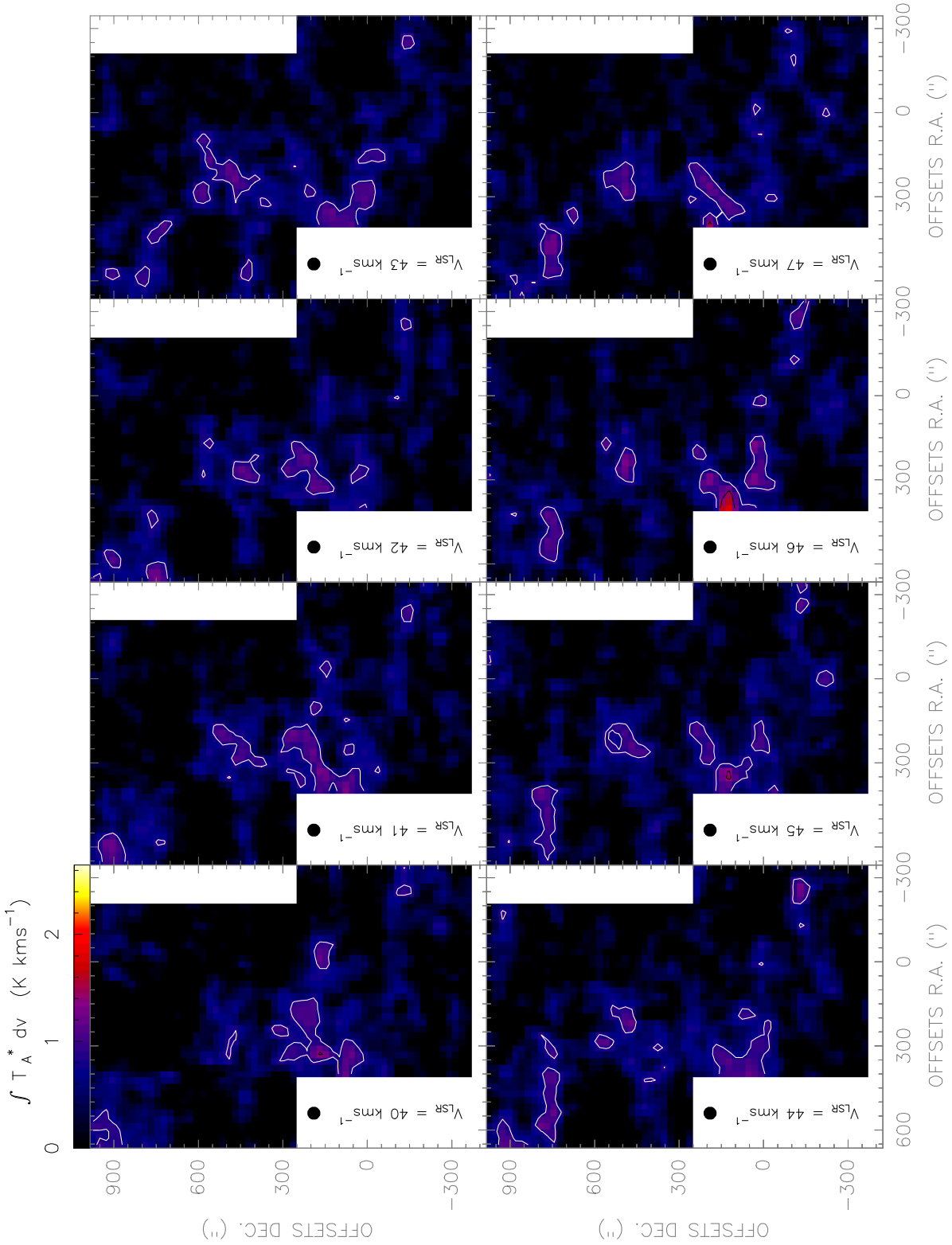

Figure. F.184: *[NII] line observed with the Herschel-HIFI satellite in Equatorial (J2000) coordinates. The spatial resolution of the maps is 46".*

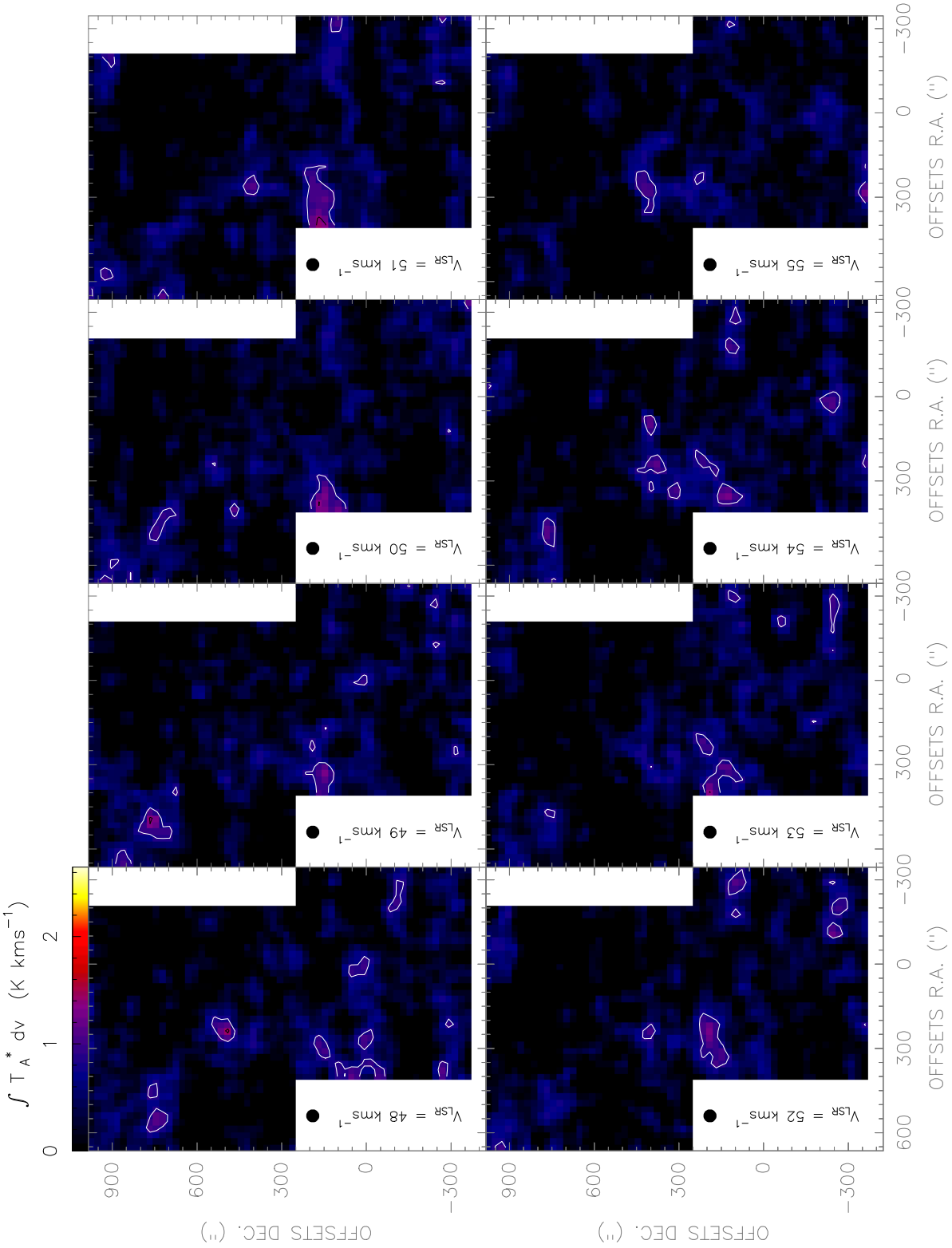

Figure. F.185: *[NII] line observed with the Herschel-HIFI satellite in Equatorial (J2000) coordinates. The spatial resolution of the maps is 46".*

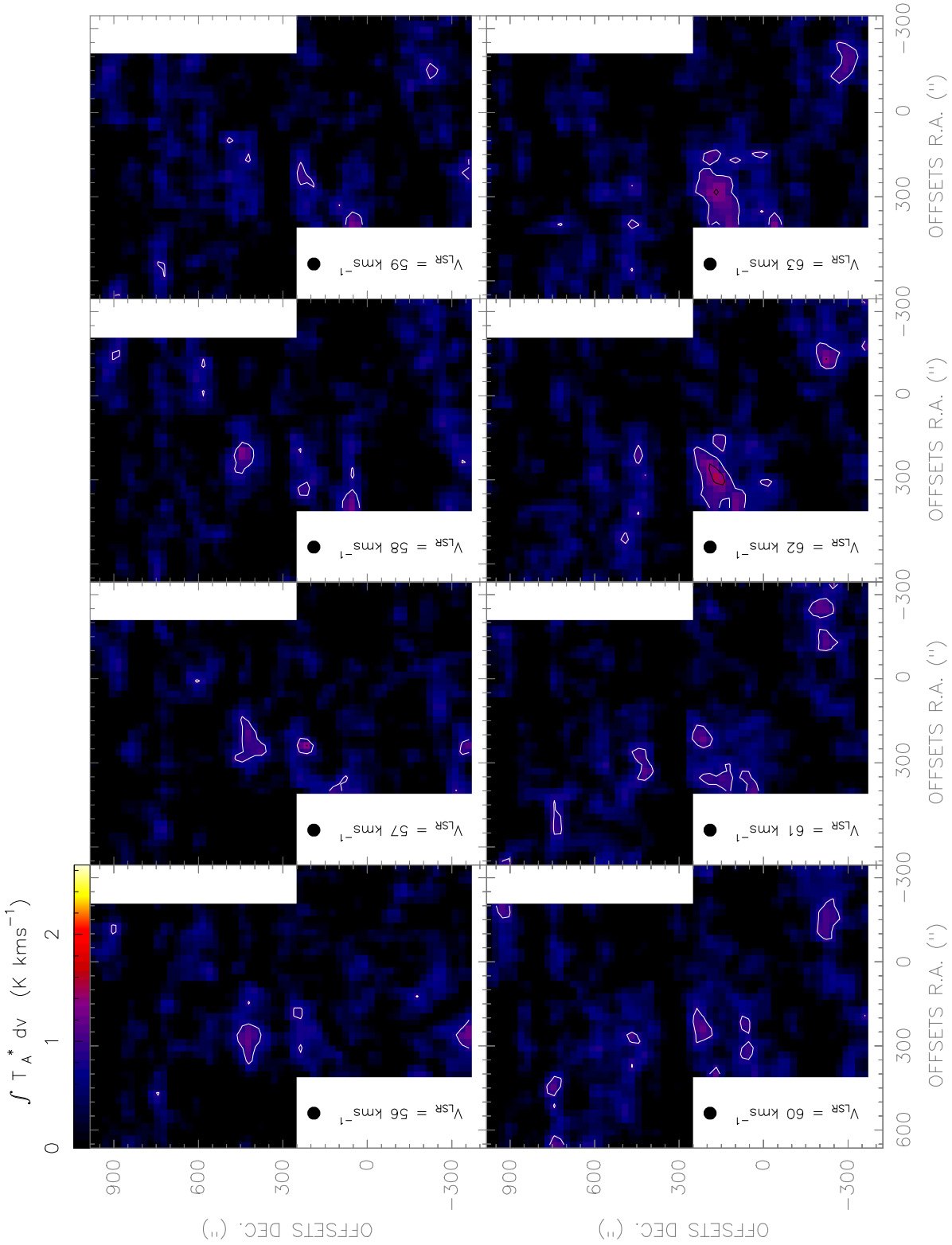

Figure. F.186: *[NII] line observed with the Herschel-HIFI satellite in Equatorial (J2000) coordinates. The spatial resolution of the maps is 46".*

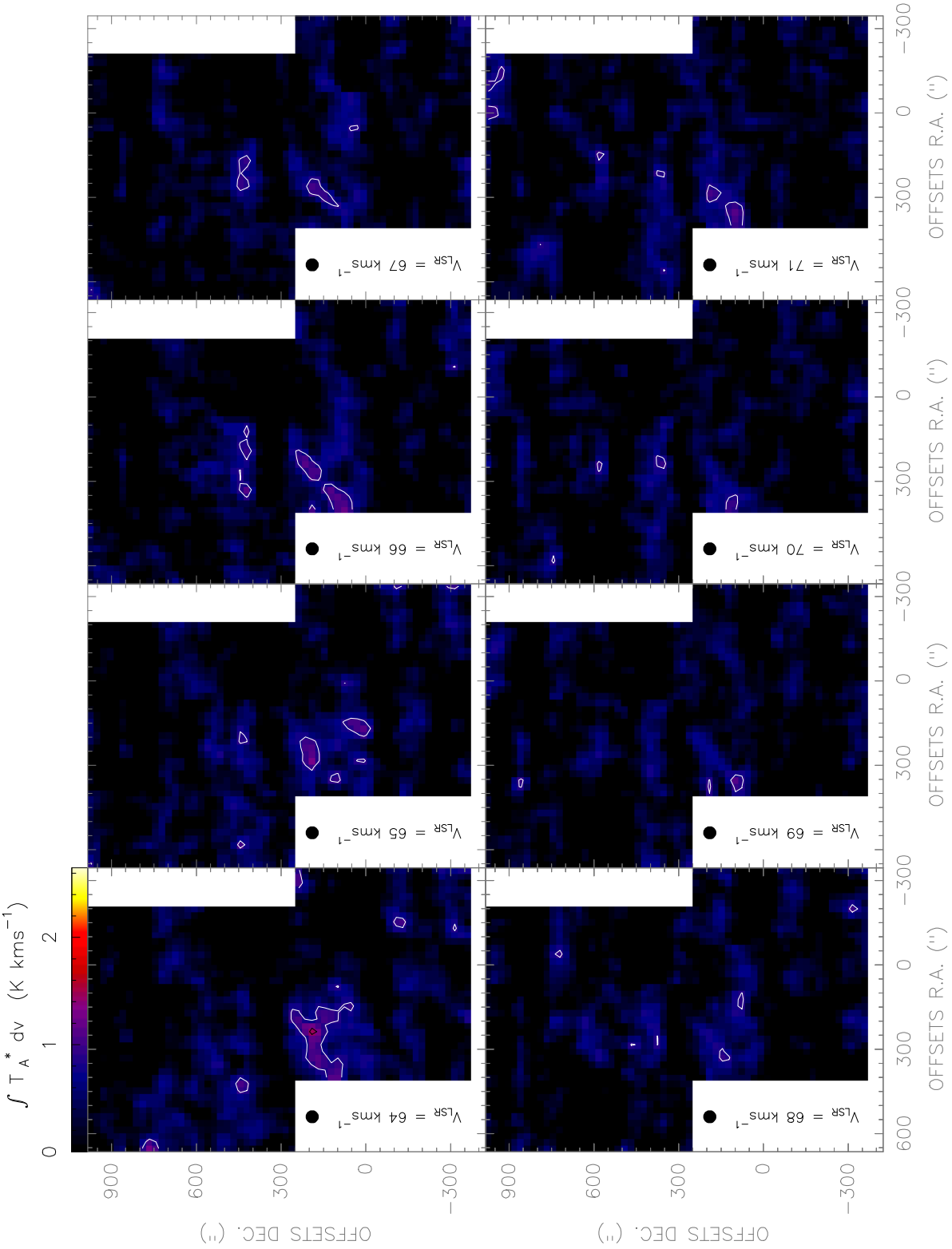

Figure. F.187: *[NII] line observed with the Herschel-HIFI satellite in Equatorial (J2000) coordinates. The spatial resolution of the maps is 46".*

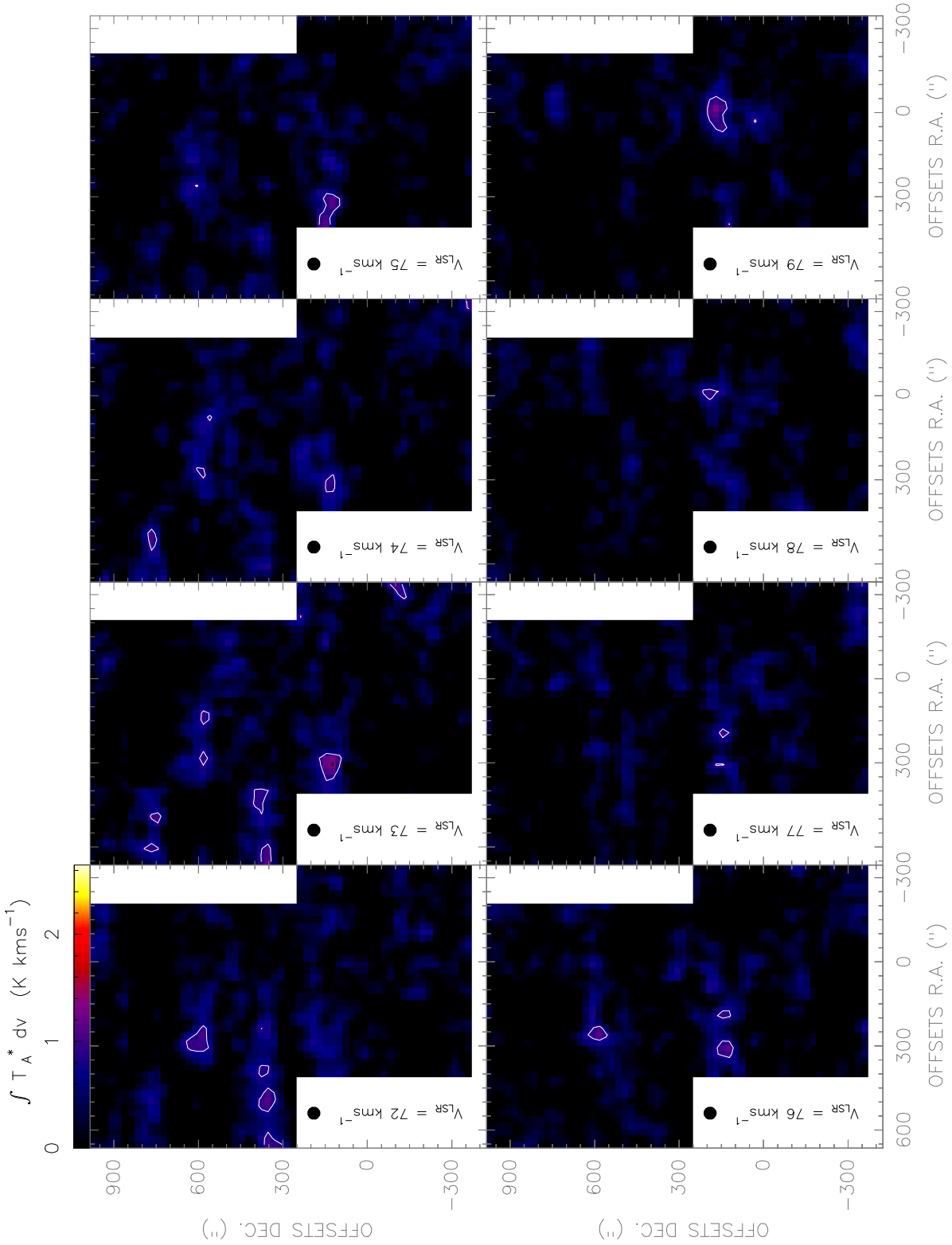

Figure. F.188: *[NII] line observed with the Herschel-HIFI satellite in Equatorial (J2000) coordinates. The spatial resolution of the maps is 46".*

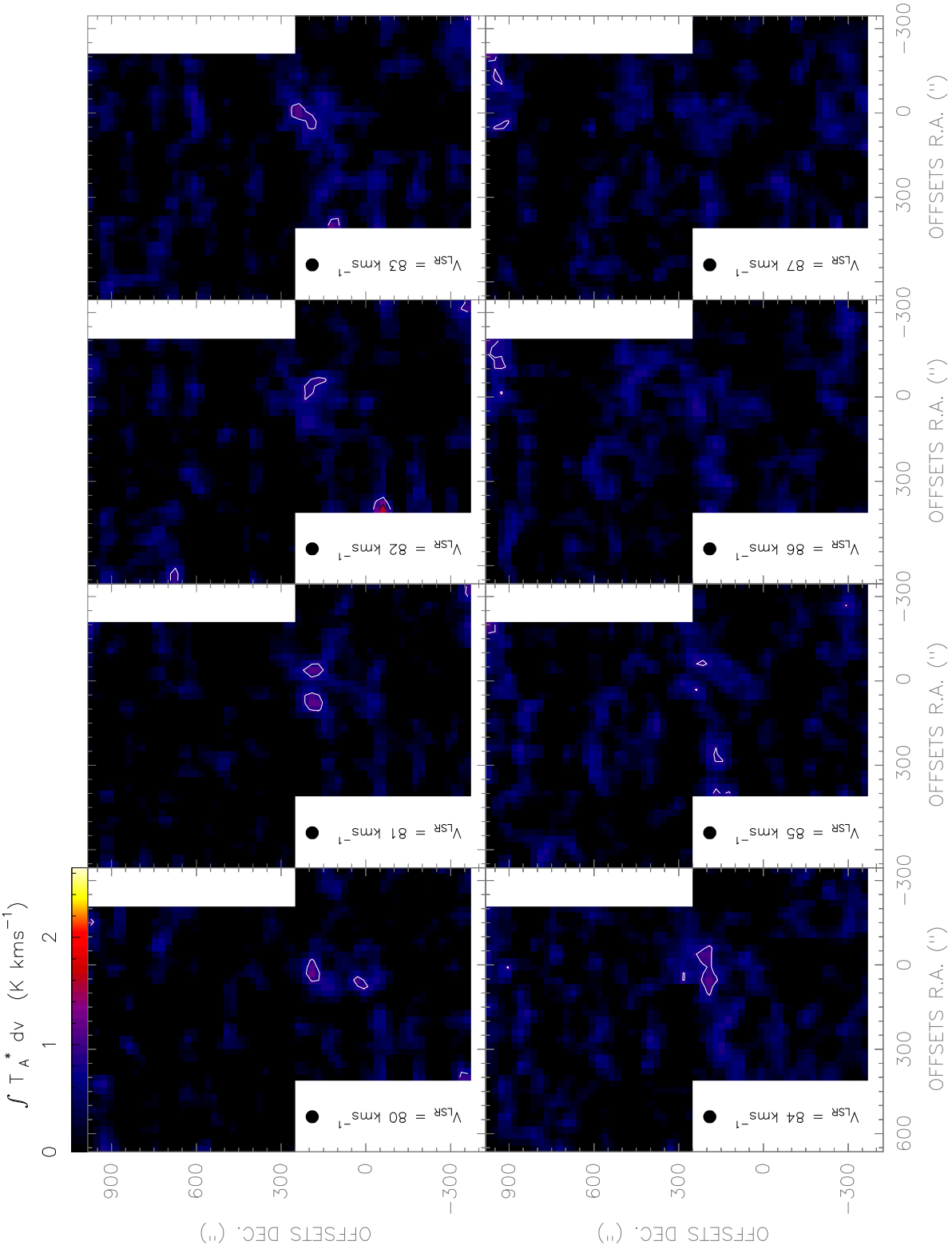

Figure. F.189: *[NII] line observed with the Herschel-HIFI satellite in Equatorial (J2000) coordinates. The spatial resolution of the maps is 46".*

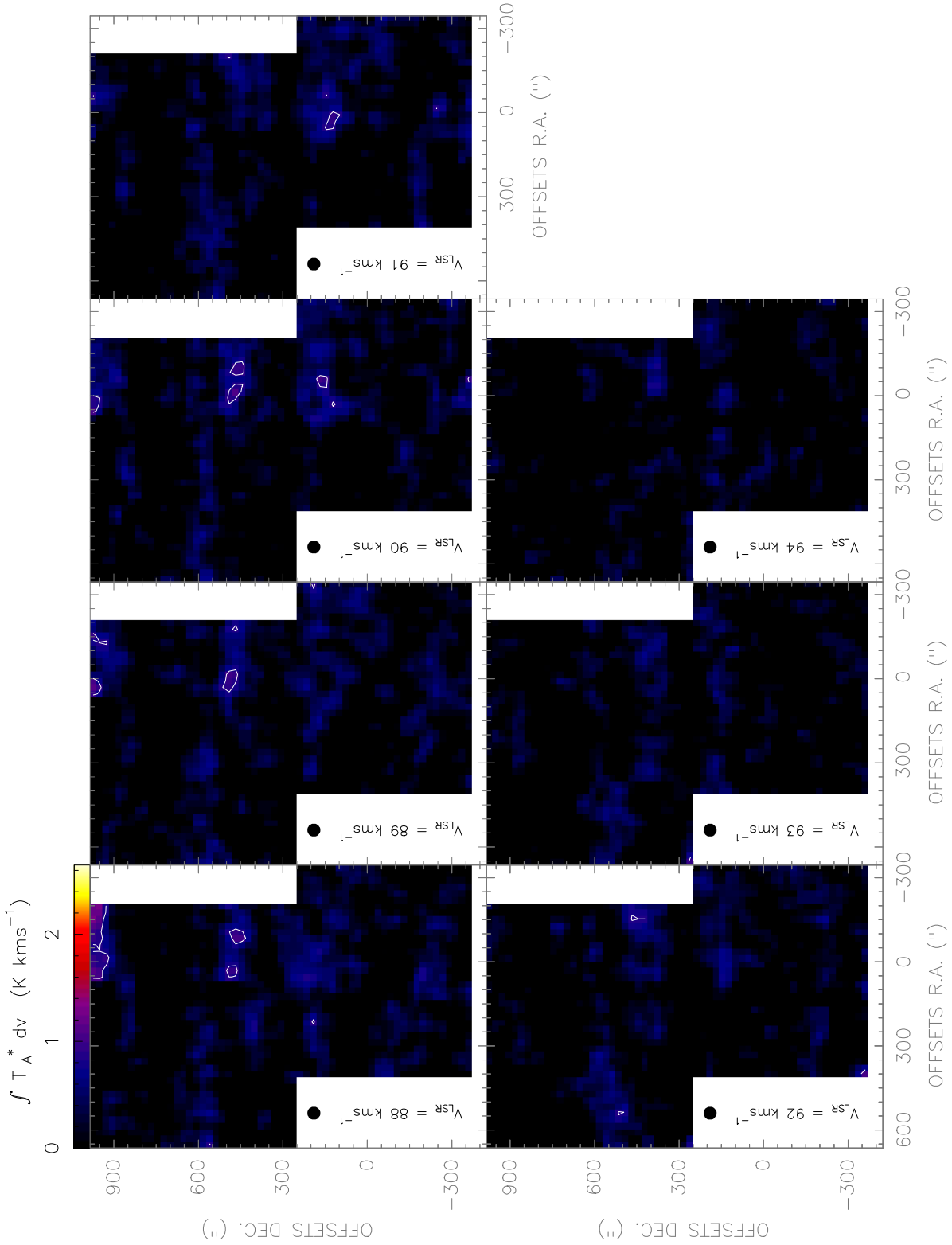

Figure. F.190: *[NII] line observed with the Herschel-HIFI satellite in Equatorial (J2000) coordinates. The spatial resolution of the maps is 46".*

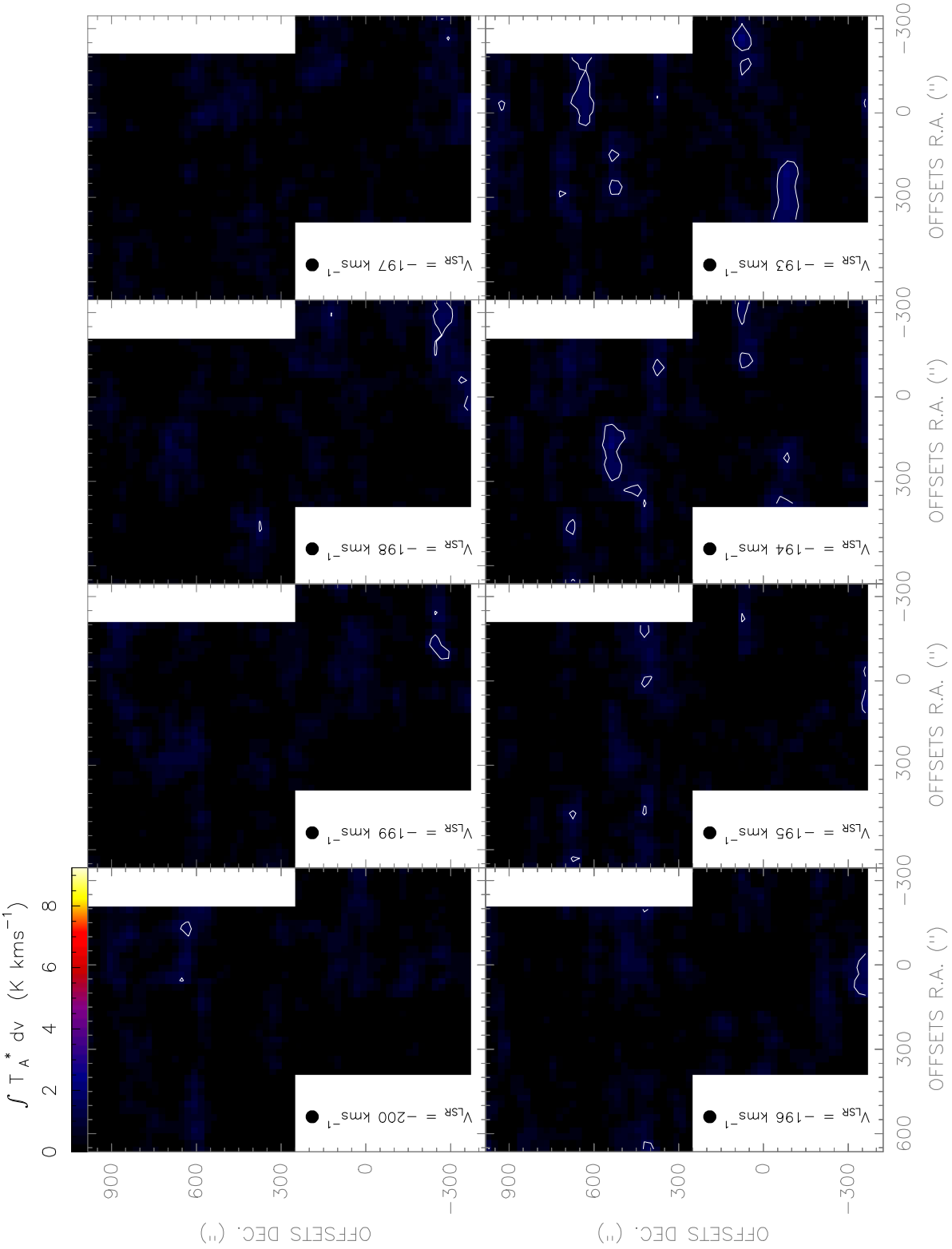

Figure. F.191: *[CII] line observed with the Herschel-HIFI satellite in Equatorial (J2000) coordinates. The spatial resolution of the maps is 46".*

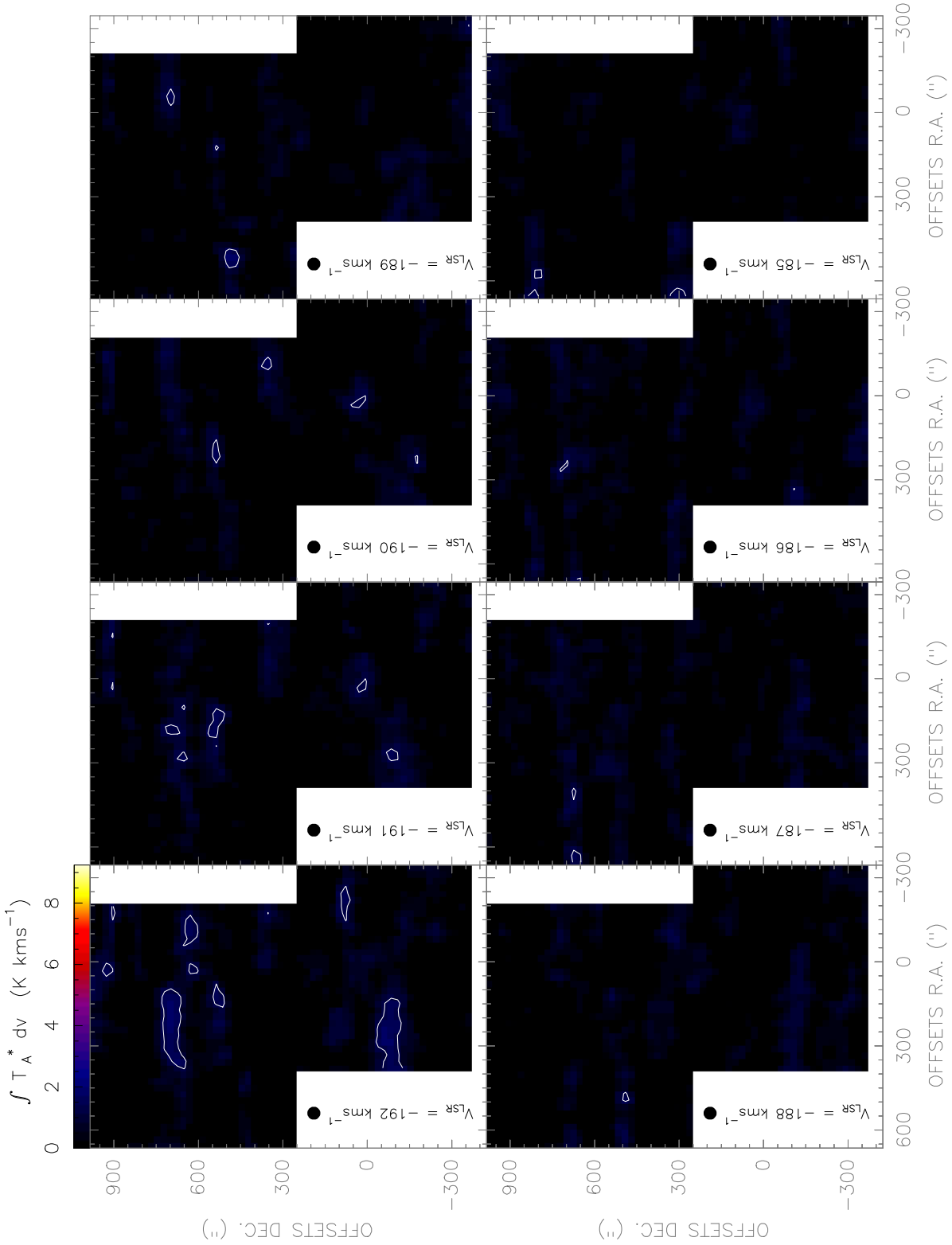

Figure. F.192: *[CII] line observed with the Herschel-HIFI satellite in Equatorial (J2000) coordinates. The spatial resolution of the maps is 46".*

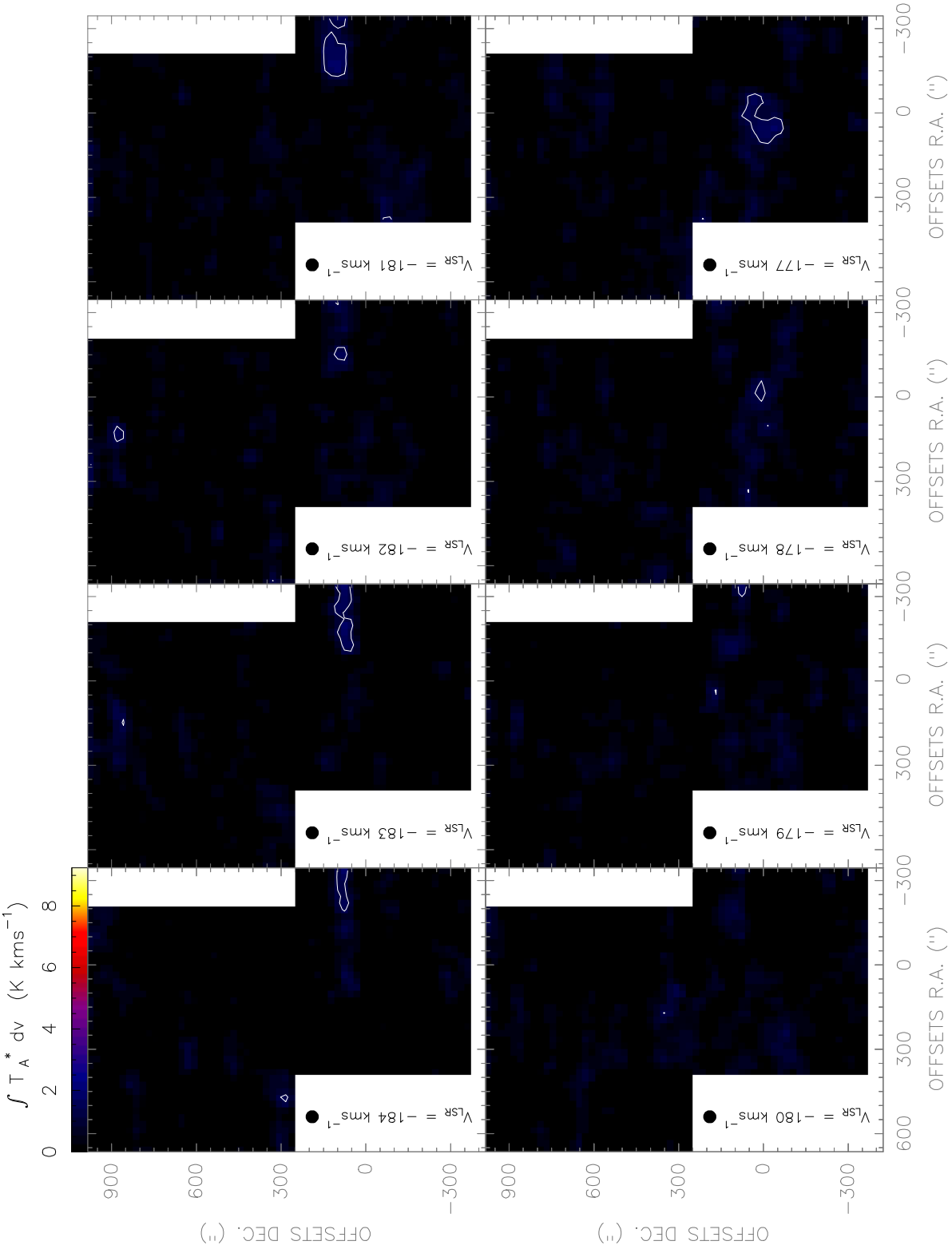

Figure. F.193: *[CII] line observed with the Herschel-HIFI satellite in Equatorial (J2000) coordinates. The spatial resolution of the maps is 46".*

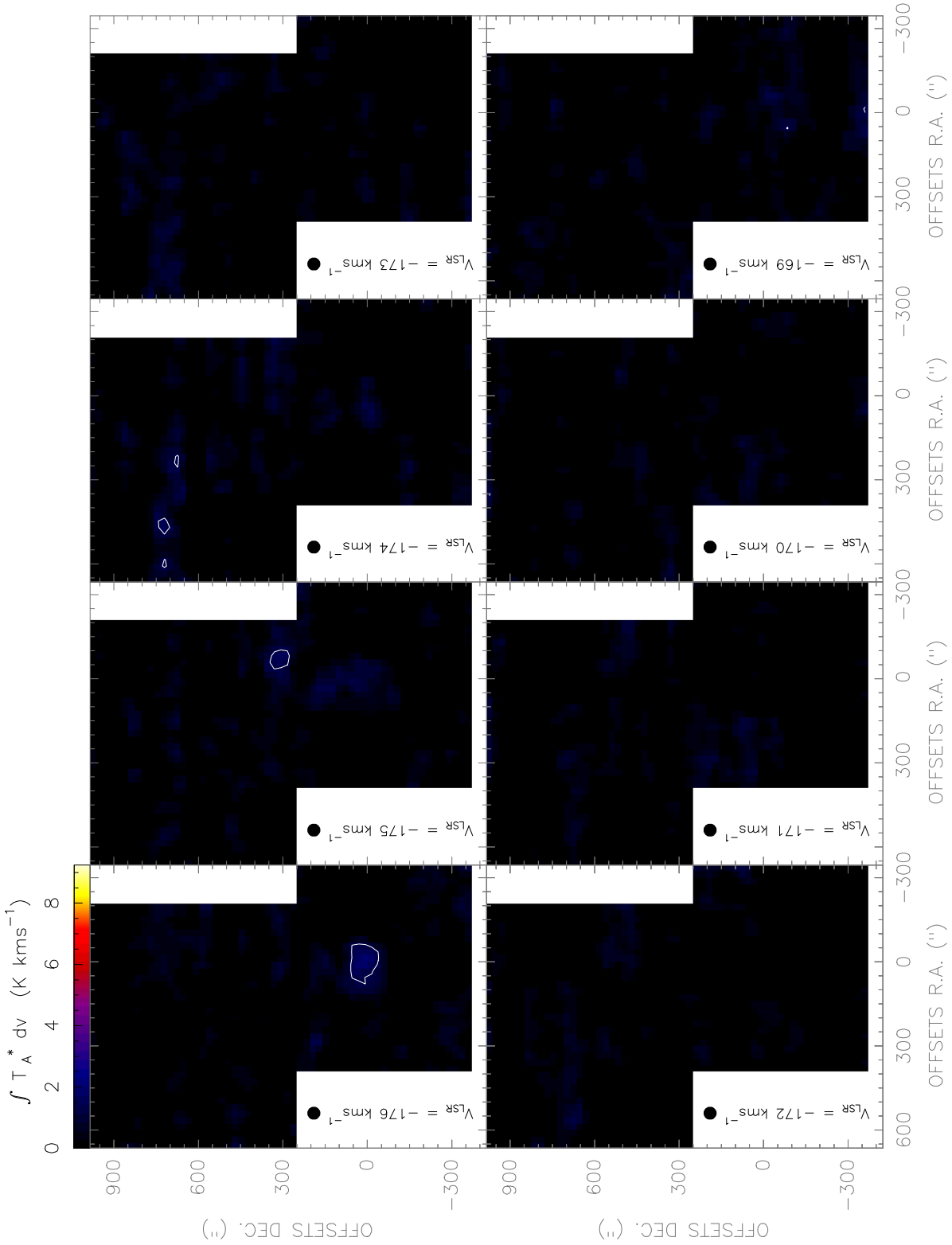

Figure. F.194: *[CII] line observed with the Herschel-HIFI satellite in Equatorial (J2000) coordinates. The spatial resolution of the maps is 46".*

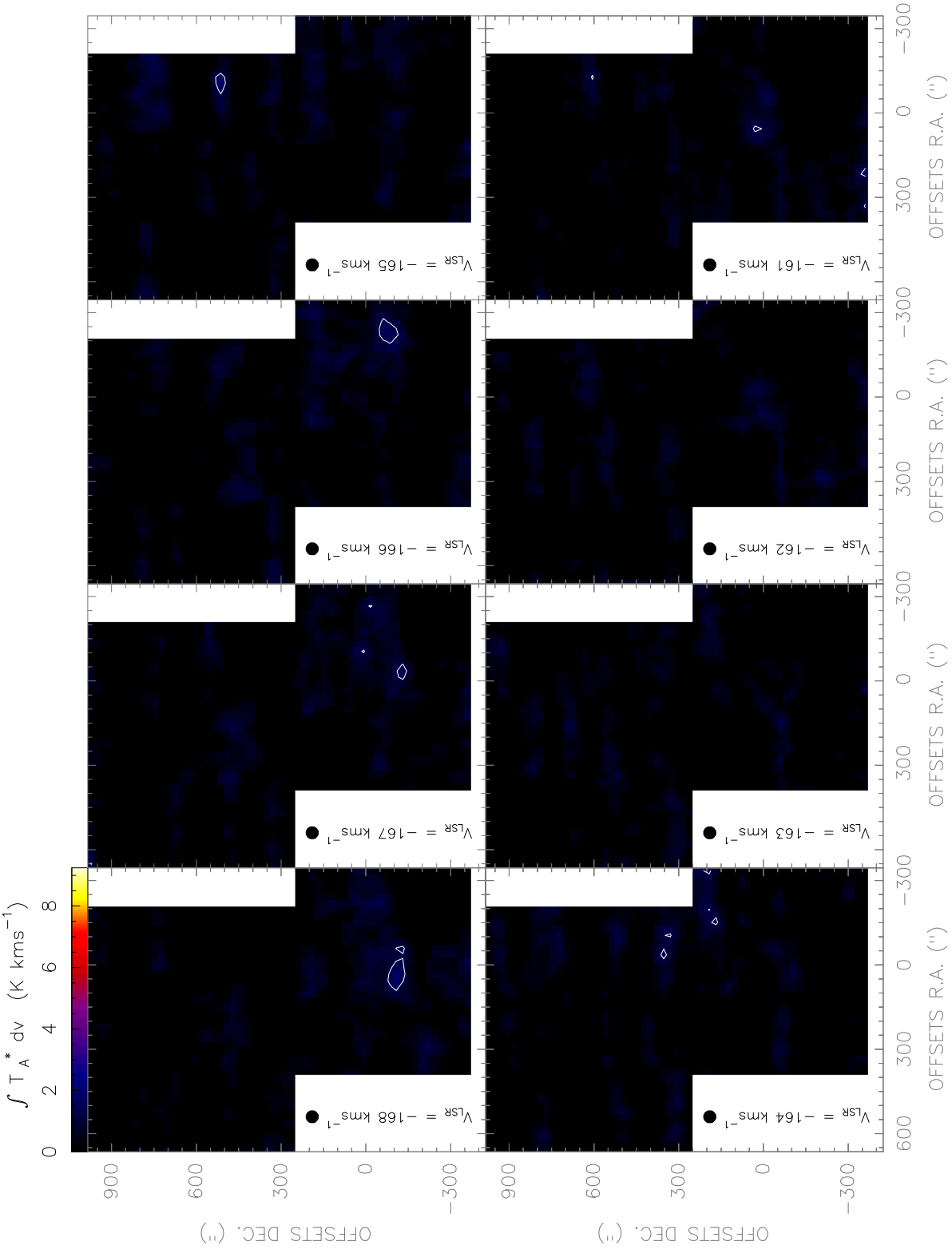

Figure. F.195: *[CII] line observed with the Herschel-HIFI satellite in Equatorial (J2000) coordinates. The spatial resolution of the maps is 46".*

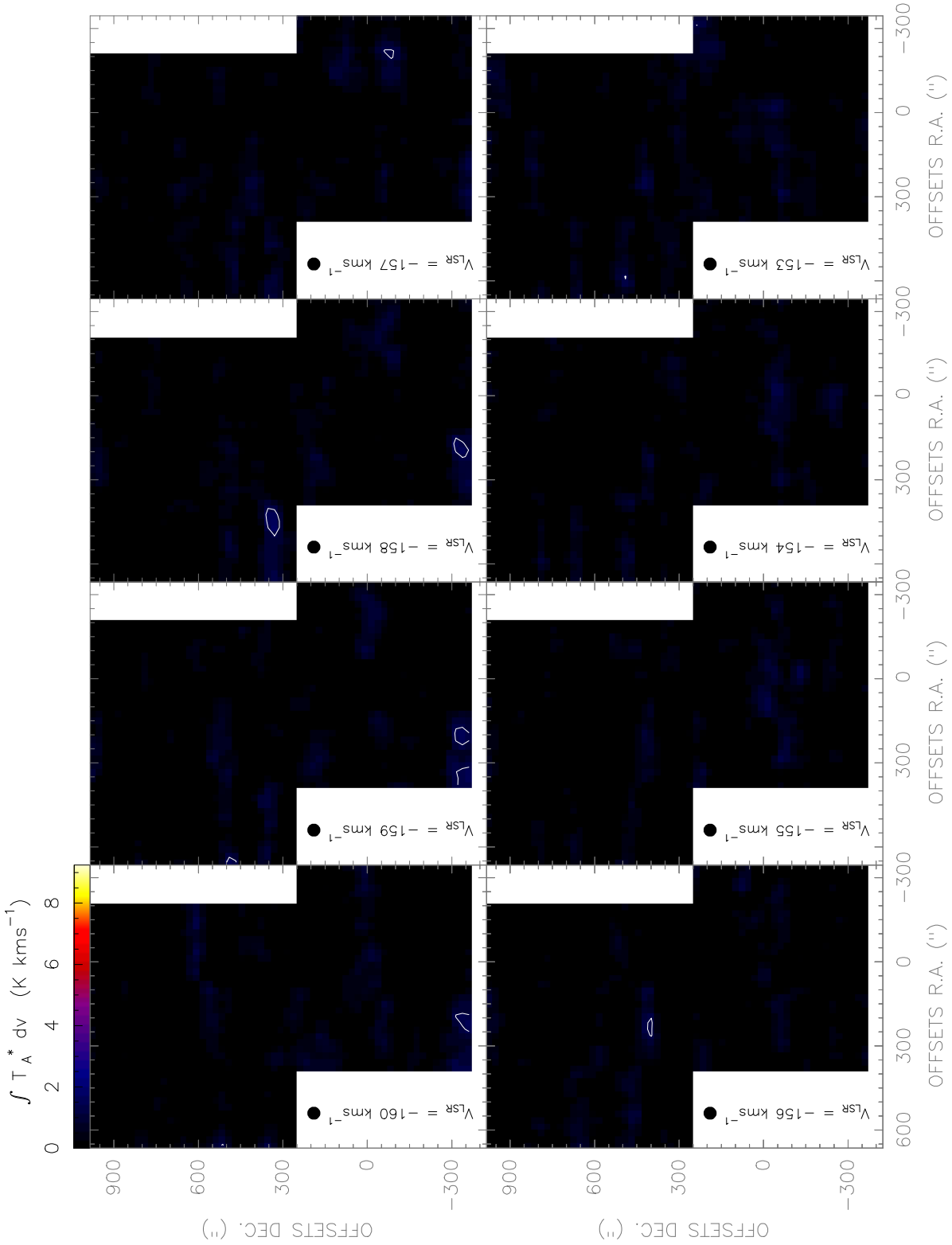

Figure. F.196: *[CII] line observed with the Herschel-HIFI satellite in Equatorial (J2000) coordinates. The spatial resolution of the maps is 46".*

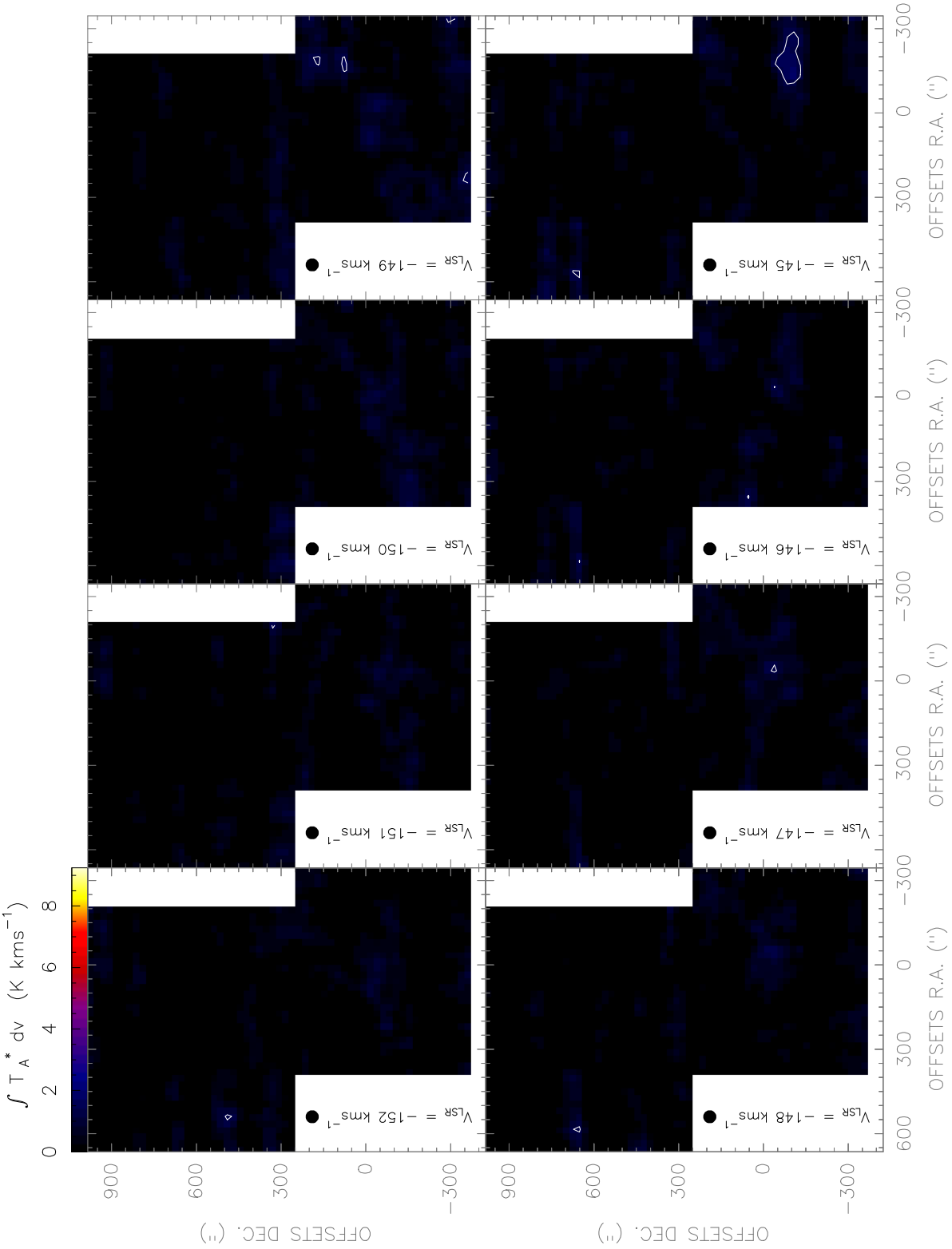

Figure. F.197: *[CII] line observed with the Herschel-HIFI satellite in Equatorial (J2000) coordinates. The spatial resolution of the maps is 46".*

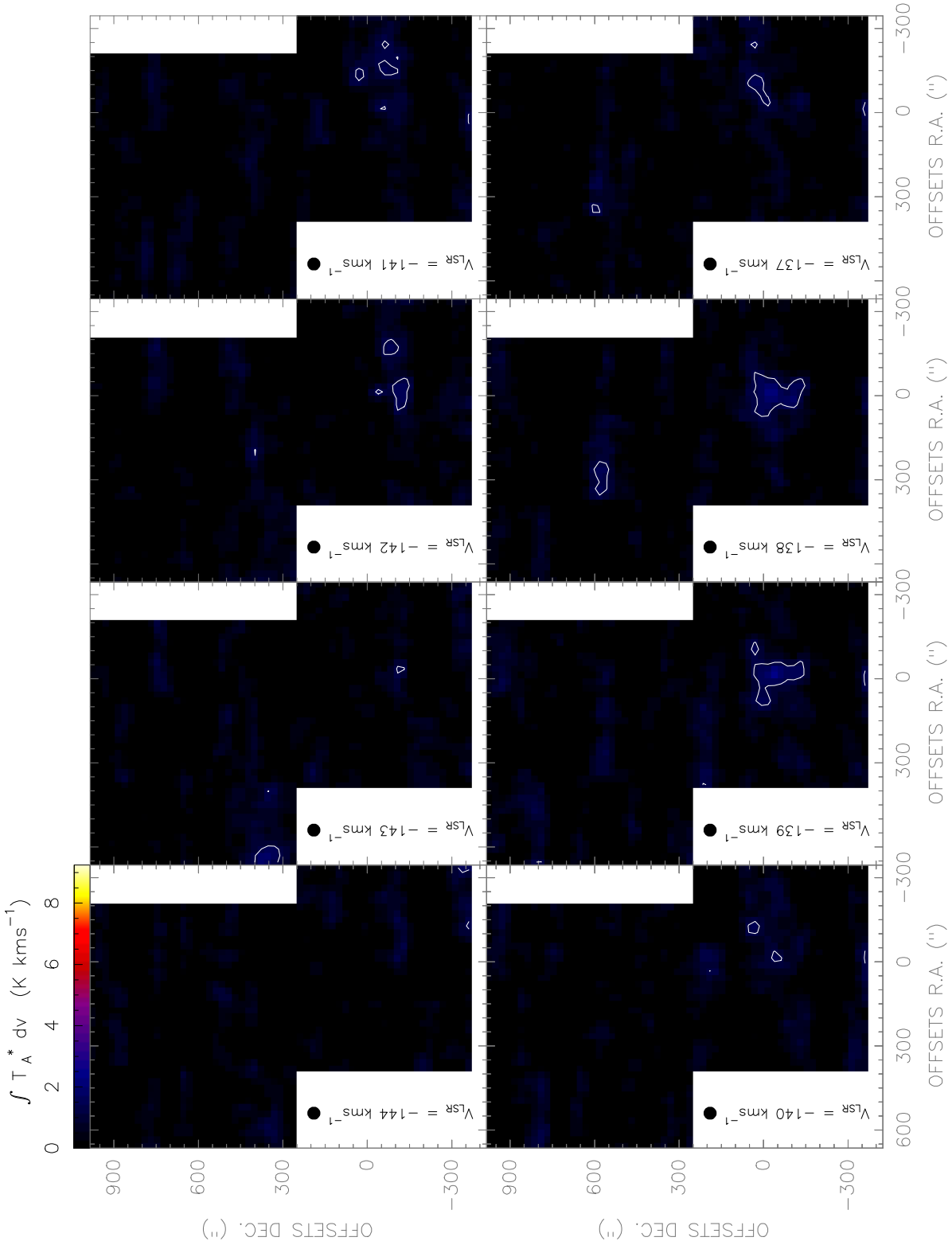

Figure. F.198: *[CII] line observed with the Herschel-HIFI satellite in Equatorial (J2000) coordinates. The spatial resolution of the maps is 46".*

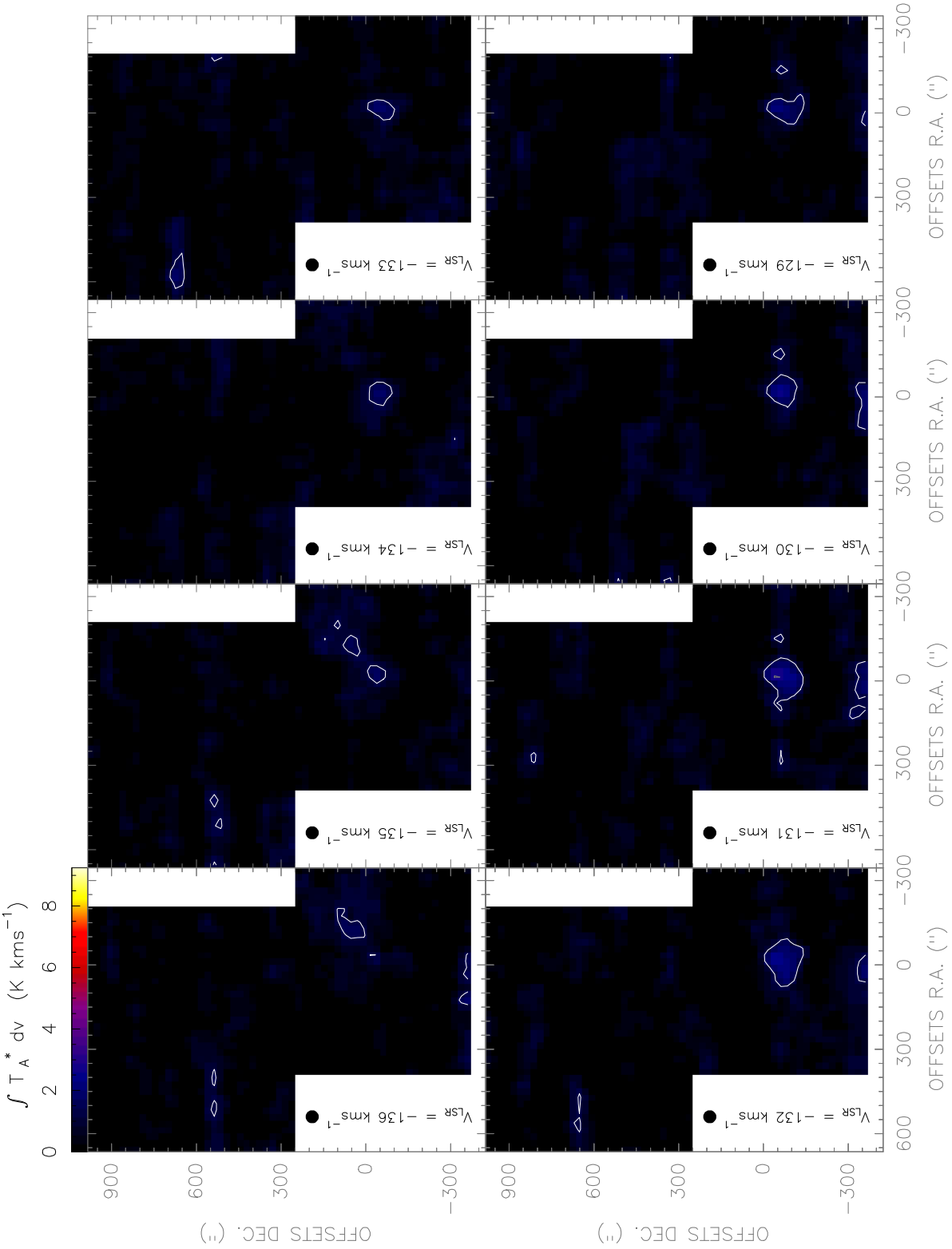

Figure. F.199: *[CII] line observed with the Herschel-HIFI satellite in Equatorial (J2000) coordinates. The spatial resolution of the maps is 46".*

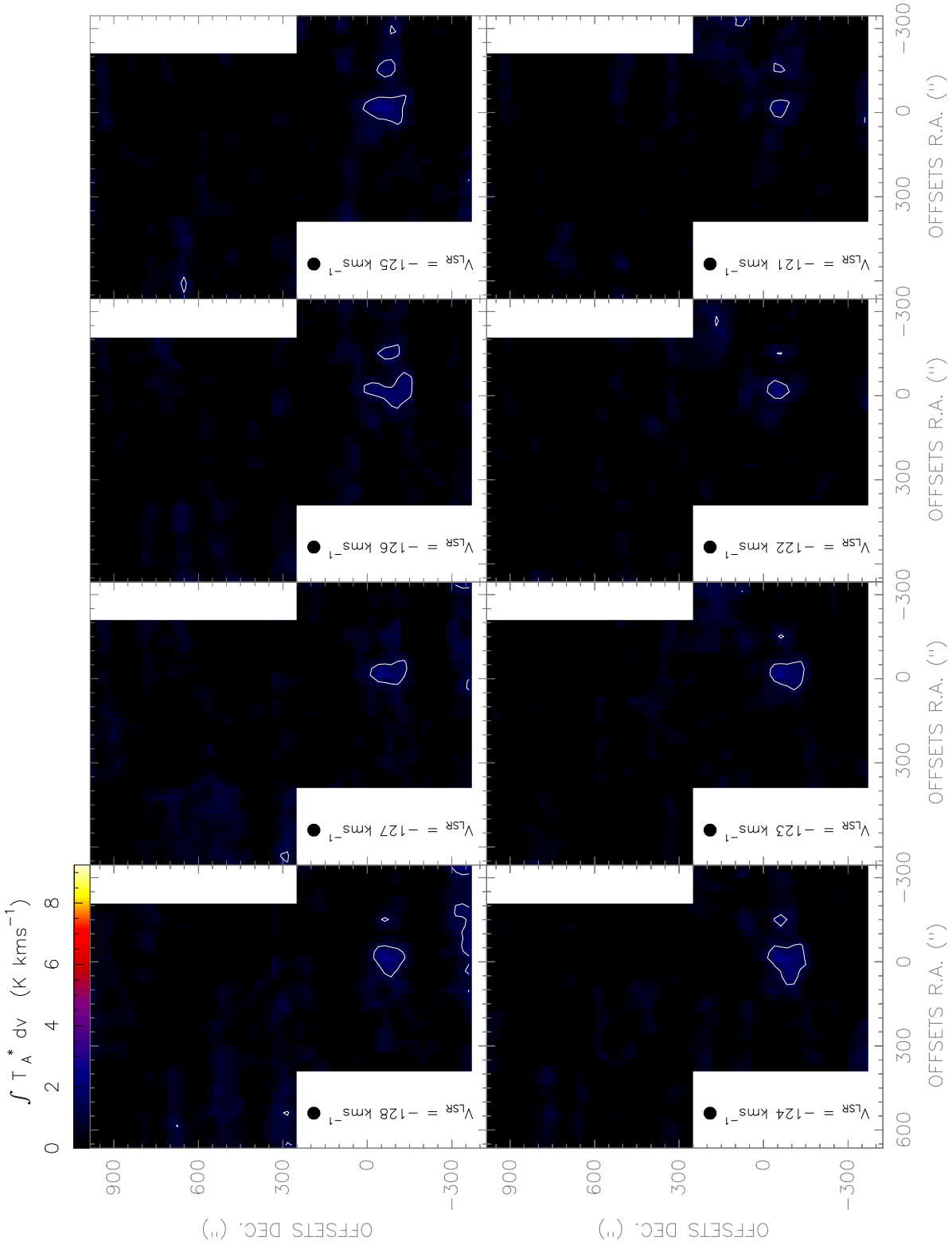

Figure. F.200: *[CII] line observed with the Herschel-HIFI satellite in Equatorial (J2000) coordinates. The spatial resolution of the maps is 46".*

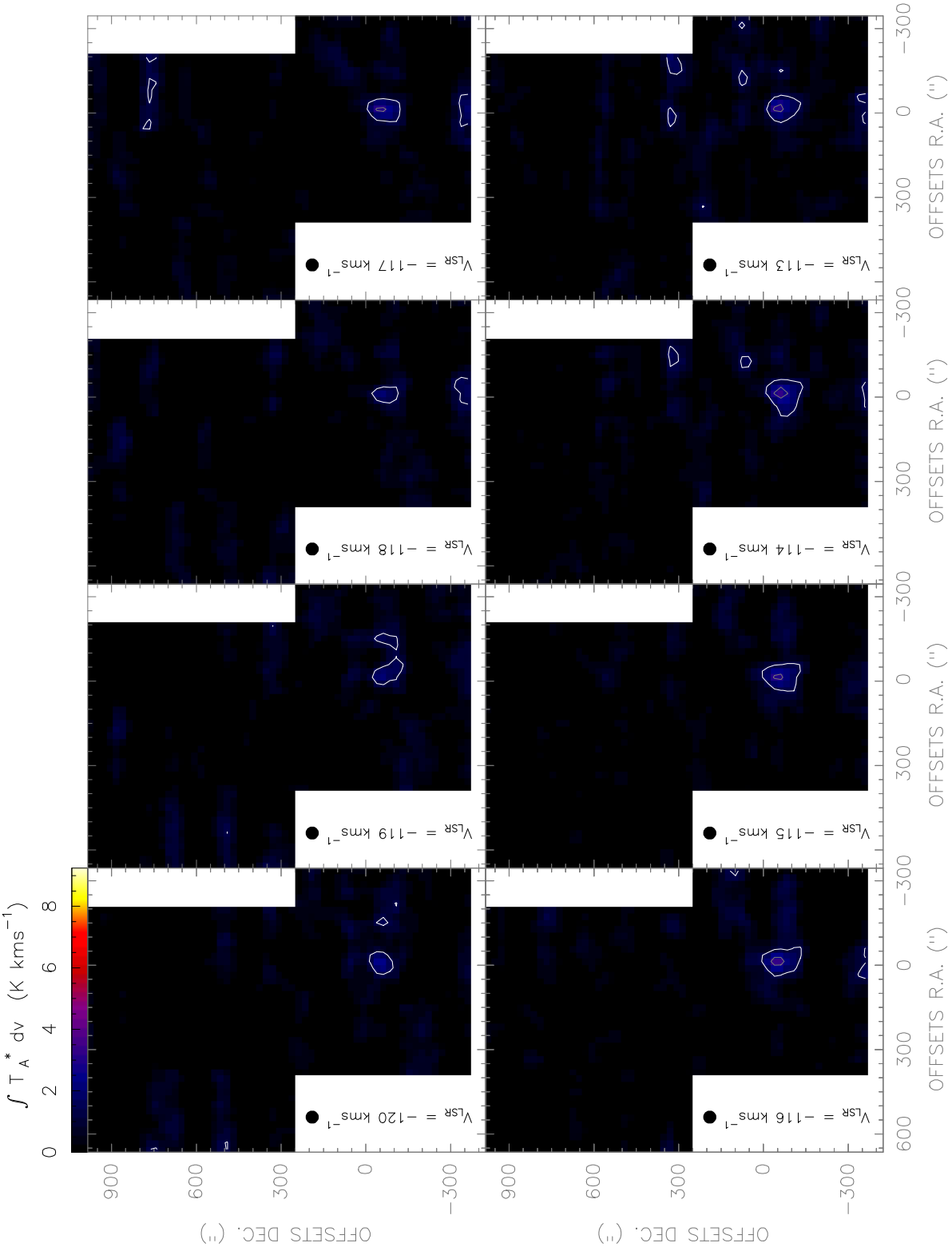

Figure. F.201: *[CII] line observed with the Herschel-HIFI satellite in Equatorial (J2000) coordinates. The spatial resolution of the maps is 46".*

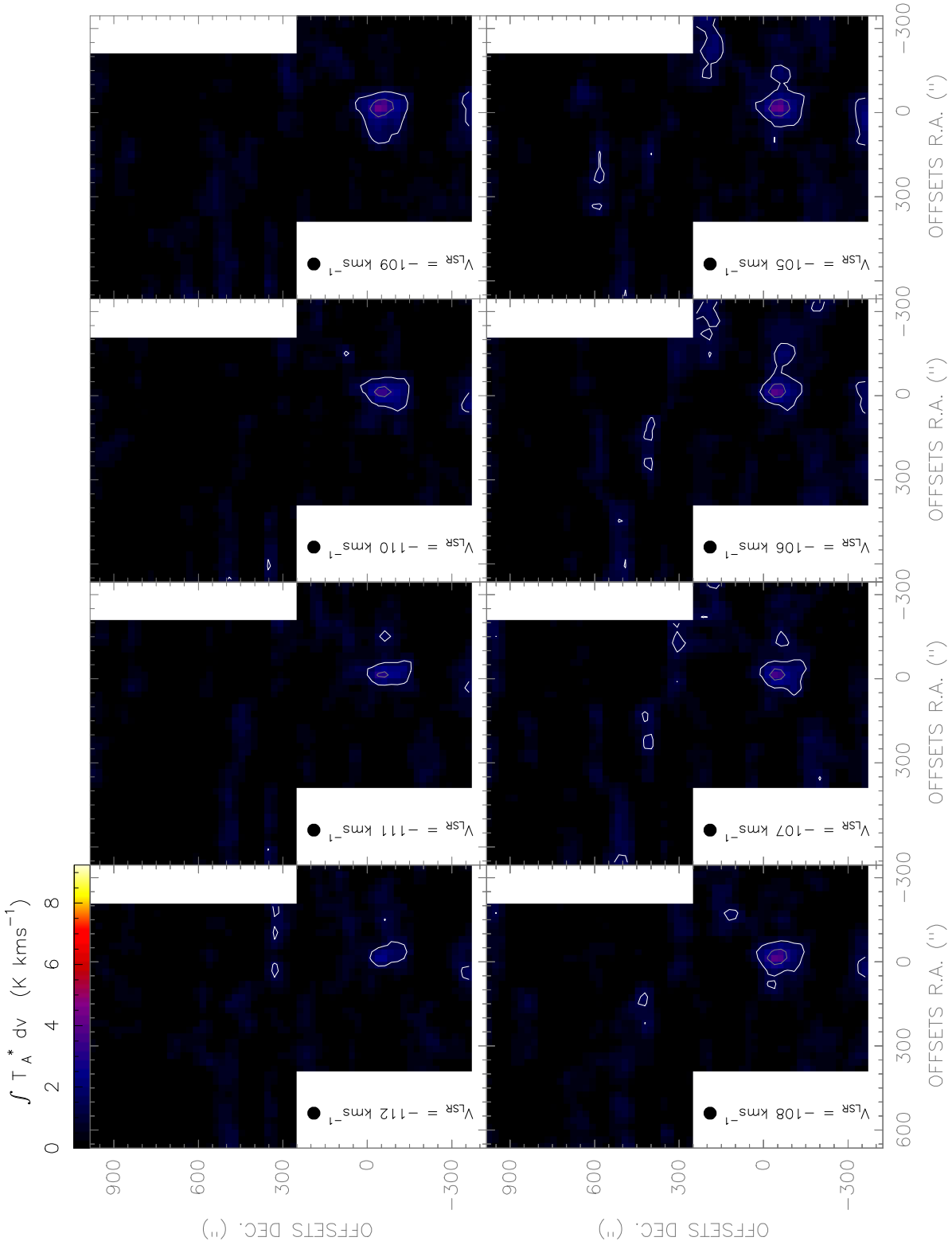

Figure. F.202: *[CII] line observed with the Herschel-HIFI satellite in Equatorial (J2000) coordinates. The spatial resolution of the maps is 46".*

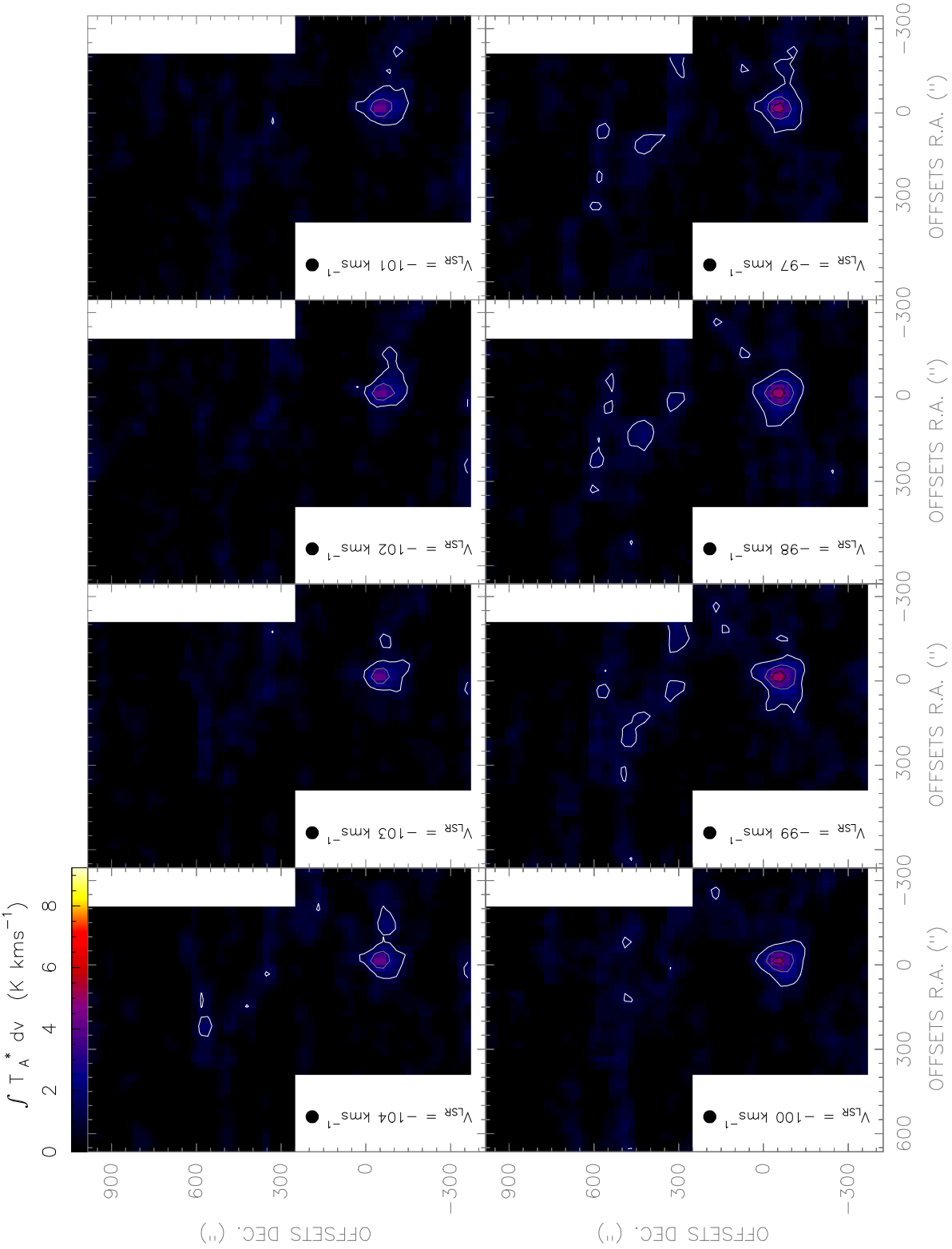

Figure. F.203: *[CII] line observed with the Herschel-HIFI satellite in Equatorial (J2000) coordinates. The spatial resolution of the maps is 46".*

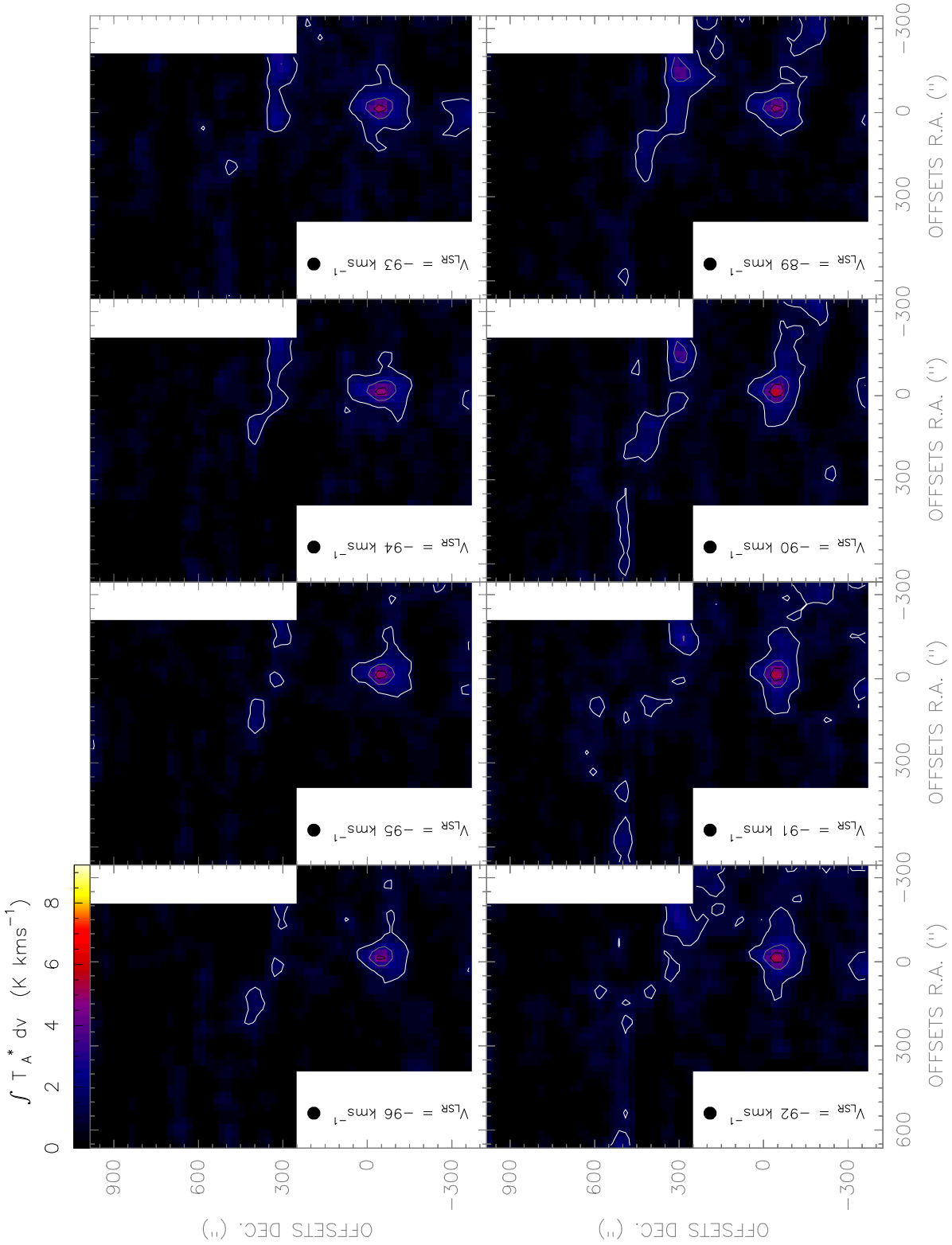

Figure. F.204: *[CII] line observed with the Herschel-HIFI satellite in Equatorial (J2000) coordinates. The spatial resolution of the maps is 46".*

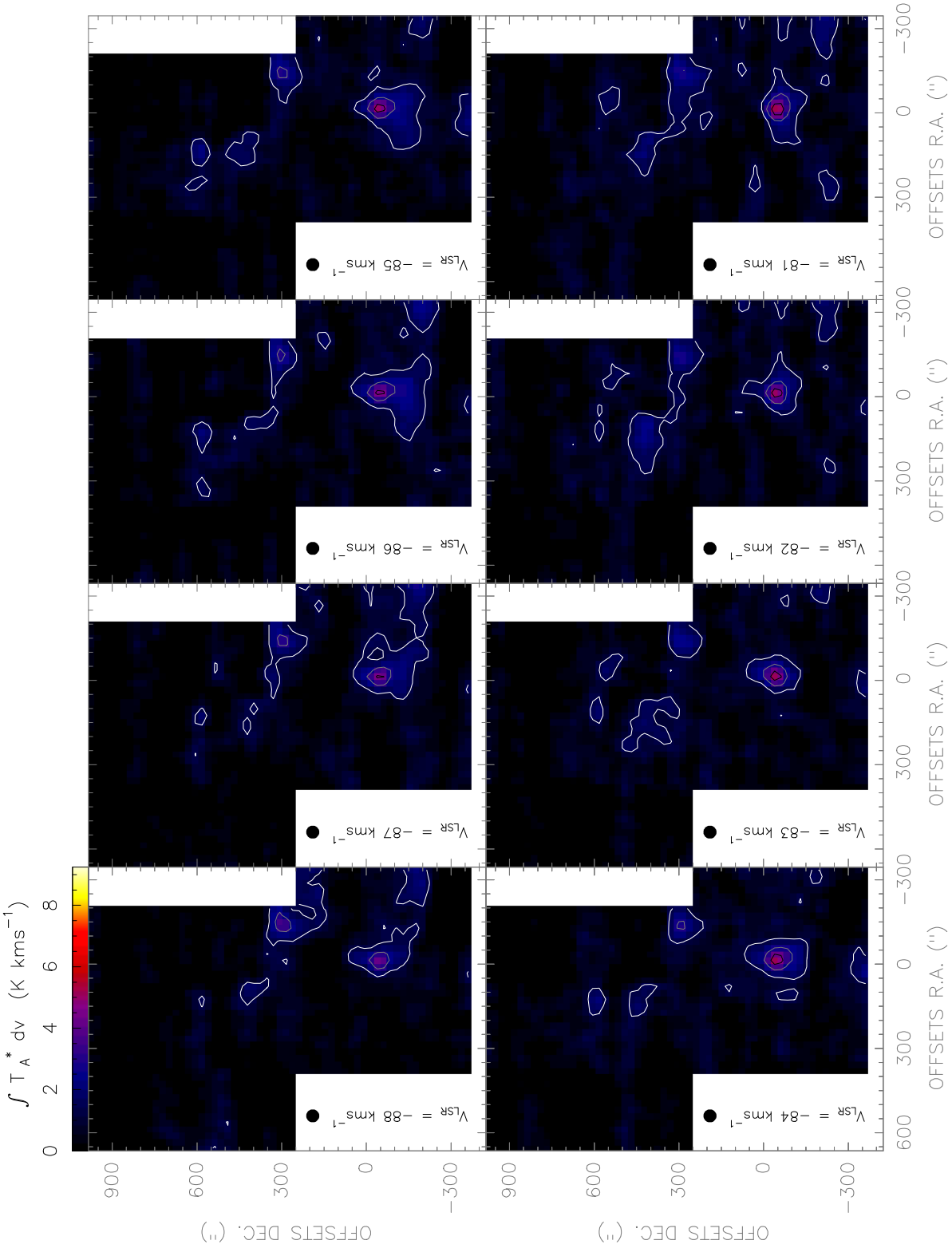

Figure. F.205: *[CII] line observed with the Herschel-HIFI satellite in Equatorial (J2000) coordinates. The spatial resolution of the maps is 46".*

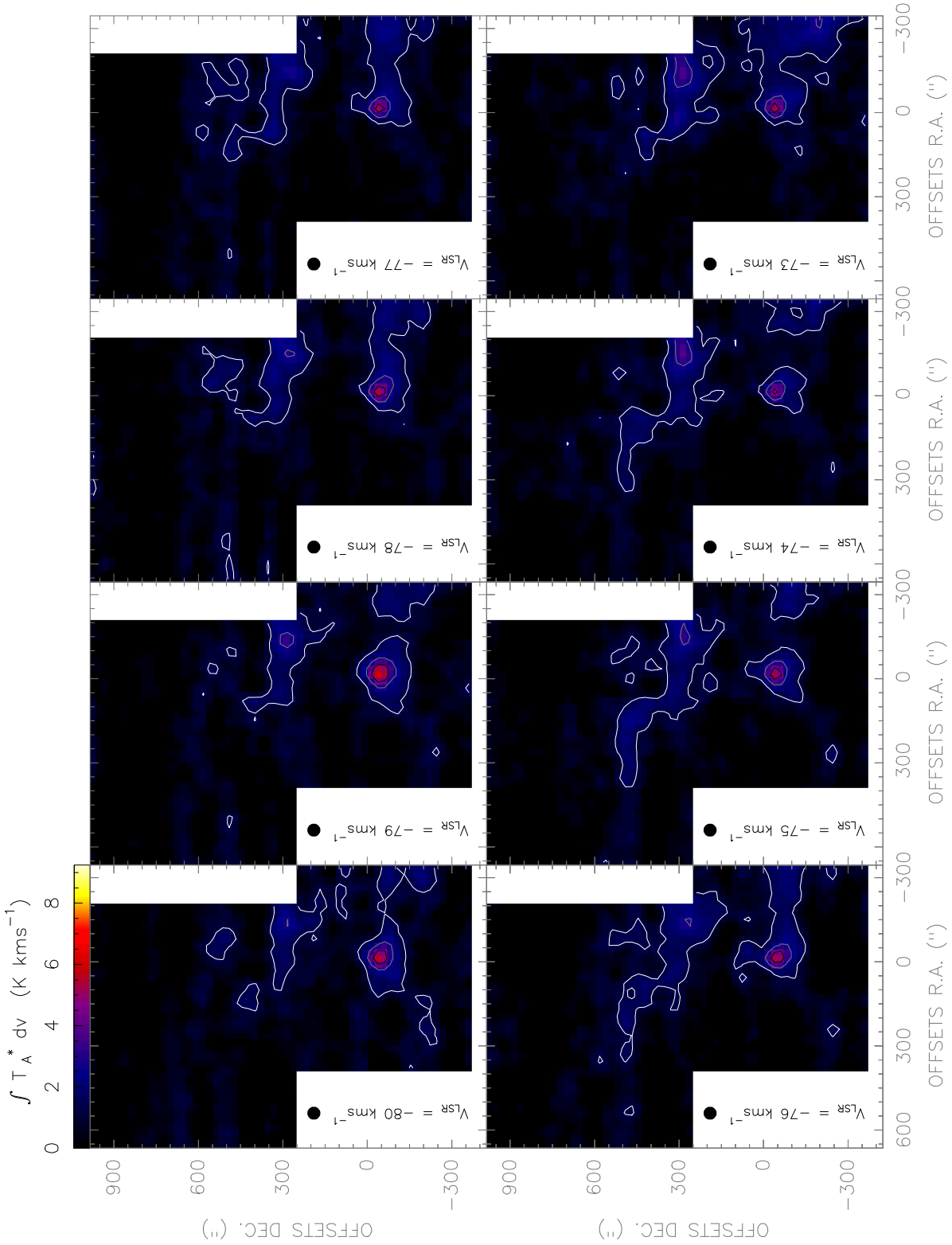

Figure. F.206: *[CII] line observed with the Herschel-HIFI satellite in Equatorial (J2000) coordinates. The spatial resolution of the maps is 46".*

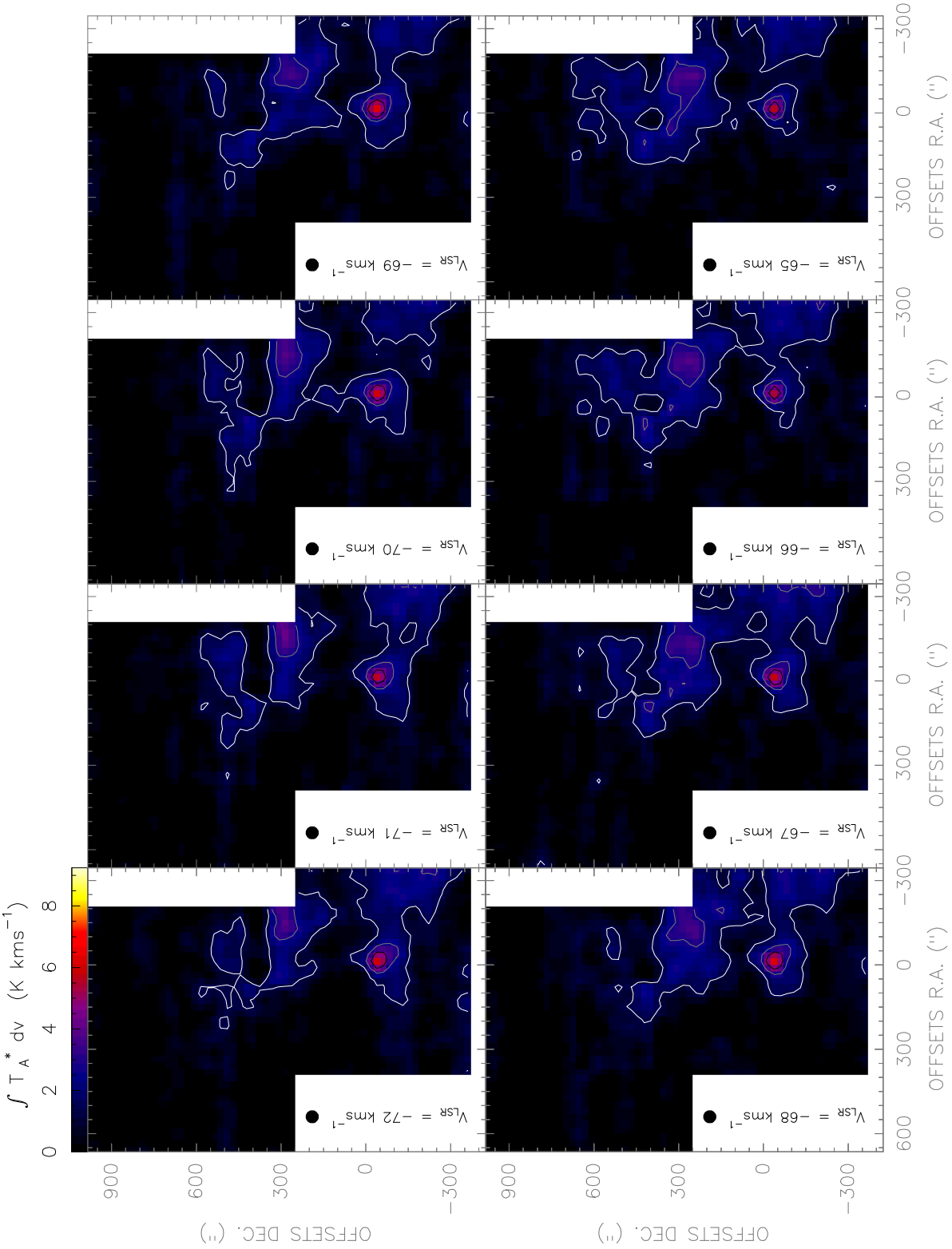

Figure. F.207: *[CII] line observed with the Herschel-HIFI satellite in Equatorial (J2000) coordinates. The spatial resolution of the maps is 46".*

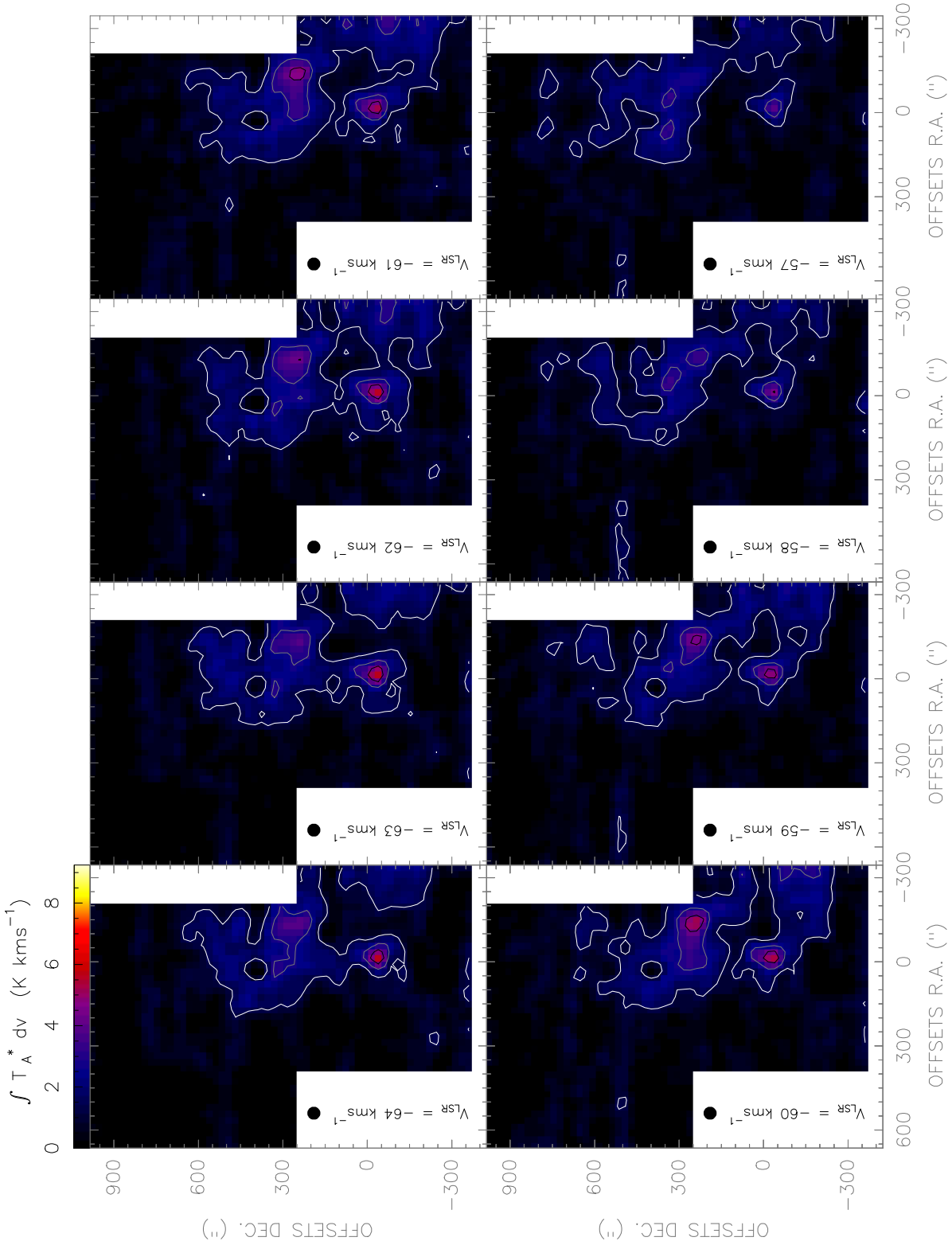

Figure. F.208: *[CII] line observed with the Herschel-HIFI satellite in Equatorial (J2000) coordinates. The spatial resolution of the maps is 46".*

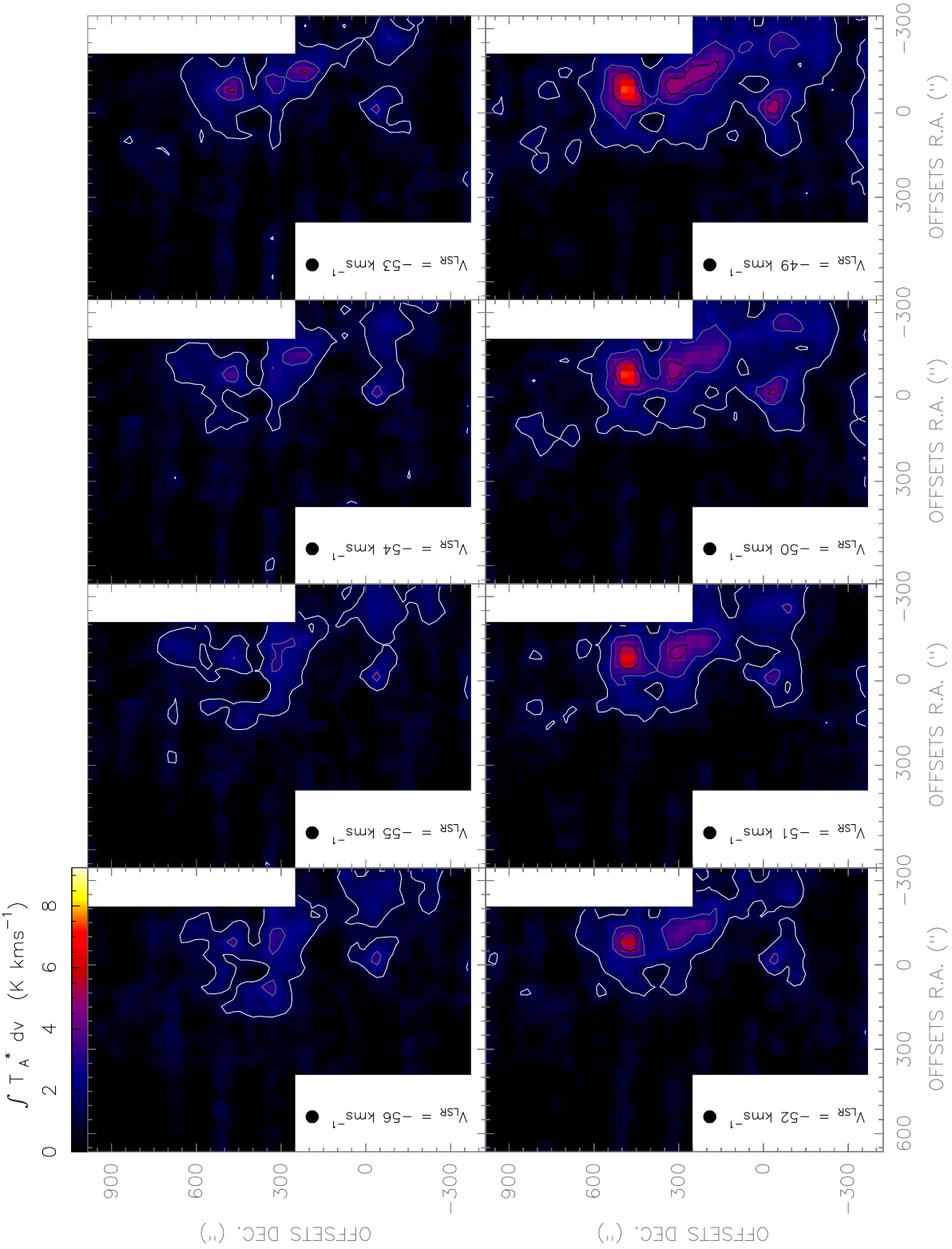

Figure. F.209: *[CII] line observed with the Herschel-HIFI satellite in Equatorial (J2000) coordinates. The spatial resolution of the maps is 46".*

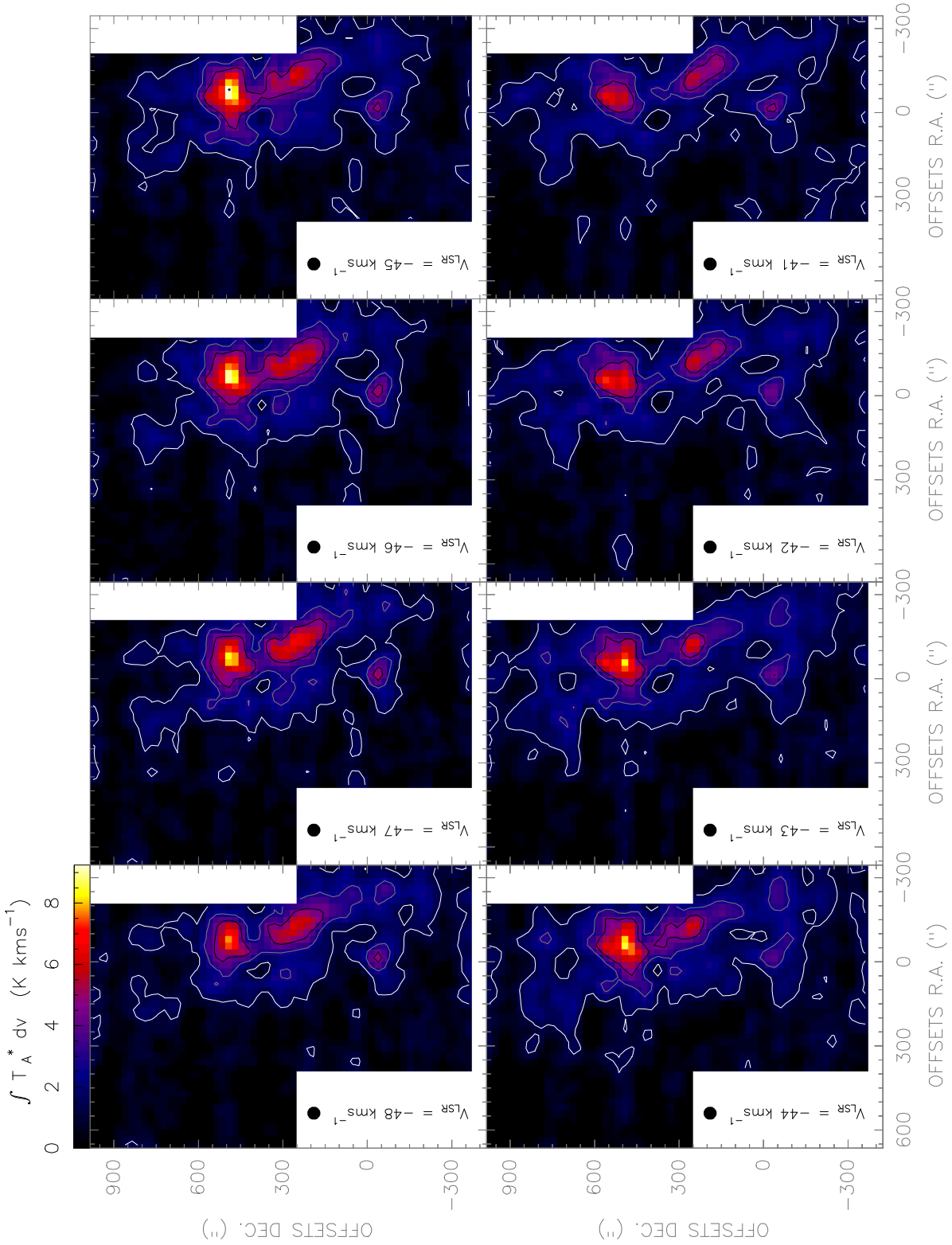

Figure. F.210: *[CII] line observed with the Herschel-HIFI satellite in Equatorial (J2000) coordinates. The spatial resolution of the maps is 46".*

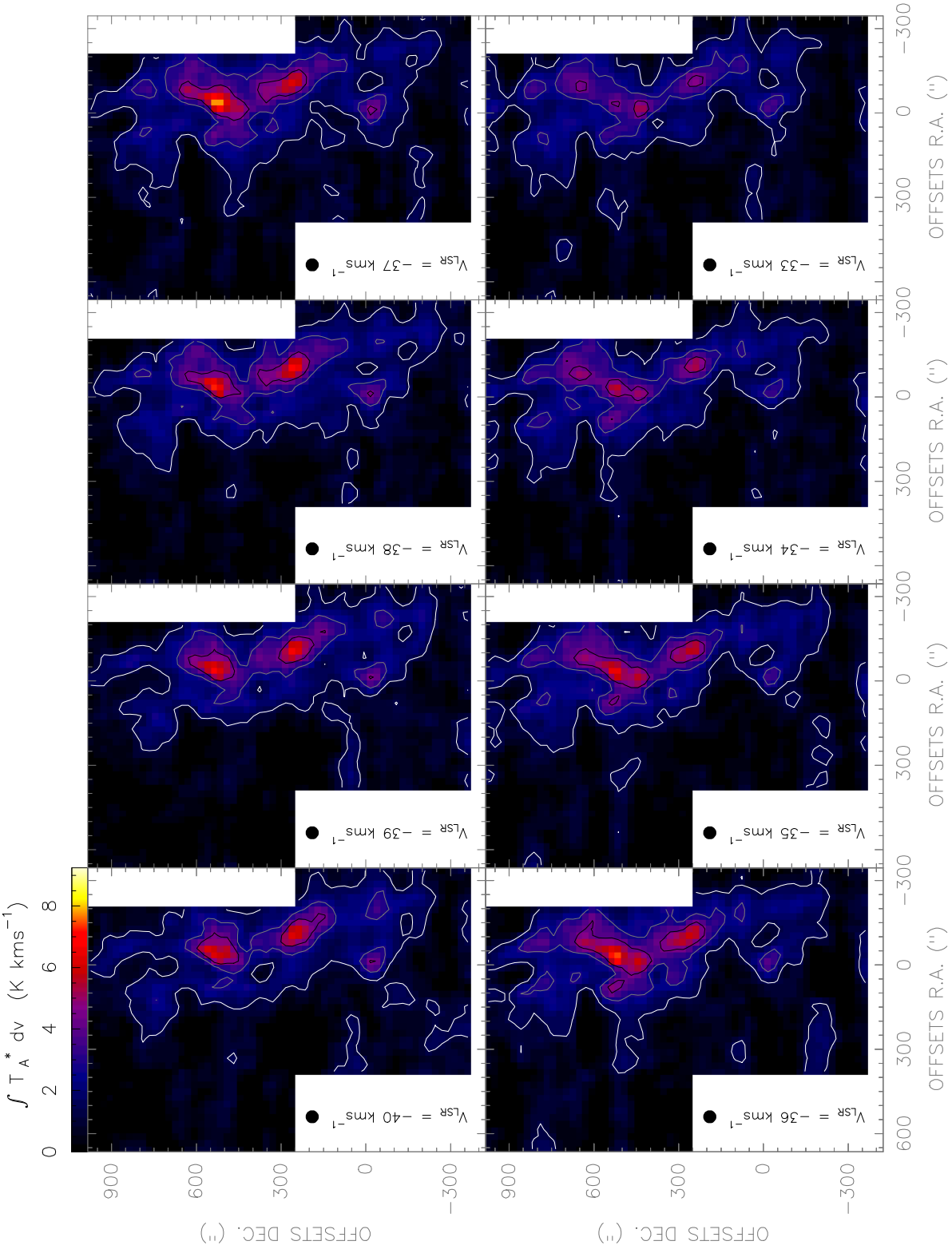

Figure. F.211: *[CII] line observed with the Herschel-HIFI satellite in Equatorial (J2000) coordinates. The spatial resolution of the maps is 46".*

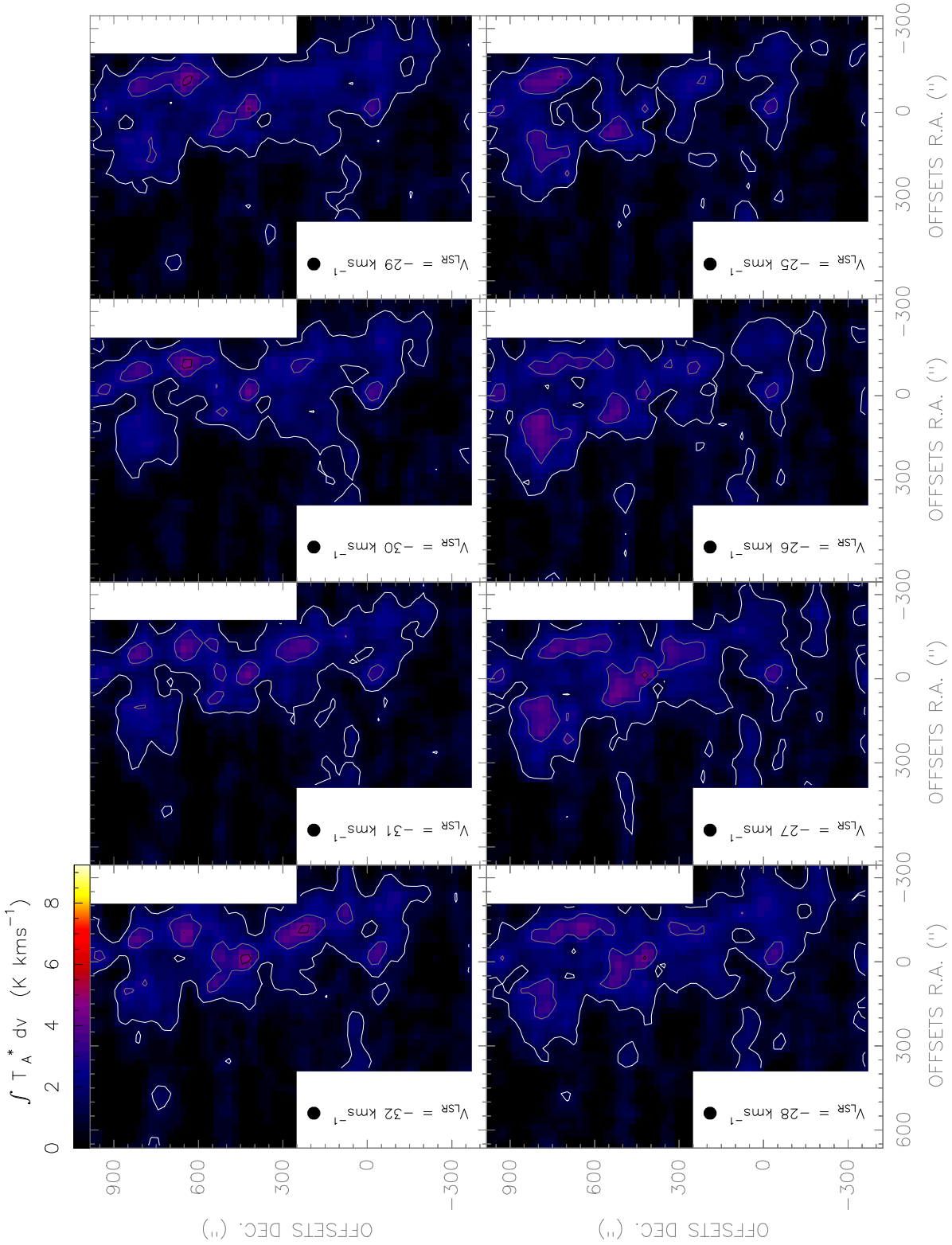

Figure. F.212: *[CII] line observed with the Herschel-HIFI satellite in Equatorial (J2000) coordinates. The spatial resolution of the maps is 46".*

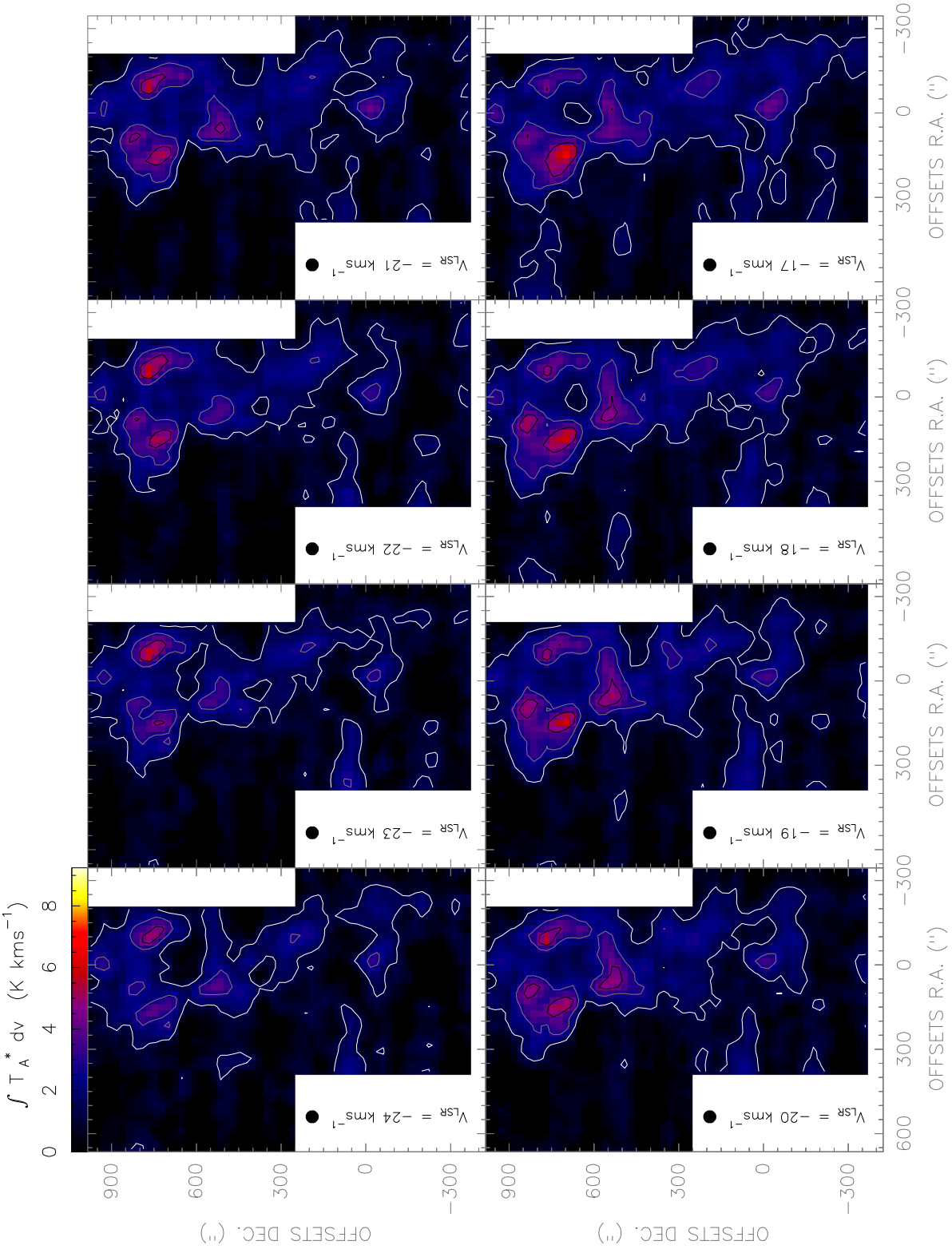

Figure. F.213: *[CII] line observed with the Herschel-HIFI satellite in Equatorial (J2000) coordinates. The spatial resolution of the maps is 46".*

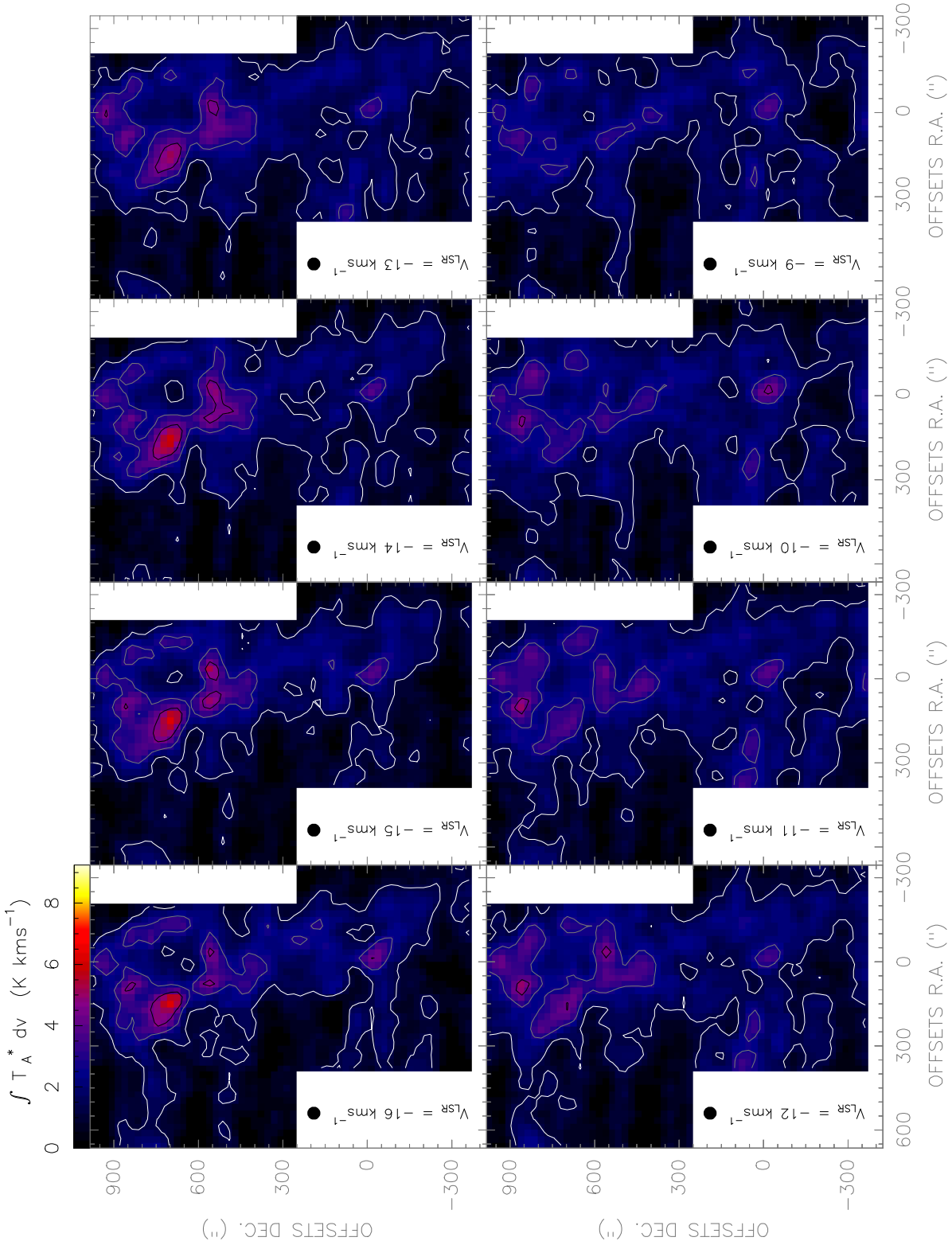

Figure. F.214: *[CII] line observed with the Herschel-HIFI satellite in Equatorial (J2000) coordinates. The spatial resolution of the maps is 46".*

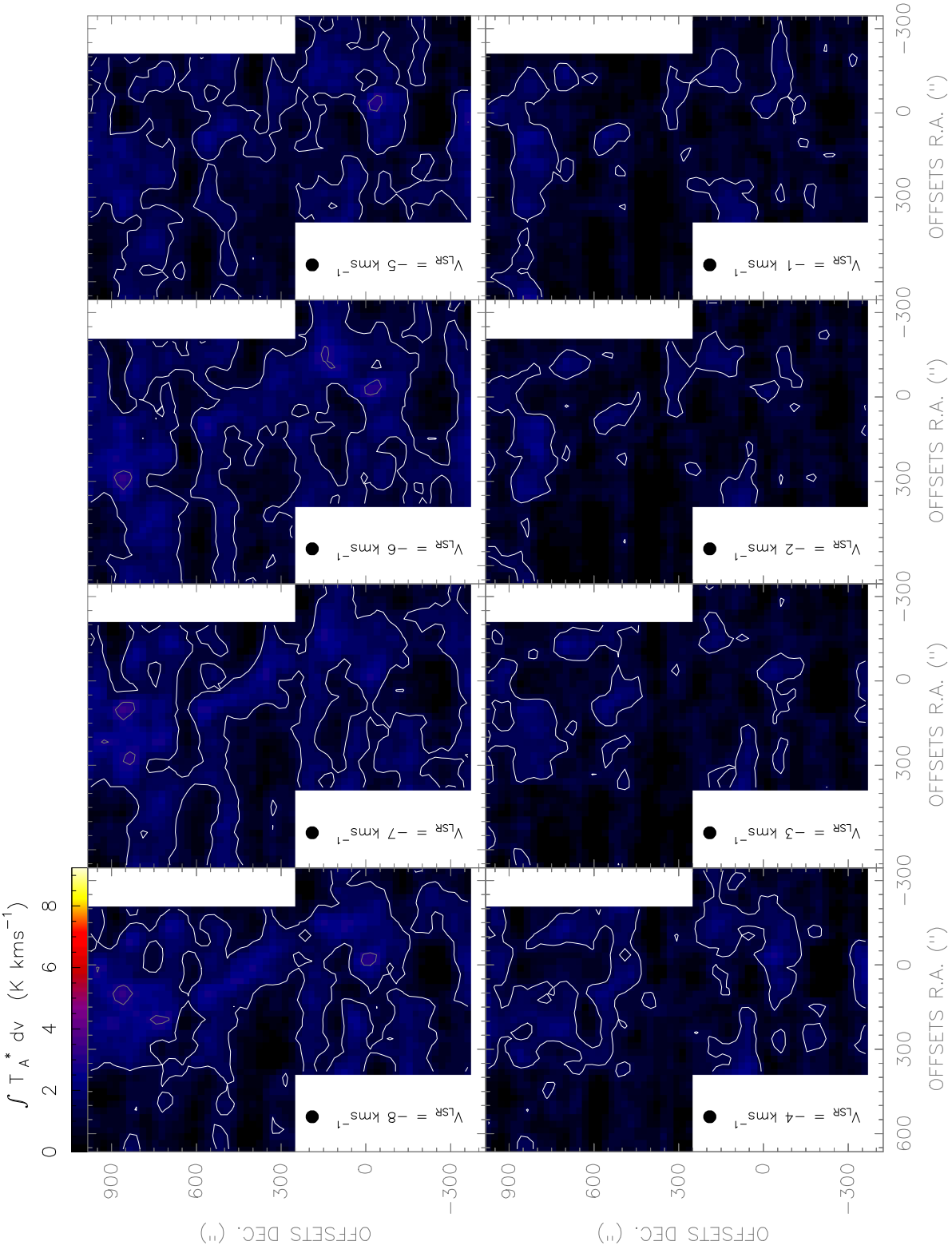

Figure. F.215: *[CII] line observed with the Herschel-HIFI satellite in Equatorial (J2000) coordinates. The spatial resolution of the maps is 46".*

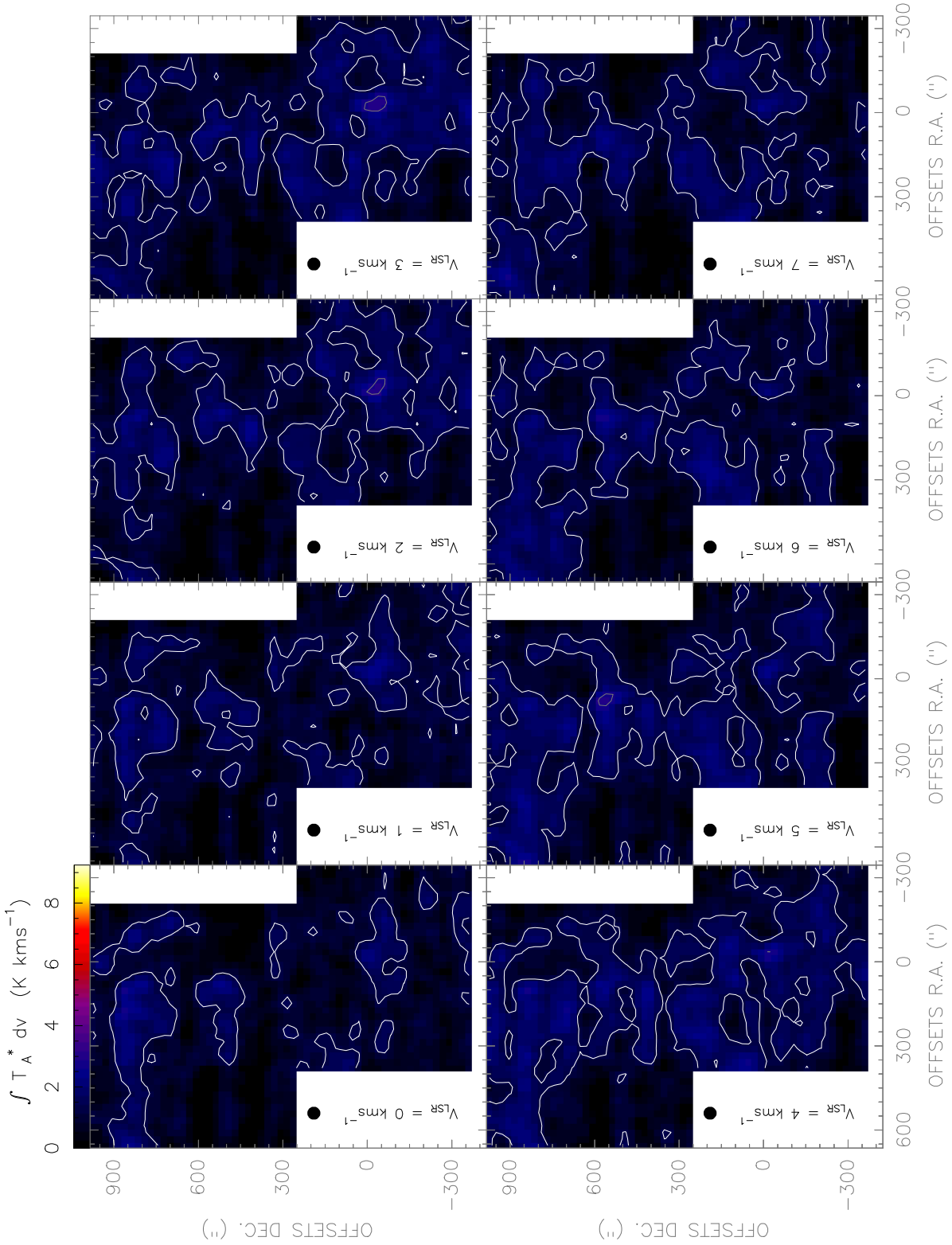

Figure. F.216: *[CII] line observed with the Herschel-HIFI satellite in Equatorial (J2000) coordinates. The spatial resolution of the maps is 46".*

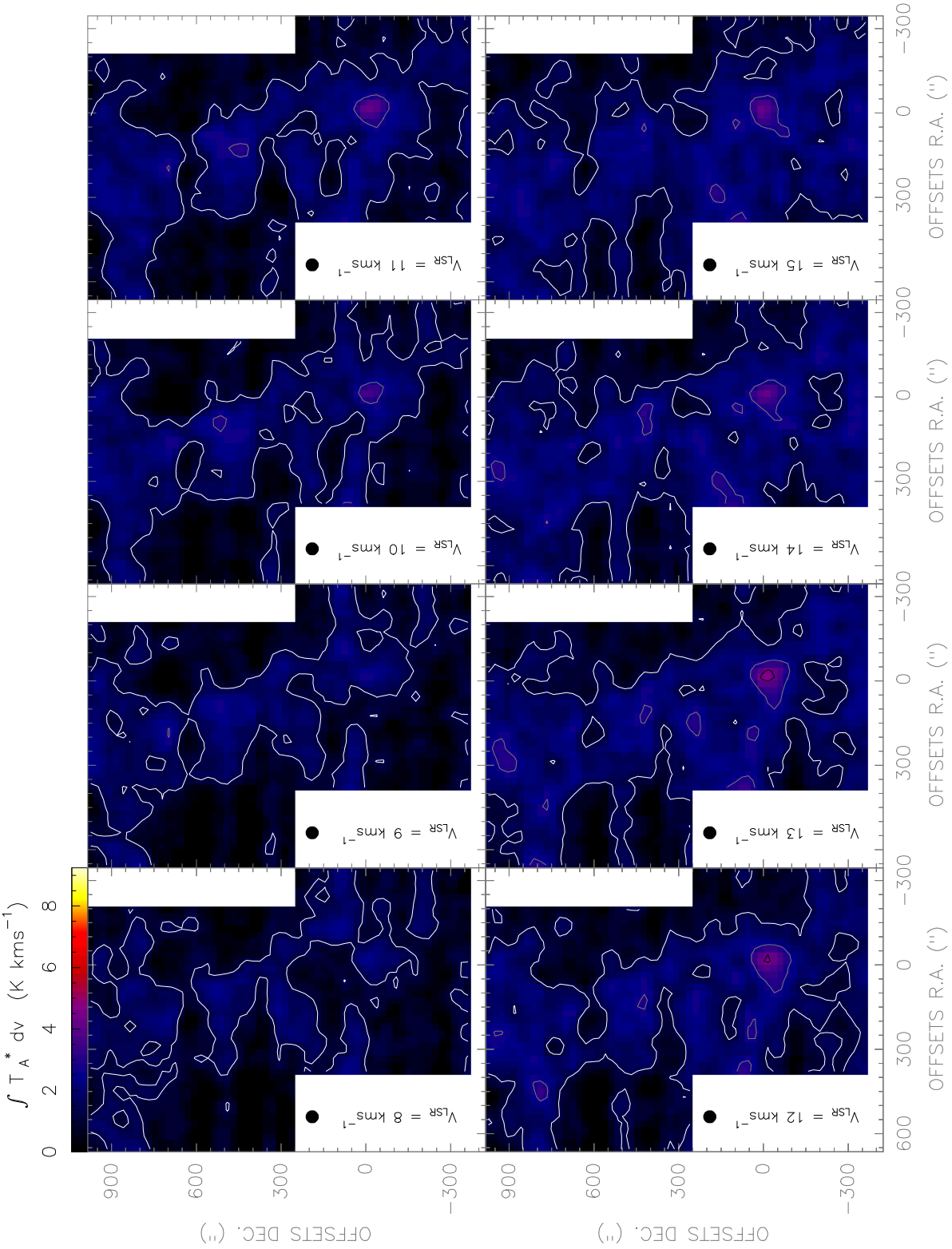

Figure. F.217: *[CII] line observed with the Herschel-HIFI satellite in Equatorial (J2000) coordinates. The spatial resolution of the maps is 46".*

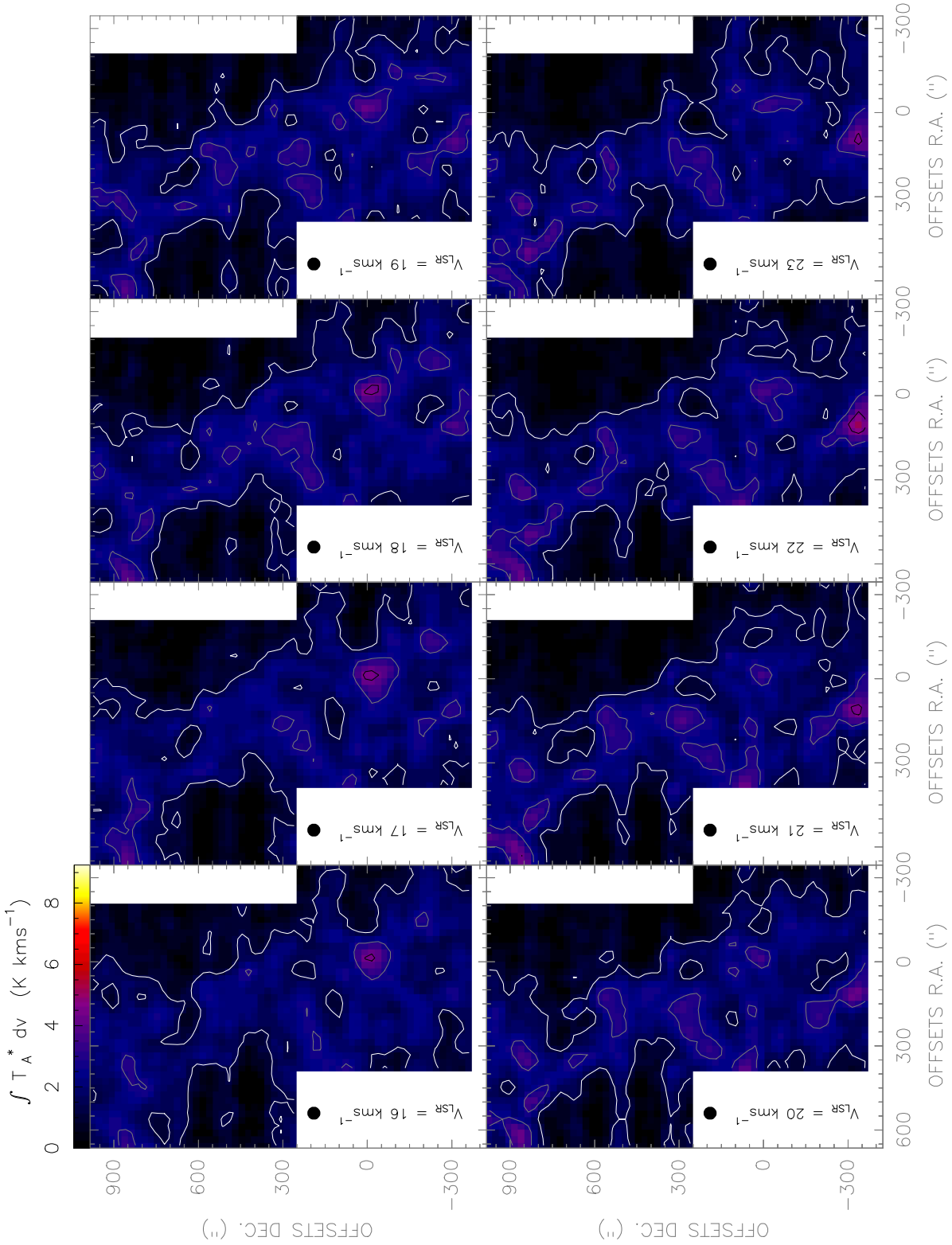

Figure. F.218: *[CII] line observed with the Herschel-HIFI satellite in Equatorial (J2000) coordinates. The spatial resolution of the maps is 46".*

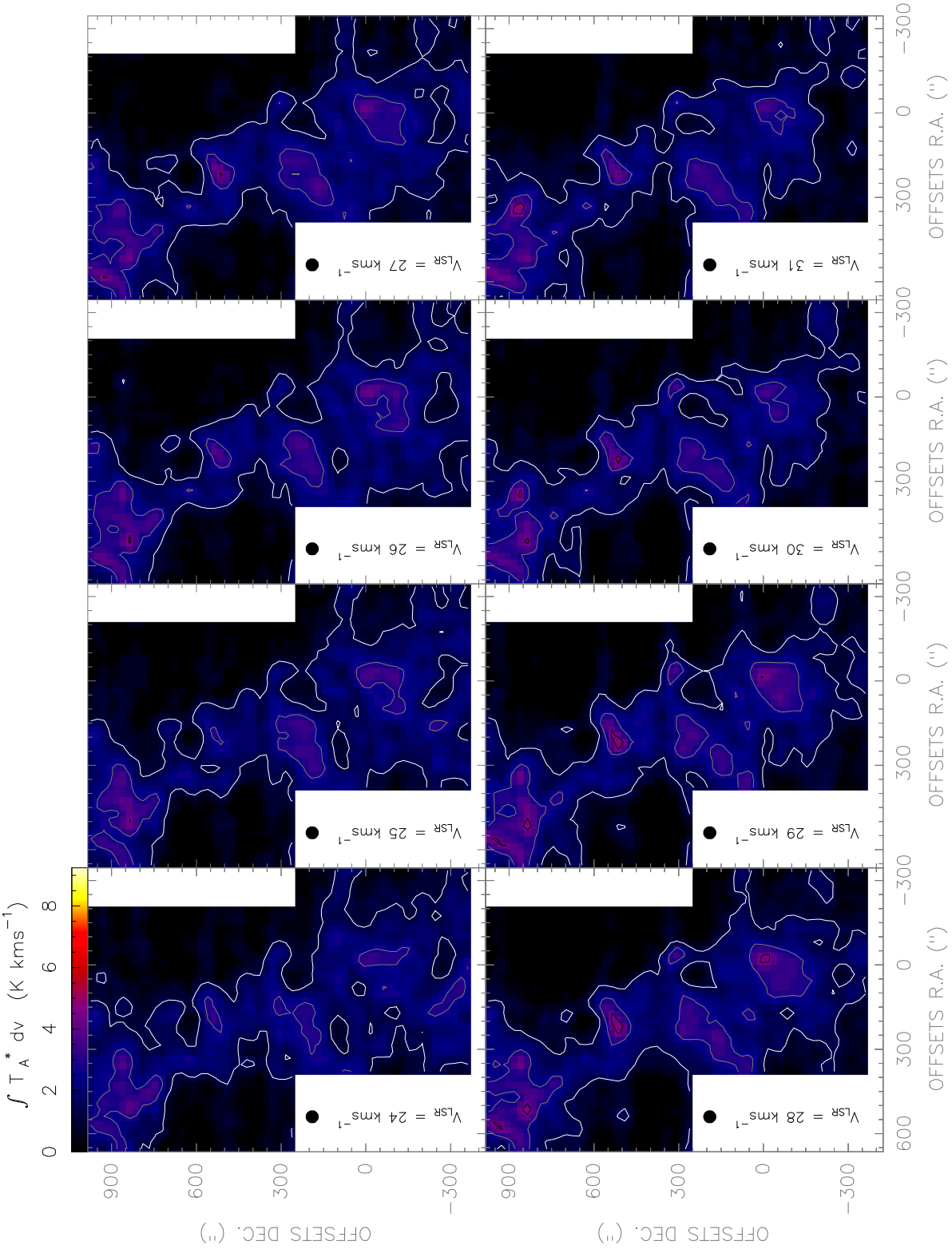

Figure. F.219: *[CII] line observed with the Herschel-HIFI satellite in Equatorial (J2000) coordinates. The spatial resolution of the maps is 46".*

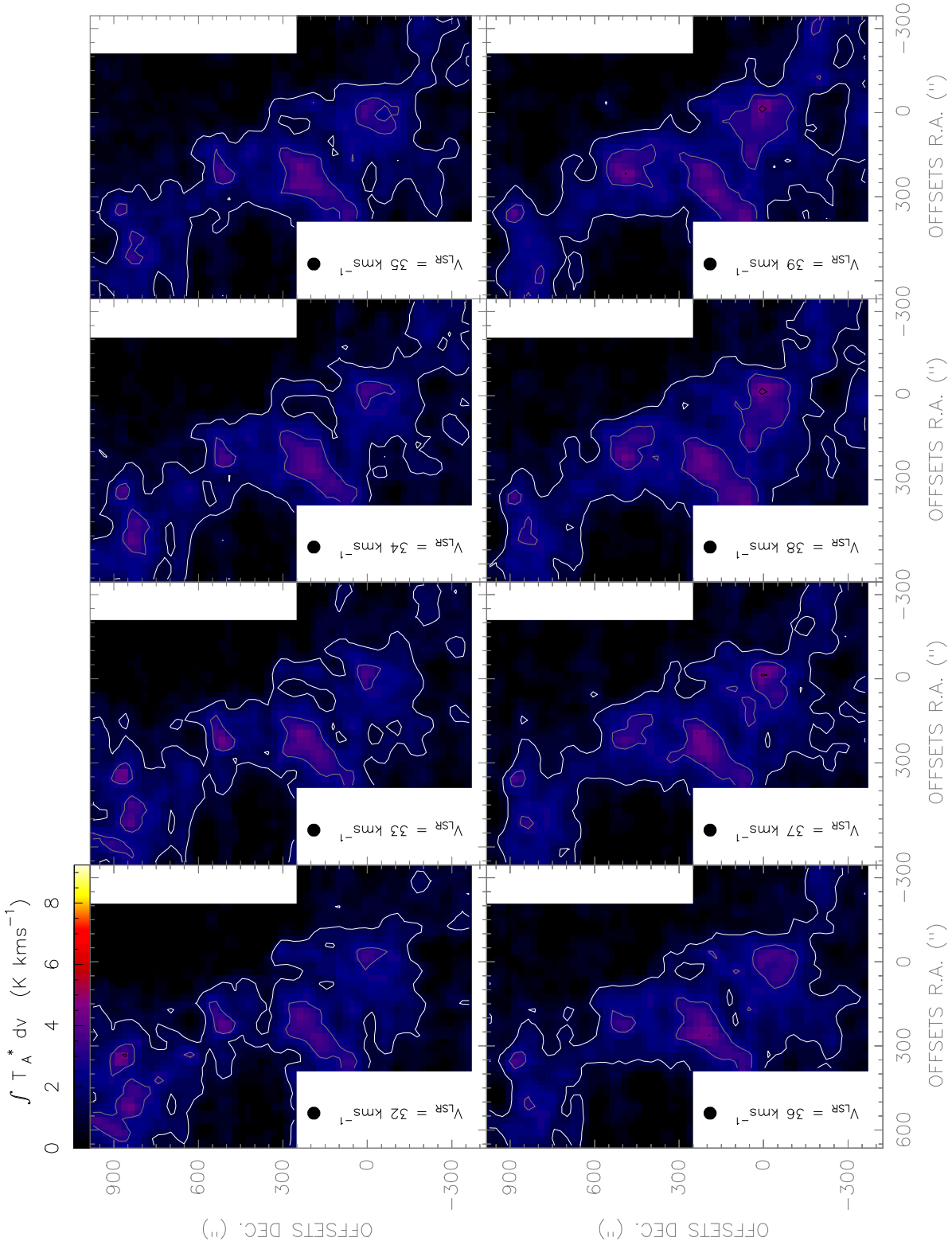

Figure. F.220: *[CII] line observed with the Herschel-HIFI satellite in Equatorial (J2000) coordinates. The spatial resolution of the maps is 46".*

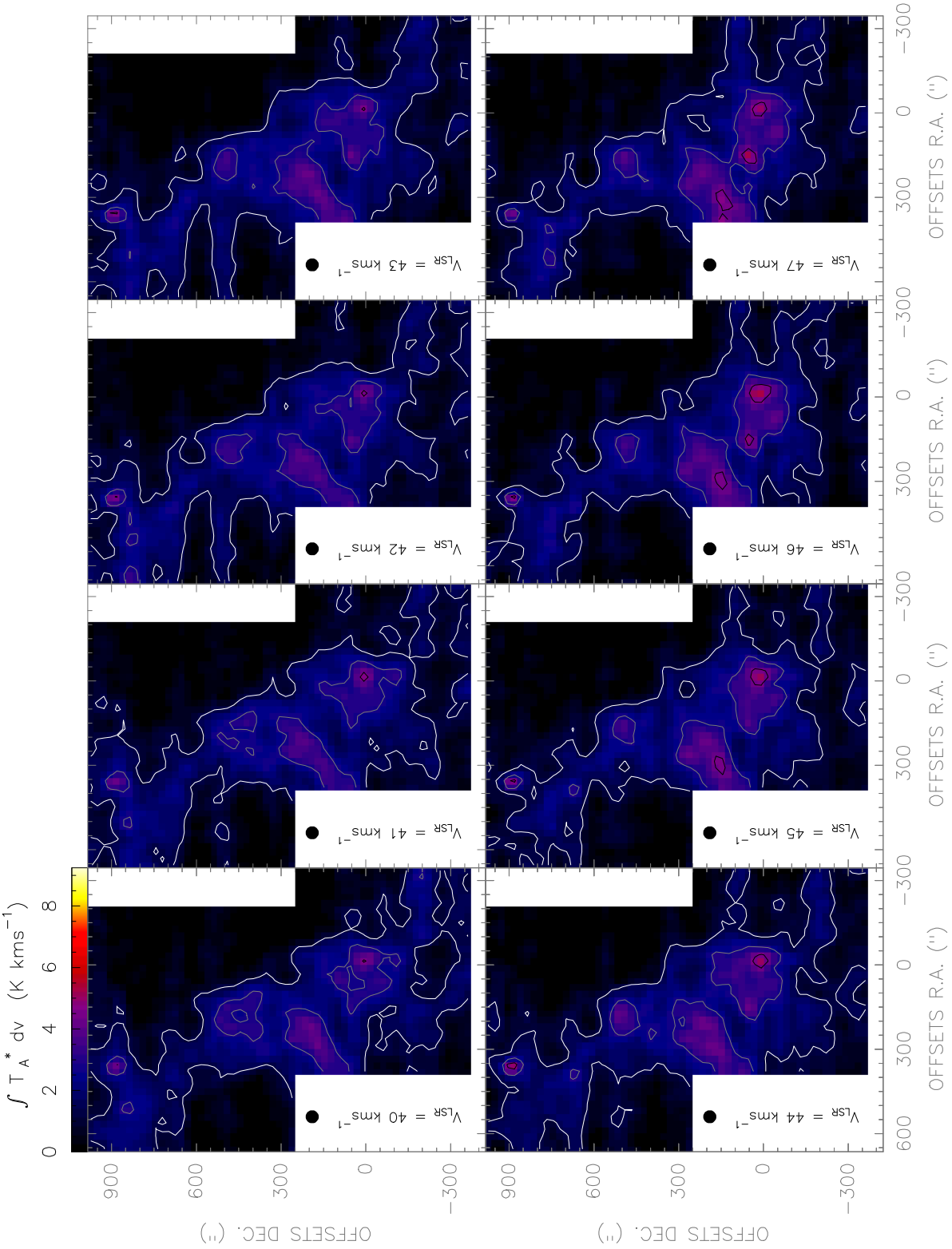

Figure. F.221: *[CII] line observed with the Herschel-HIFI satellite in Equatorial (J2000) coordinates. The spatial resolution of the maps is 46".*

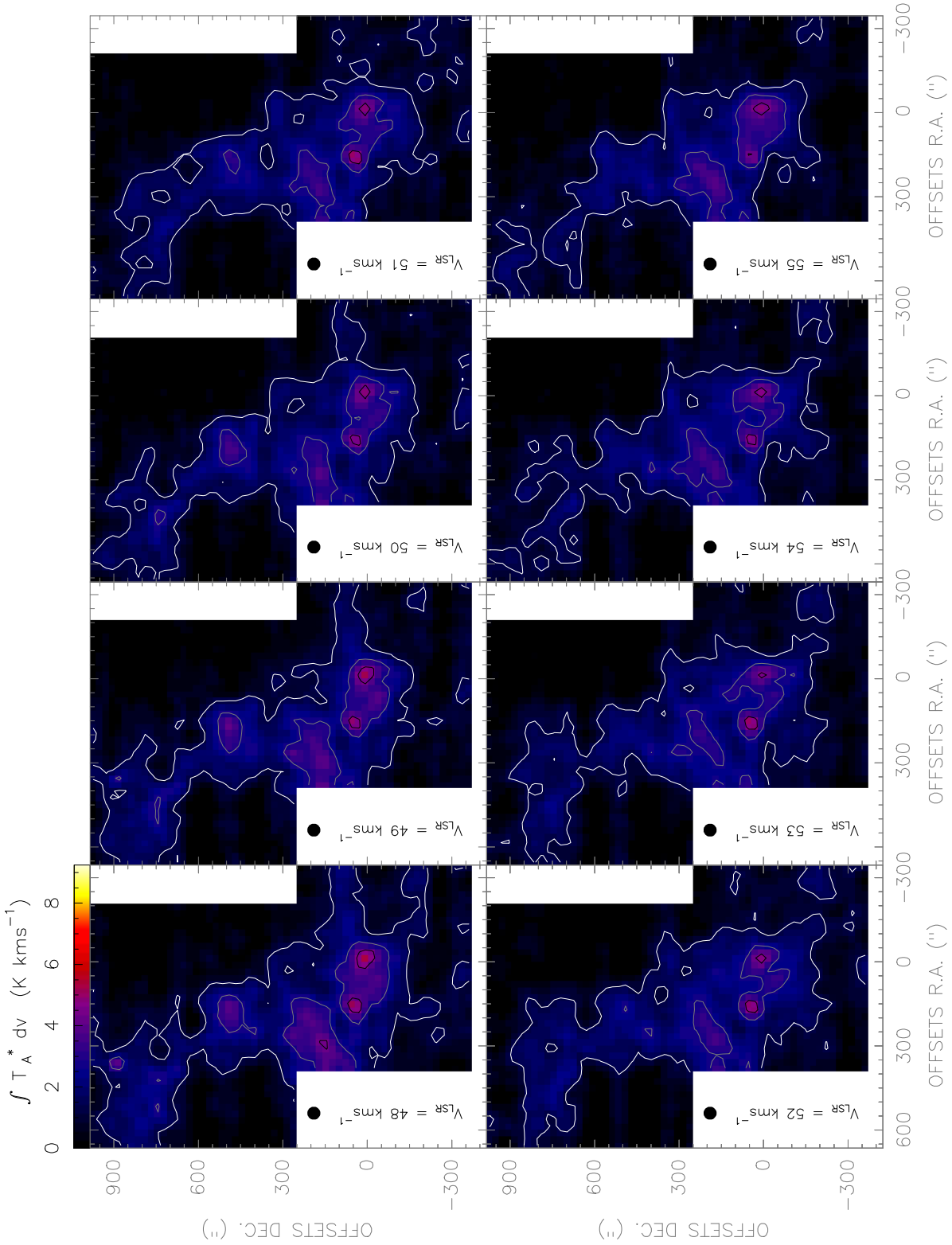

Figure. F.222: *[CII] line observed with the Herschel-HIFI satellite in Equatorial (J2000) coordinates. The spatial resolution of the maps is 46".*

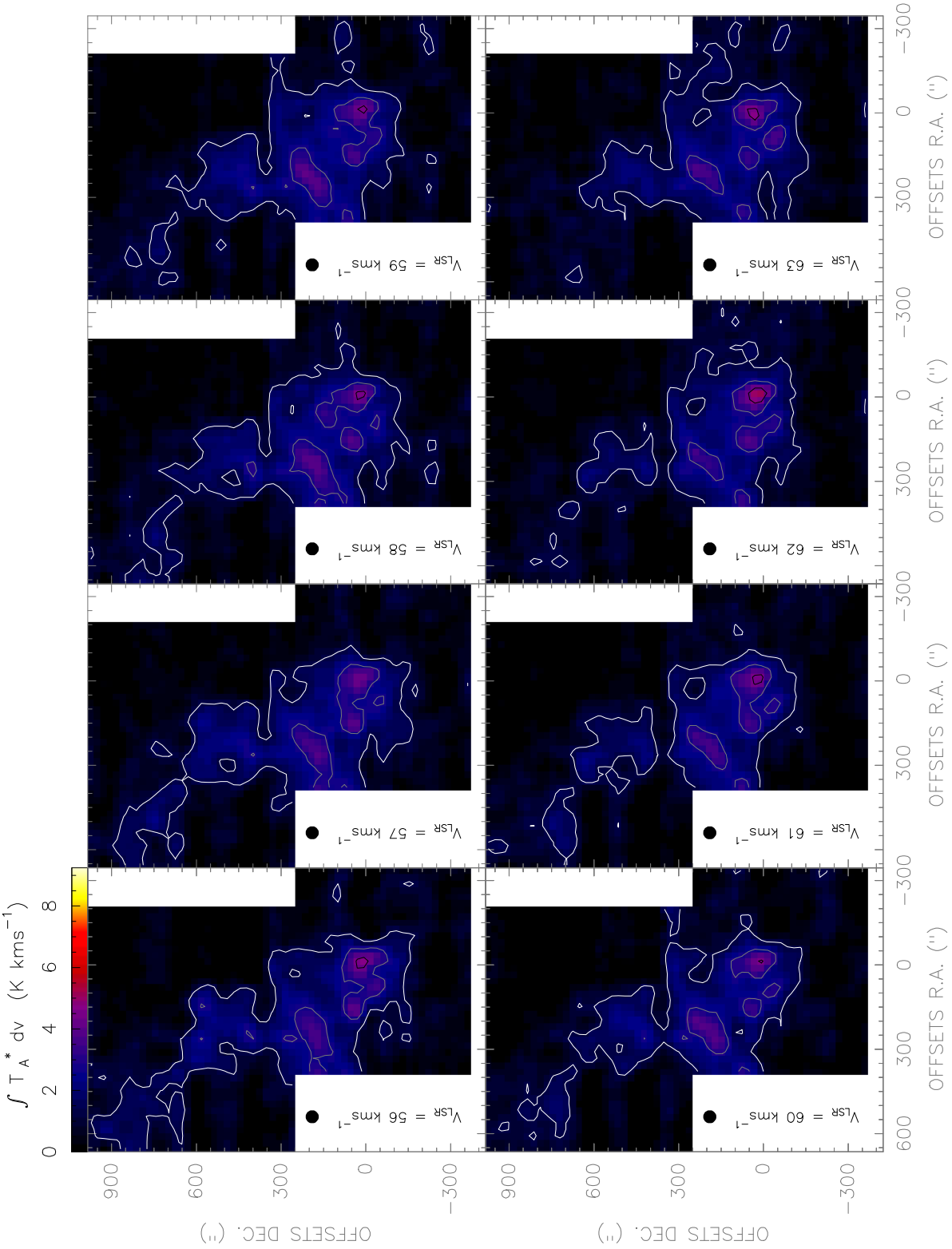

Figure. F.223: *[CII] line observed with the Herschel-HIFI satellite in Equatorial (J2000) coordinates. The spatial resolution of the maps is 46".*

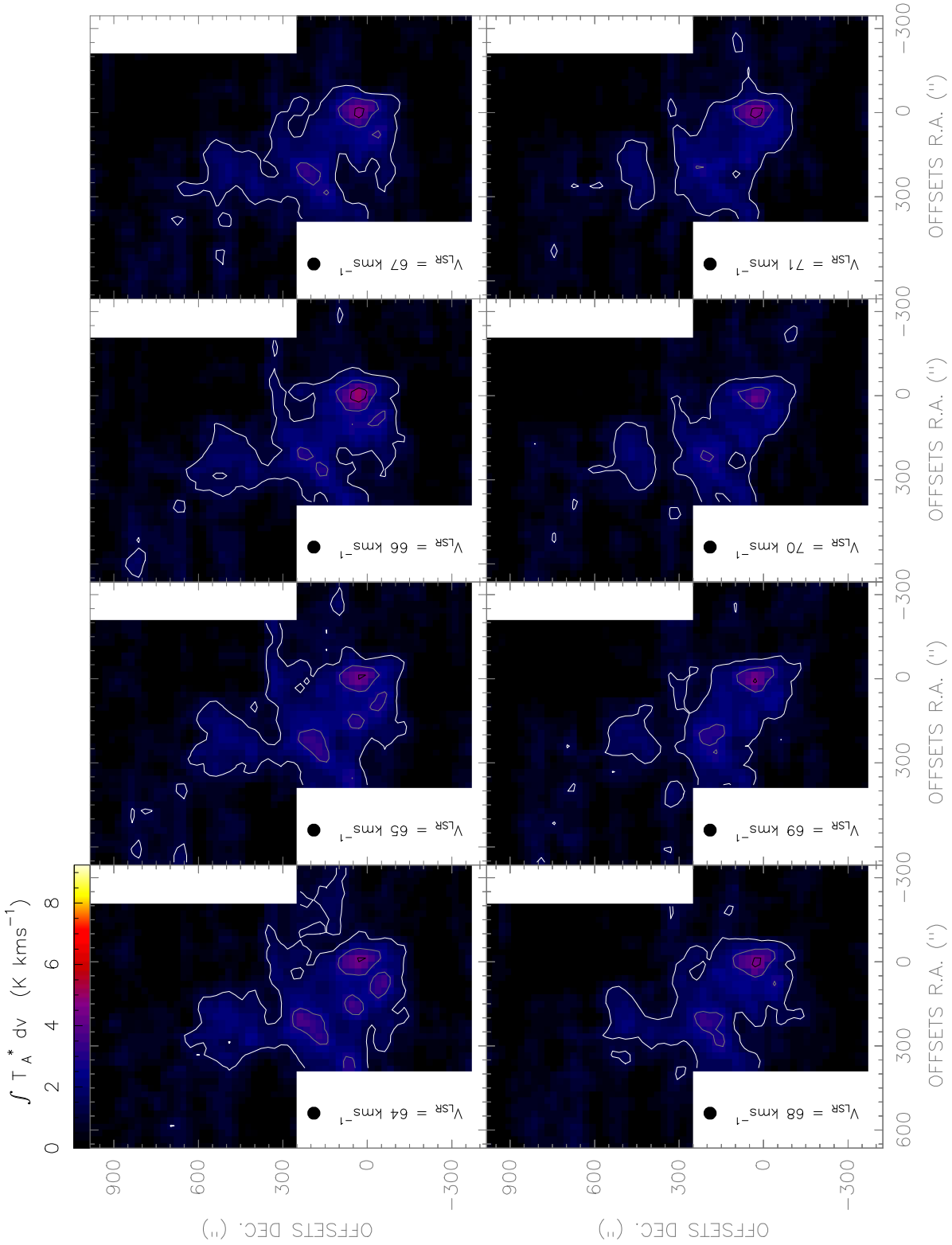

Figure. F.224: *[CII] line observed with the Herschel-HIFI satellite in Equatorial (J2000) coordinates. The spatial resolution of the maps is 46".*

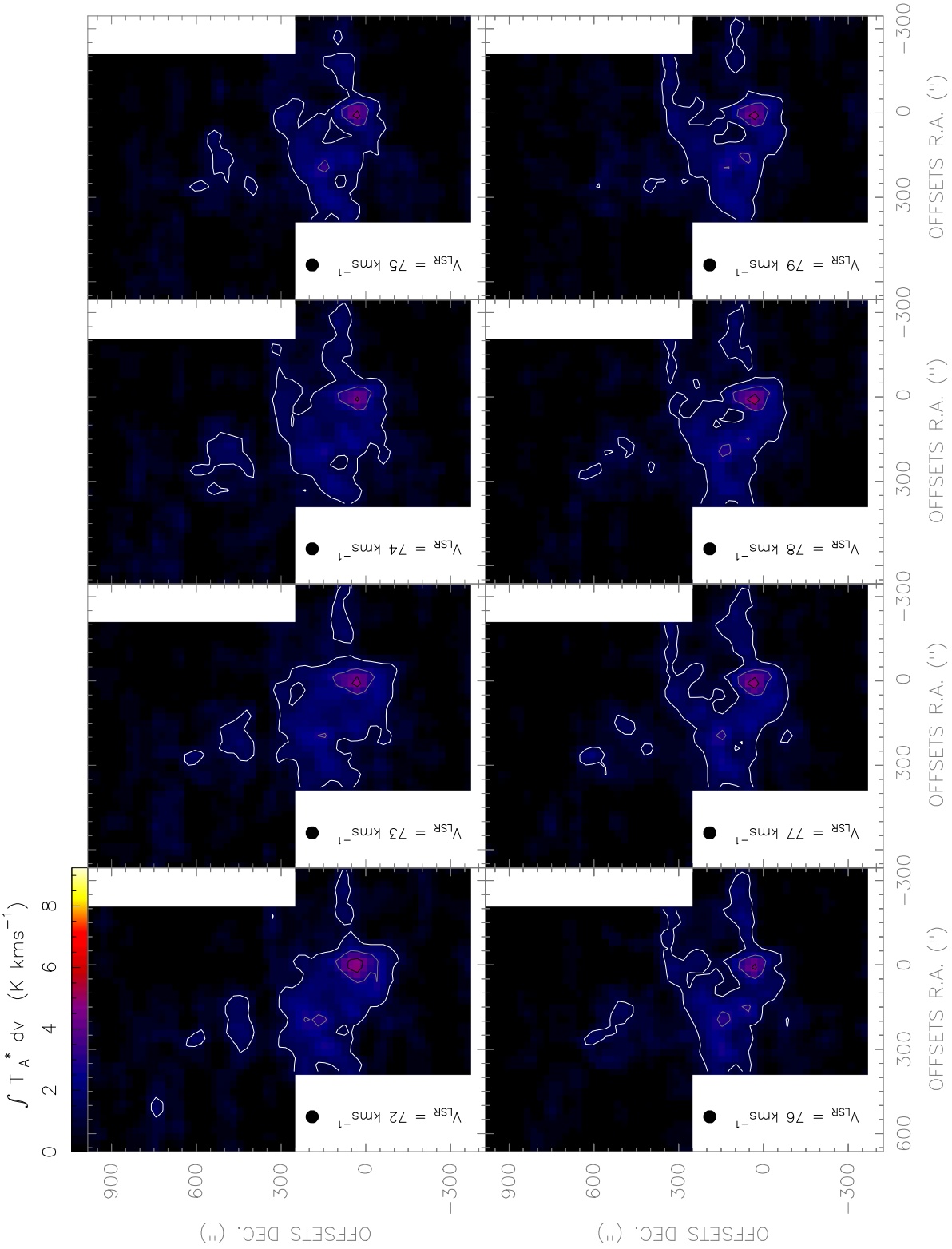

Figure. F.225: *[CII] line observed with the Herschel-HIFI satellite in Equatorial (J2000) coordinates. The spatial resolution of the maps is 46".*

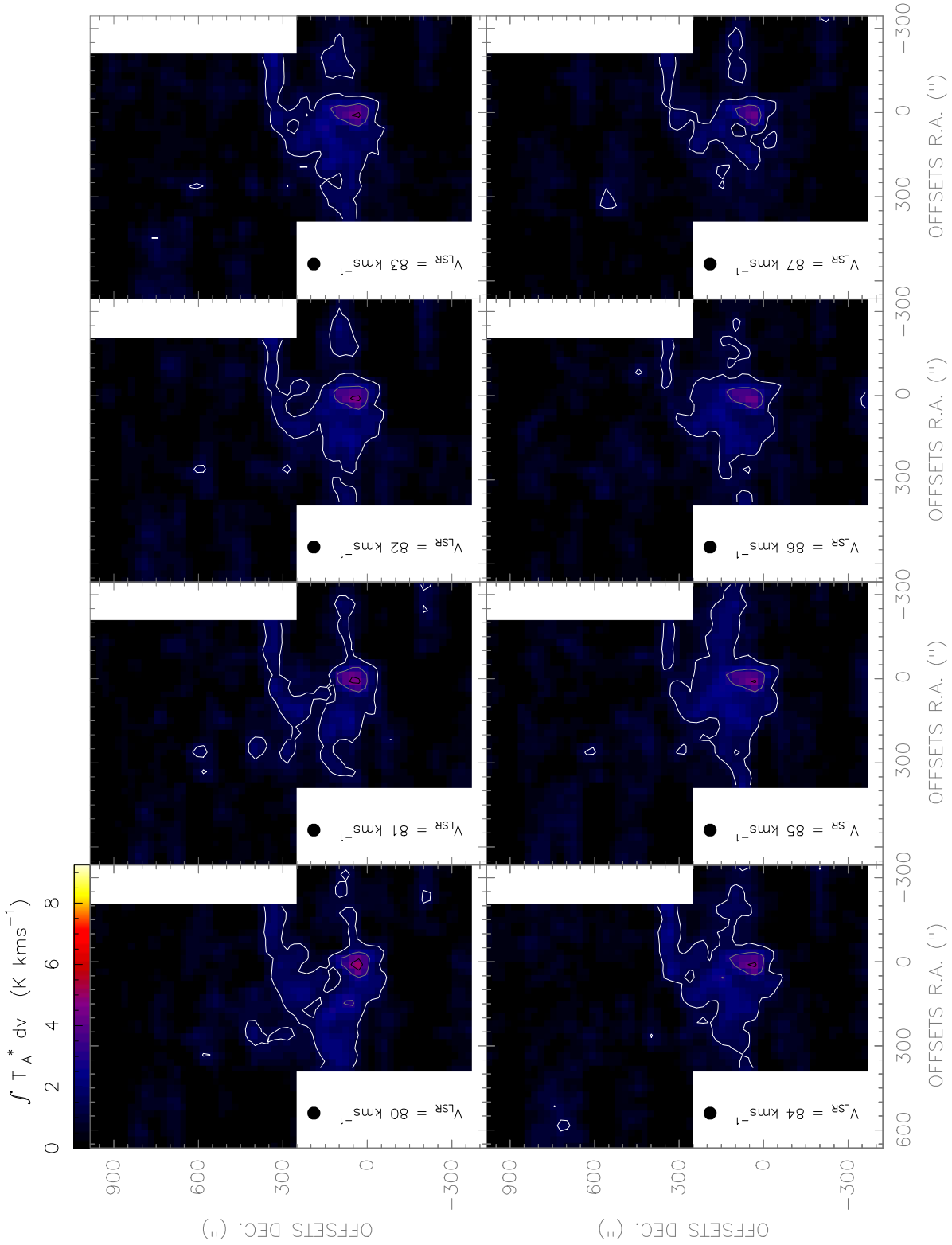

Figure. F.226: *[CII] line observed with the Herschel-HIFI satellite in Equatorial (J2000) coordinates. The spatial resolution of the maps is 46".*

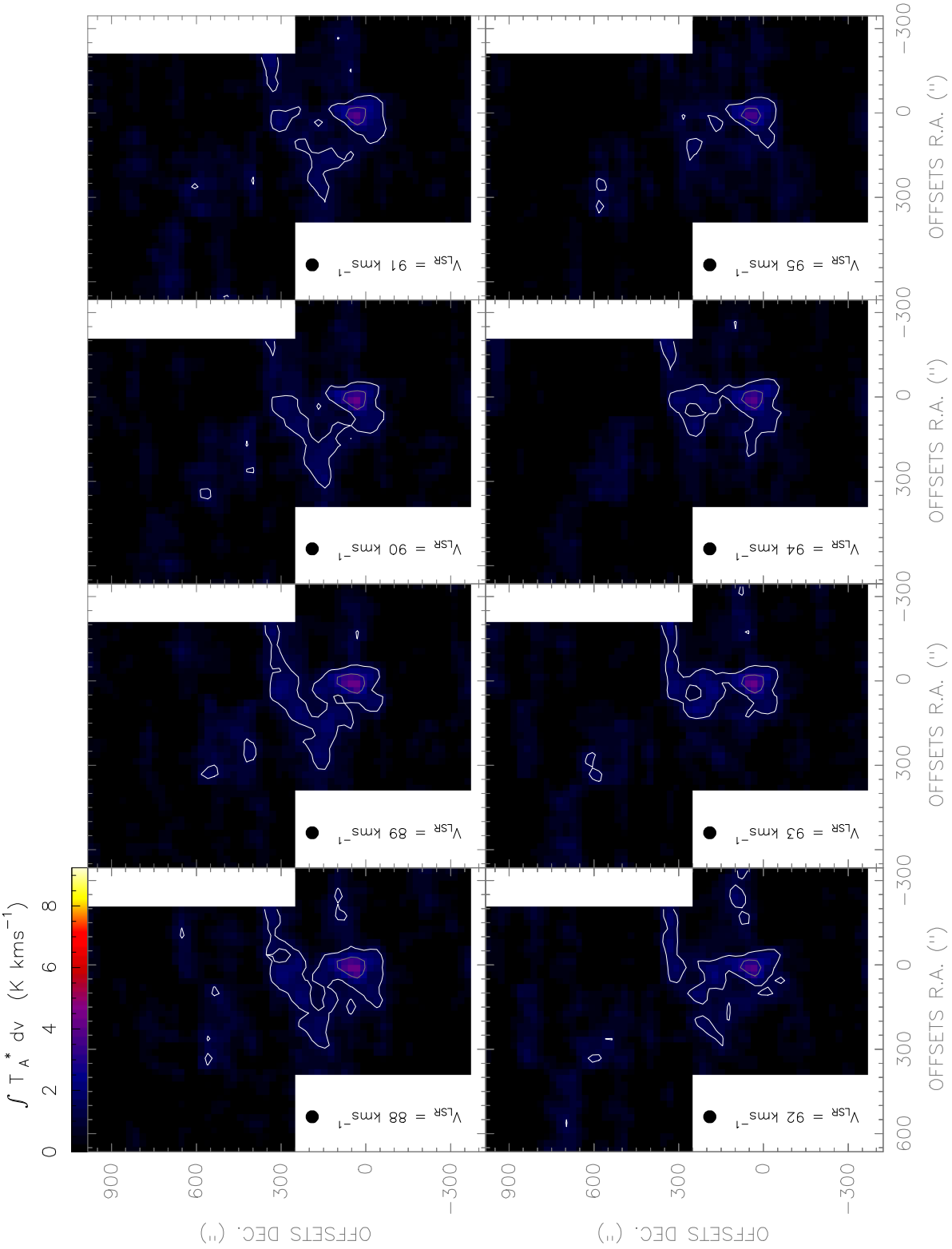

Figure. F.227: *[CII] line observed with the Herschel-HIFI satellite in Equatorial (J2000) coordinates. The spatial resolution of the maps is 46".*

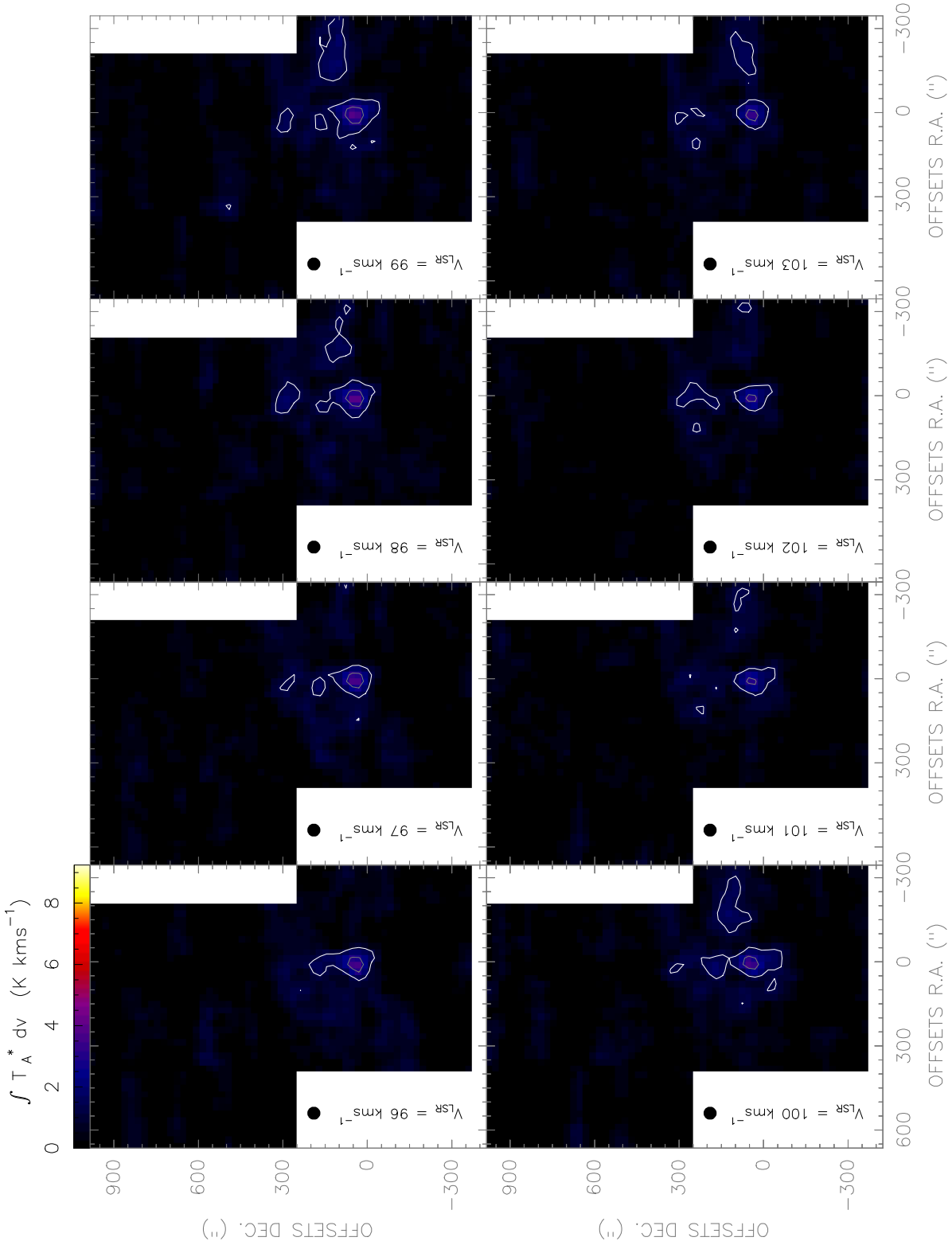

Figure. F.228: *[CII] line observed with the Herschel-HIFI satellite in Equatorial (J2000) coordinates. The spatial resolution of the maps is 46".*

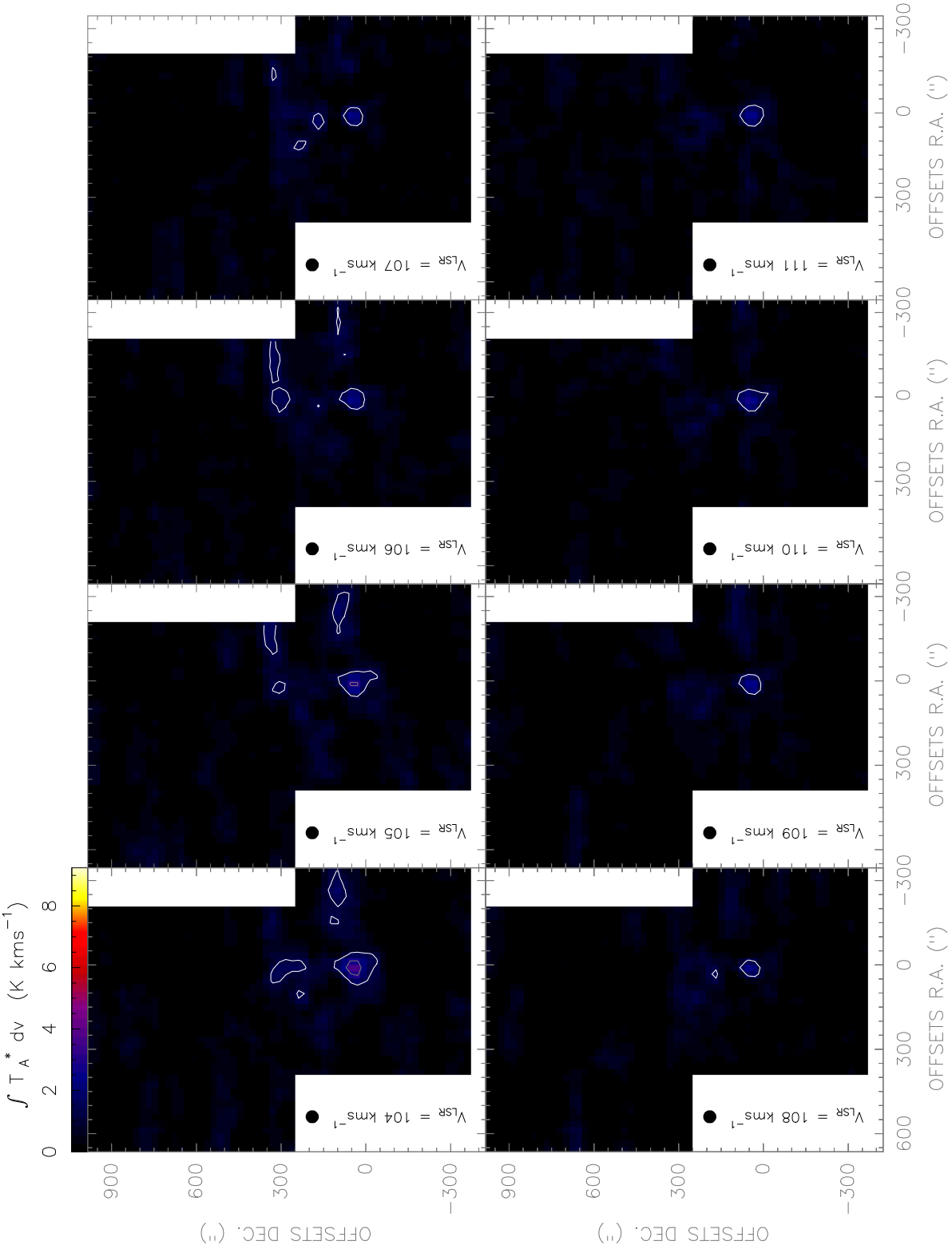

Figure. F.229: *[CII] line observed with the Herschel-HIFI satellite in Equatorial (J2000) coordinates. The spatial resolution of the maps is 46".*

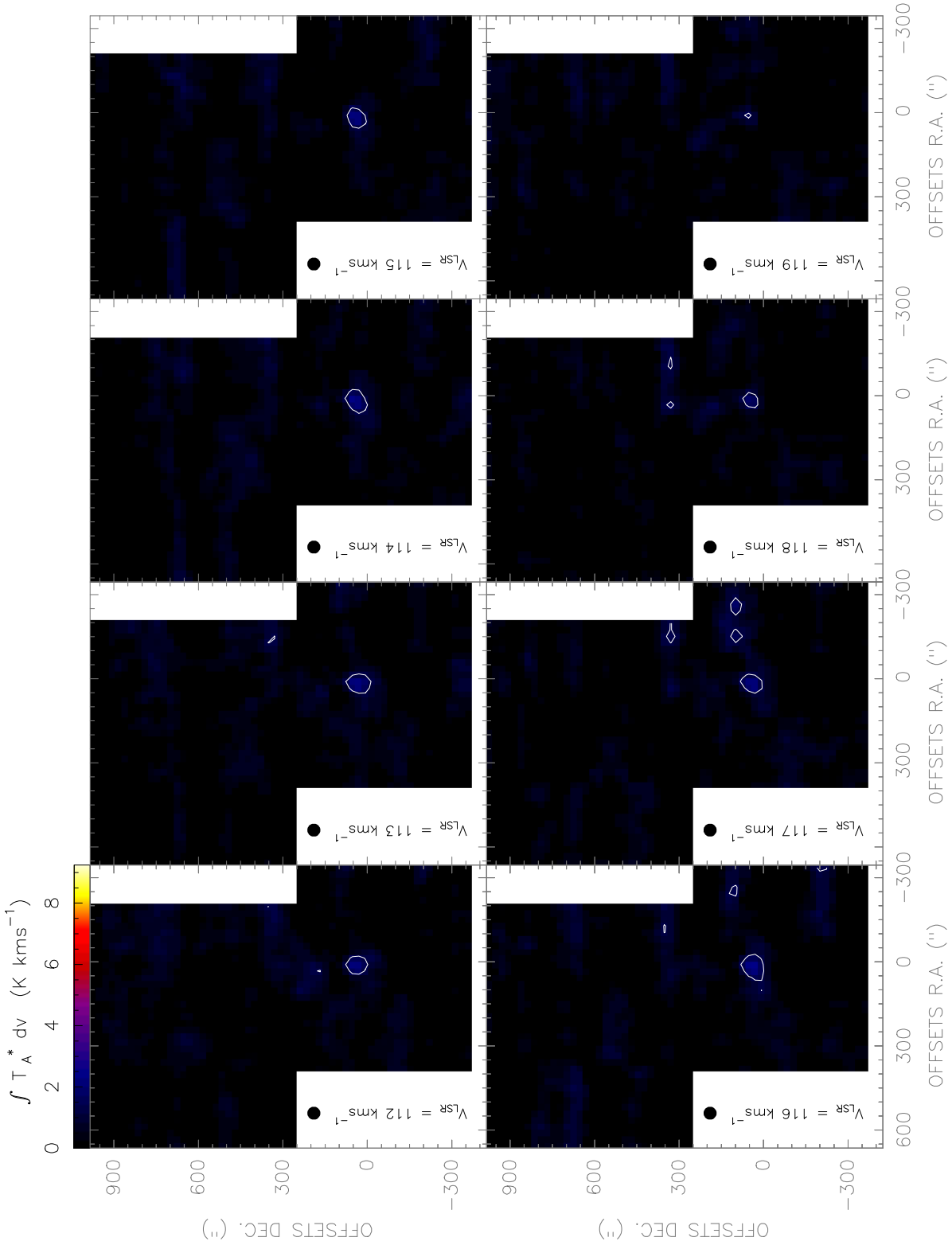

Figure. F.230: *[CII] line observed with the Herschel-HIFI satellite in Equatorial (J2000) coordinates. The spatial resolution of the maps is 46".*

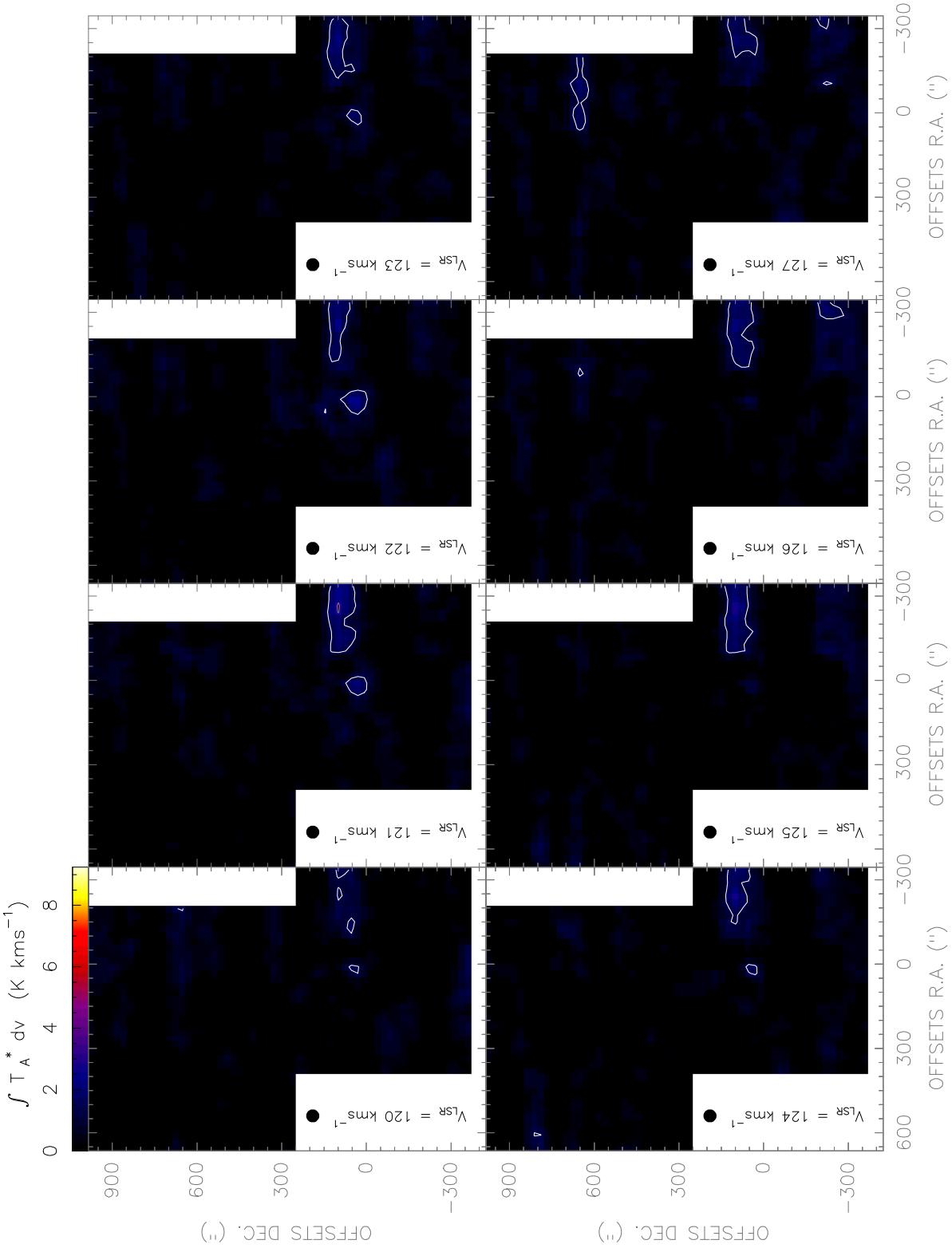

Figure. F.231: *[CII] line observed with the Herschel-HIFI satellite in Equatorial (J2000) coordinates. The spatial resolution of the maps is 46".*

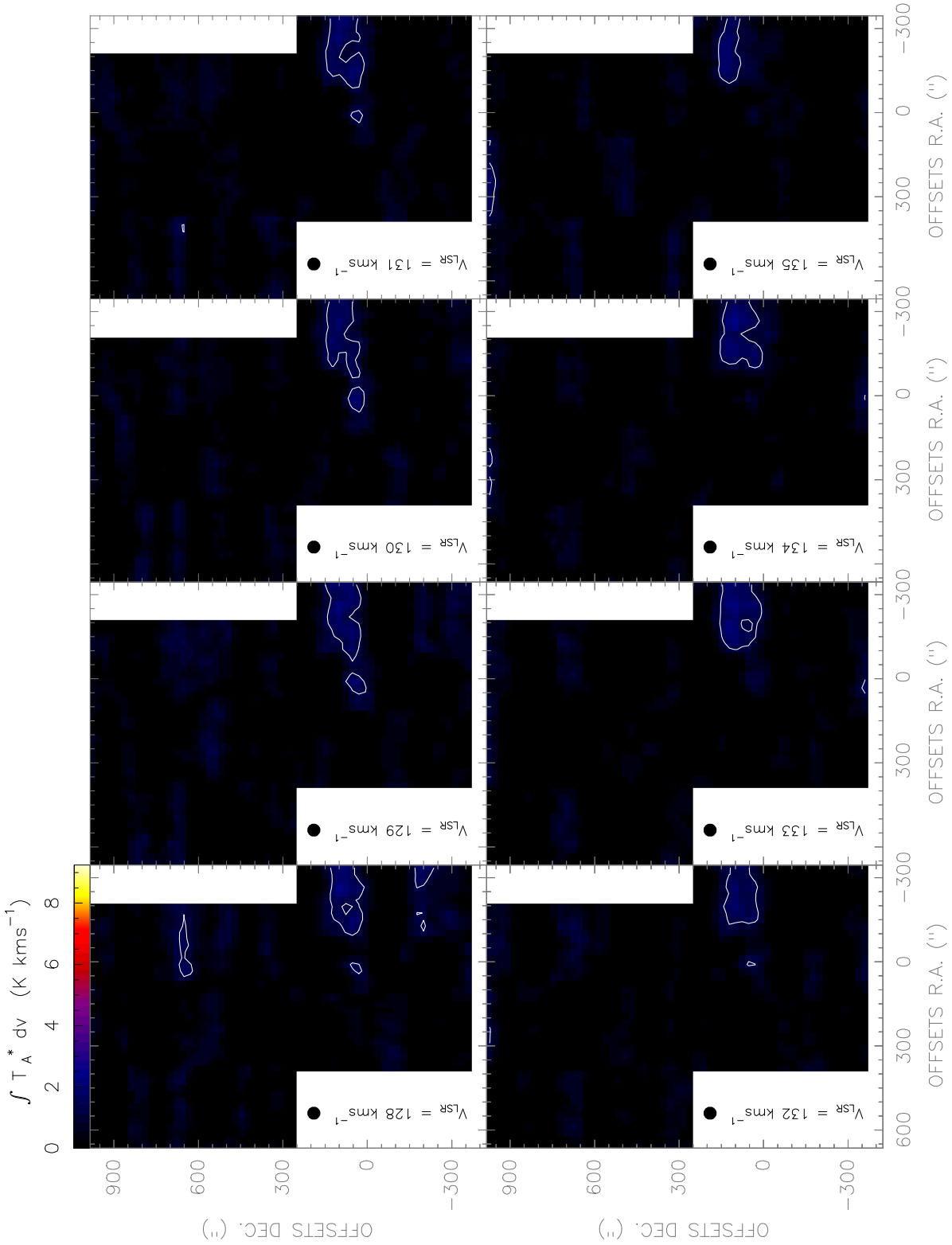

Figure. F.232: *[CII] line observed with the Herschel-HIFI satellite in Equatorial (J2000) coordinates. The spatial resolution of the maps is 46".*

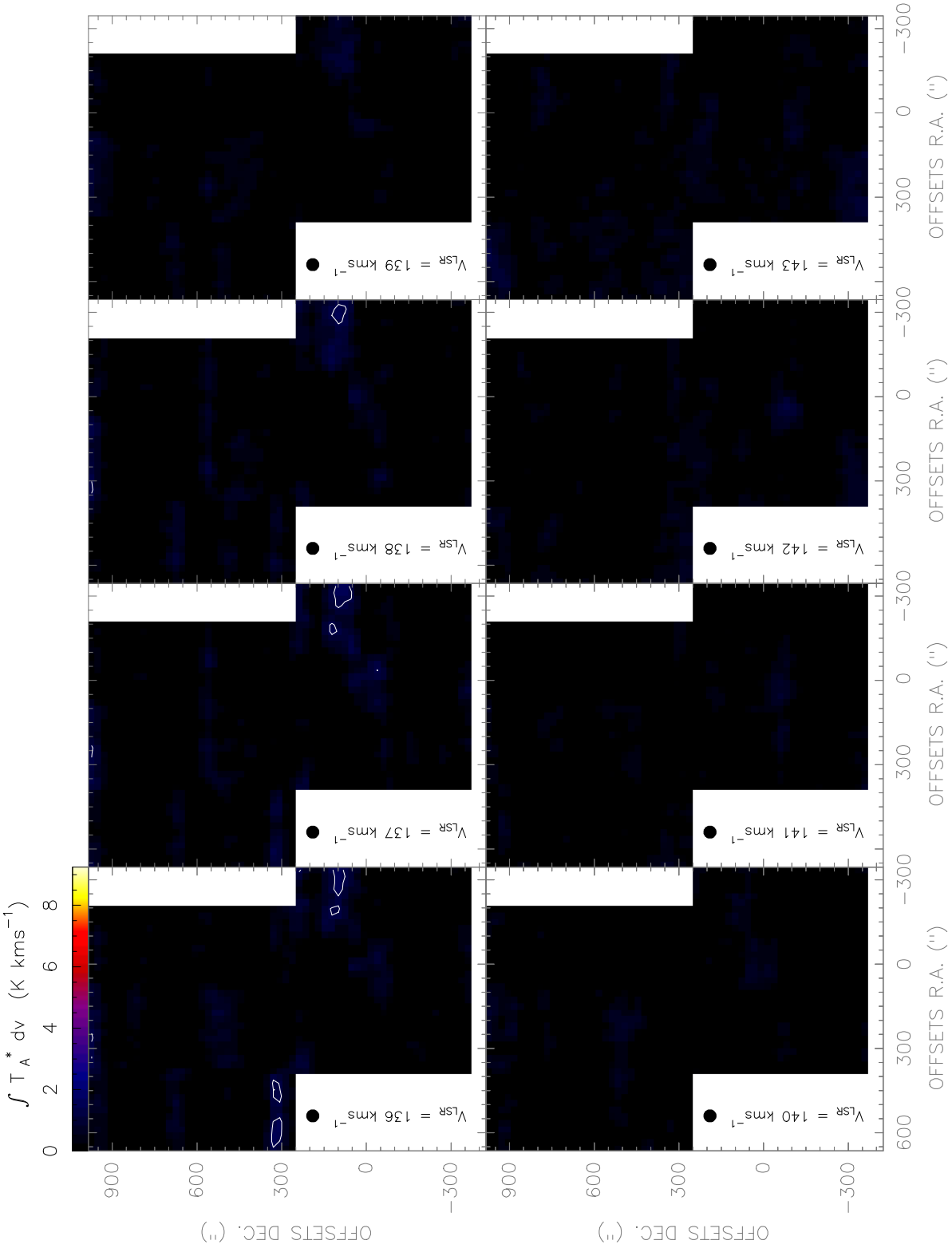

Figure. F.233: *[CII] line observed with the Herschel-HIFI satellite in Equatorial (J2000) coordinates. The spatial resolution of the maps is 46".*

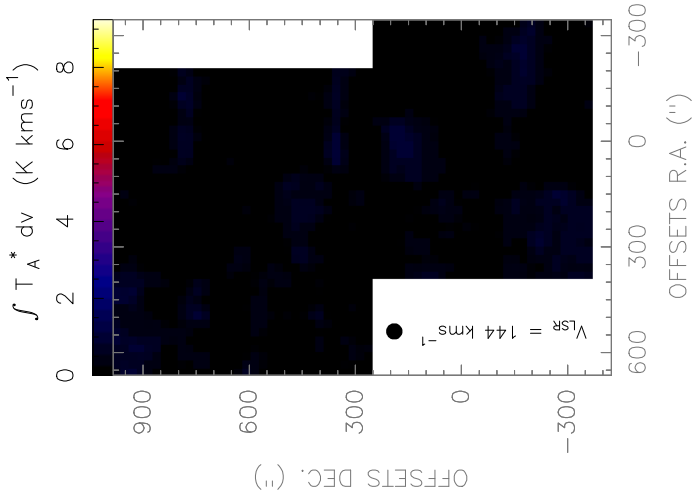

Figure. F.234: *[CII] line observed with the Herschel-HIFI satellite in Equatorial (J2000) coordinates. The spatial resolution of the maps is 46".*

List of Figures

List of Tables

Acknowledgments

Well, it's been a long time. I would say, it all started in July 1999, when I arrived in Germany for the first time as a naive exchange student (thanks YFU for the stipend), and went to live for a whole year to Leer, Ostfriesland. Without knowing any other language than a more or less decent Spanish, I had my crash course in the Teutonic language, and soon I learned that "In Aurich ist es traurig, und in Leer noch viel mehr ..." I consider that year as the beginning of a journey culminating with this PhD.

Life has strange paths that are often mistaken with fate. So, in November 2006 I took a plane to a remote location, "San Pedro de Atacama" was called. My Master Advisor, Prof. Leonardo Bronfman told me that some nice German guys were interested in having students that were willing to learn something about radio telescopes. So started my first experience with a telescope. There, there was a German guy, an astronomer, waiting for us. "I hope I do not screw it up" I was thinking when I got the welcome from Dr. Robert Simon. "I hope my German is not as horrible as I think" I was thinking. That was also my first time at such high altitude. I remember taking lots of notes of what Robert was saying and explaining. I believe, I still have them at home. It was the first time that I felt so useless in my life. Between the lack of oxygen, my very rusted German, and the tiny problem of understanding how the single pixel (what was a pixel!) test receiver worked, I was just focusing in not creating any problems (more than the ones the equipment already had, and something to remember, by then, there was a Gunn oscillator with screws and look up tables for tuning!). I remember one day Robert told me: "Why don't you go to the institute to do your PhD?". Well Robert, you gotta be careful with what you say. I hope you do not regret it. And now, here I am, writing the acknowledgments of a PhD thesis on the warm gas in the Sgr A molecular cloud at the Galactic Center..., who would have thought.

I would like to thank Prof. Jürgen Stutzki for his patience and extremely useful insight, orientation, and comments to my work. Also, I would like to thank him for what I would call "trust" in allowing me to stay at my home in Arica from time to time during the period of my thesis, so I could be with my family. Thanks also to the senior crew Robert, Markus, Urs, and Volker to whom I always came to ask (hopefully not always) silly questions, but nevertheless, had the patience and the

time to answer them.

And what would be of all of us, poor PhD students, without the knowledge and support of the PostDoc crew?. Therefore, I thank you Ronan for the fruitful discussions regarding that thing moving at 1.5 million km from Earth, you Yoko for your disposition to always give me 5 minutes to explain me several things, and to Ed, wherever you are now, for the 20 cm VLA data, that was extremely useful for my work!.

And to those who during all this years dwelt in the dark with me: to Silke for her patience to explain me her work, and to my very good friend Zoltan, the immortal, with who I shared this long, and many times, hopeless road, shared our feelings, and talked about life and that future that never comes. Also, I thank Andrea for her hospitality in Marseille, and for her patience having me there. Good days that will repeat certainly in the near future.

What would be of Germany without the Chilean crew?. It will probably fall apart. So thanks to all of you, Norma, Cristian, Denise, and Esteban, for the time together, the shared biers, conversation, and the many times we fixed the disastrous political system our beloved Chile is involved in.

I am a dwarf standing on the shoulders of giants. All this would have not been possible without the teachings of my mother, who taught me to be persevering, resilient, and to think. To my quasi mother-in-law, that helped us so much to take care of the most precious thing to me, my son. Her help can not be measured by any standards. To the mother of my son, who sacrificed so much, so I could be in Germany focusing on my PhD. To the whole Flores family, happy people even in stormy times. The world would be a better placed if we all showed that solidarity. To my younger brother, who did not teach me anything really but he is a nice guy anyway (ha ha ha!). To all my friends in Arica, people of a lot of effort, pushing their families forward with every day of work. And finally, to my son, the inspiration of my life upon which the impossible becomes possible.

Finally, I would also like to thank the Comisión Nacional de Investigación Científica y Tecnológica (CONICYT) and the Deutscher Akademischer Austauschdienst (DAAD) for their financial support during the first years of my PhD. Without them, this work would have not been possible.

The Greeks transcended through their portentous battles, poems, arts, science, philosophy, etc. I only hope to transcend through the memories of all people I have met, and through my work, sitting on the desk of a naive PhD student, scratching his head, thinking: “Oh dear, what have I put myself through...”

Acronyms

AOS	Acousto-Optical Spectrometer.
BB	Black-Body.
CDMS	The Cologne Database for Molecular Spectroscopy.
CLASS	Continuum and Line Analysis Single-dish Software.
CMB	Cosmic Microwave Background.
CMZ	Central Molecular Zone.
CND	Circum Nuclear Disk.
CNO	Carbon-Nitrogen-Oxygen.
DBS	Double SideBand.
FIR	Far Infrared.
FITS	Flexible Image Transport System.
FUV	Far Ultraviolet.
GC	Galactic Center.
GILDAS	Grenoble Image and Line Data Analysis Software.
GMC	Giant Molecular Cloud.
GREAT	German Receiver for Astronomy.
GREG	Grenoble Graphic.
HEB	Hot Electron Bolometer.
HEXGAL	Herschel EXtraGALactic.
HIFI	Heterodyne Instrument for the Far-Infrared.
HIPE	Herschel Interactive Processing Environment.
HVCC	High Velocity Compact Clump.
HVG	High Velocity Gas.
IF	Intermediate Frequency.
IRAM	Institut de Radioastronomie Millimétrique.
ISM	Inter Stellar Medium.

ISO	Infrared Space Observatory.
ISRF	Inter Stellar Radiation Field.
KOSMA	Koelner Observatorium fuer Sub-Millimeter Astronomie.
l.o.s.	line-of-sight.
LAMBDA	Leiden Atomic and Molecular Database.
LNA	Low Noise Amplifier.
LO	Local Oscillator.
LSB	Lower SideBand.
LSR	Local Standard of Rest.
LTE	Local Thermodynamic Equilibrium.
LVG	Large Velocity Gradient.
MC	Molecular Clouds.
NTF	Non Thermal Filament.
OTF	On The Flight.
PACS	Photodetector Array Camera & Spectrometer for Herschel.
PAH	Polycyclic Aromatic Hydrocarbon.
PDR	Photon-Dominated Region.
rms	root-mean-square.
SED	Spectral Energy Distribution Cosmic.
Sgr	Sagittarius.
SIS	Superconductor Insulator Superconductor.
SMART	Sub-Mm Array Receiver for Two frequencies.
SNR	Supernova Remnant.
SOFIA	Stratospheric Observatory for Infrared Astronomy.
SPIRE	Spectral and Photometric Imaging Receiver.
sub-mm	Sub-Millimeter.
UMIST	http://udfa.ajmarkwick.net/.
USB	Upper SideBand.
VLA	Very Large Array.
WBS	Wide-Band Acousto-Optical Spectrometer.
XDR	X-ray Dissociation Region.

XFFTS eXtended bandwidth Fast Fourier Transform Spectrometer.

Erklärung

Ehrenwörtliche Erklärung zu meiner Dissertation mit dem Titel: “The Warm ISM in the Sgr A Complex: Mid-J CO, Atomic Carbon, Ionized Atomic Carbon, and Ionized Nitrogen Line Observations with the Herschel-HIFI and the NANTEN2/SMART Telescopes”

Sehr geehrte Damen und Herren,

Ich versichere, dass ich die von mir vorgelegte Dissertation selbstständig angefertigt, die benutzten Quellen und Hilfsmittel vollständig angegeben und die Stellen der Arbeit - einschließlich Tabellen, Karten und Abbildungen -, die anderen Werken im Wortlaut oder dem Sinn nach entnommen sind, in jedem Einzelfall als Entlehnung kenntlich gemacht habe; dass diese Dissertation noch keiner anderen Fakultät oder Universität zu Prüfung vorgelegen hat; dass sie noch nicht veröffentlicht worden ist sowie, dass ich eine solche Veröffentlichnung vor Abschluss des Promotionsverfahrens nicht vornehmen werde.

Die Bestimmungen dieser Promotionsordnung sind mir bekannt. Die von mir vorgelegte Dissertation ist von Prof. Dr. Jürgen Stutzki betreut worden.

Ich versichere, dass ich alle Angaben wahrheitsgemäß nach bestem Wissen und Gewissen gemacht habe und verpflichte mich, jedmögliche, die obigen Angaben betreffenden Veränderungen, dem Dekanat unverzüglich mitzuteilen.

Pablo García, 

Köln, den 26ten Juni, 2015 Name, Unterschrift